2012

Mass Transport and Chalcogen-Silver Interactions on Silver Surfaces

Selena M. Russell
Iowa State University

Mass transport and chalcogen-silver interactions on silver surfaces

by

Selena M. Russell

A dissertation submitted to the graduate faculty
in partial fulfillment of the requirements for the degree of
DOCTOR OF PHILOSOPHY

Major: Physical Chemistry

Program of Study Committee:
Patricia A. Thiel, Major Professor
James W. Evans
Gordon Miller
Theresa Windus
Sriram Sundararajan

Iowa State University
Ames, Iowa
2012

Dedicated to my Mother.

TABLE OF CONTENTS

ABSTRACT

Electronegative adsorbates such as sulfur, oxygen, and chlorine can strongly affect metal transport on surfaces of coinage metals. Hence, they can affect processes of self-assembly (including nucleation and growth) and coarsening of metal nanostructures. These processes are important to many applications that exploit nanoscale particles of these metals, such as surface enhanced Raman scattering and catalysis. To understand how and why the adsorbate affects metal transport, it is necessary to first understand the basic interaction of the adsorbate with the metal surface.

Both adsorbed oxygen and sulfur reconstruct coinage metal surfaces and enhance metal island coarsening, under certain conditions. We have found that atomic S interacts strongly with Ag, inducing surface reconstruction and accelerating Ag island coarsening or sintering. In other words, S destabilizes the Ag surface and nanostructures. On the other hand, molecular H_2S interacts weakly with the Ag surface at low temperature, forming only adsorbate structures. The relative effect of O or S depends on the geometry of the substrate, in terms of the structures that appear and the rate of metal island coarsening. Sulfur reconstructs both the Ag(111) and Ag(100) surfaces resulting in long-range ordered phases composed of both S and Ag. Sulfur accelerates Ag island coarsening by 1 order of magnitude on Ag(100) and by 3 or more orders of magnitude on Ag(111). Low coverages of oxygen enhance Ag island coarsening on Ag(100), but has no effect on Ag islands on Ag(110). In addition, the nature of the chalcogen (O vs S) seems to have a larger influence on surface structures than does the nature of the metal (Cu vs Ag).

In this thesis, we describe work in which we have expanded the understanding of fundamental processes that govern nanostructure formation and dynamics by employing single crystals in ultra-high vacuum (UHV) and surface analytical techniques, including variable and low temperature scanning tunneling microscopy (STM), Auger electron spectroscopy (AES), and low-energy electron diffraction (LEED), in addition to density functional theory (DFT) calculations. This research may identify a commonality in chalcogen induced mass transport on the coinage metal surfaces and ultimately lead to controlled production of nanoclusters.

CHAPTER I

General Introduction

Systems with high surface area, such as small islands on a surface, tend to reduce that area and thus the free surface energy through morphological changes. Heterogeneous species interacting with a surface alter its surface free energy, which can lead to new surface structures. Both oxygen and sulfur adsorption enhance metal island coarsening and induce reconstructions on coinage metals.[1,2] We focus on the stability of nanoclusters and diffusion on coinage metal surfaces with chalcogens by studying elementary atomic processes on metal surfaces, in an effort to illuminate general trends between these groups.

1. Motivation

As a material shrinks to the nanoscale, surface effects become very important and can alter optical, electronic, magnetic, mechanical, and catalytic properties relative to the bulk material. The innate properties of silver and its surfaces lend it to a variety of applications, such as self-assembled monolayers,[3] analytical instruments,[4,5] heterogeneous catalysis,[6-8] and medicine. Colloidal dispersions of Ag nanoparticles find uses as bactericidal agents,[9] wound dressing anitseptics,[10] in targeted drug delivery,[11] and DNA biosensors.[12] Surface enhanced Raman scattering exploits silver's optical properties.[4,5] The catalytic properties of silver make it vitally important in industrial oxidation reactions, such as the partial oxidation methanol to formaldehyde and selective oxidation of ethylene to epoxide.[6,13-18]

As cluster size decreases, the spatial length scale of electron motion decreases,[19,20] and local surface plasmon resonance increases, which is collective conduction band electron waves/oscillations. This enhances optical absorption and scattering of the surfaces and nearby species. The optical and surface plasmon resonance of silver lends itself to nanophotonics, biology, sensing, spectroscopy, and solar energy harvesting.[20] Surface-enhanced Raman scattering (SERS) benefits from several orders of magnitude of enhancement in the scattering intensity of a molecule close to roughened coinage metal surfaces.[4,5] SERS often employs coinage metal nanoparticles, with silver most strongly enhancing the Raman scattering signal. The incident and scattered light is influenced by an

enhanced electric field resulting from excitation of surface plasmons, which depend on the metal cluster size.[5] The nanoparticles may coarsen over time which influences SERS.[21,22]

Clusters tend to coarsen (or sinter or ripen) over time, favoring fewer, larger particles instead of many, smaller particles. Coarsening is a pervasive phenomenon in ensembles of small clusters, because it serves to reduce total interfacial area or length, and thus the energy cost associated with these interfaces. The average cluster size increases while the number of clusters decreases, reducing the surface area of the clusters, and is usually irreversible. Coarsening occurs through two mechanisms: Ostwald ripening (OR) and Smoluchowski ripening (SR). OR results from mass transport *between* clusters by carriers, whose nature is generally unknown. The chemical potential difference around clusters of different sizes leads to a concentration gradient between clusters, resulting in net mass transport to regions of lower concentration, around larger clusters, maintaining local equilibrium. In other words, small clusters shrink and disappear while large clusters grow. Alternatively, SR results from cluster diffusion, coalescence, and shape relaxation. Small clusters tend to evaporate and/or diffuse faster than large clusters (relative to the average size). The best way to differentiate between OR and SR is by direct observation of cluster evolution. For example, Simonsen *et al.* monitored Pt/silica catalyst in synthetic air sintering at 923 K with *in situ* TEM.[23] The continuous observation showed small clusters shrinking and large clusters growing, a clear indicator of OR. In addition, both mechanisms may occur simultaneously. For example, Au-Cu nanoparticles migrate and coalesce on an amorphous carbon substrate at 573 K via SR, but in at least one case, the size of a small particle decreased as it approached a large particle, indicating OR also occurs in this system.[24]

In heterogeneous catalysis, the catalytic action occurs at the interface between two phases: liquid-solid or gas-solid. The details of this interaction, in particular chemical composition and geometry, dictate the kinetics and mechanism of catalytic reaction. Industrial and automotive catalysts often consist of metal clusters dispersed on high surface area substrates,[25] and must exhibit high performance regarding activity, selectivity, activation energy, and stability.[26] Catalyst activity is proportional to the number of active sites. Catalysts are often expensive, such as Pt, Pd, and Rh in the catalytic converter, so

minimizing the clusters to the most efficient size reduces material costs in addition to providing a large surface area for reaction.

Silver is an efficient and selective catalyst for the partial oxidation of ethylene to ethylene oxide.[6,13,15,27] With oxygen, ethylene may selectively oxidize to ethylene oxide ($C_2H_{4(g)} + ½O_{2(g)} \rightarrow C_2H_4O_{(g)}$), or non-selectively to acetaldeyde, which reacts further to form carbon dioxide and water ($C_2H_{4(g)} + ½O_{2(g)} \rightarrow CH_3CHO_{(g)} \rightarrow 2CO_{2(g)} + 2H_2O_{(g)}$). Epoxidation occurs with 50% selectivity without promoters. Other transition metal surfaces, activate the C-H bond, facilitating non-selective combustion.[6,28] On silver, one proposed mechanism involves a surface oxametallacycle intermediate, in which ethylene's double bond opens, bonding one carbon to the silver surface and the other to an oxygen atom on the surface.[29] From this configuration, ethylene oxide or acetaldehyde may form. Alternatively, ethylne oxide may form directly by symmetric attack of adsorbed oxygen to the double bond.[6] Atomic oxygen on silver forms a thin, oxidelike surface structure that is directly involved in epoxidation.[6,7] The catalytic activity depends on the number and effectiveness of active sites (oxygen atoms in appropriate sites) and the rate of reaction per active site. Any change to the number or quality of the active site will affect the catalytic reaction.

Poisoning, fouling, mechanical deactivation, corrosion/leaching, and thermal degradation may contribute to catalyst destabilization and deactivation.[26,30] Process conditions often require elevated temperatures leading to thermal degradation, including sintering or coarsening. Commercial epoxidation catalysts lose activity over 2 to 3 years, which requires an increase in reaction temperature. Eventually, selectivity is lost and the catalyst must be replaced. Macleod, Keel, and Lambert studied the Ag-Cs/α-Al_2O_3 catalyst and found that very significant sintering of the active Ag phase under industrial epoxidation conditions.[8] Ag clusters initially 97 nm in diameter grew slightly during the initial conditioning process (100 hr) to 117 nm. After 14 months of use, the average Ag cluster diameter was 341 nm. Fig. 1 by Macleod *et al.* shows the dramatic results of sintering.[8] The initial conditioning involves promoter redistribution (Cs) and uptake (Cl), and removal of carbonaceous material (e.g. CO_2) leftover from preparation. In this case, the promoters were not found to strongly influence coarsening.[8,31]

Additives may enhance or diminish sintering, in addition to poisoning or promoting reactions.[32,33] On Pt/alumina or Pt/silica catalysts, air exposure dramatically shifts the particle size distribution toward larger particles (7.3 to 15.6 nm r_{avg}).[23,34] Based on direct observation of cluster decay and size distributions, and energetic arguments, oxygen exposure activates OR mediated by volatile PtO_2 (as opposed to Pt atoms).[23,34,35] From other studies, oxygen is known to enhance coarsening of Pt/alumina or Pt/silica catalysts.[35-37] In contrast, additives may inhibit sintering. For example, doping α-Al_2O_3 with 1 to 2% P, considerably reduces sintering and surface area loss.[38]

Sulfur and chlorine reduce the catalytic activity of the Cu/zinc oxide–alumina catalyst used in methanol synthesis ($CO_{(g)} + 3H_{2(g)} \rightarrow CH_{4(g)} + H_2O_{(g)}$) and water gas shift ($CO_{(g)} + H_2O_{(v)} \rightarrow CO_{2(g)} + H_{2(g)}$) reactions.[39] Sulfur acts as a poison, presumably by blocking active sites.[39] If ~0.1 wt.% S adsorbed only to Cu, the catalytic activity would be severely depressed. However, adsorption of 0.4 wt.% S only reduces shift activity by 30%.[40] The poisoning effect is mitigated by S reaction with the support forming ZnS.[39,40] Chlorine, on the other hand, accelerates sintering. Under normal operation, below 563 K copper sintering does not occur due to careful support selection and catalyst preparation. Bridger, Spencer, and Twigg suggest that Cu transport occurs through the formation of mobile copper chloride compounds.[39-41]

Understanding atomic-scale chemistry, growth, and diffusion processes under controlled conditions informs our understanding of these processes in more complicated systems, such as SERS and heterogeneous catalysis.[13,42] For example, the extensive work on Ag catalysts for epoxidation has provided valuable insight into the roles of various chemical species and mechanistic, in relation to the silver surface.[13]Adsorbates influence the morphology and properties of metal surfaces, often by affecting mass transport, e.g. coarsening.[32,43] Mass transport may manifest itself through other processes such as faceting,[44] step bunching,[45] pitting,[46] smoothening during growth,[47] and reconstruction.[1,2,48,49] Reconstruction goes beyond a simple surface relaxation, e.g. atomic layer spacing deviating from the bulk spacing. The atoms of a reconstructed surface move to different positions, either preserving the number of surface atoms or not, relative to the bulk plane. The Au(111) surface is well known to reconstruct; hexagonally close-packed atoms compress laterally into

a herringbone structure. Adsorption of thiols on that surface, can lift the herringbone reconstruction, changing the clean surface structure (arrangement of Au surface atoms).[48] Our goal is to expand the understanding of fundamental processes that govern nanostructure formation and dynamics by employing single crystals in ultra-high vacuum (UHV) and surface analytical techniques, in addition to density functional theory (DFT) calculations.

2. Materials and methods

2.1. Low index silver surfaces

Due to the array of applications and interesting properties, we choose to study silver surfaces. Experimentally, silver is a convenient coinage metal to study because its surfaces do not reconstruct, it is fairly unreactive so it remains contaminant free during experiments, and dynamics on its surfaces occur on temperature and time scales accessible to our instrumentation.

Silver forms a face centered cubic (fcc) crystal with a bulk lattice constant *a*' of 0.40853 nm. The closest Ag-Ag distance is 0.289 nm. Crystals cut along one of the main crystallographic directions have a low index surface, in this case (111), (100), or (110) as illustrated in Fig. 1. A perfectly cut crystal would yield perfectly flat terraces with the appropriate arrangement of surface atoms. However, real surfaces are slightly miscut, resulting in terrace-step-kink morphology schematically shown in Fig. 2, 3, 4. These surfaces exhibit monoatomic high ledges whose edges may follow different surface directions producing kinks and corners. In addition, other defects may be present on the surface, including vacancies and dislocations. Adatoms may adsorb to terrace sites (hollow, bridge, and on-top) in addition to along step edges. Two-dimensional silver islands adopt the substrate geometry.

The hexagonally close-packed (111) surface is the most energetically favorable of the Ag low index surfaces. Fig. 2 highlights several features on the surface. The Ag(111) surface has three-fold (3-f) symmetry with *a*-*b*-*c* layer packing resulting in two three-fold hollow (3-fh) sites: hcp and fcc. The Ag atoms in the (100) surface, Fig. 3, have a square geometry and 4-f symmetry. The Ag(110) surface is less smooth or more open with a rectangular unit cell encompassing a 2-fh site, as shown in Fig. 4. The close-packed directions follow the <110>-

type directions for each of these surfaces. The Ag(111) surface is the most densely packed surface with 14 atoms/nm^2, while the surface atom density on the Ag(110) surface is only 8.5 atoms/nm^2. Features of the (110) surface are outlined in and

Adatom diffusion on the (111) and (100) surfaces occurs through hops in any direction. The potential energy surface of the (110) surface has more variation than the other two surfaces. Therefore, the diffusion barrier in-channel, along <110> between atom rows, is lower than cross-channel diffusion, along <100>.

Square brackets [ ] denote a direction vector that is related by symmetry to a family of direction vectors indicated by angle brackets < >. For example, [100] direction is in the <100> family of directions. A dash above a number in brackets indicates that the parameter equals the negative of the value, so $[2\,\bar{1}\,\bar{1}]$ can be written as [2 -1 -1]. Parentheses refer to a surface and curly brackets refer to a family of surfaces that are symmetry equivalent, e.g. {100} = (100), (010), (001), etc. For fcc crystals, the vector normal to the surface has the same index as the surface plan. For example, [100] direction is perpendicular to the (100) surface.

2.2. Electron instruments

Scanning tunneling microscopy (STM) allows us to investigate where, when, and how events, such as step fluctuations, roughening, smoothening, corrosion, and reconstruction, occur .[42,50-53] STM employs an atomically sharp metal tip that, when brought within 0.5 to 1 nm of a conducting surface at a potential difference, electrons tunnel between the tip and the sample. The tunneling current depends exponentially on the tip-sample gap distance giving STM high vertical resolution (0.01 nm). Current flowing almost exclusively at the sharp tip apex produces high lateral resolution (0.1 nm). STM creates real-space electron density maps and is particularly well suited to investigate 2-D structures, dynamic surface processes, and morphology evolution at the atomic level. Analysis can reveal the underlying atomic mechanisms for the observed structures and processes with the aid of theoretical and computational methods.

We use ultra-high vacuum (UHV, pressure less than 10^{-9} Torr or 10^{-7} Pa) to provide a well defined environment, limiting the number of variables that may affect a surface,

particularly contamination, and to allow the use of electron based techniques. The experiments on Ag(111) were conducted in a low temperature STM (LT-STM) UHV chamber, Fig. 5 at The RIKEN Advanced Science Institute, Wako, Saitama, Japan. Liquid nitrogen and liquid helium cool the STM stage (sample and tip) allowing imaging at ~5 K. Experiments on Ag(100) and Ag(110) were conducted at Iowa State University in a variable temperature STM (VT-STM) chamber, Fig 6, with imaging temperature ranges of 25 (He) or 120 K (N_2) to 750 K. The sample is cooled by a metal block around 3 sides of the sample that is in thermal contact with flowing liquid He or N_2. The tip is cooled by proximity to the sample, but the stage remains at room temperature. Both STMs are from Omicron GmbH, Germany. However, the sample is grounded in the VT-STM, but the tip is grounded in the LT-STM.

The Iowa State UHV chamber includes a low-energy electron diffraction / Auger electron spectroscopy (LEED/AES) instrument from OCI Vacuum Microengineering Inc., Canada. Low-energy electrons (30 - 200 eV) have a wavelength on the order or less of atomic separations in a crystal and a short mean free path. The incident electrons elastically collide with atoms and scatter. Therefore, LEED provides 2-D surface structure, in reciprocal space, for the surface layers (top 0.1 - 0.5 nm). I primarily used LEED to determine the surface unit cell with and without an adsorbate. AES provides chemical information by causing surface atoms (top 3 - 10 nm) to eject an electron with a characteristic energy via a three electron process. High-energy electrons (2 - 10 keV) bombard the sample creating a core hole in surface and near surface atoms. An electron from a higher energy level relaxes, replacing the core hole, and provides enough energy for a high energy level electron to escape. The energy with which the electron escapes is characteristic of the element it escapes from. In our instrument, both techniques detect the diffracted or emitted electrons with a retarding field analyzer. The electron source was either a LaB_6 single crystal or a ThO_2-W filament. AES is very sensitive to silver and sulfur, so I used it to monitor sample cleanliness and sulfur coverage.[54,55] Unfortunately, the AES detection limit for O is very high,[56] but the O/Ag intensity ratio may be used as a qualitative coverage indicator. The O coverage may be estimated by obtaining a clear LEED pattern a known superstructure.

2.3. Image processing and data analysis methods

STM images were processed and analyzed with WsXM software.[57] Microsoft Excel and WaveMetrics IGOR Pro have been used for numerical analysis and graphing. Imaging artifacts such as sample tilt, scanner bow and drift lead to images that are off level or skewed. Common leveling techniques remove tilt and curvature and are shown in Fig. 7. Plane fit subtracts a plane from the surface preserving height information. Either the whole surface (global) or regions (local) are fitted to a plane and subtracted from the original image. Rather than fitting a plane, Flatten subtracts a function from each scan line. This method is a type of filtering and can alter height information. On occasion I have used other filtering methods, such as Fast Fourier Transform (FFT) to remove noise from images. I frequently used Plane fit and Flatten to prepare images for presentation. Any image processing beyond Plane fit, Flatten, and contrast enhancement is noted in the figure caption.

Silver island coverage was determined using WsXM software, in which terrace images were flooded to give the proportion covered by islands. A few images (different areas) per experiment were analyzed to determine the average coverage and the error (reflecting the reproducibility / precision) within one standard deviation. A different source of error is associated with slight changes in flooding levels, and can be considered an absolute error. That was determined to be 6 to 28% different from the reported average coverage value and is not included in the standard deviation.

3. Dissertation organization

This dissertation includes three published papers. The first paper, Chapter II: "Low-temperature adsorption of H_2S on Ag(111)" appears in volume 133, year 2010 of *The Journal of Chemical Physics* on page 124705. The second paper, Chapter IV: "Adsorption of sulfur on Ag(100)" appears in volume 605, year 2011 of *Surface Science* on pages 520 to 527. The third paper, Appendix I: "Destabilization of Ag Nanoislands on Ag(100) by Adsorbed Sulfur" appears in volume 135, year 2011of *The Journal of Chemical Physics* on page 154701. C

Chapter II provides an example of molecular adsorption. Experiments in Chapters III and IV and Appendices II and III relate to surface reconstruction. Chapters V and VI and

Appendix I discuss silver island coarsening with oxygen or sulfur. Chapter VI is an extension of earlier work in the group, in which data from previously published experiments were analyzed to illuminate island coalescence with additives. The sulfur evaporator described in Appendix IV was built for the LT-STM chamber at RIKEN, but is similar to the evaporator used at Iowa State, built by Mingmin Shen.[58] The remaining Appendices provide databases of maintenance and STM experiments.

Figures

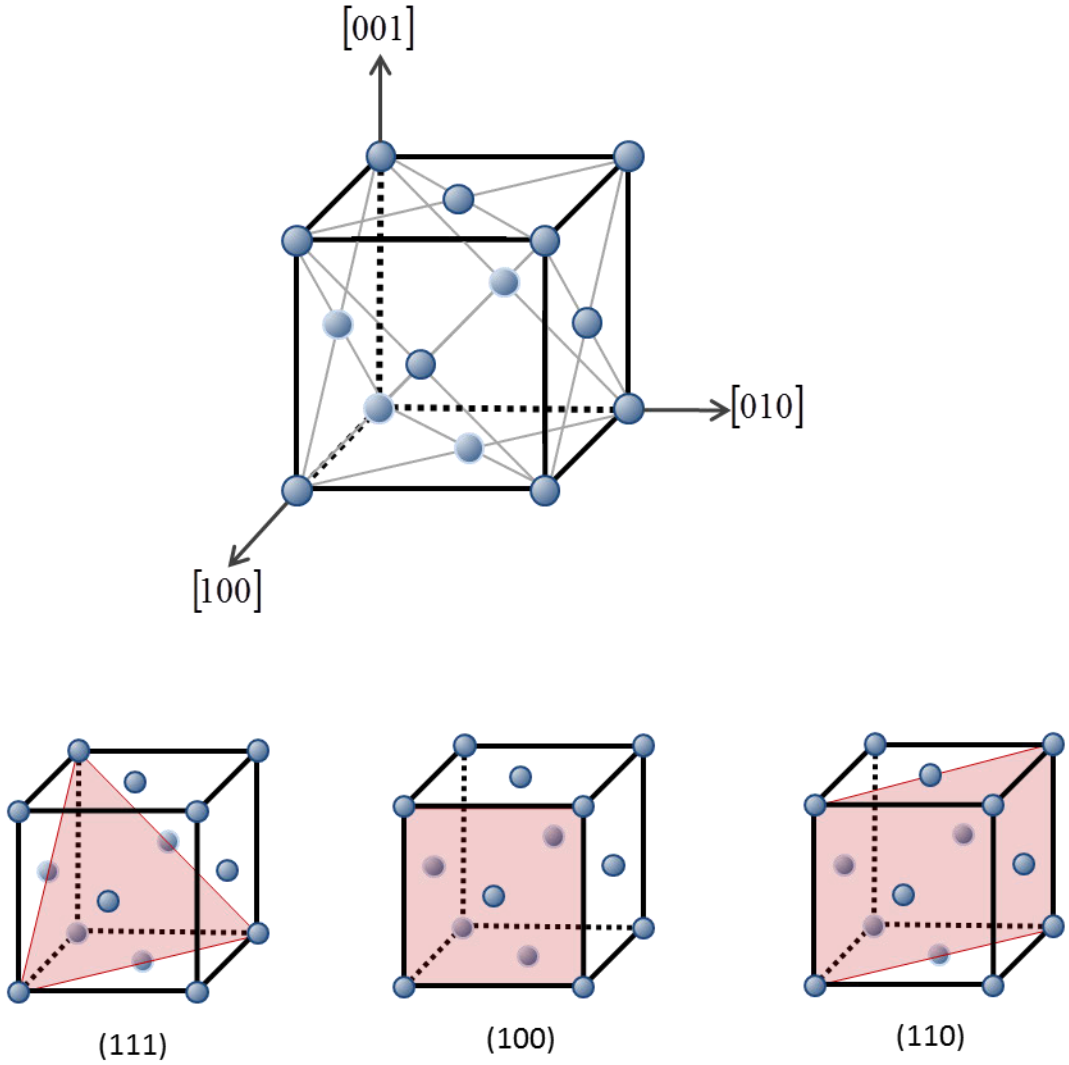

Figure 1. Face-center-cubic (fcc) crystal cut along the low-index planes. Silver forms an fcc crystal.

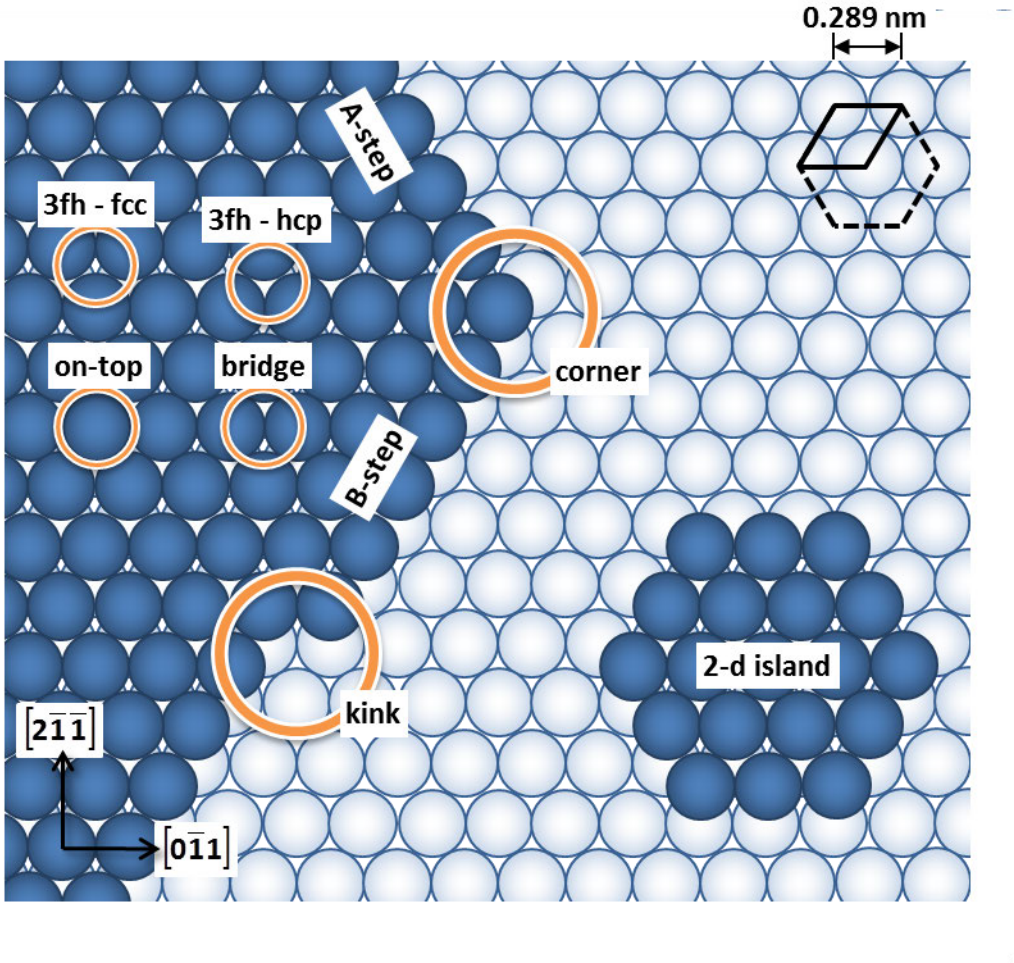

Figure 2. Features of a fcc(111) surface. The Ag surface unit cell is a rhombus with side length equal to 0.289 nm.

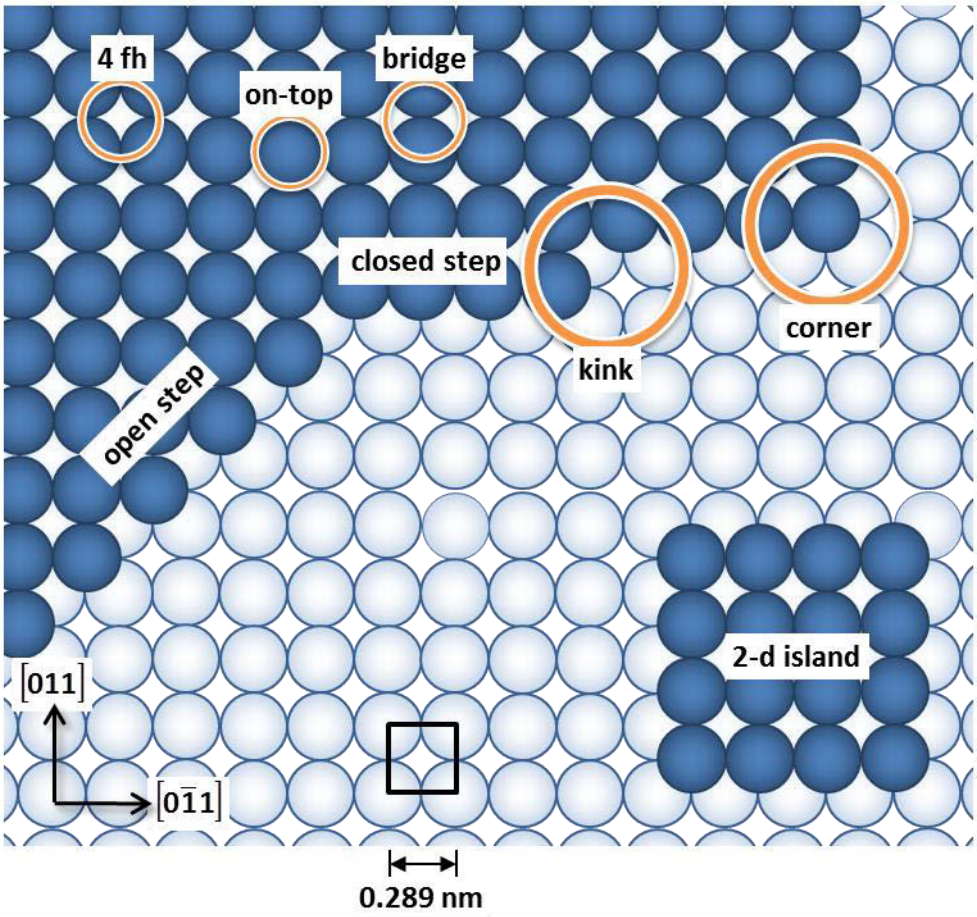

Figure 3. Features of a fcc(100) surface. The Ag surface unit cell is a square with side length equal to 0.289 nm.

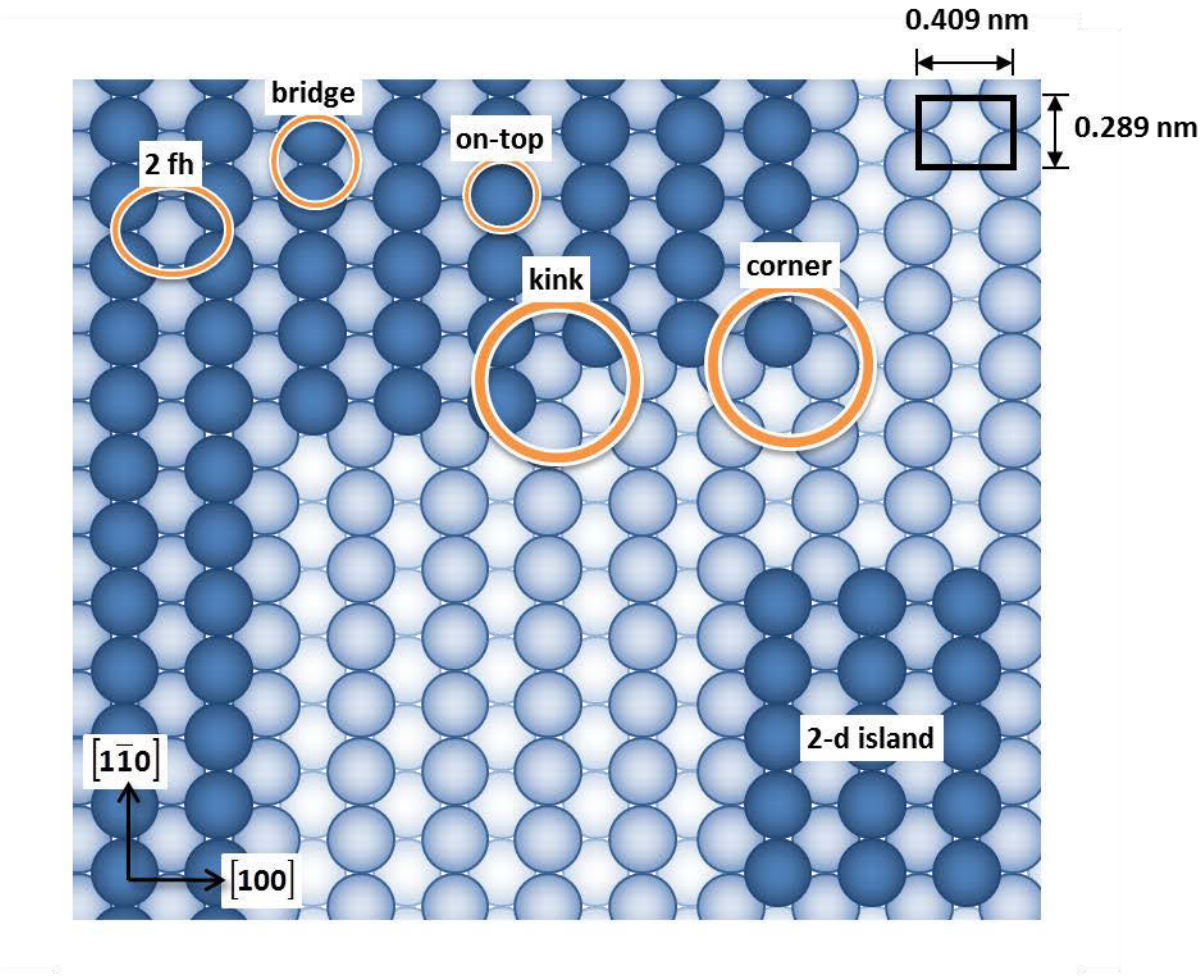

Figure 4. Features of a fcc(110) surface. The Ag surface unit cell is a rectangle with side lengths equal to 0.409 and 0.289 nm.

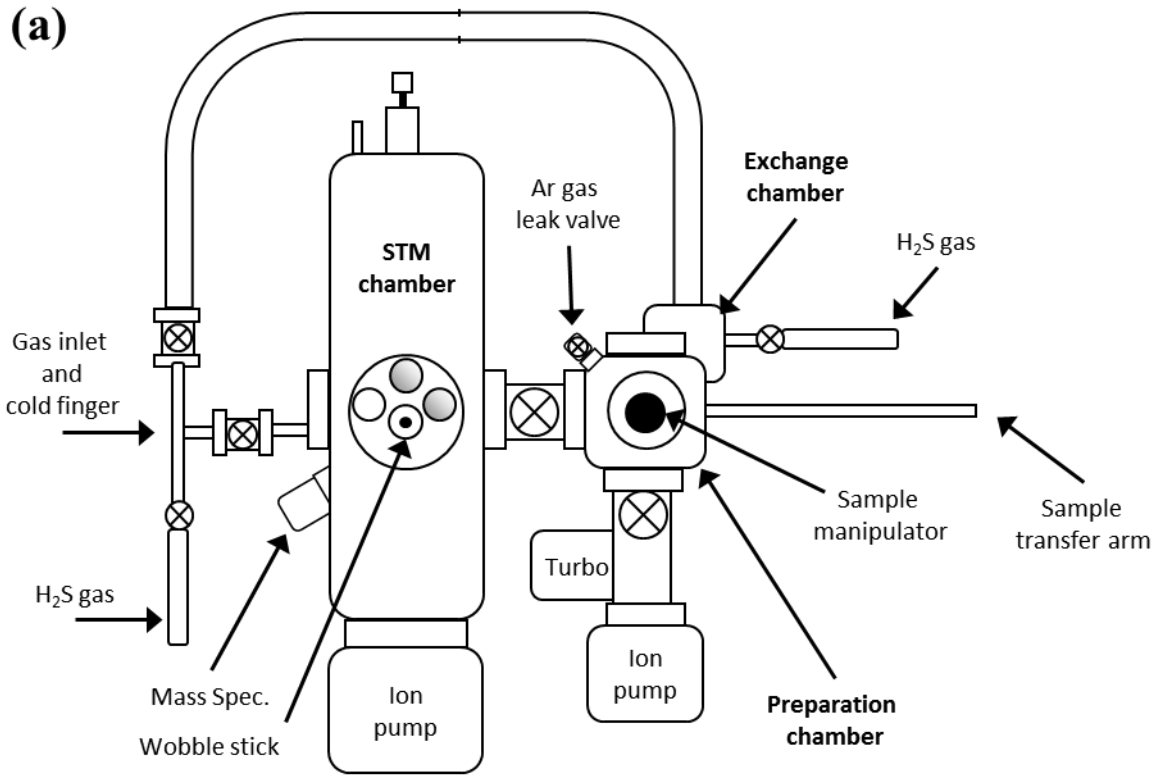

This figure continues on the following page.

Figure 5. Low temperature scanning tunneling microscope (LT-STM) chambers at RIKEN. Each chamber consists of 3 connected chambers that can be isolated by gate valves (valves of any type are drawn as ⊗). Samples are loaded in the exchange chamber (P~10^{-7} Torr) and cleaned in the preparation chamber (P~10^{-9} Torr). Experiments are performed in the STM chamber (P ≤ 10^{-10} Torr). (a) STM 2 was used for calendar year 2009 experiments with H_2S gas. (b) STM 1 was used for calendar years 2010 and 2012 experiments with S. The S evaporator was evacuated through the exchange chamber when mounted on the STM chamber (left) during the calendar year 2010 experiments. The evacuation lines are not drawn so as to not obscure the schematic. (c) Photograph of STM 1 from the opposite side illustrated in the schematic. (d) Photograph looking into the STM chamber through the view port above the wobble stick.

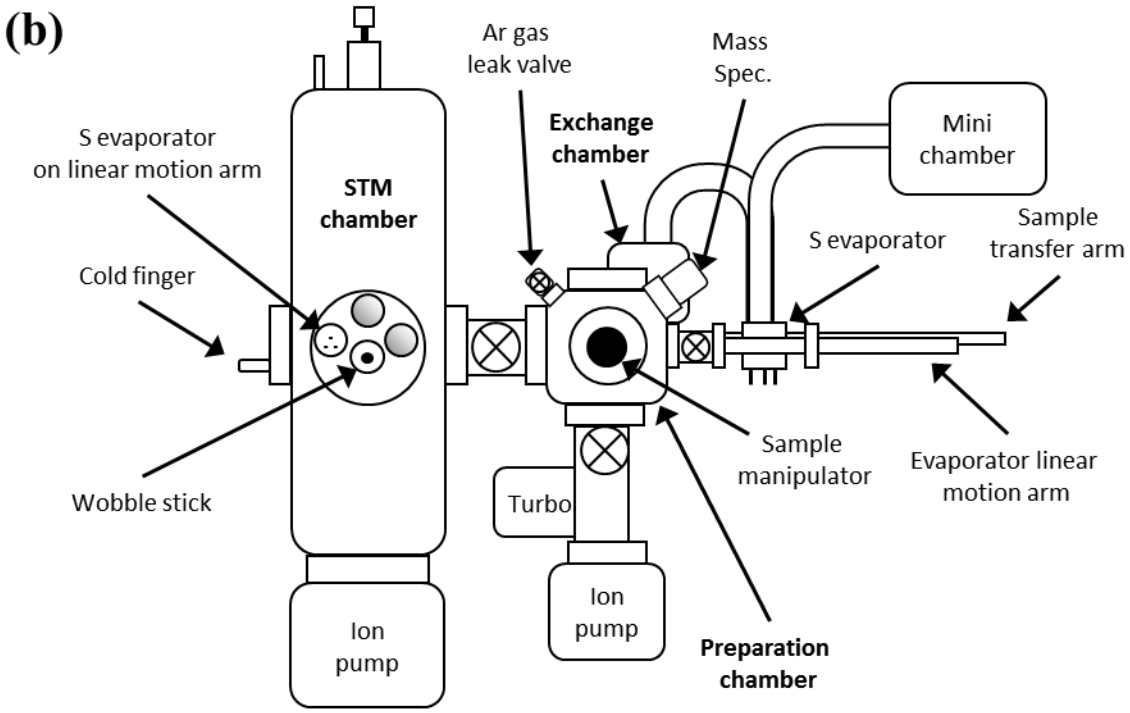

This figure continues on the following page.

Figure 5. continued

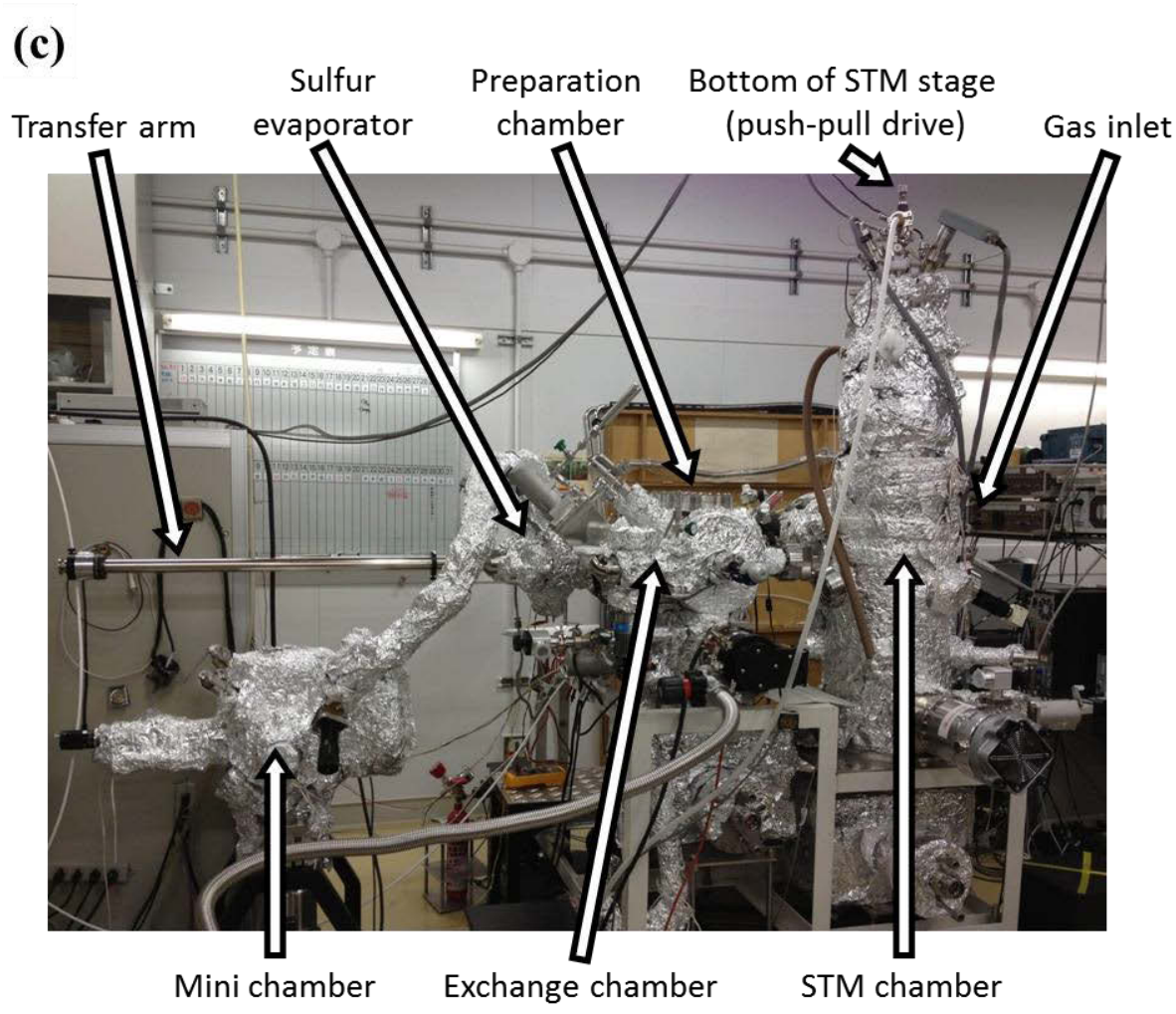

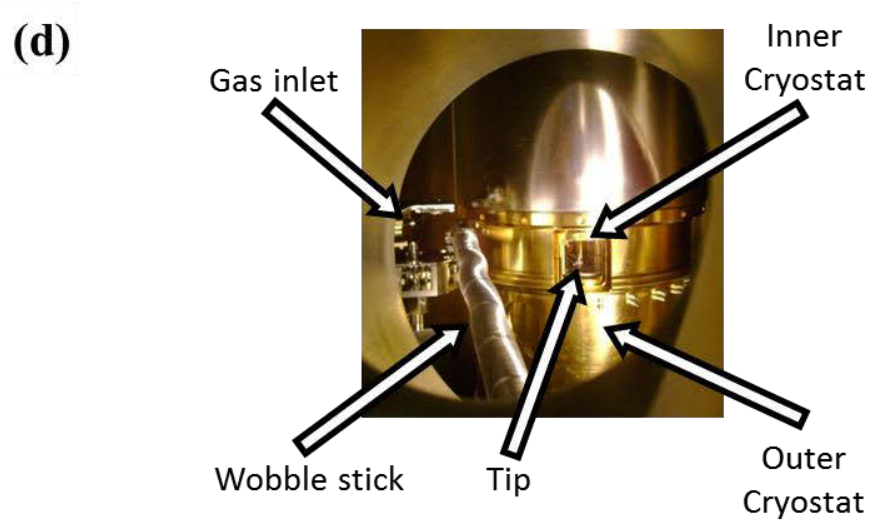

Figure 5. continued

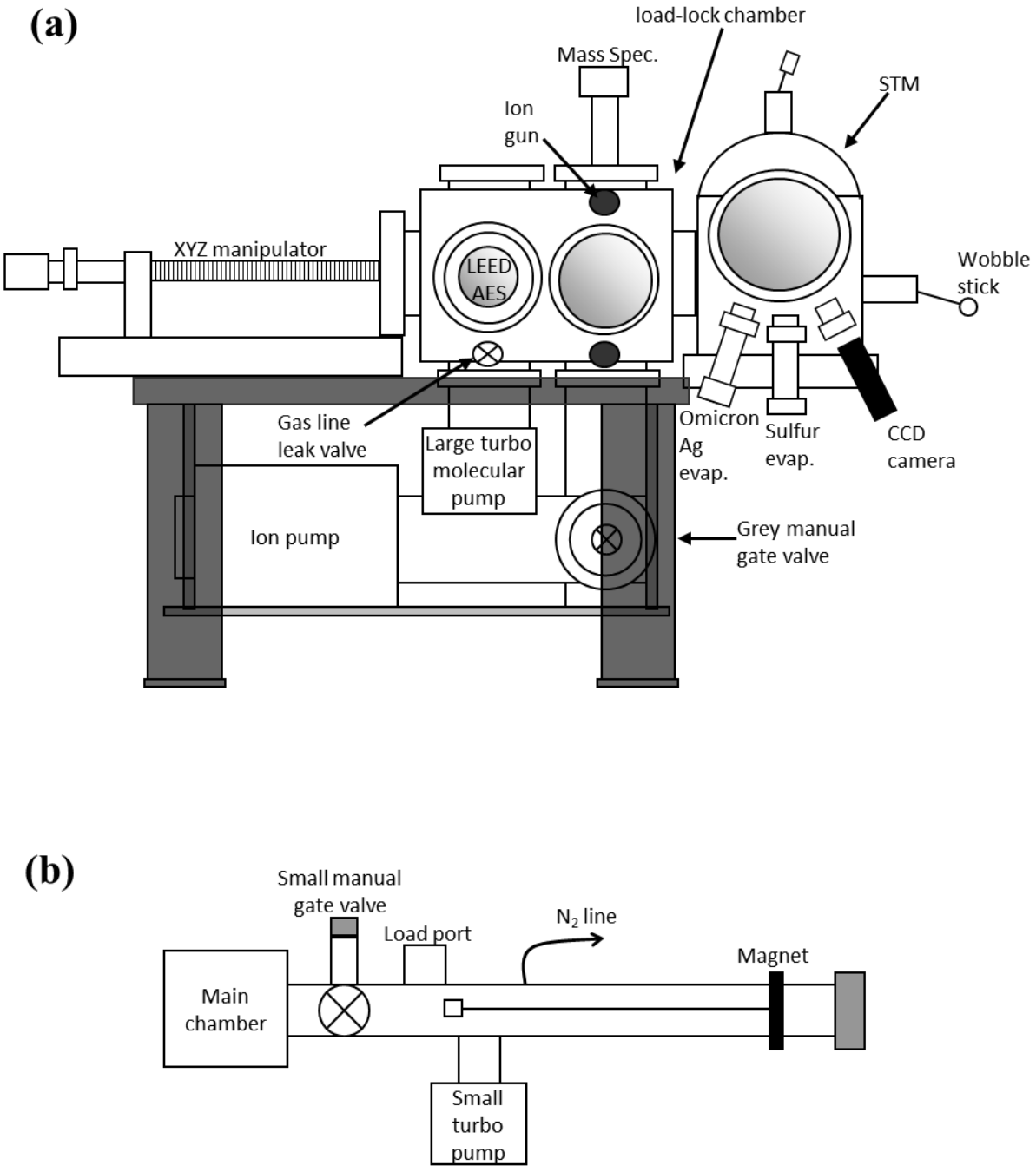

This figure continues on the following page.

Figure 6. Variable temperature scanning tunneling microscope (VT-STM) chamber at Iowa State University assembled by Conrad Stoldt. Valves of any type are drawn as ⊗. (a)The main chamber (P~10^{-10} Torr) houses the preparation area, LEED/AES, and STM. (b)Samples or tips may be transferred between UHV and atmosphere via the load-lock chamber (P~10^{-7} Torr). (c) Photograph of the chamber.

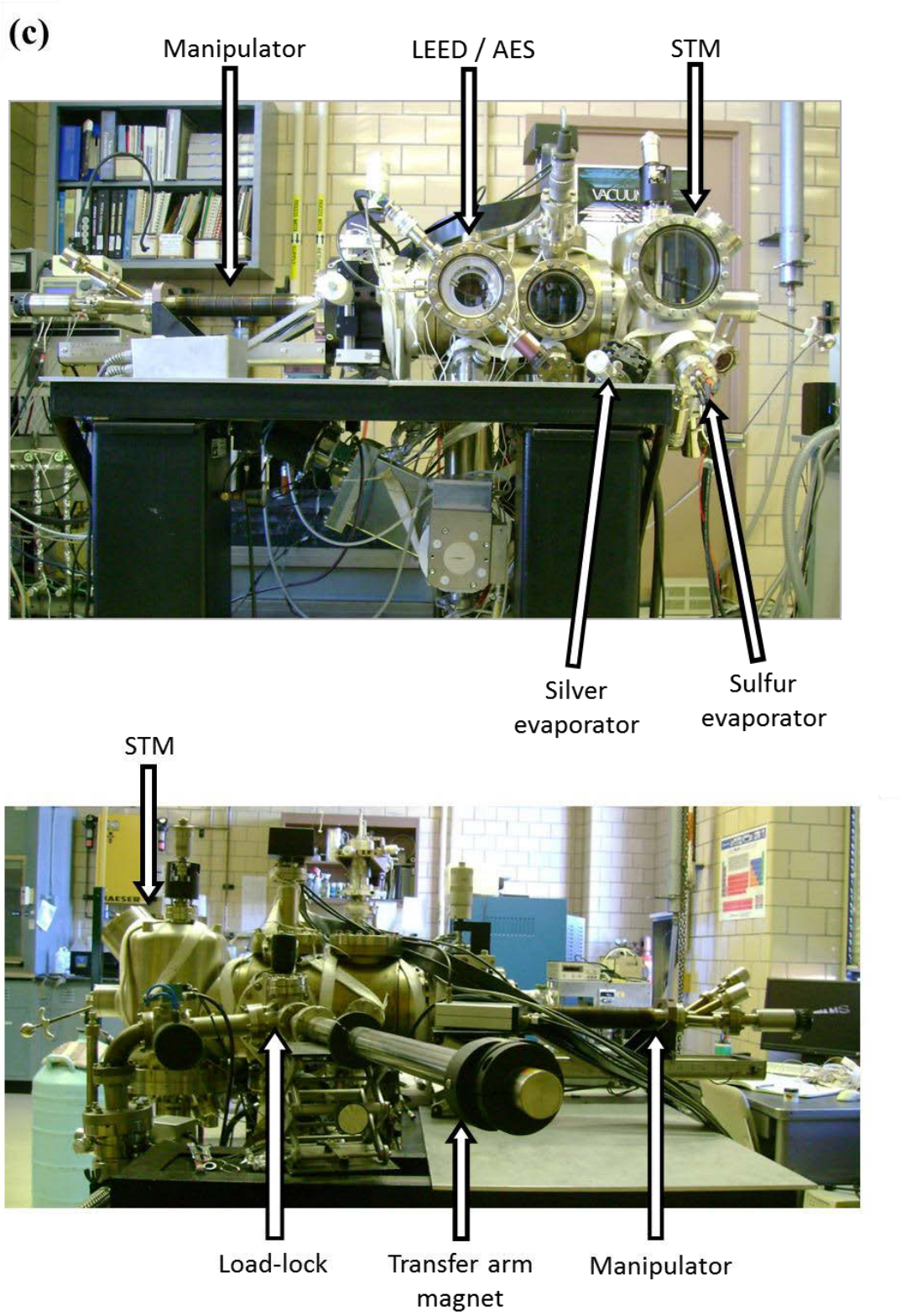

Figure 6. continued

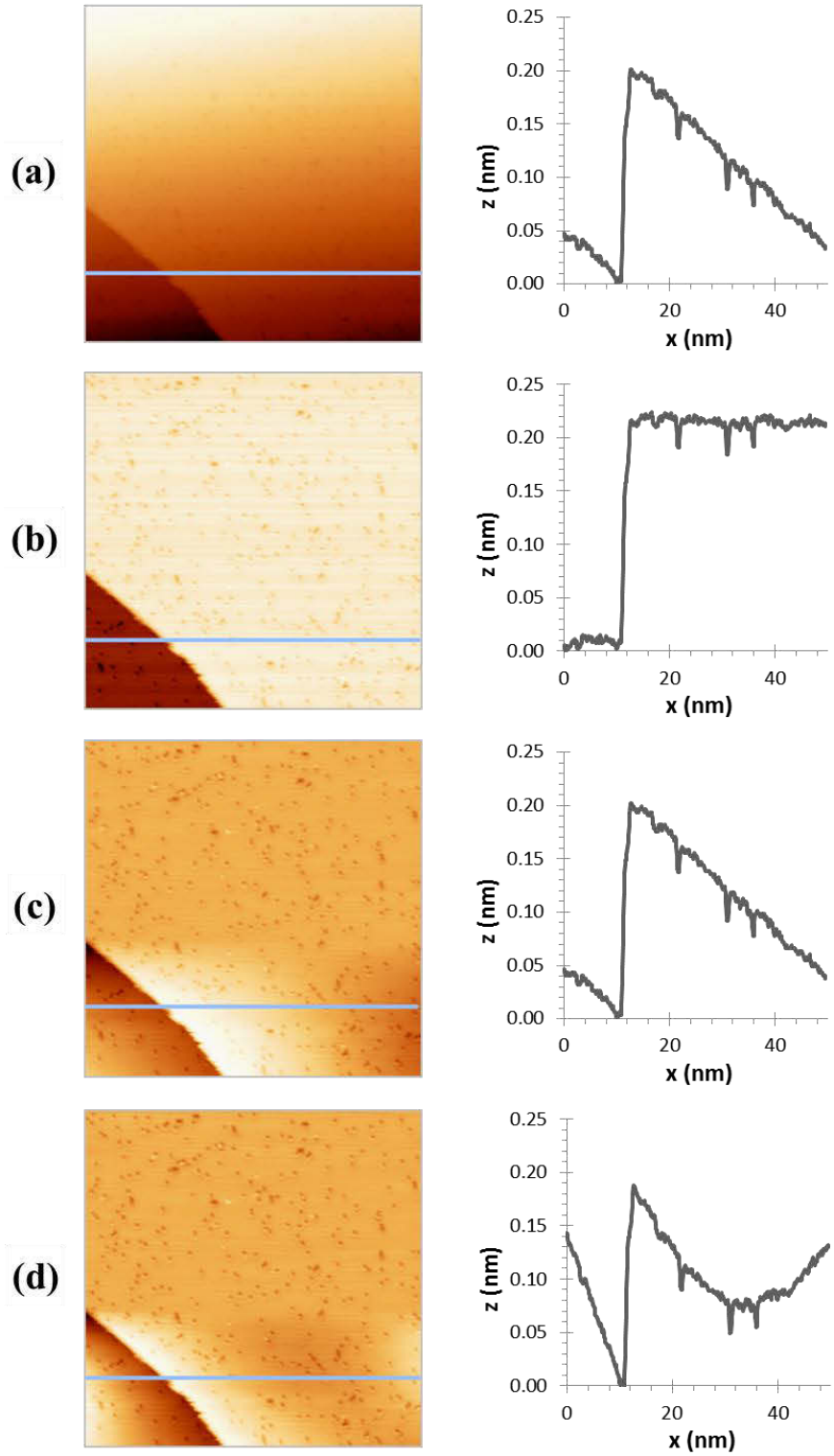

Figure 7. Ag(100) surface showing sputter damage at room temperature. STM images (left) and line profiles (right) illustrating the effect of basic image processing: (a) Raw image (b) planed or flattened subtracting a (c) linear or (d) parabolic function, 50x50 nm^2, I = 1.0 nA, U_{tip} = -1.0 V (5/27/2008 m26).

References

(1) Woodruff, D. P. *Journal of Physics: Condensed Matter* **1994**, *6*, 6067.

(2) Woodruff, D. P. *Journal of Physics: Condensed Matter* **2010**, *22*, 084016.

(3) Love, J. C.; Estroff, L. A.; Kriebel, J. K.; Nuzzo, R. G.; Whitesides, G. M. *Chemical Reviews* **2005**, *105*, 1103.

(4) Stiles, P. L.; Dieringer, J. A.; Shah, N. C.; Van Duyne, R. P. *Annual Review of Analytical Chemistry* **2008**, *1*, 601.

(5) McQuillan, A. J. *Notes and Records of the Royal Society* **2009**, *63*, 105.

(6) Ozbek, M. O.; Onal, I.; van Santen, R. A. *Journal of Catalysis* **2011**, *284*, 230.

(7) Li, W.-X.; Stampfl, C.; Scheffler, M. *Physical Review Letters* **2003**, *90*, 256102.

(8) Macleod, N.; Keel, J. M.; Lambert, R. M. *Catalysis Letters* **2003**, *86*, 51.

(9) Carmona, D.; Lalueza, P.; Balas, F.; Arruebo, M.; Santamaría, J. *Microporous and Mesoporous Materials* **2012**, *161*, 84.

(10) El-Rafie, M. H.; Shaheen, T. I.; Mohamed, A. A.; Hebeish, A. *Carbohydrate Polymers* **2012**, *90*, 915.

(11) Wang, Y.; Newell, B. B.; Irudayaraj, J. *Journal of Biomedical Nanotechnology* **2012**, *8*, 751.

(12) Peng, H.-I.; Krauss, T. D.; Miller, B. L. *Analytical Chemistry* **2010**, *82*, 8664.

(13) Serafin, J. G.; Liu, A. C.; Seyedmonir, S. R. *Journal of Molecular Catalysis A* **1998**, *131*, 157.

(14) Verykios, X. E.; Stein, F. P.; Coughlin, R. W. *Catalysis Reviews* **1980**, *22*, 197.

(15) Campbell Charles, T. In *Catalyst Characterization Science*; American Chemical Society: 1985; Vol. 288, p 210.

(16) Verykios, X. E.; Stein, F. P.; Coughlin, R. W. *Journal of Catalysis* **1980**, *66*, 147.

(17) Lefferts, L.; van Ommen, J. G.; Ross, J. R. H. *Applied Catalysis* **1986**, *23*, c.

(18) Qian, M.; Liauw, M. A.; Emig, G. *Appl. Catal. A* **2003**, *238*, 211.

(19) Link, S.; El-Sayed, M. A. *The Journal of Physical Chemistry B* **1999**, *103*, 8410.

(20) Scholl, J. A.; Koh, A. L.; Dionne, J. A. *Nature* **2012**, *483*, 421.

(21) Mock, J.; Norton, S.; Chen, S. Y.; Lazarides, A.; Smith, D. *Plasmonics* **2011**, *6*, 113.

(22) Mahmoud, M. A.; El-Sayed, M. A. *Nano Letters* **2009**, *9*, 3025.

(23) Simonsen, S. B.; Chorkendorff, I.; Dahl, S.; Skoglundh, M.; Sehested, J.; Helveg, S. *Journal of Catalysis* **2011**, *281*, 147.

(24) Gautam, A.; Howe, J. *Journal of Materials Science* **2009**, *44*, 601.

(25) The metal-support interaction can modify the catalytic activity of the metal. van den Oetelaar, L. C. A. Surface and Interface Phenomena in Heterogeneous Metal Catalysis. Ph.D. thesis, Technische Universiteit Eindhoven (1997).

(26) Moulijn, J. A.; van Diepen, A. E.; Kapteijn, F. *Appl. Catal. A* **2001**, *212*, 3.

(27) Grant, R. B.; Lambert, R. M. *Surface Science* **1984**, *146*, 256.

(28) Grant, R. B.; Lambert, R. M. *Journal of Catalysis* **1985**, *92*, 364.

(29) Linic, S.; Barteau, M. A. *Journal of the American Chemical Society* **2003**, *125*, 4034.

(30) Cao, A.; Lu, R.; Veser, G. *Physical Chemistry Chemical Physics* **2010**, *12*, 13499.

(31) Ozbek, M. O.; Onal, I.; Santen, R. A. V. *Journal of Physics: Condensed Matter* **2011**, *23*, 404202.

(32) Evans, J. W.; Thiel, P. A. *Science* **2010**, *330*, 599.

(33) Thiel, P. A.; Shen, M.; Liu, D.-J.; Evans, J. W. *Journal of Vacuum Science & Technology A* **2010**, *28*, 1285.

(34) Datye, A. K.; Xu, Q.; Kharas, K. C.; McCarty, J. M. *Catalysis Today* **2006**, *111*, 59.

(35) Wynblatt, P.; Gjostein, N. A. *Progress in Solid State Chemistry* **1975**, *9*, 21.

(36) Smith, D. J.; White, D.; Baird, T.; Fryer, J. R. *Journal of Catalysis* **1983**, *81*, 107.

(37) Larsson, E. M.; Millet, J.; Gustafsson, S.; Skoglundh, M.; Zhdanov, V. P.; Langhammer, C. *ACS Catalysis* **2012**, *2*, 238.

(38) Smith, R. L.; Yanina, S. V.; Rohrer, G. S.; Perrotta, A. J. *Journal of the American Ceramic Society* **2002**, *85*, 2325.

(39) Campbell, J. S. *Industrial & Engineering Chemistry Process Design and Development* **1970**, *9*, 588.

(40) Kung, H. H. *Catalysis Today* **1992**, *11*, 443.

(41) Spencer, M. S.; Twigg, M. V. *Annual Review of Materials Research* **2005**, *35*, 427.

(42) Besenbacher, F.; Lauritsen, J. V.; Wendt, S. *Nano Today* **2007**, *2*, 30.

(43) Shen, M.; Liu, D.-J.; Jenks, C. J.; Evans, J. W.; Thiel, P. A. *Surface Science* **2009**, *603*, 1486.

(44) Reinecke, N.; Reiter, S.; Vetter, S.; Taglauer, E. *Applied Physics A* **2002**, *75*, 1.

(45) Frank, E. R.; Hamers, R. J. *Journal of Catalysis* **1997**, *172*, 406.

(46) Min, B. K.; Alemozafar, A. R.; Biener, M. M.; Biener, J.; Friend, C. M. *Topics in Catalysis* **2005**, *36*, 77.

(47) Kalff, M.; Comsa, G.; Michely, T. *Physical Review Letters* **1998**, *81*, 1255.

(48) Iski, E. V.; Jewell, A. D.; Tierney, H. L.; Kyriakou, G.; Sykes, E. C. H. *Surface Science* **2012**, *606*, 536.

(49) Jensen, F.; Besenbacher, F.; Laegsgaard, E.; Stensgaard, I. *Physical Review B* **1990**, *42*, 9206.

(50) Binnig, G.; Rohrer, H. *IBM Journal of Research and Development* **2000**, *44*, 279.

(51) Griffith, J. E.; Kochanski, G. P. *Annual Review of Materials Science* **1990**, *20*, 219.

(52) Chen, C. J. *Introduction to Scanning Tunneling Microscopy*; Oxford University Press: Oxford, England, 2007; Vol. 1.

(53) Behm, R. J.; Garcia, N.; Rohrer, H., 1990.

(54) Davis, L. E.; MacDonald, N. C.; Palmberg, P. W.; Riach, G. E.; Weber, R. E. *Handbook of Auger electron spectroscopy: a reference book of standard data for identification and interpretation of Auger electron spectroscopy data*; 2nd ed.; Physical Electronics Industries, 1976.

(55) Schwaha, K.; Spencer, N. D.; Lambert, R. M. *Surface Science* **1979**, *81*, 273.

(56) Engelhardt, H. A.; Menzel, D. *Surface Science* **1976**, *57*, 591.

(57) Horcas, I.; Fernandez, R.; Gomez-Rodriguez, J. M.; Colchero, J.; Gomez-Herrero, J.; Baro, A. M. *Review of Scientific Instruments* **2007**, *78*, 013705.

(58) Shen, M. *Sulfur adsorption, structure, and effects on coarsening on Ag(111) and Ag(100)*. Ph.D. thesis, Iowa State University, (2009).

CHAPTER II

Low-Temperature Adsorption of H_2S on Ag(111)

A paper published in *The Journal of Chemical Physics.*[a]

Selena M. Russell,[b] Da-Jiang Liu,[c] Maki Kawai,[d,e] Yousoo Kim,[d] and P. A. Thiel[b,c]

Abstract

H_2S forms a rich variety of structures on Ag(111) at low temperature and submonolayer coverage. The molecules decorate step edges, exist as isolated entities on terraces, and aggregate into clusters and islands, under various conditions. One type of island exhibits a $(\sqrt{37}\times\sqrt{37})R25.3^o$ unit cell. Typically, molecules in the clusters and islands are separated by about 0.4 nm, the same as the S-S separation in crystalline H_2S. DFT indicates that hydrogen-bonded clusters contain two types of molecules. One is very similar to an isolated H_2S molecule, with both S-H bonds nearly parallel to the surface. The other has an S-H bond pointed toward the surface. The potential energy surface for adsorption and diffusion is very smooth.

1. Introduction

Investigations of sulfur, and sulfur-containing molecules, adsorbed on metal surfaces are motivated by applications ranging from catalysis to self-assembled monolayers. Concerning the specific interaction of H_2S with Ag(111), almost all previous studies have focused on using H_2S as a source of adsorbed S. In those studies, dissociative adsorption was achieved using high pressure and/or elevated surface temperature when H_2S was in the gas phase,[1-7] or using electrochemical methods when H_2S was in liquid solution[7,8]. In contrast,

---

[a] Russell, S. M.; Liu, D.-J.; Kawai, M.; Kim, Y.; Thiel, P. A. *The Journal of Chemical Physics* **2010**, *133*, 124705.
[b] Department of Chemistry, Iowa State University, Ames, Iowa 50011, USA
[c] Ames Laboratory US - DOE, Iowa State University, Ames, Iowa 50011, USA
[d] RIKEN Advanced Science Institute, Wako, Saitama 351-0198, Japan
[e] Department of Advanced Materials Science, The University of Tokyo, Chiba 277-8561, Japan

the present paper deals with the state of the molecule that is obtained by adsorption at low pressure and at temperatures (T) of 5 to 30 K.

Previous experiments have shown that H_2S adsorbs and desorbs without dissociation on Ag(111) at low pressure, i.e. in ultrahigh vacuum-type experiments.[9] The sticking coefficient is near unity at 80 K, and desorption occurs at T ≈ 100 K.[9] Density functional theory (DFT) calculations have shown that H_2S has an adsorption energy (E_a) of 0.17 eV on Ag(111), and that the adsorbed molecule nearly retains its gas phase geometry.[10] The structural parameters in the gas phase are 0.135 nm for the S-H bond length, and 93º for the internal bond angle, whereas the adsorbed molecule has parameters of 0.136 nm and 92º, respectively.[10] The isolated H_2S molecule adsorbs with S on top of a Ag atom, and with both S-H bonds parallel to the surface.[10]

Unlike H_2S, molecular H_2O on metal surfaces has been studied extensively, and it is useful to review the findings. The isolated H_2O molecule on Ag(111) is quite similar to H_2S, with the O atom at an on-top adsorption site, O-H bonds parallel to the surface, and E_a = 0.15 eV.[11] In general, on hexagonal metal surfaces, water forms hydrogen-bonded clusters that consist of buckled hexamers.[12-17] The importance of hydrogen bonding in the structures of H_2O aggregates on Ag(111) has been confirmed by detailed scanning tunneling microscopy (STM) and DFT studies of Morgenstern, Michaelides, *et al*.[15-26]

Like H_2O, H_2S forms H-bonds in the gas, liquid, and solid states. However, its H-bond is only about half as strong as that of H_2O,[27] and its molecular geometry is considerably different: The S-H bond is longer than the O-H bond (0.133 nm vs. 0.095 nm), and its internal bond angle is smaller (92.2º vs. 104.5º). Given these differences, it is unclear *a priori* whether H_2S will form hydrogen bonded clusters on Ag(111), and if so, what their geometry will be.

2. Experimental and computational details

All STM imaging was done at 4.7 K with a low-temperature STM (Omicron GmbH, Germany) in an UHV chamber with base pressure below 6.7×10^{-9} Pa. In an attached chamber, the Ag(111) sample (MaTecK GmbH, Germany) was cleaned by repeated cycles of Ar^+ sputtering (1 keV, ~10 μA, 10 min) and annealing (~890 K, 10 min). The clean sample

was transferred to the STM stage and cooled to the operating temperature. The surface was exposed to H_2S gas through a dosing tube located just outside of the STM cryostat. That area was at room temperature, so during exposure the sample was not cooled actively. During exposure the sample warmed to 20-30 K, depending on the time it was out of the cryostat (and hence, on exposure time). STM imaging typically began within 20 minutes after exposure ended, when the sample temperature had re-stabilized at 4.7 K. H_2S purity was checked with a mass spectrometer in the STM chamber.

STM images were acquired over a range of bias voltages from -140 mV to +112 mV, and a range of tunneling currents up to 1.0 nA. Based upon previous STM studies of H_2O on Ag(111)[17,19,24] , and also on Pt(111)[28] and Pd(111)[29], these conditions are not sufficient to induce dissociation. In addition, there was no evidence of diffusion or rearrangement during imaging if the bias potential was about 100 mV or less.

Data from three types of experiments are described in this paper. In the first, the sample was placed in front of the gas doser for about 1 s at 20 K, after which STM images were acquired continuously over a 3-hour period, and intermittently over the following 72 hours. Second, the sample was placed in front of the H_2S doser for 10 s at about 30 K, and STM images were acquired over the following 2 hours. Third, the same 10 s-exposed sample was allowed to age for 17 hours at 4.7 K, after which images were acquired again over an 8 hour period. After the 1 s exposure, 2-3% of the surface was covered by features attributable to H_2S. After the 10 s exposure, 20-30% of the surface was covered, both immediately after exposure and after aging. The surface that resulted from the two exposures will be referred to as "low $\theta^{rel}_{H_2S}$ " and "higher $\theta^{rel}_{H_2S}$ " respectively. Here the relative coverage, θ^{rel} , is simply based on the area of the STM images covered by adsorbate-related features. In the STM images, lateral (x and y) distances were calibrated using the atomic separation of Ag(111), 0.289 nm.

After deposition to higher $\theta^{rel}_{H_2S}$, aging, and scanning, the sample was allowed to warm to 200 K. When checked again with STM, the surface was clean, consistent with expectations from previous work, showing that adsorption and desorption at low temperature are reversible (non-dissociative).[9]

Total energy calculations were performed using the VASP code[30-33] with the Perdew-Burke-Ernzerhof (PBE) approximations of the exchange-correlation functional.[34] The electron-ion interactions were described by an improved version of the projector augmented wave (PAW) method for transition metals.[35] The surface was modeled by periodic slabs of varying thickness separated by 1.2 nm of vacuum, using the theoretical lattice constant 0.4149 nm. The energy cutoff was 280 eV. Molecules were adsorbed on one side of the slab, and an external potential was applied to correct the artificial dipole interactions induced by the adsorbate in the direction perpendicular to the surface,[36] when necessary. Results quoted below were obtained from averages of slab thickness varying from four to seven layers, with varying supercells up to (4×4) (16 atoms in each layer). In the calculations, absolute coverages (θ^{abs}) are relevant, and these are defined as the ratio of the density of H_2S molecules to Ag atoms in the surface plane. STM images were simulated using the Tersoff-Hamann method.[37] The simulated images were obtained from the partial charge density of the sample within ±0.1 eV of the Fermi level, and the isodensity surface at a density 1% of the average bulk density. This would correspond experimentally to an ideal point tip with spherical tip wavefunction about 0.4 nm above the surface, with low tunneling bias.

The main intermolecular interactions between H_2S molecules in a cluster should be hydrogen bond interactions, which can be reasonably described by DFT. For example, the PBE value for H_2O dimer interactions is about 0.02 eV higher than the benchmark number from high level quantum chemistry calculations.[38] It should be noted that the DFT-PBE error could be as high as 0.05 eV for highly nonlinear H bonds.[39] However, DFT at the generalized gradient approximation (GGA) level is not suitable for dispersion interactions, which may play a more important role for larger complex structures. In this paper, we report results only for small clusters where hydrogen bond interactions dominate.

3. Results

3.1. Step edges

Figure 1a shows an atomic-scale image of a region of a Ag(111) terrace. Arrows show the close-packed directions. This serves to define the crystallographic directions in all other STM images.

Figure 1b shows the smooth, straight appearance that is typical of a clean Ag(111) step at 4.7 K. The appearance changes considerably when H_2S adsorbs, as shown in Fig. 1c for low $\theta_{H_2S}^{rel}$. Clearly, molecules saturate the step edges. At higher magnification, as in Fig. 1d, a double row of protrusions is visible along the step edge. The protrusions are separated by 0.42 $\pm$ 0.09 nm, as shown in the inset in Fig. 1d. Other data to be presented in this paper will repeatedly show protrusions with similar nearest-neighbor separation of 0.4 nm, in various environments. This robust feature is reasonably assigned as an H_2S molecule hydrogen-bonded to one or more other molecules. See Table I.

At higher $\theta_{H_2S}^{rel}$, protrusions still cover the step edges, as in Fig. 1e. They have the same separation as at low $\theta_{H_2S}^{rel}$, although they comprise a wider band. After aging at higher $\theta_{H_2S}^{rel}$, one sees islands extending outward from step edges, as in Fig. 1f. The growth of these islands indicates considerable diffusion of H_2S during aging, even at 4.7 K. If two step edges border a narrow terrace, as in the center of Fig. 1f, the islands may bridge the terrace. Taken together, these data indicate that H_2S adsorbs preferentially at step edges, and the steps can serve to nucleate islands on the terraces. These are reminiscent of observations for H_2O on this surface.[20]

3.2. H_2S on terraces: Isolated molecules

At higher $\theta_{H_2S}^{rel}$, before aging, many isolated protrusions can be seen on the terraces as in Fig. 1e. These features may be isolated H_2S molecules. DFT lends some insight about whether this assignment is reasonable. Our calculations indicate that the adsorption energy of an H_2S molecule is 0.15 eV. This is in good agreement with Alfonso's value, 0.17 eV,[10] and in reasonable agreement with the value of 0.25 eV derived from experimental temperature-programmed desorption (using major simplifying assumptions).[9] The slight difference is mainly due to the different PAW potential used (and therefore different lattice constant) plus the denser k-point grids in this paper. Regarding the molecule's configuration, our DFT calculations confirm the results of Alfonso,[10] i.e. the fact that in its most stable form, the S atom is nearly at an on-top site, one of the H atoms nearly at a bridge site, and the other H atom nearly at an fcc or hcp site. This configuration is shown in Fig. 2a,b. Simulation of

STM images, based upon DFT, shows that the molecule's shape (assuming a static position) is essentially circular, as shown in Fig. 2c.

For quantitative STM dimensions, calculations show that the measured area per molecule should be about 0.18 nm^2 assuming a static position. The measured area of the isolated features in Fig. 1e is only slightly larger, about 0.23 nm^2, which is probably within the acceptable limit of such a comparison.

We also use DFT to test adsorption of an H_2S monomer with the S atom initially near an fcc or a bridge site, using a (2×2) supercell and $\theta_{H_2S}^{abs}$ = 1/4. These initial conditions result in metastable adsorption with very similar configurations and energies. The S atom is slightly higher and the H atoms are slightly lower than at the on-top site, and E_a is about 0.031 eV less favorable. These metastable adsorption configurations are near the transition states for diffusion of H_2S molecules, implying a diffusion barrier of about 0.031 eV. [Strictly speaking, this is a lower estimate. The transition state is a saddle point which should have a higher energy than a nearby metastable adsorption site. However, due to the flatness of the potential energy surface, the difference is hard to discern from numerical calculations. Our calculation of the restricted one-dimension minimal energy pathway shows no higher barrier beyond numerical uncertainties, using a (2×2×5) supercell. Furthermore, studies of various systems—our own and others'[40]—leads us to expect that the real value does not exceed this estimate by more than 10%.]

A rough, nudged elastic band calculation of the minimal energy diffusion path yields a diffusion barrier of 0.036 eV, very close to the difference in adsorption energies between the metastable and stable configurations, 0.031 eV. This is a very small diffusion barrier, suggesting that the potential energy surface is quite smooth, and that thermal diffusion at low temperature is not unreasonable. This will be discussed more fully in Section 4.

3.3. H_2S on terraces: Pinwheel and triangular clusters at low $\theta_{H_2S}^{rel}$.

Under the same conditions where the steps are decorated at low $\theta_{H_2S}^{rel}$ (Fig. 1c, d), wide terraces also exhibit clusters. These clusters are very uniform, as shown in Fig. 3a, with a diameter of 3.0 ± 0.2 nm^2. All the clusters exhibit internal protrusions arranged in a chiral

pinwheel pattern, which is evident at high magnification in Fig. 3b,c. It is faintly visible in the raw image (Fig. 3b), but is more pronounced in the differentiated image (Fig. 3c). Within experimental uncertainty, the individual protrusions in the pinwheel clusters have the same separation as the step-edge protrusions, i.e. 0.39 $\pm$ 0.07 nm. (See Table I.) The pinwheel clusters do not transform or coarsen, over a period of tens of hours in UHV at 4.7 K. The coverage of pinwheel clusters under these conditions is 0.0033 nm^{-2}, which is very low compared with the density of Ag atoms, 14.4 nm^{-2}. Thus, it is conceivable that these clusters nucleate at defects or impurities, although if that is the case, the nucleation center exerts no influence on the molecular structure within the cluster.

The H_2S pinwheel clusters can dissociate under certain tunneling conditions. They undergo increasing dissociation in the sequence in Fig. 4, leaving many small fragments finally in Fig. 4c. The small fragments, which we call triangular clusters, are shown at closer view and are also represented schematically in Fig. 5. Each triangular cluster consists of 3 unequal protrusions [labeled (a)-(c) in the schematic].

These asymmetric triangular clusters share the same orientation. This was a reproducible observation. In other words, dissociation of a pinwheel cluster always produces triangular clusters that were aligned with one anohter, even though their alignment with respect to the parent pinwheel was variable. This alignment could be produced by long-range interactions modulated by the well-known surface electronic state of Ag(111),[41,42] or by an asymmetry in the tip itself, which could induce a common spatial orientation during the dissociation process. The latter possibility is bolstered by a recent observation that spontaneous (unintentional) tip asymmetry can induce preferential molecular orientation in asymmetric alkanethiols adsorbed on Au.[43] Because of the reproducibility described above, we do not believe that the parallel alignment of the triangular H_2S clusters reflects an artifact in the imaging process itself, i.e., a multiple tip.

Morgenstern and co-workers observed similar (but not identical) triangular features, for ~0.05 bilayers H_2O and D_2O on Cu(111) and Ag(111) at 17 K.[15,17-19] They initially suggested that these features were trimers of H_2O molecules.[15] However, upon further investigation and by comparison with DFT, they later identified the feature as a 9-molecule cluster, i.e. a nonamer.[17] The nonamers consisted of a hexamer of "bilayer ice" with 3

additional H_2O molecules at the periphery, hydrogen bonded to the alternating, lower H_2O molecules of the hexamer. STM of these triangular features on Ag(111) showed a peak-to-peak distance of 0.56 nm and an internal angle of 60º, with each protrusion at the same height. In contrast, the triangular clusters of H_2S represented in Fig. 4 are smaller, the protrusions form an irregular triangle, and the protrusions are not at the same height. For example, the lengths of the sides of the triangle (as defined in Fig. 5c) are $\overline{AB} = 0.41 \pm 0.02$ nm, $\overline{BC} = 0.52 \pm 0.02$ nm, and $\overline{CA} = 0.49 \pm 0.03$ nm—all significantly smaller than the 0.56 nm of H_2O. Given that the S-H bond of H_2S in the gas phase is 40% *longer* than the O-H bond of H_2O (and that the hydrogen bond is weaker), one would *not* expect a hexamer or nonamer of H_2S to be *smaller* than the corresponding cluster of H_2O. Therefore, it is unlikely that our triangular clusters are hydrogen-bonded hexamers or nonamers.

Using DFT, we searched for clusters that might be compatible with the data. Clusters are necessarily stabilized by short-range, attractive interactions. For large intermolecular separations (0.9 to 4.6 nm), periodically arranged H_2S molecules actually repulse one another, since E_a decreases steadily with increasing coverage, from 0.15 eV at $\theta_{H_2S}^{abs}$=1/16, to 0.085 eV at $\theta_{H_2S}^{abs}$=1/3. Next examining shorter intermolecular separations, we find a *dimer* with E_a = 0.35 eV, implying an attractive interaction of about (0.35 - 2×0.15) = 0.05 eV. The distance between the two S atoms is 0.39 nm (0.38 nm in-plane). Its configuration is shown in Fig. 6a, and its predicted shape in STM is shown in Fig. 6b.

For an H_2S *trimer*, E_a is around 0.52 eV, implying 0.07 eV total attraction between molecules. We find three trimer configurations that have the same energy, to within a few meV, and these are shown in Fig. 7a-c. They have several features in common. First, they have two hydrogen bonds (S-H···S bonds) that link the molecules. Second, one molecule in each trimer is similar to an isolated H_2S molecule, with its S-H bonds nearly parallel to the surface and the S almost directly above a Ag atom. Third, each of the other two molecules has an S-H bond pointing down toward the surface. Fourth, the isolated-like molecules are always closer to the surface than the downward-pointing molecules, with the S atoms being 0.28-0.29 and 0.38-0.42 nm above the Ag atom plane, respectively. Fifth, the S-S separations in the S-H···S bonds span a wide range, from about 0.34 to 0.57 nm in-plane, or about 0.37

to 0.57 true distance. Sixth, the S-H···S bond angles are 161° to 178°, i.e. the hydrogen bonds are nearly linear. Finally, the predicted STM images are shown in Fig. 7d-f. In all trimers, the isolated-like molecule appears lower and slightly broader than the other two. In summary, these seven features are common to all the minimum-energy trimers that we have found.

There are also some differences among the trimers found in DFT. In the first two types (Fig. 7a-b), the isolated-like molecule is at the center, and it contributes all the hydrogen to the S-H···S bonds. Both these types of trimers are nearly isosceles triangles. In the third type, shown in Fig. 7c, the isolated-like molecule is at one end of the trimer (top of figure) instead of in the center. Of the three trimers, the third type fits the experimental *shape* best because it is the most irregular. The S-S *distances* for this trimer, from DFT, are 0.34, 0.36, and 0.54 nm (projected onto the surface plane). These can be compared to the observed values of 0.41 $\pm$ 0.02, 0.49 $\pm$ 0.03, and 0.52 $\pm$ 0.02 nm in the triangular clusters. Only one of the three values matches exactly. Nonetheless, the DFT calculations make it plausible to interpret the triangular clusters as some type of non-cyclic H_2S trimer.

In trimers a-c, molecules with S-H bonds pointing toward the Ag surface occupy a variety of sites. Referring to Fig. 7, these sites range from semi-on-top—as in the top molecule of trimer a and b, and the middle molecule of trimer c; to a nearly-perfect two-fold bridge site—as for the bottom molecule of type a and c; to a nearly-perfect three-fold hollow site—i.e. the bottom molecule of type b. This, plus the wide range of S-S separations, indicates that the intermolecular hydrogen bonds give rise to preferred local configurations, but these configurations are quite flexible and adaptable. The isolated-like molecule is more site-specific than the other two, because it is always found in an on-top site. In other words, the potential energy surface for the downward-pointing molecules is very smooth indeed.

3.4. H_2S on terraces: Extended islands at higher $\theta_{H_2S}^{rel}$

Initially after adsorption at ~30 K and at higher $\theta_{H_2S}^{rel}$, the molecules form large and irregularly-shaped islands that coexist with many small, isolated protrusions. The islands themselves have protrusions arranged in an irregular hexagonal-like packing, as shown in Fig. 8. The protrusions in these islands have the same nearest-neighbor separation, 0.40 $\pm$

0.05 nm, as the protrusions along the step edges in Fig. 1c, d, and in the pinwheel clusters in Fig. 3b, c. We hence assign them as H_2S molecules that are fixed in place by H-bonding with other molecules. These islands coexist with isolated protrusions on terraces which, as discussed already, are assigned as individual H_2S molecules.

With aging at 4.7 K, the features on the terraces change to those shown in Fig. 9. The individual H_2S molecules disappear. The islands with quasi-hexagonal packing of H_2S molecules also disappear, indicating that they must be metastable. They are replaced by islands that differ in several respects. One difference is found at the edges of the islands: instead of being irregular, the edges of the new islands sometimes consist of linear segments (facets), as shown in Fig. 9. Second is the internal structure, which exhibits a $(\sqrt{37}\times\sqrt{37})R25.3^o$ unit cell. This is shown in more detail in Fig. 10. The rows of protrusions highlighted by the rectangle of Fig. 10b have a lateral separation of 0.43 ± 0.16 nm, similar to that of other features (cf. Table I). Perhaps the most prominent features are dark triangles, which have alternating orientations, as shown in the inset to Fig. 9b.

4. Discussion

4.1. Molecular diffusion

One main experimental observation is that clusters of H_2S molecules can form upon adsorption at 20 K for low $\theta_{H_2S}^{rel}$ (pinwheel clusters), and upon adsorption at 30 K for high $\theta_{H_2S}^{rel}$ (irregular hexagonal islands). In addition, the latter clusters can rearrange over a time scale of about 20 hours at 4.7 K into $(\sqrt{37}\times\sqrt{37})R25.3^o$ islands, and simultaneously, individual H_2S molecules disappear. This requires that individual molecules can diffuse, while clusters can dissociate and/or rearrange at these temperatures, over the corresponding experimental time scales. Is this plausible? The clearest situation may be the aging experiment, since there T and $\theta_{H_2S}^{rel}$ are both constant. From Fig. 1e, a fair estimate is that a molecule must travel a distance of at least 1 nm during aging, corresponding to about 12 hops for a random walker. Assuming a frequency factor of 10^{14} s^{-1}, which is toward the high end, allows an estimate of the upper limit of the diffusion barrier, E_d, of 0.02 eV. This value would also be consistent with the fact that the adsorbate structures are static on the time scale

of STM imaging (2 hours) at 4.7 K. As discussed in Section 3.2, we have calculated from DFT that the diffusion barrier is 0.03 eV. Hence, both experiment and DFT support a small barrier of a few tens of meV.

Let us compare this with diffusion of H_2O on Ag(111). The upper limit of E_d for H_2O on Ag(111) has been estimated, from experimental data, at 0.2 eV.[20] From DFT, an alternate estimate for E_d is given by the difference in adsorption energies between the most-favorable site and next-most-favorable site. This difference is 0.050 eV from the present work, and 0.04 eV from others'.[44] If we focus on values of E_d for H_2O and H_2S from our calculations (to make the comparison as valid as possible), then the two values of E_d are fairly close: 0.050 eV and 0.031 eV, respectively. This similarity in E_d parallels the similarity in adsorption energies for isolated H_2O and H_2S: 0.14 eV and 0.15 eV respectively, from our calculations.

4.2. Molecular interactions

From the experimental data, the lateral separation of protrusions in clusters on terraces, or along step edges, is consistently close to 0.4 nm. See Table I. The nearest-neighbor S-S separations in crystalline H_2S are 0.40 and 0.42 nm.[45] (This is considerably longer than the O-O separation in crystalline H_2O, 0.28 nm.[46]) Therefore, we suggest that protrusions separated by 0.4 nm are individual molecules, at least some of which are linked by hydrogen bonds.

Our DFT calculations show that two types of molecules should be expected in H-bonded clusters: Molecules similar to isolated, adsorbed H_2S, and molecules with one S-H bond pointing down into the surface. The latter are farther from the surface than the former, and are predicted to be higher (brighter) in STM images, regardless of whether these molecules are hydrogen acceptors (as in Fig. 7a-b) or hydrogen donors (Fig. 7c). The molecules with one S-H bond pointing toward the surface have especially low site-specificity. The DFT calculations indicate that clusters of three molecules, linked by two hydrogen bonds, are stable relative to isolated molecules. The triangular clusters observed in experiment (Fig. 5) might be such clusters.

Larger clusters and islands also form. While we are not able to propose specific models at this time, the fact that the potential energy surface is very smooth makes coincidence lattices and metastable structures very plausible. One such extended structure has a $(\sqrt{37}\times\sqrt{37})R25.3^{o}$ unit cell. The same unit cell has been reported for H_2O on Pt(111), and a hydrogen-bonded structure was proposed.[47-49] However, the proposed structure does not match the features in our STM images, indicating that the molecular arrangement within the unit cell may be different for H_2S than for H_2O. Indeed, one would expect the molecular arrangement to be different, given the large difference in the O-O and S-S bond lengths in the solid ices (0.40-0.42 and 0.28 nm, respectively).

5. Conclusions

H_2S forms a rich variety of structures on Ag(111) at low temperature and at submonolayer coverage. The molecules decorate step edges, exist as isolated entities on terraces, and aggregate into clusters and islands, under the various conditions of our experiments. The typical molecular separation in the clusters and islands is 0.4 nm, the same as that in crystalline H_2S. The potential energy surface for adsorption and diffusion is very smooth.

Note added in proof. We recently became aware of a paper describing a new model for the $(\sqrt{37}\times\sqrt{37})R25.3°$ structure of H_2O on Pt(111), based on STM images and DFT calculations.[50]

Acknowledgments

We thank James W. Evans, Gordon J. Miller, and Jakoah Brgoch for useful discussions and helpful insights. The experimental component of this work was supported by three sources: NSF Grant CHE-0809472; a Grant-in-Aid for Scientific Research on Priority Areas “Electron Transport Through a Linked Molecule in Nano-scale”; and a Grant-in-Aid for Scientific Research(S) “Single Molecule Spectroscopy using Probe Microscope” from the Ministry of Education, Culture, Sports, Science, and Technology (MEXT) of Japan. The theoretical component of this work was supported by the Division of Chemical Sciences, BES, US Department of Energy (USDOE).

Figures

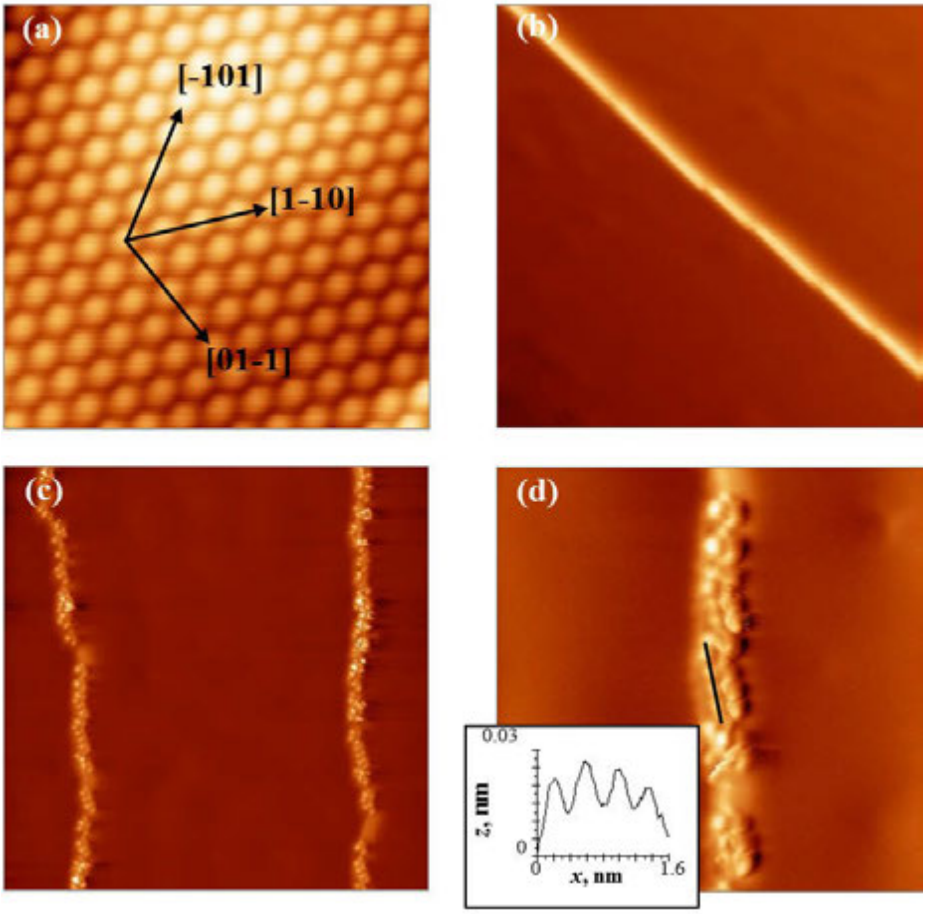

This figure continues on the following page.

Figure 1: (a) Clean Ag(111) substrate. Raw image at 1.00 nA, -100 mV, 3.6×3.7 nm^2. Close-packed directions are shown for reference, and they apply to all other images. Note that there is some deviation from ideal hexagonal packing, which is due to slight miscalibration of the XY piezoelectrics in the STM scanner. This distortion is corrected whenever distances are reported in the paper. (b-f) Images are differentiated. (b) Clean surface step. I = 0.92 nA, V_{sample} = 284 mV, 27.8×28.6 nm^2. (c, d) Step edges at low $\theta_{H_2S}^{rel}$, I = 0.20 nA, V_{sample} = 10 mV, scales of 27.8×28.6 nm^2 and 11.1×11.4 nm^2, respectively. In Panel (c), the inset shows a line profile of the topography image illustrating the peak-to-peak separation of protrusions along the step edges: 0.37 nm, 0.41 nm, and 0.36 nm. (e) Step edge at higher $\theta_{H_2S}^{rel}$ before aging, 0.84 nA, -50 mV, 27.8×28.6 nm^2. A portion of the main image, indicated by the box, is shown at higher magnification (image size of 2.6×2.7 nm^2) to highlight the isolated protrusions. (f) Step edge at higher $\theta_{H_2S}^{rel}$ after aging, I = 0.78 nA, V_{sample} = -100 mV, 27.8×28.6 nm^2. A portion of the main image, indicated by the box, is shown at higher magnification (I = 0.70 nA, V_{sample} = 28 mV, 11.1×11.4 nm^2) to highlight an example of an island, which has partially filled in the area between step edges, as discussed in the text.

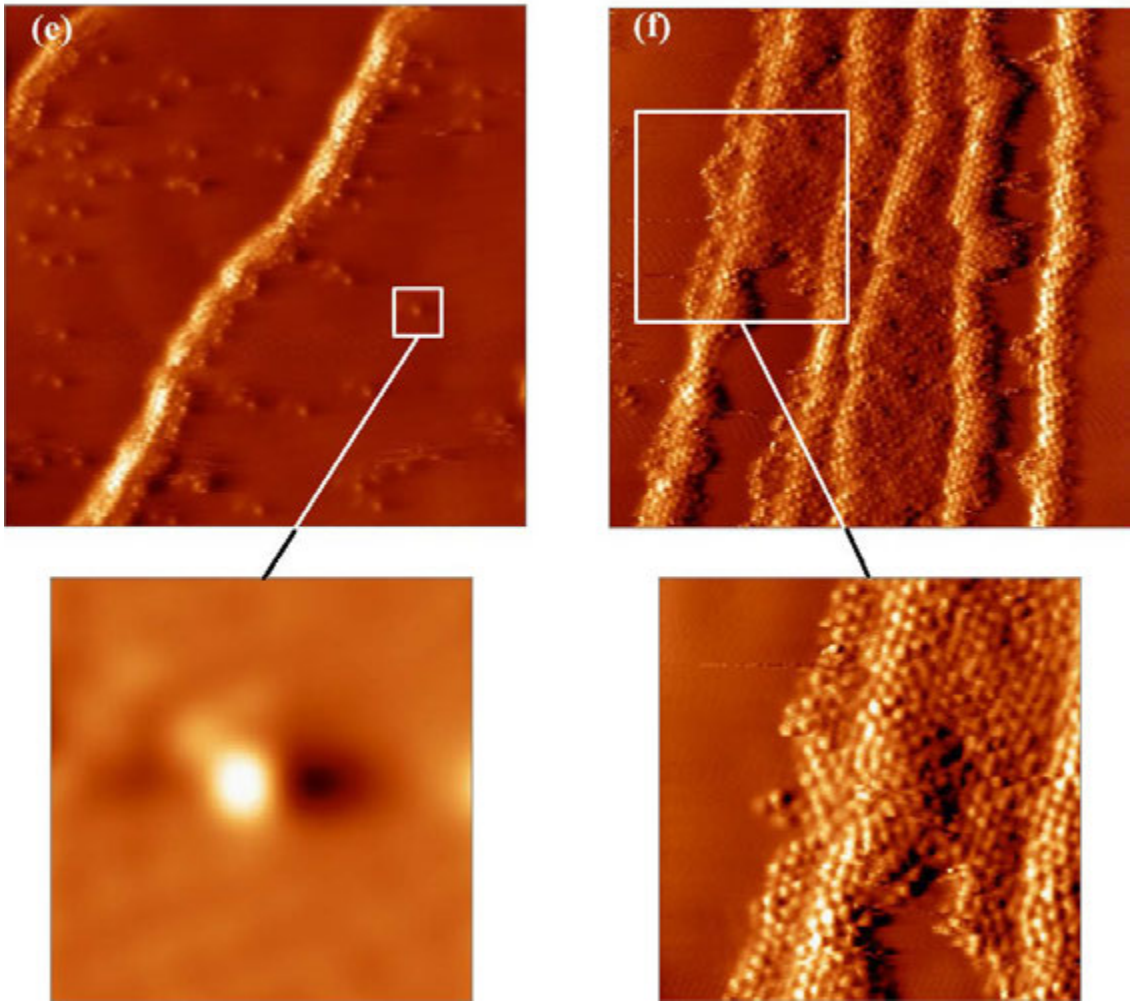

Figure 1: continued

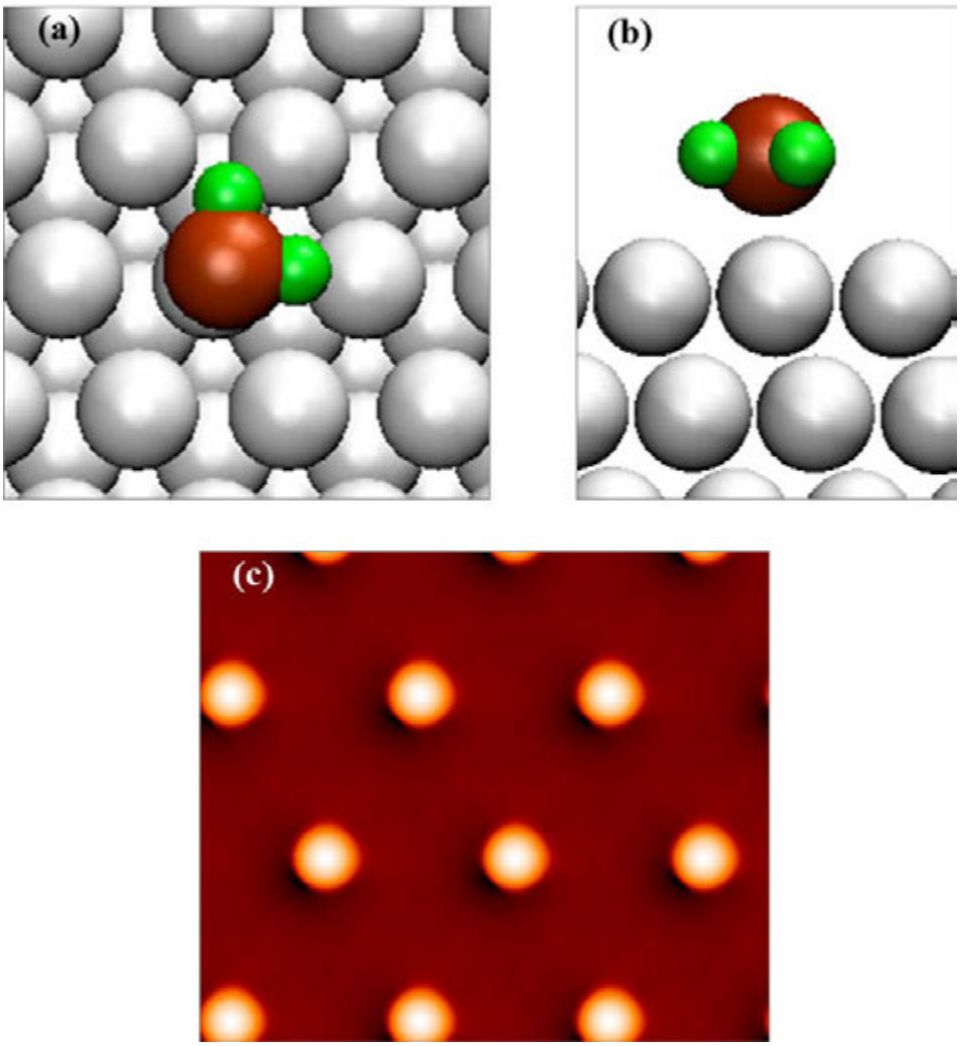

Figure 2: (a, b) Configuration of a H_2S monomer on Ag(111) optimized using DFT. The red sphere is a S atom, the green spheres are H atoms, and the grey spheres are Ag atoms. Results are obtained using a five-layer slab and 4×4 supercell. (c) Simulated STM image using the Tersoff-Hamann method.

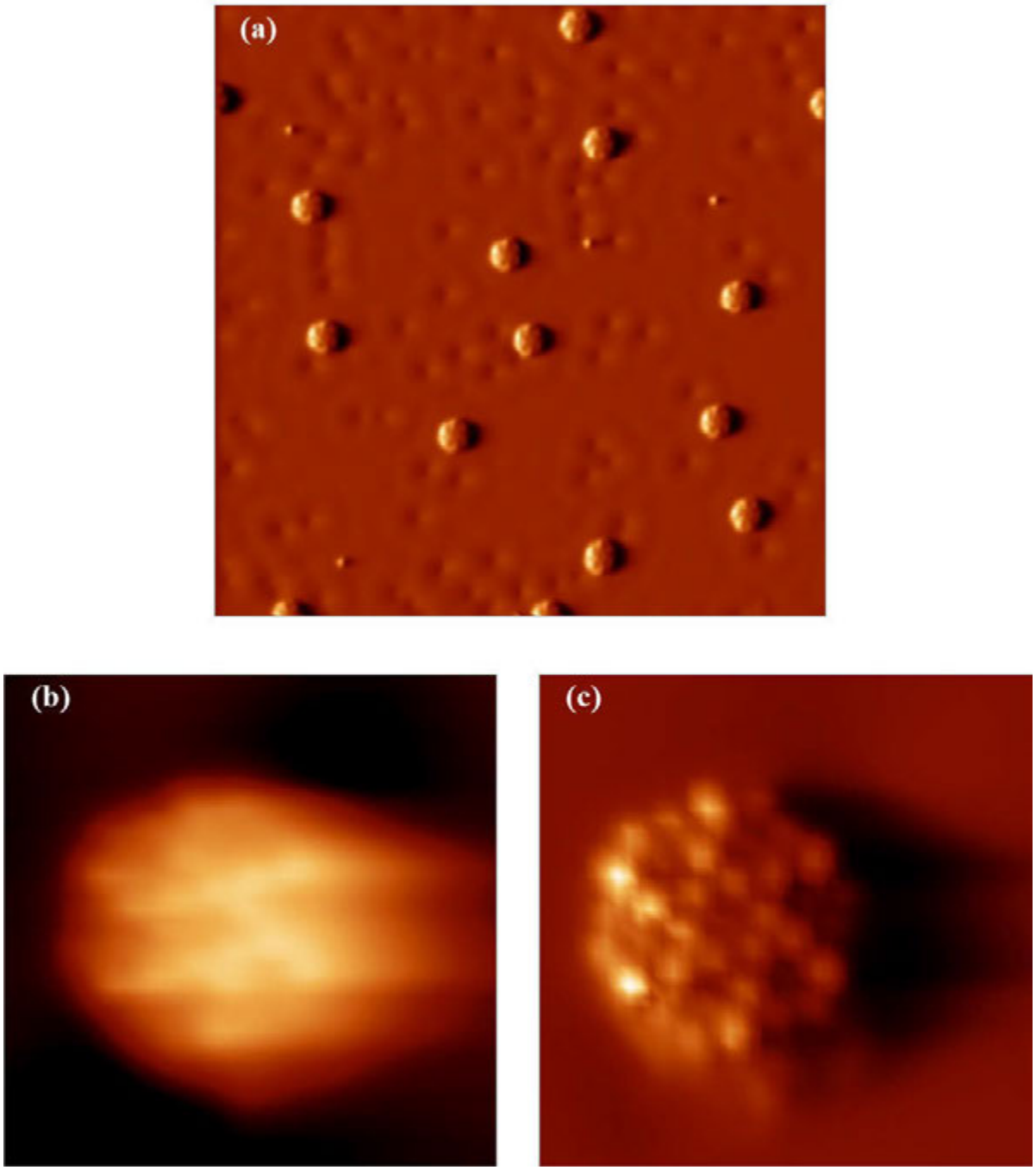

Figure 3: Isolated pinwheel clusters on terraces at low $\theta_{H_2S}^{rel}$. (a) I = 1.00 nA, V_{sample} = 100 mV, 55.6×57.2 nm^2, differentiated. (b) Untreated STM image, I = 1.00 nA, V_{sample} = 50 mV, 4.9×5.0 nm^2; and (c) differentiated form of (b).

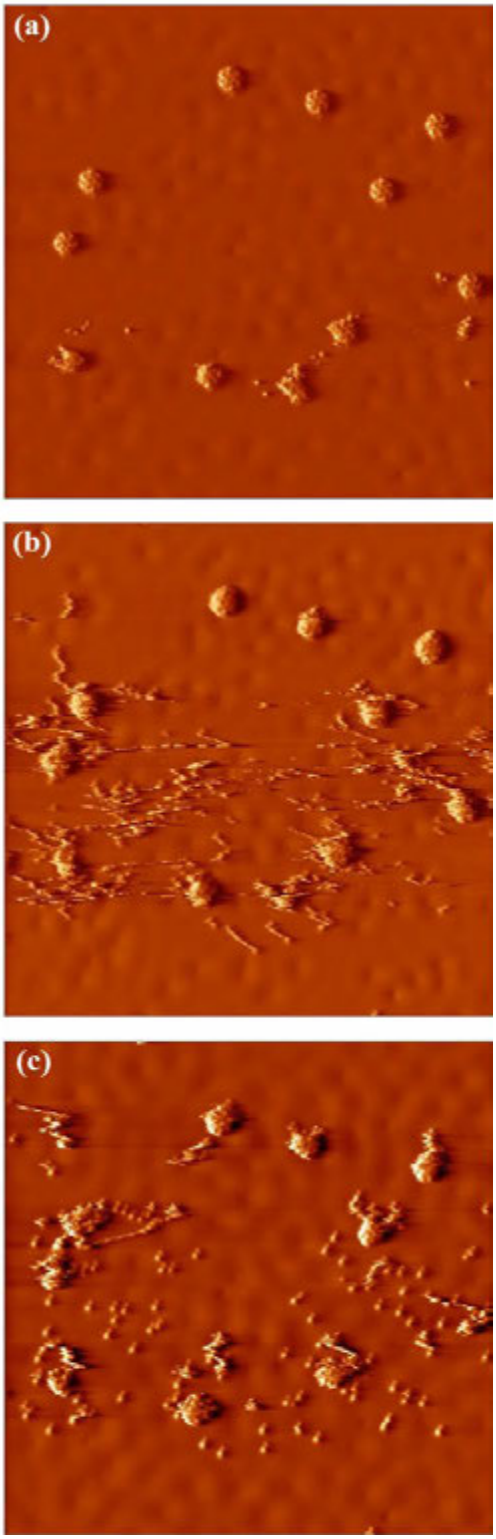

Figure 4: Dissociation of pinwheel H_2S clusters. (a) I = 1.00 nA, V_{sample} = 50 mV, (b) I = 1.00 nA, V_{sample} = 100 mV, (c) I = 0.500 nA, V_{sample} = 10 mV. All are 55.6×57.2 nm^2 and differentiated.

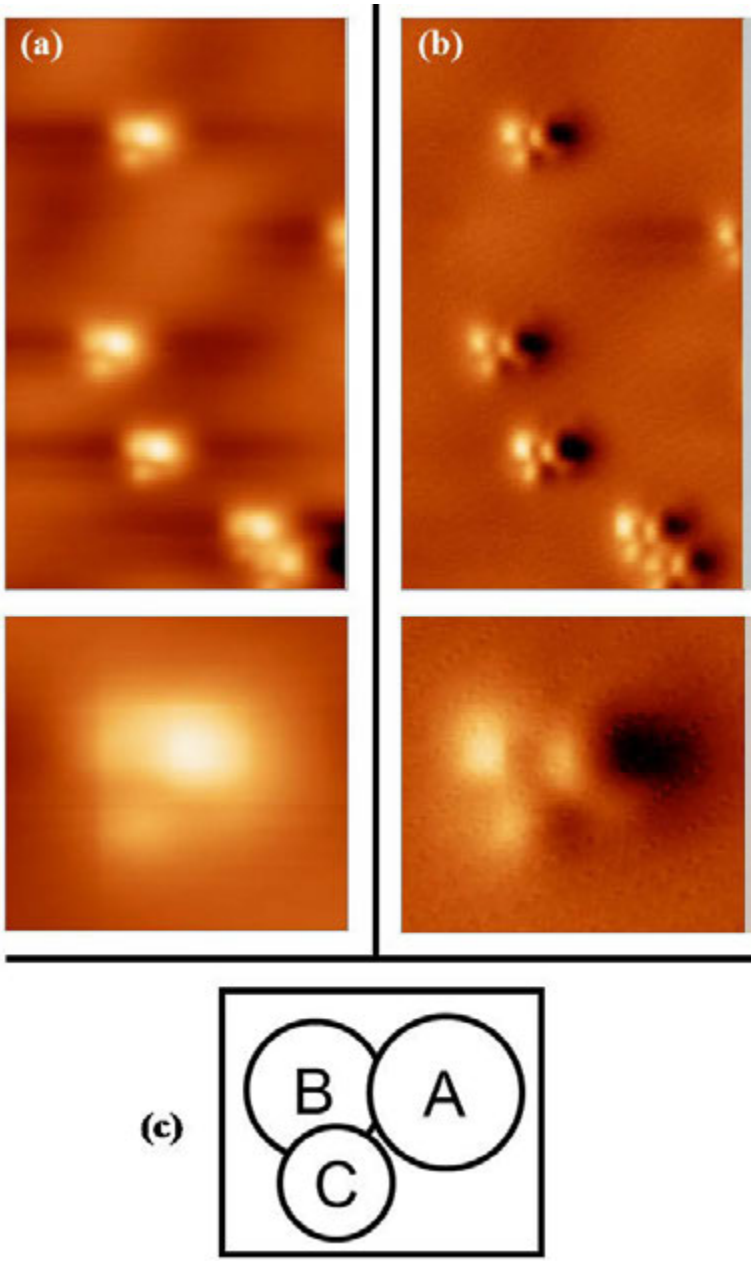

Figure 5: Isolated triangular clusters at low $\theta_{H_2S}^{rel}$. (a) Untreated image at I = 0.12 nA, V_{sample} = 5 mV, and (b) differentiated form of (a). Upper image sizes: 6.7×11.4 nm^2. Lower image sizes: 2.1×2.1 nm^2. (c) Schematic of protrusions in triangular clusters.

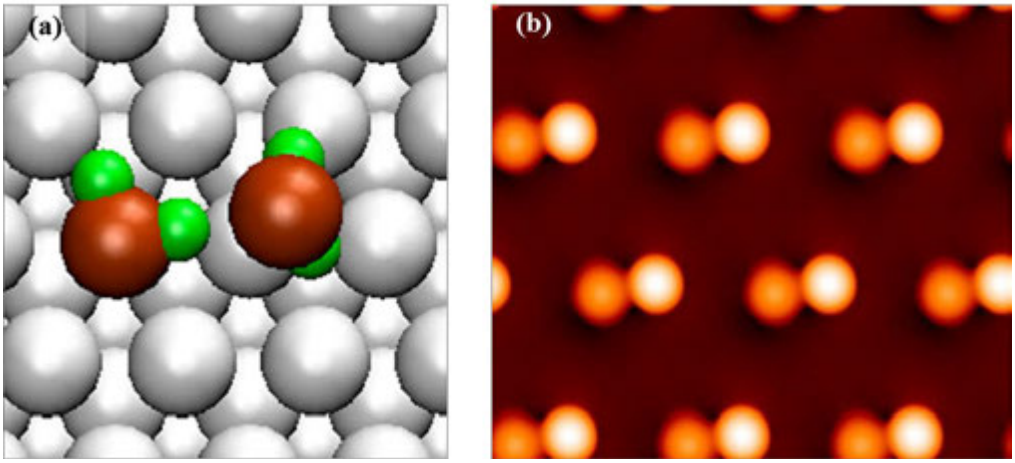

Figure 6: (a) Configuration of a H_2S dimer on Ag(111) optimized using DFT. The red spheres are S atoms, the green spheres are H atoms, and the grey spheres are Ag atoms. Results are obtained using a five-layer slab and 4×4 supercell. (b) Simulated STM image using the Tersoff-Hamann method.

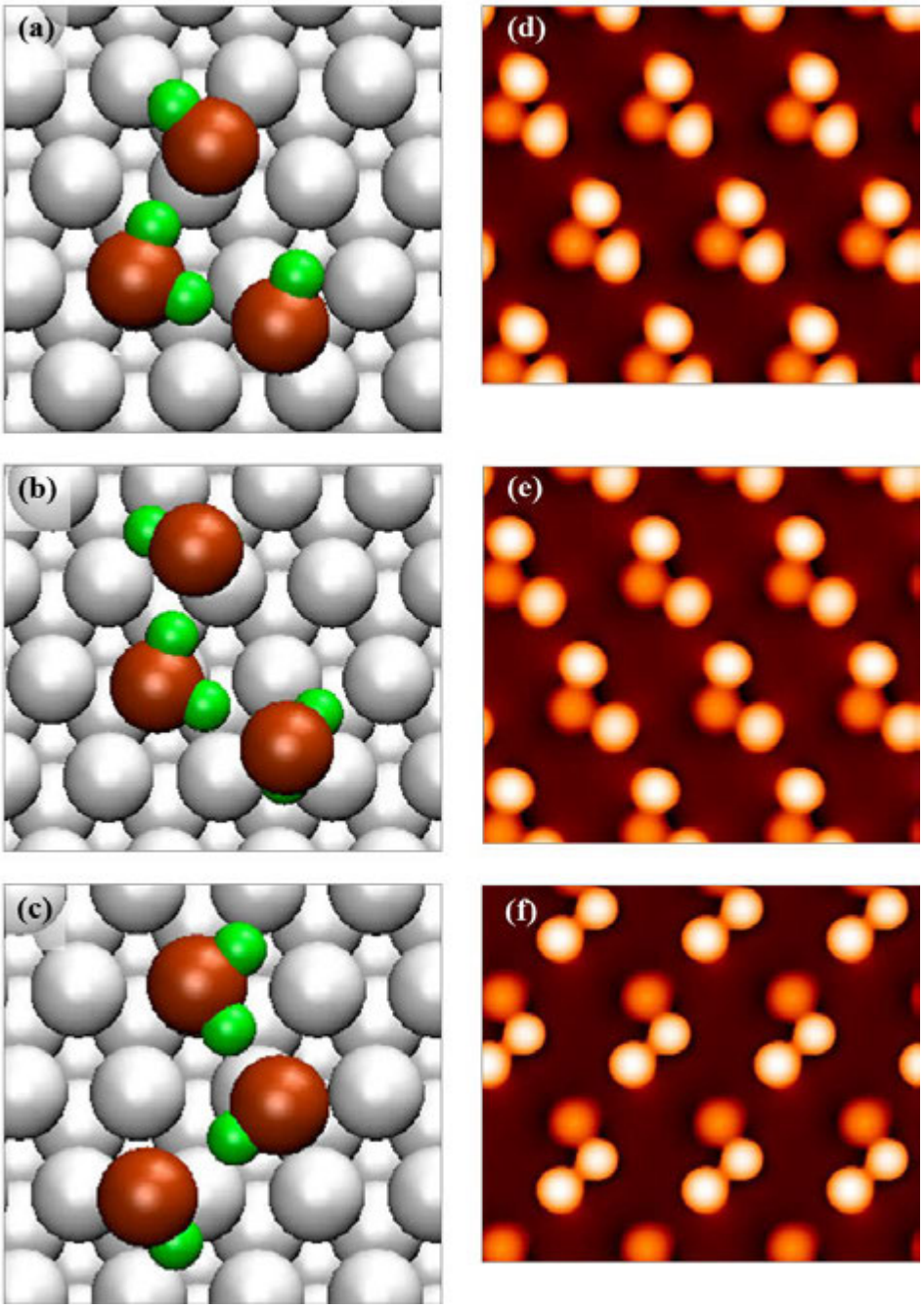

Figure 7: (a-c) Configurations of a H_2S trimers on Ag(111) optimized using DFT. The red spheres are S atoms, the green spheres are H atoms, and the grey spheres are Ag atoms. Results are obtained using a five-layer slab and 4×4 supercell. (d-f) Simulated STM image using the Tersoff-Hamann method.

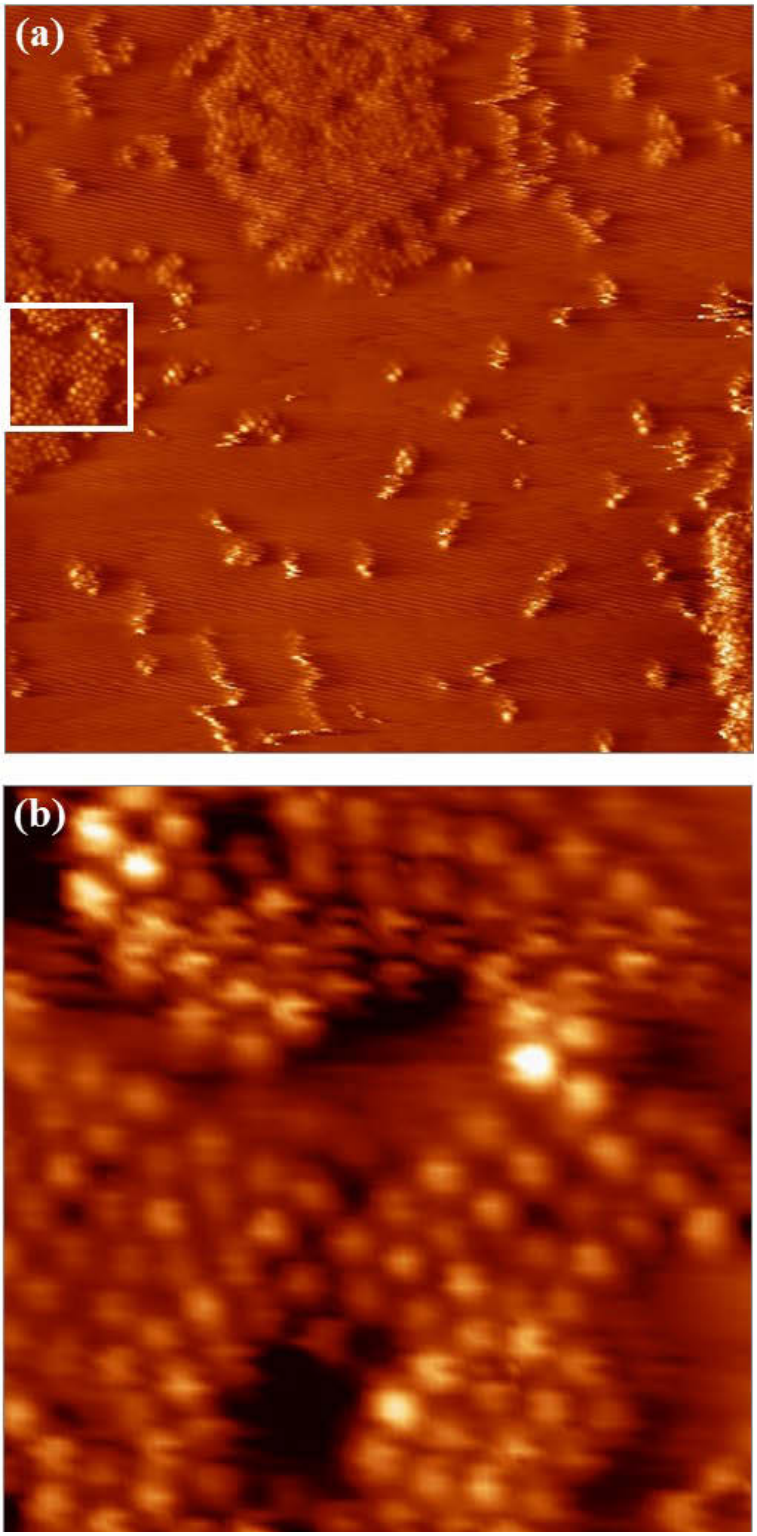

Figure 8: H_2S islands at higher $\theta_{H_2S}^{rel}$ before aging. I = 0.6611 nA, V_{sample} = -77.98 mV. Images are differentiated. (a) 33.4×34.3 nm^2 and (b) area marked in (a), 5.4×5.6 nm^2.

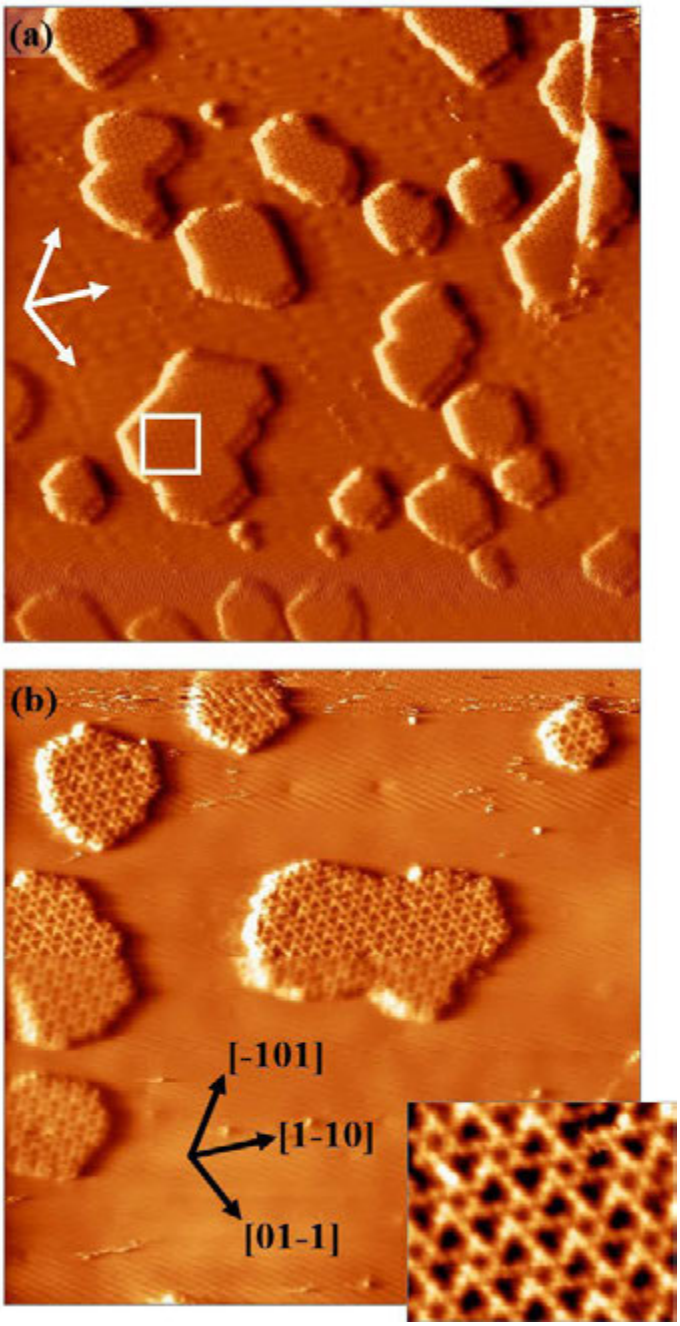

Figure 9: H_2S islands at higher $\theta_{H_2S}^{rel}$ after aging. (a) I = 1.3 nA, V_{sample} = 112 mV, 100×100 nm^2; and (b) I = 1.0 nA, V_{sample} = -140 mV, 55.6×57.2 nm^2 and the inset detail of the large island, 7.3×6.1 nm^2. Images are differentiated. Differentiation does not distort original features or introduce new features; it only extenuates the original features. Axis vectors are along the close packed directions as shown in Fig. 1(a). Note that in Fig. 9(a), there is a double tip effect that makes the lower right edges of islands appear to contain a double step, but this is not real.

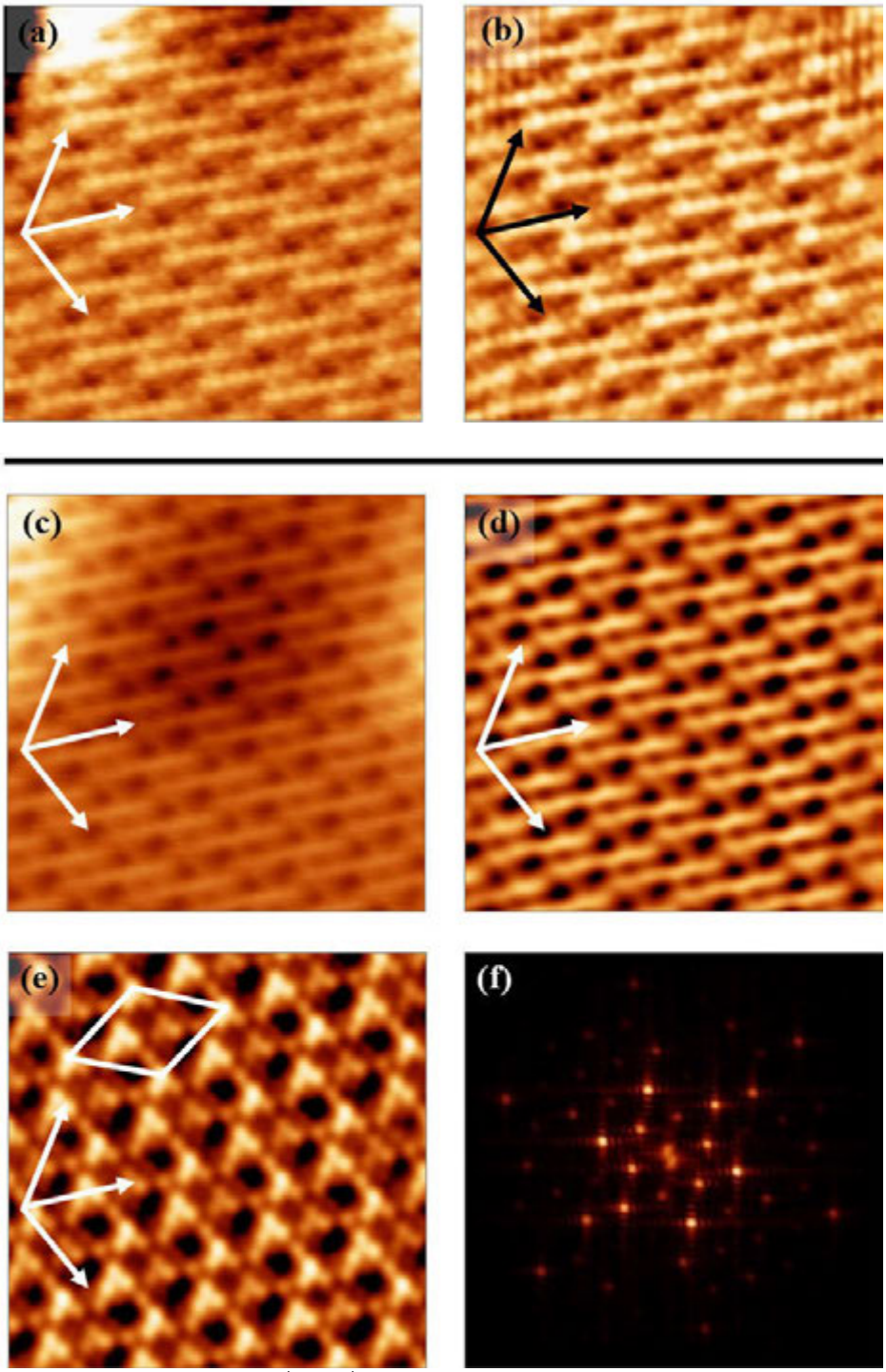

Figure 10: Fine structure of the (√37×√37)R25.3º lattice inside the largest island in Fig. 9A. Vectors show the close packed directions as in Figs. 1a and 9. (a) Raw image, I = 1.0 nA, V_{sample} = 50 mV, 11.1×11.4 nm^2. (b) Same as image (a) after Fourier transform (FT) filtering. (c) Raw image, I = 1.0 nA, V_{sample} = 46 mV, 11.1×11.4 nm^2. (d) Same as image (c) after FT filtering. (e) Differentiated version of (d), 7.8×8.0 nm^2, containing a rhombus showing the unit cell. (f) FT of (e).

Table I: Sizes and separations of protrusions in STM images. The values are all derived from raw data, i.e. with no image processing. The a-b-c notation for the isolated triangular clusters is defined in Fig. 5c. Uncertainties equal one standard deviation. Additional measurements are shown in Table .

Identity / environment of the protrusion	**Closest separation between protrusions, nm**
Step edge, low coverage	0.45 ± 0.06
Step edge, higher coverage, before aging	0.38 ± 0.05
Step edge, higher coverage, after aging	0.38 ± 0.05
Isolated pinwheel clusters	0.39 ± 0.07
Isolated triangular clusters	0.41 ± 0.02 $\overline{AB}$ 0.52 ± 0.02 $\overline{BC}$ 0.49 ± 0.03 $\overline{CA}$
Irregular islands with quasi-hexagonal internal packing	0.40 ± 0.05
(√37×√37)R25.3° islands	0.43 ± 0.16

Appendix 1. Additional measurements

Table A1.I. Sizes and separations of protrusions in STM images. The values are all derived from raw data, i.e. with no image processing. The a-b-c notation for the isolated triangular clusters is defined in Fig. 5c. Uncertainties equal one standard deviation. Measurements from drift corrected images are in regular type. Measurements from uncorrected images are lighter and italicized.

Identity / environment of the protrusion	FWHM (nm)	Closest separation between protrusions (nm)	Closest separation between features (nm)	FWHM of features (cluster or island) (nm)	Height (nm)	Angle (°)
Step edge, low coverage	~0.37 ± 0.02 *v. difficult to measure*, N = 5 *~0.25*	0.45 ± 0.06 0.387 to 0.598 N = 14 *0.42 ± 0.09*	–	–	0.01 ± 0.004 N = 9 *0.0060 ± 0.0009*	–
Step edge, higher coverage, before aging	*0.26 ± 0.04*	*0.38 ± 0.05*	–	–	*0.0057 to 0.051*	–
Step edge, higher coverage, after aging	0.31 ± 0.01 N = 7 *0.26 ± 0.04*	0.38 ± 0.05 0.271 to 0.500 N = 31 *0.38 ± 0.05*	–	–	0.072 ± 0.02 N = 12 *0.036 to 0.19*	–
Isolated protrusions on terraces, higher coverage, before aging	*0.56 ± 0.04*	–	–	–	*0.027 ± 0.004*	–
Isolated pinwheel clusters, low coverage	*0.29 ± 0.03*	*0.39 ± 0.07*	21 ± 8 6.60 to 34.8 N = 67	3.0 ± 0.2 clusters N = 20 *~5*	0.19 ± 0.01 N = 20 *0.19 ± 0.01*	–
Isolated triangular clusters, low coverage	0.70 ± 0.06 a 0.61 ± 0.06 b 0.63 ± 0.06 c N = 3 *0.83 ± 0.01 a* *0.72 ± 0.04 b* *0.51 ± 0.55 c*	0.41 ± 0.02 ab 0.52 ± 0.02 bc 0.49 ± 0.03 ca N = 3 *0.42 ± 0.02 ab* *0.47 ± 0.04 bc* *0.51 ± 0.02 ca*	3 ± 1 N = 2	–	0.0670 ± 0.0005 a 0.05 ± 0.01 b 0.05 ± 0.03 c N = 3 *0.065 ± 0.008*	61 ± 5 abc 45 ± 5 bca 63 ± 4 cab N=3 *73 ± 2 abc* *40 ± 2 bca* *57 ± 2 cab*

Table A1.I. continued

Identity / environment of the protrusion	FWHM (nm)	Closest separation between protrusions (nm)	Closest separation between features (nm)	FWHM of features (cluster or isl.) (nm)	Height (nm)	Angle (°)
Irregular isl. w/ quasi-hexagonal internal packing, high coverage	*0.26 ± 0.04*	*0.40 ± 0.05*	–	–	*0.05 ± 0.01*	–
(√37×√37)R25.3° isl., high coverage	0.36 ± 0.04 N = 24 *0.26 ± 0.04*	0.43 ± 0.16 0.233 to 0.947 N = 50 *0.54 ± 0.22*	15 ± 9 3.23 to 38.0 N = 40	11×11 ± 5×5 isl. 2.65^2 to 21.3^2 N = 15 based on area	0.19 ± 0.04 *0.13 ± 0.05*	–
Ag(111) lattice	–	0.288 ± 0.001 [-101] 0.288 ± 0.002 [1-10] 0.287 ± 0.004 [01-1]	–	–	*0.16 ± 0.02 step edge corrected to* 0.204 ± 0.03	59.4 ± 0.5 [-101]-[1-10] 59.5 ± 0.6 [1-10]-[01-1] 61 ± 1 [01-1]-[101]

Appendix 2. Room temperature H_2S exposure

Hydrogen sulfide did not dissociate under the experimetnal conditions described in the main body of the chapter. We exposed H_2S in very high doses (10^{-5} Torr) at room temperature, in an effort to promote dissociation and S adsorption. The sample was transfered to the exchange chamber for the high exposures to proctect the vacuum quality in the preparation and STM chambers. Unfortunately, the background pressure in the exchange chamber was 10^{-7} Torr, so contaminate adsorption on the surface cannot be ruled out.

After exposing 1755 L H_2S, step edges and narrow terraces are heavily decorated with a variety of protrusions. A region in Fig. A2.2c contains and adsorbed row structure. In addition, unknown species are observed on terraces as depressions regardless of tunneling conditions, see Fig. A2.2a. Allowing this surface to warm to 100 – 250 K, by holding the sample out of the STM cryostat for 20 min, induced a more organized structure on the surface as shown in Fig. A2.3. along the step edge, protrusions are closely packed. The narrow terraces also exhibit the row structure observed before warming and ladders of dimers of protrusions. In the bottom right corner of Fig. A2.3b, two row domains are rotated by 30°.

Exposing the Ag(111) surface to nearly twice the H_2S, and holding the sample at room temperature for 90 min, followd by resting at 100 – 250 K for 20 min, resulted in large ordered islands, shown at various scales in Fig. A2.4, in addition to significant adsorption of something imaged as depressions with positive or negative bias. The structure appears similar to the ladder of dimer of protrusions observed with 1755 L H_2S in Fig. A2.3.

After exposing 6931 L H_2S, the surface appears disordered, with some indication of a prefered arrangement of the surface species observed as a dimer of protrusions, Fig. A2.7.

Figures

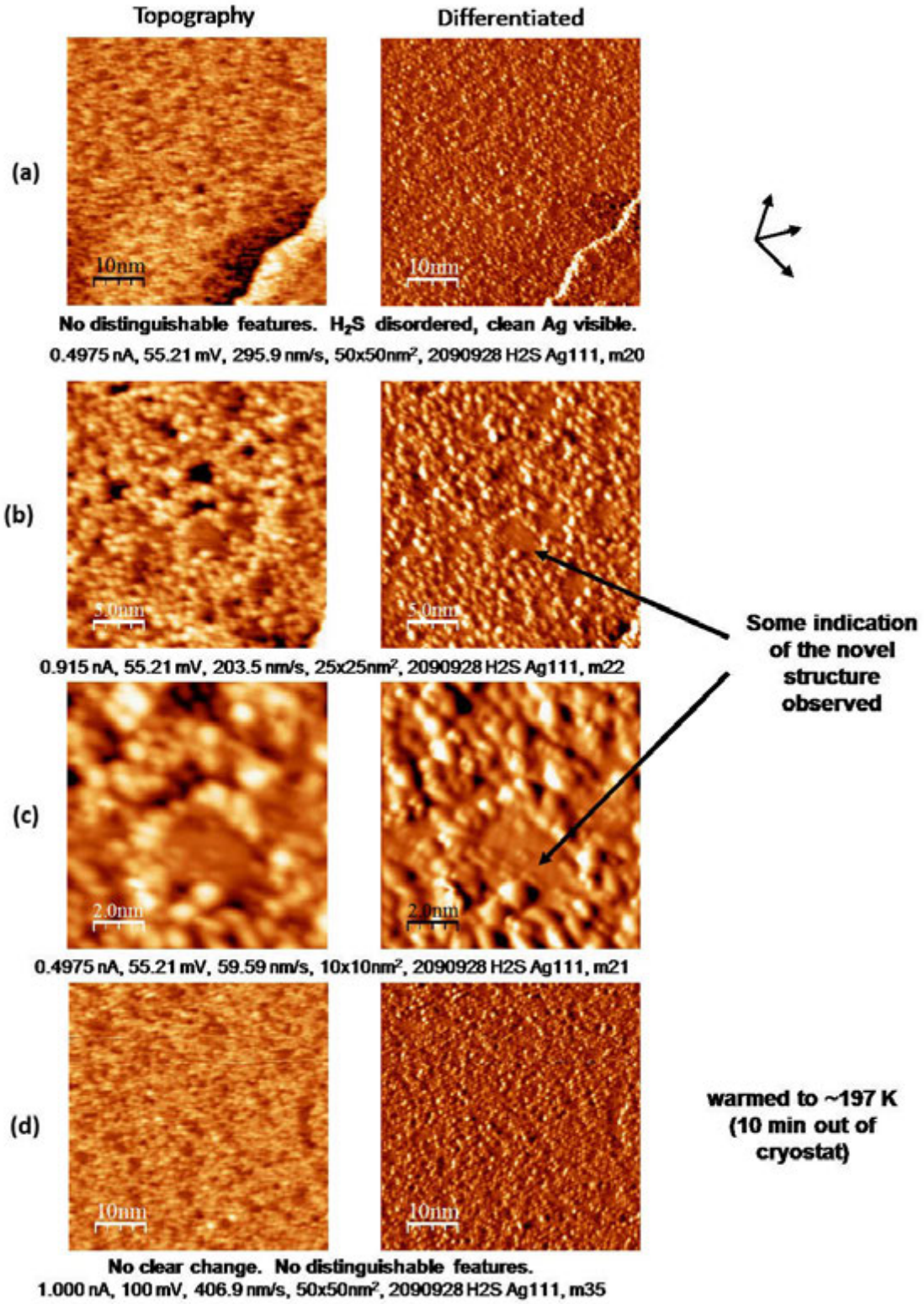

Figure A2.1.

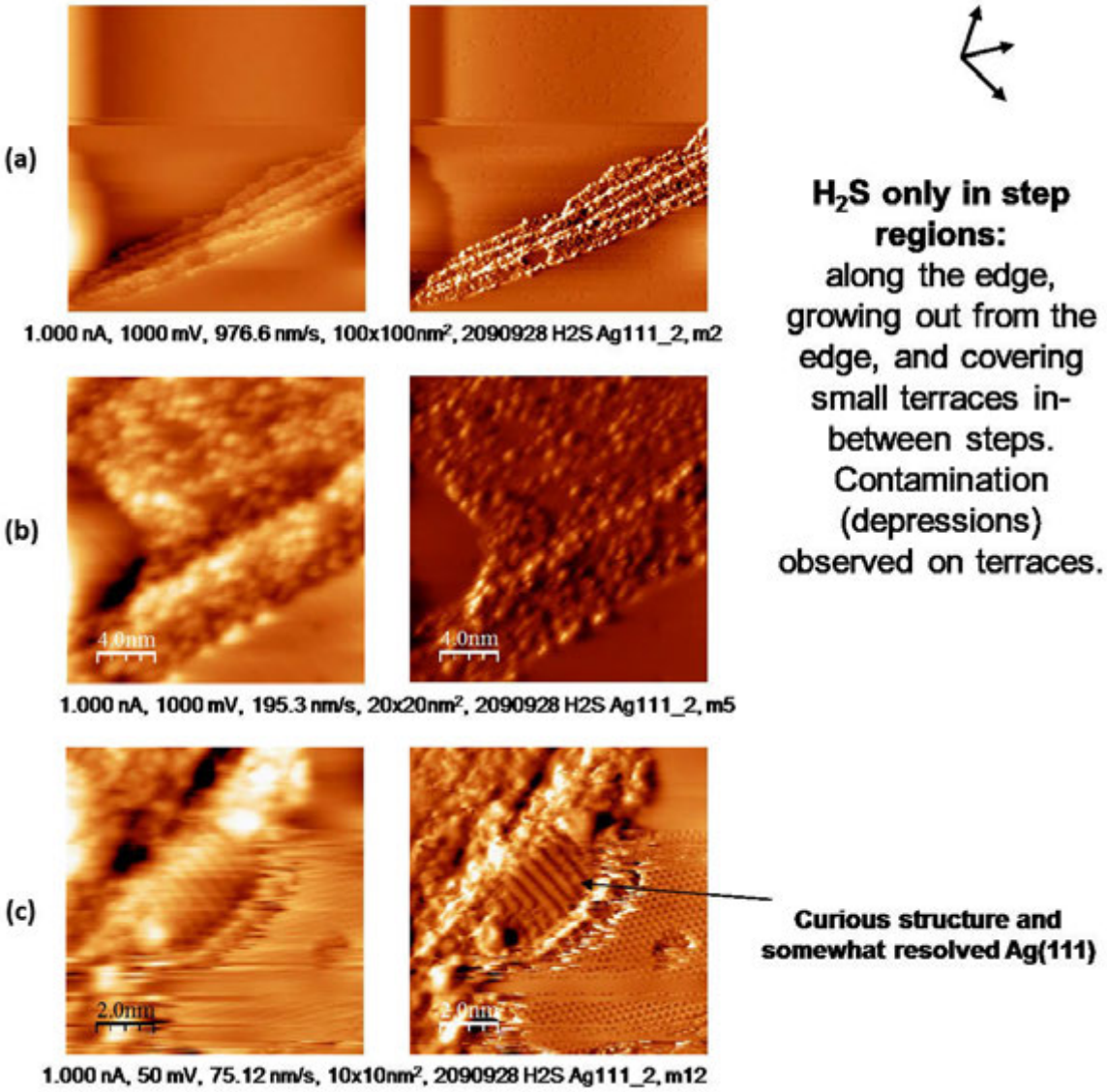

Figure A2.2.

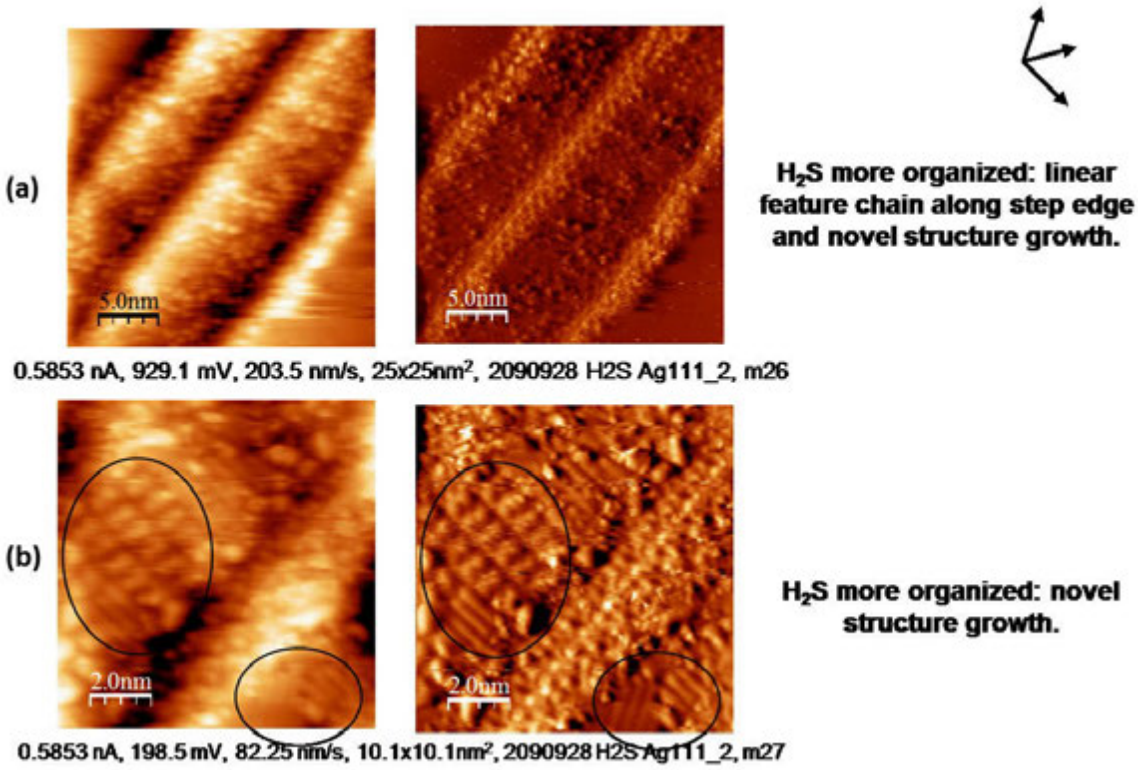

Figure A2.3.

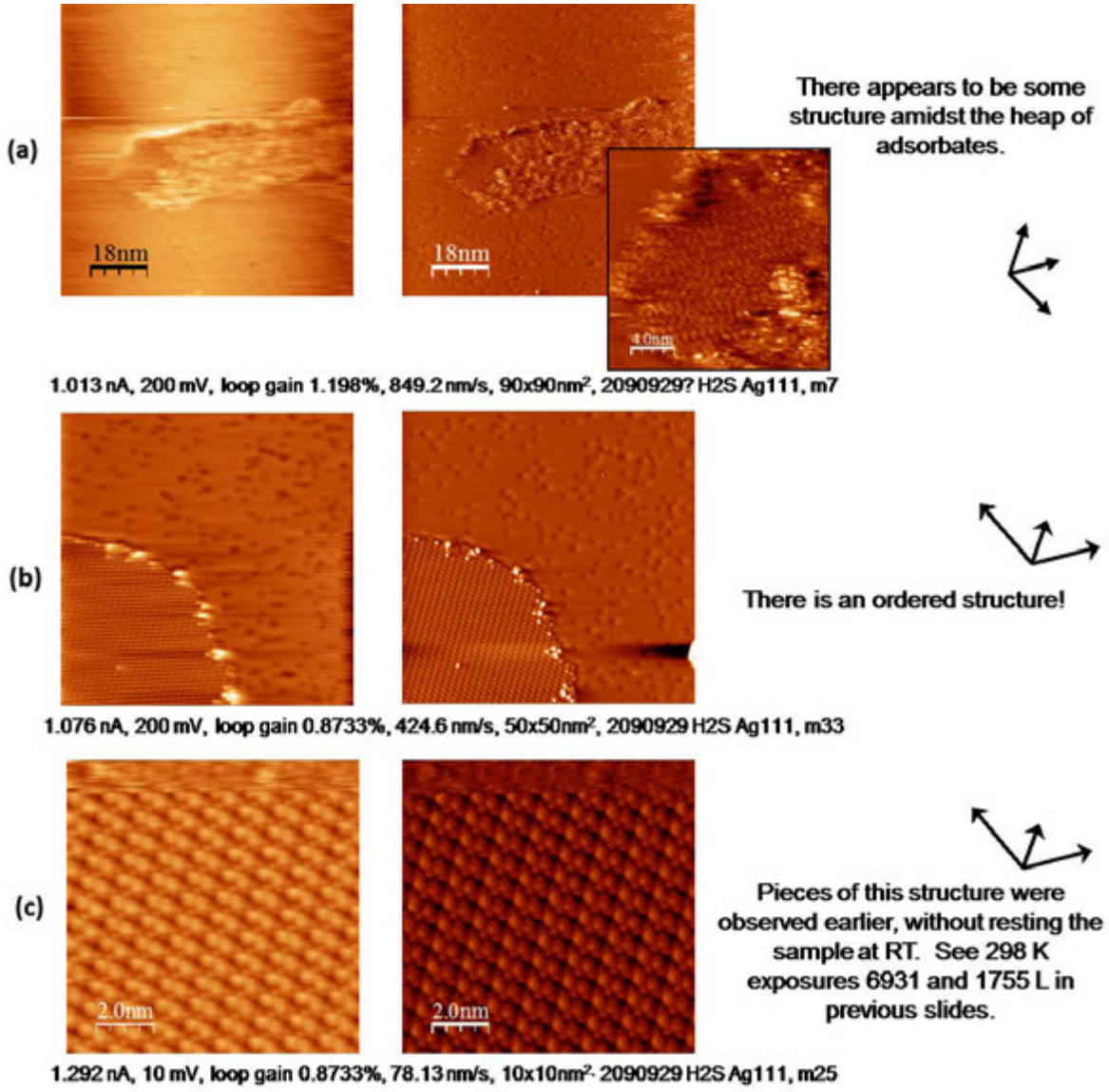

Figure A2.4.

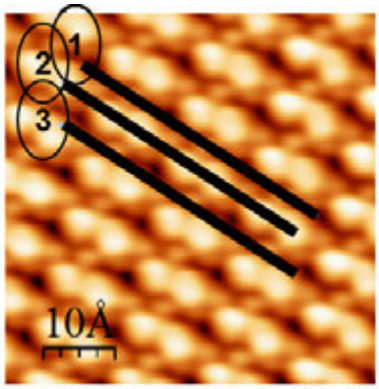

1.292 nA, 10 mV, loop gain 0.8733%, 78.13 nm/s, 5x5nm², 2090929 H2S Ag111, m25, digitally zoomed in

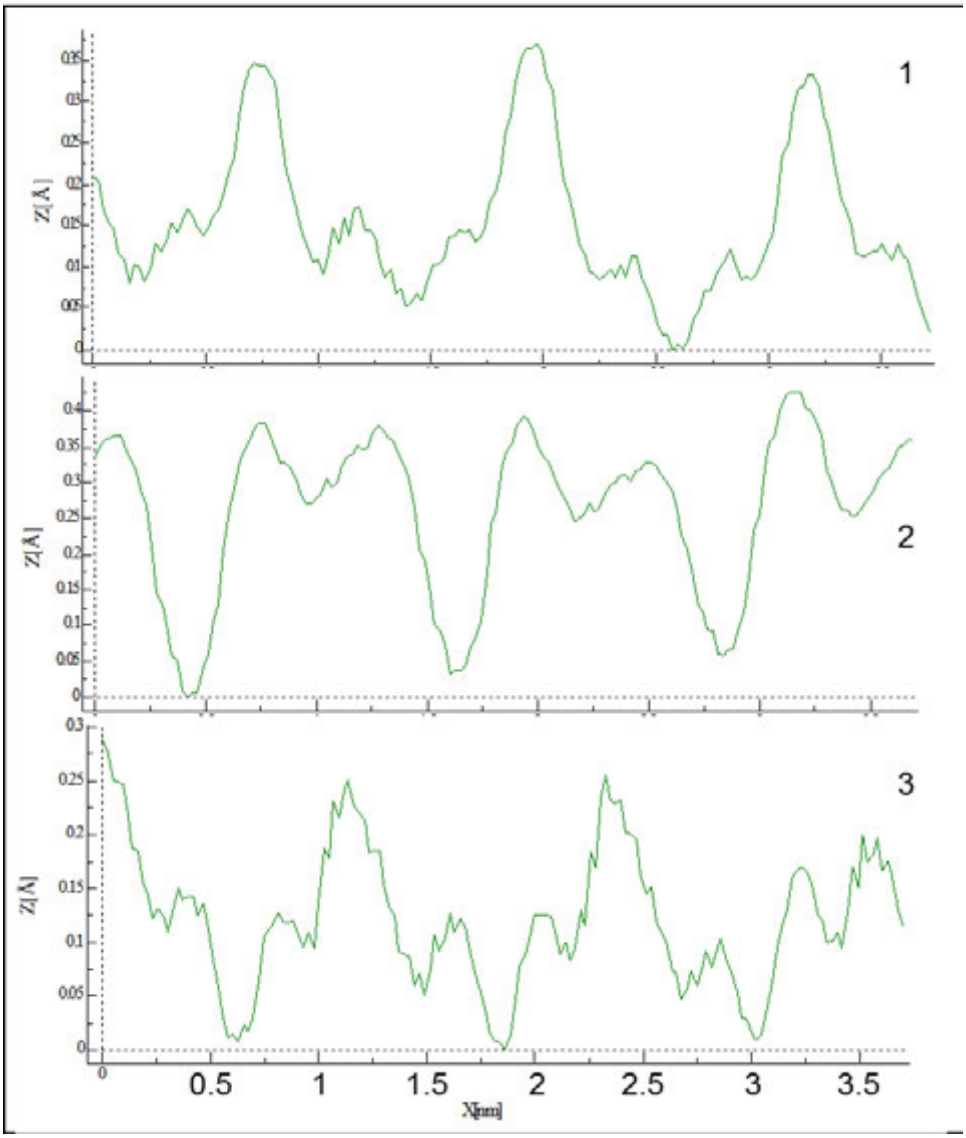

Figure A2.5.

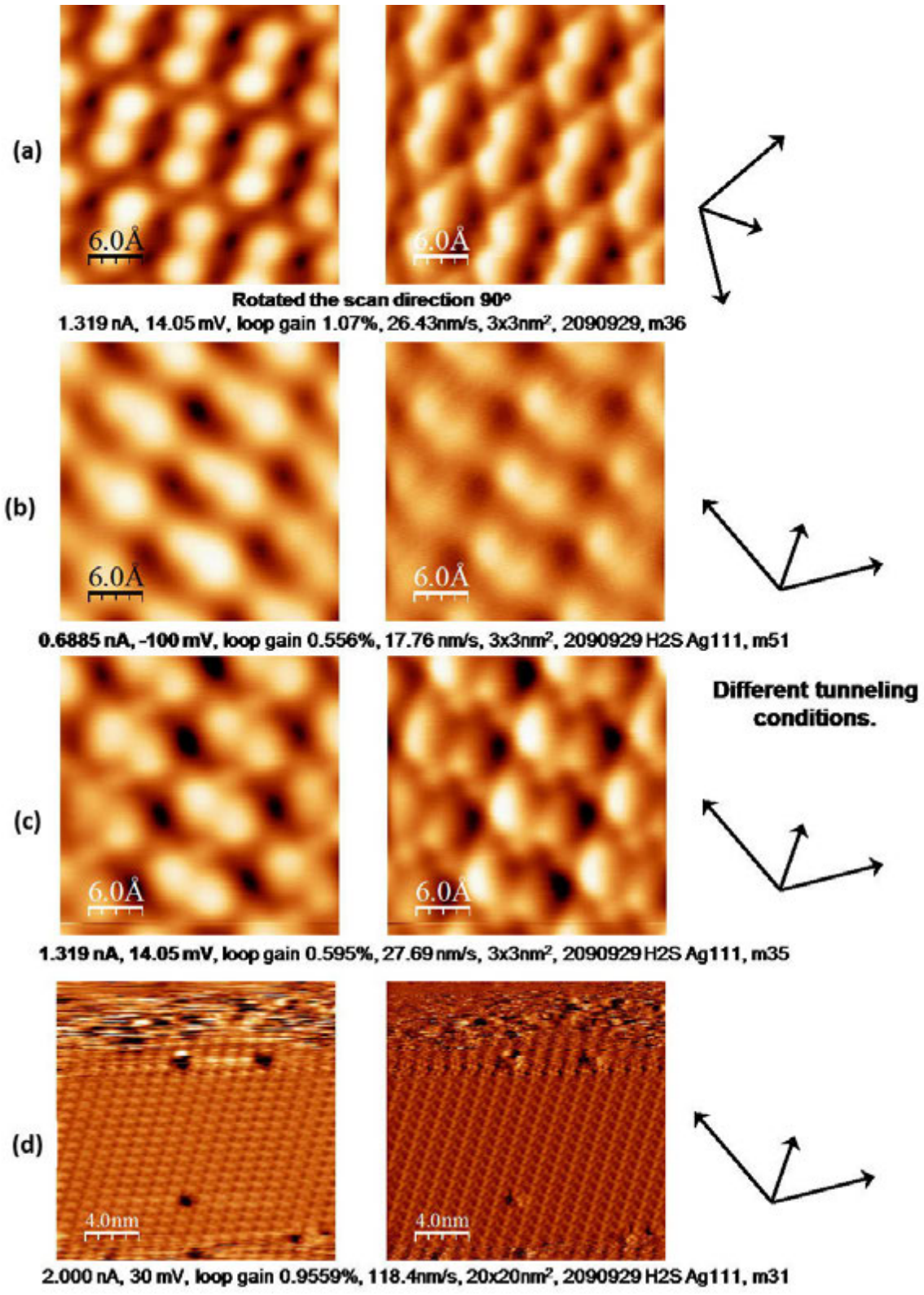

Figure A2.6.

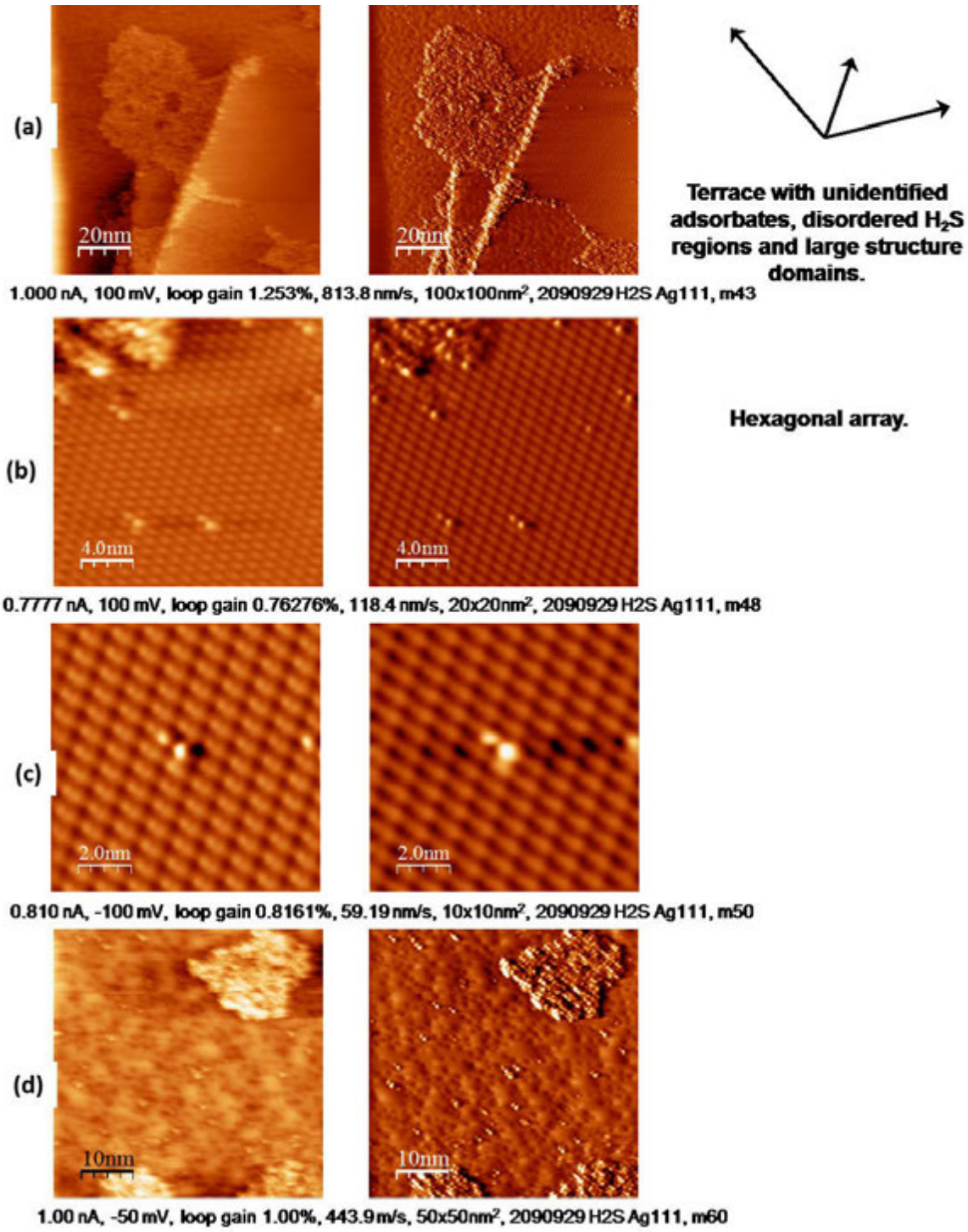

Figure A2.7.

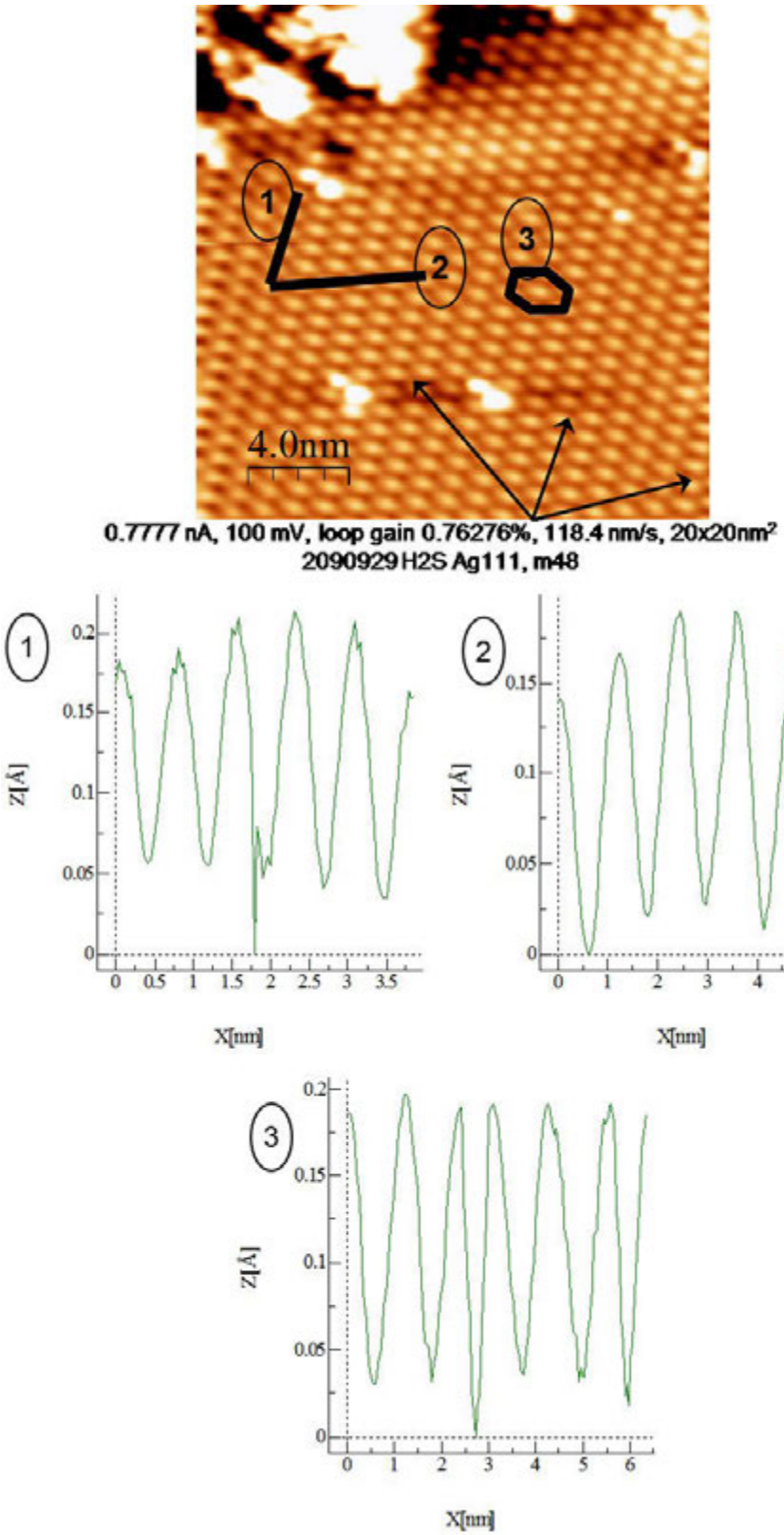

Figure A2.8.

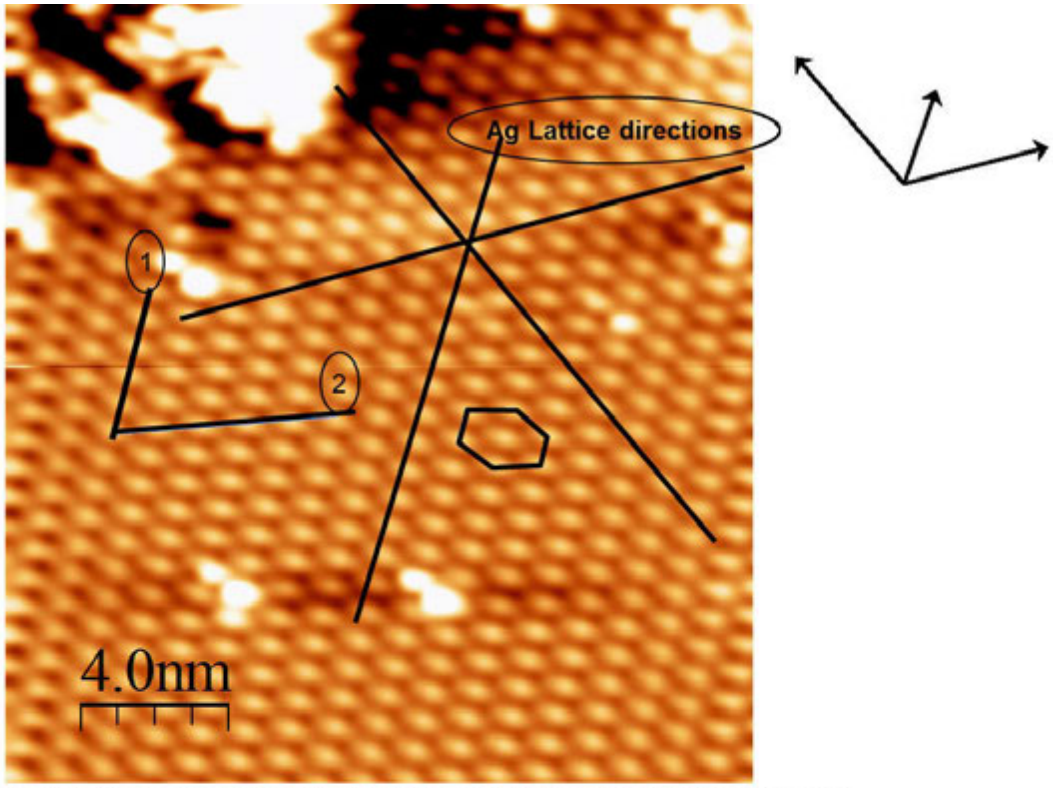

0.7777 nA, 100 mV, loop gain 0.76276%, 118.4 nm/s, 20x20nm², 2090929 H2S Ag111, m48

	1	2
avg	0.75	1.19
Std dev	0.03	0.12
N	33	28
corrected	**0.81**	**1.36**
	2.82*a*	**4.70*a***

Figure A2.9.

Appendix 3. Action spectroscopy

Injecting electrons from the STM tip into species adsorbed on a surface can cause that adsorbate to move.[51-53] Preliminary action spectroscopy (AS) results for H_2S on Ag(111) are shown here.

Figures

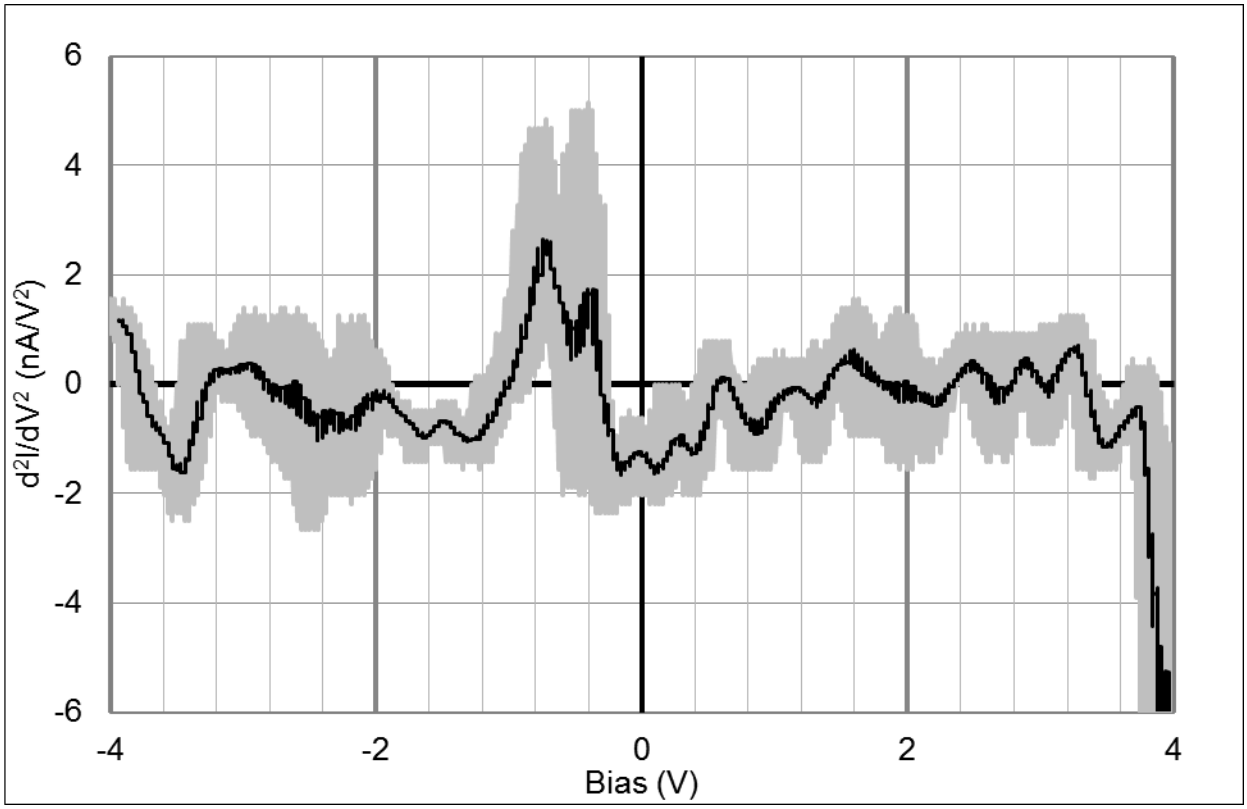

Figure A3.1. Inelastic Tunneling Spectroscopy (IETS) on Ag(111).

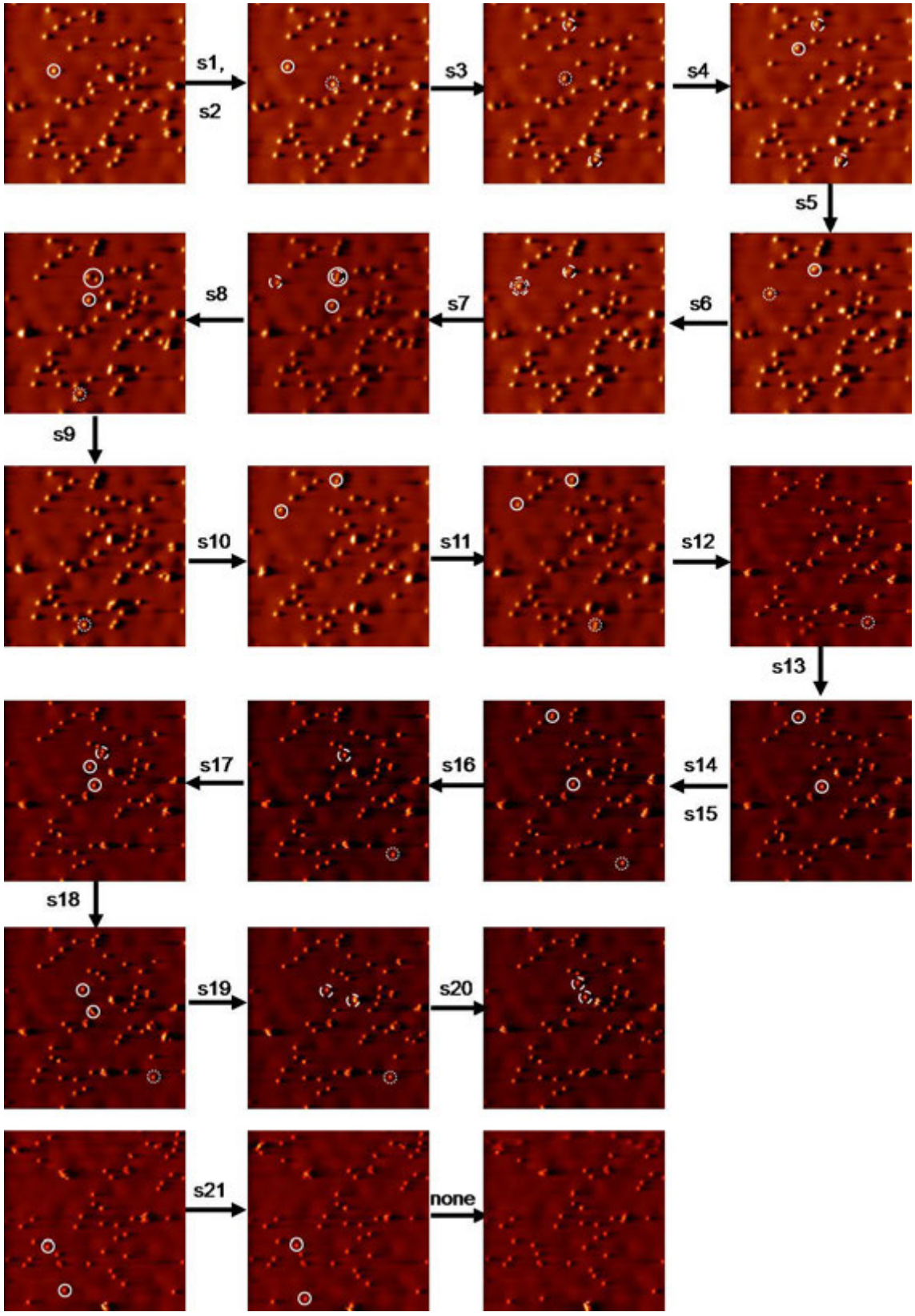

Figure A3.2. STM images of H_2S molecule displacement due to AS at 150 mV.

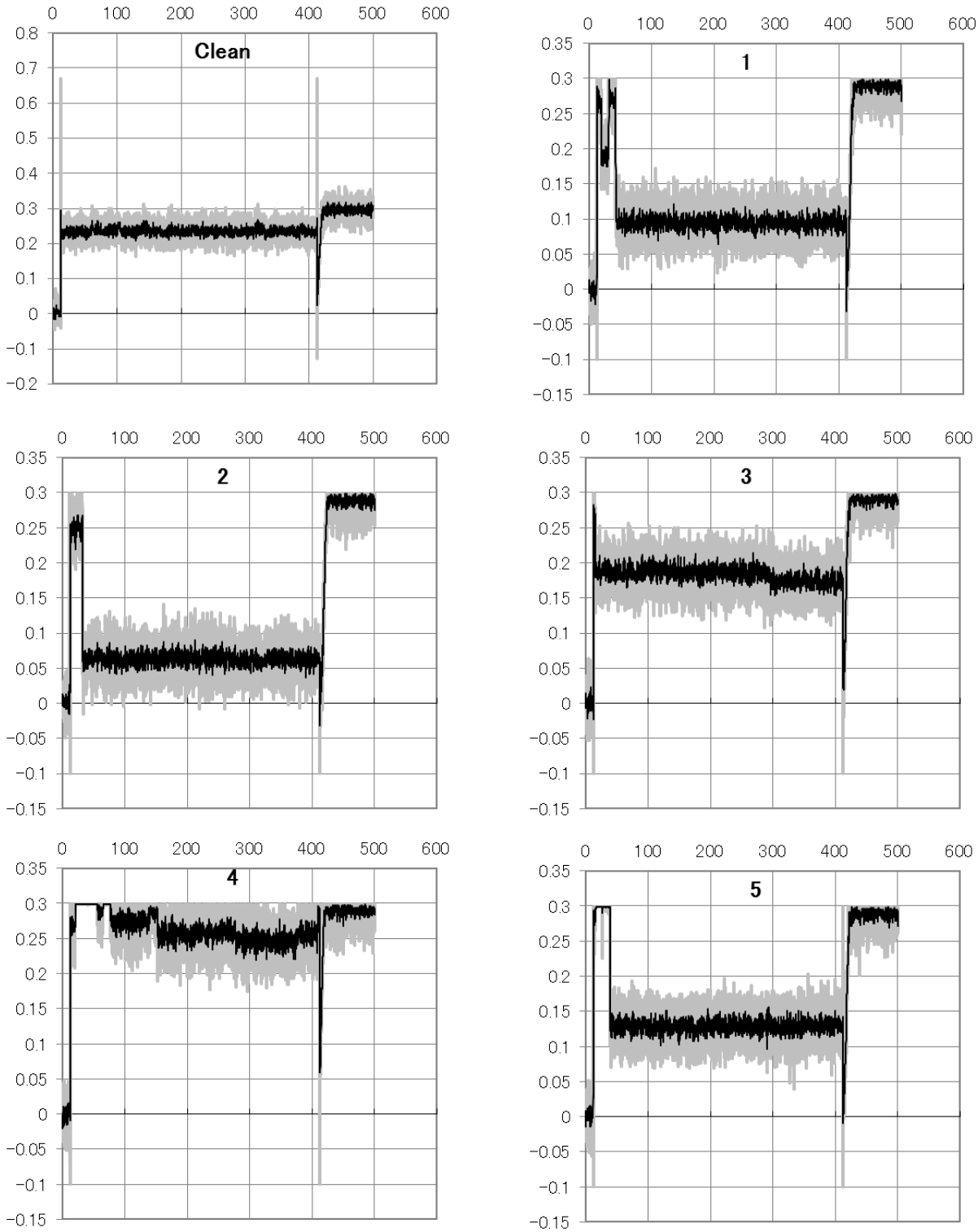

This figure continues on the following page.

Figure A3.3. AS at 150 mV corresponding to each arrow in Fig. A3.2.

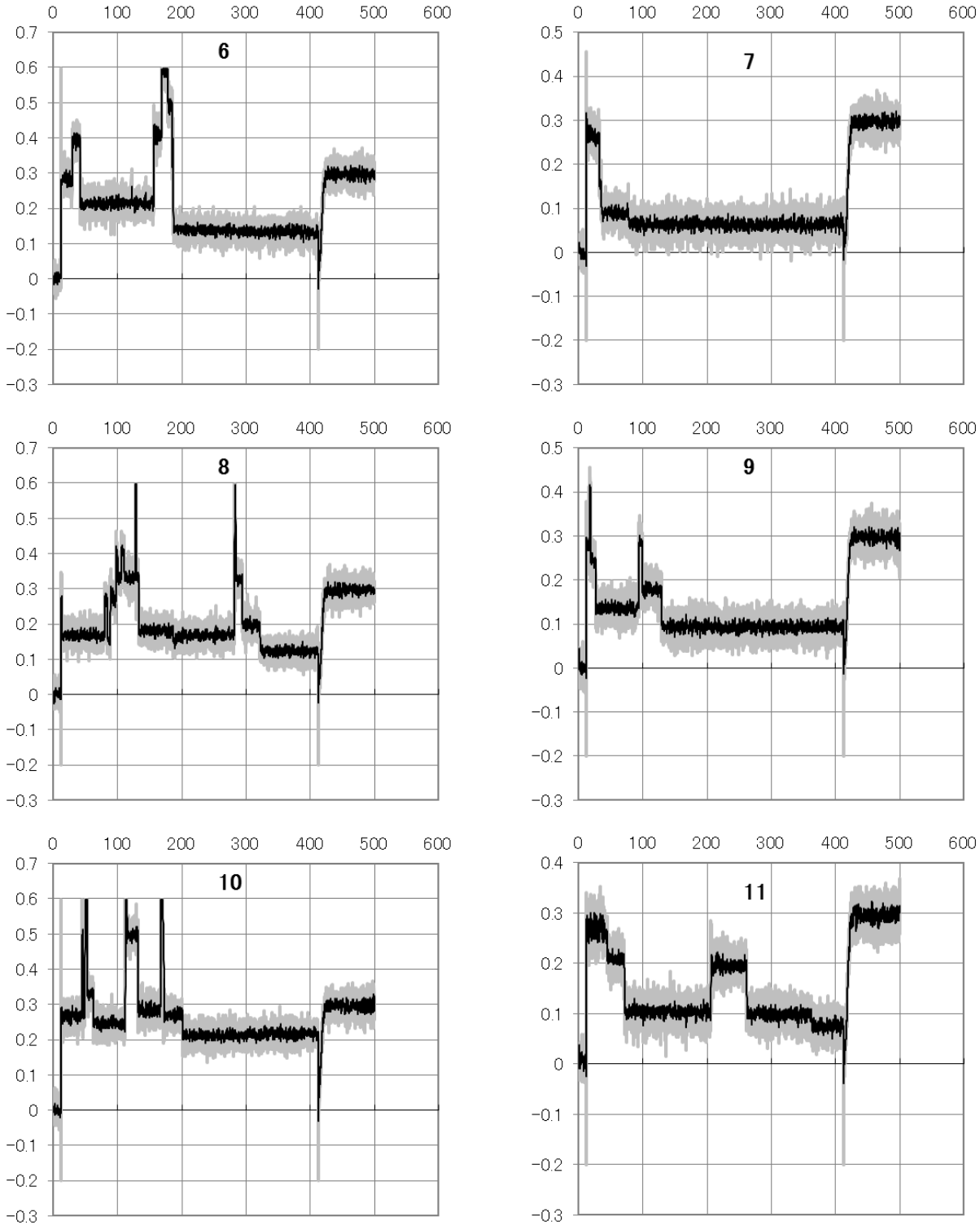

This figure continues on the following page.

Figure A3.3. continued.

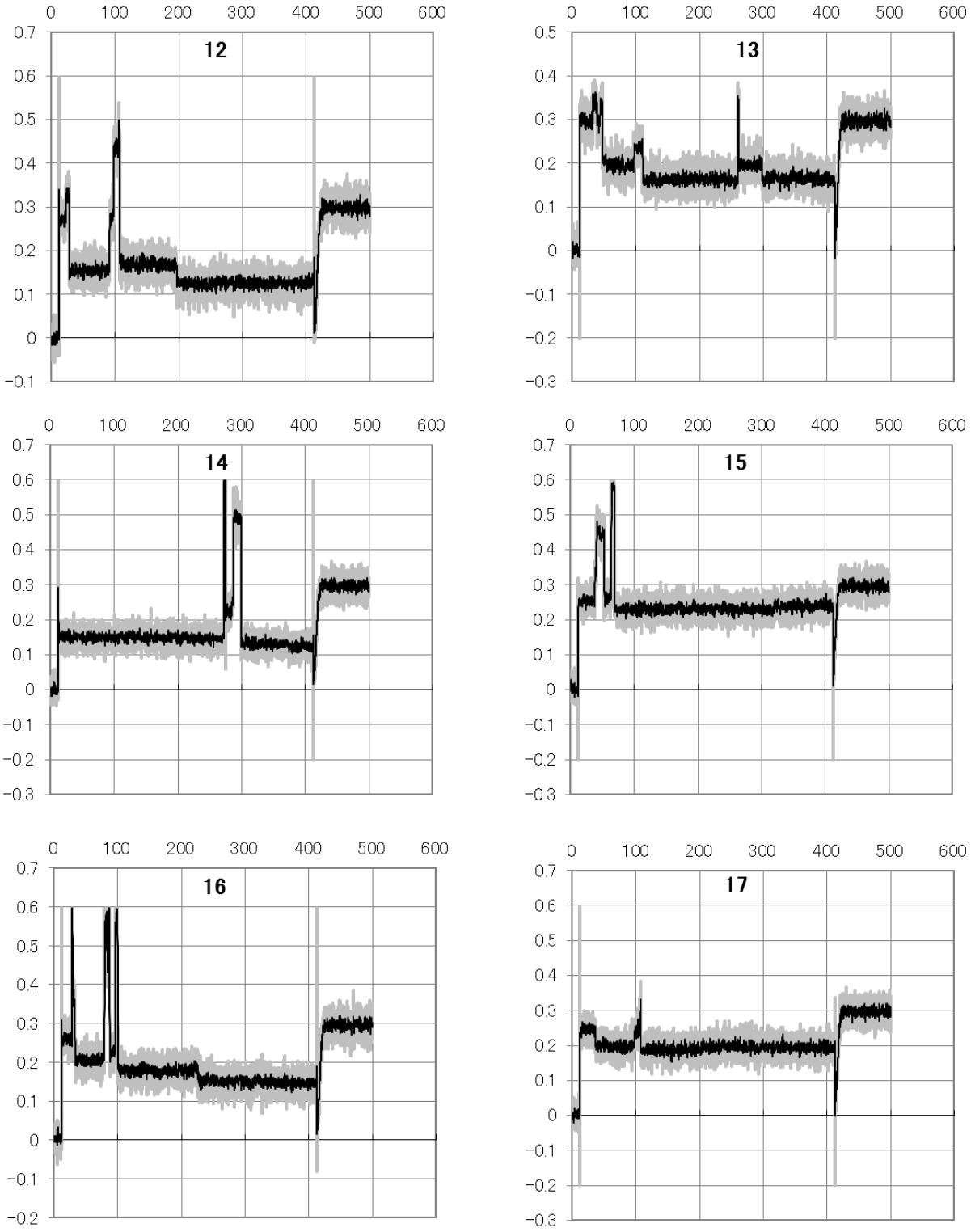

This figure continues on the following page.

Figure A3.3. continued.

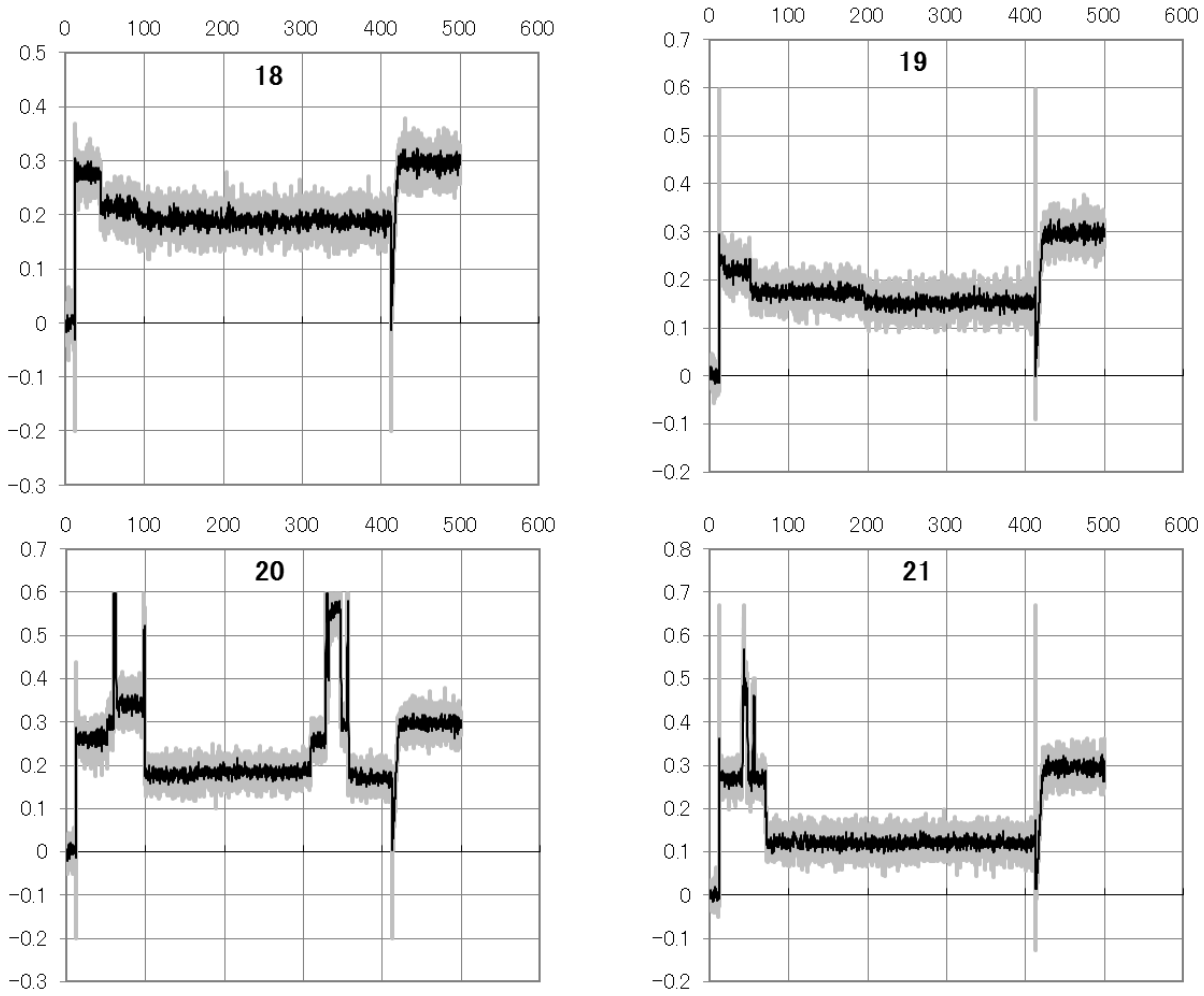

Figure A3.3. continued.

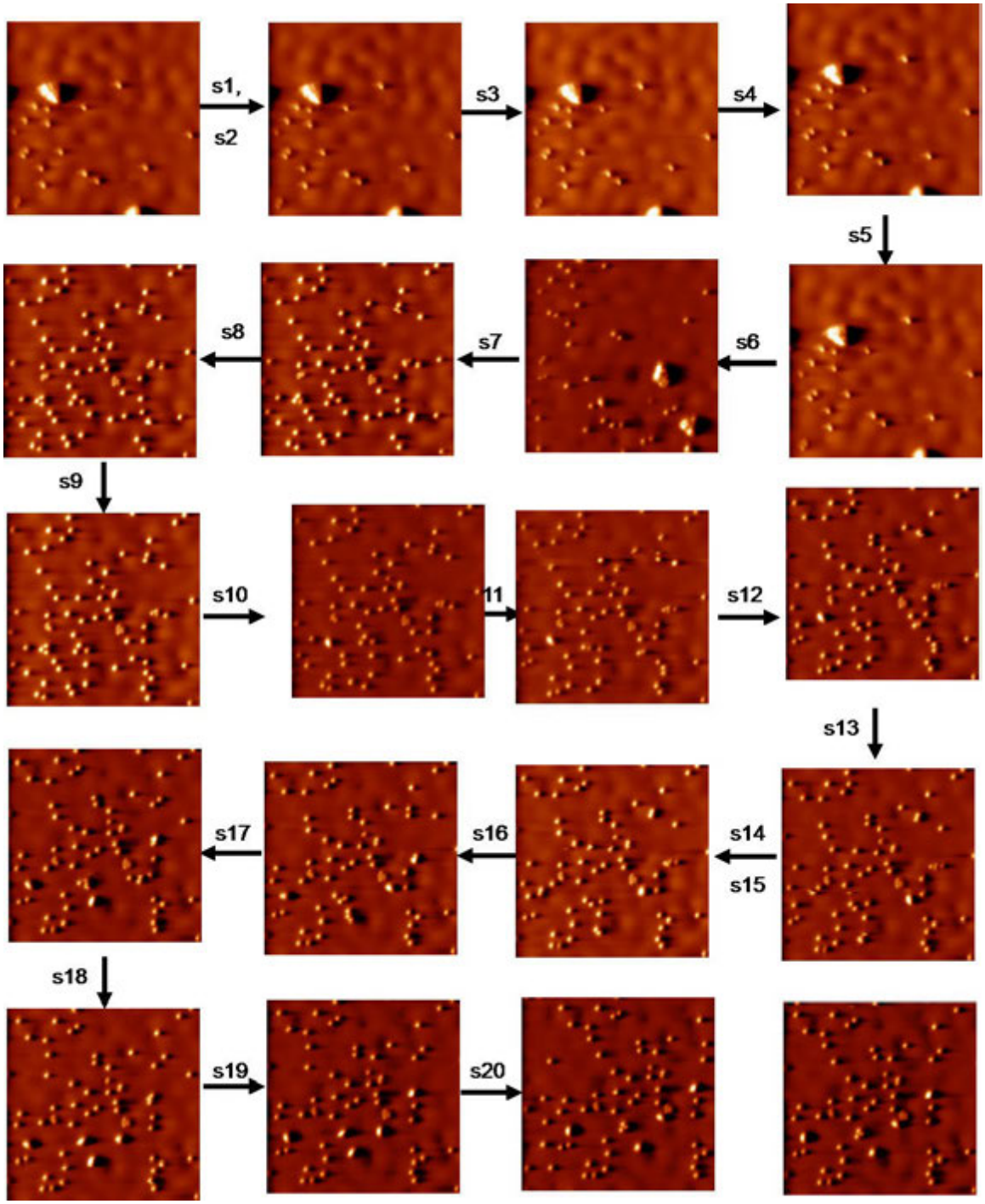

Figure A3.4. STM images of H_2S molecule displacement due to AS at 200 mV.

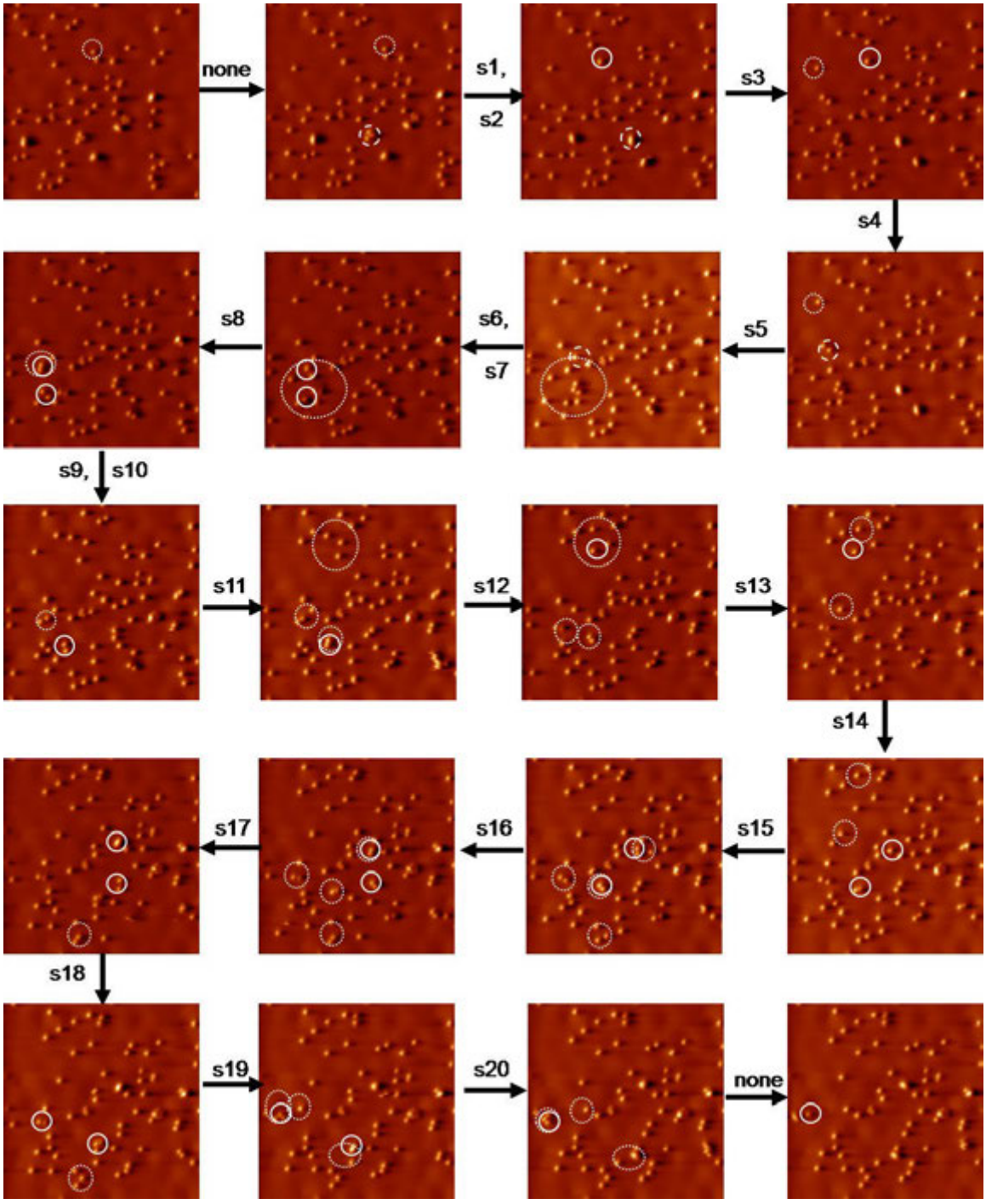

Figure A3.5. STM images of H_2S molecule displacement due to AS at 250 mV.

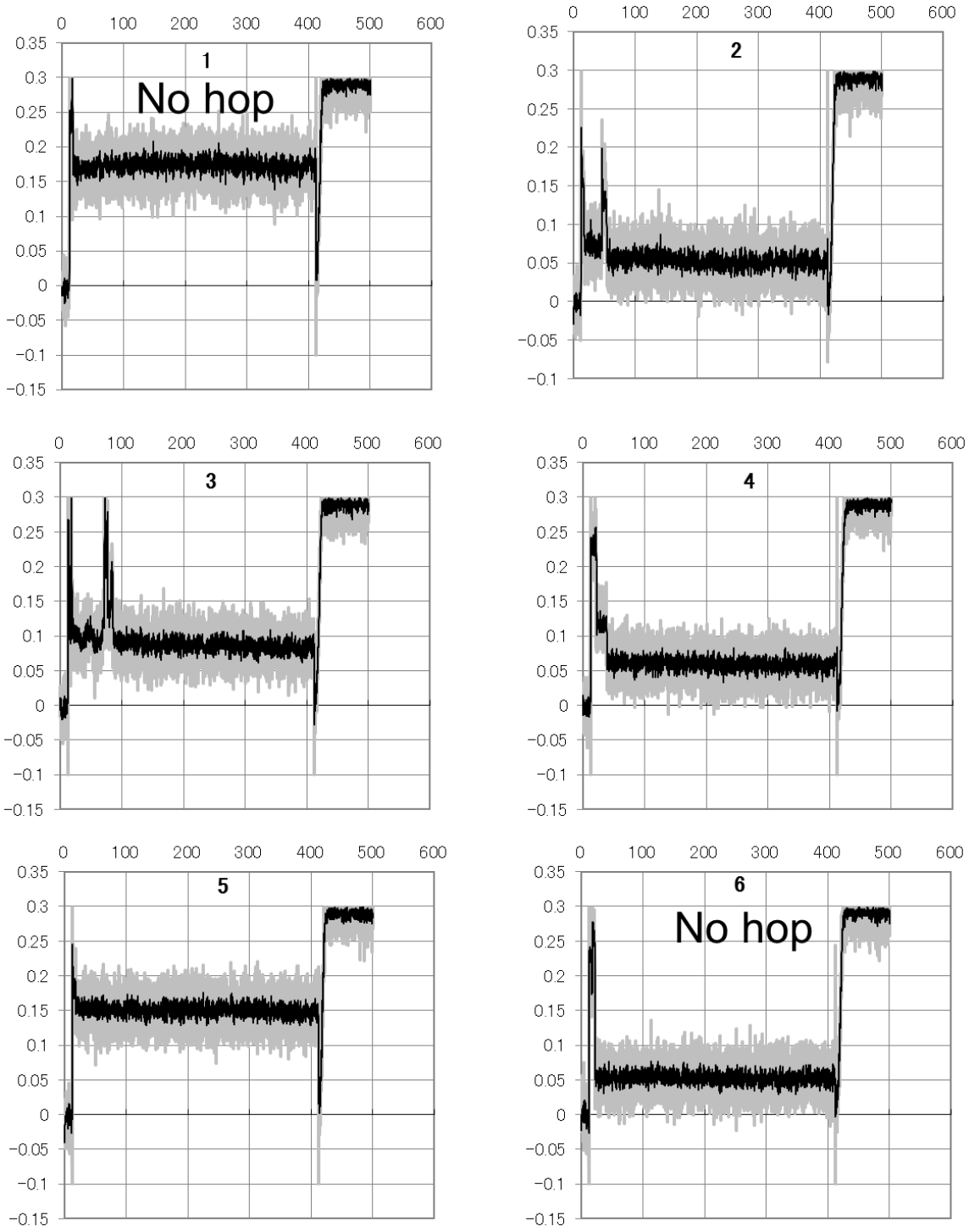

This figure continues on the following page.

Figure A3.6. AS at 250 mV corresponding to each arrow in Fig. A3.5.

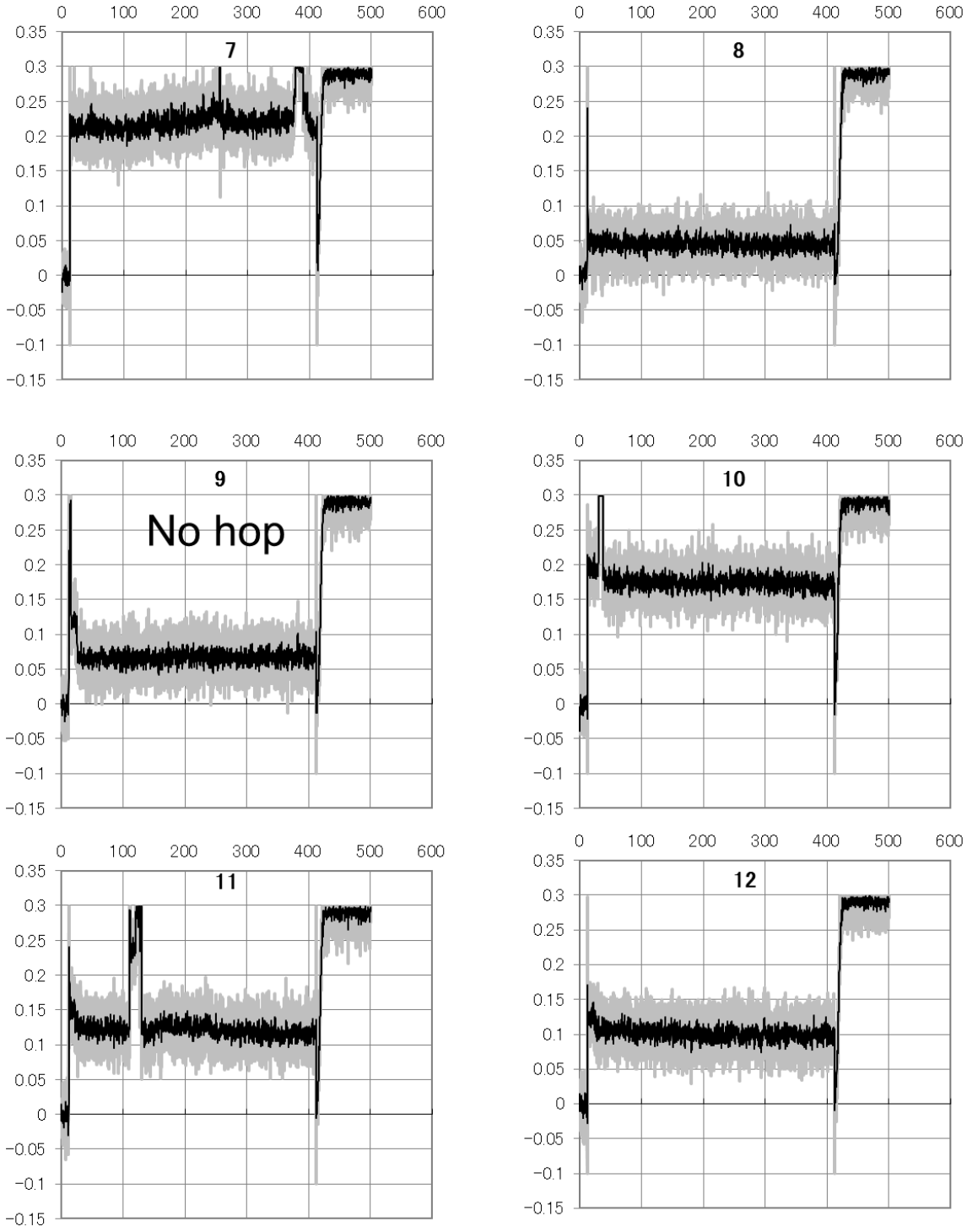

This figure continues on the following page.

Figure A3.6. continued.

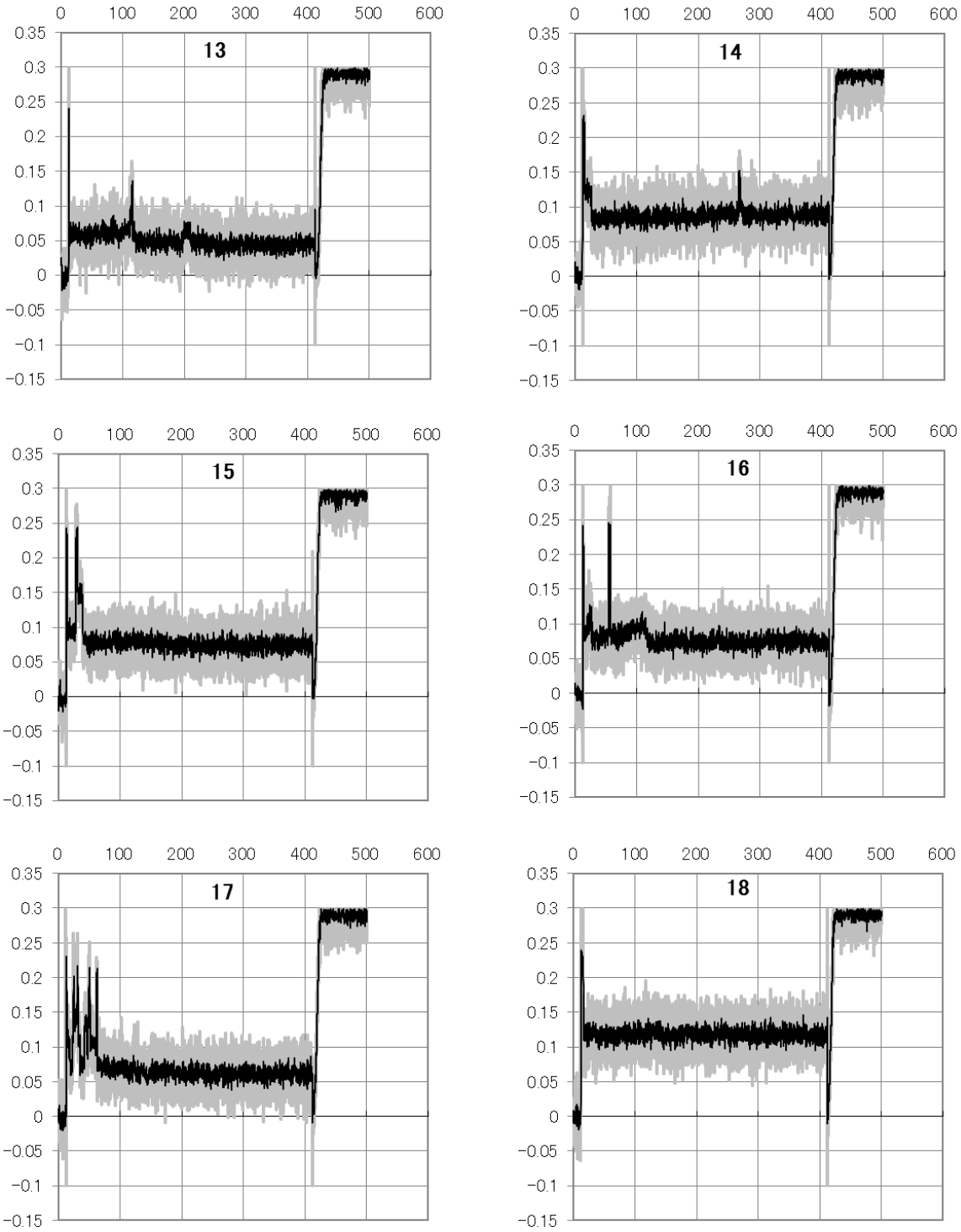

This figure continues on the following page.

Figure A3.6. continued.

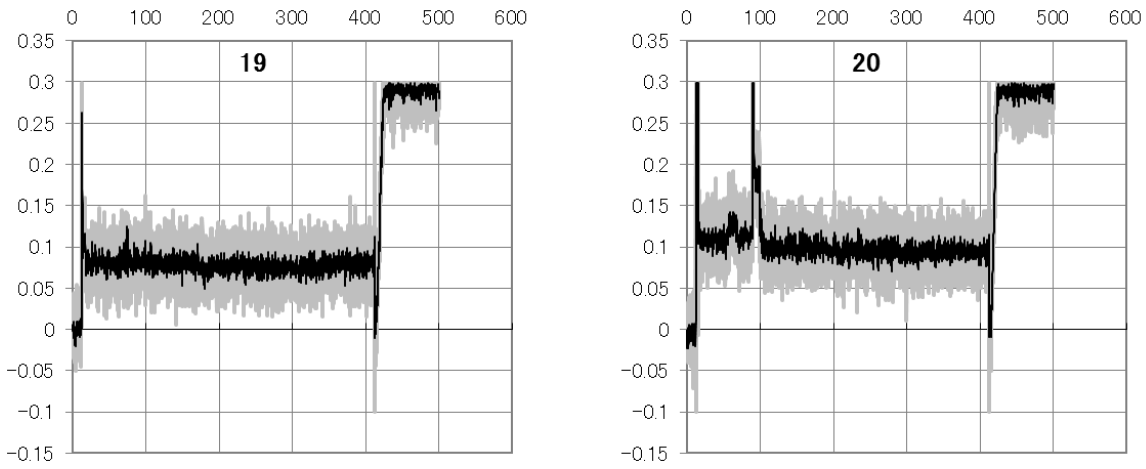

Figure A3.6. continued.

References

(1) Cabané-Brouty, F. *Journal de Chimie Physique et de Physico-Chimie Biologique* **1965**, *62*, 1045.

(2) Cabané-Brouty, F. *Journal de Chimie Physique et de Physico-Chimie Biologique* **1965**, *62*, 1056.

(3) Bénard, J.; Oudar, J.; Cabané-Brouty, F. *Surface Science* **1965**, *3*, 359.

(4) Perdereau, J.; Rhead, G. E. *Acta Metallurgica* **1968**, *16*, 1267.

(5) Rovida, G.; Pratesi, F. *Surface Science* **1981**, *104*, 609.

(6) Tibbetts, G. G.; Burkstrand, J. M.; Tracy, J. C. *Physical Review B* **1977**, *15*, 3652.

(7) Heinz, R.; Rabe, J. P. *Langmuir* **1995**, *11*, 506.

(8) Aloisi, G. D.; Cavallini, M.; Innocenti, M.; Foresti, M. L.; Pezzatini, G.; Guidelli, R. *Journal of Physical Chemistry B* **1997**, *101*, 4774.

(9) Yu, Y.; Dixon-Warren, S. J.; Astle, N. *Chemical Physics Letters* **1999**, *312*, 455.

(10) Alfonso, D. R. *Surface Science* **2008**, *602*, 2758.

(11) Carrasco, J.; Michaelides, A.; Scheffler, M. *Journal of Chemical Physics* **2009**, *130*, 184707.

(12) Thiel, P. A.; Madey, T. E. *Surface Science Reports* **1987**, *7*, 211.

(13) Henderson, M. A. *Surface Science Reports* **2002**, *46*, 1.

(14) Hodgson, A.; Haq, S. *Surface Science Reports* **2009**, *64*, 381.

(15) Morgenstern, K.; Rieder, K.-H. *Journal of Chemical Physics* **2002**, *116*, 5746.

(16) Michaelides, A. *Faraday Discussions* **2007**, *136*, 287.

(17) Michaelides, A.; Morgenstern, K. *Nature Materials* **2007**, *6*, 597.

(18) Mehlhorn, M.; Morgenstern, K. *New Journal of Physics* **2009**, *11*, 093015.

(19) Morgenstern, K.; Nieminen, J. *Journal of Chemical Physics* **2004**, *120*, 10786.

(20) Morgenstern, K. *Surface Science* **2002**, *504*, 293.

(21) Morgenstern, K.; Nieminen, J. *Physical Review Letters* **2002**, *88*, 066102.

(22) Nieminen, J.; Lahti, S.; Paavilainen, S.; Morgenstern, K. *Physical Review B* **2002**, *66*, 165421.

(23) Gawronski, H.; Morgenstern, K.; Rieder, K. H. *European Physical Journal D* **2005**, *35*, 349.

(24) Gawronski, H.; Carrasco, J.; Michaelides, A.; Morgenstern, K. *Physical Review Letters* **2008**, *101*, 136102.

(25) Mehlhorn, M.; Gawronski, H.; Morgenstern, K. *Physical Review Letters* **2008**, *101*, 196101.

(26) Mehlhorn, M.; Carrasco, J.; Michaelides, A.; Morgenstern, K. *Physical Review Letters* **2009**, *103*, 026101.

(27) Platts, J. A.; Howard, S. T.; Bracke, B. R. F. *Journal of the American Chemical Society* **1996**, *118*, 2726.

(28) Motobayashi, K.; Matsumoto, C.; Kim, Y.; Kawai, M. *Surface Science* **2008**, *602*, 3136.

(29) Mitsui, T.; Rose, M. K.; Fomin, E.; Ogletree, D. F.; Salmeron, M. *Science* **2002**, *297*, 1850.

(30) Kresse, G.; Hafner, J. *Physical Review B* **1994**, *49*, 14251.

(31) Kresse, G.; Hafner, J. *Physical Review B* **1993**, *47*, 558.

(32) Kresse, G.; Furthmüller, J. *Physical Review B* **1996**, *54*, 11169.

(33) Kresse, G.; Furthmüller, J. *Computational Materials Science* **1996**, *6*, 15.

(34) Perdew, J. P.; Burke, K.; Ernzerhof, M. *Physical Review Letters* **1996**, *77*, 3865.

(35) Kiejna, A.; Kresse, G.; Rogal, J.; De Sarkar, A.; Reuter, K.; Scheffler, M. *Physical Review B* **2006**, *73*, 035404.

(36) Neugebauer, J.; Scheffler, M. *Physical Review B* **1992**, *46*, 16067.

(37) Tersoff, J.; Hamann, D. R. *Physical Review B* **1985**, *31*, 805.

(38) Dahlke, E. E.; Truhlar, D. G. *The Journal of Physical Chemistry B* **2005**, *109*, 15677.

(39) Ireta, J.; Neugebauer, J.; Scheffler, M. *Journal of Physical Chemistry A* **2004**, *108*, 5692.

(40) Michaelides, A. *Applied Physics A: Materials Science & Processing* **2006**, *85*, 415.

(41) Ternes, M.; Pivetta, M.; Patthey, F.; Schneider, W.-D. *Progress in Surface Science* **2010**, *85*, 1.

(42) Merrick, M. L.; Luo, W.; Fichthorn, K. A. *Progress in Surface Science* **2003**, *72*, 117.

(43) Tierney, H. L. Private communication related to material later published in Tierney, H. L.; Murphy, C. J.; Sykes, E. C. H. *Physical Review Letters* **2011**, *106*, 010801.

(44) Michaelides, A.; Ranea, V. A.; de Andres, P. L.; King, D. A. *Physical Review Letters* **2003**, *90*, 216102.

(45) Sándor, E.; Ogunade, S. O. *Nature* **1969**, *224*, 905.

(46) Eisenberg, D. E.; Kauzmann, W. *The Structure and Properties of Water*; Oxford University Press: New York, 1969.

(47) Zimbitas, G.; Haq, S.; Hodgson, A. *Journal of Chemical Physics* **2005**, *123*, 174701.

(48) Harnett, J.; Haq, S.; Hodgson, A. *Surface Science* **2003**, *528*, 15.

(49) Glebov, A.; Graham, A. P.; Menzel, A.; Toennies, J. P. *Journal of Chemical Physics* **1997**, *106*, 9382.

(50) Nie, S.; Feibelman, P. J.; Bartelt, N. C.; Thürmer, K. *Physical Review Letters* **2010**, *105*, 026102.

(51) Sainoo, Y.; Kim, Y.; Okawa, T.; Komeda, T.; Shigekawa, H.; Kawai, M. *Physical Review Letters* **2005**, *95*, 246102.

(52) Outka, D. A.; Madix, R. J. *Surface Science* **1984**, *137*, 242.

(53) Motobayashi, K.; Kim, Y.; Ueba, H.; Kawai, M. *Physical Review Letters* **2010**, *105*, 076101.

CHAPTER III

Ag-S clusters on Ag(111) at Low Temperature

Selena M. Russell,[a] Yousoo Kim,[b] and P. A. Thiel[a,c]

1. Introduction

In processes involving mass transport across surfaces (such as coarsening), the nature of the transport agents or carriers is generally unknown. If we can identify the carriers, then we may discover ways to manipulate and control coarsening. Studies of chalcogen (O, S) interaction with coinage metal surfaces (Cu, Ag, Au) elucidate how those interactions affect mass transport on the surface. Both adsorbed oxygen and sulfur reconstruct coinage metal surfaces and enhance metal island coarsening, under certain conditions. On the Ag(111) surface, sulfur enhances Ag island coarsening by three or more orders of magnitude over a narrow coverage range (0 – 0.035 monolayers (ML) S) at room temperature.[1]

On Ag(111)[1] and Cu(111)[2], coarsening accelerates after S adsorption, but S does not affect the formation or diffusion energies of metal adatoms, the carrier in the clean system. Therefore, the carrier must change, for example from a Ag adatom to a Ag_xS_y cluster. After S atom adsorption, M_3S_3 clusters form on Ag(111)[1,3] and Cu(111)[2,4] in which the metal atoms are arranged in a trimer with the S atoms decorating the edges, schematically shown in Fig. 1a. If S and Co are adsorbed on Ag or Au(111), Co_3S_3S clusters form in a configuration similar to the M_3S_3 clusters where the fourth S caps the central position.[5] In studies unrelated to metal island coarsening, S on Ni(111) also forms Ni_3S_3 clusters.[6] Thiols on Au(111) surfaces undergo adatom-mediated molecular self-assembly by bonding to Au adatoms in a $Au(SR)_2$ configuration in which the S-Au-S bond is linear, schematically shown in Fig. 1b.[7,8] STM and DFT studies in our group proposed that the likely carriers during Ag island coarsening are Ag_3S_3 and AgS_2 in the S/Ag/Ag(111) system[9] and AgS_2 in the S/Ag/Ag(100) system.[10]

[a] Department of Chemistry, Iowa State University, Ames, Iowa 50011 USA
[b] RIKEN Advanced Science Institute, Wako, Saitama 351-0198, Japan
[c] Department of Material Science and Engineering and the Ames Laboratory, Iowa State University, Ames, Iowa 50011

Our identification of the Ag_3S_3 cluster derived from earlier studies of S on the smooth (without islands) Ag(111) surface.[3] With 0.03 monolayers (ML) S on Ag(111) at 200 K, a dot-row motif forms on terraces, consisting of dot-like protrusions in linear chains along the [110] direction. As the S coverage increases, dot-rows increasingly cover the surface. Pit formation within the terrace indicates that the dots consume Ag. Analysis of the STM results in conjunction with DFT, suggested that dots were likely Ag_3S_3 clusters. Of the possible clusters, Ag_3S_3 and AgS_2 form spontaneously in the presence of excess terrace S, having negative formation energies, which are lower than the formation energy of a Ag adatom by 0.68 and 0.64 eV.[11] The robust Ag_3S_3 dot-row structure exists between 0.03 and 0.5 ML around 200 K.

The Ag_3S_3 dot-row motif reversibly transforms with temperature.[3] The S structures on Ag(111) depend on temperature and S coverage, as shown in Fig. 2. Above 225 K, no organized structures are observed. The Ag_3S_3 dots are mobile on Ag(111), so at high enough temperature the clusters are highly mobile and could not be imaged on the time scale of STM imaging. At 135 K and 0.09 ML S, we observed an elongated island structure. A phase diagram for this system is shown in Fig. 2. As the coverage decreases below 0.05 ML S, the phase boundaries curve downward, for example, dot-rows were observed with 0.03 ML S at 135 K.[9,12]

DFT suggested that the low temperature elongated islands might be either single or double Ag chains with S atoms decorating either side of the chain. The models are reproduced in Fig. 3. The double chain model has the additional feature of a S atom residing on top of the chain in a pseudo 4-fold hollow site. Sulfur's strong preference for four-fold-hollow sites is exemplified by S induced reconstruction on Cu(111)[13] and Ni(111)[6,14] to a *pseudo*-M(100)-c(2×2)-S surface phase (M = Cu, Ni) and its preferred adsorption on terrace 4-fold-hollow sites on Ag(100),[15] [001] edges on stepped Cu(100),[16,17] and [01-1] edges on Ag(111)[3] surfaces. Using the spin-polarized S atom as the reference, the adsorption energy of a S atom in a 4-fold hollow site on Ag(100) is 4.16 eV, compared to 3.74 eV in a fcc 3-fold hollow site on Ag(111).[10] Sulfur is not known to induce a long-range pseudo-Ag(100) reconstruction, but S adsorbed in pseudo 4-fold hollow sites can be a local feature on Ag(111).

To date, the Ag_3S_3 cluster has been imaged only as a component of the dot-row structure, or as a diffusing fragment. It has not been imaged as a stationary, isolated cluster, nor has the proposed AgS_2 cluster. Furthermore, the structure of the elongated islands observed at low temperature is unclear. In this paper, we aim to explore further the S/Ag(111) system at liquid helium temperatures (4.7 K) to elucidate details of the previously observed structures, which may help to refine the DFT models of those structures.

2. Experimental details

All STM imaging was done at 4.7 K with a low-temperature STM (LT-STM, Omicron GmbH) in a UHV chamber with base pressure below 8×10^{-9} Pa. In an attached chamber, the Ag(111) sample (MaTecK GmbH) was cleaned by repeated cycles of Ar^+ sputtering (1 keV, ~10 μA, 10 min) and annealing (~670 K). The clean sample was transferred to the STM stage and cooled to the operating temperature. Tunneling conditions are given in the figure captions.

Sulfur adsorption occurred by exposing the room temperature surface to a S_2 beam generated by a solid-state electrochemical $Ag|AgI|Ag_2S|Pt$ cell following the design of Wagner and is shown in Appendix IV. The evaporator was mounted on a linear motion arm in a small chamber pumped via the exchange chamber or a standalone miniature chamber to 2×10^{-6} Pa. The small evaporator chamber was connected to the preparation chamber (base pressure 3×10^{-9} Pa or lower), but was isolated by a gate valve. Once the cell was fully warmed up, the gate valve to the preparation chamber was opened and the evaporator was moved to within 10 mm of the sample as pictured. The sample plane was a few millimeters lower than the evaporator opening. STM imaging typically began within 30 minutes after deposition ended, when the sample temperature had re-stabilized at 4.7 K. Bias voltage is the sample potential referenced to the tip.

Two general experiments were conducted, distinguished by the sulfur coverage (low and high). The sample was always cleaned before each S deposition. In the two low coverage experiments, ~ 5% of the surface is covered with features. To achieve a low S coverage, the deposition time was limited to 1 min or less and an evaporator cell voltage of 250 mV.

Longer deposition times and/or higher evaporator cell voltages were used to deposit large amounts of S in the three high coverage experiments, so that the entire surface was covered. The results of these experiments are discussed in Section A.1, at the end of this chapter. The details of each S deposition are shown in Table I. The sample was sometimes held overnight in the STM stage at 4.7 K to continue observation the following day. Fig. 4 outlines when each experiment took place and the conditions.

In an effort to promote ordering, (e.g. dot-row formation) during either experiment, we held the sample between 200 and 300 K. To do this, the sample was placed in the cold finger in the STM chamber and nitrogen gas from the cryogen dewar flowed through the cold finger at a rate to maintain about 200 K on the inlet tube. (The thermocouple at the cold finger was damaged, so the exact sample temperature is unknown.)

The clean surface is shown for reference in Fig. 5; the delineated directions apply to all low temperature (LT) images. Note that there is some deviation from ideal hexagonal packing, in that the atomically resolved image in Fig. 5 shows shortened bond distances and corrupted bond angles that vary across the image. The atom rows also bow, especially near the image edges. The distortion may be due to slight miscalibration of the XY piezo-electrics in the STM scanner and drift during scanning. All images presented here are uncorrected for distortion. In extracting dimensions from the images, a rough correction was sometimes applied by measuring the peak-to-peak separation of Ag atoms in atomically resolved images and comparing those values with the expected value of 0.289 nm. The lateral dimensions are systematically contracted by 17 to 26% and the bond angles differ from 60°. Details of these measurements are shown in Table II. An overall rough correction factor (abbreviated RC) of 1.2650 has been applied to all measured in-plane measurements, i.e. without regard to the directionality of the distortion. Both the raw (RAW) and roughly corrected (RC) values are reported in this paper. The standard deviation of all measurements is also reported, but does not reflect the absolute error associated with image distortion. Reported widths are measured at the full-width-at-half-max (FWHM) of the line profile across a feature.

The clean step height from STM images in this study is -5.8% different than the expected value of 0.250 nm, ignoring tunneling conditions. Measuring the height is very

difficult in that features are usually surrounded by a shadow or depression. The height was measured from a feature's apex to where the substrate levels (not the shadow).

All dimensions are taken from the topographic images.

3. Low S coverage results

Three features arise from ***low*** S coverage deposition on the Ag(111) surface, namely step decoration, triangular clusters, and chains. These are all shown in Fig. 6.

3.1. Step decoration

Fig. 7 illustrates faceted step edges along the close-packed directions. The steps show evenly spaced protrusions, which are separated by 0.47 ± 0.04 nm (RAW), and by 0.58 ± 0.04 nm (RC for each direction in Table II, not overall factor of 1. 2650), N = 129. Statistics are shown in Table III. This separation is double the Ag atom separation, 2a = 0.578 nm, along <1 -1 0> directions. This decoration is consistent with S occupying every other site along the close-packed directions, which we have also concluded from earlier experiments.[3]

3.2. Triangular clusters

The small roundish cluster boxed in Fig. 6 appears to consist of three protrusions arranged in a triangle; higher resolution images are shown in Fig. 8. The topography of the cluster is delineated in a series of line profiles in Fig. 9. Along the edges of the cluster (solid lines), the peaks are separated by 0.36 ± 0.04 nm (RAW), 0.45 ± 0.05 nm (RC) and the peaks are 0.023 ± 0.007 nm (RAW), 0.021 ± 0.006 nm (RC) above the surface. The dashed profiles bisecting the peaks give 0.71 ± 0.02 nm (RAW), 0.90 ± 0.03 nm (RC) as an estimate of the cluster diameter, at a tunneling bias of 7.641 mV. Details are given in Table IV. Moving down Fig. 8, from c to h, the bias voltage increases from 4.155 to 999.9 mV. The small voltage difference of about 3 mV between Fig. 8c-f does not appreciably alter the appearance of three lobes of the triangular cluster or the dimensions. (The FWHM decreases by 1%, the peak-to-peak separation increases by 2%, and the height increases by 6%.) At nearly 1 V, the cluster in Fig. 8g-h appears much more compact and the protrusions less discrete, so that the peak-to-peak separation is 0.26 ± 0.03 nm (RAW), 0.33 ± 0.03 nm (RC), and the peaks are

0.017 ± 0.004 nm (RAW), 0.016 ± 0.004 nm (RC) above the surface. The diameter of the cluster is 0.64 ± 0.03 nm (RAW), 0.81 ± 0.04 nm (RC). Measurements of the clusters in Fig. 8g-h and Fig. 8c-d are given in Tables V and VI. As the bias voltage increases from 4.155 to 999.9 mV, the diameter contracts by 0.08 to 0.1 nm and the height decreases by 0.004 nm. (All of the cluster dimensions decrease between 4.155 and 999.9 mV: FWHM by 11%, peak-to-peak separation by 12%, and height by 19%.) We assign this cluster as Ag_3S_3, for reasons that will be given in Section 4.2.

Other similarly sized features are visible on the surface, for example the images in Fig. 10. The feature in Fig. 10e exhibits a three-lobed shape like the triangular cluster discussed above and is 0.95 nm (RAW), 1.2 nm (RC) in diameter, and 0.023 nm (RAW), 0.021 nm (RC), with a tunneling bias of -874.1 mV. The diameter of the feature in Fig. 10e is larger and taller than the cluster in Fig. 8g-h by 48%. The cluster orientation differs between the images, the triangle points up in Fig. 10e, but points down in Fig. 8g-h. Also, the orientation / adsorption site with respect to the substrate is unknown. Most of the other observed features look like spheres without the three lobe shape or extensive surface modification (shadow), e.g. Fig. 10a-d, so it is difficult to verify if they are triangular clusters or something else. The tunneling current ranged from 0.155 to 1.00 nA and the bias ranged from -2.00 to 1.00 V. Fig. 10f-g shows histograms of the FWHM and height of 25 potential triangular clusters and the values are summarized in Table VII. Most of the widths are in agreement with the triangular cluster. However, the features are all taller than the triangular cluster in Fig. 9.

The dimensions of the triangular clusters in Fig. 8 and Fig. 10 vary, but do not appear to depend on the tunneling bias. Fig. 11 shows that average height is 0.07 ± 0.01 nm (RAW & RC) and the FWHM is 0.78 ± 0.07 nm (RAW), 0.98 ± 0.09 nm (RC) from -1 V to +1V, ignoring the three very large clusters (FWHM greater than 1.0 nm RAW, 1.3 RC). Neither height nor FWHM vary consistently with bias.

3.3. Chains

Chains, like those circled in Fig. 6, predominate on the surface at low S coverage. Their 2-fold shape is unexpected based on the 3-fold symmetry of the substrate. Closer

inspection reveals that the chains consist of cross-like units with a bright central protrusion and diamond-like arms over a wide range of tunneling conditions (-6 to +7 V and 0.046 to 2.0 nA). Variation of the chain appearance with tunneling conditions will be discussed, together with scanning tunneling spectroscopy (STS), in Appendix 2 at the end of this chapter. Fig. 12(a) shows a single cross-like unit, while Fig. 12(b) shows a two-unit chain. We will call the arms that span the short width of the chain the 'equatorial' arms, and those that connect the units 'axial' arms. The equatorial arms appear narrower and shorter than the axial arms. The axial arms (links) between central protrusions in the longer chains often appear as two bumps parallel to the equator and the equatorial arms appear as single bumps on either side of the central protrusion within a unit, rather than as diamond shaped. Compare the arms in Fig. 12a-b. Figures 12b and 13 illustrate several examples.

Fig. 13 and 14 show that the chains vary in length, but have a consistent width. The chains tend to be short, with most containing only a single central protrusion (one unit), as illustrated by the chain-length histogram in Fig. 15 and summarized in Table VIII. A single unit is 1.6 ± 0.1 nm (RAW), 2.0 ± 0.2 nm (RC) long, and 1.2 ± 0.2 nm (RAW), 1.5 ± 0.2 nm (RC) wide (N=25). Fig. 16 shows the line profiles of a single unit. Fig. 17 shows the line profiles of a double unit chain. Two-unit chains are 2.7 ± 0.1 nm (RAW), 3.4 ± 0.1 nm (RC) long, which is less than double the length of a single unit (3.2 nm RAW, 4.0 nm RC). Therefore, the two-unit chains are not simply stacked single units. In multiple unit chains, two units share one axial arm between the central protrusions. The width of the single and double chains are the same. For multiple unit chains, the central protrusion-to-central protrusion separation remains constant at 1.12 ± 0.06 nm (RAW), 1.41 ± 0.07 nm (RC) (N=99). The width of the shallow maxima along the line profile d in Fig. 17, across the interior axial arm, is 0.9 ± 0.3 nm (RAW), 1.2 ± 0.4 nm (RC) (N=32). Dimension statistics are shown in Tables IX, X, and XI for single, double, and all chains.

Fig. 18 shows a highly stepped region and a variety of edge features. As discussed in Section 3.1 and shown in Fig. 6, steps are often decorated with S atoms, pointed out by white arrows in Fig. 18. In addition, partial chains emerge adjacent to descending step edges, as noted by black arrows in Fig. 18. The chains may either be oriented along (nearly parallel to) the edge or rotated away from (more nearly perpendicular to) the edge. The latter type of

chain fragments often appear to be nearly complete single units that interact with the step just at the point of an axial arm and are especially visible in Fig. 19. Zigzag shaped features are also visible along descending step edges in Fig. 18 and 19e-f marked by patterned arrows. Fig. 18c and 19e-f show examples. The zigzags are 0.57 ± 0.08 nm (RAW), 0.7 ± 0.1 nm (RC) (N=16) wide. The zigzag shapes most often appear in a single row along a step, but occasionally double rows of staggered zigzags arise as in Fig. 18b. The zigzag-like features are different from the normal step decoration and both can exist along the same edge, Fig. 18c upper left and 19e-f right hand side.

3.4. Stability

Over the course of the low coverage experiments, the surface rested at 4.7 K for several days, and was also warmed to just above 200 K and to 300 K. The surface remained unchanged. Fig. 20 shows that the chain length is very stable with aging, always about 2 units long. In addition, the step decoration and triangular clusters are always present, though there are not many examples of the triangular cluster overall.

4. Discussion

4.1. Comparison of triangular clusters with previously-identified Ag_3S_3 clusters

Fig. 21 summarizes previous DFT and STM results from our group regarding the Ag_3S_3 dot cluster.[3] The STM observations are illustrated in Fig. 21a. The dots were observed in a range of sulfur coverages from 0.03 to 0.48 ML and at temperatures of 175 to 225 K. For the most part, the dots were arranged in rows parallel to the close-packed Ag(111) directions. The dots measured 0.70 ± 0.06 nm wide and 0.13 ± 0.01 nm tall, at a tunneling bias of -2.0 V.[3] These dimensions were compatible with predictions of a Ag_3S_3 cluster from DFT, shown in Fig. 21a-b.

In the present work, the triangular clusters are 0.81 ± 0.04 nm (RC) in diameter and 0.016 ± 0.004 nm (RC) tall, at a sample bias of +1 V and comparable tunneling current. Thus the clusters observed in both studies have similar dimensions (compatible within experimental error), and the experimental shapes and dimensions in both works are compatible with the DFT.

4.2. Chain comparison with elongated islands

An earlier experiment by Shen and co-workers showed that the Ag_3S_3 dot-row motif reversibly transforms into elongated islands between 200 and 135 K with 0.09 ML S.[3] Representative images of the elongated islands from that earlier work in our group are shown in Fig. 22 and 23. The islands extend along the close-packed directions and vary in length from 2.92 to 65.9 nm (N=112) and are 1.93 ± 0.36 nm wide. Chains are 1.2 ± 0.2 nm (RAW), 1.5 ± 0.2 nm (RC) wide. (Note that in this previous work, the image correction factor differs from that in the present work.) There are regular bumps down the length of the islands separated by 1.3 ± 0.1 nm (N=49), especially visible in Fig. 22e-f and Fig. 23e-f., suggesting that the islands consist of a repeating unit. The peak-to-peak separation in the chains is 1.12 ± 0.06 nm (RAW), 1.41 ± 0.07 nm (RC).

The elongated islands in the previous work[3] appear very similar to the chains identified in the present work. Both have an anisotropic shape and are composed of a regular unit. Both the chain and island structures have similar widths and peak-to-peak separations, c.f. Tables XI and XII. In addition, the chains and islands are oriented along the close packed directions of the Ag(111) substrate. Both structures are frequently observed along upper step edges and jutting out of descending step edges, in addition to being isolated on the terrace. The density and lengths of elongated islands in the previous work[3] are much higher than the chain density and lengths in our experiments. In the previous work,[3] the elongated islands cover approximately 38% of the surface by area, resulting from a S coverage of 0.09 ML. In the present work, the chains cover approximately 5% of the surface by area. The S coverage in the present work appears to be substantially lower than that in the previous work. Comparing the elongated island and chain area coverage between the studies, we estimate that the S coverage was about 0.01 ML in the present study. Based on visual comparison, similar dimensions, and experimental conditions (i.e. below 200 K), we conclude that the elongated islands and chains are the same structure.

4.3. Proposed chain structure

Based on the data available at the time, our group proposed that the elongated islands were a Ag-S single or double-chain structures shown in Fig. 3.[3] In the double-chain structure, depicted in Fig. 3b, two rows of Ag atoms align along the close packed directions with S atoms occupying every other 4-fold site in the middle of the rows and decorating either side of the rows.[3] New calculations performed by Da-Jiang Liu in association with our group, are refining the earlier model based upon the higher-quality STM images now available. Liu's DFT calculations suggest one possibility that the chain units are $Ag_{10}S_7$ clusters depicted in Fig. 24. The model cluster consists of a S atom in a pseudo 4-fold hollow site formed by four Ag atoms, forming a pyramid; the Ag atoms are the base of the pyramid and the S atom is the apex. The red arrows in Fig. 24b cross at the pyramid's apex. The pyramid is ringed by a set of three quasi-linear AgS_2 fragments (blue lines) separated by three Ag atoms. Four of the ring S atoms reside at the corners of the Ag_4S pyramid. Moving along the red lines in Fig. 24b, across the central Ag_4S pyramid, the S and Ag atoms alternate. The $Ag_{10}S_7$ cluster is elongated along the close-packed <-1 0 1> directions, while the equator lies along the open <1 -2 1> directions. The $Ag_{10}S_7$ cluster is an intuitive match to experimental data based on simulated STM images and features such as the AgS_2 units and 4-fold hollow site. However, this is only one possible structure and further calculations are in progress. Other potential models include the key features of the central Ag_4S pyramid and AgS_2 units.

If the chains are $Ag_{10}S_7$ clusters, then the bright central protrusion corresponds to the Ag-S pyramid, the axial arms to the intersection of two linear AgS_2 pieces pointing away from the pyramid, and the equatorial arms to one linear AgS_2 piece at either side of the pyramid. The topography most closely corresponds to Ag atoms in the model. Fig. 25 compares the model $Ag_{10}S_7$ cluster and high resolution STM images of chains. The $Ag_{10}S_7$ cluster appears as an irregular hexagon with discrete lobes and a bright central protrusion in the STM image simulated via the Tersoff-Hamann method shown in Fig. 24c. The experimental image, Fig. 12a and Fig 25a, reveals more detail than can be replicated in the simulated image. For example, the diamond-like shape of the arms is not articulated in the calculation. On the other hand, there exist examples in which the point of the axial arms is

not always clearly visible. In Fig. 12b and 13 the axial arm appears as two bumps parallel to the equator.

In Fig. 25b, we suggest how the chain units may be linked. Experimentally, the two-unit chains are 0.52 nm (RAW), 0.65 (RC) nm shorter than double the length of a single unit and are observed to have one axial arm between the bright central protrusions. We propose that the chains share an axial arm and are linked the S atom at the point of the Ag-S ring.

The zigzag-like features along step edges resemble chain arms. Compare the arm details in Fig. 12a with Figures 16 and 17. The equatorial and axial chain arms are 0.038 ± 0.009 nm (RAW), 0.036 ± 0.008 nm (RC) (N=16) above the substrate, while the zigzags are 0.03 ± 0.02 nm (RAW), 0.03 ± 0.02 nm (RC) (N=16) above the substrate. The zigzags are approximately 0.57 ± 0.08 nm (RAW), 0.7 ± 0.1 nm (RC) (N=16) wide and the axial arms are 0.76 ± 0.06 nm (RAW), 0.96 ± 0.07 nm (RC) (N=8) wide. Linking axial arms in chain units do not have any neighbors in the equatorial direction (the central protrusions neighbor in the axial direction). However, the zigzags often share corners, so the measured width is shorter than it would be for an isolated feature, like the linking axial arms. From the $Ag_{10}S_7$ model, the zigzag features correspond to the point of the Ag-S ring where two AgS_2 units intersect; a schematic is shown in Fig. 26a. Sometimes the zigzag features surround a bright protrusion like in Fig. 19a-b and e-f, down pointing black arrows. These appear to be partial chain units parallel to the step. Fig. 26b illustrates how these features may be equatorial arms aligned parallel to a step edge, with a S atom on the upper step. The features along step edges, other than the normal S decoration, are mixtures of AgS_2 units.

5. Conclusions

Room temperature deposition of S and cooling to 4.7 K result in three main adsorbate structures: step decoration, triangular clusters, and chains. Each corresponds to previously observed features.[3] S atoms occupy every other site along step edges resulting in decoration. We propose that the triangular clusters observed here are Ag_3S_3 dots observed with 0.03 to 0.47 ML S on Ag(111) at 175 to 225 K. The chains may consist of large Ag-S units, such as $Ag_{10}S_7$, aligned along the close packed directions of the substrate. Key features of potential

models include a S atom in a pseudo 4-fold hollow site and AgS_2 units. The chains and earlier observed elongated islands are the same structure.

Acknowledgements

We thank Da-Jiang Liu for preliminary DFT results. We thank Tomoko Shimizu, Hiroshi Imada, Ju-Hyung Kim, and Hyun Jin Yang for assistance with the experiments. SMR thanks Steven L. Yeninas for assistance writing procedures in Igor Pro to process and organize the STS data discussed in Appendix 2 of this chapter. The experimental component of this work was supported by three sources: NSF Grant CHE-1111500; a Grant-in-Aid for Scientific Research on Priority Areas "Electron Transport Through a Linked Molecule in Nano-scale"; and a Grant-in-Aid for Scientific Research(S) "Single Molecule Spectroscopy using Probe Microscope" from the Ministry of Education, Culture, Sports, Science, and Technology (MEXT) of Japan. The theoretical component of this work was supported by the Division of Chemical Sciences, BES, US Department of Energy (USDOE).

Figures

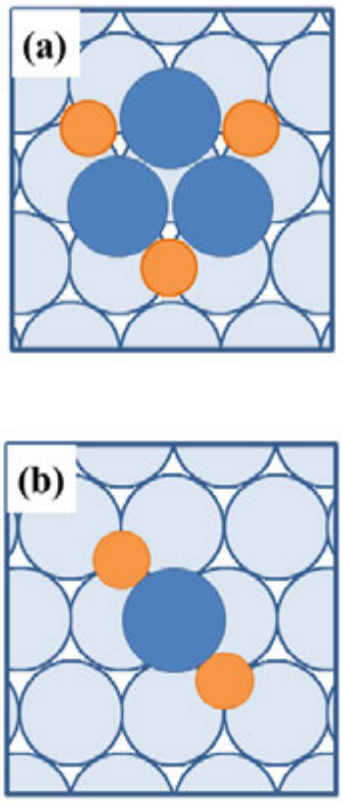

Figure 1. Metal-sulfur clusters on M(111): (a) M_3S_3 and (b) linear MS_2.

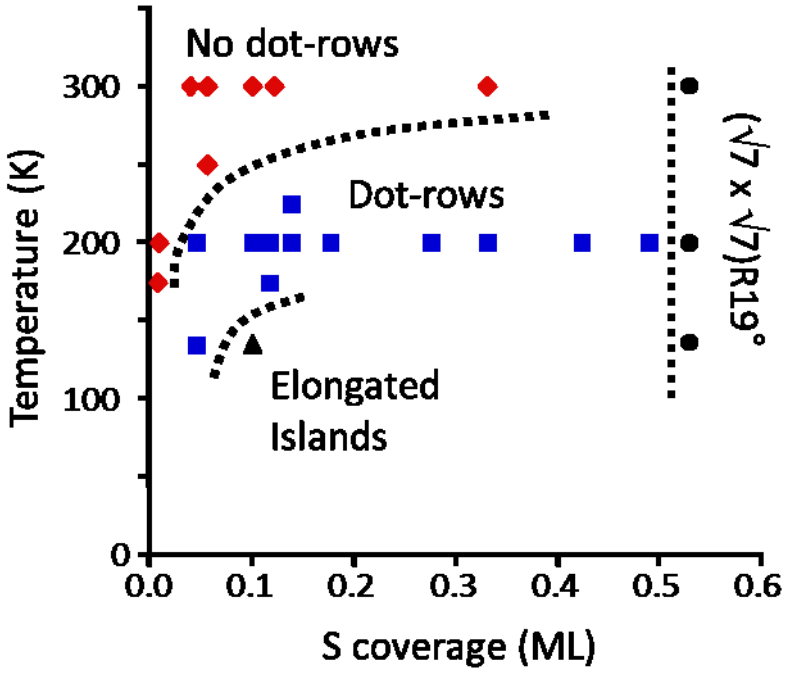

Figure 2. Temperature-coverage diagram for the S/Ag(111) system based on STM results previously published. Additional data include all √7 points and the no dot-row point at 0.33 ML and 300 K. Adapted with permission from Shen, M.; Liu, D. J.; Jenks, C. J.; Thiel, P. A. *Journal of Physical Chemistry C* 2008, *112*, 4281. Copyright 2008 American Chemical Society.

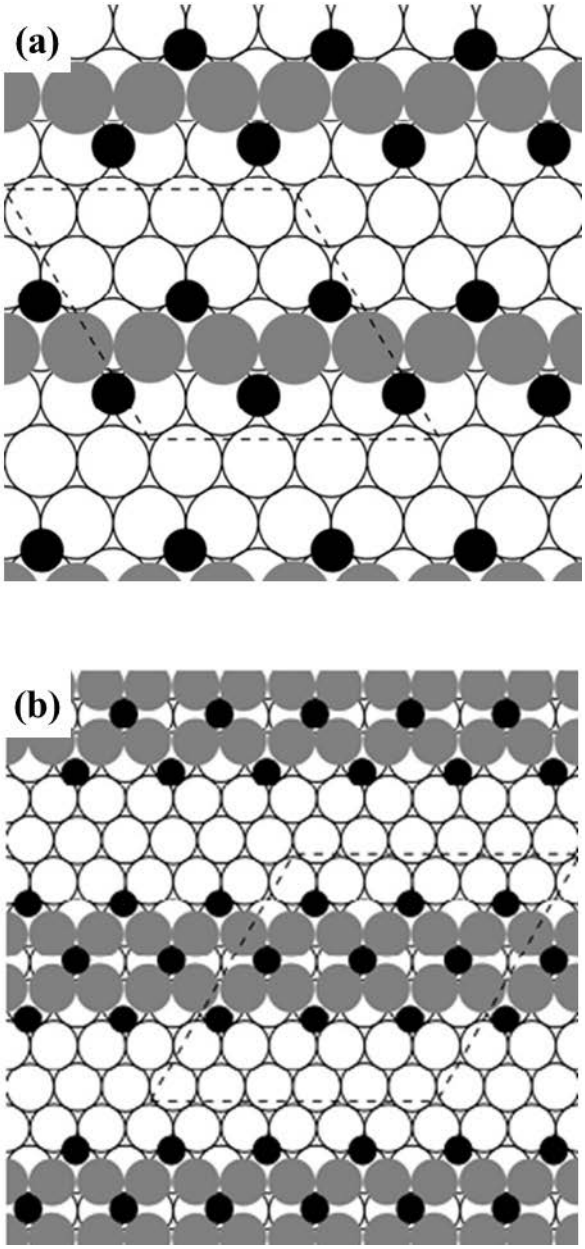

Figure 3. DFT models of Ag-S single-chain (a) and Ag-S double-chain (b) structures. Reprinted with permission from Shen, M.; Liu, D. J.; Jenks, C. J.; Thiel, P. A. *Journal of Physical Chemistry C* 2008, *112*, 4281. Copyright 2008 American Chemical Society.[9]

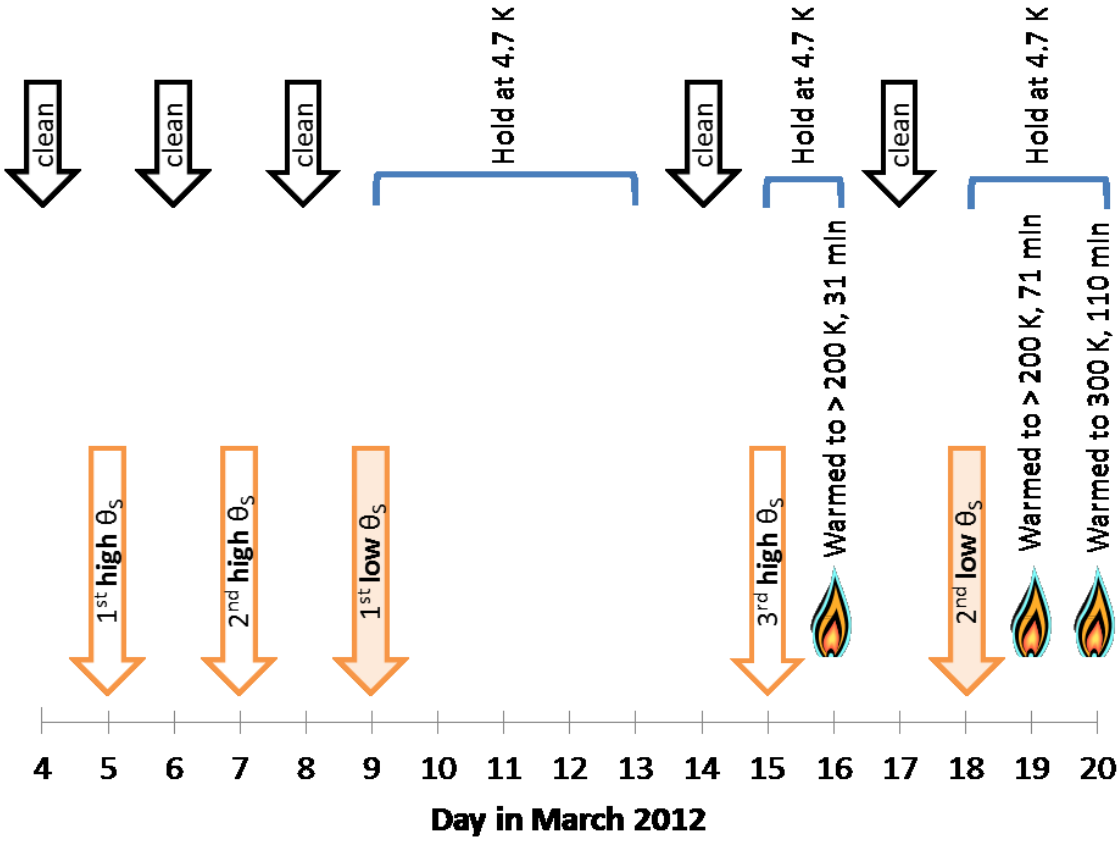

Figure 4. Top black arrows indicate days when the sample was cleaned in the preparation chamber. The blue brackets mark time when the sample was held in the STM stage at 4.7 K. The lower orange arrows indicate when S was deposited. The low coverage experiments are discussed in the main body of this chapter (filled orange arrows). The flame indicates when the sample was warmed to 200 K or higher by removing it from the STM stage and placing it in the cold finger, which was at room temperature or actively cooled by N_2 gas.

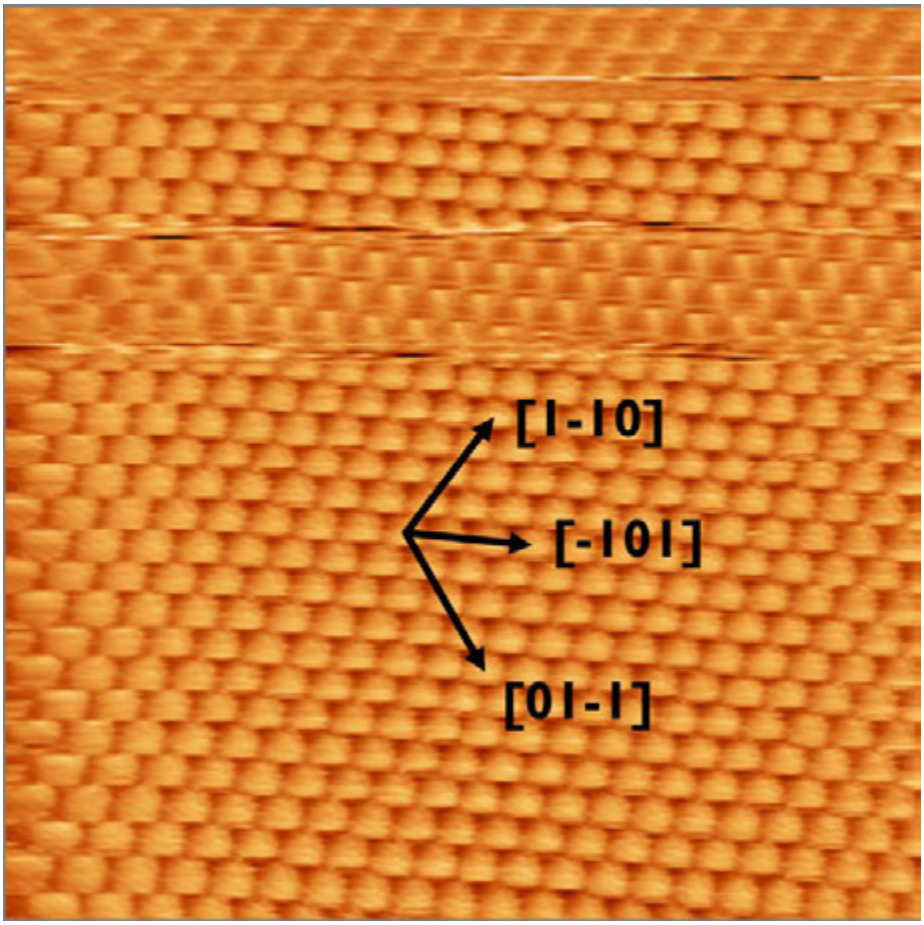

Figure 5. Topographic image of the clean Ag(111) surface. The close-packed <110> crystallographic directions defined here apply to subsequent images, unless otherwise noted. Scanning parameters: I = 2.02 nA, V_{sample} = 6.765 mV, loop gain 1%, 10 nm/s, 5×5 nm^2 (1120310 S_Ag111 continued, m21).

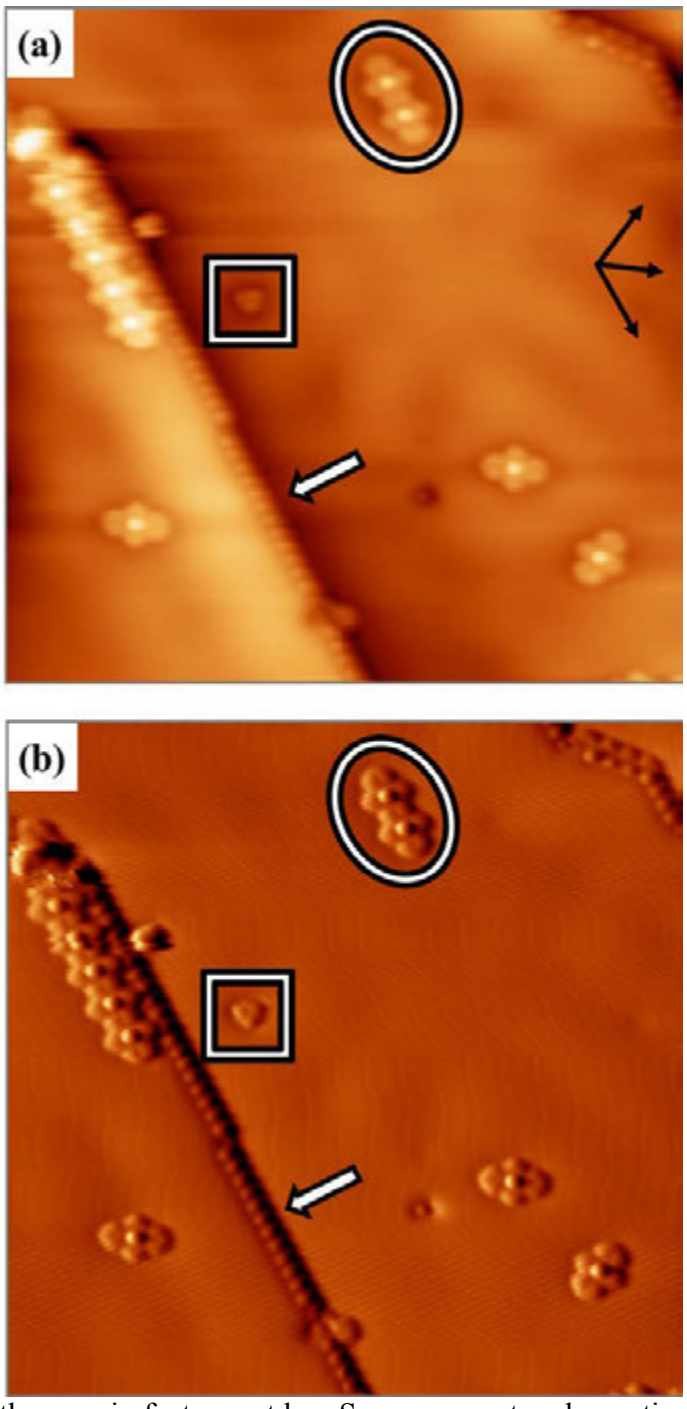

Figure 6. There are three main features at low S coverage: step decoration (black and white arrow), triangular clusters (box), and chains (ellipses). (a) Topographic and (b) differentiated images of the same region. The black arrows on the right hand side in (a) represent the <110> directions. Scanning parameters: I = 2.062 nA, V_{sample} = 7.641 mV, loop gain 1%, 50 nm/s, 20×20 nm^2 (1120311 S_Ag111, m2). Third day of the first low coverage experiment.

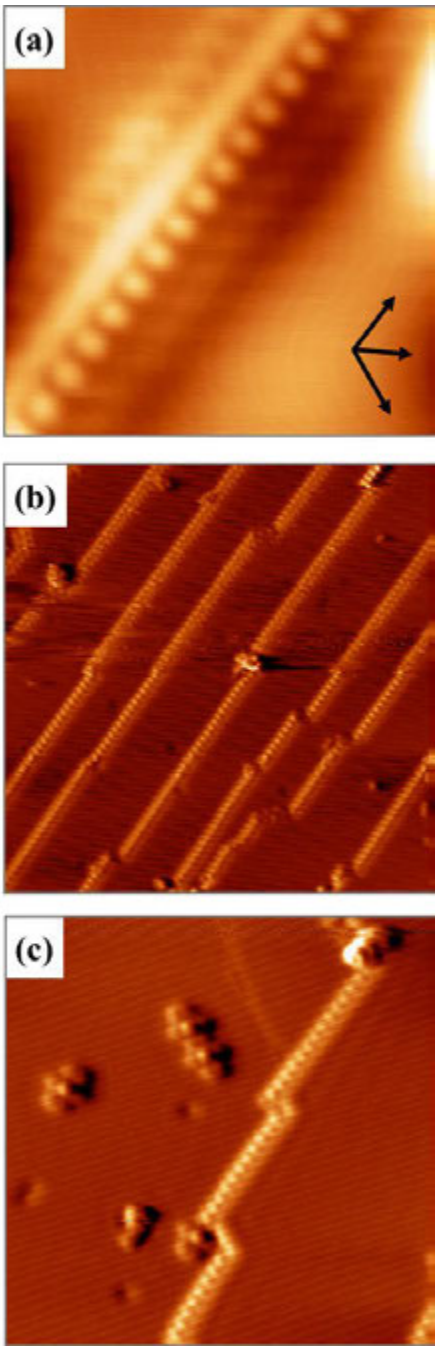

Figure 7. S atom step decoration. These images resulted from the same S deposition (on 3/9), but (b) and (c) were recorded after the surface aged at 4.7 K over one and four nights, respectively. (a) Topography. I = 0.300 nA, V_{sample} = -1.0 V, loop gain 1%, 25 nm/s, 5×5 nm^2, (1120309 S_Ag111, m60). First day of the first low coverage experiment. (b) Differentiated. I = 0.500 nA, V_{sample} = 1.0 V, loop gain 1%, 150 nm/s, 24.9×24.9 nm^2 (1120310 S_Ag111, m16). Second day of the first low coverage experiment. (c) Differentiated. I = 0.500 nA, V_{sample} = 1.0 V, loop gain 1%, 50 nm/s, 15×15 nm^2 (1120313 S_Ag111, m1). Fifth day of the first low coverage experiment.

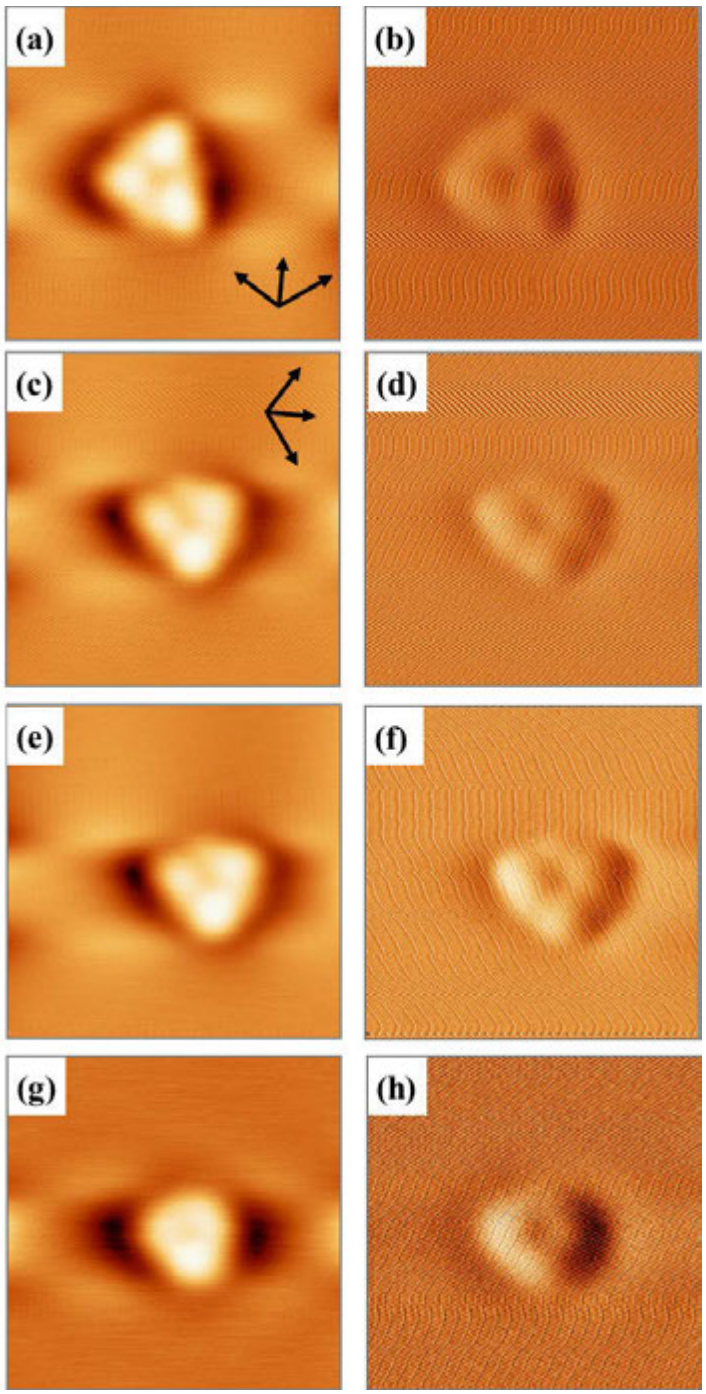

Figure 8. Images of the triangular cluster boxed in Fig. 5 at different voltages and scan directions. Topography images are shown in the left column. Differentiated images are shown in the right column. Scanning parameters: I = 2.062 nA, loop gain 1%, 6.3 nm/s, 2.5×2.5 nm^2 (1120311 S_Ag111). (a-b) V_{sample} = 4.155 mV, scan direction rotated 90^o (m5). (c-d) V_{sample} = 4.155 mV (m4). (e-f) V_{sample} = 7.641 mV (m3). (g-h) V_{sample} = 999.9 mV (m6). Third day of the first low coverage experiment.

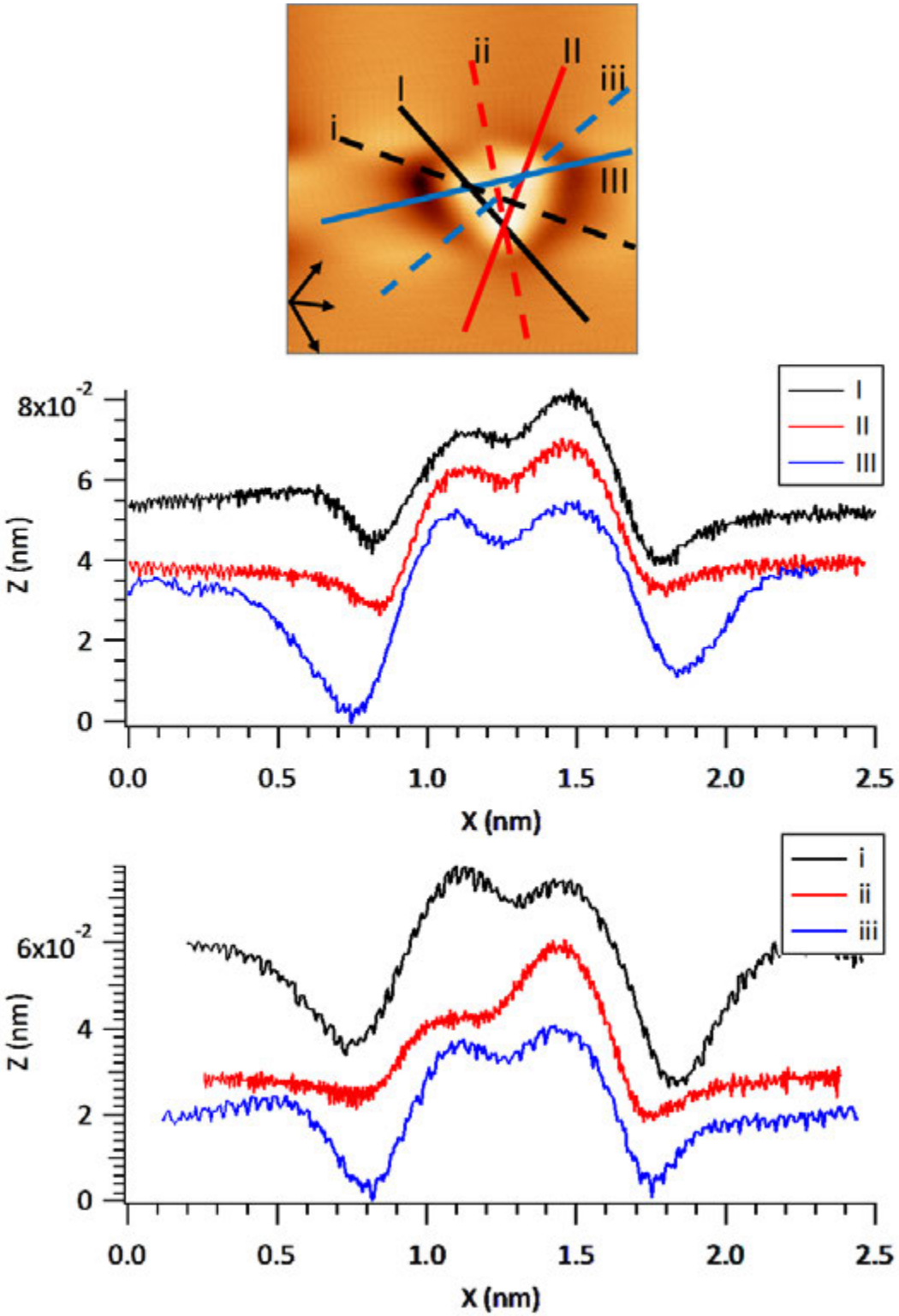

Figure 9. Line profiles across the cluster in Fig. 7e. I = 2.062 nA, V_{sample} = 7.641 mV, loop gain 1%, 6.3 nm/s, 2.5×2.5 nm^2 (1120311 S_Ag111, m3).

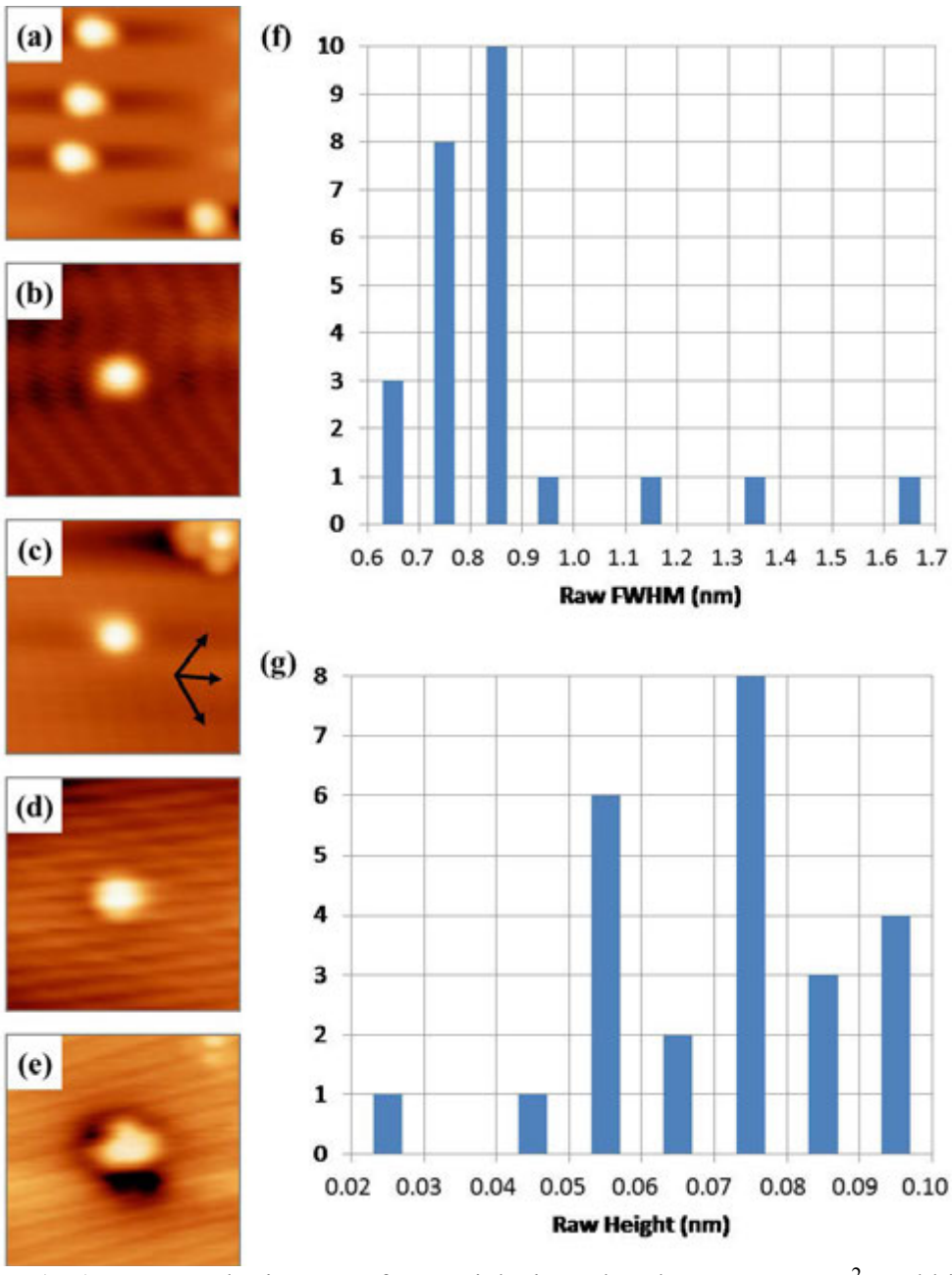

Figure 10. (a-e) Topography images of potential triangular clusters, 5×5 nm^2, and histograms of FWHM (f) and height (g) from the RAW measurement of 25 such features. Scanning parameters: (a) I = 0.9456 nA, V_{sample} = -2.0 V, loop gain 0.5%, 12 nm/s (1120309 S_Ag111, m44). First day of the first low coverage experiment. (b) I = 0.300 nA, V_{sample} = -1.0 V, loop gain 1%, 40 nm/s (1120309 S_Ag111, m48). First day of the first low coverage experiment. (c) I = 1.00 nA, V_{sample} = -0.500 V, loop gain 1%, 41 nm/s (1120309 S_Ag111, m54). First day of the first low coverage experiment. (d) I = 0.5247 nA, V_{sample} = -0.9874 V, loop gain 1.5%, 174 nm/s (1120310 S_Ag111, m3). Second day of the first low coverage experiment. (e) I = 0.8001 nA, V_{sample} = -0.8741 V, loop gain 1%, 188 nm/s (1120318 S_Ag111, m37). First day of the second low coverage experiment.

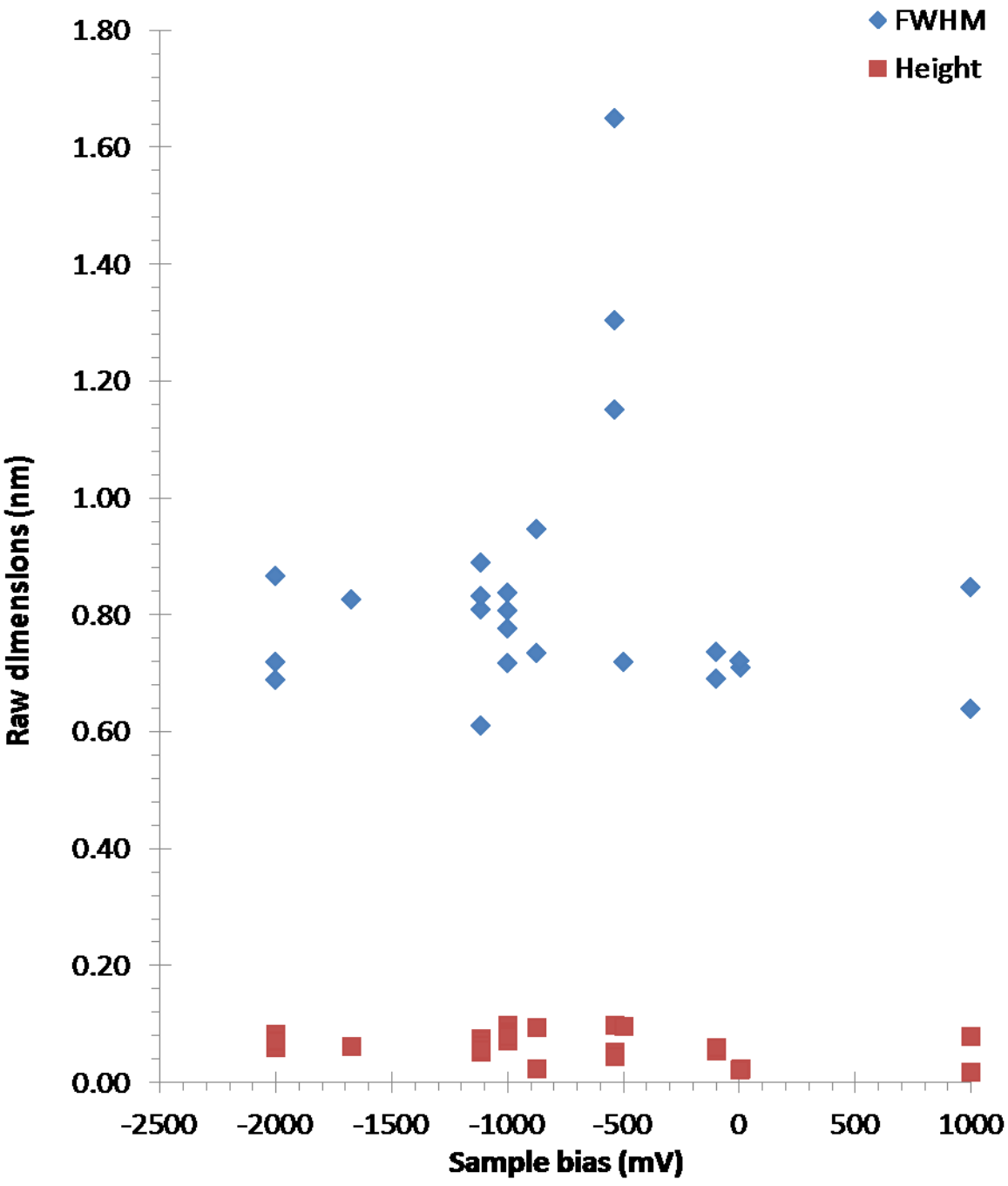

Figure 11. Triangular clusters and possible triangular clusters dimensions as a function of sample bias for clusters in Fig. 8 and 10.

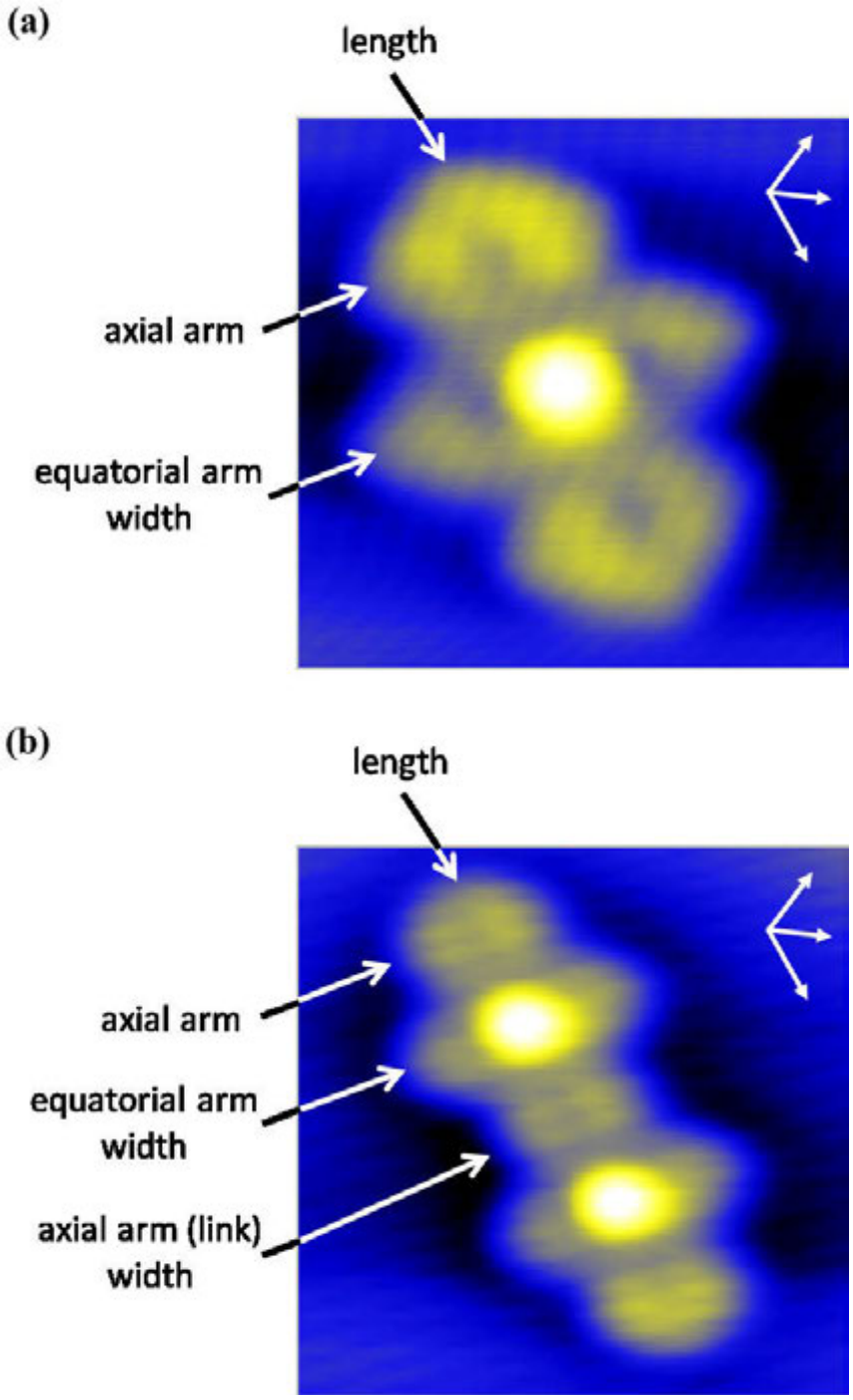

Figure 12. High resolution images of small chains. (a) Single chain unit. I = 0.04599 nA, V_{sample} = 1.0 V, loop gain 0.508%, 6.3 nm/s, 2×2 nm^2 (1120309 S_Ag111, m25). First day of the first low coverage experiment. (b) Double chain unit. I = 2.062 nA, V_{sample} = 7.641 mV, loop gain 1%, 50 nm/s, 3×3 nm^2 (1120311 S_Ag111, m2). Third day of the first low coverage experiment.

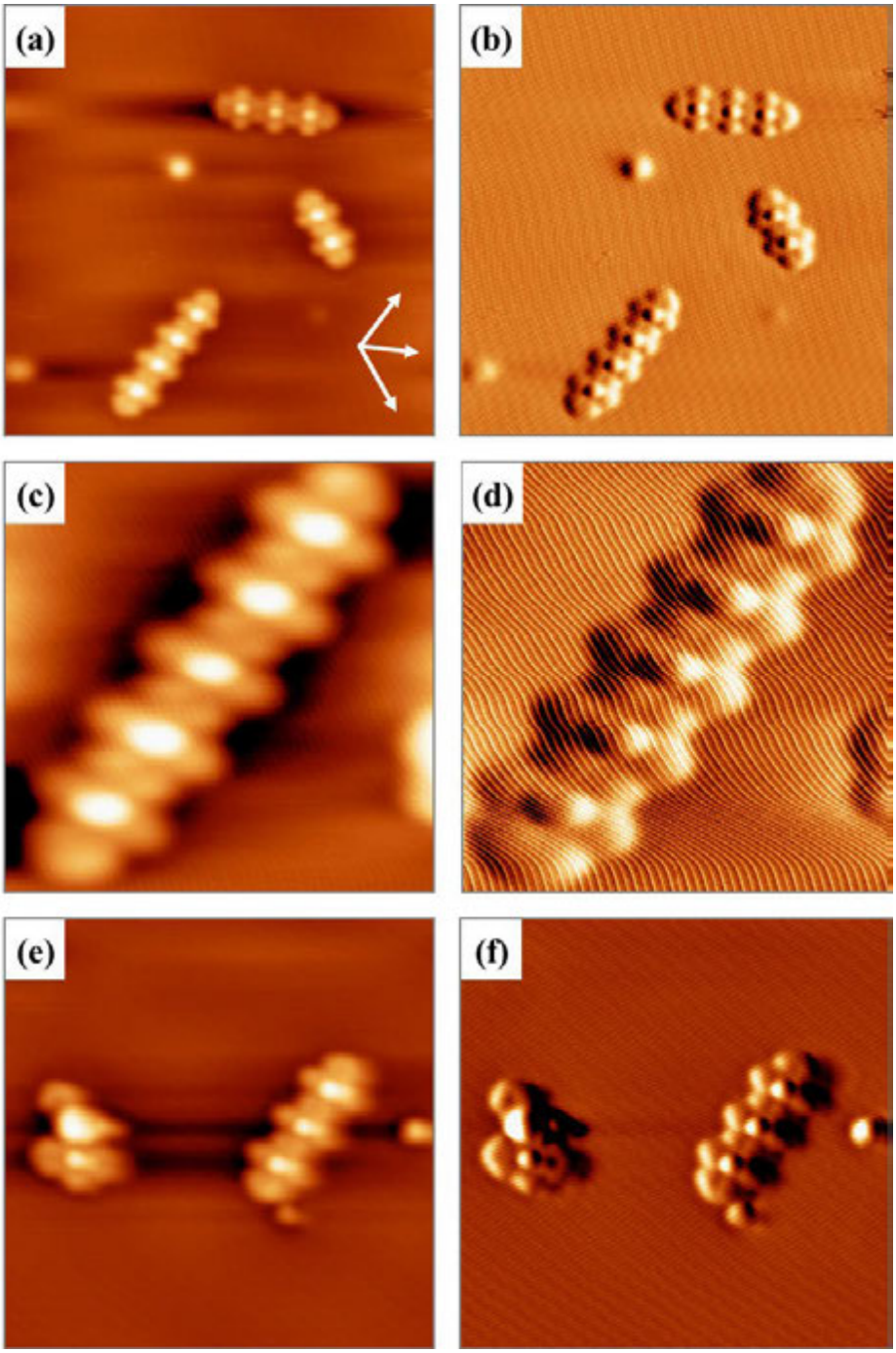

Figure 13. Examples of longer chains. Topography images are shown in the left column. Differentiated images are shown in the right column. Scanning parameters: (a-b) I = 1.0 nA, V_{sample} = -0.500 V, loop gain 1%, 41 nm/s, 15×15 nm^2 (1120309 S_Ag111, m54). First day of the first low coverage experiment. (c-d) I = 0.3715 nA, V_{sample} = -0.6851 V, loop gain 1%, 10 nm/s, 5×5 nm^2 (1120309 S_Ag111, m7). First day of the first low coverage experiment. (e-f) I = 0.5507 nA, V_{sample} = -0.1687 V, loop gain 0.9777%, 45 nm/s, 10×10 nm^2 (1120320S_Ag111, m5). Third day of the second low coverage experiment.

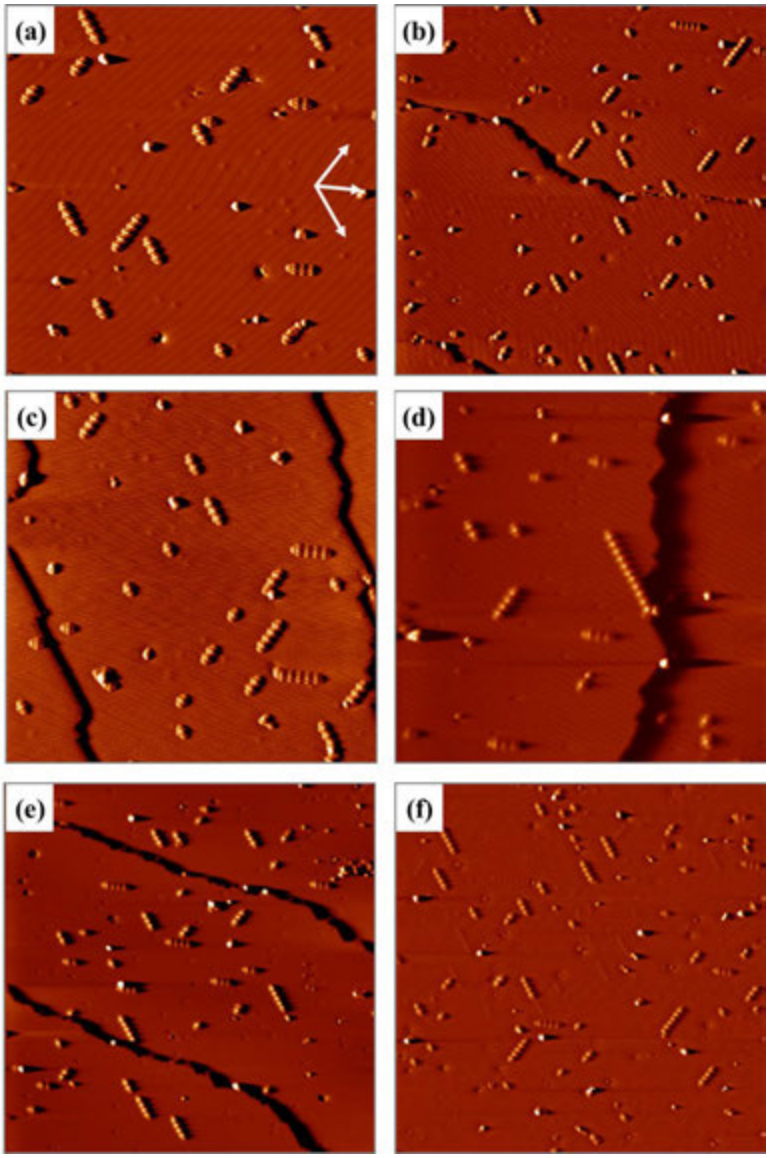

Figure 14. Sulfur on Ag(111) at 4.7 K. Large scale differentiated images showing the chains oriented along the close-packed directions and their varying lengths, (a,c,d) 50×50 nm^2 and (b,e,f) 75×75 nm^2. (a) I = 0.3223 nA, V_{sample} = -1.115 V, loop gain 1.61%, 200 nm/s, 50×50nm^2 (1120309 S_Ag111, m2). First day of the first low coverage experiment. (b) I = 0.2912 nA, V_{sample} = -1.0 V, loop gain 1%, 161 nm/s, 75×75 nm^2 (1120309 S_Ag111, m50). First day of the first low coverage experiment. (c) I = 0.5247 nA, V_{sample} = -0.9874 V, loop gain 1.5%, 174 nm/s, 50×50 nm^2, (1120310 S_Ag111, m2). Second day of the first low coverage experiment. (d) I = 0.178 nA, V_{sample} = 1.0 V, loop gain 1%, 150 nm/s, 50×50 nm^2 (1120312 S_Ag111, m38). Fourth day of the first low coverage experiment. (e) I = 1.0 nA, V_{sample} = 1.0 V, loop gain 1%, 225 nm/s, 75×75 nm^2 (1120313 S_Ag111, m8). Fifth day of the first low coverage experiment. (f) I = 0.8001 nA, V_{sample} = -0.8741 V, loop gain 1%, 188nm/s, 75×75 nm^2 (1120318 S_Ag111, m36). First day of the second low coverage experiment.

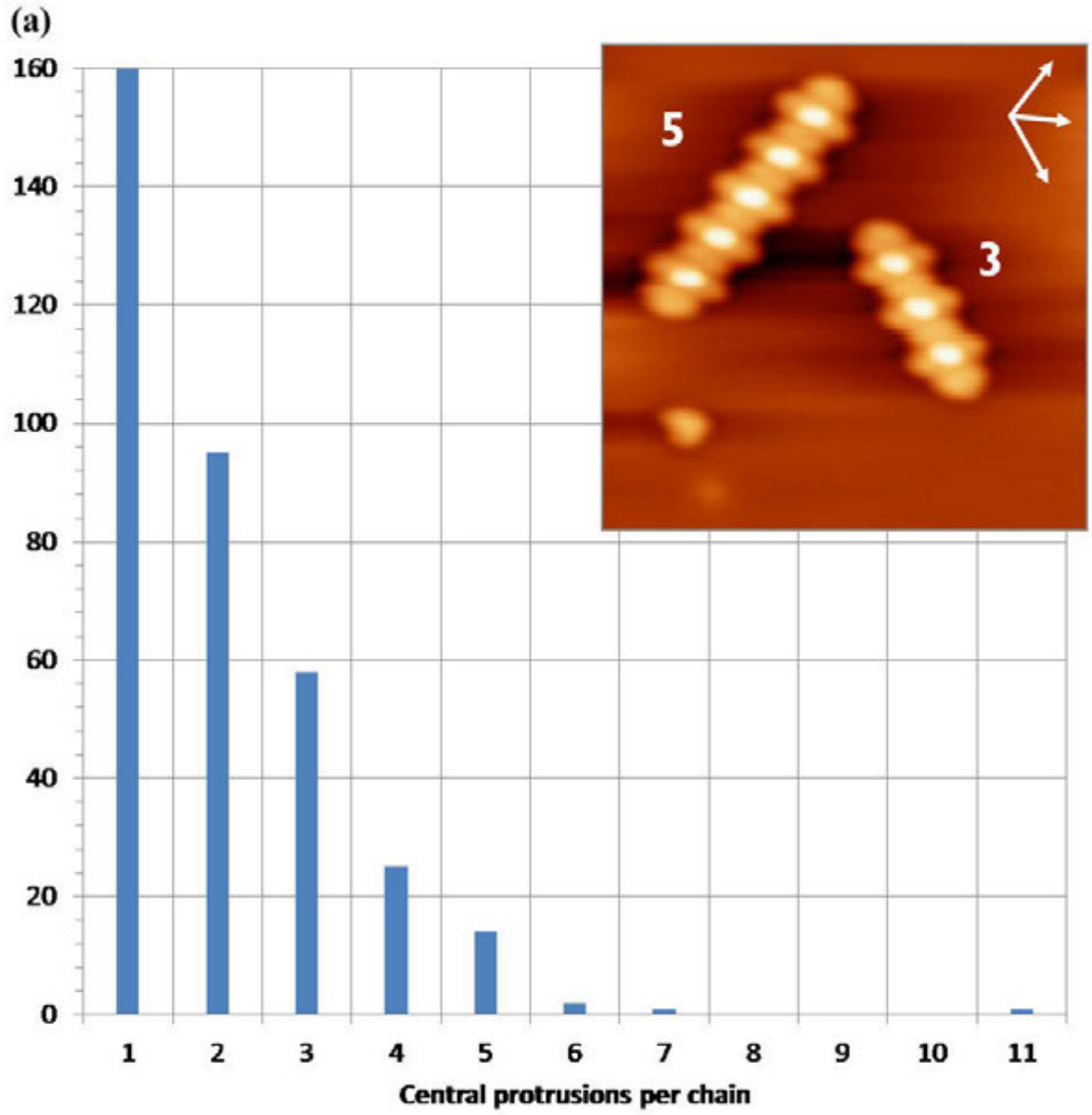

This figure continues on the following page.

Figure 15. Chain length histogram in terms of chain units indicated by the number of central protrusions per chain (1 central protrusion = 1 chain unit) over 23 regions, several days, and two different S depositions. Inset: Topographic image recorded at I = 0.3715 nA, V_{sample} = -1.115 V, loop gain 1%, 20nm/s, 10×10 nm^2 (1120309 S_Ag111, m6) illustrating 5 and 3 unit chains. First day of the first low coverage experiment. (a) Distribution of chain lengths for 356 chains regardless of proximity to step-edge or pinning. (b) Distribution of chain lengths for 294 chains away from step-edges and without pinning.

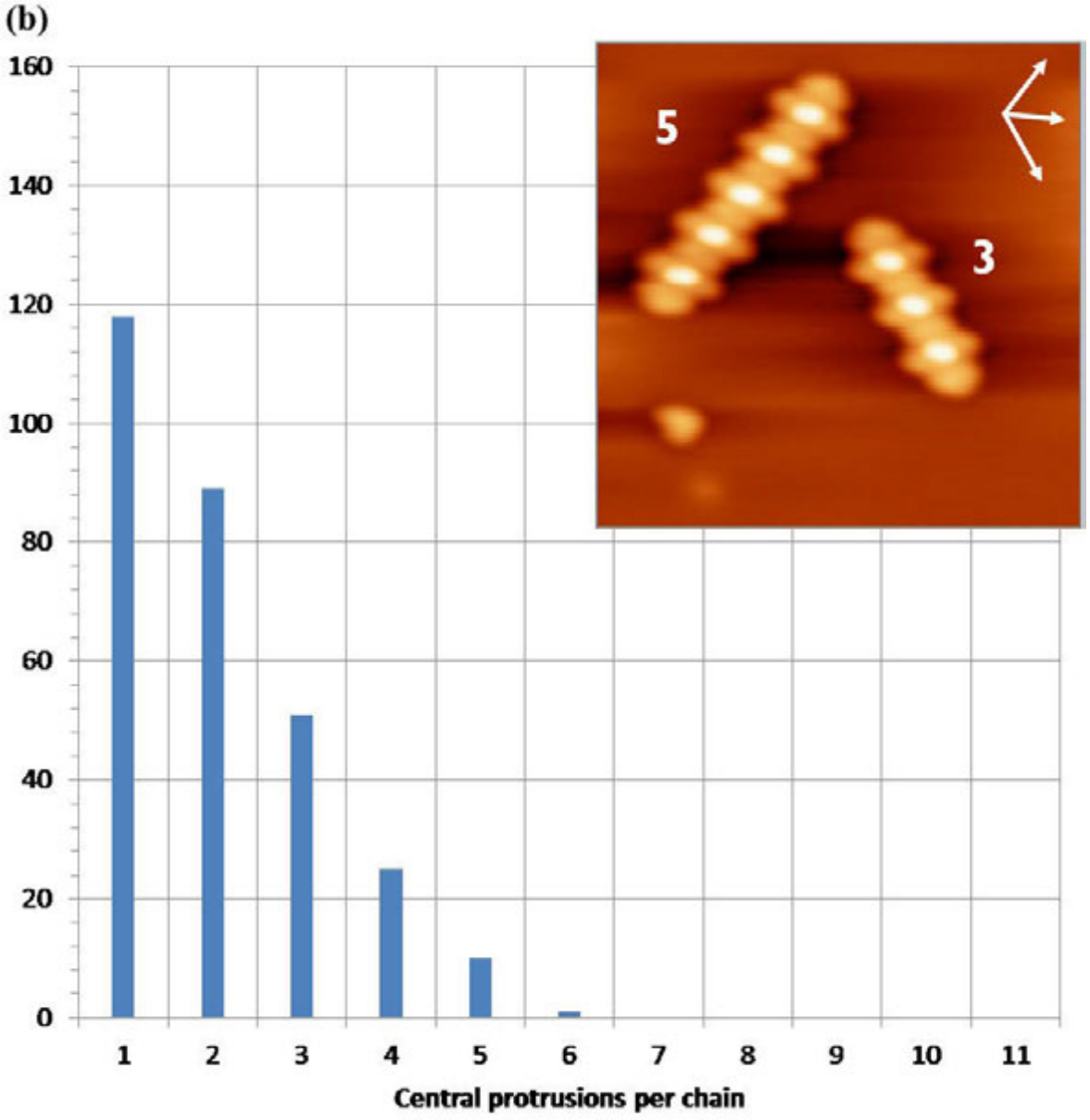

Figure 15. continued

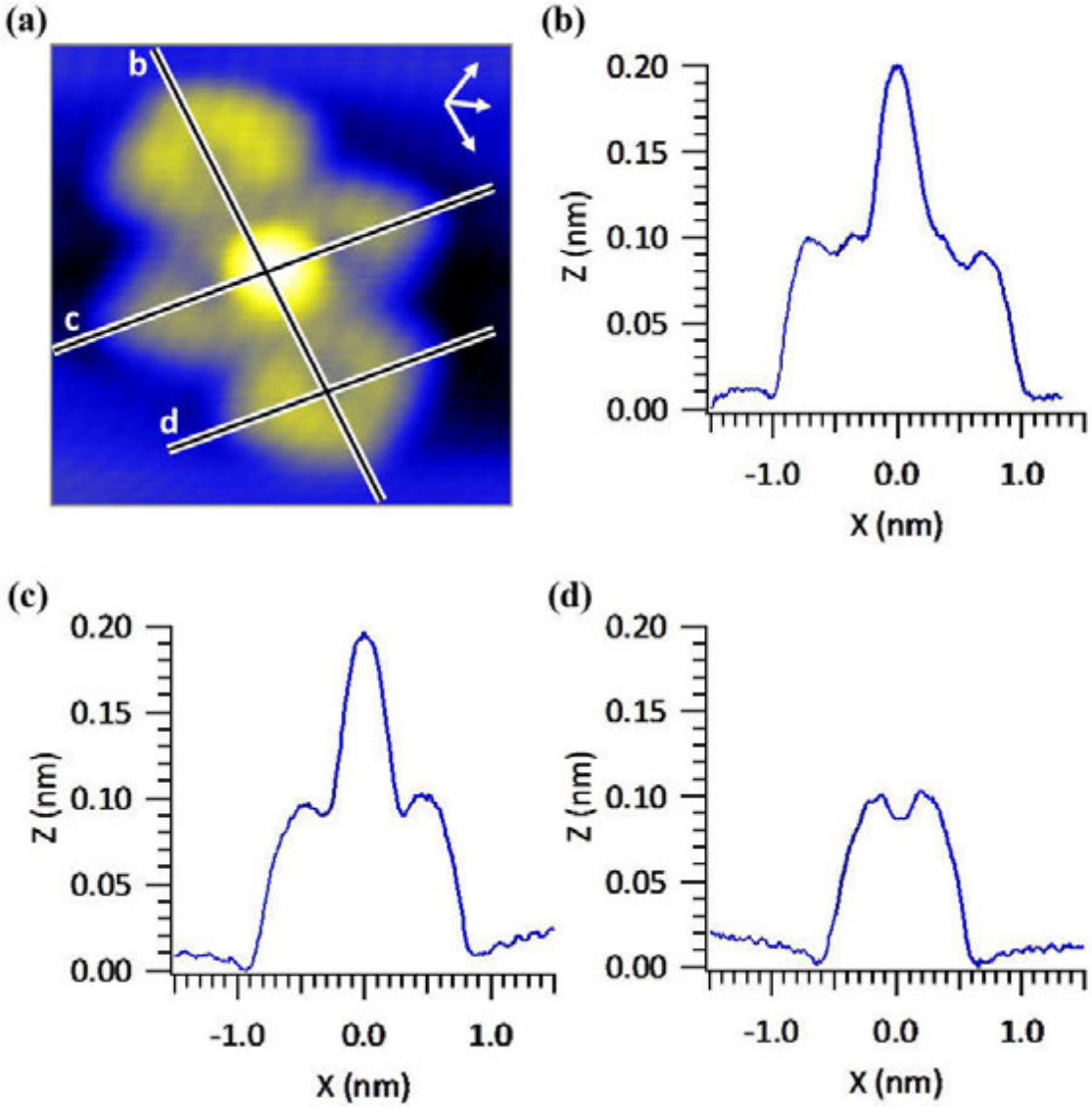

Figure 16. (a) Same image as 10a: I = 0.04599 nA, V_{sample} = 1.0 V, loop gain 0.508%, 6.3 nm/s, 2×2 nm^2 (1120309 S_Ag111, m25). First day of the first low coverage experiment. (b-d) Line profiles along the lines marked in (a), length (b), equatorial arm width (c), and axial arm width (d).

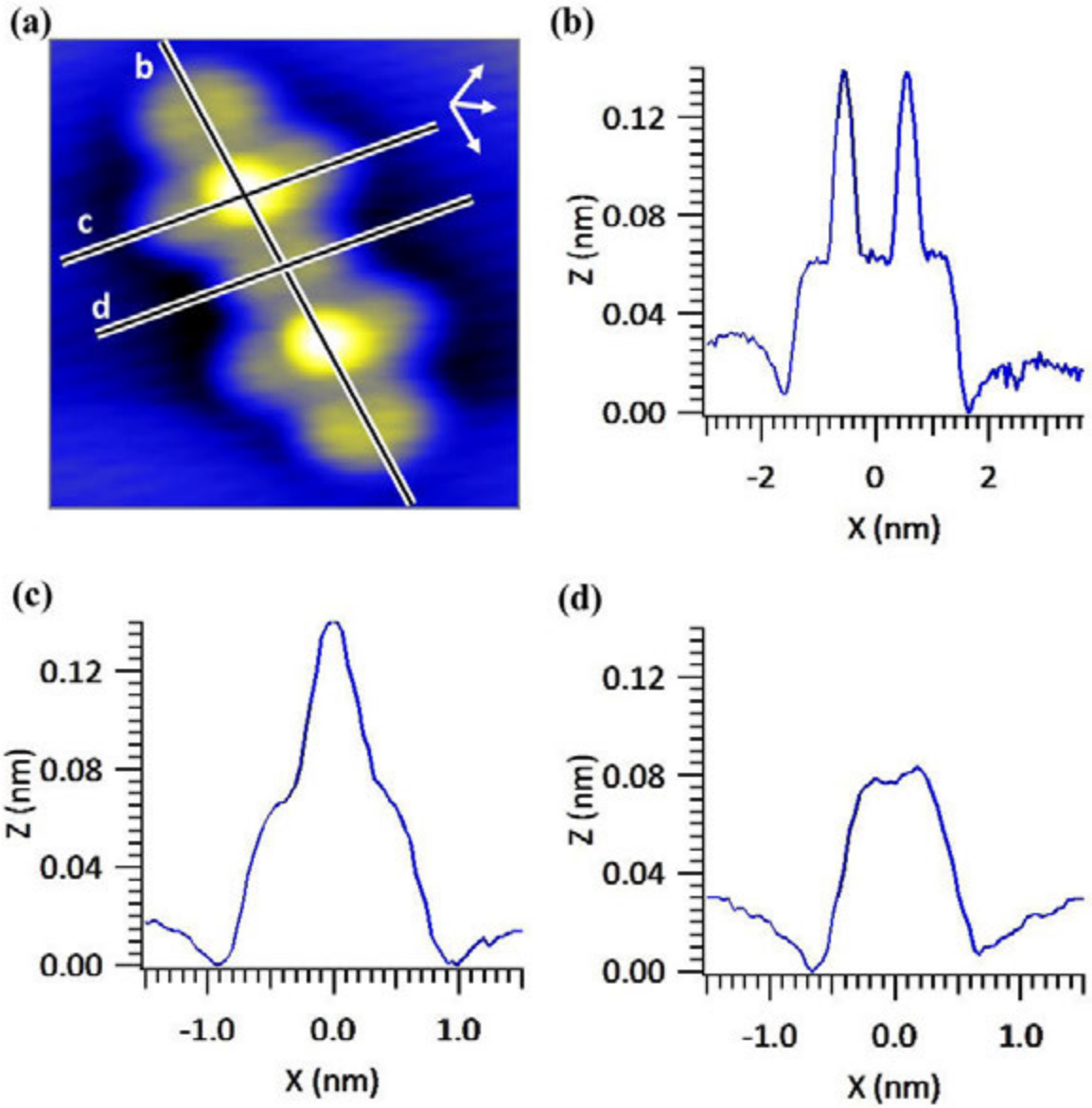

Figure 17. (a) Same image as 10b: I = 2.062 nA, V_{sample} = 7.641 mV, loop gain 1%, 50 nm/s, 3×3 nm^2 (1120311 S_Ag111, m2). Third day of the first low coverage experiment. (b-d) Line profiles along the lines marked in (a), length (b), equatorial arm width (c), and interior axial arm width (d).

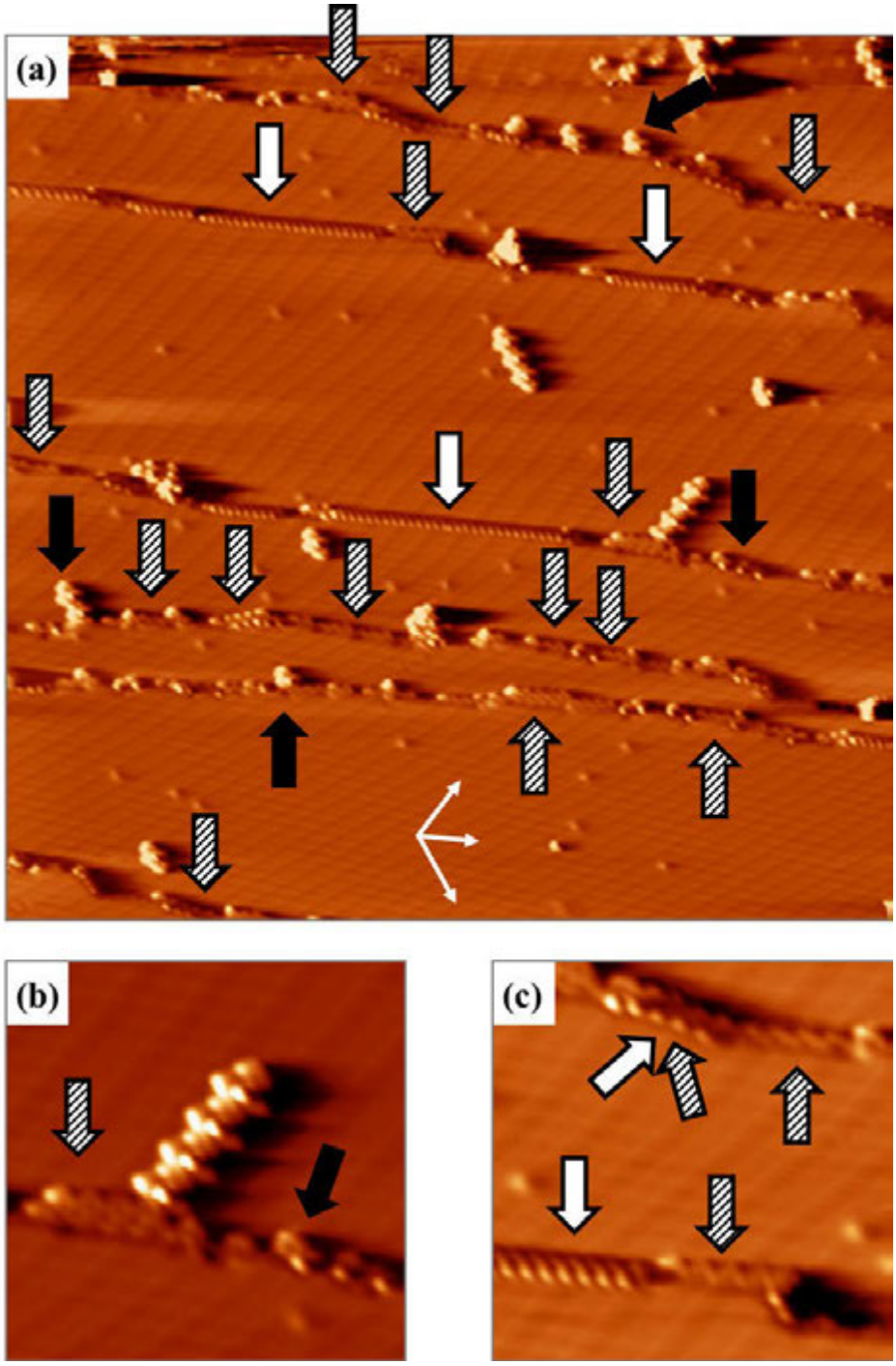

Figure 18. Step edge features including chain fragments (black arrows), decoration (white arrows), and zigzags (patterned arrows). The white arrows point to step decoration like that in Fig. 6. Differentiated images with scanning parameters: I = 0.2853 nA, V_{sample} = -0.9874 V, loop gain 1%, 199 nm/s, (1120309 S_Ag111, m21). First day of the first low coverage experiment. (a) 50×50 nm^2, (b-c) 10×10 nm^2.

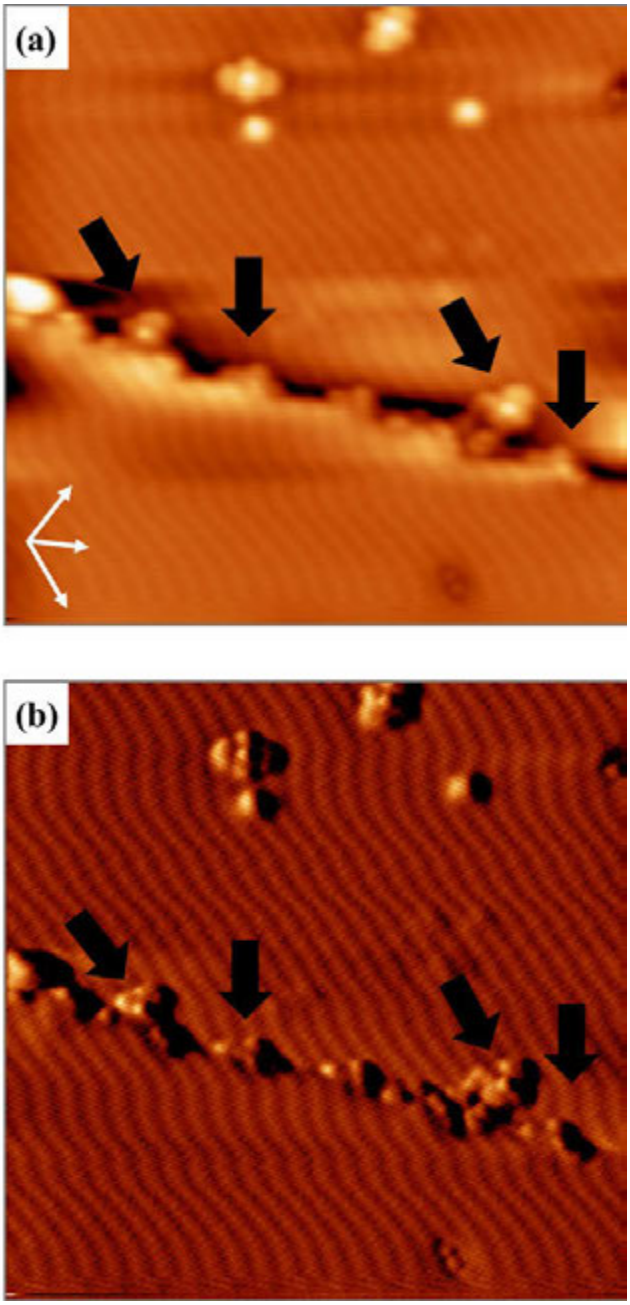

This figure continues on the following page.

Figure 19. Step edge features including chain fragments (black arrows), decoration (white arrows), and zigzags (patterned arrows). The white arrows point to step decoration like that in Fig. 6. Topography (top) and differentiated (bottom). The boxes in (c) and (d) are magnified in (e) and (f), respectively. (a-b) I = 0.300 nA, V_{sample} = -1.0 V, loop gain 1%, 40 nm/s, 20×20 nm^2 (1120309 S_Ag111, m48). First day of the first low coverage experiment. (c-f) I = 2.0 nA, V_{sample} = 0.020 V, loop gain 1%, 40 nm/s, (1120311 S_Ag111, m10). Third day of the first low coverage experiment. (c-d) 20×20 and (e-f) 10×10 nm^2.

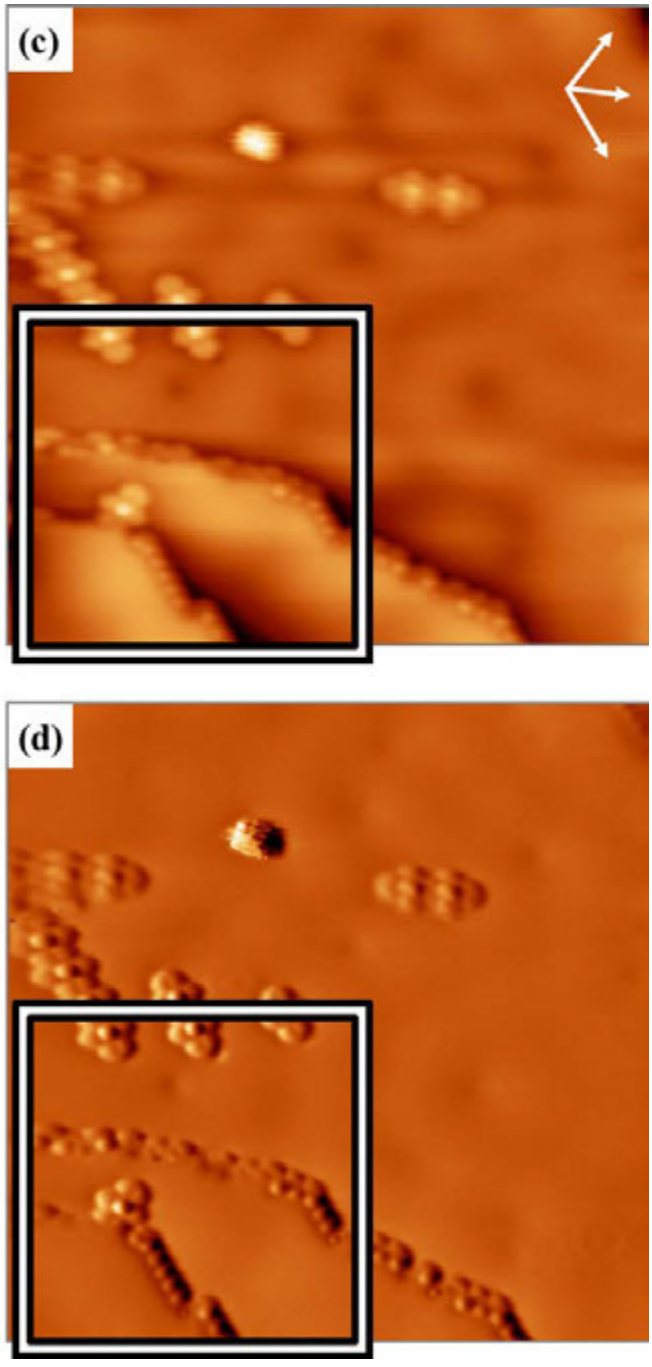

This figure continues on the following page.

Figure 19. continued.

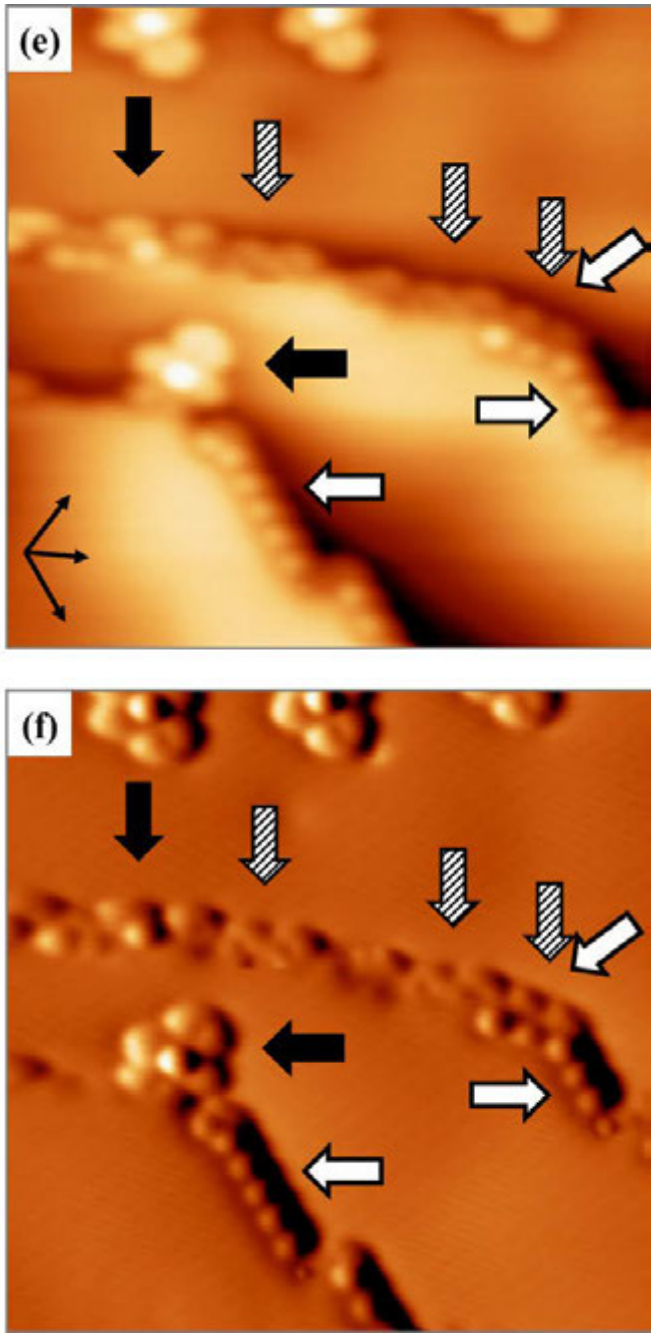

Figure 19. continued.

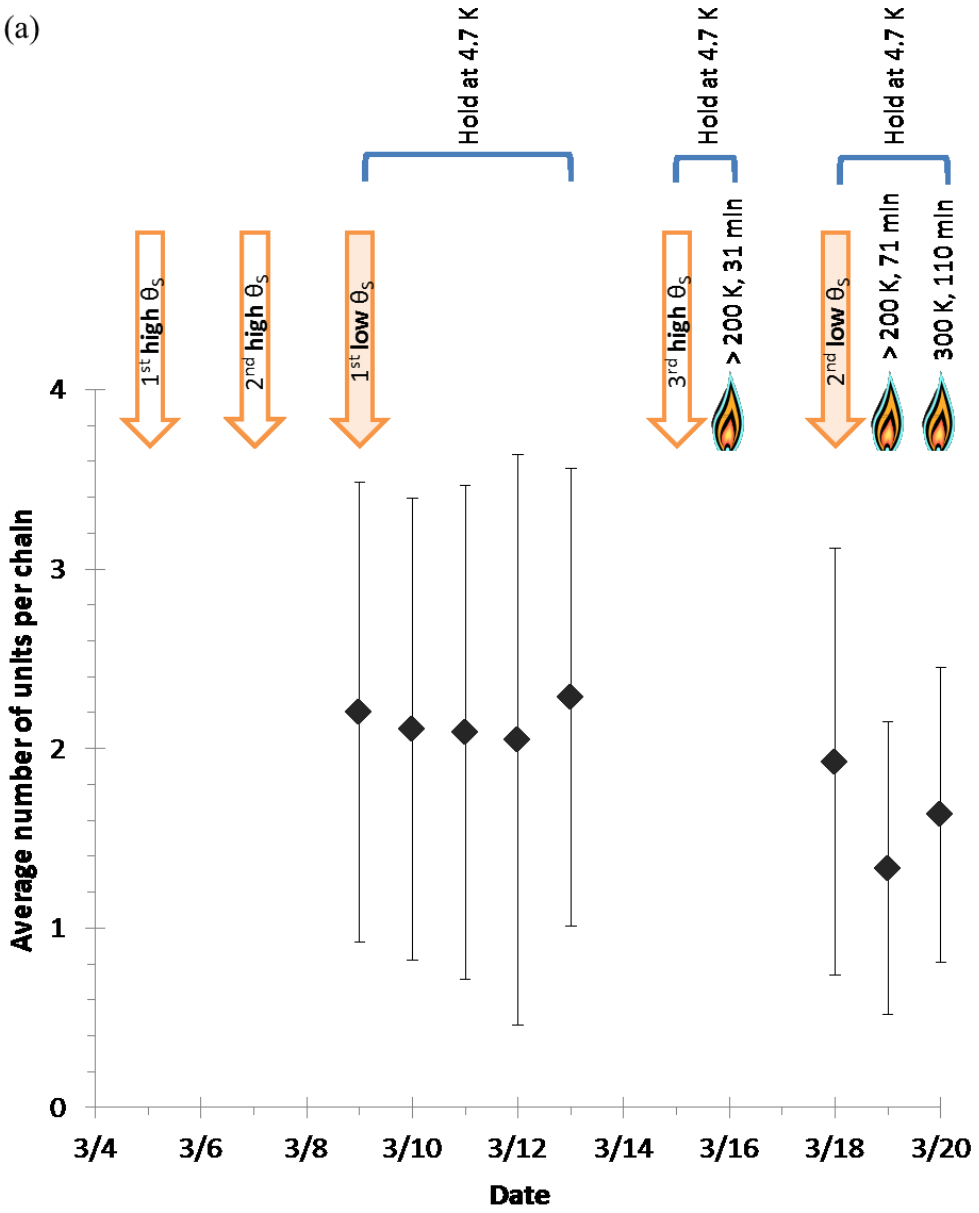

This figure continues on the following page.

Figure 20. The orange arrows indicate when S was deposited. The blue brackets mark time when the sample was held in the STM stage at 4.7 K. The flame indicates when the sample was warmed to 200 K or higher by removing it from the STM stage and placing it in the cold finger. (a) Average chain lengths for 356 chains regardless of proximity to step-edge or pinning. (b) Average chain lengths for 294 chains away from step-edges and without pinning. The error bars are the standard deviation. The statistics are summarized in Table XIII. (c-f) Chain length histogram in terms of chain units for (c-d) the first and (e-f) second low coverage experiments. (c, e) Distribution of all chains. (d, f) Distribution of chains on terraces, not pinned or connected to steps.

(b)

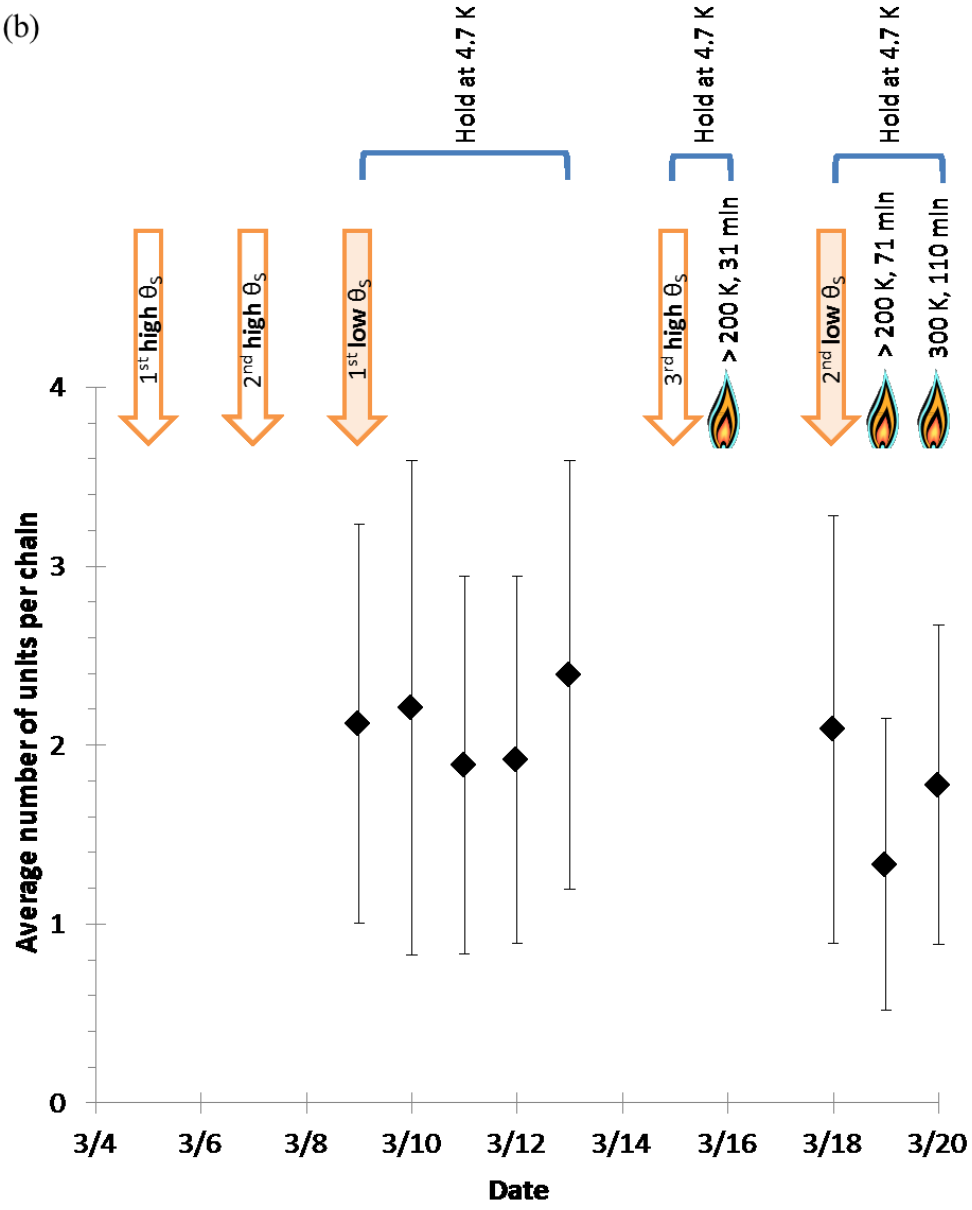

This figure continues on the following page.

Figure 20. continued

(c)

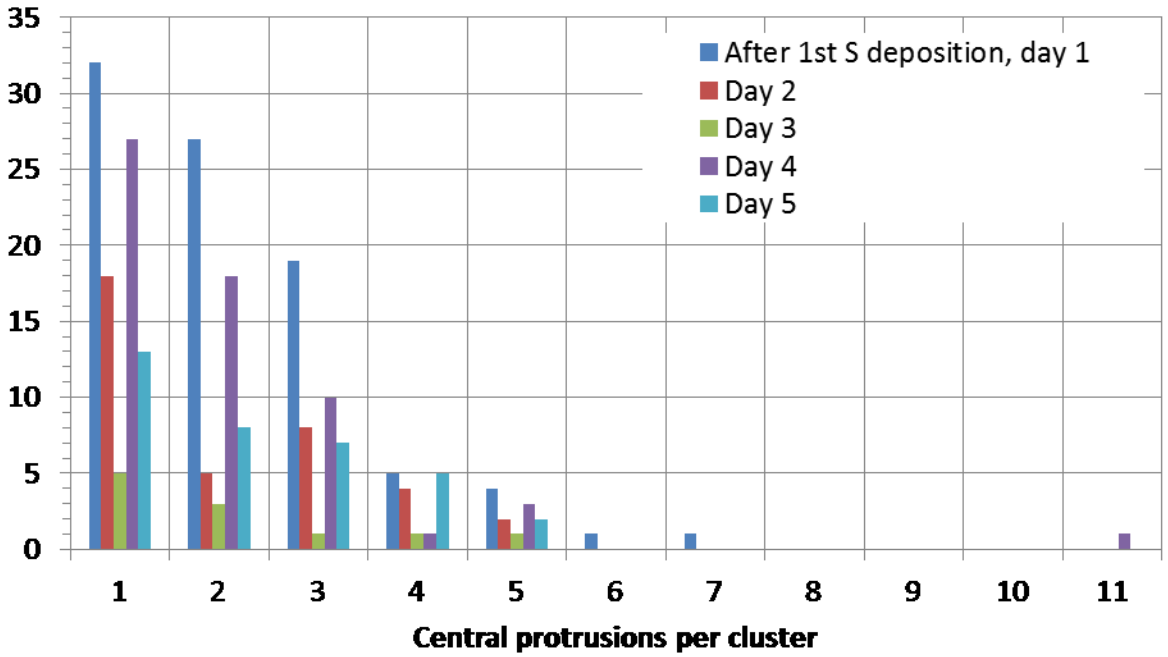

(d)

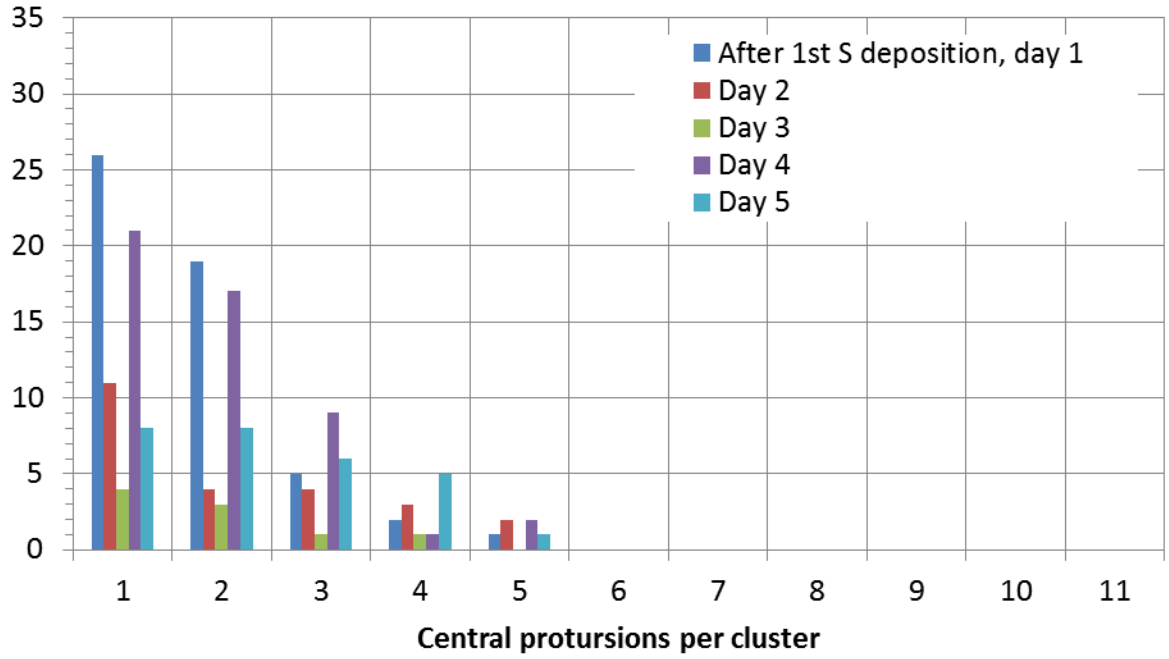

This figure continues on the following page.

Figure 20. continued

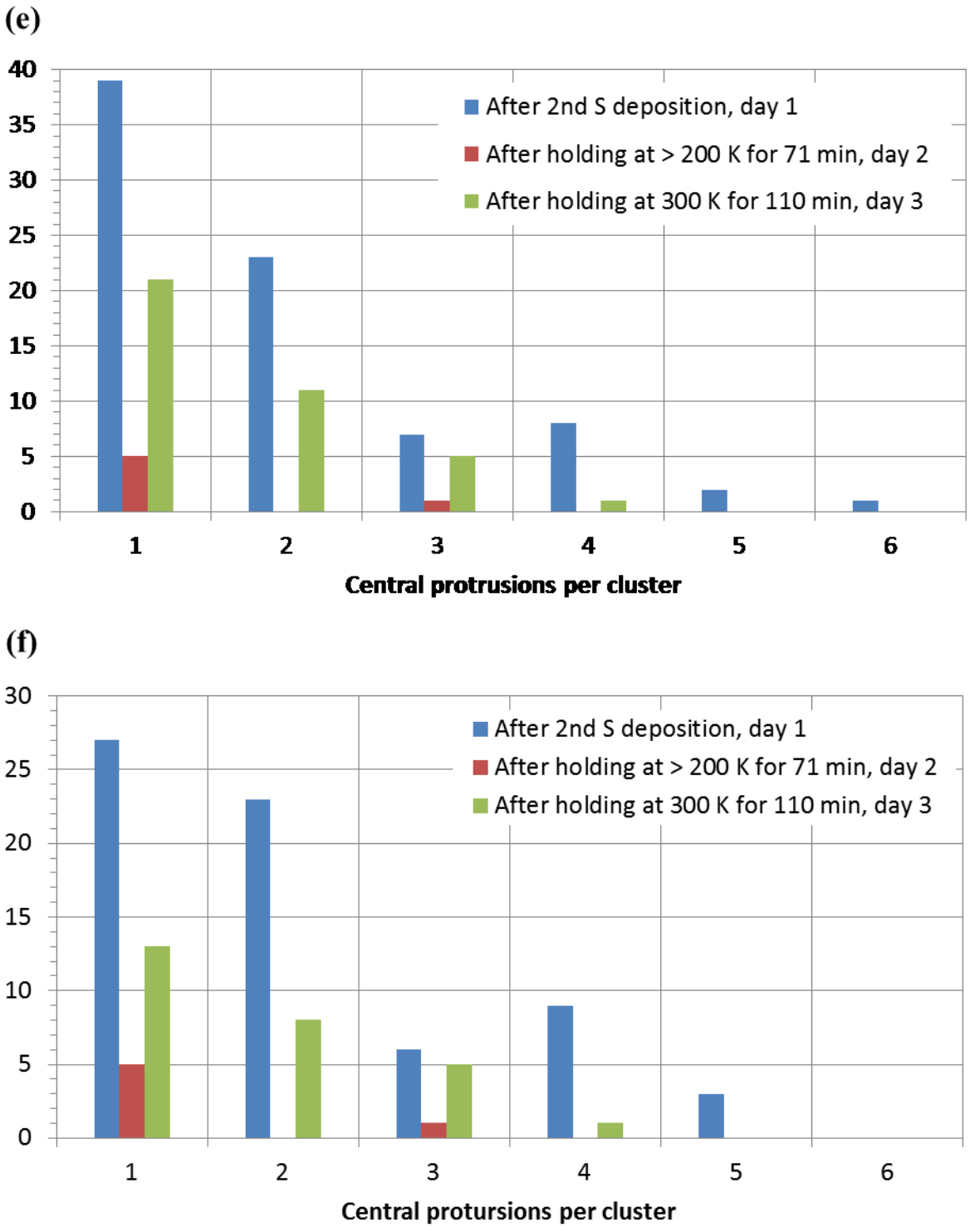

Figure 20. Continued

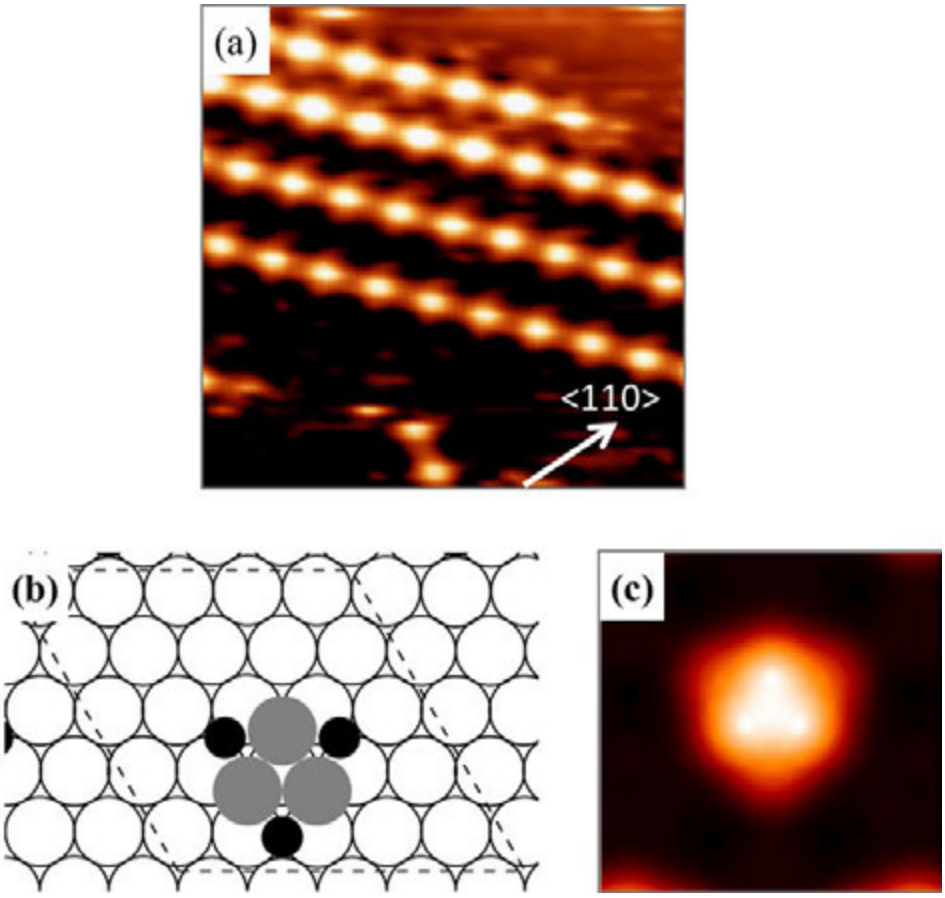

Figure 21. (a) Ag_3S_3 cluster in the dot row motif with 0.03 ML S at 200 K, 15×15 nm^2, I = 1.0 nA, V_{tip} = -2.0 V. (b) Ag_3S_3 cluster configuration from DFT calculations. Results were obtained using a 5×5 supercell denoted by the dashed line. (c) Simulated STM image, bias = -2 V, via the Tersoff-Hamann method.[18] All of the images in this figure are reprinted or adapted with permission from Shen, M.; Liu, D. J.; Jenks, C. J.; Thiel, P. A. *Journal of Physical Chemistry C* 2008, *112*, 4281. Copyright 2008 American Chemical Society.[9]

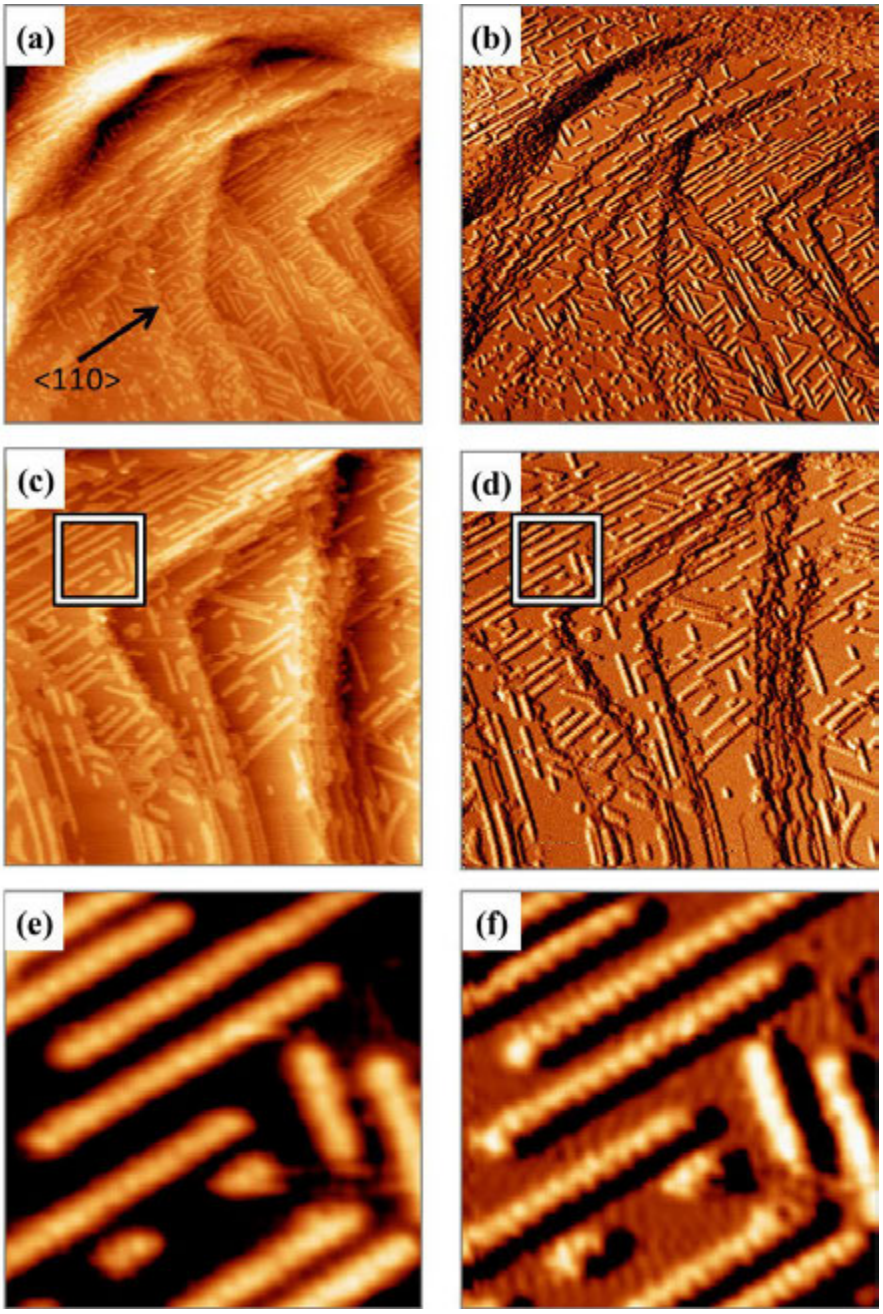

Figure 22. Elongated island topography (left) and differentiated (right) STM images from earlier experiments at 135 K with 0.09 ML S. (a-b) I = 1.00 nA, V_{tip} = 2.00 V, loop gain 3%, 732 nm/s, 250×250 nm^2, (01-11-2007, m55). (c-f) I = 1.00 nA, V_{tip} = 2.00 V, loop gain 3%, 732 nm/s (01-11-2007, m57), (c-d) 146.5×146.5 nm^2 and (e-f) 25.5×25.5 nm^2, FFT filtered (Blackman-Harris pass). The boxes in (c) and (d) are magnified in (e) and (f), respectively. A 120×120 nm^2 portion of (c) is adapted with permission from Shen, M.; Liu, D. J.; Jenks, C. J.; Thiel, P. A. *Journal of Physical Chemistry C* 2008, *112*, 4281. Copyright 2008 American Chemical Society.[9]

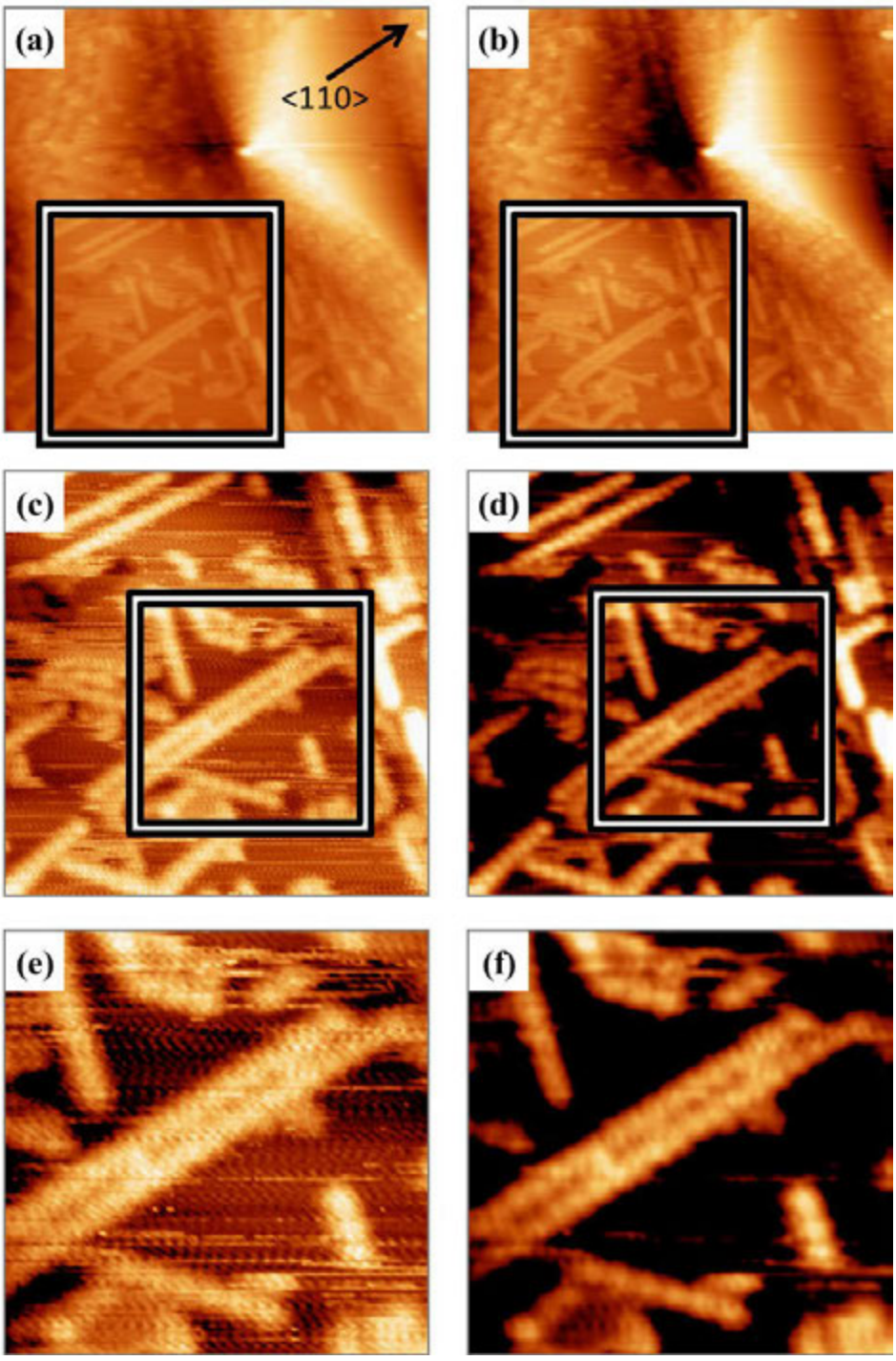

Figure 23. Another view of the elongated islands observed at 135 K with 0.09 ML S. All images are topographic. The images in the left column are unprocessed, while those in the right column have been smoothed. Scanning parameters: I = 1.00 nA, V_{tip} = 2.00 V, loop gain 3%, 502 nm/s, (01-11-2007, m54). (a-b) 100×100 nm^2, (c-d) 50×50 nm^2, and (e-f) 25.1×25.1 nm^2. The boxes in (a) and (b) are magnified in (c) and (d), respectively. The boxes in (c) and (d) are magnified in (e) and (f), respectively.

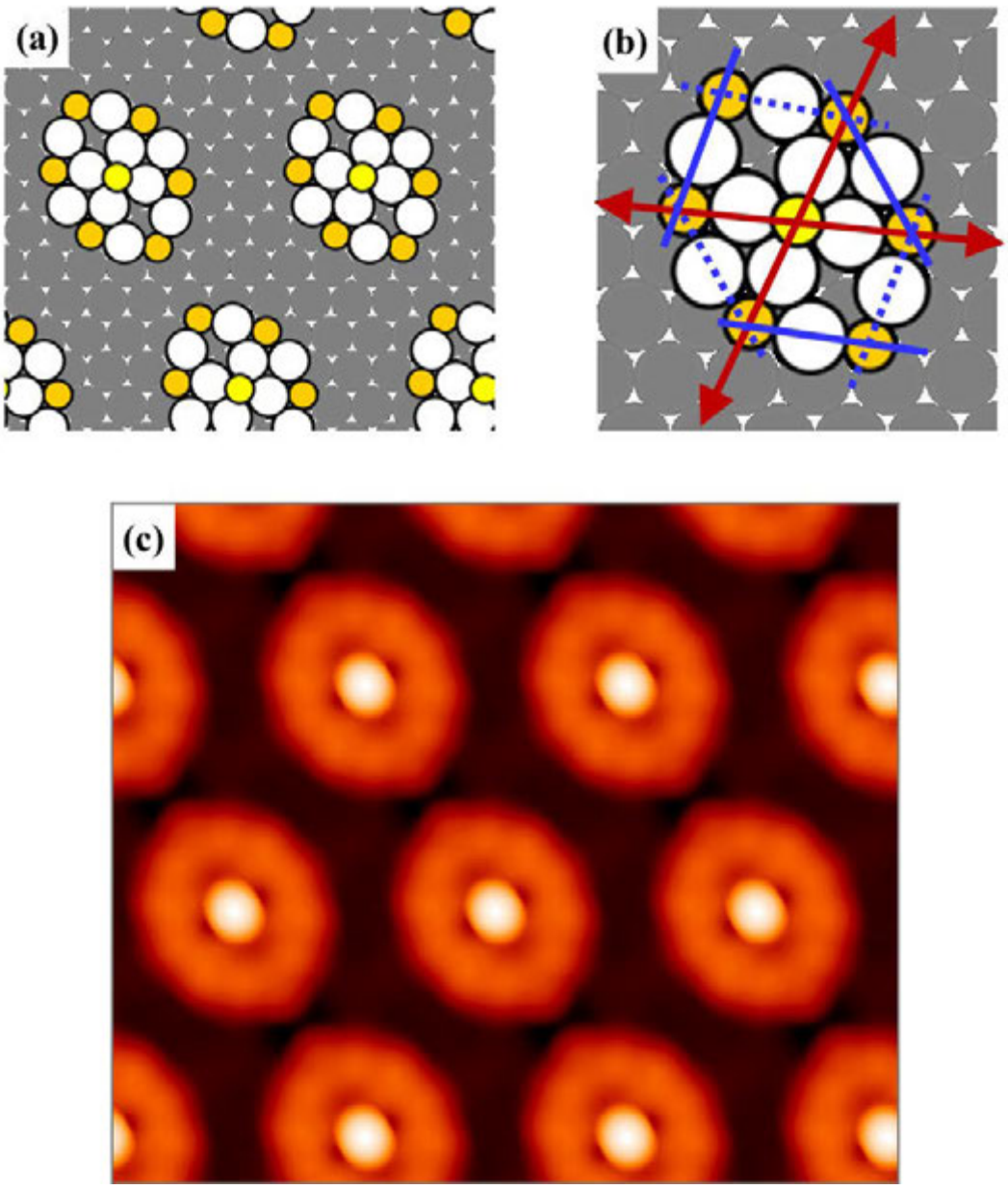

Figure 24. (a) DFT $Ag_{10}S_7$ cluster model in (6×6) unit cell and (b) detail view of (a) outlining structural features. Red arrows cross at apex of the Ag_4S pyramid. Blue lines mark AgS_2 units. (c) Tersoff-Hamann simulated STM image of (a).

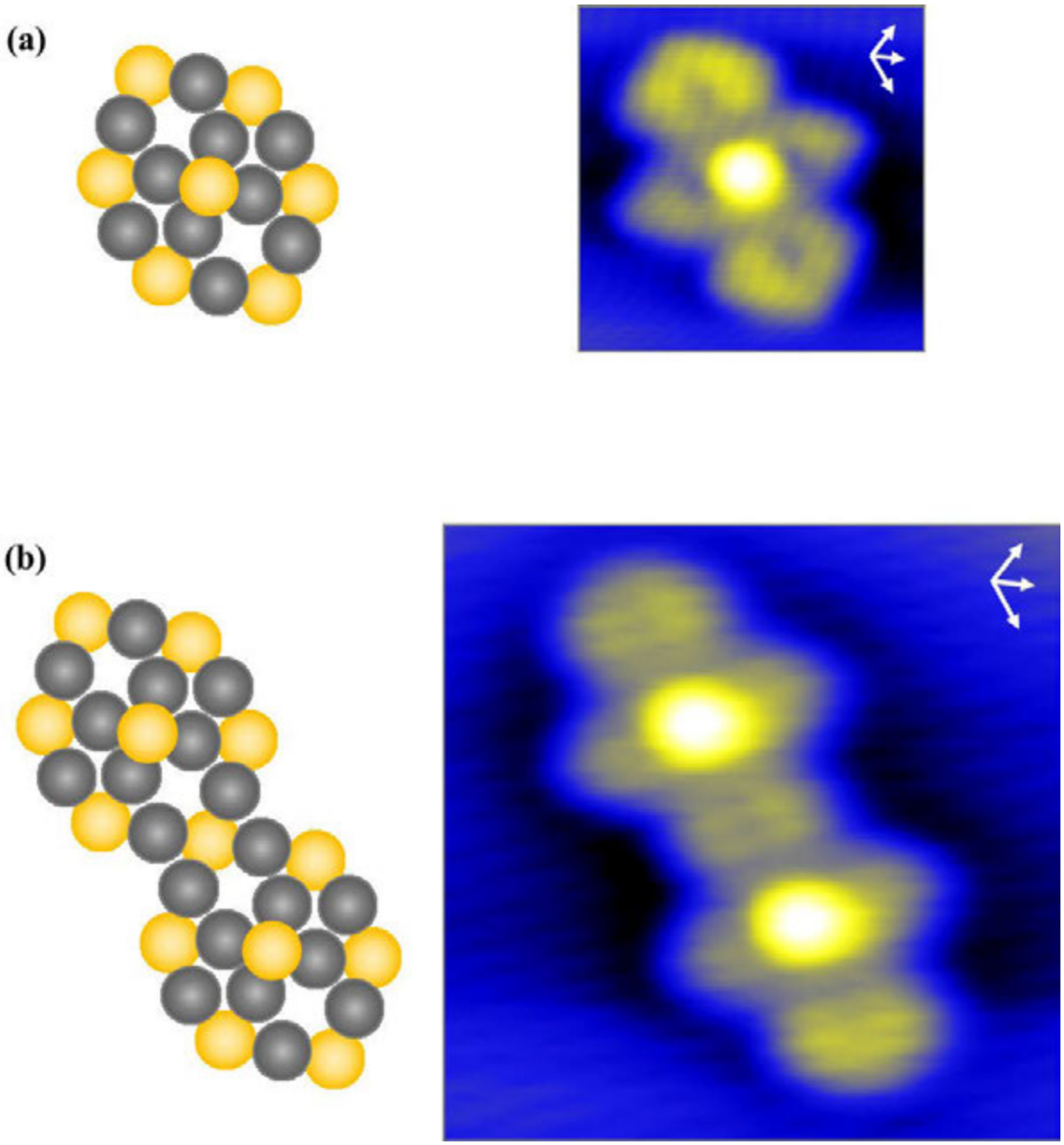

Figure 25. Comparison with DFT model and STM images: (a) Single chain unit. I = 0.04599 nA, V_{sample} = 1.0 V, loop gain 0.508%, 6.3 nm/s, 2×2 nm^2 (1120309 S_Ag111, m25). First day of the first low coverage experiment. (b) Double chain unit. I = 2.062 nA, V_{sample} = 7.641 mV, loop gain 1%, 50 nm/s, 3×3 nm^2 (11203011 S_Ag111, m2). Third day of the first low coverage experiment.

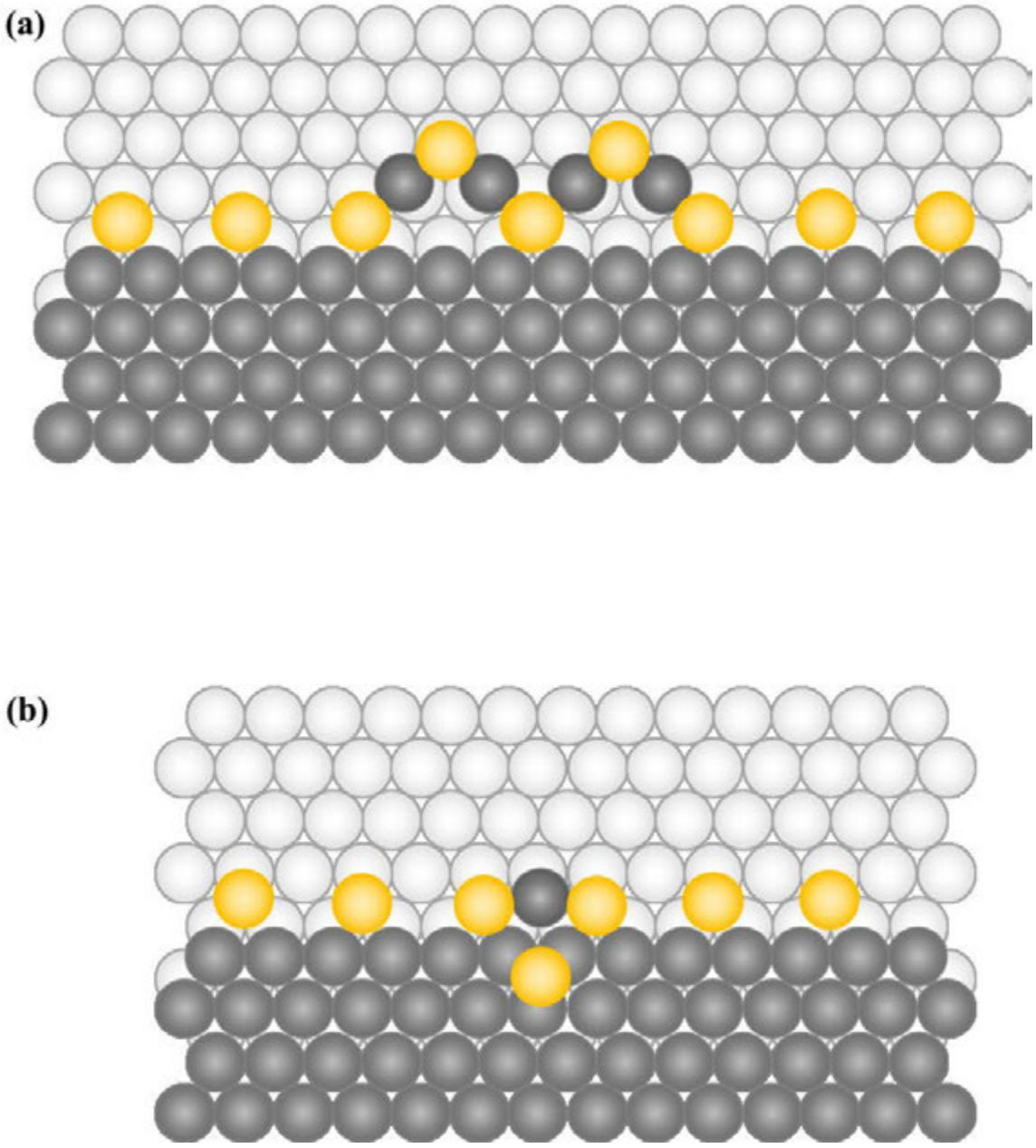

Figure 26. Illustration of possible configurations of step species including the normal step decoration in which a S atom occupies every other site along a step edge, the zigzag-like features (a), and partial chains parallel to step edges (b).

Tables

Table I: Sulfur deposition parameters for each experiment.

Date Description	Filament		Evaporator temperature (K)	Cell		Exposure time	Preparation chamber pressure (Pa)	STM notes
	(A)	(V)		(mV)	(mA)	(s)		
3/5/2012 1st **high** θ_S	1.3	3	477	210 to 58	10	281	8.73×10^{-7}	Failed (cell potential dropped)
3/7/2012 2nd **high** θ_S	1.1	2.9	451	250	~80	240	1.17×10^{-6}	High coverage with linear features
3/9/2012 1st **low** θ_S	1.4	3.3	467	268 to 239		60	5.51×10^{-7}	Step decoration & clusters
3/15/2012 3rd **high** θ_S	1.4	2.4	503	270		54	2.91×10^{-6}	High coverage, poor resolution. No improvement upon warming to >200 K.
3/18/2012 2nd **low** θ_S	1.3	2.9	469	238		47		Step decoration & clusters. Stable upon warming to >200 and 300 K.

Table II: Peak-to-peak separation between Ag atoms along the close-packed directions. The expected value is a = 0.289 nm. Average is over one atomically resolved image. The percent difference was calculated as the difference between the measured and expected value divided by their average. The percent difference was calculated as the difference between the measured and expected value divided by the expected value. The required correction to recover the expected value is given for each direction, as well as the overall RC factor.

	[1 -1 0]	[-1 0 1]	[0 1 -1]	All
average	0.240	0.214	0.233	0.229
std. dev.	0.020	0.013	0.013	0.013
maximum	0.270	0.252	0.250	0.270
minimum	0.214	0.199	0.200	0.199
percent difference	-19%	-30%	-21%	-23%
percent change	-17%	-26%	-19%	-21%
correction factor	1.204	1.351	1.241	1.265

Table III: Peak-to-peak separation between protrusions decorating step edges like those in Fig. 6 along the directions defined in Fig. 4. The percent difference between all of the measured values and the expected value of 2a = 0.578 nm is also shown as a check against the overall rough correction factor based on the clean surface (RC = 0.2650). The percent difference was calculated as the difference between the measured and expected value divided by their average.

(nm)		[1 -1 0]	[-1 0 1]	[0 1 -1]	All	% difference
	N	86	13	30	129	129
RAW	average	0.486	0.440	0.442	0.471	20.73
	std. dev.	0.038	0.021	0.021	0.039	8.03
	maximum	0.614	0.484	0.481	0.614	35.20
	minimum	0.409	0.410	0.405	0.405	-6.04
rough correction (RC)	correction factor	0.2040	0.3505	0.2405	–	
	average	0.585	0.594	0.549	0.577	
	std. dev.	0.046	0.028	0.026	0.044	–
	maximum	0.739	0.654	0.597	0.739	
	minimum	0.492	0.554	0.502	0.492	

Table IV: Values corresponding to the line profiles in Fig. 8 of the triangular cluster in Fig. 7e-f, imaged at a tunneling bias of 0.007641 V.

(nm)		Along edge: I, II, III			Through center: i, ii, iii	
		FWHM	peak-to-peak	height	FWHM	peak-to-peak
RAW	average	0.719	0.360	0.023	0.710	0.338
	std. dev.	0.051	0.038	0.007	0.023	0.017
	maximum	0.777	0.400	0.030	0.736	0.356
	minimum	0.689	0.325	0.015	0.691	0.323
rough correction (RC)	average	0.906	0.454	0.021	0.895	0.426
	std. dev.	0.064	0.048	0.006	0.030	0.021
	maximum	0.979	0.504	0.029	0.928	0.449
	minimum	0.868	0.410	0.014	0.871	0.407

Table V: Dimensions of the triangular cluster in Fig. 7g-h, imaged at a tunneling bias of 0.9999 V.

(nm)		Along edge: I, II, III			Through center: i, ii, iii	
		FWHM	peak-to-peak	height	FWHM	peak-to-peak
RAW	average	0.62	0.263	0.017	0.639	0.290
	std. dev.	0.02	0.025	0.004	0.034	0.034
	maximum	0.64	0.284	0.023	0.669	0.327
	minimum	0.61	0.235	0.013	0.602	0.261
rough correction (RC)	average	0.78	0.331	0.016	0.805	0.366
	std. dev.	0.02	0.032	0.004	0.043	0.042
	maximum	0.80	0.358	0.022	0.843	0.412
	minimum	0.77	0.296	0.012	0.759	0.329

Table VI: Dimensions of the triangular cluster in Fig. 7c-d, imaged at a tunneling bias of 0.004155 V.

(nm)		Along edge: I, II, III			Through center: i, ii, iii	
		FWHM	peak-to-peak	height	FWHM	peak-to-peak
RAW	average	0.703	0.349	0.0213	0.720	0.331
	std. dev.	0.038	0.025	0.0059	0.045	0.024
	maximum	0.747	0.375	0.0297	0.751	0.356
	minimum	0.679	0.326	0.0146	0.669	0.309
rough correction (RC)	average	0.886	0.439	0.0201	0.908	0.418
	std. dev.	0.048	0.031	0.0056	0.056	0.030
	maximum	0.942	0.473	0.0280	0.947	0.449
	minimum	0.856	0.411	0.0138	0.843	0.389

Table VII: Measurements of 25 potential triangular clusters presented in Fig. 10f-g.

(nm)		FWHM	height
RAW	average	0.86	0.071
	std. dev.	0.22	0.070
	maximum	1.65	0.018
	minimum	0.61	0.097
rough correction (RC)	average	1.06	0.065
	std. dev.	0.41	0.014
	maximum	1.85	0.092
	minimum	0.80	0.017

Table VIII: Summary of the data presented in Fig. 15. 23 different regions were analyzed from several days.

	All chains		Chains on terraced, not pinned or connected to steps	
	region area (nm^2)	**central protrusions per chain**	**region area (nm^2)**	**central protrusions per chain**
Number of chains	356		294	
average	2008	2	2008	2
std. dev.	1744	1	1744	1
maximum	5625	11	5625	6
minimum	100	1	100	1

Table IX: Measurements of 25 single chains. Peak refers to the bright central protrusion.

(nm)		**chain length**	**equatorial arm width (across peaks)**
RAW	average	1.60	1.16
	std. dev.	0.13	0.15
	maximum	1.89	1.52
	minimum	1.37	0.91
rough correction (RC)	average	2.02	1.47
	std. dev.	0.16	0.19
	maximum	2.38	1.91
	minimum	1.73	1.15

Table X: Measurements of 9 double chains. Peak refers to the bright central protrusion of each unit.

(nm)		**peak-to-peak separation**	**chain length**	**equatorial arm width (across peaks)**	**axial arm (link) width (between peaks)**
RAW	average	1.11	2.68	1.18	1.03
	std. dev.	0.05	0.11	0.16	0.17
	maximum	1.20	2.86	1.50	1.28
	minimum	1.02	2.51	0.84	0.76
rough correction (RC)	average	1.40	3.38	1.49	1.29
	std. dev.	0.07	0.13	0.20	0.22
	maximum	1.52	3.61	1.89	1.62
	minimum	1.29	3.16	1.06	0.96

Table XI: Measurement of chains of varying length from 1 to 11 units. Peak refers to the bright central protrusion of each unit.

(nm)		peak-to-peak separation	equatorial arm width (across peaks)	axial arm (link) width (between peaks)
	N	99	56	32
RAW	average	1.12	1.21	0.93
	std. dev.	0.06	0.16	0.29
	maximum	1.27	1.51	1.28
	minimum	1.02	0.84	0.25
rough correction (RC)	average	1.41	1.52	1.18
	std. dev.	0.07	0.21	0.36
	maximum	1.60	1.90	1.62
	minimum	1.29	1.06	0.31

Table XII: Elongated island measurements from an experiment performed by Shen *et al*.[3]

(nm)	peak-to-peak separation	length	width
N	49	112	117
average	1.34	12.4	1.93
std. dev.	0.14	8.6	0.36
maximum	1.70	65.9	2.84
minimum	0.88	2.92	1.16

Table XIII. Summary of the data presented in Fig. 20.

		All days		3/9/2012		3/10/2012		3/11/2012		3/12/2012	
		image area (nm^2)	units per chain	image area (nm^2)	units per chain	image area (nm^2)	units per chain	image area (nm^2)	units per chain	image area (nm^2)	units per chain
All chains	N_{areas} or N_{chains}	23	356	6	89	2	37	2	11	5	60
	average	2008	2.0	1958	2.2	2500	2.1	400	2.1	1645	2.1
	std. dev.	1744	1.3	2083	1.3	0	1.3	0	1.4	1185	1.6
	max	5625	11	5625	7	2500	5	400	5	2500	11
	min	100	1	100	1	2500	1	400	1	100	1
Chains on terraces, not pinned or connected to steps	N_{areas} or N_{chains}	23	294	6	82	2	24	2	9	5	50
	average	2008	2.1	1958	2.1	2500	2.2	400	1.9	1645	1.9
	std. dev.	1744	1.1	2083	1.1	0	1.4	0	1.1	1185	1.0
	max	5625	6	5625	6	2500	5	400	4	2500	5
	min	100	1	100	1	2500	1	400	1	100	1

Table XIII. continued.

		All days		3/13/2012		3/18/2012		3/19/2012		3/20/2012	
		image area (nm^2)	units per chain	image area (nm^2)	units per chain	image area (nm^2)	units per chain	image area (nm^2)	units per chain	image area (nm^2)	units per chain
All chains	N_{areas} or N_{chains}	23	356	1	35	4	80	1	6	2	38
	average	2008	2.0	5625	2.3	2288	1.9	625	1.3	2500	1.6
	std. dev.	1744	1.3		1.3	2416	1.2		0.8	0	0.8
	max	5625	11	5625	5	5625	6	625	3	2500	4
	min	100	1	5625	1	400	1	625	1	2500	1
Chains on terraces, not pinned or connected to steps	N_{areas} or N_{chains}	23	294	1	28	4	68	1	6	2	27
	average	2008	2.1	5625	2.4	2288	2.1	625	1.3	2500	1.8
	std. dev.	1744	1.1		1.2	2416	1.2		0.8	0	0.9
	max	5625	6	5625	5	5625	5	625	3	2500	4
	min	100	1	5625	1	400	1	625	1	2500	1

Appendix 1. High sulfur coverage

At higher S coverage the surface appears quite different from the experiments discussed above in which only ~5% of the substrate was covered by chains. Deposition of large amounts of S yield a surface completely covered so that no bare substrate is visible, illustrated in Fig. A1.1. While much of the surface appears disordered, the step edges are occasionally faceted, Fig. A1.1a and e, and vaguely linear features exist separated by ~ 3.09 nm. Fig. A1.2 shows that these linear features exist in two domains rotated by ~60°. Unfortunately, the resolution during the high coverage experiments was not sufficient to elucidate the adsorbate structure.

Attempts to probe the high coverage regime by warming the sample to just over 200 K yielded inconclusive results. The surface does look different before, Fig. A1.3, and after, Fig. A1.4, warming. An ordered structure appears in Fig. A1.4c-f, but doesn't seem consistent with results discussed above and may be contaminated.

Figures

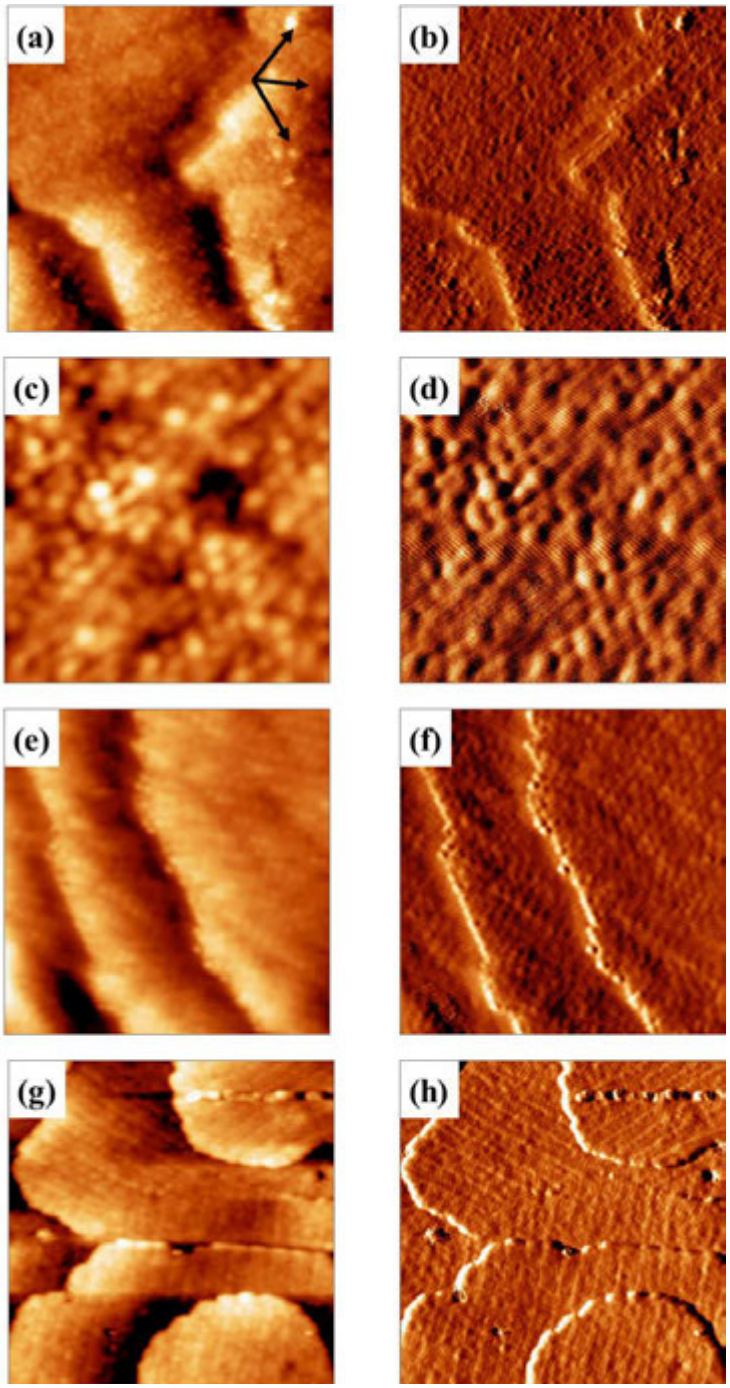

Figure A1.1. High S coverage topography (left) and differentiated (right) images from the second high coverage experiment. (a-b) I = 0.3032 nA, V_{sample} = -1.816 V, loop gain 1%, 40 nm/s, 20×20 nm^2 (1120307 S_Ag111, m17). (c-d) I = 0.3715 nA, V_{sample} = -1.185 V, loop gain 0.7457%, 10 nm/s, 5×5 nm^2 (1120307 S_Ag111, m22). (e-f) I = 0.3715 nA, V_{sample} = -1.185 V, loop gain 0.7457%, 30 nm/s, 15×15 nm^2 (1120307 S_Ag111, m24). (g-h) 0.3223 nA, 1.115 V, loop gain 1.607%, 80nm/s, 50×50 nm^2 (1120307 S_Ag111, m35).

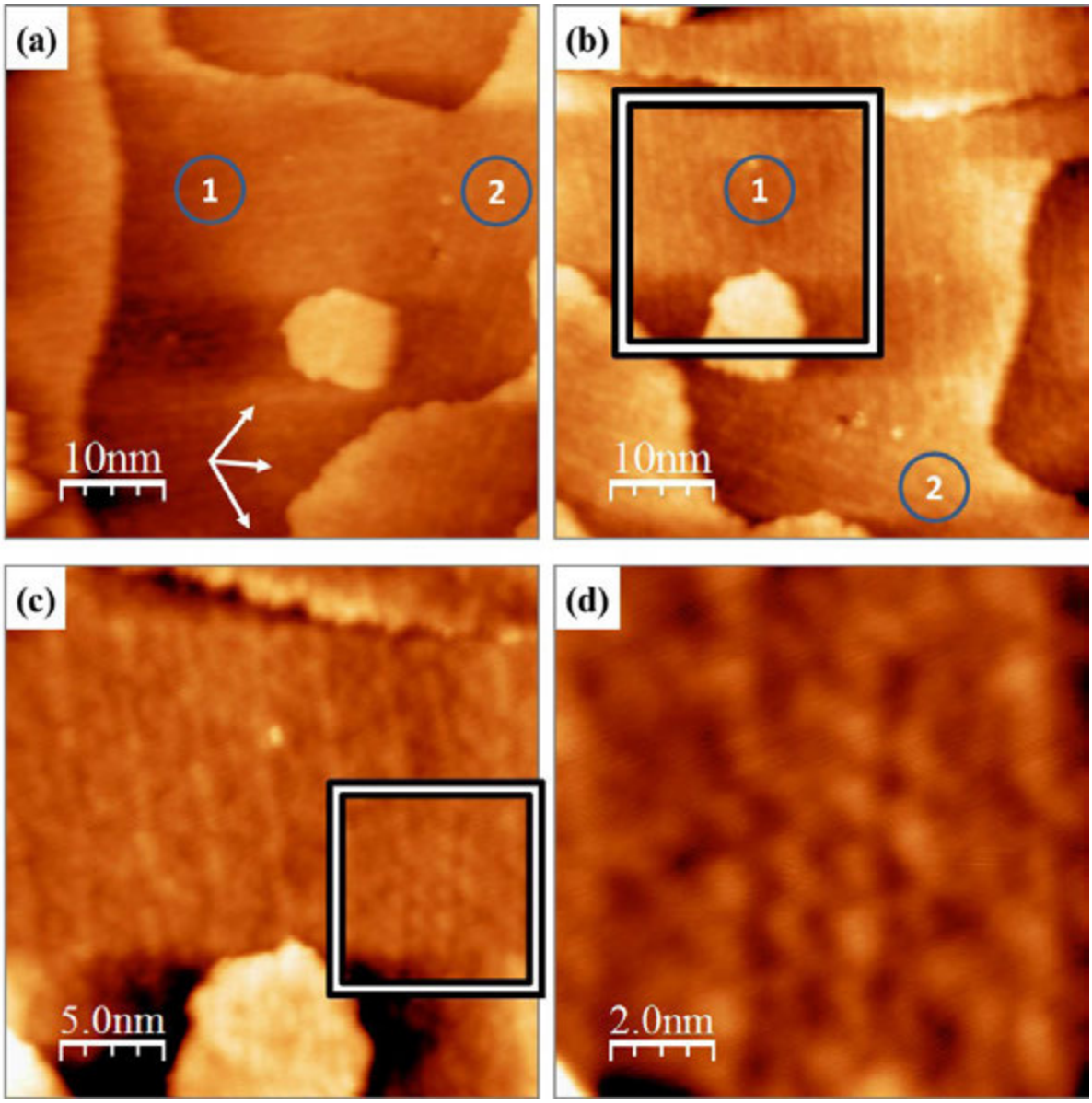

Figure A1.2. High S coverage topographic images exhibiting two domains of linear features from second high coverage experiment. Scanning parameters: I = 0.149 nA, V_{sample} = 1.359 V, loop gain 2.581%, 174nm/s, (1120307 S_Ag111, m1) with normal scan direction (a) and rotated 90° (b-d). (a-b) 50×50 nm^2, (c) 25×25 nm^2 region boxed in (b), and (d) 10×10 nm^2 region boxed in (c).

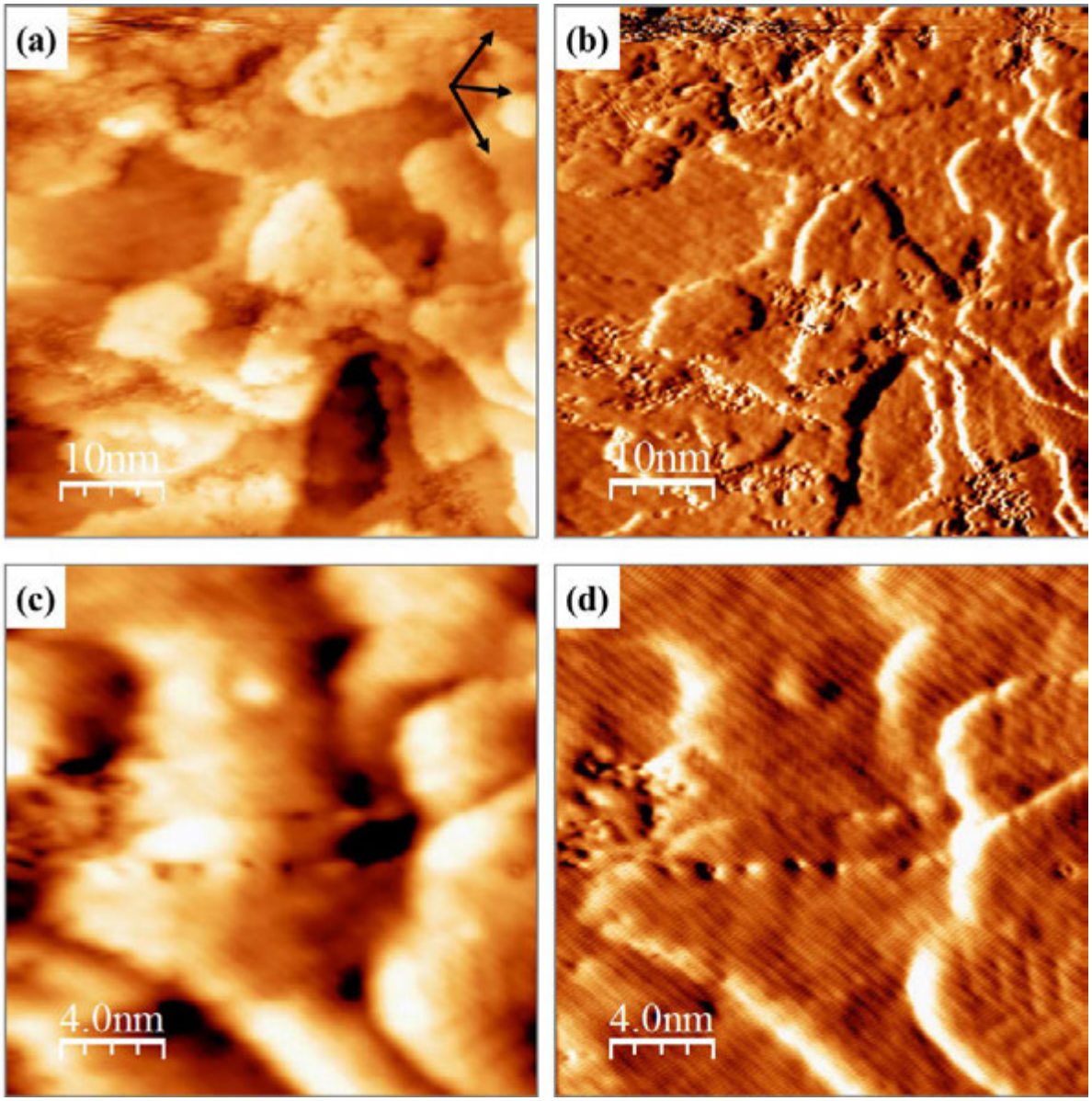

Figure A.1.3. High S coverage topographic (left) and differentiated (right) images in a rough region from the third high coverage experiment. (a-b) I = 0.300 nA, V_{sample} = 1.00 V, loop gain 5%, 150 nm/s, 50×50nm^2 (1120315 S_Ag111, m2). (c-d) 0.300 nA, 1.00 V, loop gain 3%, 60 nm/s, 20×20nm^2 (1120315 S_Ag111, m6).

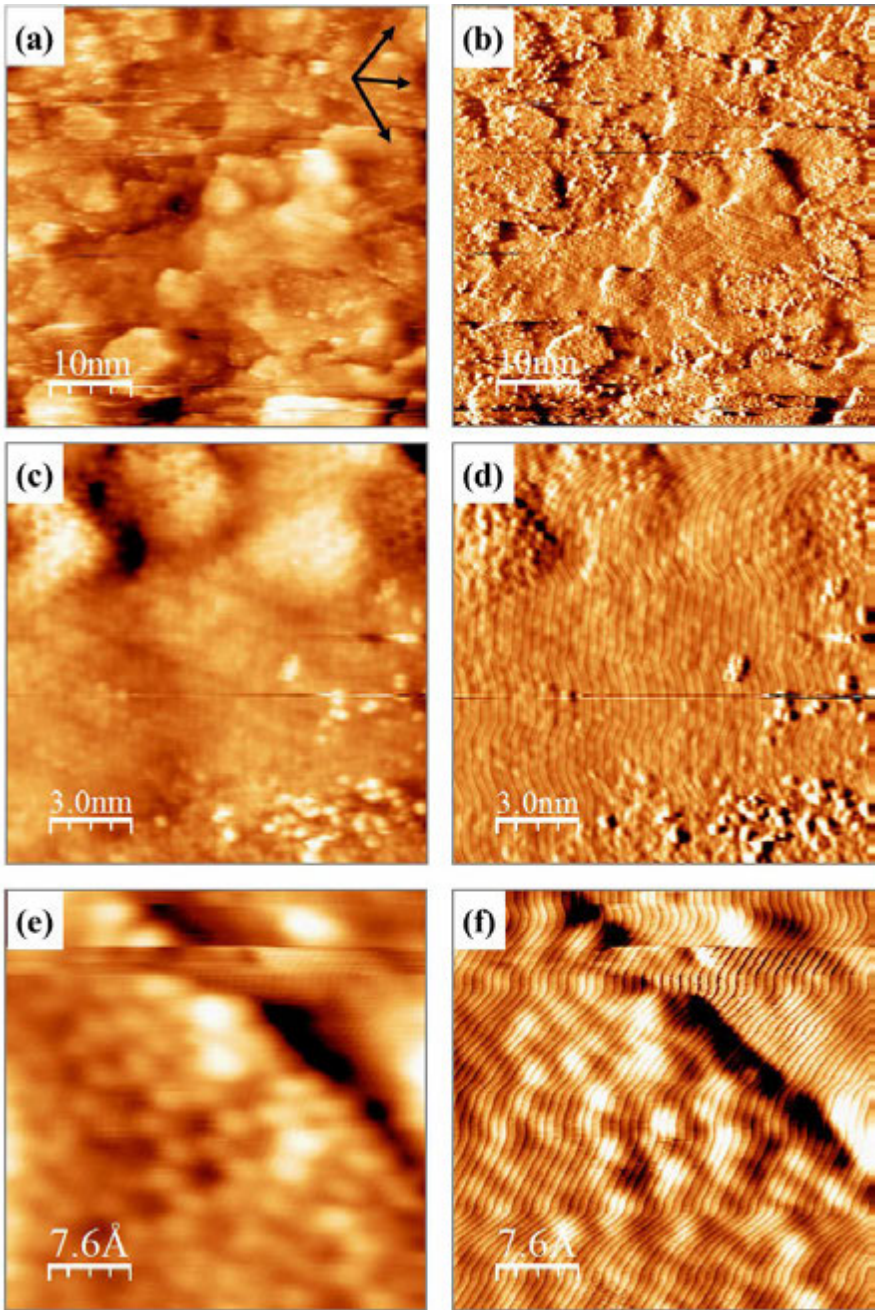

Figure A.1.4. High S coverage topographic (left) and their differentiated (right) images in a rough region after warming to just above 200 K from the second day of the third high coverage experiment. (a-b) I = 0.2934nA, V_{sample} = -1.744 V, loop gain 1%, 112 nm/s, 50×50 nm^2, (1120316 S_Ag111 continued warmed, m2). (c-d) I = 0.2934nA, V_{sample} = -1.744 V, loop gain 1%, 34 nm/s, 15×15 nm^2, (1120316 S_Ag111 continued warmed, m3). (e-f) I = 0.2934nA, V_{sample} = -1.744 V, loop gain 0.5%, 8.5 nm/s, 3.8×3.8 nm^2, (1120316 S_Ag111 continued warmed, m4). (g-h) I = 0.5396 nA, V_{sample} = -2.0 V, loop gain 2%, 60 nm/s, 20×20 nm^2 (1120316 S_Ag111 continued warmed, m8). (i-j) I = 0.5396 nA, V_{sample} = -2.0 V, loop gain 0.5%, 15 nm/s, 7.5×7.5 nm^2 (1120316 S_Ag111 continued warmed, m9).

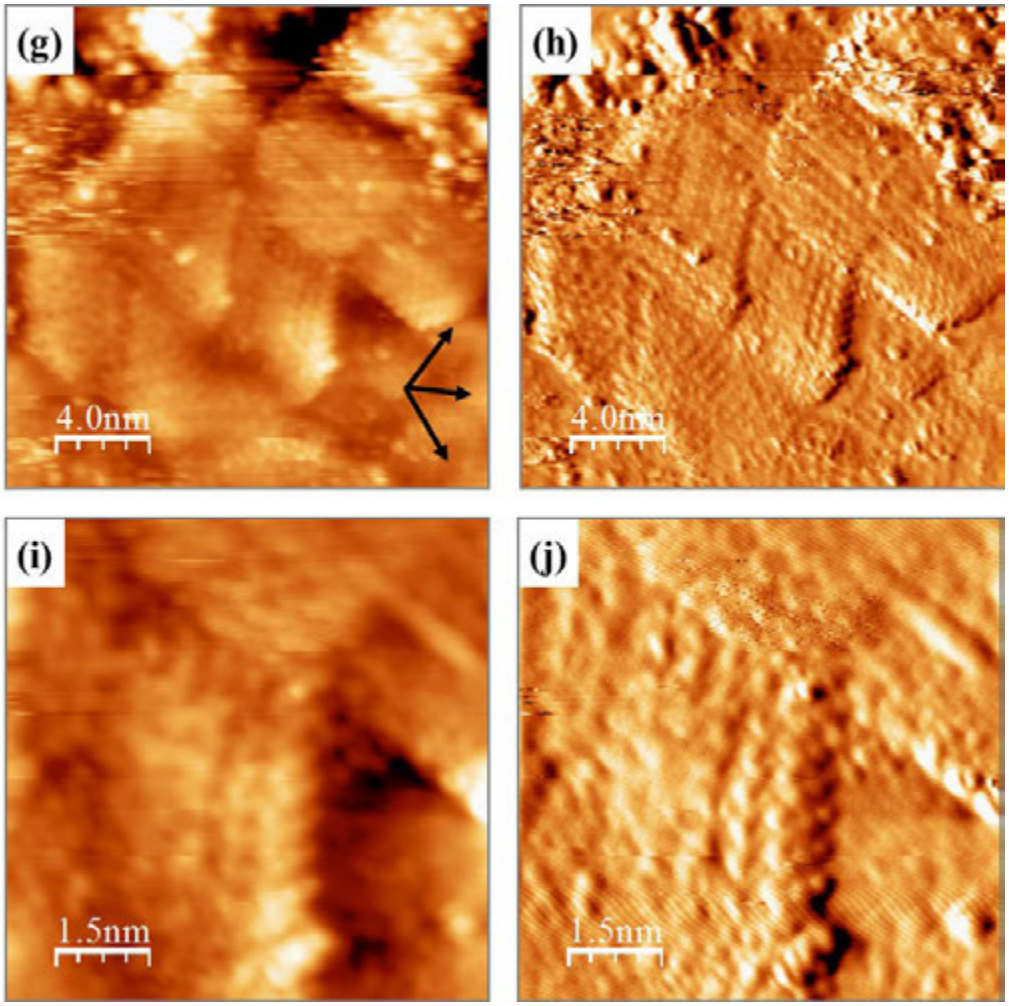

Figure A.1.4. continued

Appendix 2. Scanning tunneling spectroscopy

1. Contrast bias dependence

Scanning the chains over a wide bias range does not affect the structure; the chains remain stable between -7 and +7 V. However, between +5 and +6 V, Fig. A2.1d-e, the image topography inverts, which may be a real effect or due to tip contamination or deformation. Contrast changes may arise from tunneling near the resonance level of the adsorbate, high LDOS or phase differences between different tunneling channels of the adsorbate.[19]

2. dI/dV spectra

To explore the electronic structure of the chains, scanning tunneling spectroscopy (STS) was performed. The STS data was acquired through lock-in detection of the ac tunneling current driven by a 50 mV bias modulation and 0.025 Hz signal added to the junction bias under open-loop conditions. The dI/dVsignal can provide information about the local density of states (LDOS) of the surface, the spatial variation of electronic wave functions, and single-electron tunneling (SET) phenomena.

The dI/dV spectrum taken on the clean surface gives an onset of the surface states at ~ -40 mV, which later than the reported experimental value of -65 ± 5 mV for large terraces.[20] See Fig. A2.2 The difference between the spectra recorded on the chain and the substrate shows that the chain is less metallic than the substrate. The spectra are shown in Fig. A2.3d.

3. dI/dV map

A dI/dV or differential conductivity spectrum probes the density of states as a function of energy at a particular spatial position. The conductivity map of a 4 unit chain is shown in Fig. A2.5. In addition, spectra on a grid over this chain (similar to the experiment in the previous section) were also recorded, but are not shown.

Figures

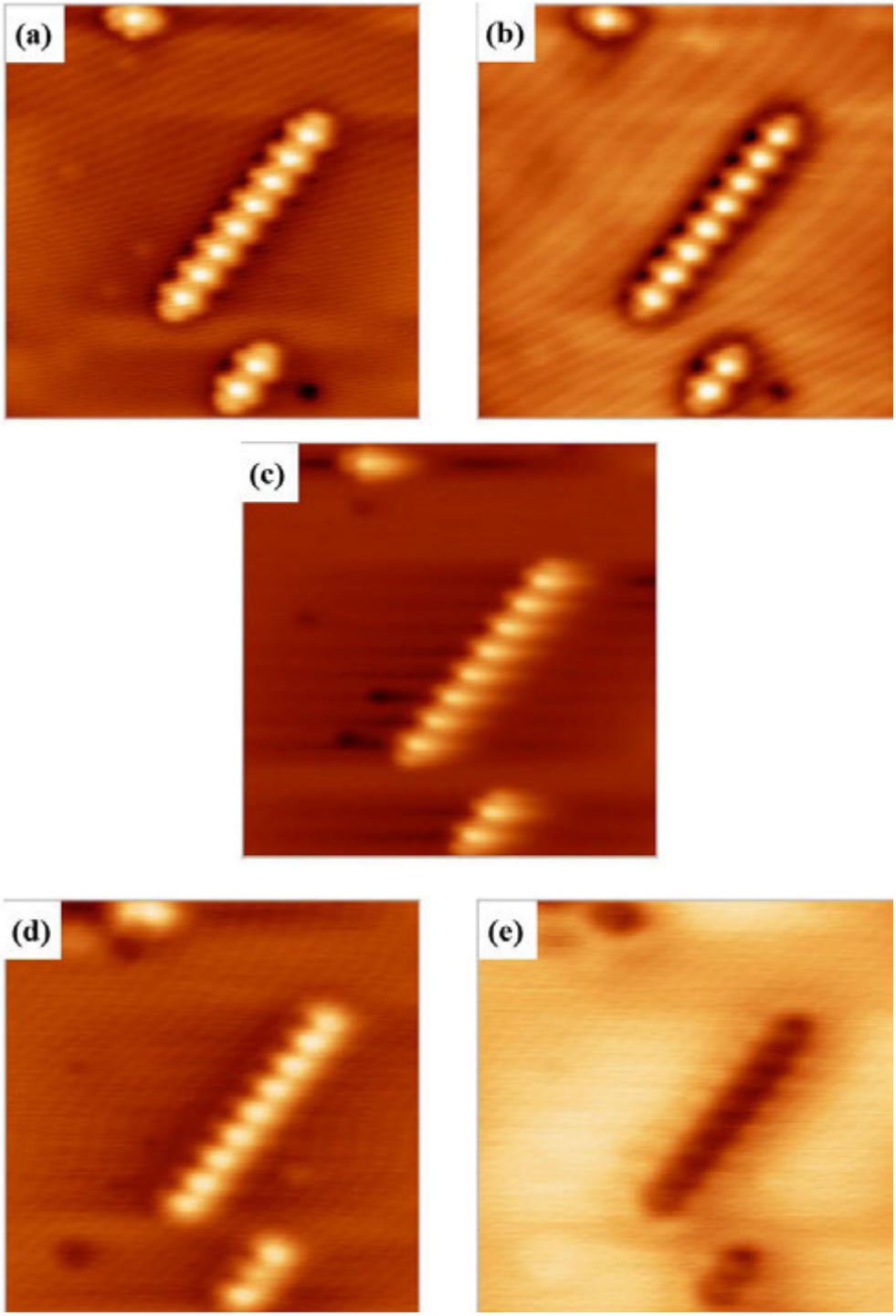

Figure A2.1. Bias dependence of STM images at 1 nA and -5 V (a), -6 V (b), 1 V (c), +5 V (d), and +6 V (e). Loop gain 0.25%, 80 nm/s, 15×15 nm^2 (1120309 S_Ag111: m69, m70, m62, m66, m67).

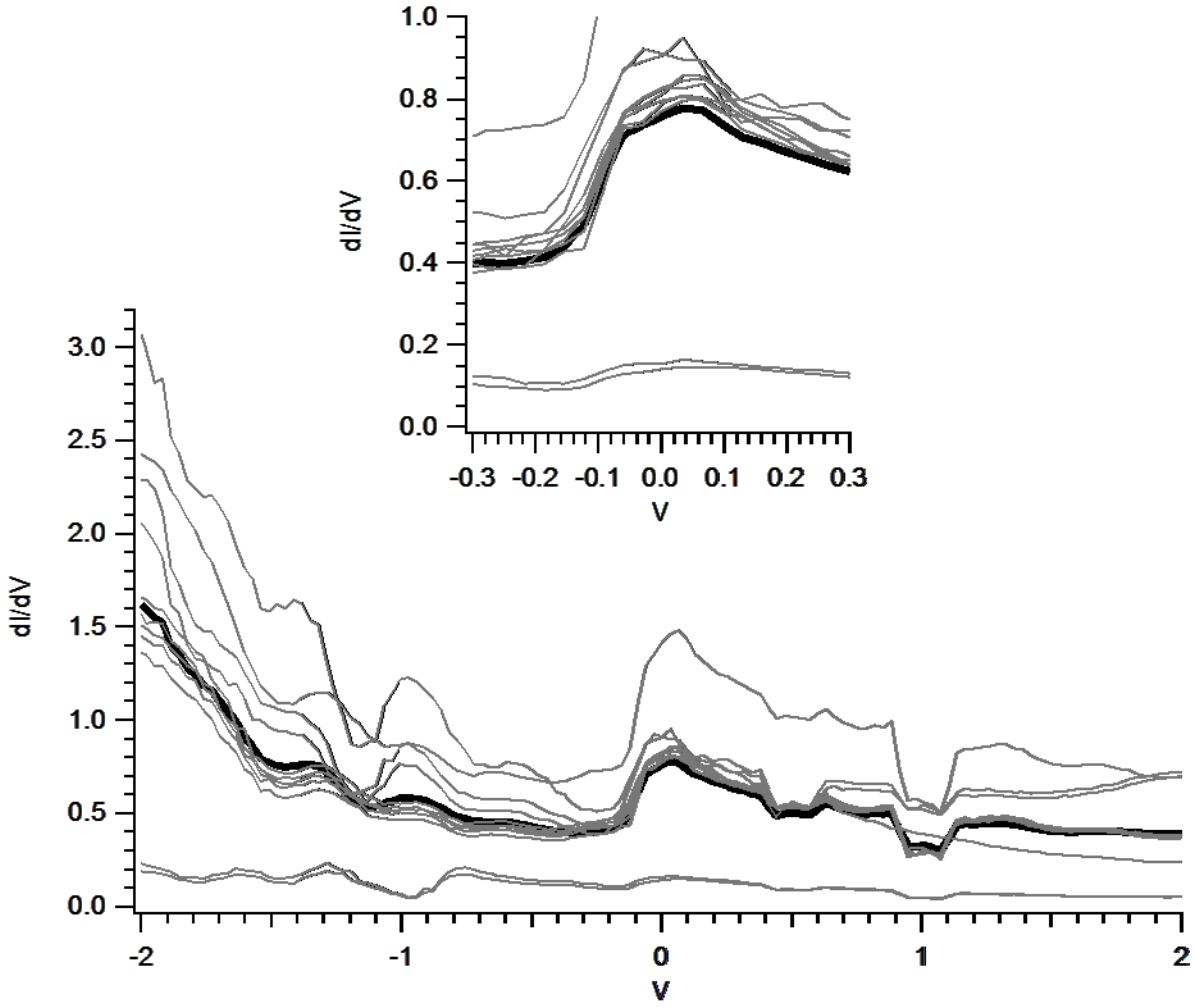

Figure A2.2. dI/dV spectra of the clean Ag(111) surface. The bold black curve represents the average of all of the spectra in grey. (Graph_120312_S_Ag111_neg2to2V_clean).

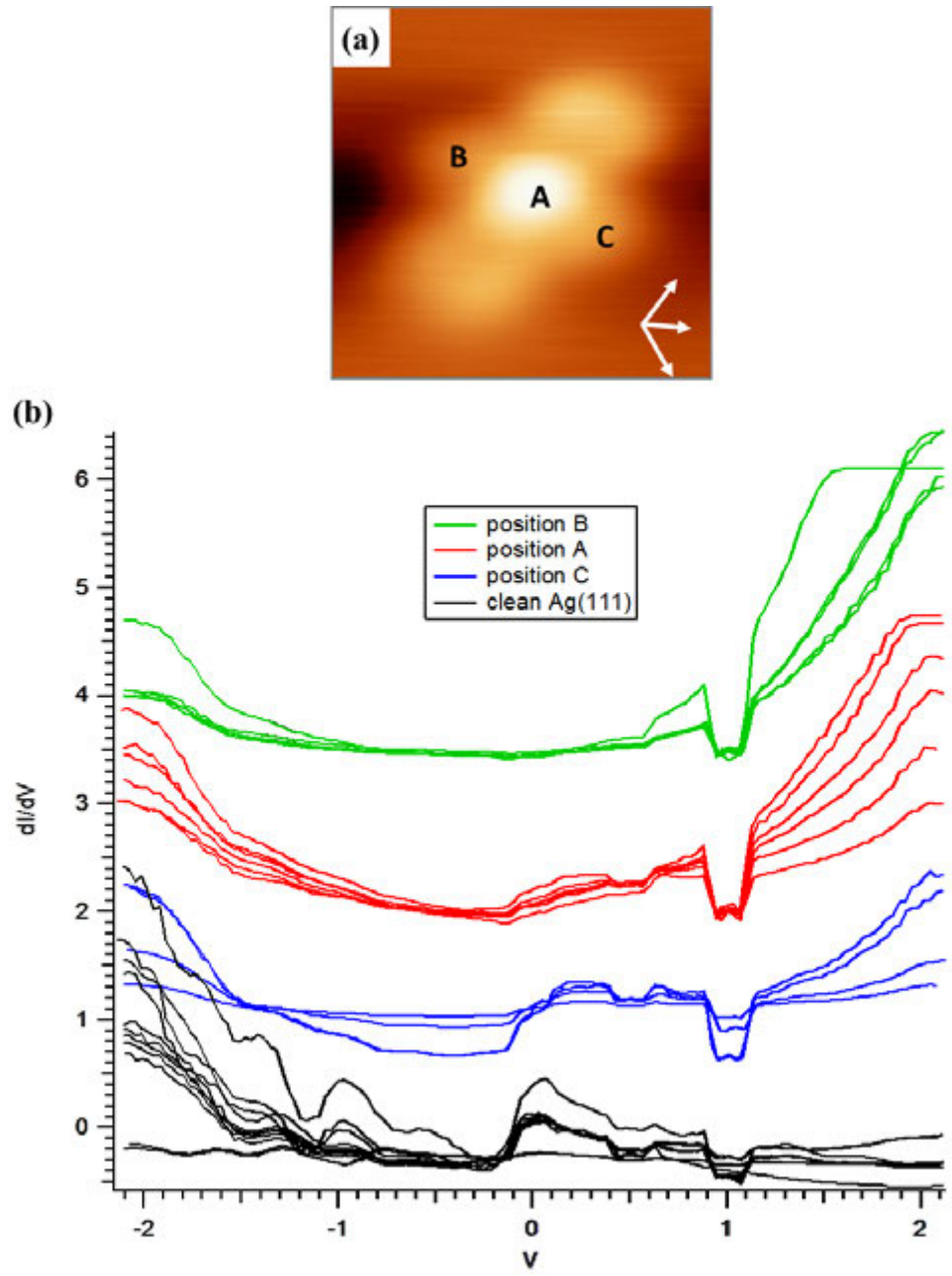

This figure continues on the following page.

Figure A2.3. (a) Topographic image of a single chain unit. Scanning parameters: 0.176 nA, 1.0 V, loop gain 1%, 15 nm/s, 6×6 nm^2 (11203012 S_Ag111, m18). (b) dI/dV spectra at three point across the equator of the chain, defined in (a), and spectra on the clean substrate (Graph_120312_S_Ag111_neg2to2V). (c) The average spectra at each position (Graph_120312_S_Ag111_neg2to2V_average). (d) The difference between each position on the chain and the clean surface, based on the averaged dI/dV spectra (Graph_120312_S_Ag111_neg2to2V_difference).

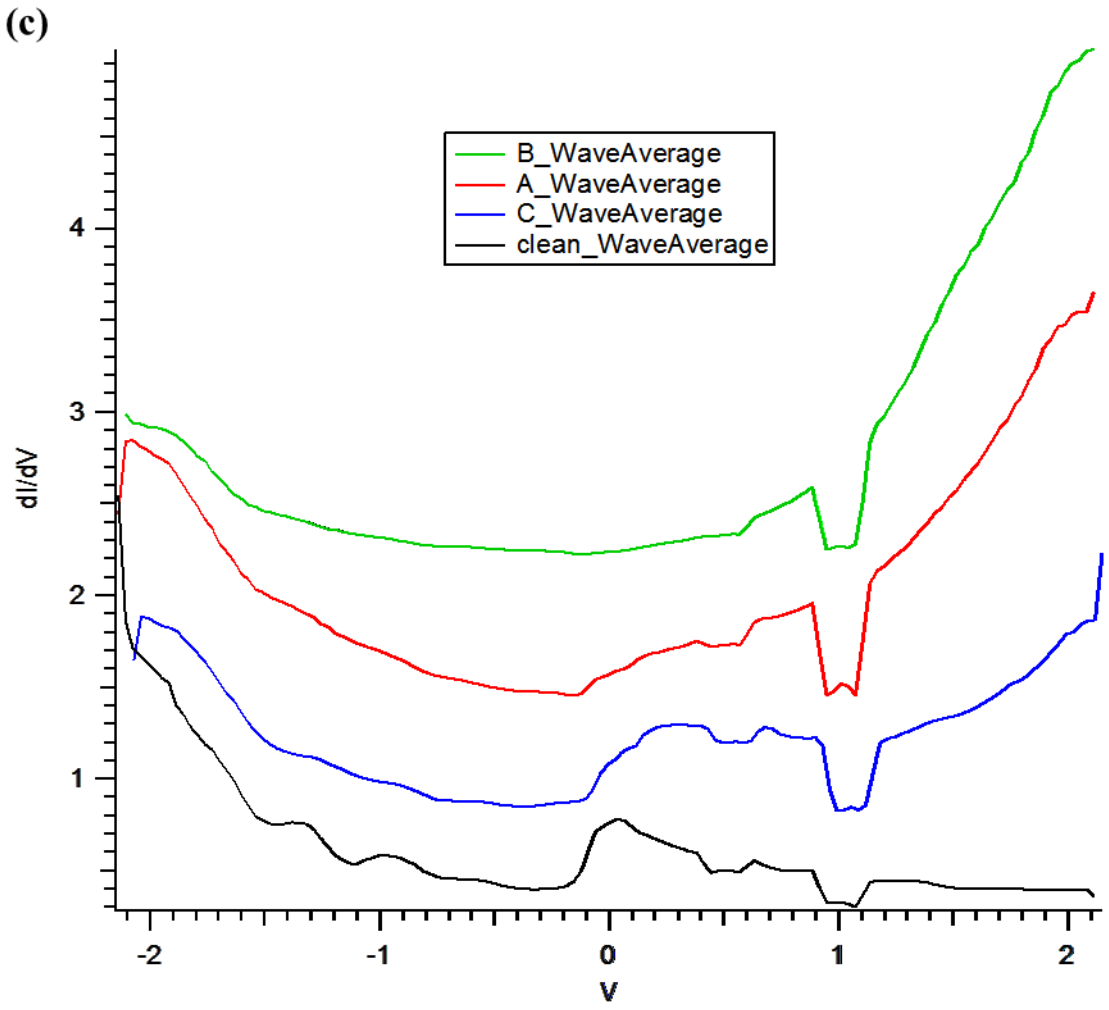

This figure continues on the following page.

Figure A2.3. continued.

(d)

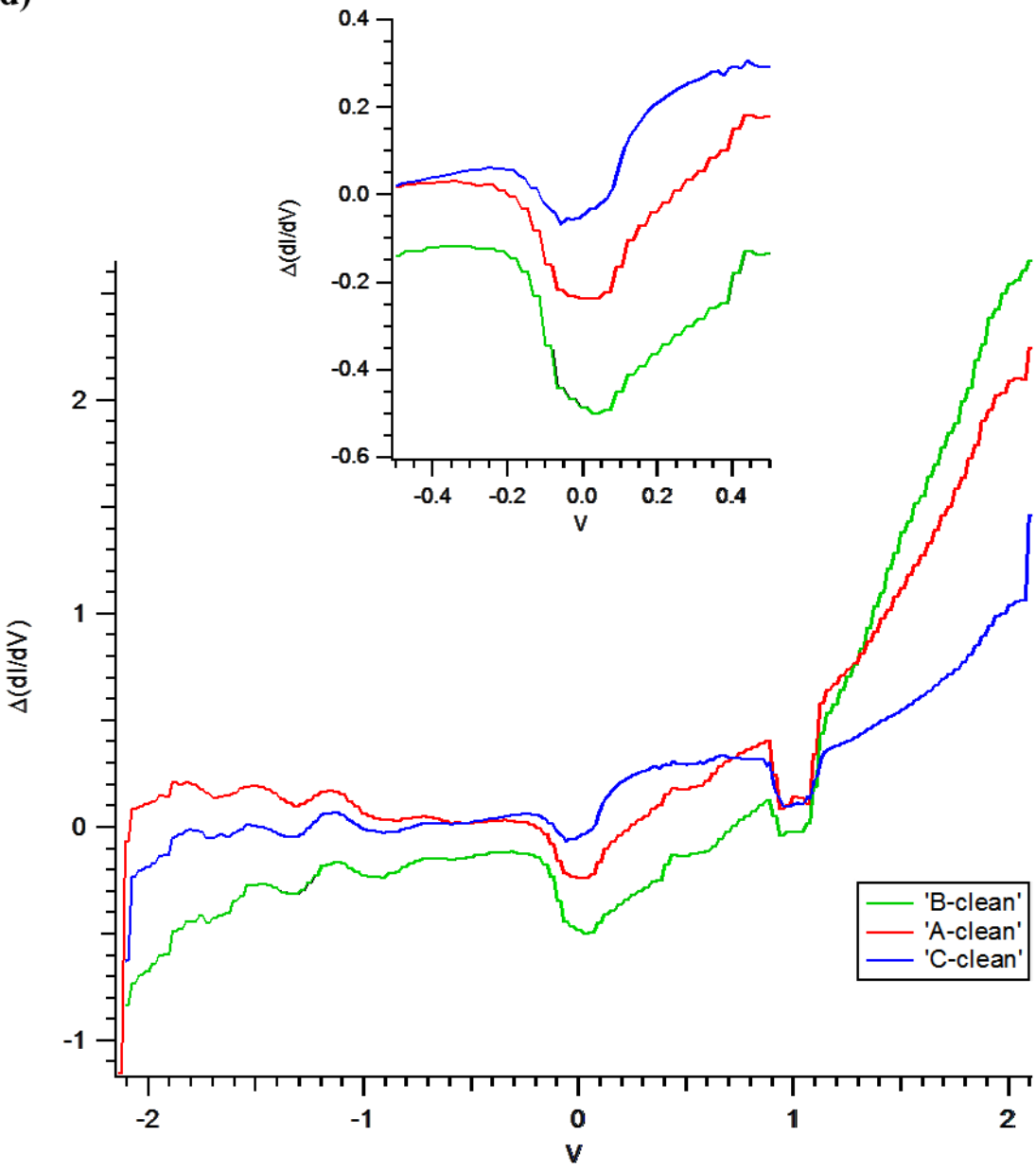

Figure A2.3. continued.

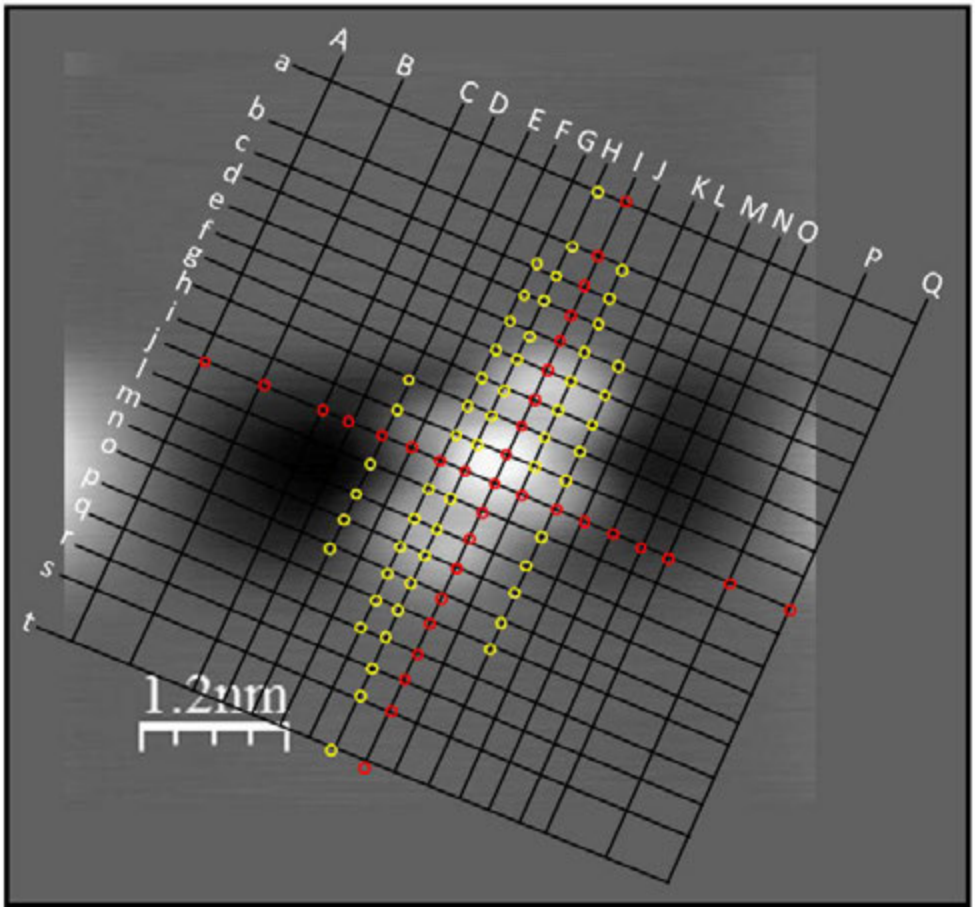

This figure continues on the following page.

Figure A2.4. dI/dV line cut of a single unit. I = 0.176 nA, V_{sample} = 1.0 V, loop gain 1%, 15 nm/s, 6×6 nm^2, 11203012 S_Ag111, m2-m25.

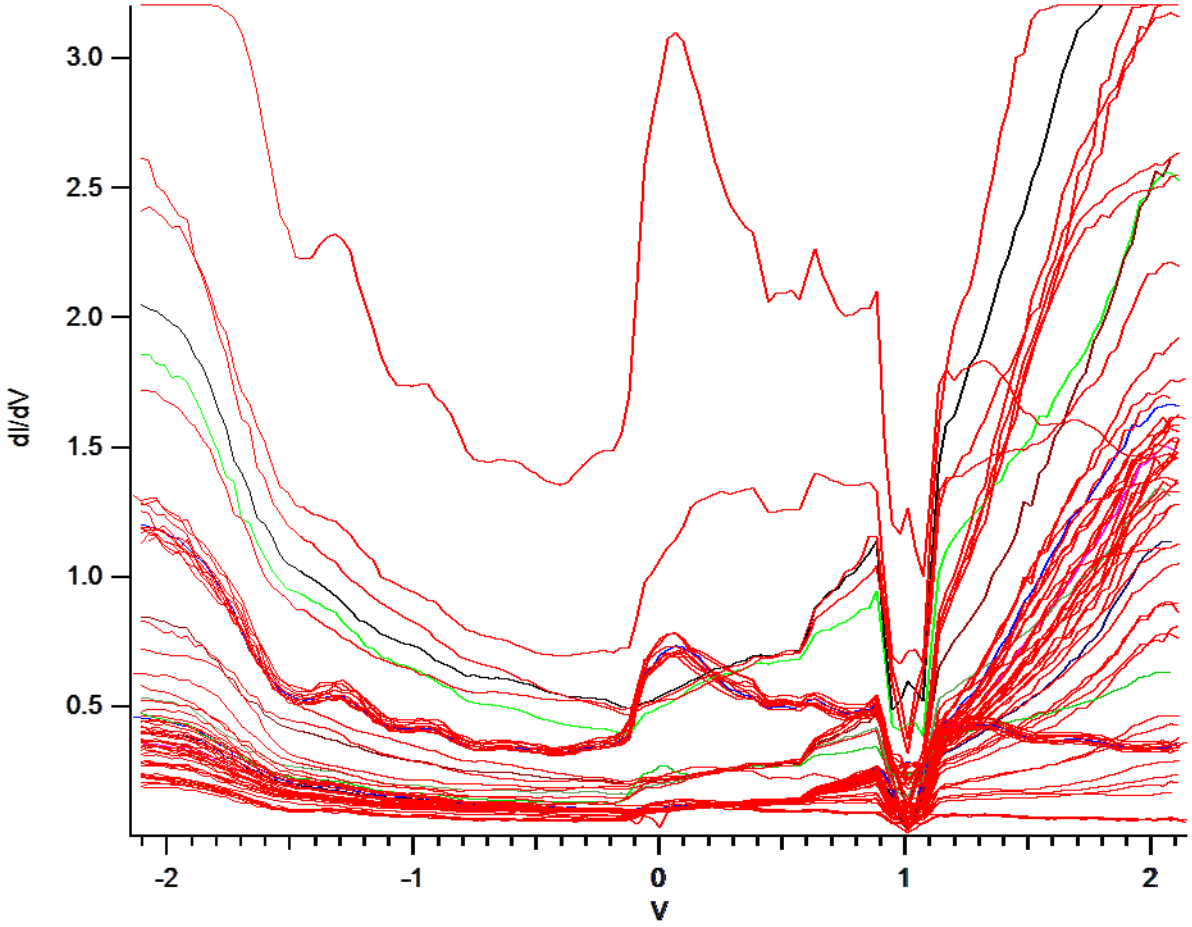

Figure A2.4. continued.

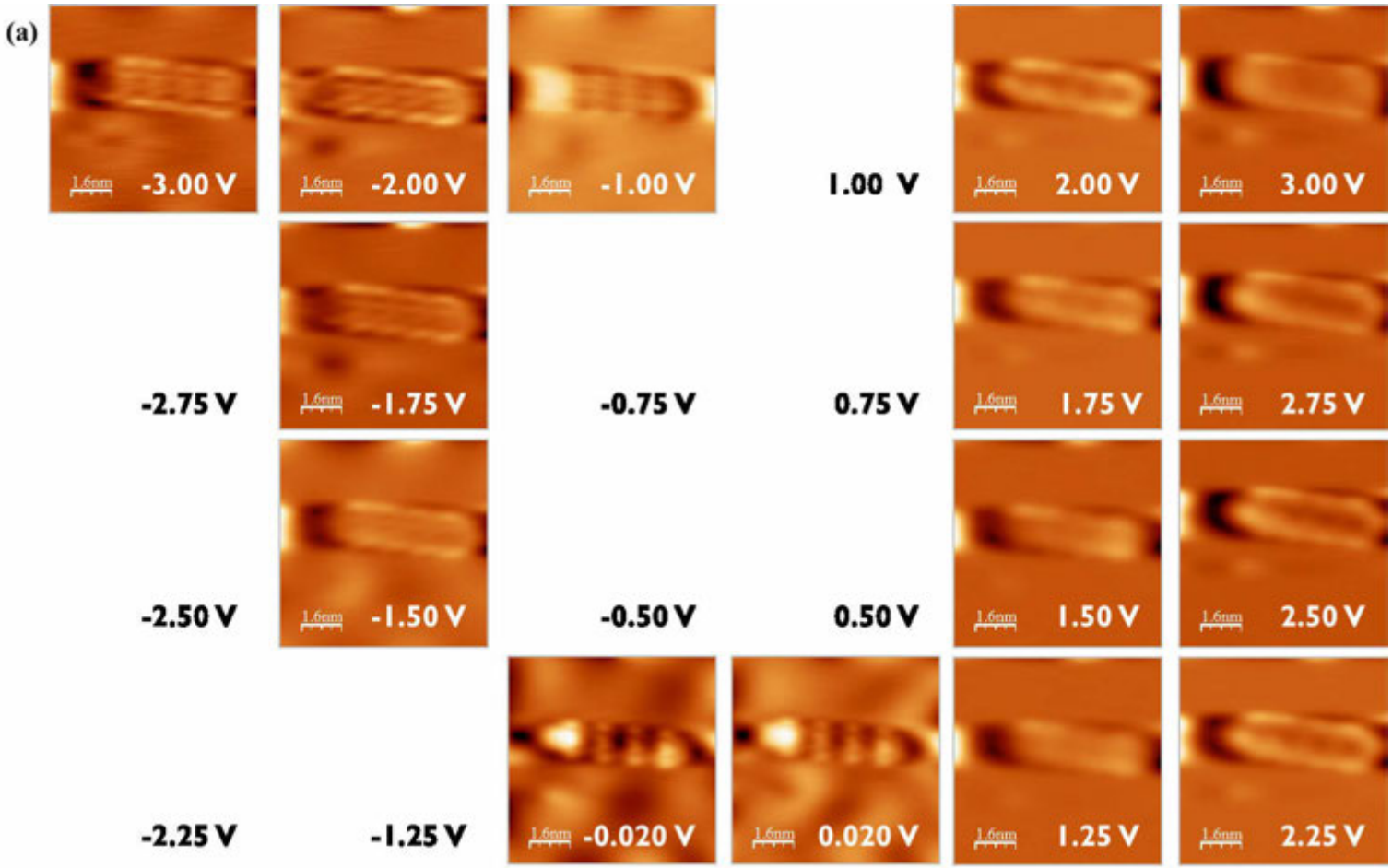

This figure continues on the following page.

Figure A2.5. (a) dI/dV map showing the local density of states (LDOS) of a 4 unit chain at different biases. The topography (b) and differentiated (c) images were captured simultaneously. Scanning parameters: 0.050 modulation V, 0.0250 Hz, 1.0 nA, loop gain 1%, 15 nm/s, 8×8 nm^2 (11203013 S_Ag111, m10-48). Note that the scale bar has not been calibrated and reflects the raw dimensions.

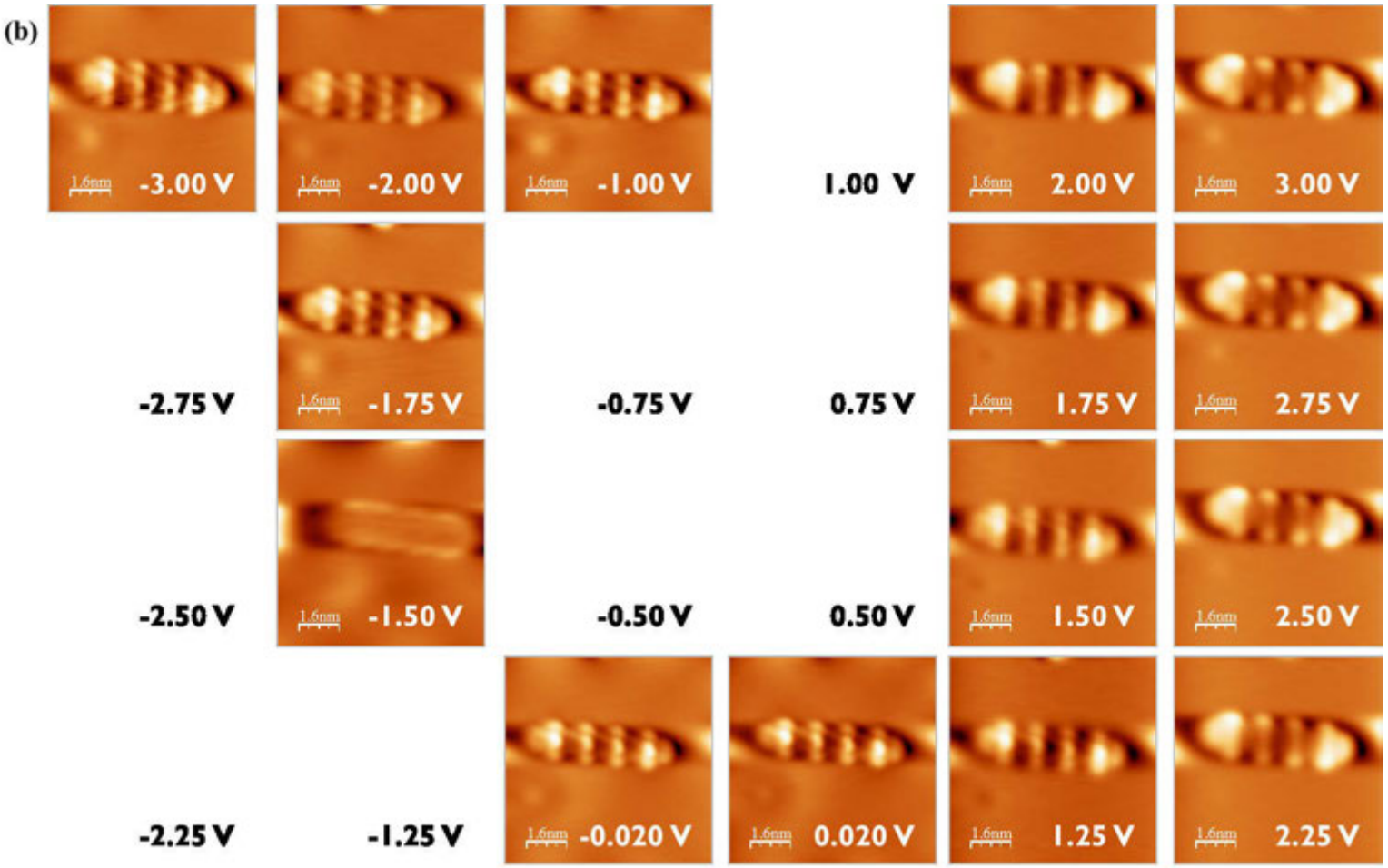

This figure continues on the following page.

Figure A2.5. continued.

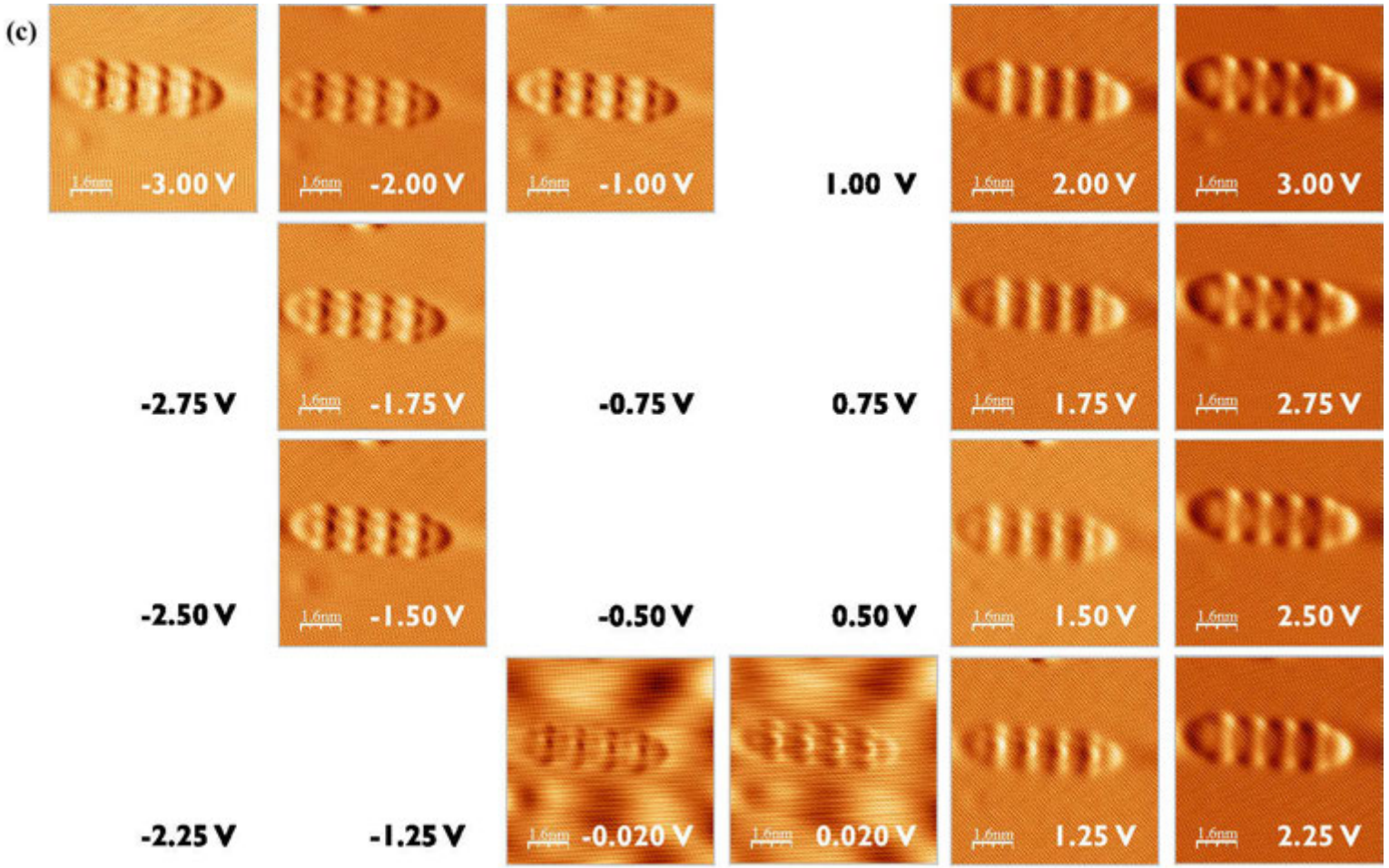

Figure A2.5. continued.

Appendix 3. Low-temperature deposition

These experiments were performed the summer of 2010, prior to those discussed above. During the 2010 visit I built and tested the S evaporator described in Appendix III. The evaporator was mounted on the STM chamber of STM-1 (as opposed to the preparation chamber as in the 2012 experiments above). The sample temperature during S deposition was less than 90 K, and usually less than 70 K. Fig. A3.1. summarizes the experiments. All STM imaging was at 4.7 K.

The atomically resolved image of the Ag(111) surface in Fig. A3.2. shows the crystallographic directions of this sample. All image sizes are based on the raw measurement.

1. After low-temperature deposition

Material adsorbs on the surface as amorphous agglomerations on terraces and step edges. Fig. A3.3, A3.4, and A3.5 show examples of the surface after different S depositions. The chemical composition of the adsorbed species is unknown, it might be some combination of S and contamination. (The mass spectrum of the evaporator's output is shown in Appendix III.) These agglomerations can be sensitive to scanning conditions and break up.

2. After warming

Warming the sample appeared to lessen contamination and induce ordering of the surface species. Holding the sample outside of the cryostat allowed its temperature to increase in a known way, so that sample temperatures with ±5 K of the desired temperature could be achieved, if only very briefly. The surface appears somewhat cleaner after warming to 200 K, but random agglomerations remain, though these are more compact than just after LT deposition. Fig. A3.6 gives example images of the surface after S deposition and warming to 200 K. The step edges retain much of the surface material. The edges appear to be eroded.

After warming to 250 K, the terrace agglomerations feature ordered domains in a stripe, as shown in Fig. A3.7. Larger, more organized islands appear along step edges, with the stripes parallel or rotate away from the steps. Fig. A3.8 gives several examples of these islands, including some high resolution images. The islands sometimes have a border that

differs from the interior structure, which is especially evident in Fig. A3.8g-h. The surface remains unchanged after being held in the STM stage at 4.7 K overnight. See Fig. A3.9. An edge island imaged that day has the stripe interior and a boarder of repeating roughly circular features. Several images of this island are shown in Fig. A3.10. For terrace island shown in Fig. A3.11, the contrast of the striped interior of depends on the sample bias. When the bias is +50 mV the stripes are visible in high contrast, but at -50 mV the stripes are no longer visible and the structure appears flatter. Increasing the bias to 91 mV enhances the contrast of the stripes.

The experiment was repeated, but the large ordered islands did not appear. See Fig. A3.12. It is possible that the coverage of that species was lower in the second experiment. At 250 K, most of what was on the surface congregated at step edges and eroded the steps, which is shown in Fig. A3.13.

The surface appeared much cleaner after warming the sample to 275 K, as shown in Fig. A3.14. In some areas, nearly circular features exist that appear similar to the stripe island boarder, c.f. Fig. A3.10 and A3.15.

Figures

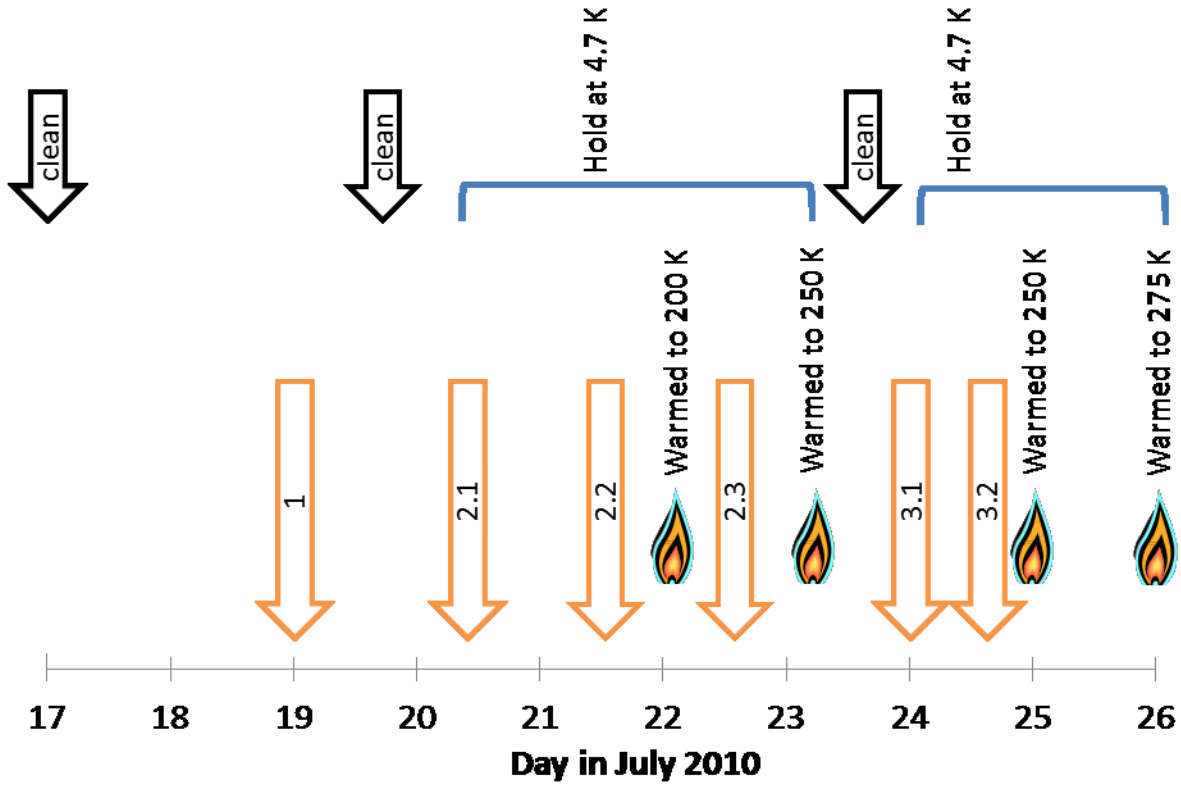

Figure A3.1. Top black arrows indicate days when the sample was cleaned in the preparation chamber. The blue brackets mark time when the sample was held in the STM stage at 4.7 K. The lower orange arrows indicate when S was deposited. The numbers within the arrows refer to the experiment number. The flame indicates when the sample was warmed to 200 K or higher by removing it from the STM stage and allowed to warm to the indicated temperature. The sample was not actively heated, nor held at temperatures above 4.7 K.

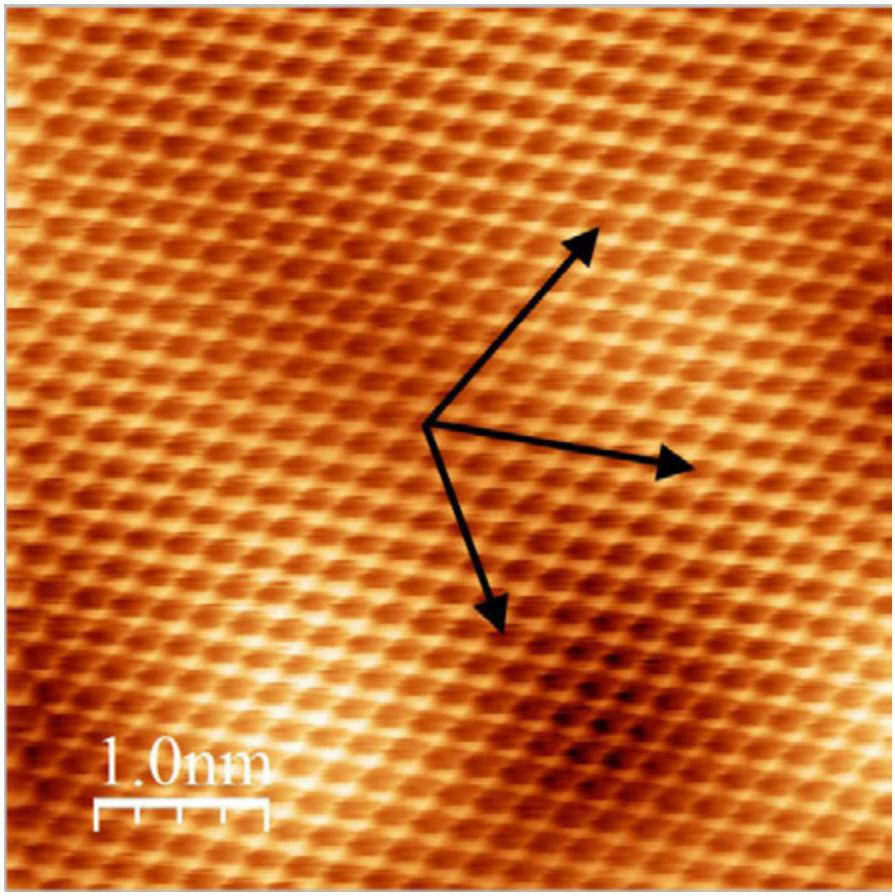

Figure A3.2. Topographic STM image of atomically resolved Ag(111). I = 0.09924 nA, V_{sample} = 6.495 mV, loop gain 1%, 15 nm/s, 5×5nm^2 (1100721 S Ag111, m15).

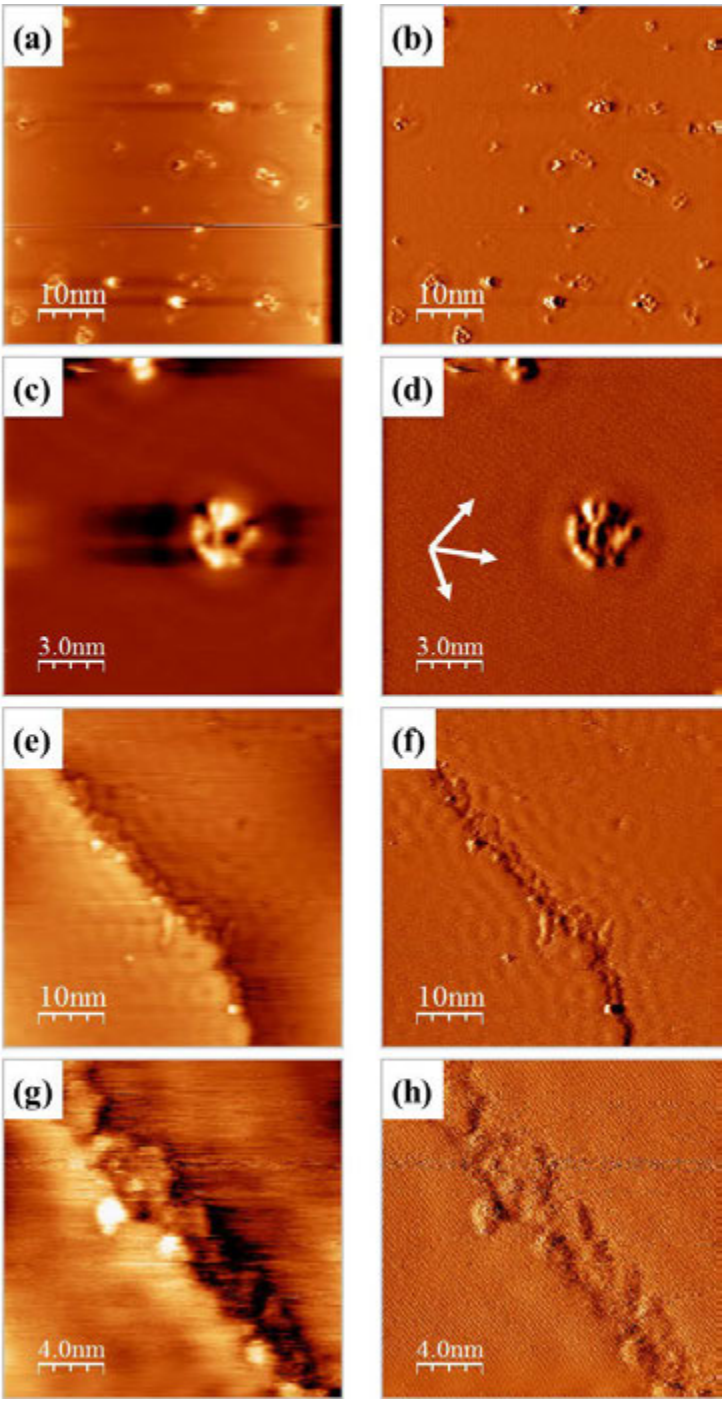

Figure A3.3. Ag(111) surface after 28 and 34 s of S deposition (experiments 2.1 and 2.2 at T_{sample} ~ 42 and 49 K). Topographic (left) and differentiated (right) STM images (1100721 S Ag111, m10, 29, 39, 42). (a-b) I = 0.717 nA, V_{sample} = 124 mV, loop gain 1%, 200 nm/s, 50×50nm^2. (c-d) I = 0.05396 nA, V_{sample} = 168.7 mV, loop gain 1%, 55 nm/s, 15×15nm^2. (e-f) I = 0.04495 nA, V_{sample} = 10.36 mV, loop gain 3%, 180 nm/s, 50×50nm^2. (g-h) I = 1.00 nA, V_{sample} = -10.36 mV, loop gain 1.75%, 60 nm/s, 20×20nm^2.

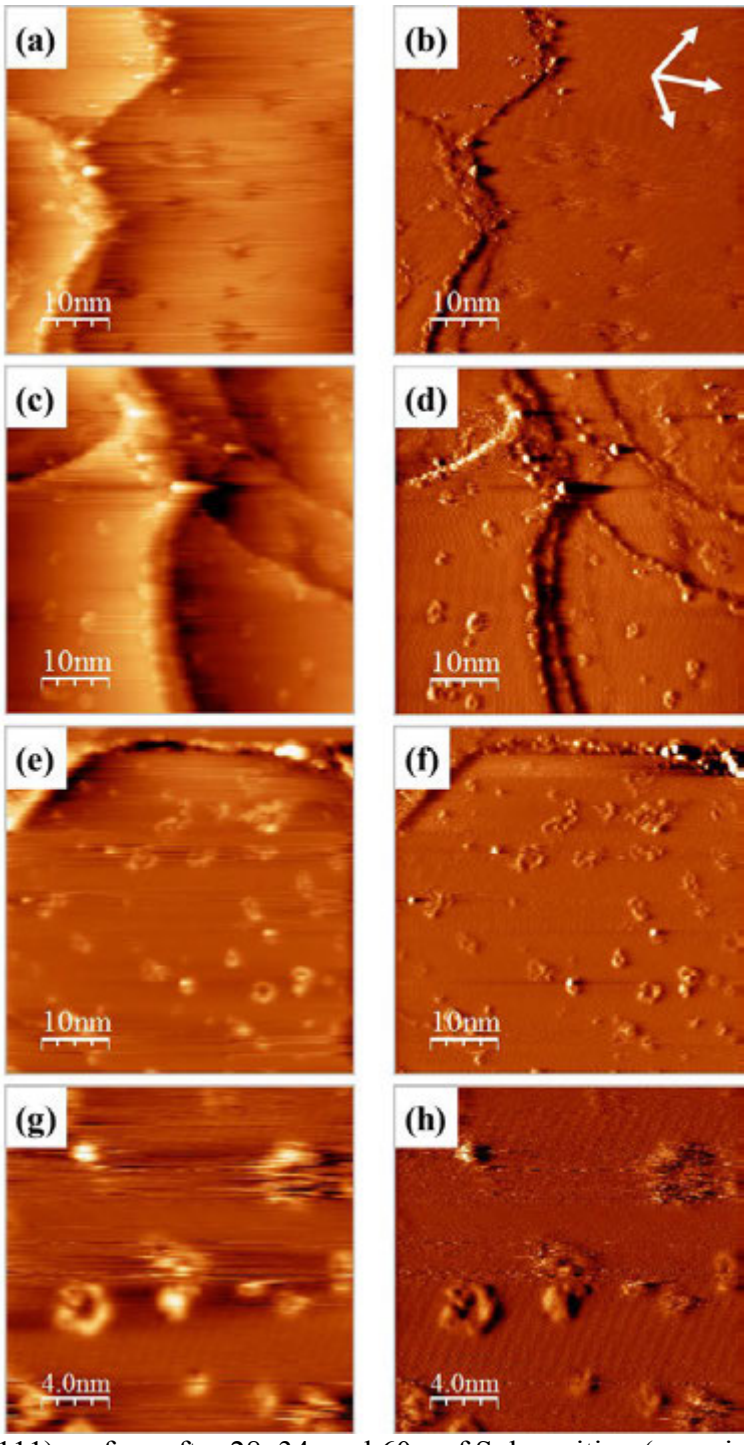

Figure A3.4. Ag(111) surface after 28, 34, and 60 s of S deposition (experiments 2.1, 2.2, and 2.3 at T_{sample} ~ 42, 49, and 63 K). Topographic (left) and differentiated (right) STM images, (a-f) 50×50nm^2 and (g-h) 20×20nm^2 (1100722 S Ag111, m9, 15, 20, 21). (a-b) I = 0.4112 nA, V_{sample} = -124 mV, loop gain 1%, 200 nm/s. (c-d) I = 0.700 nA, V_{sample} = -100 mV, loop gain 1%, 195 nm/s. (e-f) I = 0.3248 nA, V_{sample} = 365 mV, loop gain 1%, 200 nm/s. (g-h) I = 0.1766 nA, V_{sample} = 6713 mV, loop gain 0.8%, 80 nm/s.

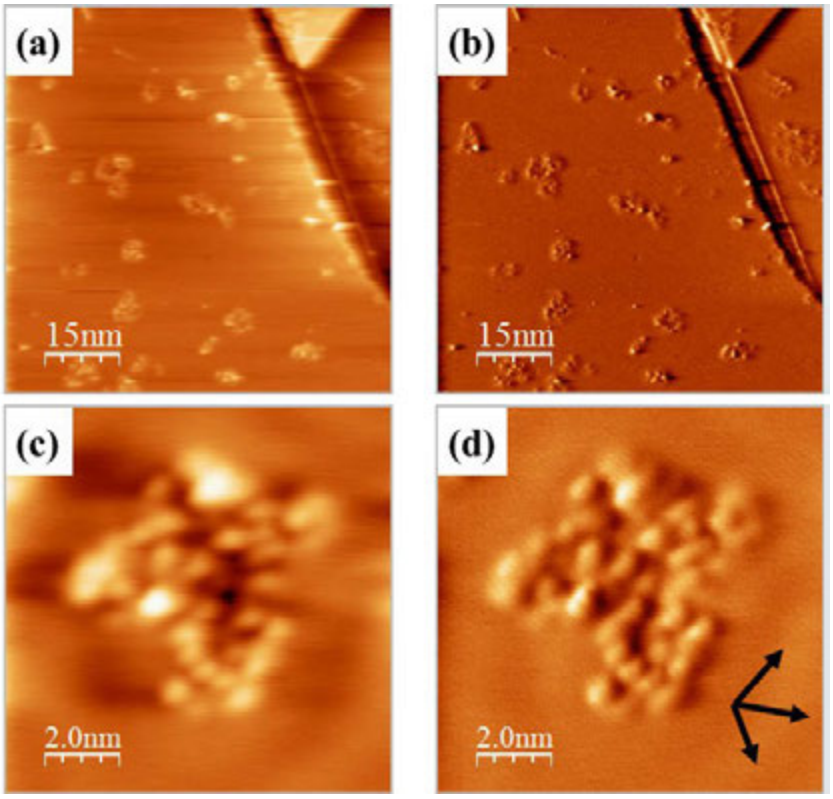

Figure A3.5. Ag(111) surface after 75 and 30 s of S deposition (experiment 3.1 and 3.2 at T_{sample} ~ 67 and 45 K). Topographic (left) and differentiated (right) STM images (1100724 S Ag111, m16, 26). (a-b) I = 0.02253 nA, V_{sample} = 269.2 mV, loop gain 2.2%, 225.4nm/s, 75×75nm^2. (c-d) I = 0.02253 nA, V_{sample} = 143.4 mV, loop gain 0.83%, 30.05 nm/s, 10×10nm^2.

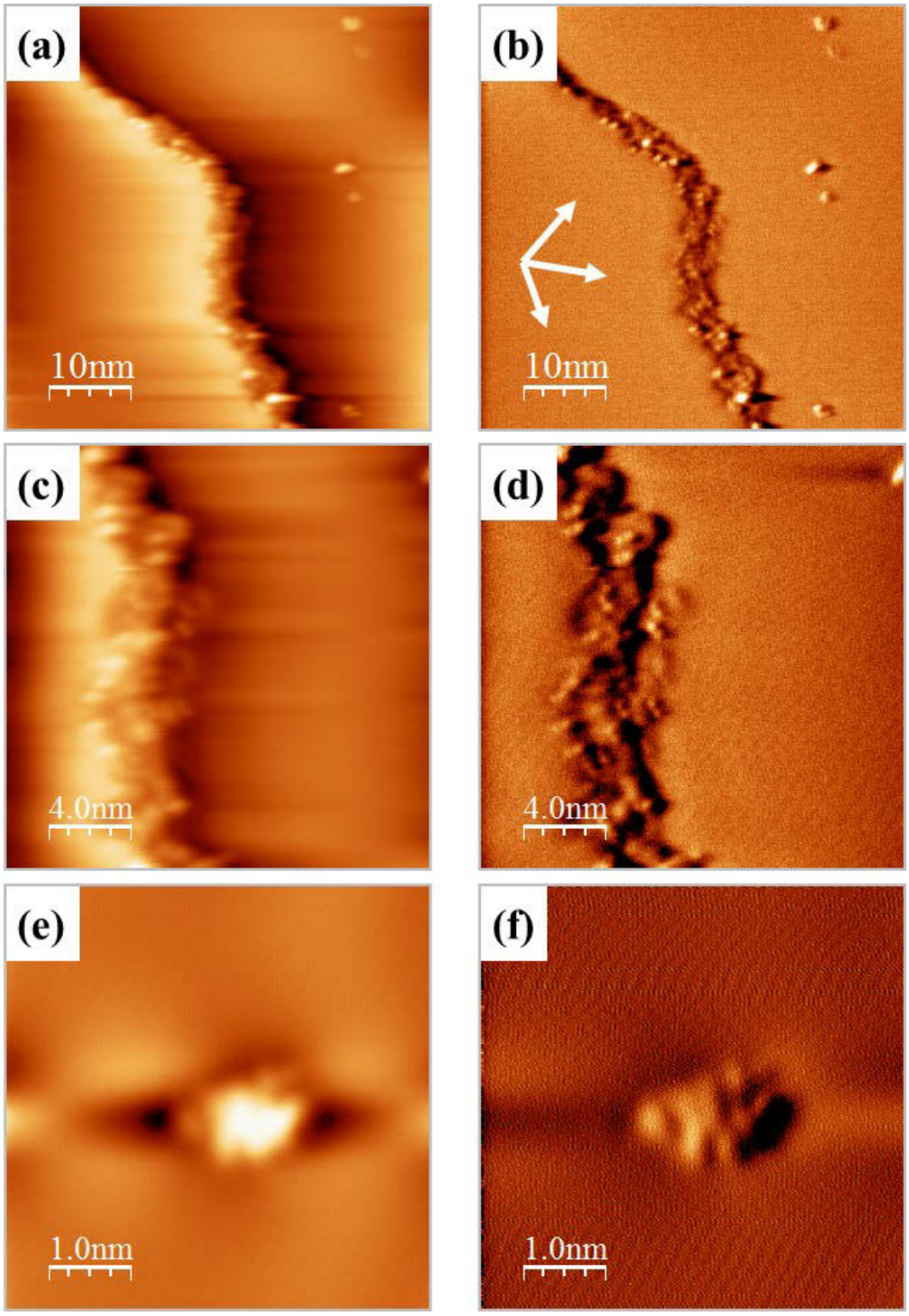

Figure A3.6. Ag(111) surface after S deposition and warming the sample to 200 K (experiment 2.2). Topographic (left) and differentiated (right) STM images (1100721 S Ag111 warmed, m15, 12, 6). (a-b) 0.025 nA, -452.9 mV, loop gain 2%, 200 nm/s, 50×50nm^2. (b-c) I = 0.030 nA, V_{sample} = -246.3 mV, loop gain 1%, 80 nm/s, 20×20nm^2. (e-f) I = 0.1098 nA, V_{sample} = 22.42 mV, loop gain 0.8%, 20 nm/s, 5×5nm^2.

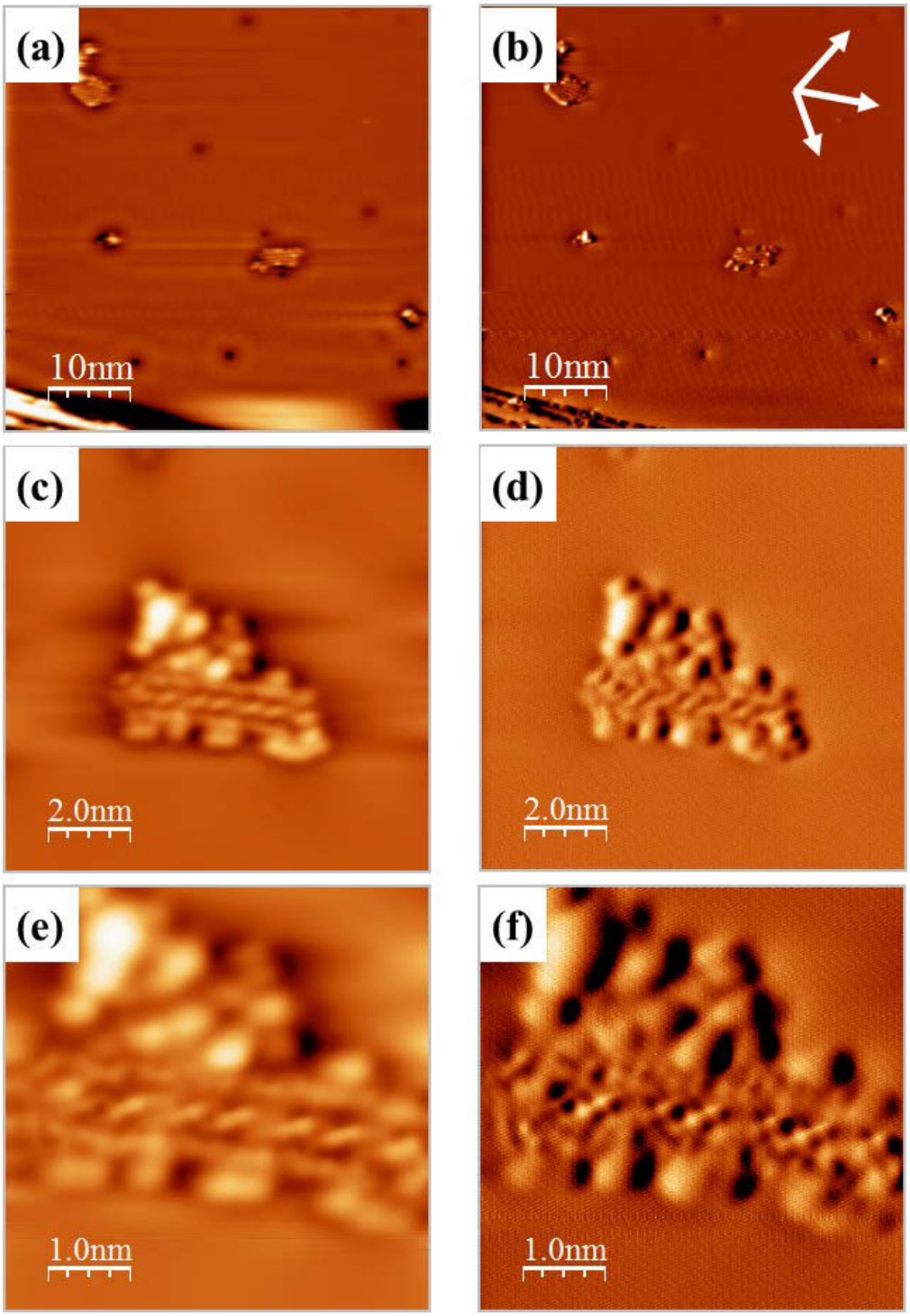

Figure A3.7. Terrace structures on the Ag(111) surface after S deposition and warming the sample to 250 K (experiment 2.3). Topographic (left) and differentiated (right) STM images (1100722 S Ag111 warmed, m20, 30, 31). (a-b) I = 0.1595 nA, V_{sample} = -165.3 mV, loop gain 0.8%, 150 nm/s, 50×50nm^2. (c-d) I = 0.100 nA, V_{sample} = -194.5 mV, loop gain 1%, 30 nm/s, 10×10nm^2. (e-f) I = 0.500 nA, V_{sample} = -47 mV, loop gain 1%, 15 nm/s, 5×5nm^2.

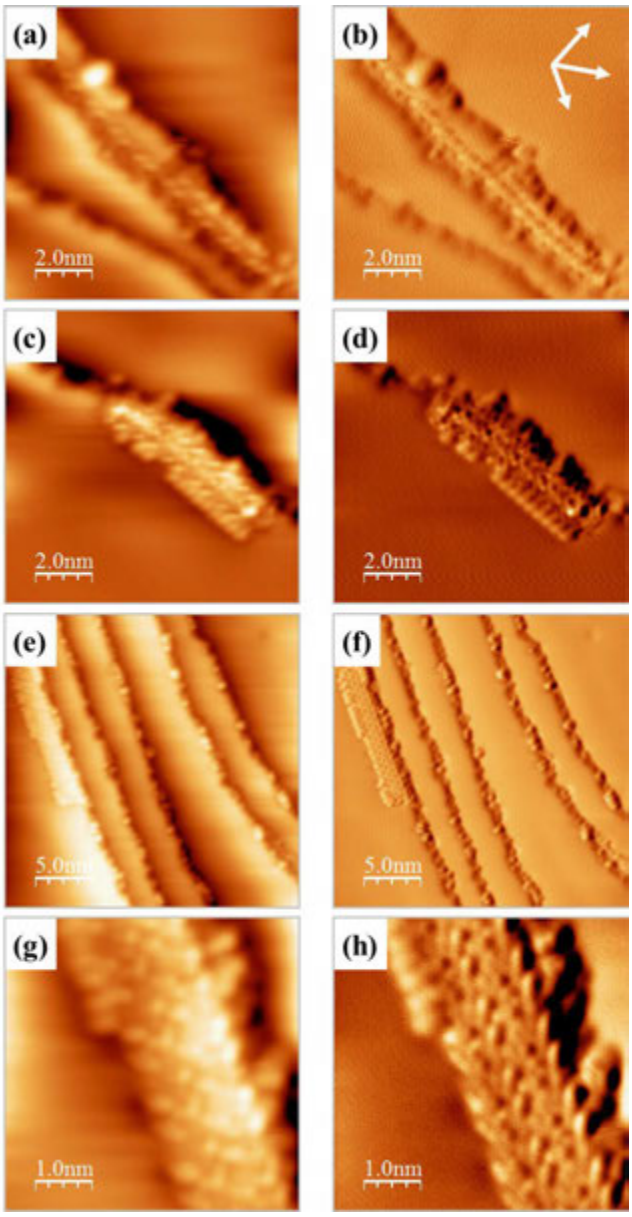

This figure continues on the following page.

Figure A3.8. Step regions on the Ag(111) surface after S deposition and warming the sample to 250 K (experiment 2.3). Topographic (left) and differentiated (right) STM images, (e-f) $25\times25nm^2$, (i-j) $20\times20nm^2$, (a-b, c-d, m-n) $10\times10nm^2$, and (g-h) $5\times5nm^2$ (1100722 S Ag111 warmed, m5, 10, 34, 36, 23, 25, 49, 51). (a-b) I = 0.6095 nA, V_{sample} = 657.8 mV, loop gain 2%, 40 nm/s. (c-d) I = 0.5396 nA, V_{sample} = -55.21 mV, loop gain 2%, 50 nm/s. (e-f) I = 0.146 nA, V_{sample} = -47 mV, loop gain 1.75%, 75 nm/s. (g-h) I = 0.146 nA, V_{sample} = -47 mV, loop gain 0.8%, 15 nm/s. (i-j) I = 0.500 nA, V_{sample} = -46.93 mV, loop gain 2%, 60 nm/s. (k-l) I = 0.500 nA, V_{sample} = -46.93 mV, loop gain 1%, 15 nm/s. (m-n) I = 0.08266 nA, V_{sample} = -54.1 mV, loop gain 1%, 30 nm/s. (o-p) I = 0.02934 nA, V_{sample} = -618.9 mV, loop gain 0.8%, 15 nm/s.

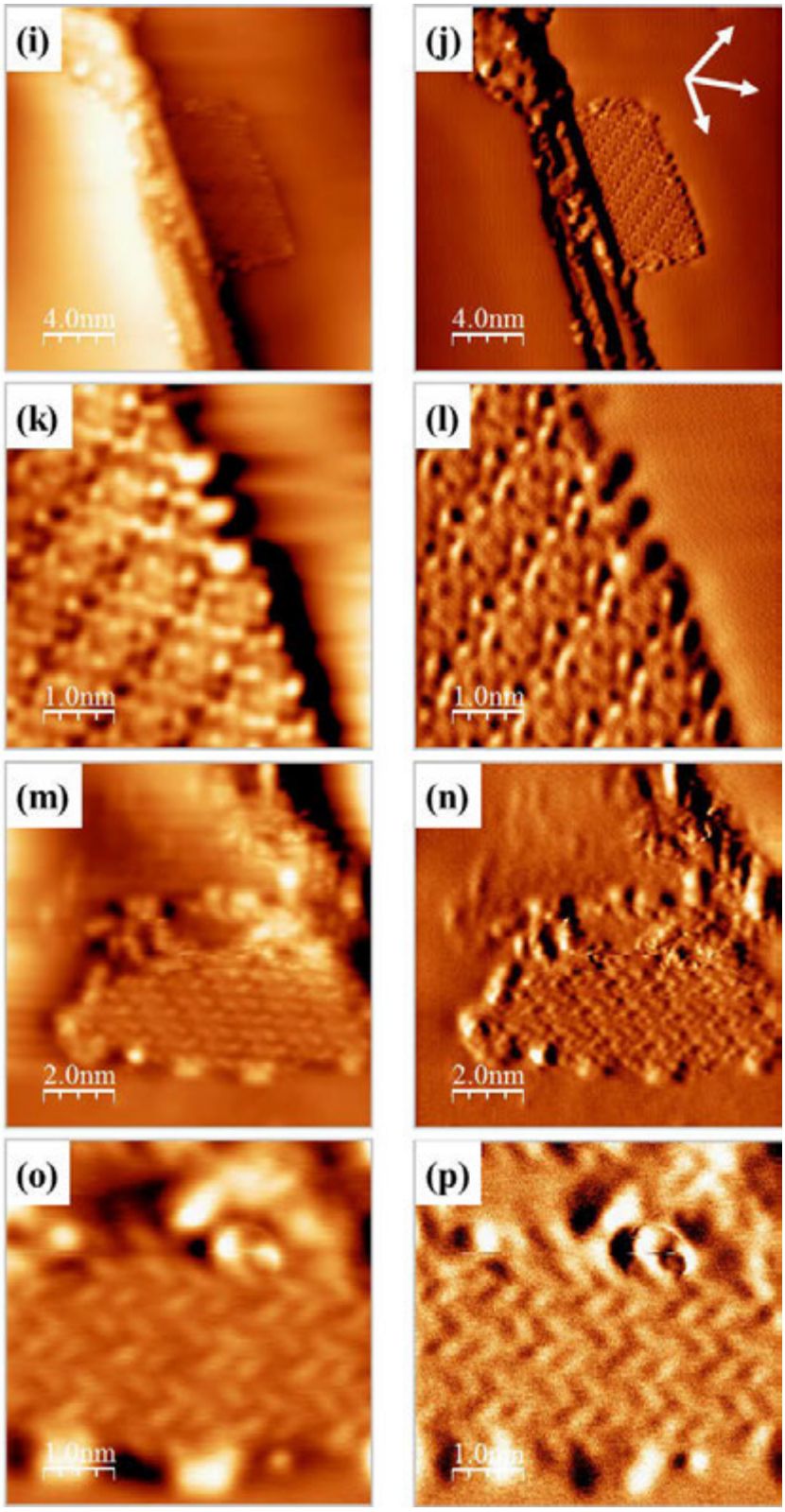

Figure A3.8. continued.

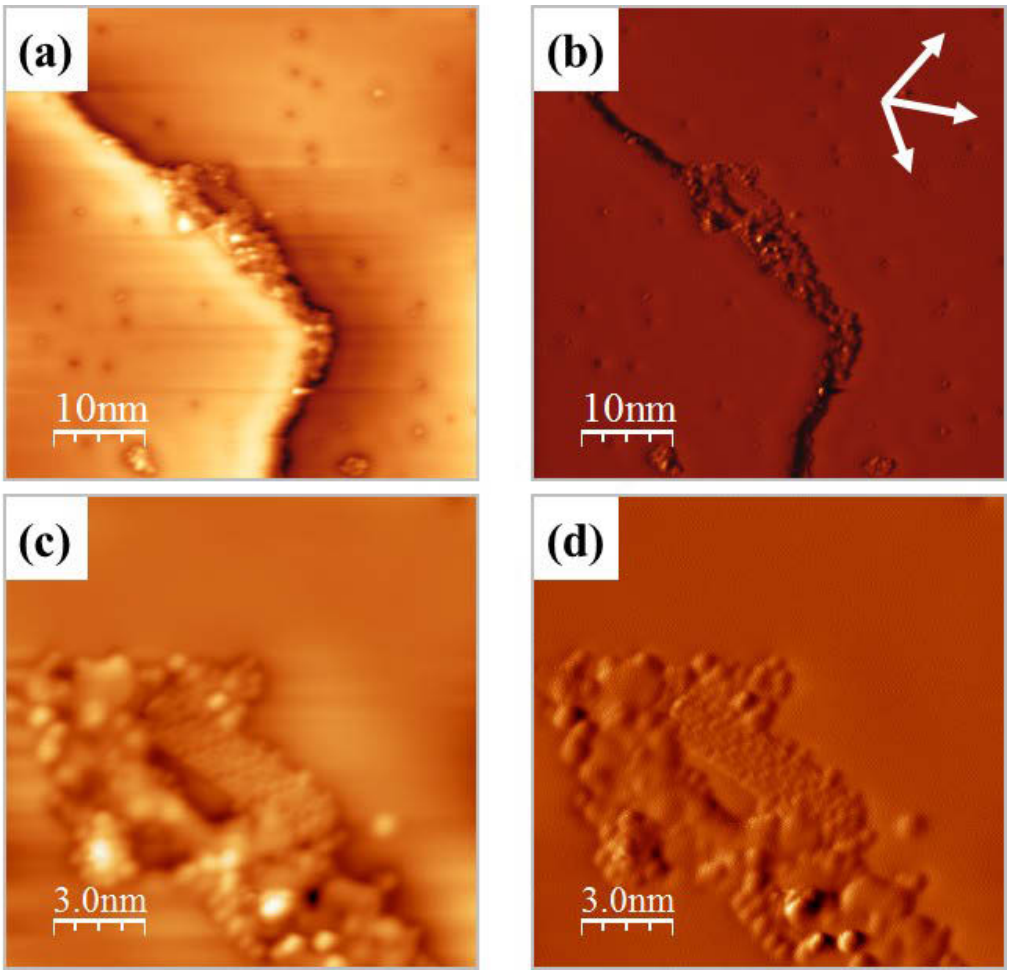

Figure A3.9. Step region on the Ag(111) surface after S deposition, warming to 250 K, and holding the sample overnight at 4.7 K (experiment 2.3). Topographic (left) and differentiated (right) STM images (1100723 S Ag111 warmed contd, m1, 4). (a-b) I = 0.1683 nA, V_{sample} = -54.1 mV, loop gain 1%, 180 nm/s, 50×50nm^2. (c-d) I = 0.1683 nA, V_{sample} = -54.1 mV, loop gain 1%, 55 nm/s, 15×15nm^2.

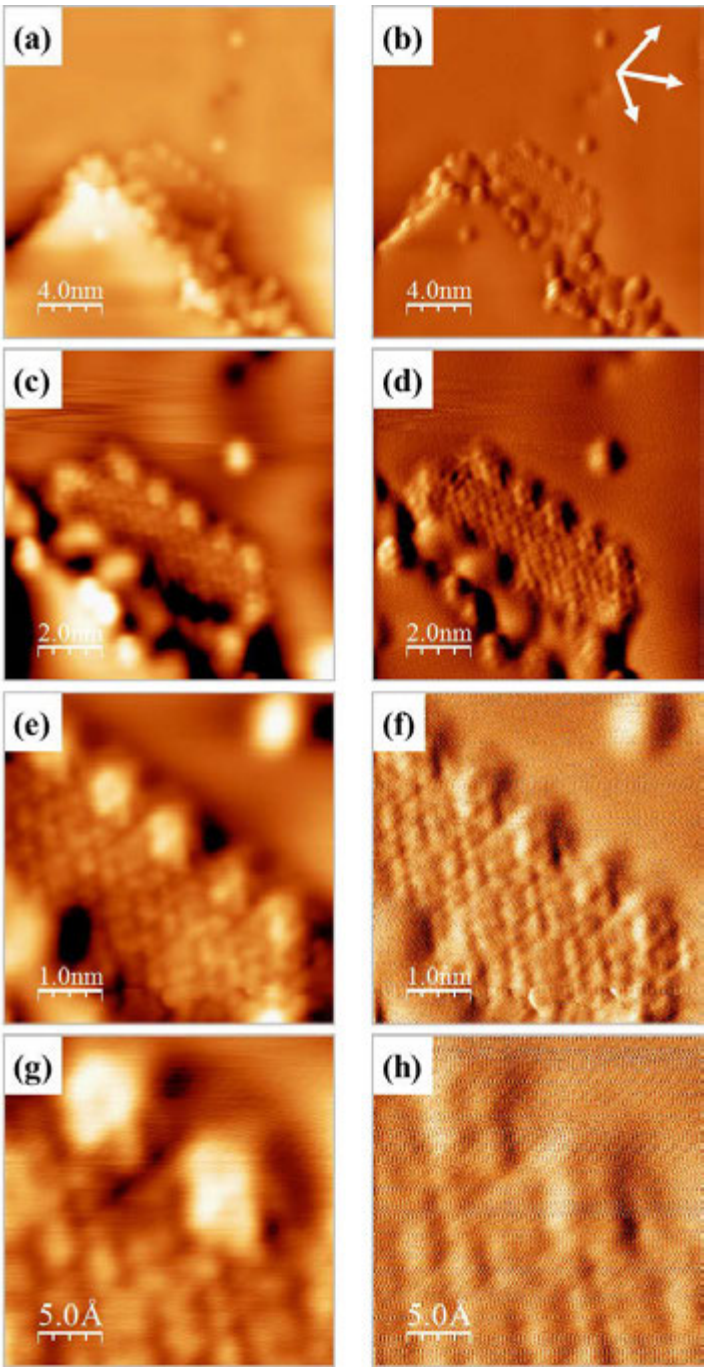

Figure A3.10. Ordered island along a step edge on the Ag(111) surface after S deposition, warming to 250 K, and holding the sample overnight at 4.7 K (experiment 2.3). Topographic (left) and differentiated (right) STM images of progressively smaller areas (1100723 S Ag111 warmed contd, m8, 19, 10, 18). (a-b) I = 1.00 nA, V_{sample} = -50 mV, loop gain 0.8%, 73 nm/s, 20×20nm^2. (c-d) I = 0.2796 nA, V_{sample} = -14.34 mV, loop gain 0.5%, 30 nm/s, 10×10nm^2. (e-f) I = 1.00 nA, V_{sample} = -50 mV, loop gain 0.8%, 15 nm/s, 5×5nm^2. (g-h) I = 0.2796 nA, V_{sample} = -14.34 mV, loop gain 0.5%, 5 nm/s, 2.5×2.5nm^2.

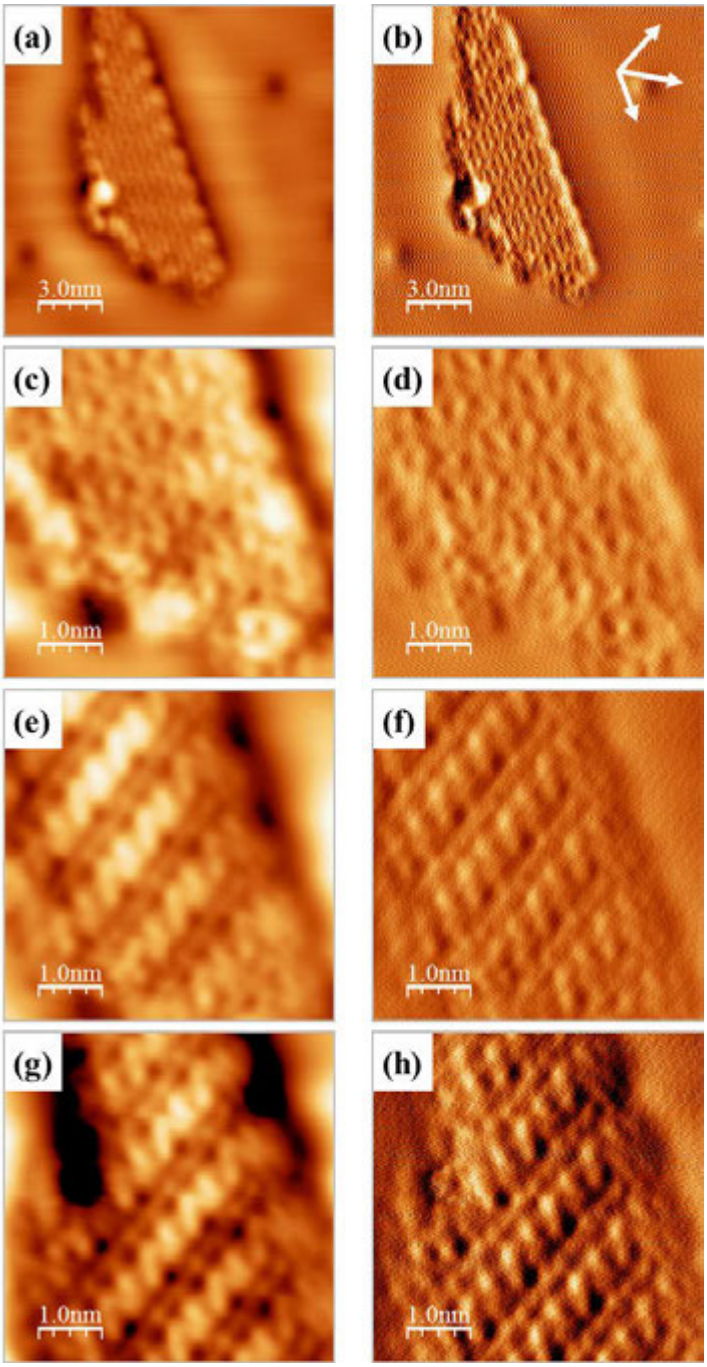

Figure A3.11. Ordered terrace island on the Ag(111) surface after S deposition, warming to 250 K, and holding the sample overnight at 4.7 K (experiment 2.3). Topographic (left) and differentiated (right) STM images, (a-b)15×15 nm^2 and (c-d) 5×5nm^2 (1100723 S Ag111 warmed contd, m36, 39, 40, 44). (a-b) I = 0.4552 nA, V_{sample} = -50 mV, loop gain 0.8%, 22.54 nm/s. (c-d) I = 0.5355 nA, V_{sample} = -50 mV, loop gain 0.6661%, 15.02 nm/s. (e-f) I = 0.5355 nA, V_{sample} = 50 mV, loop gain 0.6661%, 15.02 nm/s. (g-h) I = 1.0 nA, V_{sample} = 91.74 mV, loop gain 0.6661%, 19.93 nm/s.

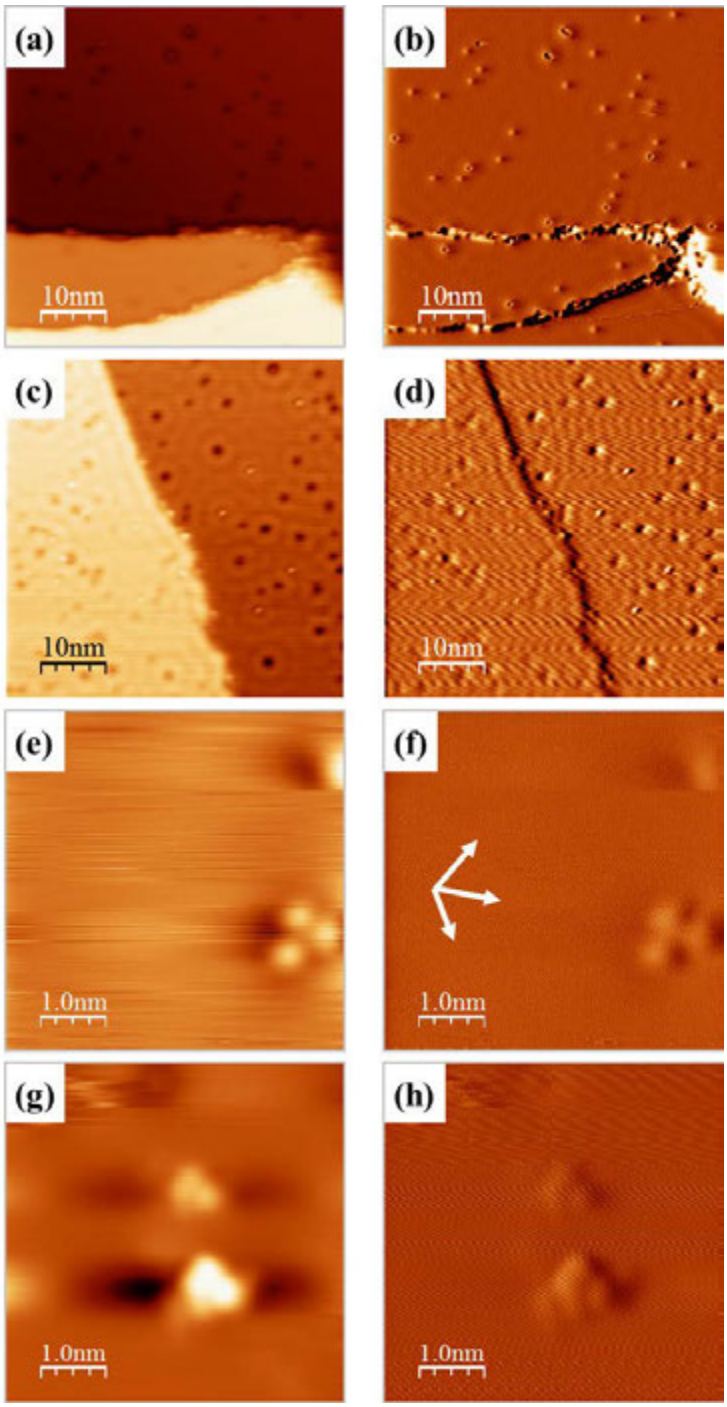

Figure A3.12. Ag(111) surface after S deposition and warming the sample to 250 K (experiment 3.2). Topographic (left) and differentiated (right) STM images, (a-d) 50×50 nm^2 and (e-h) 5×5nm^2 (1100725 S Ag111 warmed, m4, 51, 21, 46).(a-b) I = 0.500 nA, V_{sample} = -400 mV, loop gain 0.5%, 199.3 nm/s. (c-d) I = 0.5355 nA, V_{sample} = 54.1 mV, loop gain 1%, 199.3 nm/s. (e-f) I = 0.05396 nA, V_{sample} = -400 mV, loop gain 0.4967%, 15.02 nm/s. (g-h) I = 0.403nA, V_{sample} = -536.9 mV, loop gain 0.5436%, 25.04 nm/s.

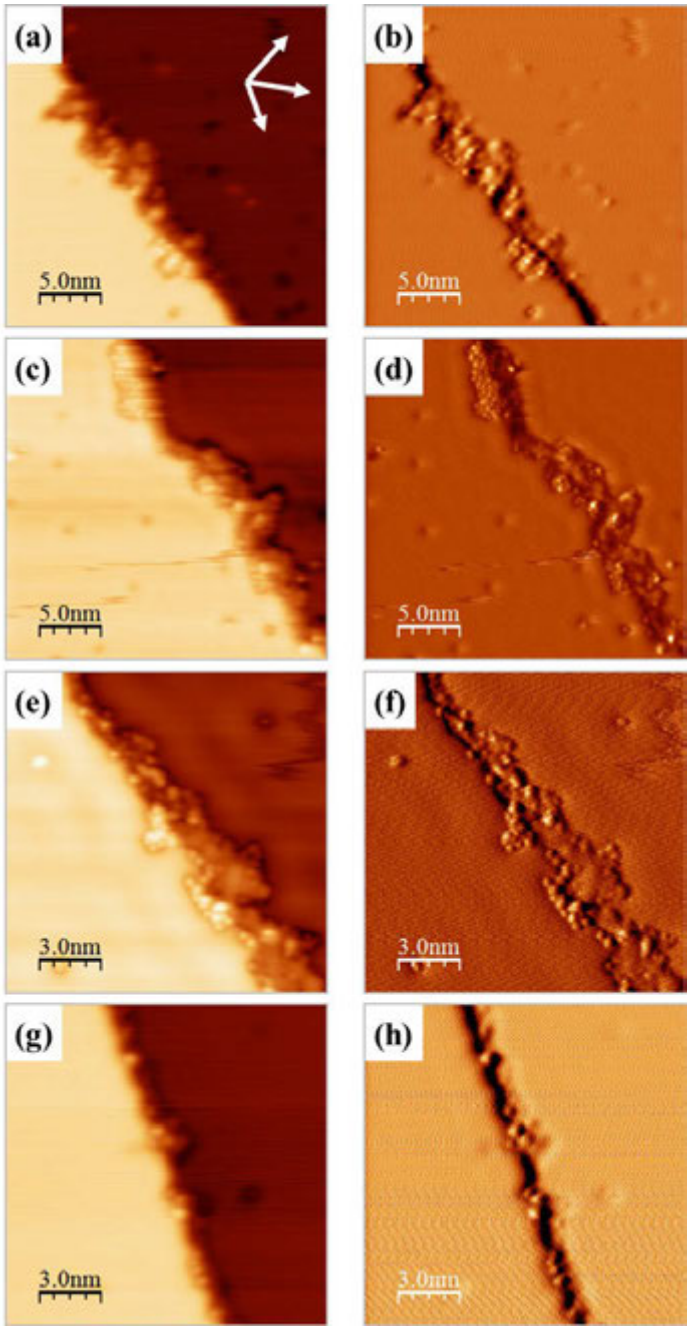

Figure A3.13. Step modification after S deposition and warming the sample to 250 K (experiment 3.2). Topographic (left) and differentiated (right) STM images, (a-d) 25×25 nm^2 and (e-f) 15×15 nm^2 (1100725 S Ag111 warmed, m70, 86, 96, 62). (a-b) I = 0.2191 nA, V_{sample} = 485.1 mV, loop gain 0.5%, 75.12 nm/s. (c-d) I = 0.1434 nA, V_{sample} = 143.4 mV, loop gain 0.508%, 99.65 nm/s. (e-f) I = 0.403 nA, V_{sample} = 62.37 mV, loop gain 1%, 52.32 nm/s. (g-h) I = 0.4851 nA, V_{sample} = 485.1 mV, loop gain 0.7%, 49.66 nm/s.

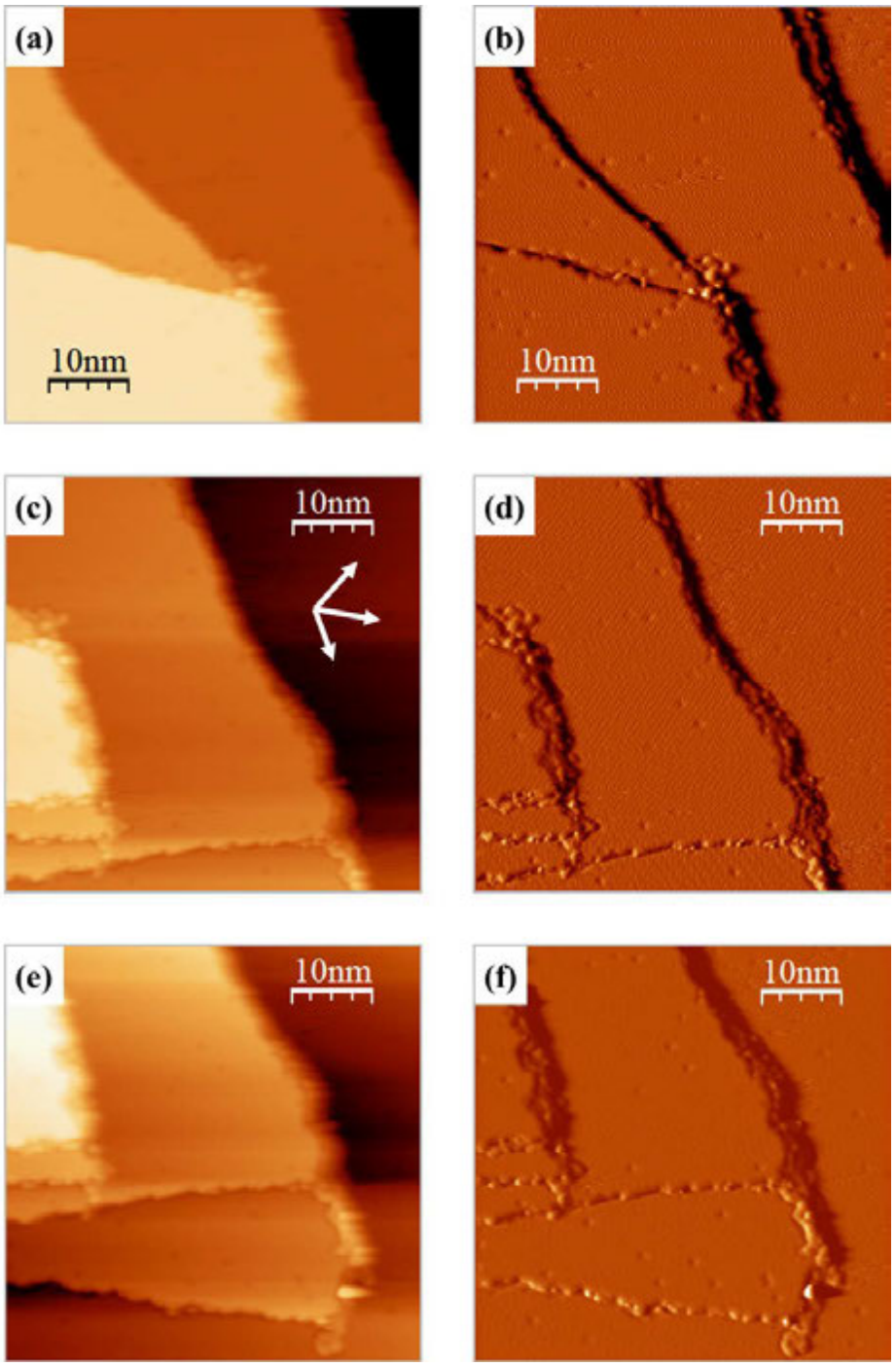

Figure A3.14. Step modification after S deposition, warming the sample to 250 K, holding overnight at 4.7 K, and warming to 275 K (experiment 3.2). Topographic (left) and differentiated (right) STM images, 50×50 nm^2 (1100726 S Ag111 rewarmed, m19, 10, 11). (a-b) I = 0.5355 nA, V_{sample} = 412 mV, loop gain 0.7%, 162.8 nm/s. (c-d) I = 1.0 nA, V_{sample} = 412.3 mV, loop gain 1%, 150.2 nm/s. (e-f) I = 0.5355 nA, V_{sample} = 412.3 mV, loop gain 0.6968%, 150.2 nm/s.

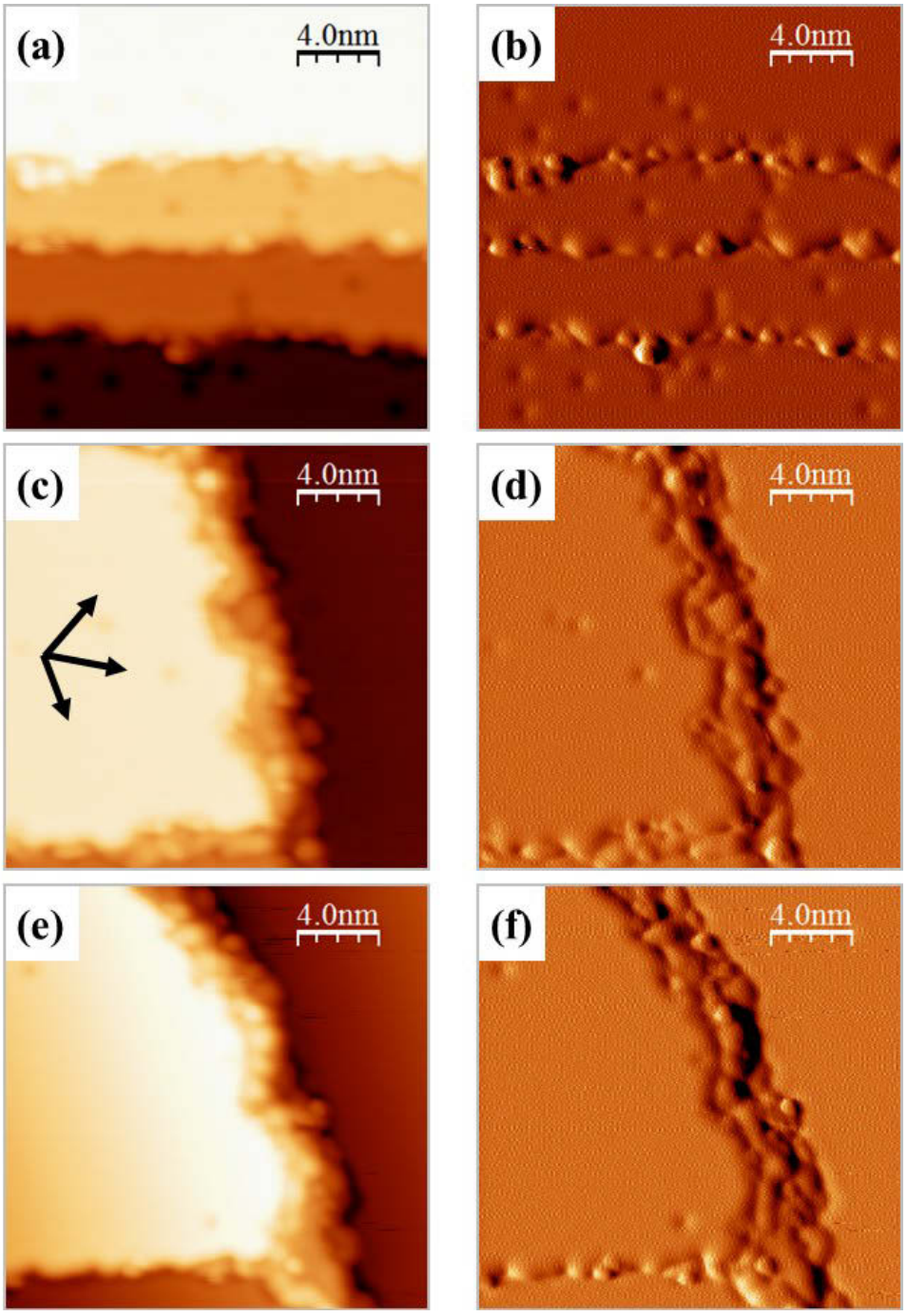

Figure A3.15. Step modification after S deposition, warming the sample to 250 K, holding overnight at 4.7 K, and warming to 275 K (experiment 3.2). Topographic (left) and differentiated (right) STM images, 20×20 nm^2 (1100726 S Ag111 rewarmed, m16, 14, 12). (a-b) I = 0.5355 nA, V_{sample} = 412 mV, loop gain 0.7%, 65.1nm/s. (c-d) I = 1.0 nA, V_{sample} = 412.3 mV, loop gain 0.8%, 65.1nm/s. (e-f) I = 0.965 nA, V_{sample} = 412.3 mV, loop gain 0.8%, 65.1nm/s.

References

(1) Shen, M.; Liu, D.-J.; Jenks, C. J.; Thiel, P. A.; Evans, J. W. *Journal of Chemical Physics* **2009**, *130*, 094701.

(2) Ling, W. L.; Bartelt, N. C.; Pohl, K.; de la Figuera, J.; Hwang, R. Q.; McCarty, K. F. *Physical Review Letters* **2004**, *93*, 166101.

(3) Shen, M.; Liu, D. J.; Jenks, C. J.; Thiel, P. A. *Journal of Physical Chemistry C* **2008**, *112*, 4281.

(4) Feibelman, P. J. *Physical Review Letters* **2000**, *85*, 606.

(5) Kibsgaard, J.; Morgenstern, K.; Lægsgaard, E.; Lauritsen, J. V.; Besenbacher, F. *Physical Review Letters* **2008**, *100*, 116104.

(6) Yamada, M.; Hirashima, H.; Kitada, A.; Izumi, K.; Nakamura, J. *Surface Science* **2008**, *602*, 1659.

(7) Maksymovych, P.; Voznyy, O.; Dougherty, D. B.; Sorescu, D. C.; Yates Jr., J. T. *Progress in Surface Science* **2010**, *85*, 206.

(8) Häkkinen, H. *Nature Chemistry* **2012**, *4*, 443.

(9) Shen, M. M.; Liu, D. J.; Jenks, C. J.; Thiel, P. A. *Journal of Physical Chemistry C* **2008**, *112*, 4281.

(10) Shen, M.; Russell, S. M.; Liu, D.-J.; Thiel, P. A. *Journal of Chemical Physics* **2011**, *135*, 154701.

(11) Shen, M.; Liu, D.-J.; Jenks, C. J.; Evans, J. W.; Thiel, P. A. *Surface Science* **2009**, *603*, 1486.

(12) Schwaha, K.; Spencer, N. D.; Lambert, R. M. *Surface Science* **1979**, *81*, 273.

(13) Driver, S. M.; Woodruff, D. P. *Surface Science* **2001**, *479*, 1.

(14) Woodruff, D. P. *Journal of physics: Condensed Matter* **1994**, *6*, 6067.

(15) Qin, C.; Whitten, J. L. *Surface Science* **2005**, *588*, 83.

(16) Sotto, M. P.; Boulliard, J. C. *Surface Science* **1985**, *162*, 285.

(17) Boulliard, J. C.; Sotto, M. P. *Surface Science* **1988**, *195*, 255.

(18) Tersoff, J.; Hamann, D. R. *Physical Review B* **1985**, *31*, 805.

(19) Nieminen, J.; Lahti, S.; Paavilainen, S.; Morgenstern, K. *Physical Review B* **2002**, *66*, 165421.

(20) Li, J.; Schneider, W.-D.; Berndt, R. *Physical Review B* **1997**, *56*, 7656.

CHAPTER IV

Adsorption of Sulfur on Ag(100)

A paper published in *Surface Science.*[a]

Selena M. Russell,[b] Mingmin Shen,[b,c] Da-Jiang Liu,[d] and Patricia A. Thiel[b,d,e]

Abstract

We have used scanning tunneling microscopy and density functional theory to investigate the structures formed by sulfur on Ag(100). As indicated by previous low-energy electron diffraction studies, the main phases have unit cells of p(2×2) and (√17×√17)R14°. We show that the latter is a reconstruction. The favored structural model is one in which 5 Ag atoms are missing from the (100) surface plane per unit cell. The ejected Ag atoms combine with sulfur to form islands of the reconstructed phase on the terraces. The (√17×√17)R14° phase coexists with the p(2×2), at sulfur coverages slightly above 0.25 monolayers. In addition, chain-like structures are observed in STM, both at room temperature (where they are dynamic) and below (where they are not). These results are compared with relevant literature for copper surfaces.

1. Introduction

Electronegative adsorbates such as sulfur,[1-8] oxygen,[8-14] chlorine[15] can strongly affect metal transport on surfaces of coinage metals. Hence, they can affect processes of self-assembly (including nucleation and growth[16,17]) and coarsening[18,19] of metal nanostructures. These processes are important to many applications that exploit nanoscale particles of these metals, such as surface enhanced Raman scattering and catalysis. To understand how and why the adsorbate affects metal transport, it is necessary to first understand the basic

[a] Russell, S. M.; Shen, M.; Liu, D.-J.; Thiel, P. A. *Surface Science* **2011**, *605*, 520.
[b] Department of Chemistry, Iowa State University, Ames, IA 50011
[c] Current address: Materials and Chemical Sciences Division, Fundamental and Computational Sciences Directorate, Pacific Northwest National Laboratory, Richland, WA 99352
[d] Ames Laboratory – USDOE, Iowa State University, Ames, IA 50011
[e] Department of Materials Science & Engineering, Iowa State University, Ames, IA 50011

interaction of the adsorbate with the metal surface. We have investigated sulfur on Ag(100) for that purpose, using (primarily) STM and DFT.

There have been no prior studies of this system using these techniques, to our knowledge. Previous experimental studies have used low-energy electron diffraction (LEED), Auger electron spectroscopy (AES), and isothermal measurements.[20-24] These have shown that at 0.25 monolayers (ML) of sulfur, a p(2×2) surface phase exists, while at higher coverage a (√17×√17)R14° phase (abbreviated √17) forms.[23,24] The √17 phase is stable from room temperature to 420 K, when it transforms reversibly to a (4√2×4√2)R45° phase.[23,24] A model was proposed for the √17 phase, consisting of chemisorbed sulfur in a coincidence lattice.[23] However, a √17 phase of sulfur on Cu(100) was assigned as a reconstruction, based partly on STM results.[25] This naturally leads to the question of whether the √17 phase on Ag(100) could be assigned similarly.

In terms of theory, there has been a previous study of sulfur on Ag(100) using configuration interaction theory.[26] The Ag surface was modeled as an embedded cluster. This showed that an isolated sulfur atom occupies the fourfold hollow site.

In this paper, we will show that the √17 phase on Ag(100) is a reconstruction that is virtually identical to the √17 phase on Cu(100). The √17 phase on Ag(100) can coexist with the p(2×2). In addition, chain-like structures are observed, both at room temperature (where they are dynamic) and below (where they are not).

2. Experimental and computational details

The Ag(100) sample was grown by the Ames Laboratory Materials Preparation Center.[27] The details of sample preparation and experimental procedures were very similar to those reported in a previous study of sulfur on Ag(111).[28] Notably, S_2 gas was generated within UHV in a solid-state electrochemical Ag|AgI|Ag_2S|Pt cell, following the design of Wagner.[29] Sulfur flux was in the range of 0.010 to 0.023 ML/minute. Unless stated otherwise, tunneling conditions for the STM images (all constant-current) were 1.00 nA current and -1.00 V tip bias. Data file names are provided in the figure captions: the date refers to the experiment date and folder name, and "m#" refers to the image file. We used the

p(2×2) structure as a reference to define crystallographic directions and lateral dimensions in STM.

Sulfur coverage, θ_S, is given as the ratio of S atoms to Ag atoms, also expressed as ML. Sulfur coverage was determined in two ways. First, after each STM experiment the S(LMM)/Ag(MNN) AES intensity ratio was measured and converted to coverage, following a calibration established by Schwaha, et al.[30] and corroborated by Rovida and Pratesi.[23] Coverage was also calculated from the fractional areas of p(2×2) and √17 in the STM images at 300 K, at coverages where the two coexisted. Each method of coverage determination was subject to its own sources of error. For example, AES probes an area at least 10^6 times larger than does STM, and the gross average coverage could differ from local coverage because of inhomogeneous flux or surface morphology. In STM, coverage determinations could be affected by domain boundaries and poorly-ordered regions. Nonetheless, the two measurements gave the same value within 12%. STM-based sulfur coverages are reported in this paper, because these gave slightly better agreement with ideal coverages.

Density-functional theory (DFT) calculations were performed using the VASP[31-33] total energy code, with Perdew-Burke-Ernzerhof (PBE)[34] generalized gradient approximation (GGA). The effects of various GGA approximations were tested, and the results are given in the supplemental materials. The projected augmented-wave (PAW)[35] method was used, utilizing a new PAW potential with improved treatment of the f channels[36] for Ag instead of the potential in the standard VASP package. Energetic values were obtained from Ag slabs, as described below, with the bottom layer of atoms fixed at their bulk positions. Adsorbates were attached to one side of the slab, with the induced artificial dipole interactions compensated by an external electrostatic field.[37] The lattice constant was set to 0.415 nm, the bulk PBE value at zero temperature using the new PAW potential (versus the experimental value of 0.409 nm). Methfessel-Paxton[38] smearing of the occupancy function (with $N = 1$ and $\sigma = 0.2$ eV) was used for efficiency. The energy cutoff was 280 eV for all calculations. The vacuum spacing between slabs was 1.2 nm.

Due to the need to compare energetics from calculations using various supercells, it is necessary to carefully consider convergence of DFT numbers to their bulk limit from calculations on finite slab thickness and with finite k-point grids. The supplemental materials

illustrate the effect of slab thickness on convergence. We find that surface energetics on Ag(100) and Cu(100) generally display variations with the slab thickness with a period of 5 ML.[39] An effective method to achieve highly accurate energetics on these surfaces is to average over results for a range of slab thickness. In this work, that range is 5 to 9 ML. The numerical errors, which are mainly due to finite slab thickness and finite k-point grids, can be estimated from the standard deviation of the results divided by the number of samples (5 in this paper). Note that this is different from the calculation of errors that are due to statistical noise in the samples.

3. Results and Analysis

3.1. STM and LEED observations of ordered structures at room temperature

Figure 1 shows a series of STM images after deposition of sulfur at 115 K, and various subsequent thermal treatments. The sulfur coverage is 0.28 and 0.35 ML. Results for both coverages are qualitatively similar. Immediately after deposition, there are many small, irregular islands, as shown in Fig. 1a. These may be islands of molecular sulfur, since they transform irreversibly upon heating. The same assignment has been suggested for irregular islands observed after Ag(111) exposure to S_2 at 135 K.[28]

Heating to about 230 K produces islands that are more well-defined, as shown in Fig. 1b. These may be precursors of larger islands that develop upon heating to 300 K, which are shown in Fig. 1c. In addition to these larger islands, there are two kinds of regions that are embedded in the terraces after heating to 300 K. All three regions are shown at higher magnification in Fig. 1d, and mapped schematically in Fig. 1e. The islands, and one of the embedded regions, show a fine structure like an irregular checkerboard. For reasons given shortly, we assign the checkerboard pattern as a $\sqrt{17}$ lattice with defects. Hence, regions of $\sqrt{17}$ exist within the terraces, and also as islands on top of the terraces.

The second kind of region embedded within the terrace exhibits a square arrangement of protrusions. The tops of the protrusions are about 0.17 nm below the $\sqrt{17}$ islands. At a coverage of 0.28 ML, LEED shows a clear p(2×2) pattern, as shown in Fig. 2a. At 0.35 ML, STM shows that a greater fraction of the surface is covered by the checkerboard pattern, than at 0.28 ML. Correspondingly, the LEED pattern shows a fainter p(2×2) and higher

background, but no distinguishable √17 LEED pattern. Together, these observations provide a basis for assigning the square arrangement of protrusions in STM as a p(2×2) structure, which is shown at high magnification in Fig. 2b.

The justification for assigning the checkerboard regions as √17 lies in details of the STM images, shown in Fig. 3. First, Fig. 3a shows that the checkerboard actually consists of bright protrusions, grouped in sets of 4 (tetramers) or sets of 6 (rectangular hexamers). One of each is encircled in Fig. 3a. We regard the hexamers (sets of 6) to be defects in the structure. This is because a surface prepared at higher sulfur coverage, and annealed above room temperature, consists mainly of tetramers. An image of such a surface is shown in Fig. 3b. Therefore, to assign the ideal structure, we consider only checkerboard regions comprised of tetramers. One such region is shown by the island at the top of Fig. 3c, where the unit cell of the lattice and its rotation [measured relative to the p(2×2)] are illustrated. The edge of the unit cell is 1.18 $\pm$ 0.03 nm long, compatible with the value of 1.192 nm expected for a √17 lattice. The measured angle of rotation is 13 $\pm$ 3^{o}, also compatible with the expected angle of 14^{o}.

In summary, the experiments show that a p(2×2) structure coexists with a √17 structure, slightly above the ideal p(2×2) coverage of 0.25 ML. As sulfur coverage increases, the fraction of surface area covered by √17 increases. The √17 exists both as islands on top of terraces, and within terraces. The main structural motif of the √17 is a tetramer.

3.2. Chemical potentials of possible structures

DFT can be used to judge the relative stabilities of ordered sulfur structures. The figure of merit is the chemical potential of sulfur, which is defined at 0 K as

$$\mu_S = [E_{\mathrm{ad}}(\mathrm{Ag}_m\mathrm{S}_n, L) - E_{\mathrm{clean}}(L) - m\,\mu_{Ag}] / n \qquad (1)$$

where $E_{\mathrm{clean}}(L)$ is the energy of a clean slab of thickness L, and $E_{\mathrm{ad}}(\mathrm{Ag}_m\mathrm{S}_n, L)$ is the energy of an adsorbate structure with m Ag atoms and n sulfur atoms (per supercell) on top of an L-layer slab. Note that m can be negative in the case of vacancies. μ_{Ag} is the chemical potential

of Ag in the bulk. Above 0 K, the chemical potential also has an entropy term. A lower (more negative) value of μ_S corresponds to a more stable structure.

Values of μ_S have been calculated for numerous structures. The most relevant ones are reported in this paper. Others are described in the supplemental material. There are two main types: those that just involve a chemisorbed overlayer of sulfur; and those that include Ag adatoms or vacancies. Figure 4 shows results for the most favorable structures. Some tie lines are drawn to suggest phase co-existence.

A stable p(2×2) structure exists with ideal coverage of 1/4 ML, involving chemisorbed sulfur at four-fold hollow sites.[26] Stable p(2×2) structures are often observed for chalcogens on metal(100) surfaces, and they reflect very strong nearest-neighbor (NN) repulsions and substantial second-NN repulsions. However, additional interactions are necessary to stabilize the p(2×2) against one-dimensional disorder. These can be third-NN attractions [as for O/Pd(100)[40,41] and O/Ni(100)[42]], or fourth-NN repulsions [as for Se/Ni(100)[43] and O/Rh(100)[44]], or both. For S/Ag(100), a fourth-NN repulsion exists, based upon comparison of μ_S of three very dilute chemisorbed structures. One is a ($\sqrt{5}\times\sqrt{5}$)R26^o structure, which is dominated by fourth-NN interactions. This structure's μ_S is 0.02 to 0.03 eV higher than c(4×4) and p(3×3) structures, which have longer-range and extremely weak interactions. Because of this fourth-NN repulsion, one expects the phase region of p(2×2) order to be quite narrow at 200-300 K, similar to Se/Ni(100)[43] and O/Rh(100)[44]. In Fig. 4, the low-coverage limit (the end-point of the left-most tie-line) is taken as the average μ_S of the c(4×4) and p(3×3) structures, which is assumed to be a proxy of μ_S for a low-coverage disordered phase.

Above 0.25 ML, a mixed p(2×2) and √17 structure can exist as suggested by the tie-line between 0.25 and 0.47 ML. The experimental observations at 300 K fall in this coverage range and agree very well with DFT. The c(2×2) at 0.5 ML is not predicted to be a stable phase, but we show it in Fig. 4 to demonstrate the relative stability of the competing p(2×2)and √17 phases. A chemisorbed layer, with μ_S slightly below the p(2×2)-√17 tie line, will be addressed later. First, the √17 structure is analyzed in more detail.

3.3. The √17 phase

A structural model has been proposed for a √17 structure observed on Cu(100),[25] based both on STM[25] and sulfur coverage measurements on that surface.[45] Two variants of this model are shown in Fig. 5a and 5c. DFT indicates that this model is viable also on Ag(100). In Fig. 5a and 5c, the atomic positions have been optimized with DFT for Ag(100). Within each unit cell, there are eight sulfur atoms, as was originally proposed on Cu(100).[45] The coverage is 8/17 ≈ 0.47 ML. Four sulfur atoms sit above the surface plane, and four replace Ag atoms within the surface plane (or nearly so), creating sites that can be called Ag vacancies. Following the nomenclature established for the Cu(100) model,[25] we call the sulfur atoms "surface sulfur" and "in-plane sulfur," respectively. On Ag(100), DFT shows that in-plane sulfur atoms are shifted slightly away from the lateral positions occupied by the original Ag atoms. In the earlier work with Cu(100), it was proposed that one additional in-plane metal atom might be missing per unit cell.[25] If it is missing on Ag(100), the structure contains 5 Ag vacancies per unit cell–relative to a clean Ag(100) terrace–as shown in Fig. 5a; otherwise, it contains 4 vacancies as shown in Fig. 5c.

The chemical potentials of both types of √17 are shown in Fig. 4 for Ag(100). The 5-vacancy structure has lower μ_S and hence is predicted. This form of the √17 is also supported by the following comparison between simulated and measured STM images. Figure 5b shows a simulated STM image using the Tersoff-Hamann method for the 5-vacancy model. Figure 5D is the corresponding picture for the 4-vacancy model. The main difference is that in the 5-vacancy model, there is a depression at the center of 4 tetramers (corresponding to a missing in-plane Ag atom). In the 4-vacancy model, there is a slight protrusion at this spot. The 5-vacancy model agrees better with experiment, since we observe a depression, but never a protrusion, between tetramers. See Fig. 3a.

Other models with large unit cells, including √17, were tested and results are given in the supplemental materials. None is as favorable as the 5-vacancy √17 model shown in Fig. 5a. However, several are fairly close (within 0.05 eV), suggesting that they could be observed at higher temperatures. This interpretation is supported by the experimental observation that the √17 transforms to a larger-unit-cell structure upon heating to 420 K.[23,24]

However, the size of the unit cell observed experimentally–4√2*a*–makes direct DFT simulations impractical in our studies.

As an aside, for the √17 on Cu(100), we have also calculated μ_S for the 5-vacancy and 4-vacancy models with DFT. Similar to Ag(100), the 5-vacancy model is significantly more stable, by about 0.11 eV per sulfur, on Cu(100).

The structural model of Fig. 5 requires that Ag atoms be displaced from the terrace. This explains the origin of the √17 islands in the STM images; they consist of ejected Ag, plus additional sulfur. Step edges can compete with islands as repositories for ejected Ag atoms. We ascribe the faceted appearance of step edges in Fig. 1c to outward growth of √17 from the step edges. In fact, at a coverage of 0.35 ML, the tops of step edges are entirely covered by √17, while interiors of terraces and bottoms of steps are only partially covered by √17. Thus, the √17 preferentially grows outward from existing steps.

Hexamers appear at boundaries between domains of √17, as shown in Fig. 3a. Hexamers occur with higher frequency in √17 terrace domains than in √17 islands. For instance, the hexamers in Fig. 3a exist in a domain embedded in a terrace, but there are no hexamers in the small island of Fig. 3c. Perhaps √17 domains in embedded regions cannot merge as freely as in islands, either during or after growth. It is also interesting that features larger than hexamers and smaller than tetramers are never observed. The upper limit may mean that units larger than hexamers can easily dissociate into smaller units.

3.4. Transition from the mixed p(2×2)-√17 phase

Returning to Fig. 4, the data point slightly below the p(2×2)-√17 tie line represents a family of structures that is more stable than the coexisting phases by about 0.02 eV. These can be thought of as p(2×2) areas with domain walls having local c(2×2) structure. One form is illustrated in Fig. 6. (Other forms of domain walls were also tested, but were not energetically competitive.) The structures in this family should form a continuum above 0.25 ML. The prediction from DFT is that below T=200 K (corresponding to 0.02 eV), one will see a p(2×2) chemisorbed layer with domain wall structure at 0.25 to 0.38 ML. Above 200 K, one should see mixed p(2×2) and √17 at these coverages, as observed.

There is experimental evidence to support a phase transition in this temperature range, both at 0.28 and 0.35 ML. STM images are given in Fig. 7, showing a surface with 0.28 ML that has been cooled from 300 K to 230 K. Except for small and rare patches, the p(2×2) has disappeared. It is replaced by regions that do not have long-range order, but frequently exhibit local stringy features. Examples are shown in Fig. 7b-d. At this temperature, 230 K, the surface does not change during observation.

It is possible that as the surface cools below 300 K, the transition to the domain wall structure begins. However, for kinetic reasons, the transition cannot be completed and the surface becomes frozen into a disordered state that contains remnants of the original phases, as well as harbingers of the new phase. On the other hand, the structures present at 230 K often resemble chain structures, with a height that is higher than expected for domain walls: 0.07 + 0.03 nm measured in STM, vs. 0.01 nm predicted from DFT for domain walls. Hence, another possibility is that there exists another energetically-competitive, chain-like structure that has not been predicted to be a equilibrium phase by DFT. Chains are discussed in more detail in the next section.

3.5. Surface dynamics at 300 K

Figures 8 and 9 demonstrate that the surface is dynamic at 300 K, at a coverage of 0.35 ML and on the time scale of our STM imaging. In Fig. 8, four STM images are acquired at intervals of 190 s. One interesting feature is the evolution of a subgrain boundary within a √17 island over time, in the large island near the center of the image. At the beginning (Fig. 8a), the rows of √17 are in two domains, separated by a boundary in the middle containing several hexamers. The boundary is indicated by the white arrow. By the end (Fig. 8d), the hexamers have rearranged to form the first dislocation in a subgrain boundary, also marked by an arrow. These observations show that there is motion and rearrangement of material within the √17 islands at 300 K.

There is also evidence of motion and rearrangement outside of the √17 islands. This comes from *transient* regions which contain material that is intermediate in height between the p(2×2) and the √17. In Fig. 8, several such regions are connected to the central large √17 island. These are encircled. Other transients are enclosed in squares. This shows that

considerable material is transported on the time scale of STM imaging, leading to observable density fluctuations at 300 K. Fluctuations are not observed at 230 K.

Several transient regions are shown at higher magnification in Fig. 9. There is some horizontal streaking associated with the horizontal scanning direction in STM, but non-horizontal, linear segments are visible nonetheless. The clearest example is in Fig. 9c. The linear segments are usually parallel to rows of p(2×2). They are 0.11 $\pm$ 0.03 nm higher than the top of the p(2×2). We propose that these linear features are Ag-S chains.

One type of chain could consist of linear Ag-S-Ag-S units. Several variations are shown in Fig. 10a-c. DFT shows that if Ag and S atoms are constrained to adjacent four-fold hollow sites, the chain is relatively unstable, with μ_S = -4.49 eV. This low stability is due to the separation between Ag and S atoms, d, which is too large for a bonding interaction. In fact, there is some repulsion between Ag and S atoms at a distance of one Ag(100) surface lattice constant, a, which is 0.293 nm in the DFT simulations. For relaxed, isolated pairs of Ag and S atoms, as shown in Fig. 10a, the interaction is only slightly more favorable. However, a S-Ag-S cluster–which can be considered a very short chain–is much more stable (Fig. 10b). According to DFT, $d = 0.836a$ = 0.245 nm, and μ_S = -4.84 eV. An example of a longer linear chain is shown in Fig. 10c, and the chemical potentials of several are shown in Fig. 10d. In these, the general trend is that some Ag and S atoms are displaced from high-symmetry sites to achieve shorter Ag-S bonds. These chains are most stable if they are S-terminated, so the stoichiometry is always Ag_mS_{m+1}. The most stable one that has been tested in this work is Ag_2S_3, but even it is not as stable as the p(2×2)-$\sqrt{17}$ mixed phase, as shown by the chemical potential-coverage diagram of Fig. 10d.

Another possible type of chain is a zig-zag, which is simply a denser row of Ag, decorated by sulfur at alternating positions along the sides. Examples are shown in Fig. 11a-b, and values of μ_S are given in Fig. 11c. The chemical potentials of these (infinite) zig-zag chains are not as low as the p(2×2)-$\sqrt{17}$ mixed phase, but are comparable to the linear chains shown in Fig. 10. Hence, according to DFT, chain structures cannot represent an equilibrium surface phase.

DFT predicts that in STM, the heights of both types of chains should be intermediate between the p(2×2) and the √17, as observed. The heights, relative to the top of the p(2×2), are essentially identical in experiment and theory, at about 0.10 nm.

One possible explanation for the transient regions is that they consist of chains that form in the presence of a very slight supersaturation of isolated, mobile Ag adatoms. Values of μ_S, for structures that contain Ag adatoms or vacancies, depend strongly on the chemical potential of the Ag adatoms, μ_{Ag} in Eq. 1. In the DFT calculations, μ_{Ag} is taken as the bulk value, which is the same as assuming that Ag adatoms are in equilibrium with the bulk. However, if diffusion of Ag adatoms is slow, or if attachment to the step edge is slow, there can be a surplus of Ag adatoms. This will lower μ_S of structures containing Ag adatoms, like the chains, and it will change the relative stabilities of such structures. The transient surplus of Ag adatoms could be associated with Ag ejection from terraces as the √17 forms. This could possibly account for the transients in Fig. 8.

4. Discussion

4.1. Comparison with prior studies of sulfur on Ag(100)

Our work is generally consistent with the two earlier studies of sulfur on Ag(100) that implemented LEED.[23,24] Both reported that a p(2×2) pattern emerged first, followed by a √17 pattern, with increasing sulfur coverage at 300 K. In one of those studies, the √17 pattern was observed at 0.5 ML and above, somewhat higher than in the present work (0.28 ML and above), although that difference could be attributed to the higher sensitivity for small domains–especially small domains of a structure with a large unit cell–in STM compared with LEED.

4.2. Comparison with prior studies of sulfur on Cu(100)

There have been both LEED and STM studies of sulfur on Cu(100).[25,46] There are strong similarities with S/Ag(100), but also some differences.

Sulfur on Cu(100) forms p(2×2)[25,46] and √17[25] structures, as well as c(4×2)[25,46] and c(6×2)[46] structures. On Ag(100), we find no evidence for the latter two structures, nor was there any report of them in the previous LEED studies for this system.[23,24]

STM images of the √17 on Cu(100)[25] show local motifs that are essentially identical to the tetramers observed in the present study, suggesting a common origin. Our DFT analysis supports the idea that the model proposed for S/Cu(100) can be applied to S/Ag(100) as well (Fig. 5). Hexamers were also reported as a minority species on Cu(100).[25] Our DFT calculations support the 5-vacancy model over the 4-vacancy one, for the √17 structure on both Ag(100) and Cu(100).

One difference can be found in the temperature necessary to produce the √17 superstructure, and the associated tetramers. On Cu(100), it is necessary to anneal above room temperature (to at least 500 K),[25] whereas on Ag(100), room temperature suffices (although the quality of the LEED pattern can be improved by annealing above room temperature).[23] This difference in temperatures is explained by the lower cohesive energy of Ag, in light of the fact that the √17 requires displacement of metal atoms.

Another difference between Cu and Ag is that transient structures were not reported for sulfur on Cu(100), perhaps because surfaces were imaged at room temperature. Extrapolating from Ag(100), a temperature of 500 K would be more appropriate for observing transients on Cu(100). One-dimensional chains were also reported on Cu(100),[25] but their structure was not discussed, and they were static at 300 K.

4.3. Chain structures

The chain-like structures observed in this work are reminiscent of the mobile Cu-O-Cu-O chains observed on Cu(110). Those chains are the building blocks of the added-row reconstruction, and in STM they were observed to move independently on the Cu(110) terraces at 300 K.[12-14] They are structurally similar to the linear chains in Fig. 10c, except that they are longer and are in perfect registry with the Cu(110) substrate. Additionally, there may be some buckling in the Cu-O chains.[47]

However, DFT indicates that μ_S of analogous linear Ag-S chains is at least 0.1 eV higher than that of the p(2×2)-√17 mixed phase on Ag(100). Their relative instability arises because if the Ag and S atoms are in perfect registry, the Ag-S separation is too long for a favorable interaction. If the Ag and S atoms are allowed to relax, the chain loses perfect registry with the substrate, which is obvious in Figs. 10b-c, and this is energetically costly.

On Ag(100), chains are observed under two conditions: As transients at 300 K, and as static features at 230 K. It is not clear whether the chains produced under the two conditions are the same. Either these are non-equilibrium structures, or else DFT does not correctly capture all the features of the S/Ag(100) system. However, DFT is quite successful in predicting the structure of the √17 phase, and the p(2×2)-√17 phase coexistence. It is possible that the chains exist as metastable phases due to Ag supersaturation (at 300 K), and due to quenching during a phase transition (at 230 K). In fact, a phase transition to a p(2×2) with c(2×2)-like domain walls, below 300 K, is predicted by DFT. Further investigation of the chains is warranted.

5. Conclusions

We have used STM and DFT to investigate the co-existence of the known p(2×2) and √17 phases of adsorbed sulfur. The √17 phase is virtually identical to a sulfur-induced reconstruction with the same unit cell on Cu(100). The main structural motif is a tetramer. Hexamers can be observed as well, but these are interpreted as defects in the √17 structure. The favored structural model is one in which 5 Ag atoms are missing from the (100) surface plane per √17 unit cell. The ejected Ag atoms combine with sulfur to form islands of the reconstructed phase on the terraces. The √17 phase coexists with the p(2×2), at sulfur coverages slightly above 0.25 monolayers. In addition, chain-like structures are observed in STM, both at 300 K (where they are dynamic) and below (where they are static). The nature of the chains is unclear, although scenarios are presented in which they could exist as metastable phases.

Acknowledgements

We thank Danny Shechtman for an enlightening discussion about dislocations, and we thank Jim Evans for a careful reading. The experimental component of this work was supported by NSF Grant CHE-0809472. The theoretical component was supported by the Division of Chemical Sciences, BES, US Department of Energy (USDOE).

Figures

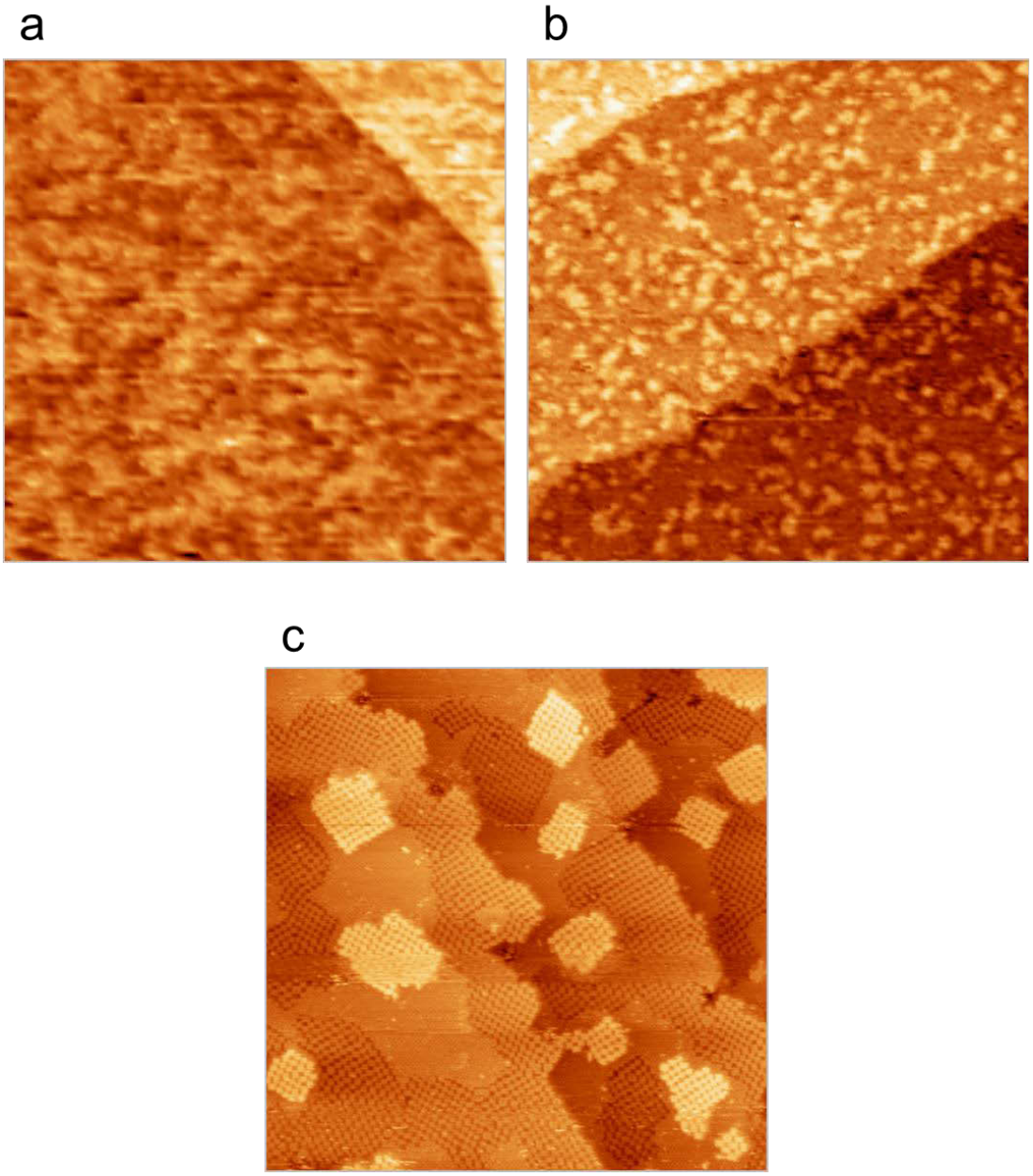

This figure continues on the next page.

Figure 1. STM images (100×100 nm^2) following adsorption of sulfur at 120 K. (a) 0.28 ML, no heating (7/30/2008 m13). (b) 0.35 ML. The sample was heated to, and imaged at, 230 K (7/22/2008 m55). (c) 0.35 ML. After (b), the sample was heated to 300 K, cooled to 230 K, and finally imaged at 300 K (7/22/2008 m141). (d) Same conditions as in (c), but higher magnification: 25×25 nm^2. (e) Schematic map of image (d). I = 1.0 nA, V_{tip} = -1.0 V.

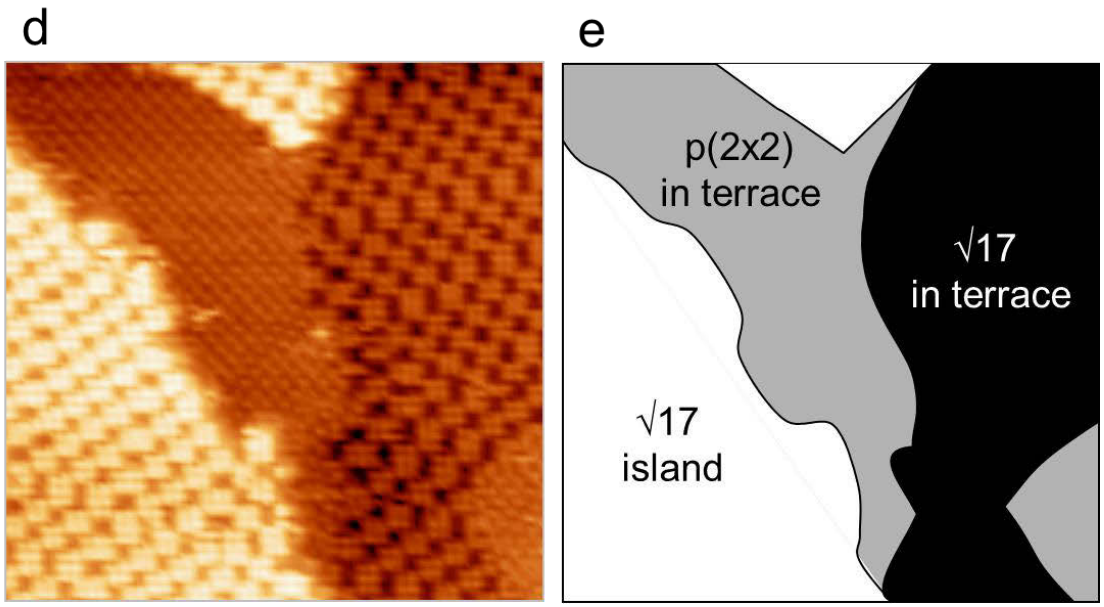

Figure 1. continued.

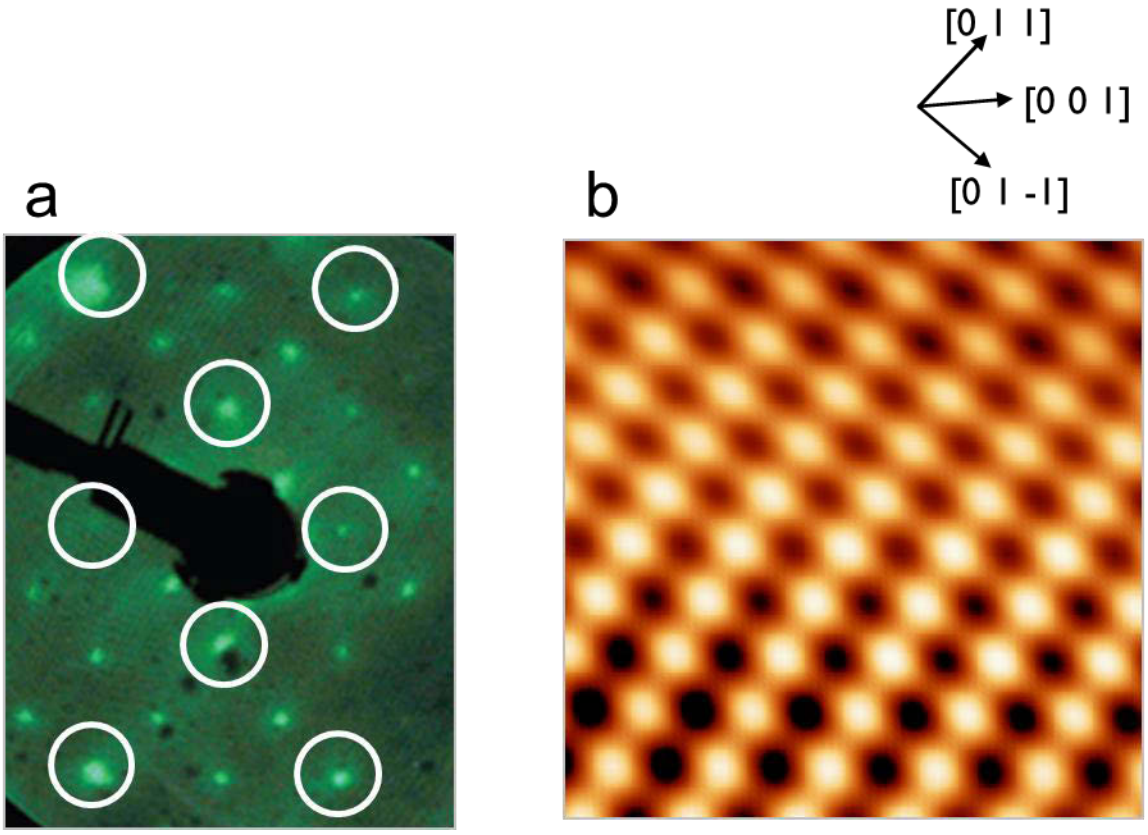

Figure 2. p(2×2) structure at 0.28 ML sulfur. The surface was prepared by adsorption at 120 K and heating to 300 K. Data were acquired at 300 K. (a) LEED pattern at incident beam energy of 162 eV (7/31/2008). White circles show positions of integral-order spots. (b) FFT filtered STM image of a 5×5 nm^2 region, I = 1.0 nA, V_{tip} = -1.0 V (7/30/2008 m75).

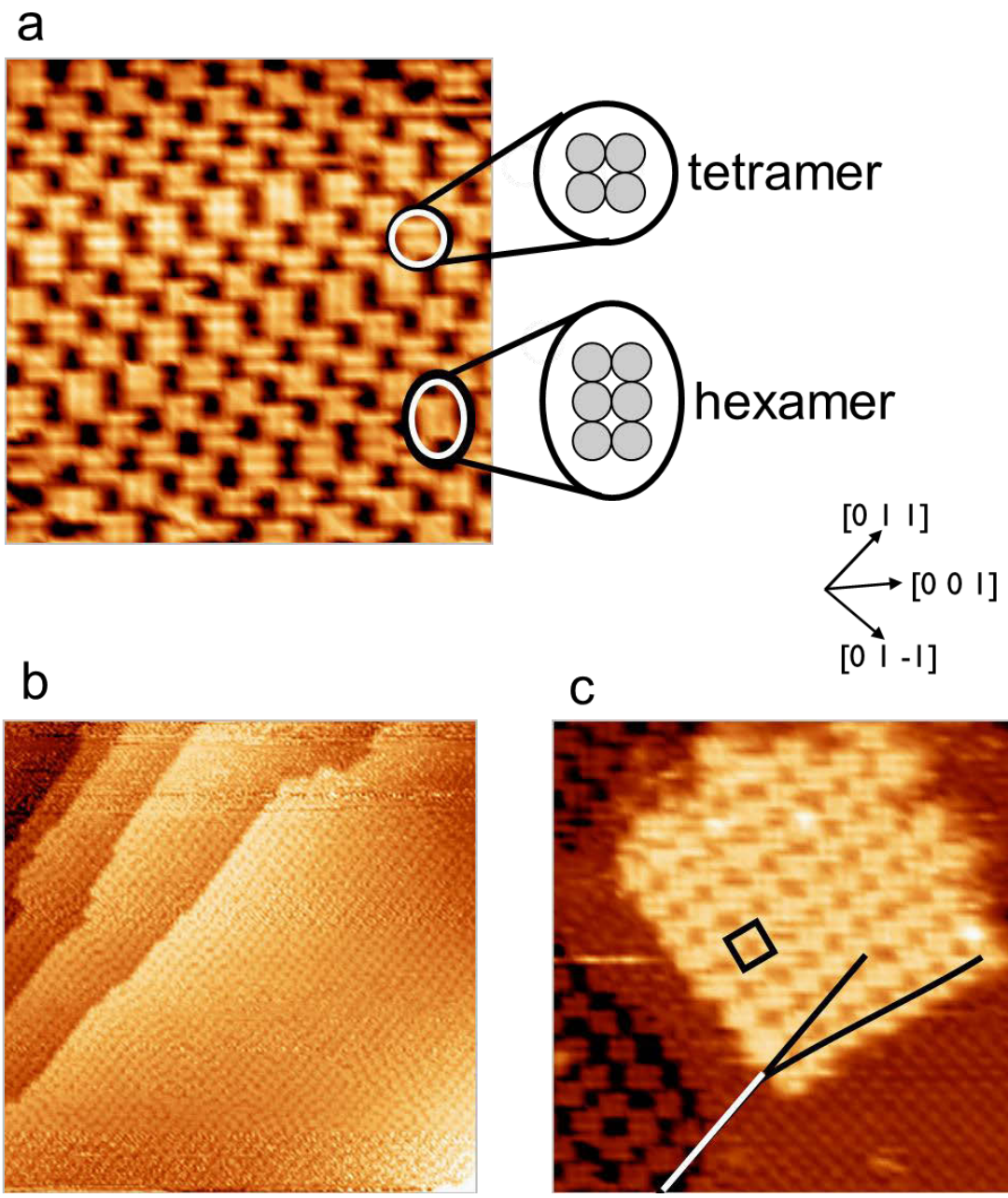

Figure 3. Illustrations of the √17 structure. (a) 15×15 nm^2. Prepared by adsorption of 0.35 ML sulfur at 120 K, followed by heating to (and imaging at) 300 K. The ovals show tetramers and hexamers. (b) 50×50 nm^2. Tunneling conditions: 1.55 nA, -1.00 V. Prepared by adsorption of 0.47 ML sulfur at 120 K, followed by heating to 670 K, and imaging at 300 K. (c) 20×20 nm^2. Prepared by adsorption of 0.35 ML sulfur at 120 K, followed by heating to, and imaging at, 300 K. The crystallographic directions apply to panels (a) and (c). Straight lines indicate the angle of rotation of the √17 with respect to the p(2×2), and the box shows the √17 unit cell. Scanning parameters: (a,c) I = 1.0 nA, V_{tip} = -1.0 V (7/22/2008 m141). (b) I = 0.954 nA, V_{tip} = -3.85V (11/19/2009 m49).

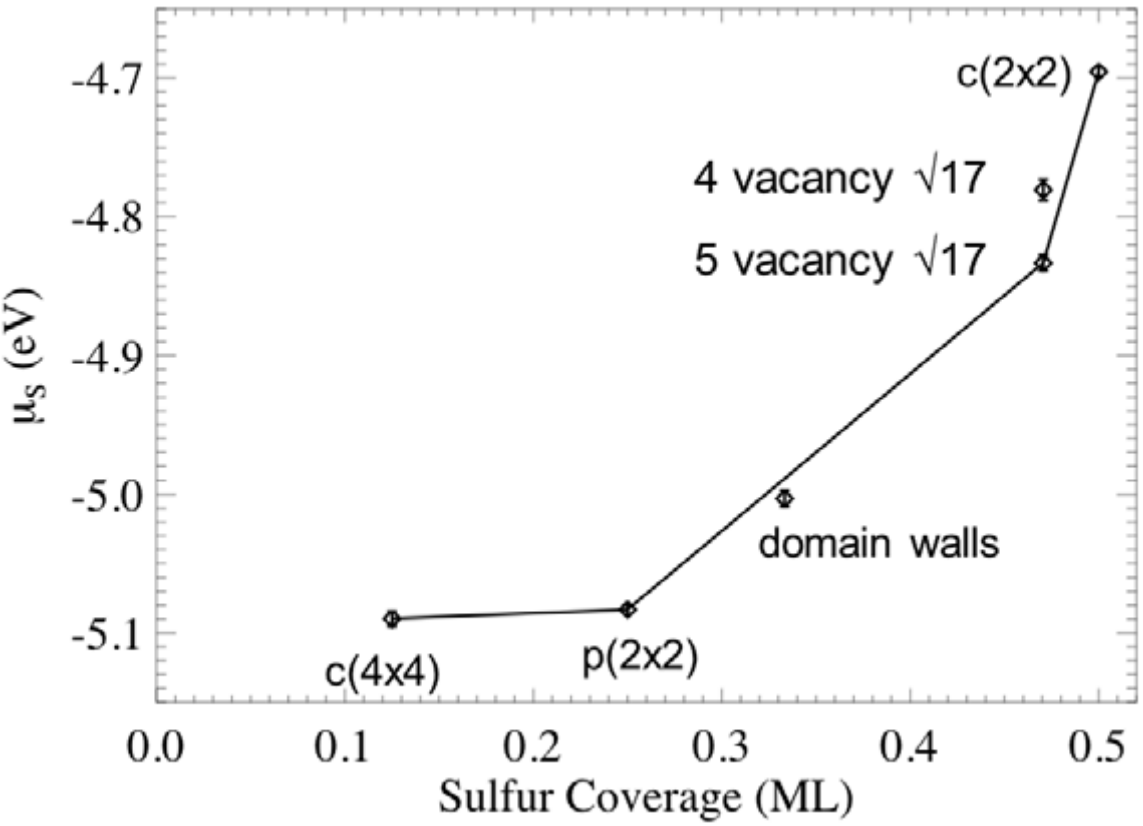

Figure 4. Chemical potential of S on Ag(100) vs. sulfur coverage. Two different √17 structures are included, one with 5 Ag vacancies and one with 4 Ag vacancies in each supercell. Data points are obtained by averaging results using slabs from five to nine layers. The zero coverage limit is from the average of c(4×4) and p(3×3) structures with 1/8 and 1/9 ML coverage, respectively. The error bars, which are about the same size as the symbols in this figure, are calculated as described in Section 2.

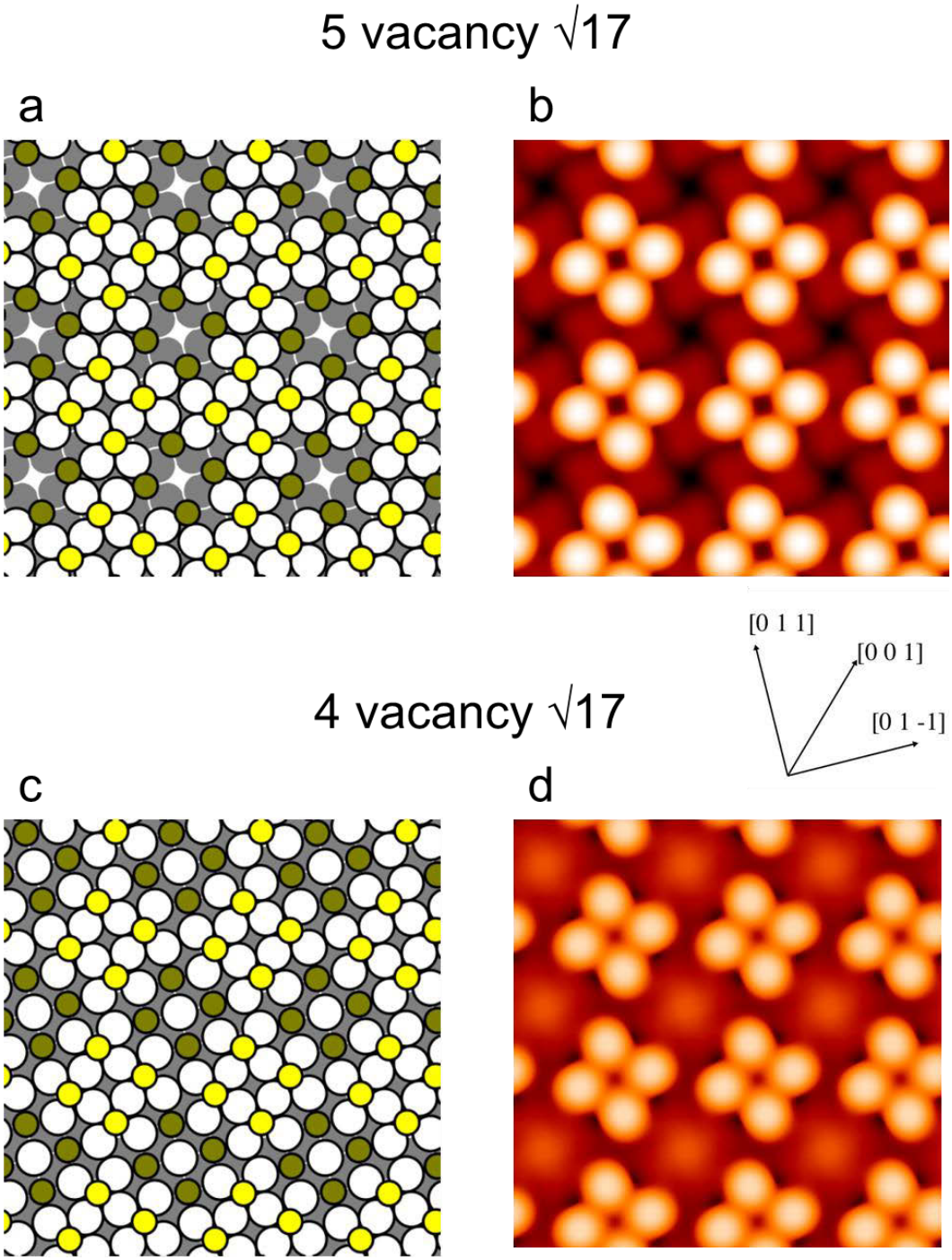

Figure 5. Two possible structures of the √17, based on DFT. (a, c) show atomic locations. Small circles are sulfur atoms, and large circles are Ag atoms. Light yellow (color on-line) denotes surface sulfur atoms and dark yellow denotes in-plane sulfur atoms. White circles are in-plane Ag atoms, and gray circles are Ag atoms in the plane below. (b, d) show simulated STM images encompassing the same area. According to the simulations, each bright spot in the STM images is a surface sulfur atom.

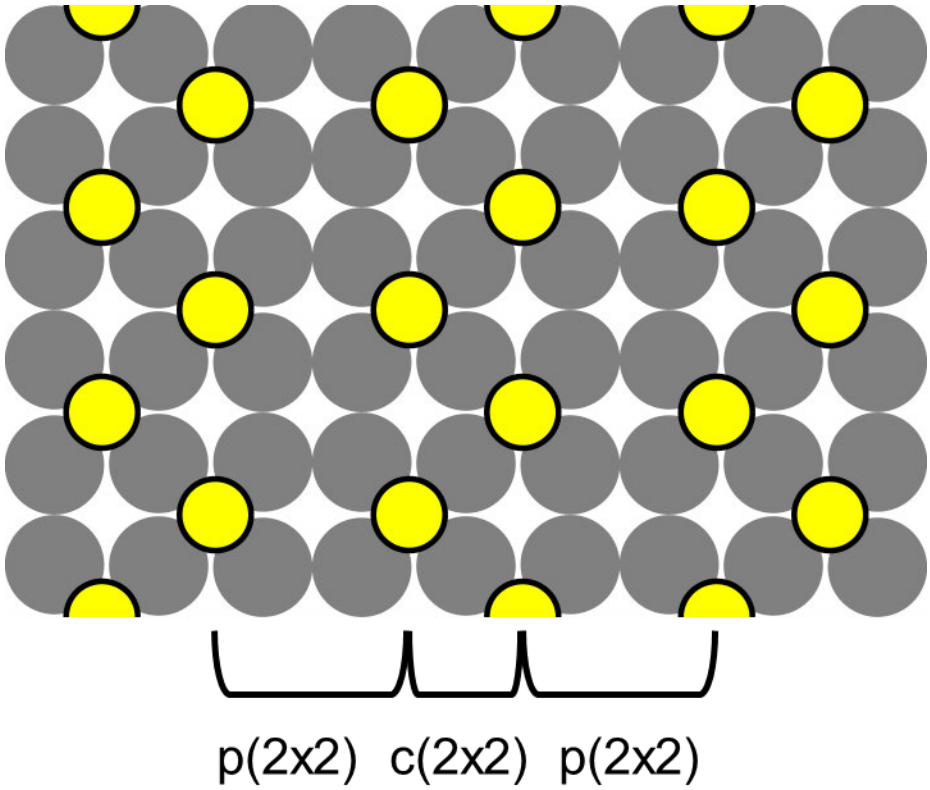

Figure 6. Schematic of p(2×2) domain wall structure at its maximum sulfur coverage, 0.38 ML. From DFT, the most stable domain wall has a local c(2×2) structure, as shown. Small (yellow) circles are chemisorbed sulfur atoms, and large (gray) circles are silver atoms.

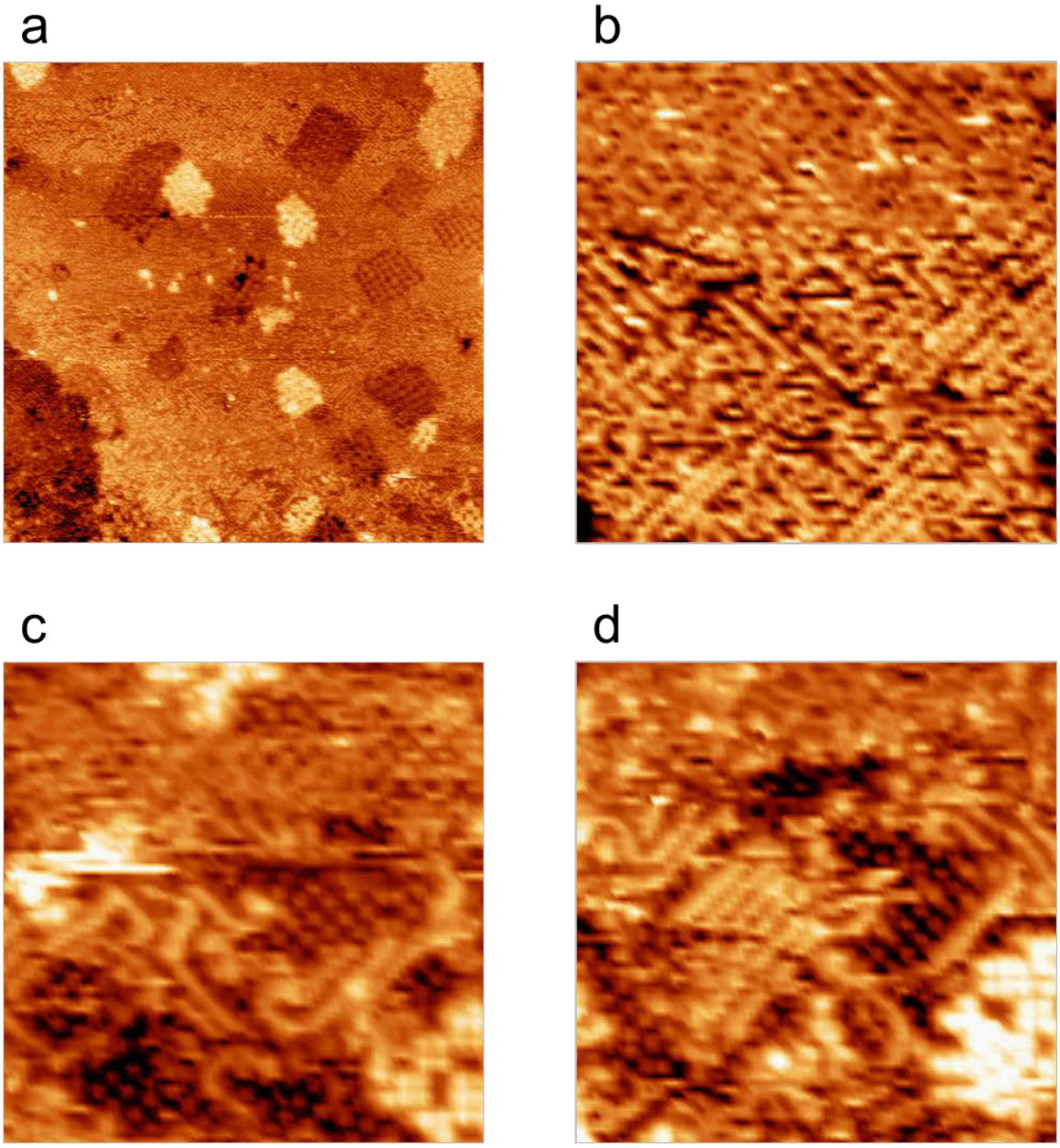

Figure 7. STM images providing evidence of a structural transition between 300 and 230 K. Surface was prepared by adsorption of 0.28 ML sulfur at 115 K, heated to 300 K, then re-cooled and imaged at 230 K. (a) Large scale image, 80×80 nm^2. (b-d) Small-scale images, 14.6×14.6 nm^2. (a-d) I = 1.0 nA, V_{tip} = -1.0 V (7/30/2008 m103).

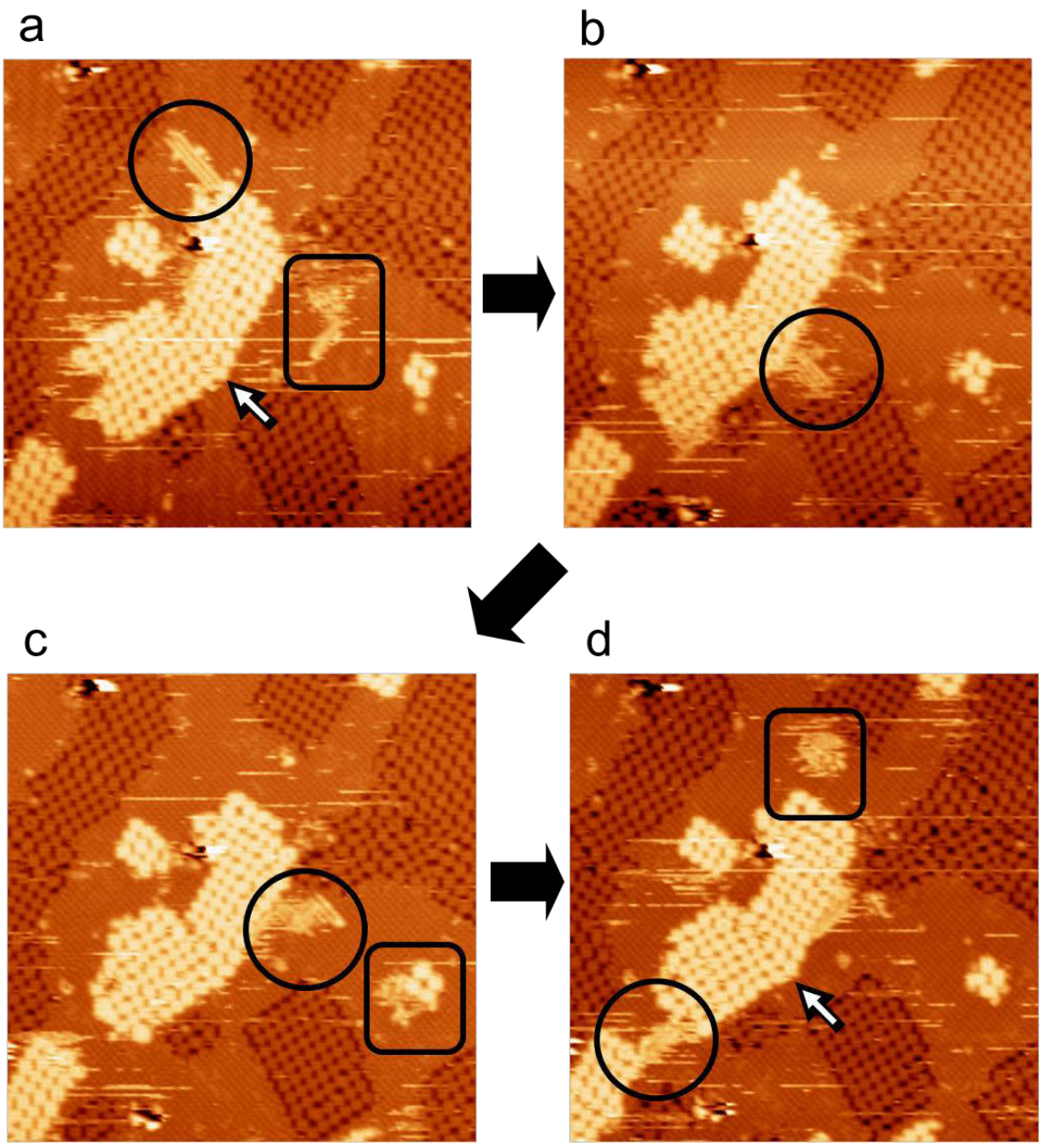

Figure 8. Evidence of transient density fluctuations (enclosed in circles and rectangles) and dislocation evolution (see arrow) at 300 K. Successive STM images, 190 s/image, 50×50 nm^2. The sample was prepared by adsorption of 0.35 ML sulfur at 120 K, followed by heating to 300 K. The images were acquired at 300 K. (a-d) I = 1.0 nA, V_{tip} = -1.0 V (7/22/2008 m90, 91, 92, 93)

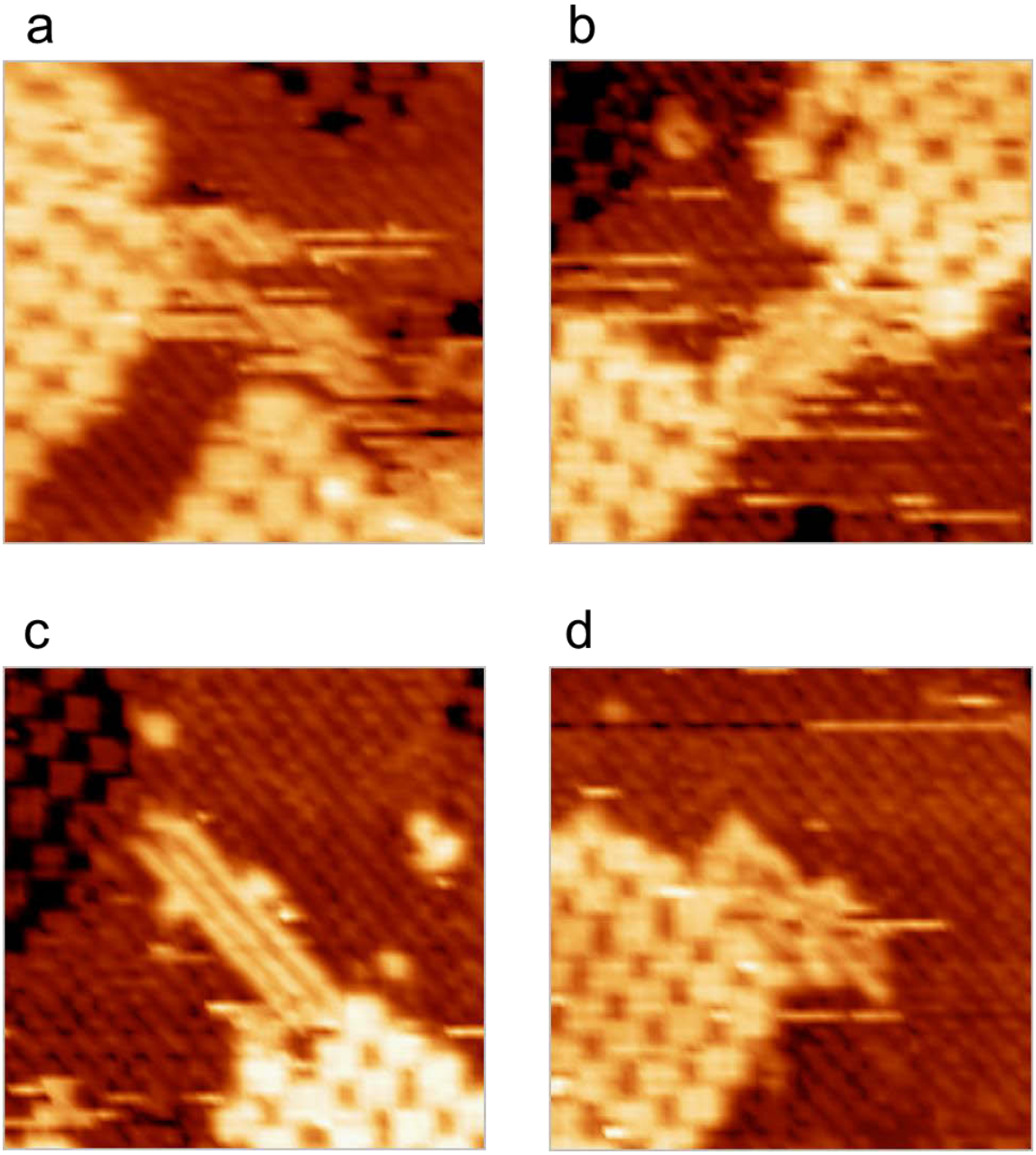

This figure continues on the next page.

Figure 9. High-magnification STM images of transient regions at 300 K. Conditions are the same as in Fig. 8. All image sizes are 14.6×14.6 nm^2. (a-f) I = 1.0 nA, V_{tip} = -1.0 V (7/22/2008 m95, 93, 90, 90, 92, 90).

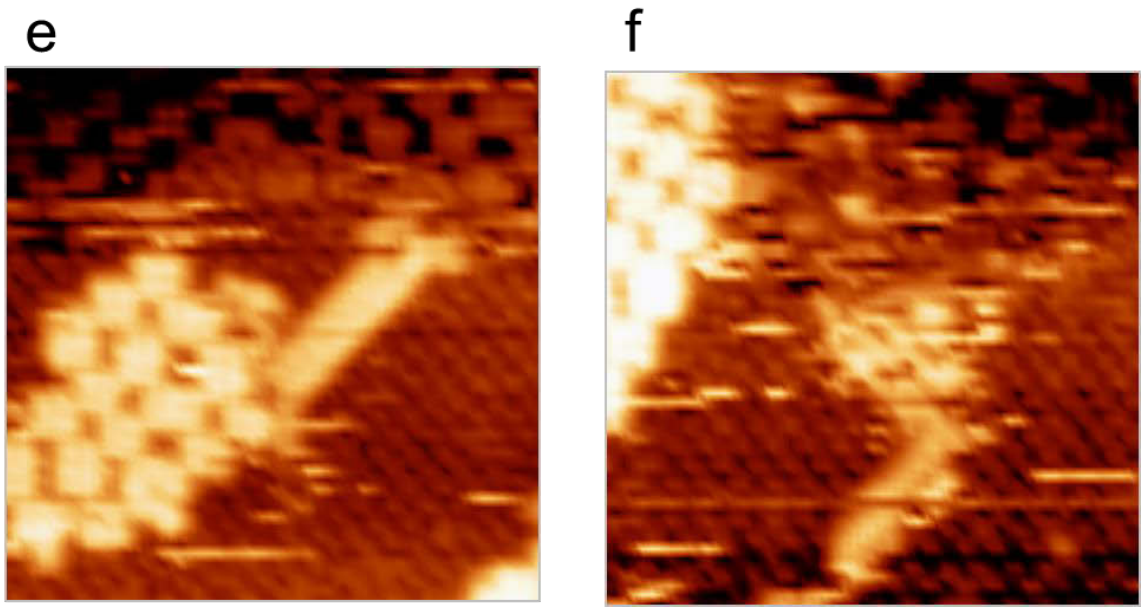

Figure 9. continued.

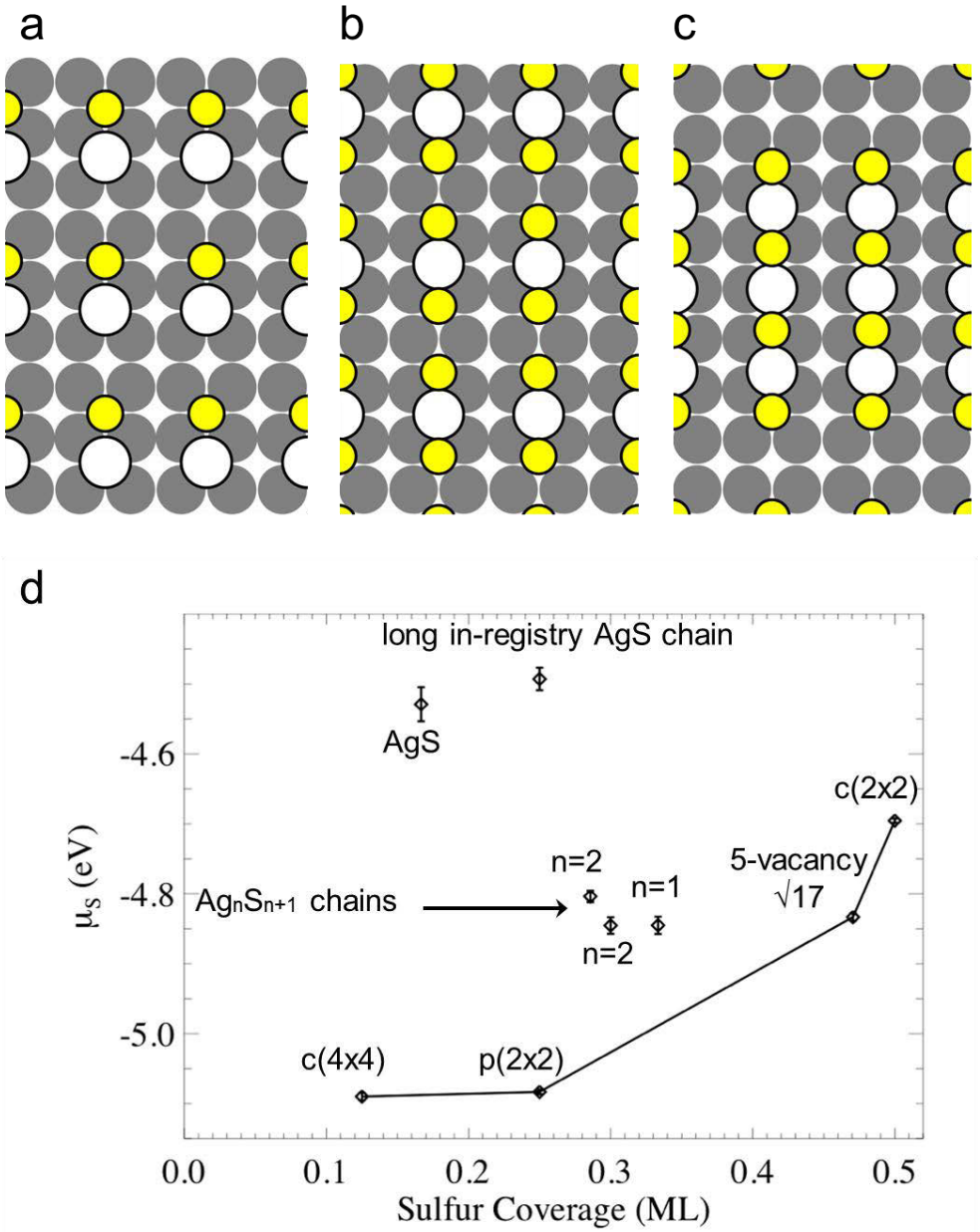

Figure 10. (a-c): Atomic positions in DFT-optimized structures that are related to linear Ag-S chains. Small (yellow) circles are sulfur atoms in the surface plane, large white circles are in-plane Ag atoms, and large gray circles are Ag atoms below the surface plane. (a) shows a relaxed AgS "chain" in a (3×2) unit cell. Panels (b-c) show longer relaxed chains in larger unit cells. These chains are capped on both ends by sulfur atoms, implying a stoichiometry of Ag_mS_{m+1}. For (b) m=1, and for (c) m=3. (d): Chemical potential vs. coverage of various linear chain structures. The point labeled "AgS" corresponds to the structure in Panel A. The point labeled "long in-registry AgS chain" is similar to Panel a, but the Ag-S units are constrained to a (2×2) unit cell, i.e. Ag atoms occupy every other four-fold hollow site. Other chemical potential values are indexed by m. The separation between chains is always $2a$, as illustrated in Panels (a-c).

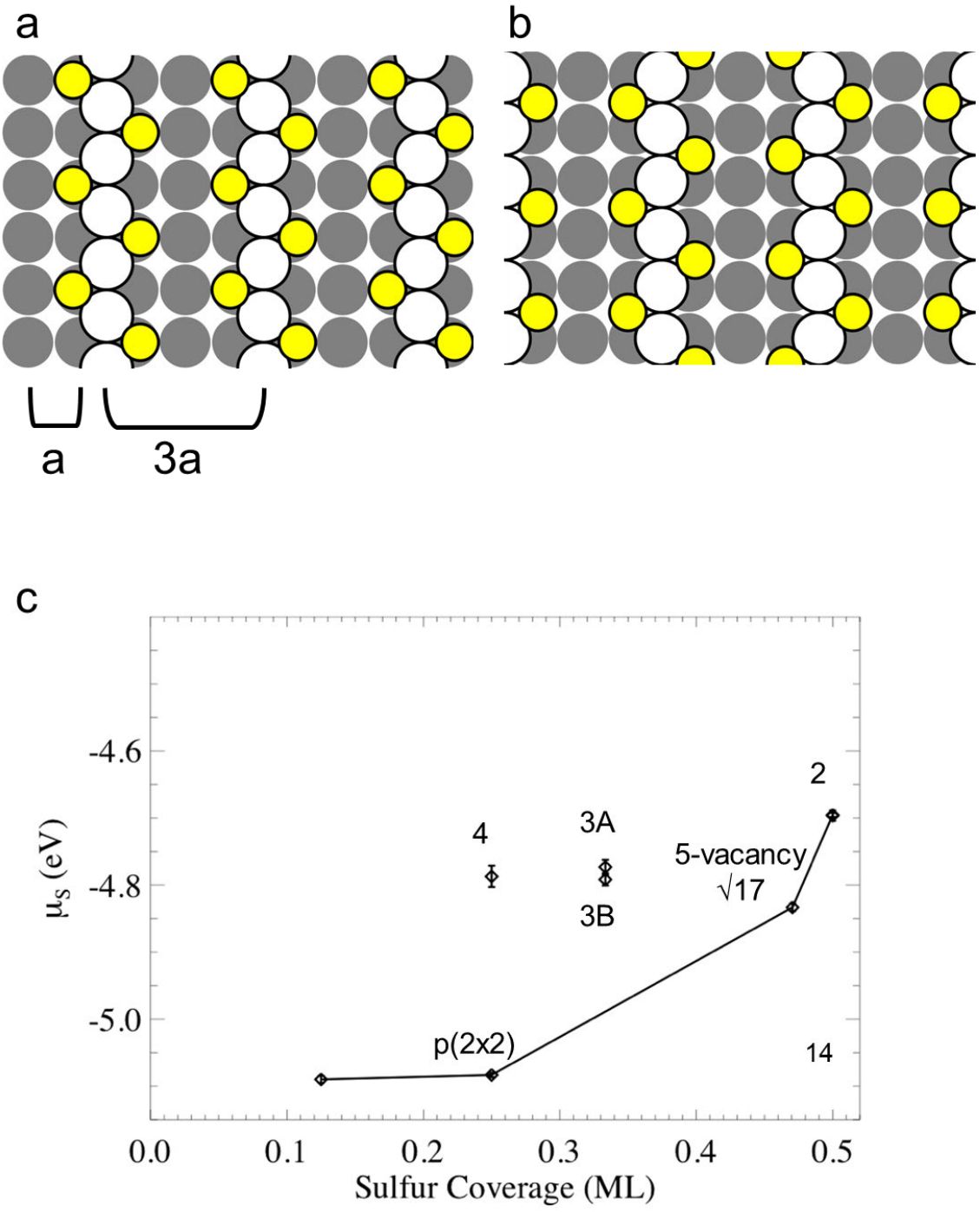

Figure 11. (a,b): Examples of DFT-optimized, infinite zig-zag Ag-S chains where S atoms decorate a linear Ag row. The key is the same as for Fig. 10. (c) Chemical potential vs. coverage of various zig-zag chain structures. Each numeric label indicates the separation between rows (in units of *a*), with 3a and 3b corresponding to the configurations in Panels (a) and (b), respectively.

Appendix. Supplementary Information

Table A.I. Effects of various GGA approximations of the exchange-correlation functional on the Ag-S bond (calculated from a Ag-S dimer in vacuum) and the lattice constant of the Ag crystal. The energy cutoff is 280 eV. The best theoretical values are in boldface.

	LDA	PBEsol	PBE	RPBE	HSE06	exp
AgS bond length (nm)	0.222	0.223	0.228	0.229	0.229	
Ag bond strength (eV)	3.08	2.76	2.61	2.28	2.23	
bulk Ag lattice constant (nm)	0.4016	**0.4053**	0.4149	0.4210	0.415	0.405
bulk Ag cohesive energy (eV)	3.64	**3.16**	2.58	2.05	2.05	2.97
S_2 atomization energy (eV)	5.84	5.55	5.28	5.05	**4.63**	4.41

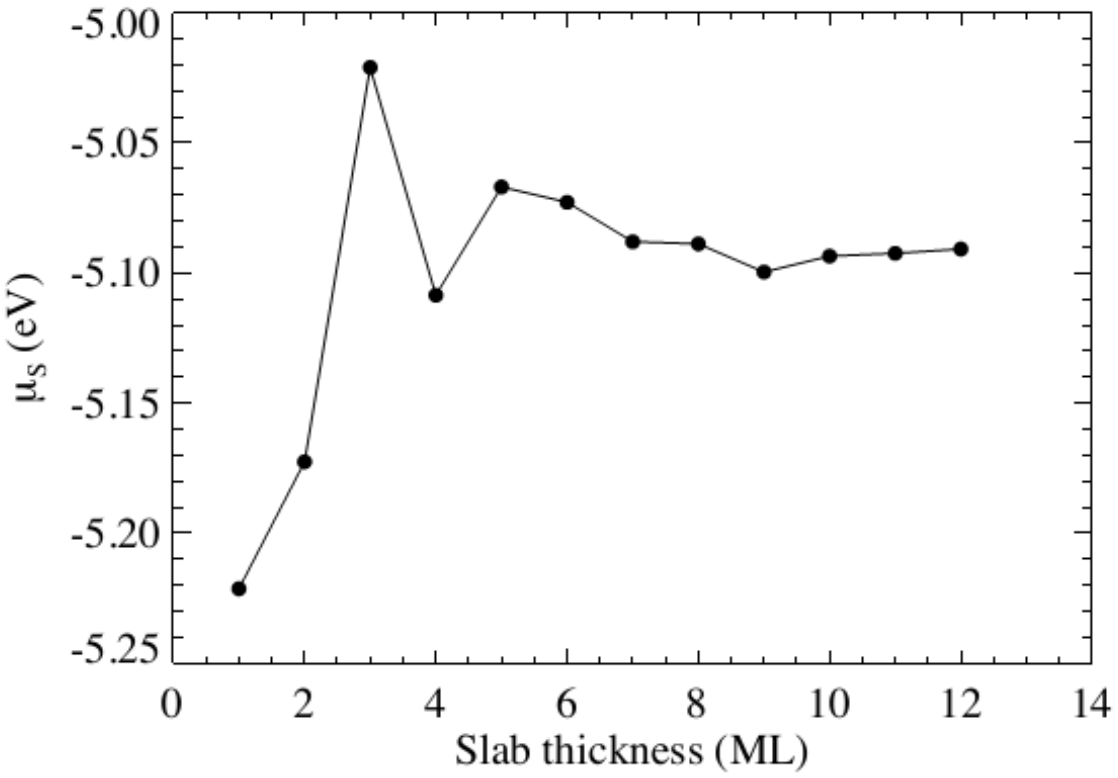

Figure A.1. Calculated adsorption energy of S on Ag(100) at 1/4 ML and p(2×2) ordering with various slab thickness. The *k*-point grid is (12×12).

Table A.II. μ_S for various Ag-S chains.

	super cell	*k*-points	slab thickness (ML)	μ_S (eV)
(a) Ag_2S_3	5 × 2	(2 × 6)	5 to 9	-4.84
(b) Ag_5S_5	8 × 2	(1 × 6)	4 to 7	-4.71
(c) Ag_2S	2 × 2	(6 × 6)	4 to 7	-4.25
(d) Ag_2S_2 (hol)	3 × 2	(4 × 6)	4 to 7	-4.73
(d) Ag_2S_2 (top)	3 × 2	(4 × 6)	4 to 7	-4.62

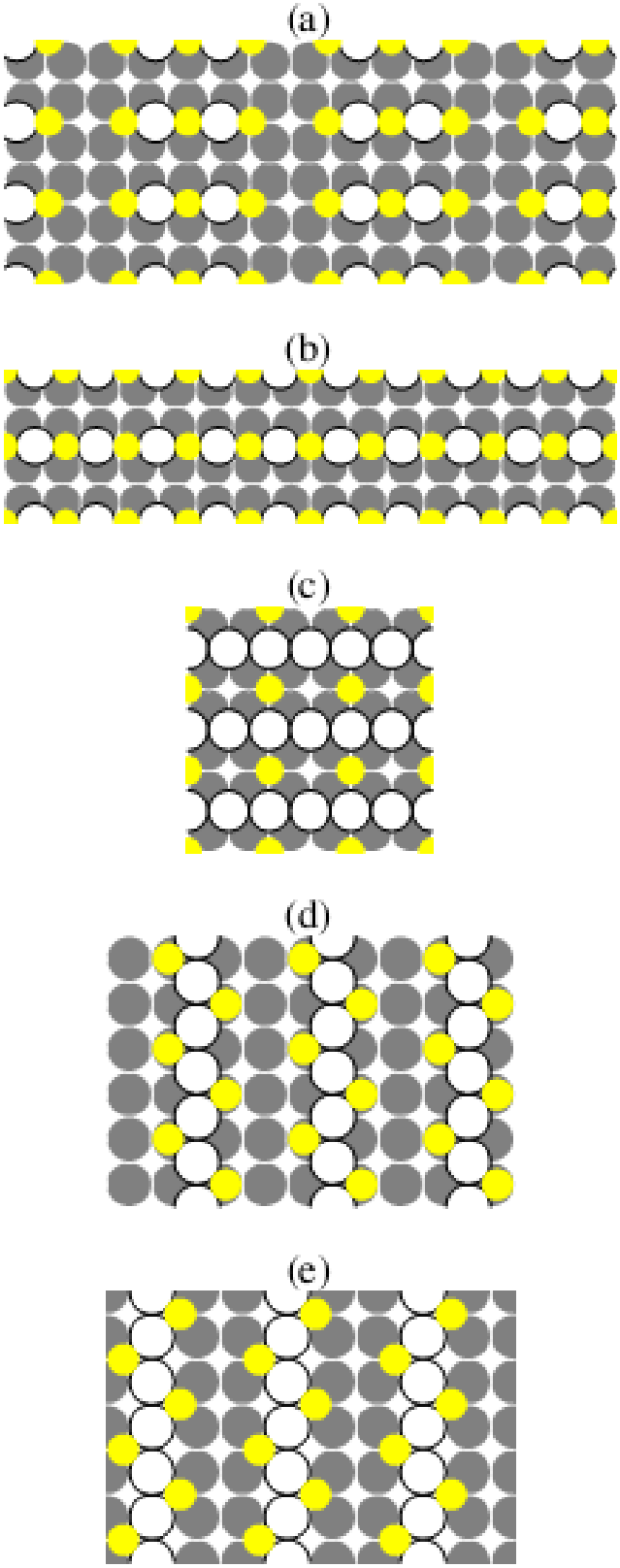

Figure A.2. Schematics of the Ag-S chain structures in Table A.II.

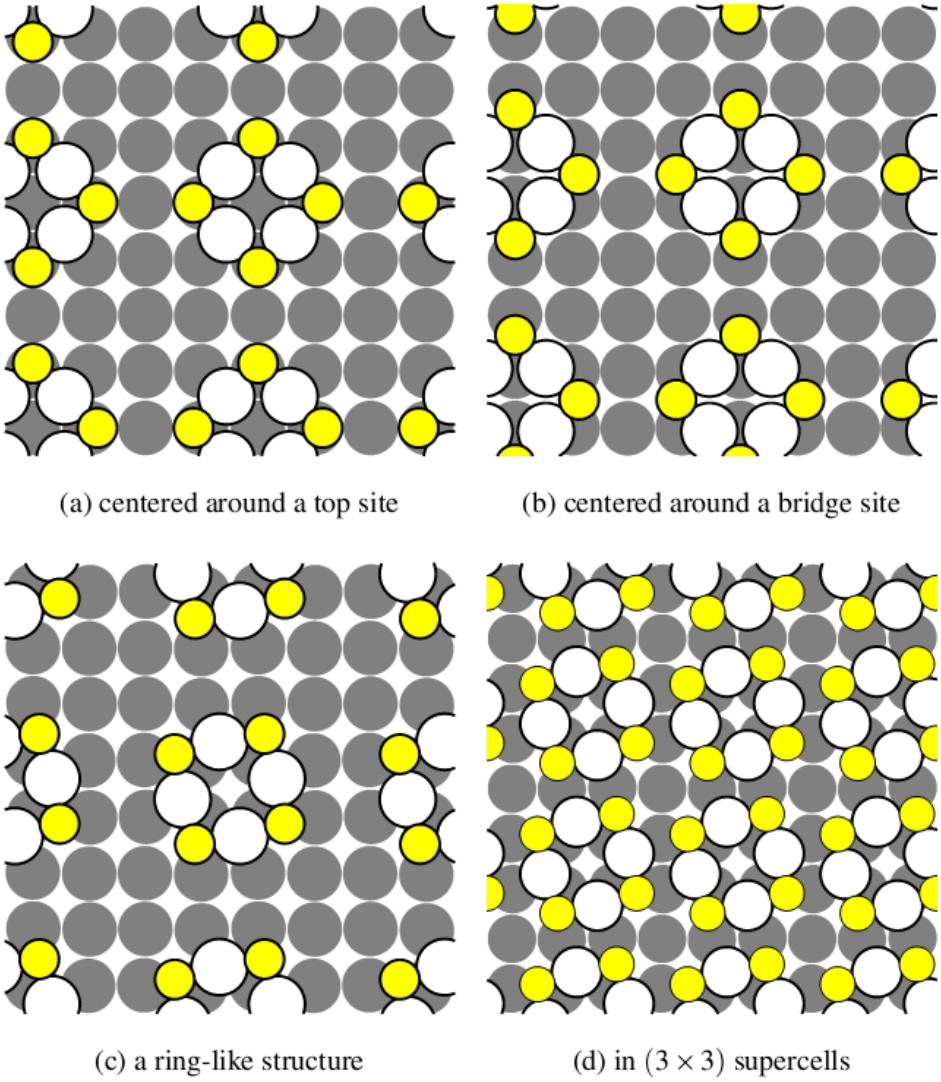

Figure A.3. Various Ag_4S_4clusters. (a) Ag occupying near hollow sites, μ_S = -4.75 eV; (b) Ag occupying near bridge sites, μ_S = 4:76 eV; and (c) a ring-like structure, μ_S = -4.79 eV. Compared with the p(2×2) overlayer structure with μ_S = -5.09 eV, the Ag_4S_4 cluster is about 0.30 eV less favorable per S atom, so the formation energy is 1.2 eV (4 S in each cluster). (d) Ag_4S_4 in (3× 3) supercells, with θ_S = 0.444 ML, and μ_S = -4.80. Compared with the tie-line between the p(2×2) and the 5-vacancy √17 structure, it is only 0.07 eV (per S atom) less stable.

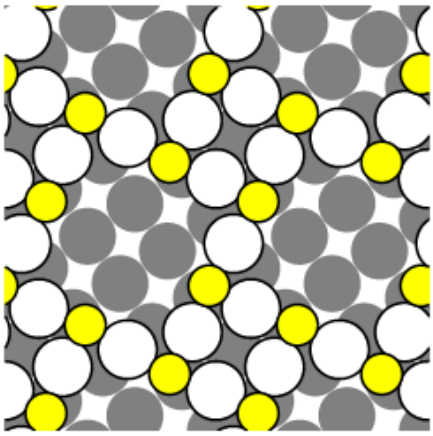

(a) $(\sqrt{13} \times \sqrt{13})R33.7°$

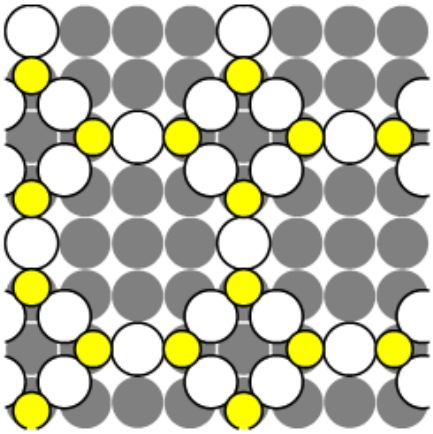

(b) (4×4)

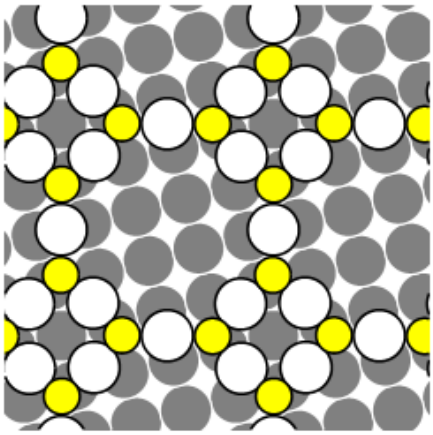

(c) $(\sqrt{17} \times \sqrt{17})R14.0°$

Figure A.4. Various Ag_6S_4 structures: (a) in (√13×√13)R33.7° supercells, with θ_S = 0.308 ML and μ_S = -4.60 eV; (b) in a (4×4) supercell, with θ_S = 0.25 ML and μ_S = -4.75 eV; and (c) in (√17×√17)R14.0°, with θ_S = 0.235 ML and μ_S = -4.60 eV.

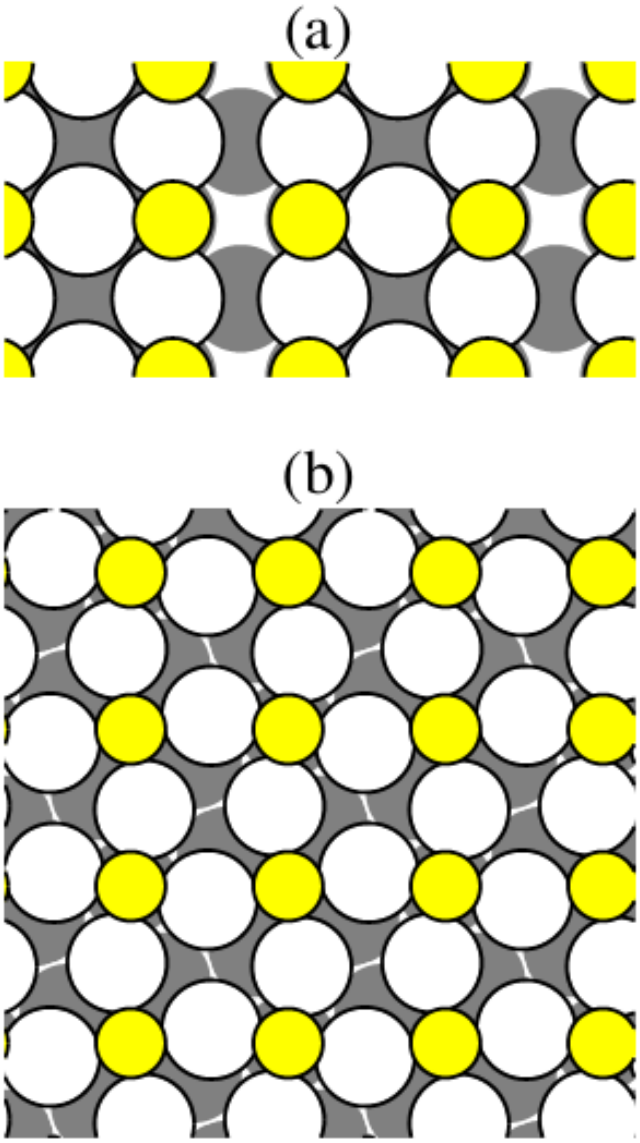

Figure A.5. Other possible structures: (a) a Ag_3S_2, or missing row structure in $(2\sqrt{2}\times\sqrt{2})R45°$ supercells, with $\theta_S = 0.5$ ML and $\mu_S = -4.48$ eV. (b) a Ag_8S_4 structure in $(\sqrt{10}\times\sqrt{10})R18.4°$ supercells, with $\theta_S = 0.4$ ML and $\mu_S = -4.69$ eV. These two structures, motivated by the structures of O/Ag(100) and O/Ag(111), are not favorable according to DFT calculations.

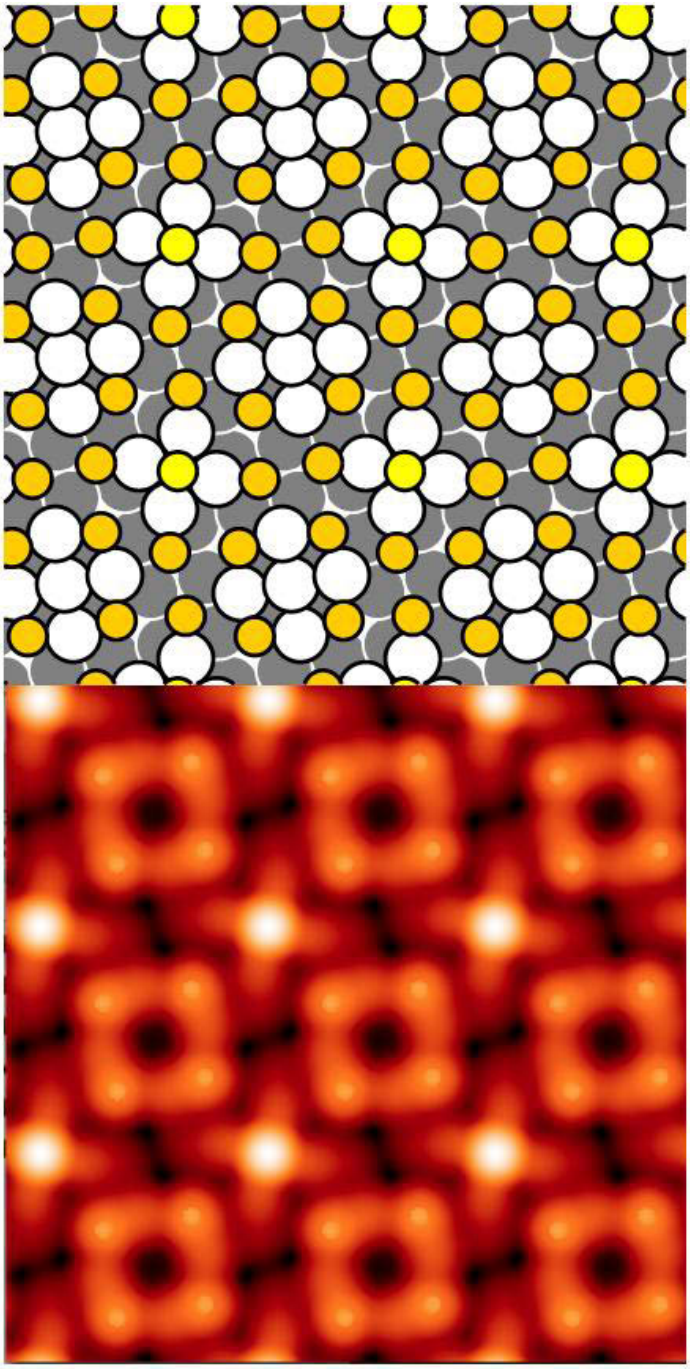

Figure A.6. An alternative structure with Ag_9S_9 in $\sqrt{17}\times\sqrt{17}$ supercell. μ_S = -4.68 eV, which is 0.15 eV less favorable than the 5-vacancy $\sqrt{17}$ structure. The lower panel is a simulated STM image. Note that θ_S is 0.53 ML versus 0.47 ML for the 5-vacancy $\sqrt{17}$ structure. The structure consists of a Ag_5S_4 cluster, and a Ag_4S_5 cluster. Also note that by taking off the top S (shown here in lighter yellow) from the Ag_4 increases μ_S to -4.56 eV, while lower the coverage to 0.5 ML, therefore not competitive.

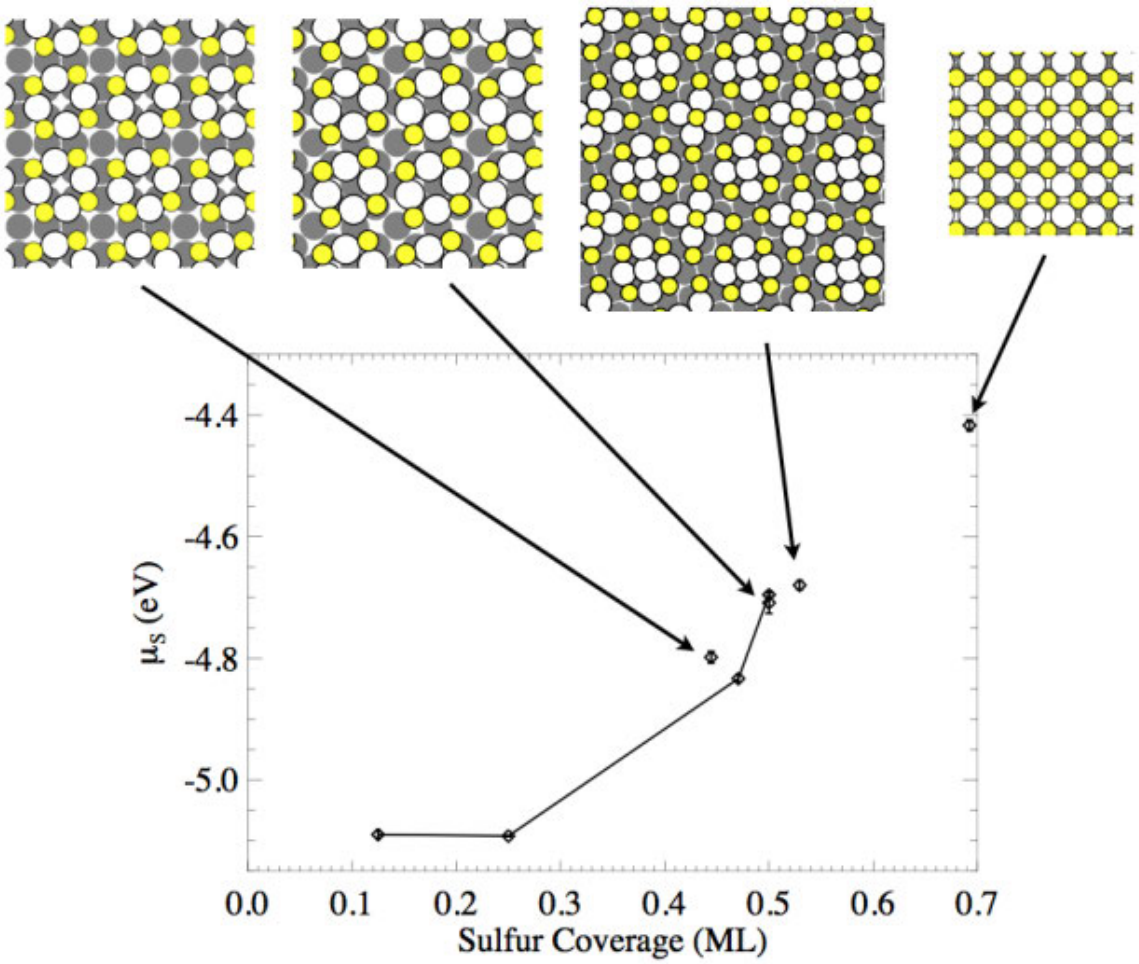

Figure A.7. μ_S for a family of AgS clusters. From left to right, they are Ag_4S_4 in (3×3) cells, Ag_4S_4 in c(4×4) cells, Ag_9S_9 in √17 cells, and Ag_9S_9 in √13 cells.

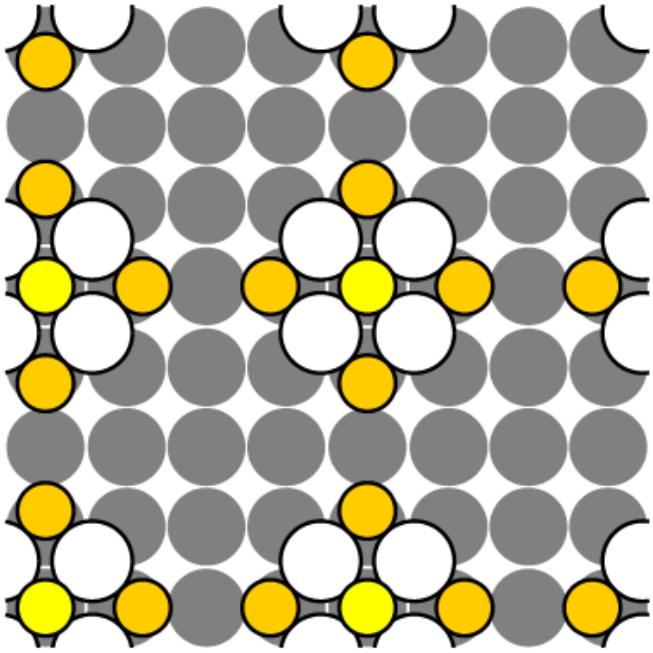

(a) $\mu_S = -4.44$ eV

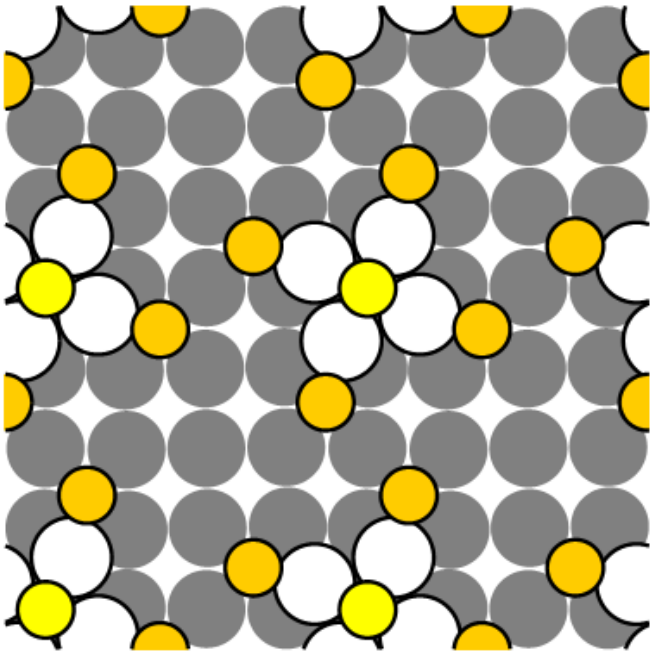

(b) $\mu_S = -4.94$ eV

Figure A.8. Two pyramidal Ag_4S_5 clusters: (a) with in-plane S (darker yellow) attaching to the edges, and (b) with in-plane S attaching to the corners. Configuration (b) is 0.50 eV more stable than (a).

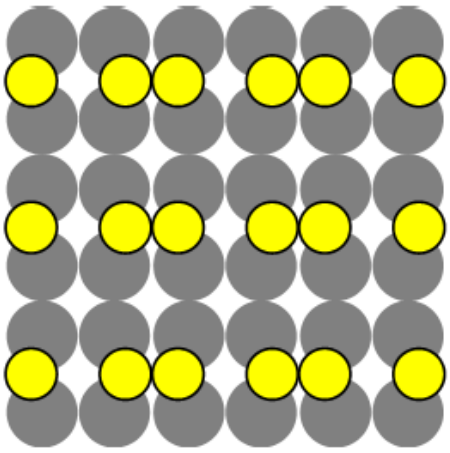

(a) $\mu_S = -4.58$ eV

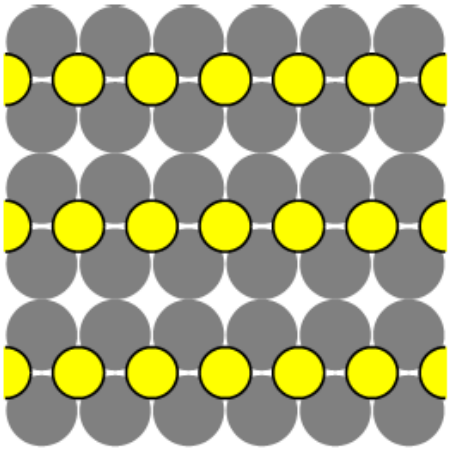

(b) $\mu_S = -4.40$ eV

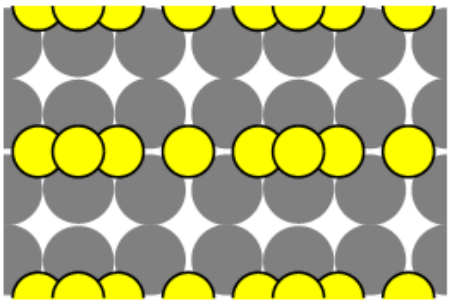

(c) $\mu_S = -4.31$ eV

Figure A.9. Examples of pure S chains: (a) a S_2 molecule in (2×2) supercells, with μ_S = -4.57 eV. In contrast, a chemisorbed in-registry S chain (b) is less stable. Both (a) and (b) are less stable than the c(2×2) configuration at the same θ_S = 0.5 ML. (c) Combinations of S on a hollow site and a S_3 chain, with θ_S = 0.667 ML. The S at the center of the S_3 chain is 0.13 nm higher than the other two. Longer chains tend to be unstable and fragment into shorter chains.

References

(1) Perdereau, J.; Rhead, G. E. *Surf. Sci* **1967**, *7*, 175.

(2) Stranick, S. J.; Parikh, A. N.; Allara, D. L.; Weiss, P. S. *J. Phys. Chem.* **1994**, *98*, 11136.

(3) Ling, W. L.; Bartelt, N. C.; Pohl, K.; de la Figuera, J.; Hwang, R. Q.; McCarty, K. F. *Phys. Rev. Lett.* **2004**, *93*, 166101.

(4) Shen, M.; Liu, D.-J.; Jenks, C. J.; Thiel, P. A. *Surf. Sci.* **2009**, *603*, 1486.

(5) Shen, M.; Liu, D.-J.; Jenks, C.; Thiel, P.; Evans, J. *J. Chem. Phys.* **2009**, *130*, 094701.

(6) Feibelman, P. J. *Phys. Rev. Lett.* **2000**, *85*, 606.

(7) Biener, M. M.; Biener, J.; Friend, C. M. *Surf. Sci* **2007**, *601*, 1659.

(8) Min, B. K.; Alemozafar, A. R.; Biener, M. M.; Biener, J.; Friend, C. M. *Topics in Catalysis* **2005**, *36*, 77.

(9) Ozcomert, J. S.; Pai, W. W.; Bartelt, N. C.; Reutt-Robey, J. E. *Phys. Rev. Lett.* **1994**, *72*, 258.

(10) Layson, A. R.; Evans, J. W.; P.A.Thiel *Phys. Rev. B* **2002**, *65*, 193409.

(11) Layson, A. R.; Thiel, P. A. *Surf. Sci.* **2001**, *472*, L151.

(12) Kuk, Y.; Chua, F. M.; Silverman, P. J.; Meyer, J. A. *Phys. Rev. B* **1990**, *41*, 12393.

(13) Coulman, D. J.; Wintterlin, J.; Behm, R. J.; Ertl, G. *Phys. Rev. Lett.* **1990**, *64*, 1761.

(14) Jensen, F.; Besenbacher, F.; Laegsgaard, E.; Stensgaard, I. *Phys. Rev. B* **1990**, *41*, 10233.

(15) Frank, E. R.; Hamers, R. J. *J. Catalysis* **1997**, *172*, 406.

(16) Layson, A. R.; Evans, J. W.; Fournée, V.; Thiel, P. A. *J. Chem. Phys.* **2003**, *118*, 6467.

(17) Shen, M.; Jenks, C. J.; Evans, J. W.; Thiel, P. A. *Topics in Catalysis* **2011**, *in press*.

(18) Thiel, P. A.; Shen, M.; Liu, D.-J.; Evans, J. W. *J. Vac. Sci. Technol. A* **2010**, *28*, 1285.

(19) Thiel, P. A.; Shen, M.; Liu, D.-J.; Evans, J. W. *J. Phys. Chem. C* **2009**, *113*, 5047.

(20) Cabané-Brouty, F. *Journal de Chimie Physique et de Physico-Chimie Biologique* **1965**, *62*, 1056.

(21) Cabané-Brouty, F. *Journal de Chimie Physique et de Physico-Chimie Biologique* **1965**, *62*, 1045.

(22) Bénard, J.; Oudar, J.; Cabané-Brouty, F. *Surf. Sci.* **1965**, *3*, 359.

(23) Rovida, G.; Pratesi, F. *Surf. Sci* **1981**, *104*, 609.

(24) Sotto, M. P.; Boulliard, J. C. *Surf. Sci.* **1985**, *162*, 285.

(25) Colaianni, M. L.; Chorkendorff, I. *Phys. Rev. B* **1994**, *50*, 8798.

(26) Qin, C. Y.; Whitten, J. L. *Surf. Sci.* **2005**, *588*, 83.

(27) Samples were synthesized at the Materials Preparation Center, Ames Laboratory USDOE, Ames, IA, USA. See: www.mpc.ameslab.gov.

(28) Shen, M.; Liu, D.-J.; Jenks, C.; Thiel, P. A. *J. Phys. Chem. C* **2008**, *112*, 4281.

(29) Wagner, C. *J. Chem. Phys.* **1953**, *21*, 1819.

(30) Schwaha, K.; Spencer, N. D.; Lambert, R. M. *Surf. Sci* **1979**, *81*, 273.

(31) Kresse, G.; Furthmüller, J. *Phys. Rev. B* **1996**, *54*, 11169.

(32) Kresse, G.; Hafner, J. *Phys. Rev. B* **1994**, *49*, 14251.

(33) Kresse, G.; Hafner, J. *Phys. Rev. B* **1993**, *47*, 558.

(34) Perdew, J. P.; Burke, K.; Ernzerhof, M. *Phys. Rev. Lett.* **1996**, *77*, 3865.

(35) Kresse, G.; Joubert, D. *Phys. Rev. B* **1999**, *59*, 1758.

(36) Kiejna, A.; Kresse, G.; Rogal, J.; De Sarkar, A.; Reuter, K.; Scheffler, M. *Phys. Rev. B* **2006**, *73*, 035404.

(37) Neugebauer, J.; Scheffler, M. *Phys. Rev. B* **1992**, *46*, 16067.

(38) Methfessel, M.; Paxton, A. T. *Phys. Rev. B* **1989**, *40*, 3616.

(39) Liu, D.-J. *Phys. Rev. B* **2010**, *81*, 035415.

(40) Liu, D.-J.; Evans, J. W. *Surface Sci.* **2004**, *563*, 13.

(41) Zhang, Y.; Blum, V.; Reuter, K. *Phys. Rev. B* **2007**, *75*, 235406.

(42) Caflisch, R. G.; Berker, A. N. *Phys. Rev. B* **1984**, *29*, 1279.

(43) Bak, P. *Phys. Rev. Lett.* **1985**, *54*, 1539.

(44) Liu, D.-J. *J. Phys. Chem. C* **2007**, *111*, 14698.

(45) Domange, J. L.; Oudar, J. *Surf. Sci.* **1968**, *11*, 124.

(46) Spaenig, A.; Broekmann, P.; Wandelt, K. *Z. Phys. Chem.* **2003**, *217*, 459.

(47) Liu, P.; Wang, Y. *Surf. Sci.* **2000**, *468*, 122.

CHAPTER V

Silver island coarsening on the anisotropic Ag(110) surface with and without oxygen

Selena M. Russell,[a] Anthony R. Layson,[a,b] Chad D. Yuen,[a] Holly Walen,[a] J. W. Evans,[c] and Patricia A. Thiel[a,d]

1. Introduction

Available surface area plays a key role in a variety of chemical reactions. For example, as surface area increases so do the number of catalytic sites.[1,2] There is a drive to make ever smaller nanoparticles to increase surface area and introduce size dependent properties[3]. However, particles tend to coarsen or sinter over time, favoring fewer, larger particles instead of many, smaller particles. This leads to decreased catalytic activity,[4] formation of monodispersed particles in solution[5], and tunable nanowires[6].

Diffusion on metal surfaces has been of great interest, in particular its relevance to controlled production of useful nanoparticles.[7] Coarsening can occur by two mechanisms: Ostwald[8] and Smolushowski[9] ripening, abbreviated OR and SR respectively. During the more common OR, small islands decrease in size and eventually disappear, while large island increase in size (sizes relative to the average island size). During SR, islands diffuse and merge. While both mechanisms can occur simultaneously, one will dominate depending on the particular nature of the system. In both cases, the island density decreases while the average island size increases, resulting from overall mass transport. OR may be limited by either terrace diffusion or attachment-detachment of mass transport agents. Several carriers are viable candidates in OR, including adatoms, vacancies, and clusters or complexes. The process of coarsening not only depends on diffusion, but can also provide insight into the diffusion process itself.

[a] Department of Chemistry, Iowa State University, Ames, Iowa 50011
[b] Current address: Jannen School of Arts and Sciences, Trine University, One University Avenue, Angola, Indiana 46703
[c] Departments of Mathematics and Physics & Astronomy, Iowa State University, Ames, Iowa 5011
[d] Department of Material Science and Engineering, Iowa State University, Ames, Iowa 50011

Extensive experimental and theoretical studies have investigated diffusion and coarsening on the isotropic Ag(100) and Ag(111) surfaces.[10-33] However, the details of the coarsening mechanism are inherently different on Ag(110) due to surface anisotropy. Prior work on the (110) has been summed up well in Ref. 43, as follows: "The Ag(110) surface offers several advantages in the study of anisotropic materials. Unlike the (110) surfaces of Au [Ref. 34] and Pt [Ref. 35], Ag(110) does not undergo a surface reconstruction. It is therefore possible to examine true (110) atomic interactions. In addition, Monte Carlo simulations have been performed to examine the nucleation and growth characteristics of submonolayer islands.[36,37]" Homoepitaxial deposition, coarsening and diffusion processes on the clean Ag(110) surface are well characterized.[36-51]

In this paper, we will describe Ag island coarsening experiments between 140 and 260 K with and without oxygen. Morgenstern *et al.*[39] and De Giorgi *et al.*[43] performed experiments similar to ours, without oxygen. Below 175 K, no coarsening of submonlayer silver islands was observed with STM.[39,42,49,50] Upon heating and up to 220 K, "1D" island decay occurs where atoms detach from the narrow, <001> chain ends and diffuse in any direction on the surface. Above 220 K, islands tend toward their equilibrium shape (aspect ratio = 2.9 at 250-270 K) and decay 2-dimensionally. Simulations give similar results.[36,40,48] Both De Giorgi *et al.* and Mottet *et al.* observe a break in the island density between 190 and 220 K, corresponding to the transition from "1D" to "2D" coarsening, and relate it to the onset of in-channel bond breaking above 200 K.[36,43] Furthermore, Morgenstern *et al.* determined that the critical temperature of 220 K, when the transition from anisotropic to isotropic coarsening occurs, corresponds to the temperature at which detachment from kink sites is possible, and because the islands are not perfectly rectangular but rather have rounded edges, a sufficient number of kink sites should exisit.[39,42] OR on the clean surface is probably terrace diffusion (TD) limited as there should be no extra barrier for Ag attachment-detachment (AD). In addition, Morgenstern and coworkers' analysis of the evolution of individual island dimensions with time supports TD-limited OR.

Investigations of the Ag(100) surface with oxygen[52,53] and sulfur[54], and the Ag(111) surface with sulfur[55-57] have revealed that these chalcogens enhance Ag island coarsening. Little is known about how the effect of chalcogens depends on surface crystallography,

except for the sulfur-silver system on the (100) and (111) surfaces for which we have comparative data. One of the goals of this study is to compare coarsening, after oxygen exposure, on the silver (100) and (110) surfaces.

While coarsening with oxygen has not been studied on Ag(110) to our knowledge, due to the prevalence of silver catalysts in epoxidation reactions[58-66], oxygen's behavior on the (110) surface is well-characterized[67-114] and it induces an "added-row" reconstruction on Ag and Cu(110)[115-135]. We expect the initial sticking coefficient s_0 for room temperature O_2 gas to range between 0.008 and 0.003 for sample temperatures between 126 and 300 K.[70,71] Below 150 K on Ag(110), O_2 adsorbs molecularly in-channel and mostly dissociates upon heating due to electron transfer from the Ag surface to the O_2 antibonding orbital, weakening the O–O bond.[136] Above 150 K, O_2 dissociatively absorbs on the Ag(110) surface forming p(n × 1) superstructures, where n = 7 to 2 with increasing coverage ($\theta \sim 1/n$), consisting of –O–Ag–O– chains perpendicular to the close-packed direction. The p(n × 1)-O "added-row" structures become more ordered above room temperature. Diffusion of Ag on Cu(110) is greatly reduced in the presence of the oxygen "added-row" reconstruction.[137-139]

In these experiments, we evaluate Ag island coarsening on Ag(110) in terms of the changes in island density and individual island area, dimensions, and aspect ratios, and the dependence of these changes on temperature. This provides a benchmark for determining what affect oxygen might have on Ag islands.

2. Experimental details

All experiments were performed in a stainless-steel ultrahigh vacuum (UHV) chamber with base pressure of 1×10^{-10} Torr (1.33×10^{-8} Pa), equipped with a variable temperature scanning tunneling microscope (VT-STM) (Omicron GmbH, Germany). The Ag(110) samples were cleaned by repeated cycles of Ar^+ sputtering (1 keV, ~ 2 μA, 8 – 16 min) and annealing (625 – 670 K, 10 min). One of the authors, ARL, conducted experiments from 1999 to 2001 on a sample prepared at the Materials Preparation Center of the Ames Laboratory[140]. The primary author, SMR, conducted experiments from 2010 to 2012 on two samples from the Surface Preparation Laboratory in the Netheralnds[141,142]. A third author,

CDY, participated in some of the experiments with SMR in 2010. A fourth author, HW, participated in some of the experiments with SMR in 2012.

All STM images were collected using electrochemically etched W tips and cut PtIr tips in an Omicron VT-STM. The true temperature of the sample is within ± 5 K of the reported value and was held constant during each experiment, unless otherwise noted. Tunneling conditions are given in the figure captions. With the sample actively cooled in the STM stage to 173 – 260 K, silver was deposited via an Omicron EFM3 UHV evaporator containing Ag (99.99% pure). Ag coverage was determined using WsXM software, in which terrace images were flooded to give the proportion covered by islands. A few images (different areas) per experiment were analyzed to determine the average coverage and the error (reflecting the reproducibility / precision) within one standard deviation. A different source of error is associated with slight changes in flooding levels, and can be considered an absolute error. That was determined to be 6 to 28% different from the reported average coverage value and is not included in the standard deviation. In the experiments discussed below, the Ag coverage ranged from 0.086 ± 0.007 to 0.31 ± 0.05 monolayer (ML). The Ag flux ranged from 6.6 to 70 mML/s and was determined from coverage and deposition time. Previously in our group it has been shown that island density is independent of flux over a limited range of fluxes (2 to 80 mML/s) on this surface.[53] In these experiments, Ag islands were always prepared in this range, so comparison between experiments utilizing different Ag flux is reasonable for a given temperature.

Prior to O_2 exposure, the surface was allowed to stabilize for 139 ± 54 min. The chamber was then backfilled with O_2 gas through a leak valve to the desired pressure. It was continuously pumped with an ion pump. In two experiments, we continued scanning during exposure, but in both we were unable to observe the surface after exposure for more than one hour, because of tip instability and thermal drift. One such experiment is included in the results summary. In all other experiments, the surface was observed for 119 ± 101 min. Oxygen exposure is reported in Langmuir (1 L = 10^{-6} Torr s). In temperature programmed desorption (TPD), oxygen desorbs between 515 and 565 K. Therefore, we do not expect oxygen to desorb at our experimental temperatures, 173 to 242 K.[143] Oxygen coverage will be determined solely by the adsorption probability (sticking coefficient).

Throughout this paper, visual clues are used to quickly differentiate between experiment types: blue indicates an image without O and orange indicates an image after O exposure. Data file names are provided in the figure captions: the date refers to the experiment date and folder name and "m#" refers to the image file.

3. Results

3.1. Island density

At room temperature, Ag islands on Ag(110) disappear in a matter of minutes, and only their remnants are observed as large "fingers" flowing from step edges. At 260 K and below, discrete islands form and change slowly enough that experimental observations are possible. Therefore, all of our measurements are made below room temperature.

Starting from 175 K, Fig. 1a illustrates that with increasing temperature, islands coarsen more readily: the island density deceases and the island size increases. In comparison, the island density over the same time range at 175 K remains stable. From the top images, where temperature increases and coarsening accelerates, we can also see a growing depletion zone around step edges, especially at descending edges. This means that the descending step edges act as sinks, or traps, for Ag from the islands.

We monitored the initial island density N as a function of deposition temperature from 140 to 260 K, with a constant deposition flux of 45 mML/s, and results are shown in Fig. 2a. As temperature increases, N decreases and island size increases. The semi-log plot in Fig. 2b shows a smooth variation of N with T.

The decay of the island density with time, after Ag deposition stops, is shown in Fig. 3. The N decay appears rather shallow for most temperatures, except at 260 K, where N rapidly decreases. (ARL's data in Fig. 2b were taken from the initial island densities shown in Fig. 3.)

Fig. 4 visually compares three experiments at 175 K: Ag/Ag(110) without O_2, with 0.52 L O_2, and with 1.1 L O_2. Exposing Ag islands to oxygen appears to have little or no effect on island coarsening; the island density does not change abruptly, nor do the islands' shapes. At 193 K, Fig. 5, shows that oxygen exposure at higher temperature does not seem to affect island coarsening either. The Ag islands appear wider and less dense with time, but

these are the effects of normal coarsening for this system and not due to oxygen. A more quantitative proof lies in the decay of N with time, shown in Fig. 6. There, the decay rates remain unperturbed with O_2 exposure.

3.2. Individual island decay: Temperature dependence

Analyzing individual island decay provides another way to characterize coarsening quantitatively, as shown in Fig. **7**. At 175 K, islands less than 6 nm^2 decay at a rate of 0.002 ± 0.001 nm^2/s soon after Ag deposition. After almost an hour, similarly sized islands decay at 0.0012 ± 0.002 nm^2/s. At 190 K, islands ranging in area from 7.6 to 13 nm^2 decay at 0.0062 ± 0.0016 nm^2/s. At 220 K, an island of area 71 nm^2 decays at 0.15 nm^2/s. At 240 K, the decay rate is 0.59 ± 0.19 nm^2/s for islands 427 to 188 nm^2. These values are summarized in Table I.

Islands at 260 K clearly illustrate TD-limited OR in Fig. **7**; as neighboring islands disappear the individual island decay rate increases. The islands range in size from 98 to 3046 nm^2 initially. Islands d and e show the strongest dependence. The decay of island d bends down sharply after islands c and f disappear. The largest island, e, increases in size until it is the only island remaining after d disappears, when the rate changes from increasing at 0.43 nm^2/s to decaying at 1.6 nm^2/s. If we only consider rates at 260 K that were determined after close-neighboring islands disappeared, then the average individual island decay rate is 2.4 ± 0.7 nm^2/s. Table I gives the details of each island analysis. From the values quoted above and shown in Table I., there is no obvious trend in decay rate with island size over a factor of 2 to 3 in initial island size at a given temperature.

With 0.52 L O_2 at 173 K, islands of initial area of 1.9 to 4.1 nm^2 in area decay at 0.0015 ± 0.005 nm^2/s in Fig. 8. With 1.0 L O_2 at 194 K, islands ranging in size from 18 to 45 nm^2 decay at a rate of 0.0110 ± 0.0004 nm^2/s as shown in Fig. 8. Above the reported transition temperature of 220 K, at 242 K and with 14 L O_2, most islands, including the smallest, actually increase in area over the 14 min we are able to image. This 242 K experiment differs from the others in that we observed the same islands before, during, and after O_2 exposure. (The period of O_2 exposure at 242 K is denoted by the vertical lines in Fig. 8.) Islands c and e in Fig. 8 are about the same size, yet coarsen differently, with island c decaying and island e increasing in size. In order for the majority of island areas to increase,

mass must actually be net transferred *from* step edges *to* islands. One possible explanation is that the islands are contamination pinned, and hence cannot coarsen by losing mass to the step edges. The data set is shown to illustrate that, in spite of the anomalous behavior, all of the islands change in a way that is indifferent to the presence of oxygen. The initial areas and all rates are given in Table II.

The Arrhenius plot of the individual island decay rates in Fig. 9 shows that the rate decreases regularly with decreasing temperature. Island decay with oxygen very closely follows the clean decay trend, again supporting the conclusion that oxygen does not affect Ag island coarsening.

3.3. Individual island decay: Aspect ratio

While oxygen may not enhance island coarsening, perhaps it affects island shape. On the clean surface at 175 to 220 K, island length along <110> decays about an order of magnitude faster than island width along <001>, as shown in Fig. 10. The short island edges fluctuate with time, appearing arrow-, L-, or flat-shaped. At 240 K, island decay differs by a factor of 5 between the long and short dimensions. At 260 K, the difference between dimensions varies. However, for island e, which was observed for a long time isolated on the terrace, the dimension decay differs by a factor of 7.

The change in island dimensions, for the clean, Fig. 10, and oxygen, Fig. 11, experiments at ~190 K are similar. The decay of the long vs. short dimensions of the small island at 173 K with 0.52 L O_2 differs by a factor of 3. The short rate is 5 times faster with 0.52 L O_2 at 173 K compared to the clean surface at 175 K. However, islands at these temperatures decay slowly and were not observed for long periods of time leading to a small data set from which to extract approximate rates with large errors, see Tables I and II. At 242 K with 0.070 ML Ag and 14 L O_2, the length actually increases for each island, while the short dimension slightly decreases. This is consistent with the area increase shown in Fig. 8 for these islands. As discussed above, the experiment, while anamolous, does illustrate that oxygen has no affect.

There appears to be no relationship between aspect ratio decay and temperature for the analyzed islands on the clean surface in Fig. 12 nor after oxygen exposure in Fig. 13. The

particular islands considered at 175 K on the clean surface have an aspect ratio decay rate of 0.001 ± 0.002 s^{-1}, which is faster than the rate of 0.0004 ± 0.0032 s^{-1} at 173 K with 0.52 L O_2. However, theses data are noisy. With 1.0 L O_2 at 194 K, the aspect ratio decreases at a rate of 0.0011 ± 0.0007 s^{-1}, which is comparable to the clean rate of 0.00095 ± 0.00007 s^{-1} at 190 K. At 240 K, the islands' aspect ratios oscillate about 3.0 ± 0.2. The aspect ratio behavior is unaffected by 14 L O_2 exposure as shown in Fig. 13 for the 242 K experiment, where the surface was observed before, after, and during O_2 exposure. At 260 K without oxygen, the mean aspect ratio is 3.3 ± 0.2 for all of the islands

4. Discussion

4.1. Comparison with previous work

De Giorgi *et al.* performed experiments in the same temperature range (140 – 250 K) and with the same deposition method as ours, but with lower silver coverage (0.16 ML) and flux (25 mML/s).[43] Morgenstern and coworkers also investigated the Ag/Ag(110) system at temperatures ranging from 155 to 255 K, but prepared the Ag islands via two methods: deposition from a tungsten basket and by sputtering the clean surface.[39]

Our island decay as a function of temperature is in excellent agreement with Morgenstern *et al.*'s work, as illustrated in Fig. 14.[39] In addition, their work also showed a minimal dependence of decay rate on island size. For example, the decay rate for the same island varied by a factor of 3 over a size difference of 1 order of magnitude, c.f. data at 255 K.[39] Our data with and without oxygen, combined with Morgenstern *et al.*'s data are highly correlated, with R^2 equal to 0.9957, as shown by the linear fit in Fig. 14b. From the same Figure, the effective activation barrier E_{eff} to OR is 0.34 ± 0.01 eV.

Morgenstern and coworkers found that below 220 K, Ag islands coarsen 1-dimensionally: the long dimension decays rapidly while the short dimension is stable until the island has almost vanished (less than 10 nm^2 at 199 K).[39] Between 200 and 220 K, island coarsening changes from 1D to 2D in the literature.[39,43,48] However, the change in decay rates along the long and short dimensions in our data does not definitively show this transition. The dimension decay data at 220 K and lower is consistent with 1D coarsening. In 2D coarsening, one expects the decay of the short dimension to approach that of the long

dimension. While the long and short decays of islands at 240 K in Fig. 10 are closer to eachother (differing by a factor of 5) than at lower temperature, the decays still do not mimic Morgenstern *et al.*'s work at 242 K where the long and short rates are nearly equal, differing by a factor of 2 or less.[39] The discrepancy may be due to island choice, as coarsening is TD-limited and therefore depends on island environment. In addition, Morgenstern and coworkers utilized a fast-scanning STM, so they can more readily observe rapid fluctuations on the surface and produce finer statistics.[39] In our work, decay rates along *both* dimensions increase by 3 orders of magnitude between 175 and 260 K. Above the reported transition to 2D coarsening at 220 K, we expect the short decay rate to increase more rapidly with temperature.

De Giorgi *et al.*'s work showed that island morphology transitions from small, nearly isotropic clusters at 140 K to large, highly aniostropic clusters at higher temperatures. The STM images in Fig. 2, qualitatively agree with this trend. At 140 and 160 K, Ag islands appear small and almost square. As temperature increases to 220 K, the islands become more anisotropic. Above 220 K, the anisotropy of the islands appears to decrease with temperature. At low temperatures, Morgenstern *et al.'s* equilibrium aspect ratio R_{eq} (2.9 ± 0.4, 250 - 270 K)[39] seems irrelevant as might be expected due to the low temperature and therefore inhibited equilibration: in Fig. 12 the islands at 175 K reside above R_{eq}, while the islands at 190 K trail below R_{eq}, the island at 220 K appears to have no relationship to R_{eq}, the measured ratio oscillates about R_{eq} at 240 K and above R_{eq} at 260 K. With 1.0 L O_2 at 194 K, the aspect ratio decay crosses R_{eq}. Only a few, relatively small, islands were analyzed at each temperature. For example, at 175 K without oxygen the initial average aspect ratio is 12 ± 8, ranging between 1.5 and 41, but the ratio of the six analyzed islands are all below the mean, 2.9 to 8.5 initially. The data set at 260 K without oxygen, has a mean aspect ratio of 3.3 ± 0.2.

4.2. Oxygen

Additives may enhance or diminish coarsening by altering the carrier or altering the effective activation energy of the original carrier.[144] In these experiments oxygen does not enhance Ag island coarsening. There are two possible explanations for our observations.

i. Energetics –Oxygen does not affect the energetics.

   a. General energetics of coarsening. The two main steps involved in coarsening are diffusion of the mass-transporting agent across the terraces in between islands, and attachment/detachment of the mass-transporting agent at island or step edges. Either one can be rate-limiting. Terrace-diffusion (TD)-limited OR is typical of metal homoepitaxial systems and depends on the island environment, specifically, on the carrier diffusion rate and density.

   b. Energetics specific to Ag(110). For the clean Ag(110) surface, both De Giorgi *et al*. and Mottet *et al.* report an in-channel diffusion barrier of 0.28 eV based on experiments and Monte Carlo simulations.[36,43] Ag adatom formation energy is 0.16 - 0.20 eV.[144] In this scenario, oxygen would need to reduce one of these barriers to enhance coarsening.

ii. Oxygen coverage. The second possible explanation is that little or no oxygen adsorbs on the surface as a result of exposure under these conditions: 0.52 to 14 L at 175 to 242 K. Pai and Reutt-Robey[126] quote an initial sticking coefficient s_0 of 0.006 for O_2 gas on Ag(110) based on others' earlier determinations, without specifying the temperature.[70,89] Pai and Reutt-Robey's own experiments were performed at room temperature.[126] Engelhardt and Menzel report $s_0 = 0.003$ at room temperature based on LEED measurements, and is the most commonly referenced value.[70] Barteau and Madix report $s_0 = 0.008$ at 126 K based on thermal desorption spectroscopy (TDS) using isotopic and LEED measurements.[71] From Engelhardt & Menzel's[70] and Barteau & Madix's[71] work plotted in Fig. 15, we see that s_0 exponentially decreases with increasing temperature. Both experiments are consistent, and both experimental conditions are similar to our conditions. Based on this data, we can estimate s_0 for our experimental temperatures, and then use that to estimate the oxygen coverage in monolayers (ML) in our experiments. We expect s_0 to range from 0.007 to 0.004 for the sample temperatures used in our experiments. We assume that the sticking

coefficient is coverage-independent at low exposure. The results, shown in Table III, indicate that coverage is low: 0.003 to 0.08 ML.

The calculated oxygen coverages achieved with our exposures on Ag(110) seem extremely low, but it is informative to compare them with coverages probably achieved in previous work with Ag(100). There, the sticking coefficient is 1.3×10^{-4} at 250 K, and exposures of 12 to 36 L were typically used, which would result in coverages of 0.002 to 0.005.[145] These values are comparable to the lowest coverages achieved in our experiments. However, for Ag(100), exposures of 20 L (0.003 ML) consistently resulted in strong acceleration of Ag island coarsening and a change in the dominant mechanism of coarsening from SR to OR. Thus, we can say that very small coverages of oxygen on Ag(110) (roughly 0.003 to 0.08 ML) have a much less dramatic effect than very small coverages on Ag(100) (roughly 0.002 to 0.005 ML).

5. Conclusions

The rate of Ag island decay on Ag(110) follows an Arrhenius dependence on temperature between 175 and 260 K, being more rapid at higher temperature, and is in good agreement with previous studies. However, the island dimensions and aspect ratio do not show a trend with varying temperature and there is no strong evidence for a transition from 1D to 2D coarsening at 220 K. While it is difficult to quantitatively determine the rate-limiting step in OR from the data presented here, we do have strong support for TD-limited kinetics.

Oxygen has no effect on Ag island density, area, dimension, or aspect ratio decay in our experiments on Ag(110). However, the likely oxygen coverage was low and studies should be performed at higher O_2 exposure to fully illuminate oxygen's influence on mass transport on the Ag(110) surface. Based on the results presented here, oxygen does not affect Ag island coarsening at 173 to 242 K and 0.52 to 14 L O_2 exposures, which correspond to oxygen coverages of 0.003 to 0.08 ML. For comparison, oxygen coverages of only 0.002 to 0.005 ML served to strongly accelerate Ag island coarsening and change the coarsening mechanism, on Ag(100). This suggests that the effect of trace amounts of oxygen has a strong dependence on Ag crystallography.

Acknowledgements

We thank J. W. Evans for beneficial discussions and M. Wallingford for his assistance to H. Walen. This work was supported by the National Science Foundation (NSF) Grant No. CHE- 1111500. The work was performed at Ames Laboratory which is operated for the USDOE by Iowa State University under Contract No. DE-AC02-07CH11358.

Figures

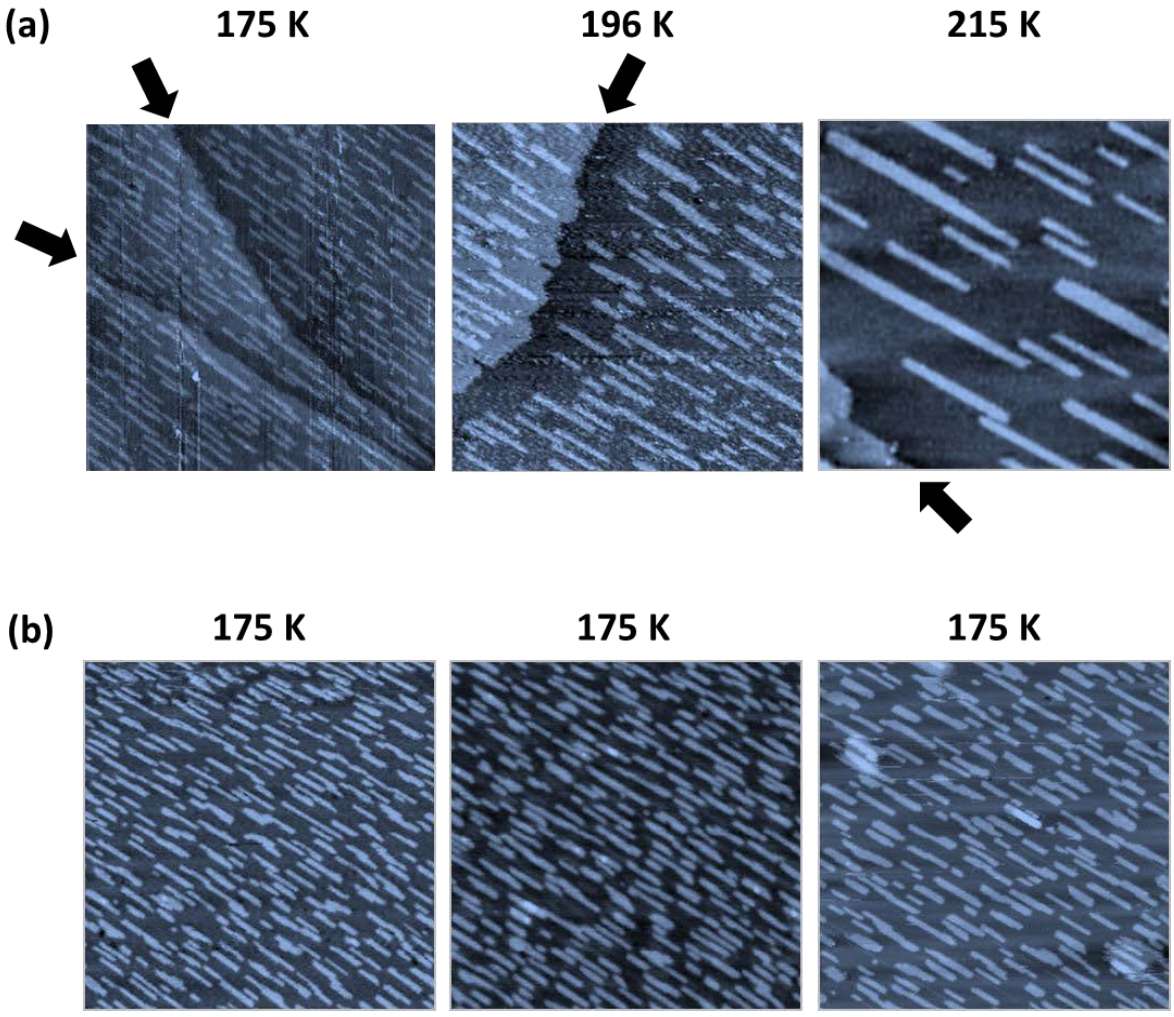

This figure continues on the following page.

Figure 1. Effect of temperature on Ag islands. (a) 0.28 ML Ag was deposited at a flux of 16 mML/s at 175 K. The arrows point to step edges. The sample was heated to 196 and 215 K as shown in (c). Note that the temperature increase is not linear with time as drawn, but rather, increases rapidly initially then plateaus at the set temperature. (b) 0.26 ML Ag was deposited at a flux of 45 mML/s at 175 K. Images were recorded at the specified temperature 53 min, 1 hr 38 min, and 3 hr 8 min after Ag deposition in (a), denoted as "×" in (c), and at constant temperature 53 min, 1 hr 38 min, 3 hr 5 min after Ag deposition in (b). All images digitally zoomed in to ~99×99 nm^2, except (b) right. Image parameters are (a) Left, 175 K: -3.49 V, 0.74 nA, 99.2×99.2 nm^2 (2010-05-13, m52). Middle, 196 K,: V_{tip} = -1.34 V, I = 1.13nA, 99.1×99.1 nm^2 (m63, 17:07). Right, 215 K: V_{tip} = -2.58 V, I = 0.149 nA, 99.1×99.1 nm^2 (m94, 18:37), FFT filtered. (b) Left: V_{tip} = -1.22 V, I = 0.114 nA, 99.6×99.6 nm^2 (1999-12-12, m35). Middle: V_{tip} = 1.00 V, I = 0.158 nA, 99.7×99.7 nm^2 (m62). Right: V_{tip} = -1.27 V, I = 0.129 nA, 91.6×91.6 nm^2 (m105).

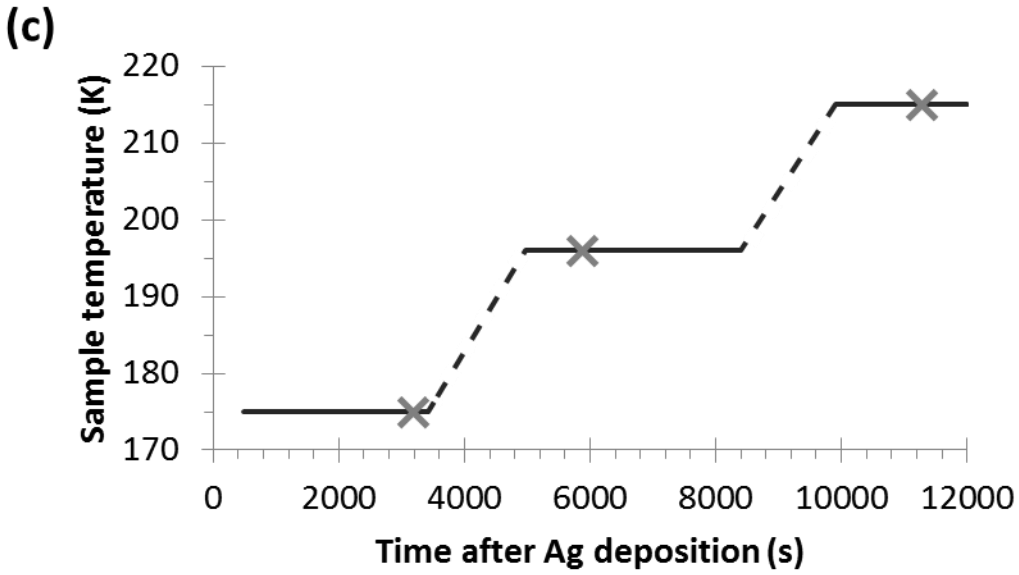

Figure 1. continued.

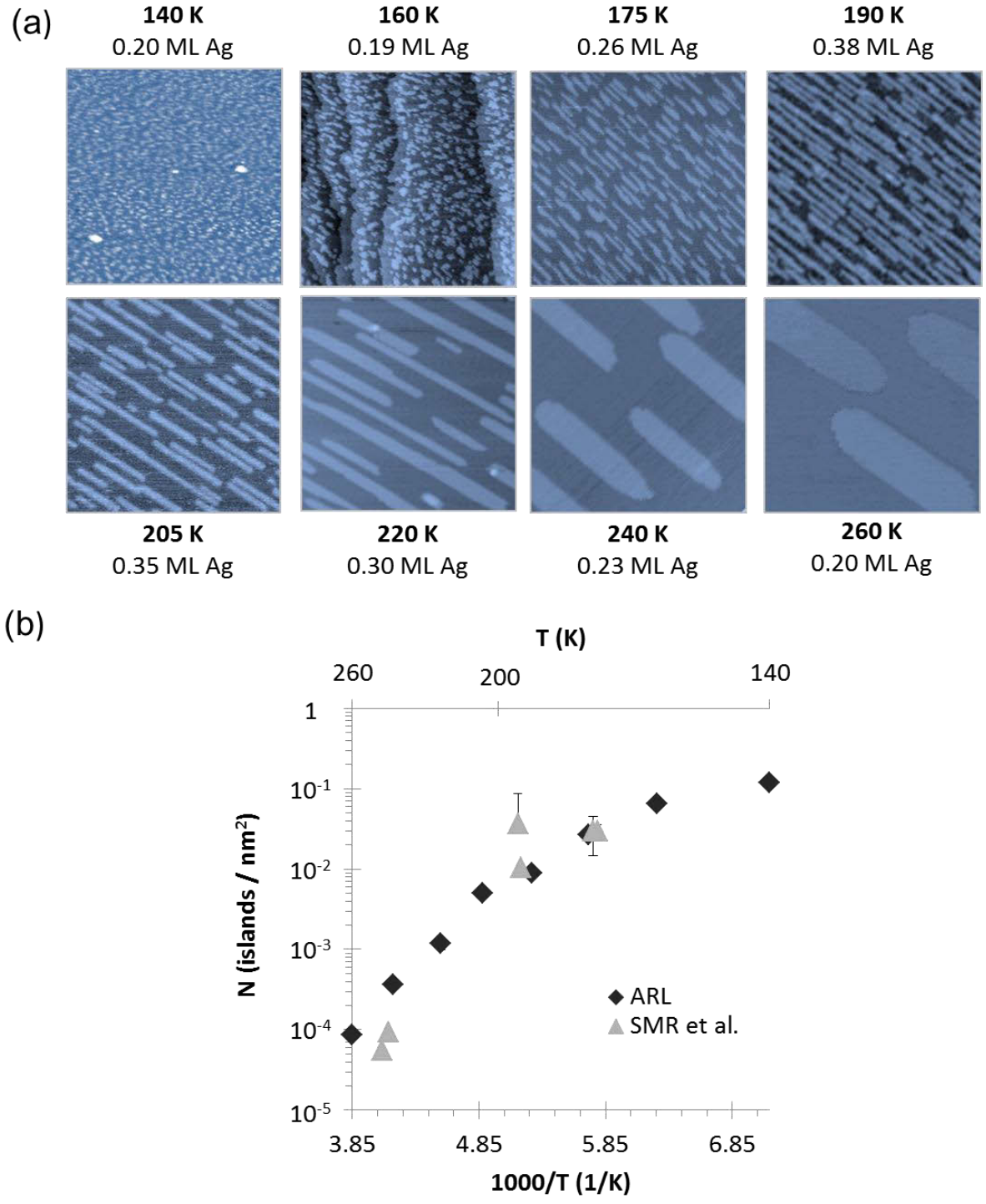

Figure 2. Island density as a function of temperature. (a) STM images showing Ag Islands at various temperatures. All images are 100 × 100 nm^2. (b) Arrhenius plots for the island density, comparing ARL's data, all flux = 45 mML/s, and SMR *et al.*'s data at various fluxes.

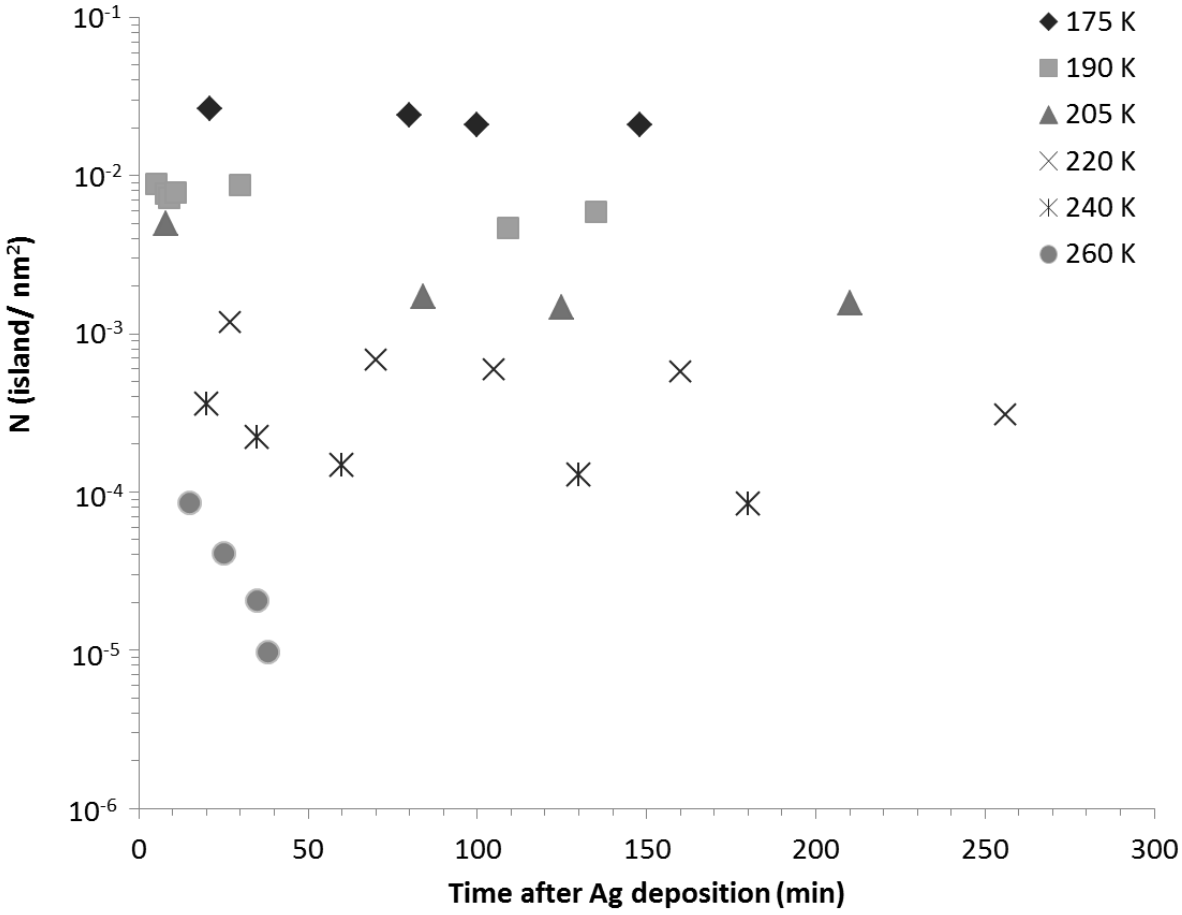

Figure 3. Island density decay of (0.28 ± 0.06) ML silver islands deposited at 45 mML/s on Ag(110) at different temperatures.

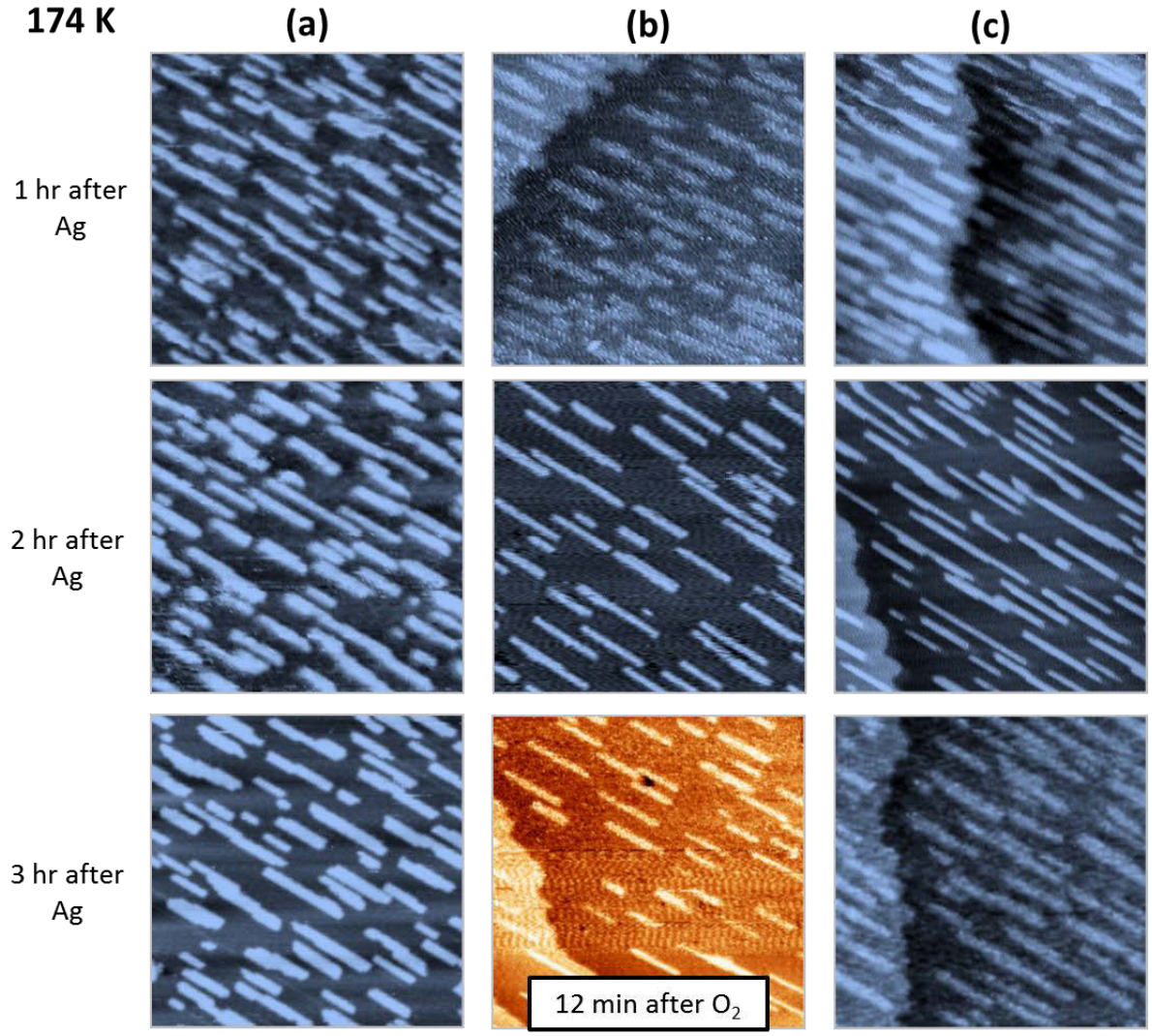

This figure continues on the following page.

Figure 4. Ag island coarsening at 174 K under different conditions. (a) 0.26 ML Ag (45 mML/s), clean, -0.68 ± 1.1, V_{tip} = -1.27 to 1.00 V and I = 0.098 to 0.13 nA (12/12/1999, m43, 82, 104). (b) 0.25 ML Ag (17mML/s) with 0.52 L O_2, V_{tip} = -1.50 to -1.01 V and I = 0.97 to 1.01 nA (5/20/2010, m71, 99, 104, 129). (c) 0.31 ML Ag (23 mML/s) with 1.1 L O_2, V_{tip} = -1.35 to 1.50 V and I = 0.93 to 1.14 nA (5/24/2010, m63, 77, 102, 122, 144, 172). Images are 49.6×49.6 to 50×50 nm^2.

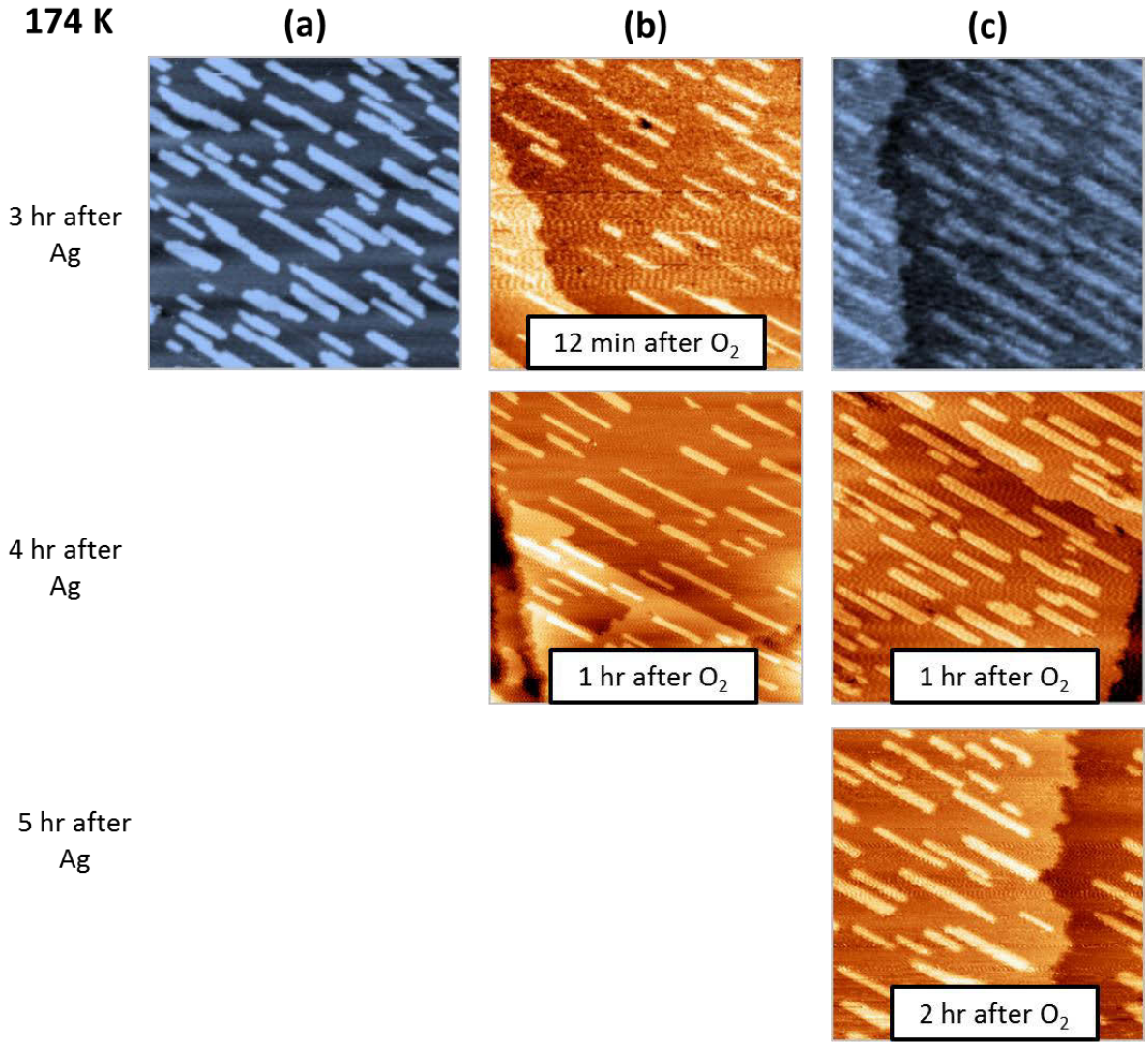

Figure 4. continued.

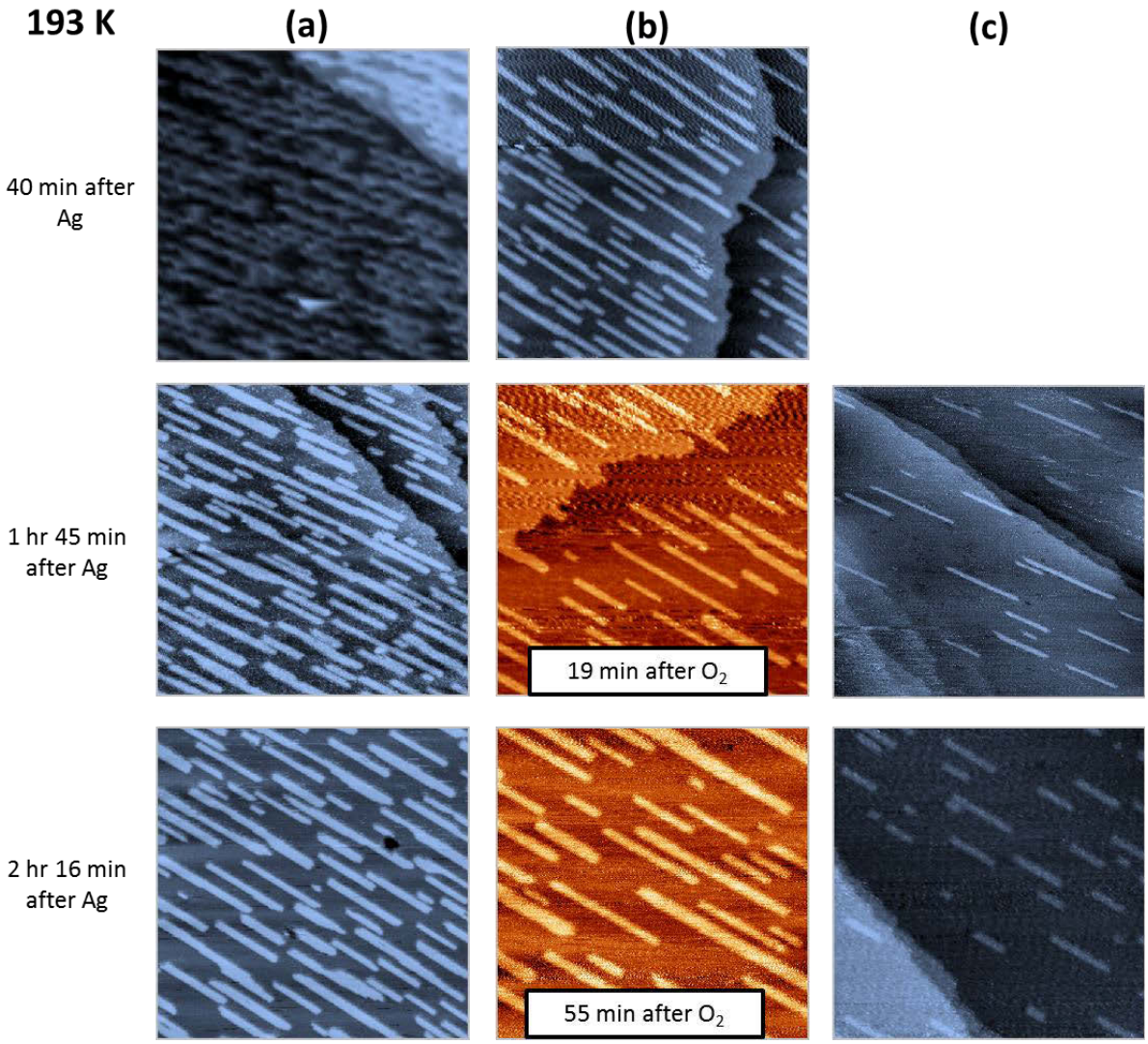

This figure continues on the following page.

Figure 5. Ag island coarsening at 190 to 194 K under different conditions. (a) 0.38 ML Ag (45 mML/s), clean, V_{tip} = 1.00 V and I = 0.232 to 0.316 nA (12/19/1999, m24, 25, 45). (b) 0.27 ML Ag (18 mML/s) with 1.0 L O_2, V_{tip} = -1.47 to -0.38 V and I = 0.184 to 1.19 nA (5/26/2010, m50, 73, 90, 100, 122, 150). (c) 0.099 ML Ag (6.6 mML/s) with 13 L O_2, V_{tip} = -1.87 to -1.42 V and I = 1.00 to 1.23 nA (7/7/2010, m158, 173, 207, 233). Images are 99×99 to 100×100 nm^2.

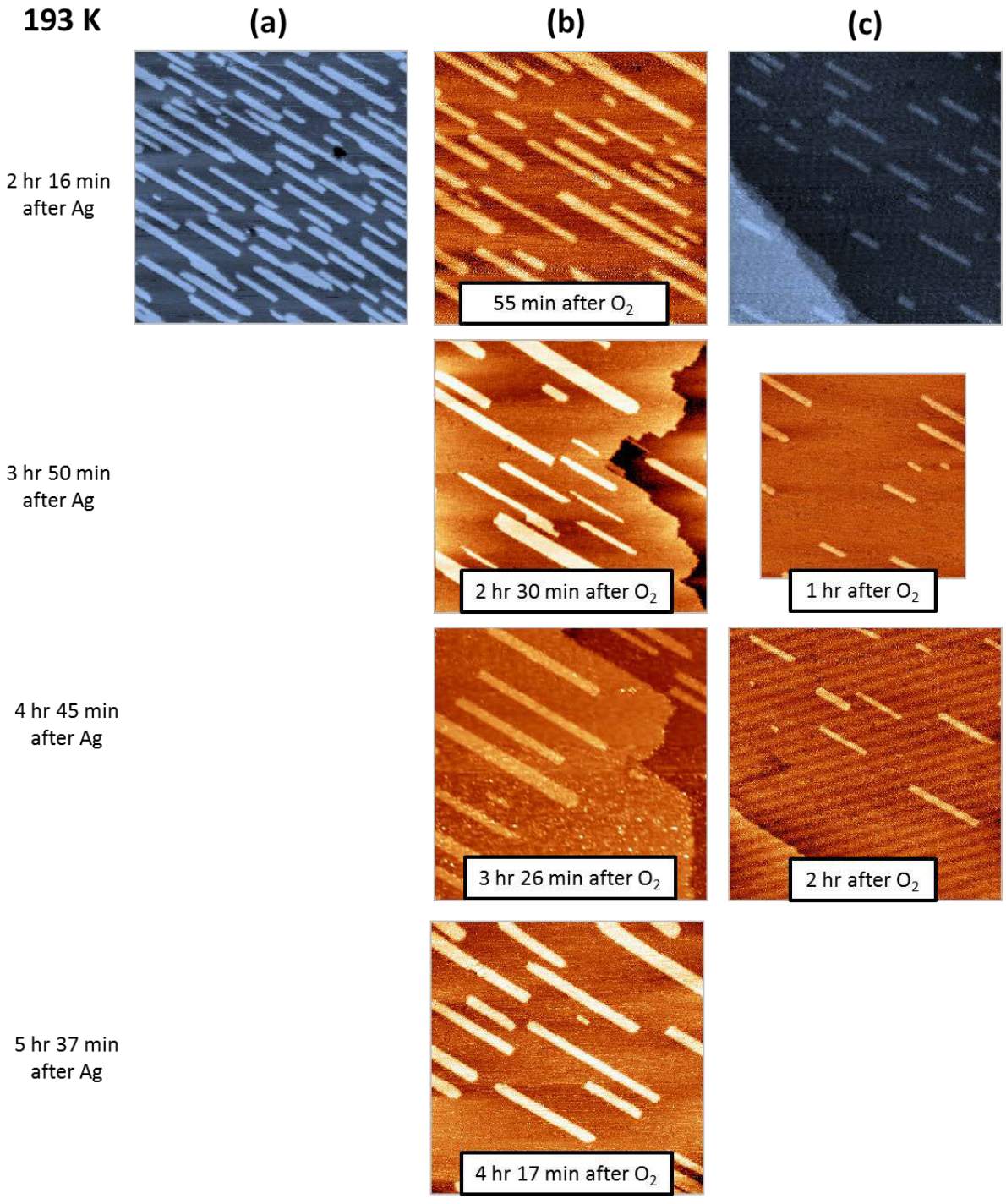

Figure 5. continued.

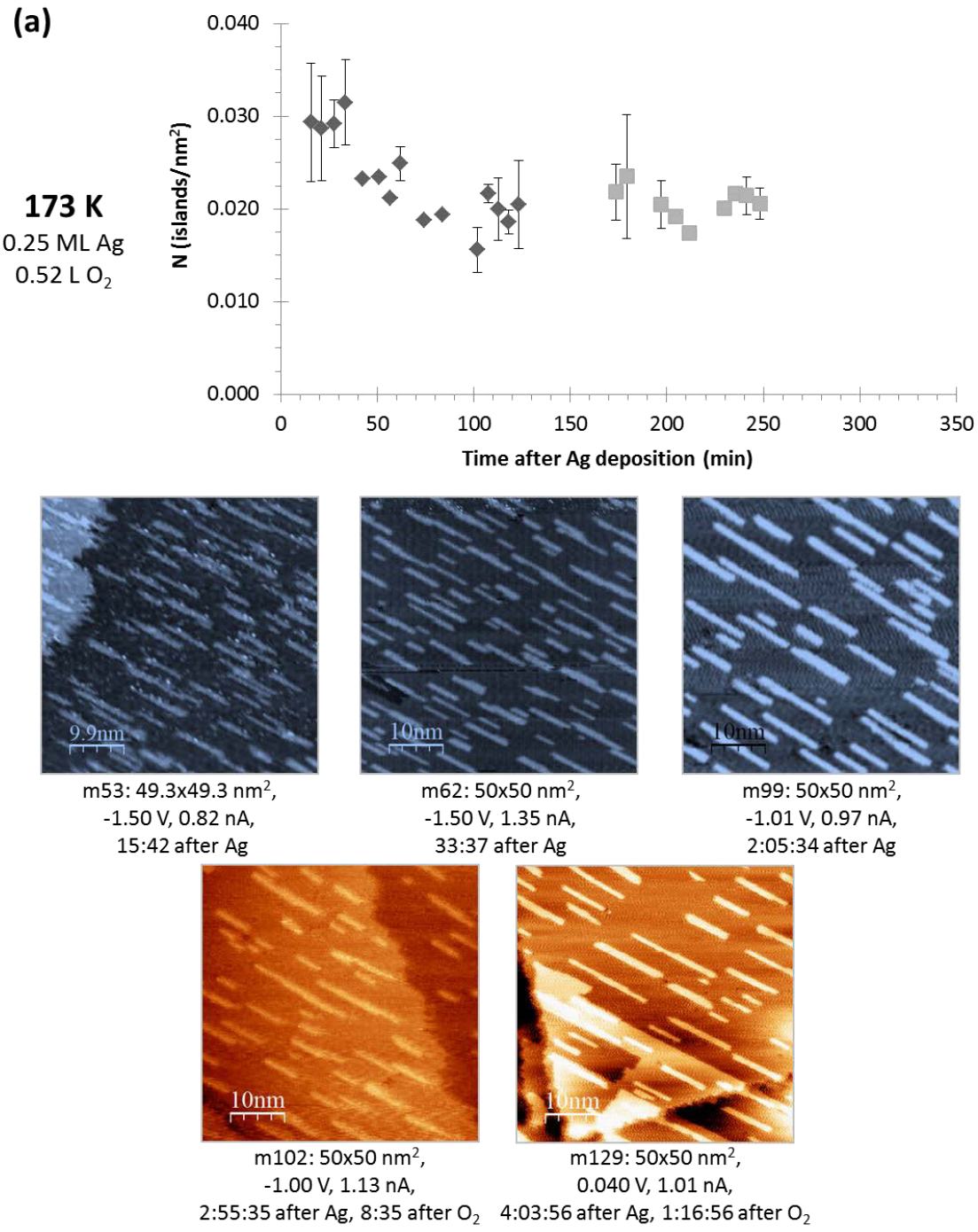

This figure continues on the following page.

Figure 6. Island density decay of silver islands on Ag(110) at different temperatures before (diamonds) and after (squares) oxygen exposure at 173 K (a), 174 K (b), 194 K, 193 K (d), and 242 K (e).

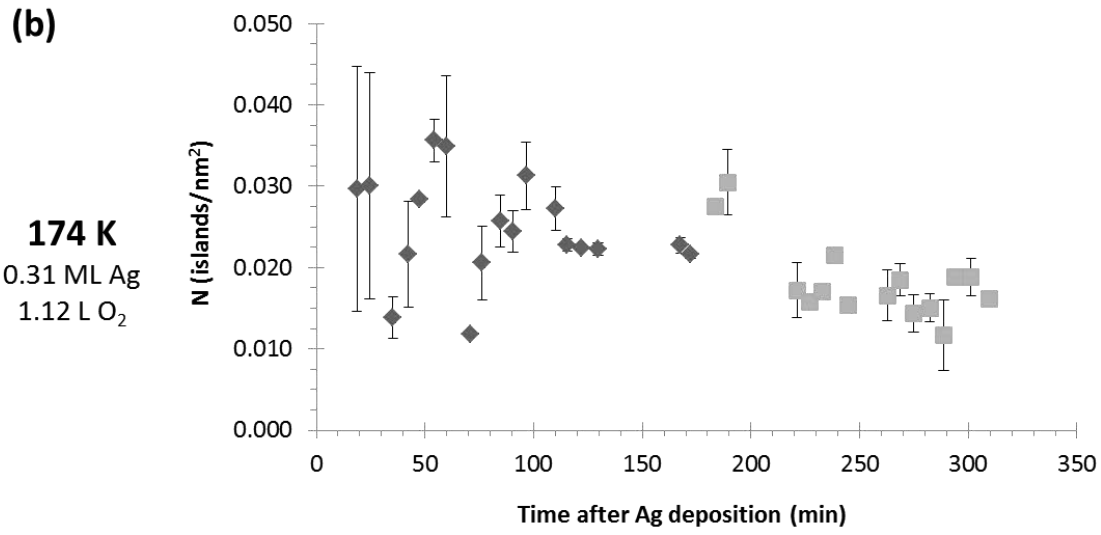

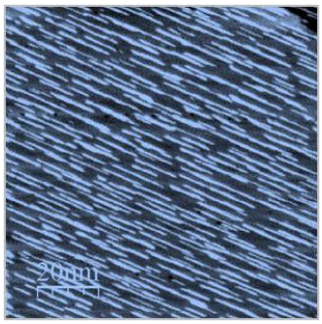

m62: 100x100 nm^2,
1.50 V, 0.99 nA,
18:38 after Ag

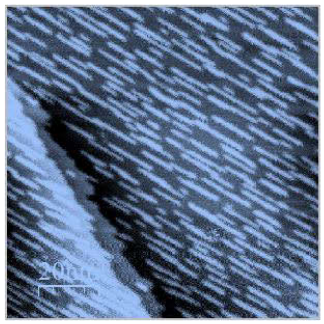

m92: 100x100 nm^2,
1.50 V, 0.93 nA,
1:30:26 after Ag

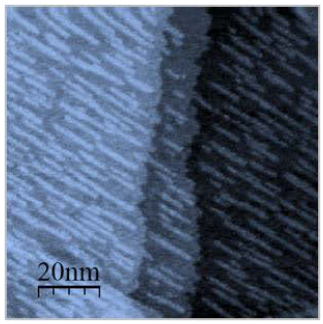

m122: 100x100 nm^2,
-1.35 V, 0.93 nA,
2:52:12 after Ag

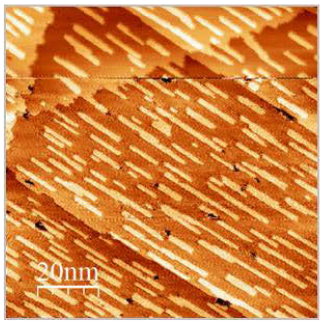

m140: 100x100 nm^2,
-2.00 V, 1.0 nA,
3:49:00 after Ag, 0:54:00 after O_2

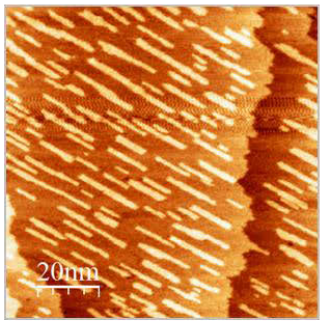

m174: 100x100 nm^2,
-1.50 V, 0.72 nA,
5:06:39 after Ag, 2:11:39 after O_2

This figure continues on the following page.

Figure 6. continued.

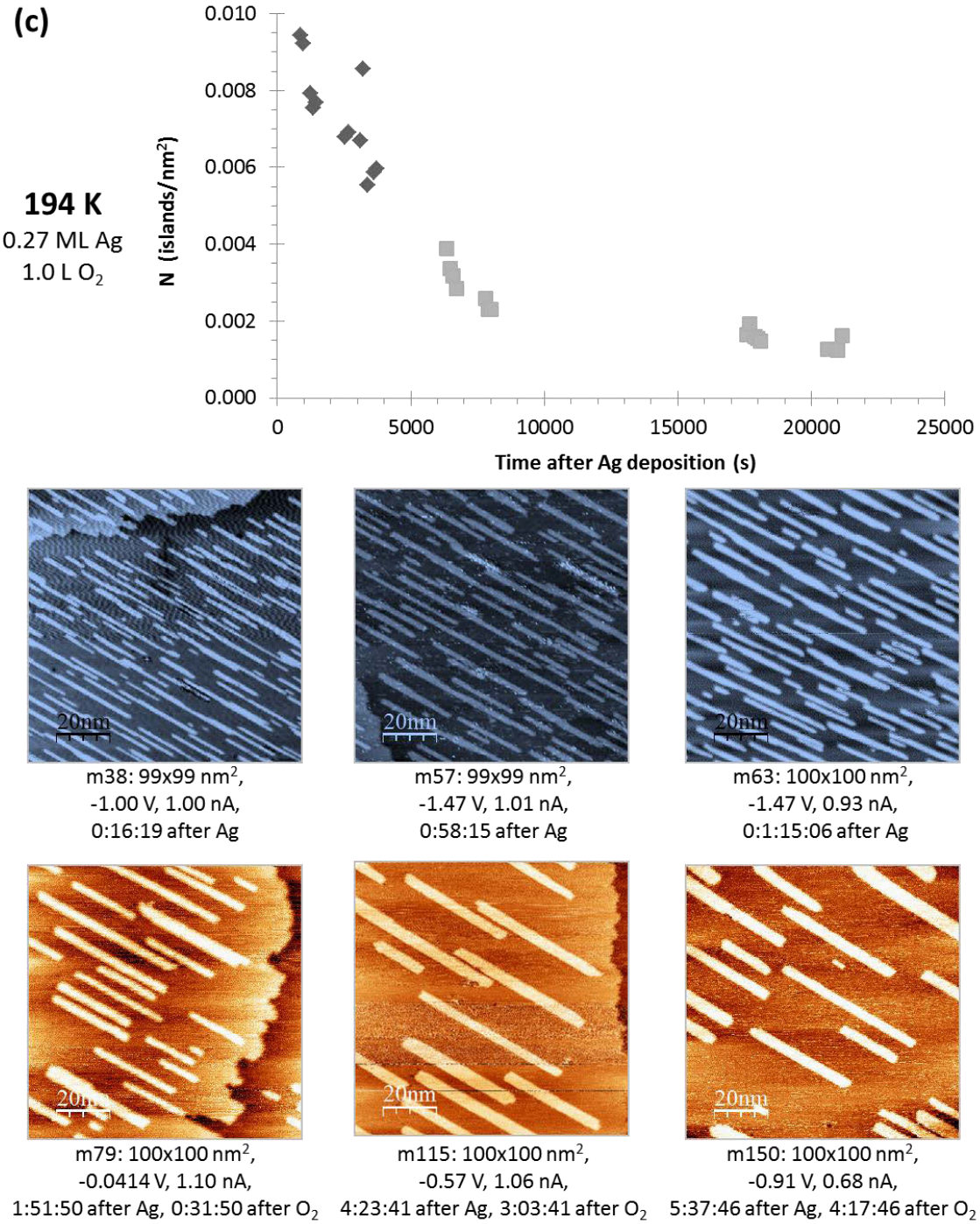

This figure continues on the following page.

Figure 6. continued.

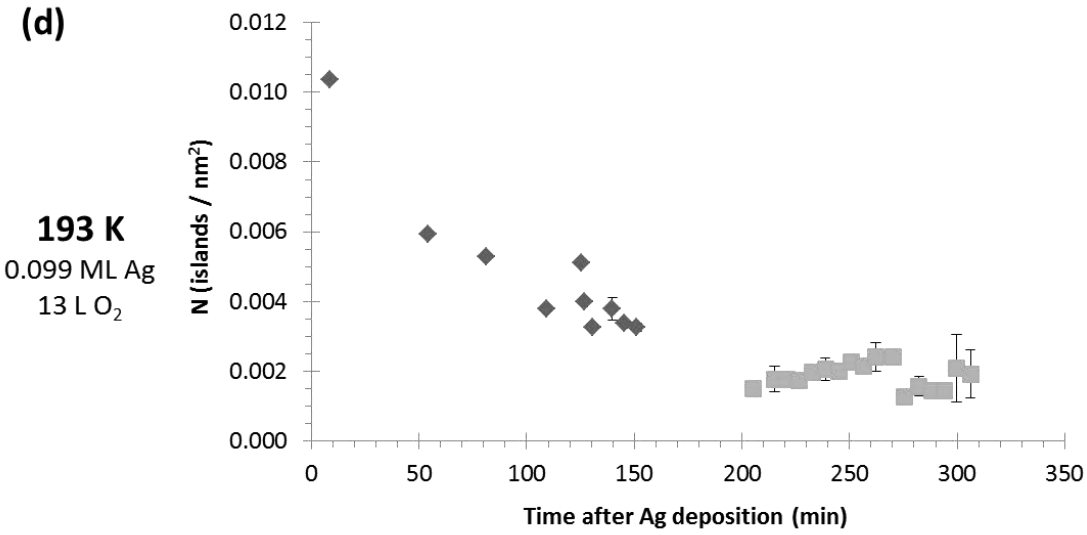

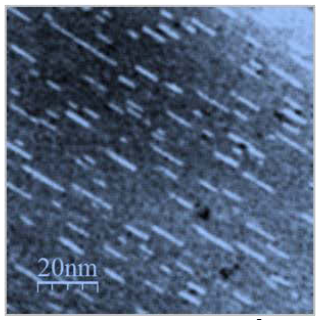

m116 : 100x100 nm^2,
-1.50 V, 0.88 nA,
8:44 after Ag

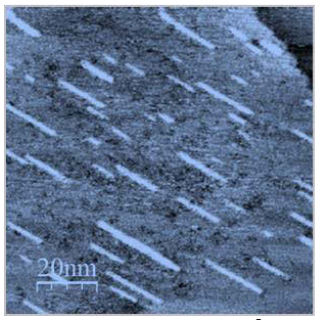

m147 : 100x100 nm^2,
-2.38 V, 1.00 nA,
1:21:10 after Ag

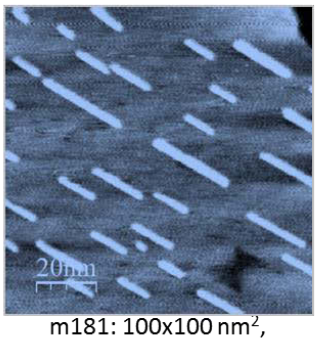

m181: 100x100 nm^2,
-1.42 V, 0.99 nA
2:32:55 after Ag

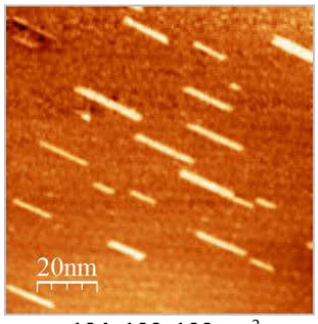

m194 :100x100 nm^2,
-1.42 V, 1.15 nA,
3:23:09 after Ag, 39:09 after O_2

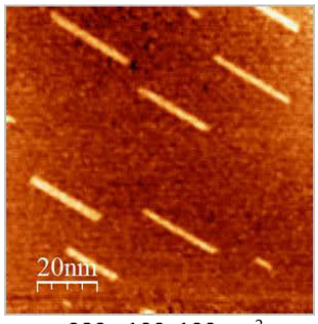

m232 : 100x100 nm^2,
-1.42 V, 1.02 nA,
4:42:21 after Ag, 1:58:21 after O_2

This figure continues on the following page.

Figure 6. continued.

(e)

242 K
0.070 ML Ag
14 L O_2

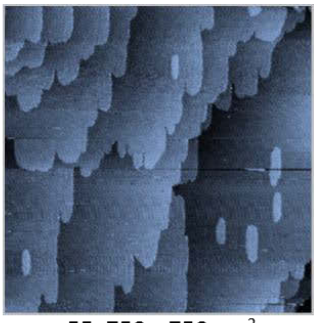

m55: 750 x 750 nm^2,
-2.26 V, 0.216 nA,
2:27:04 after Ag

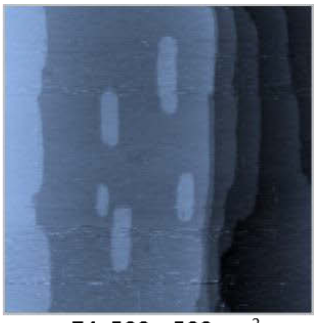

m74: 500 x 500 nm^2,
-2.39 V, 0.119 nA,
3:42:55 after Ag,
just before O_2 exposure

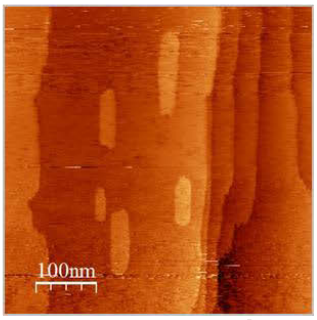

m75: 500 x 500 nm^2,
-2.37 V, 0.120 nA,
3:44:40 after Ag,
during O_2 exposure

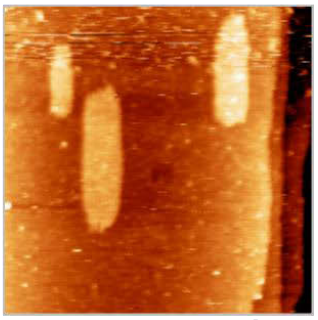

m80: 250 x 250 nm^2,
-2.30 V, 0.0883 nA,
3:57:02 after Ag,
0:07:02 after O_2

Figure 6. continued.

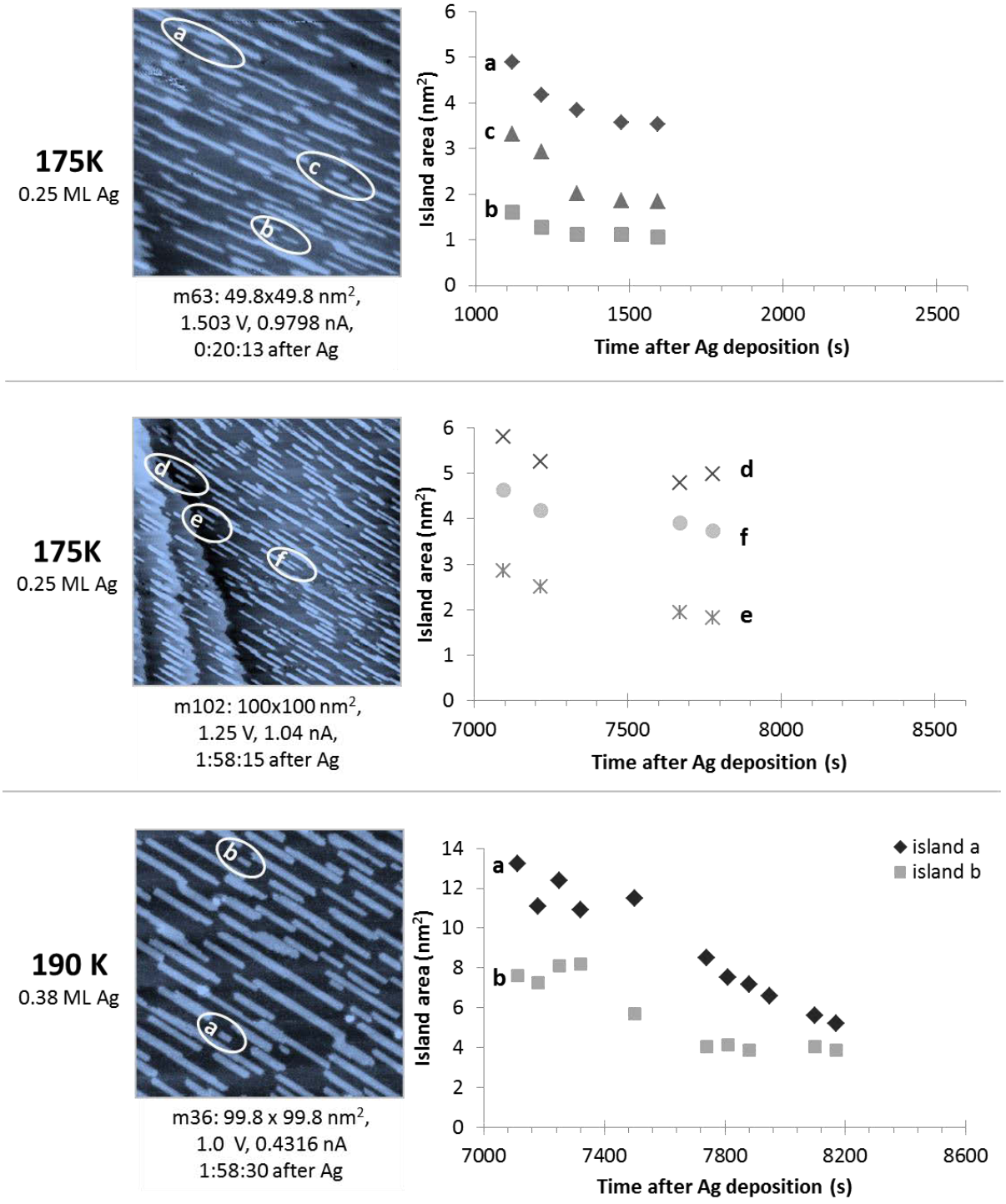

This figure continues on the following page.

Figure 7. Clean-surface, individual island decay at different temperatures, 175 – 260 K. All Ag deposited with flux = 45 mML/s, except at 175 K where the flux was 21 mML/s.

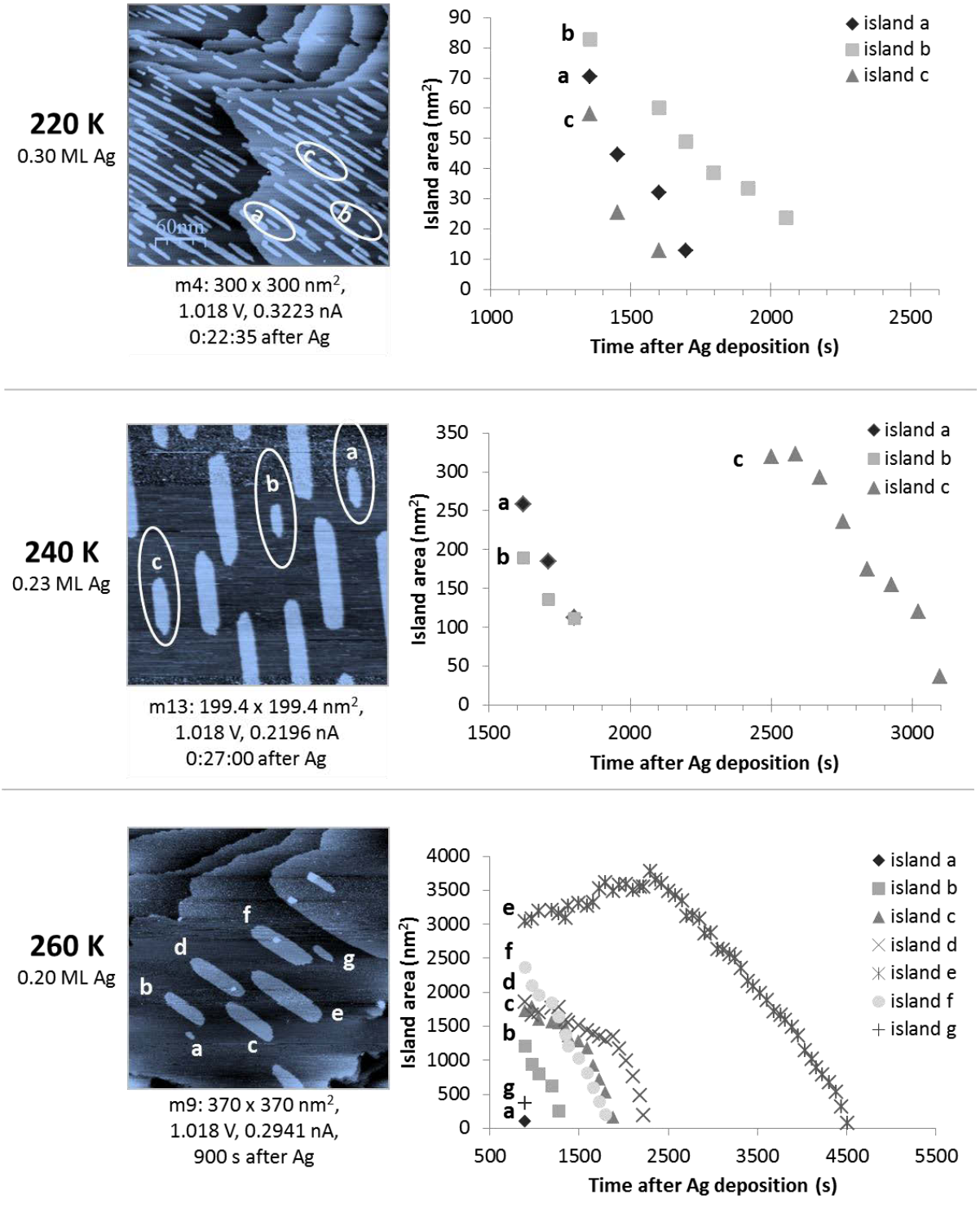

Figure 7. continued.

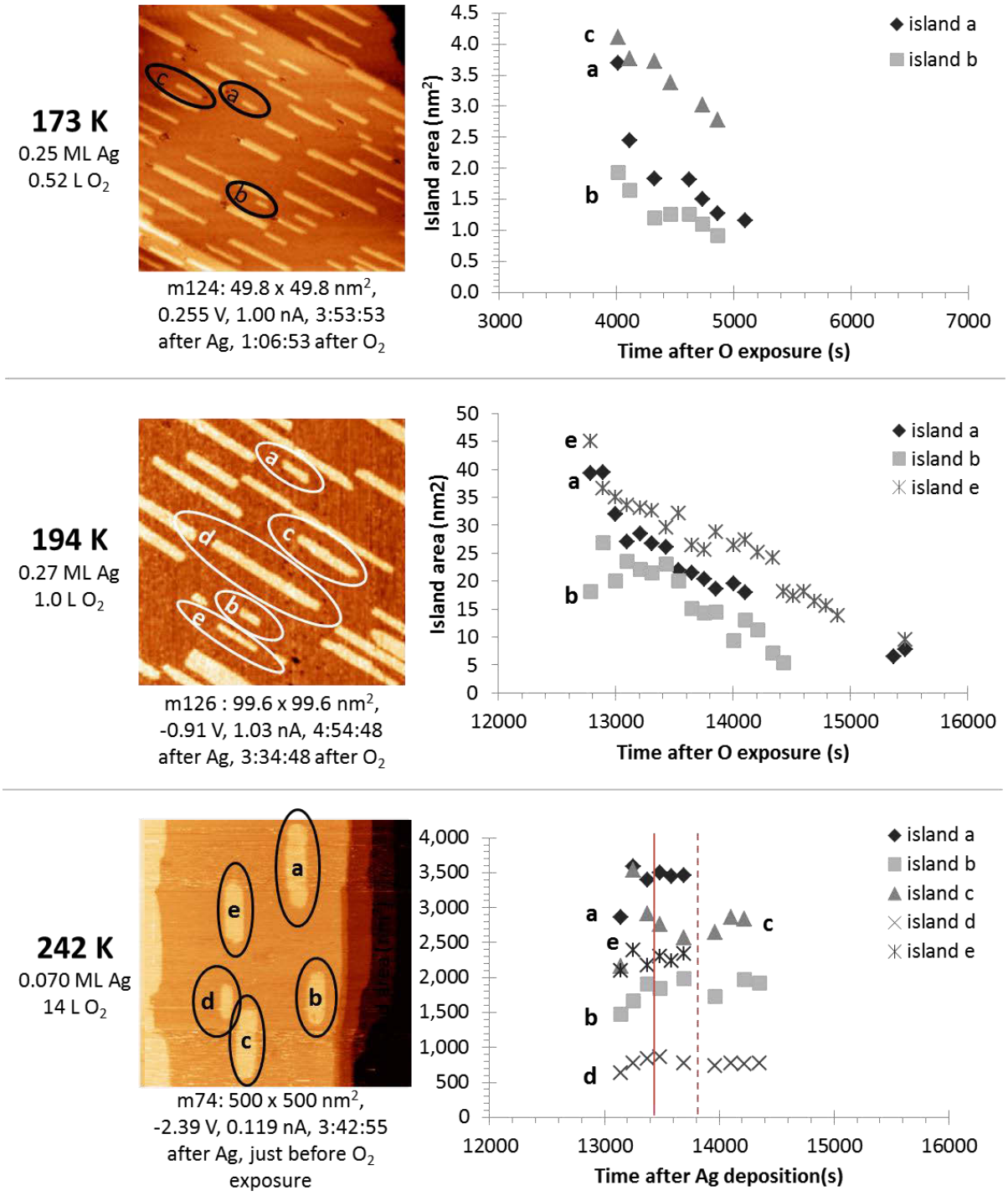

Figure 8. Individual island decay at different temperatures and oxygen exposures. At 242 K, unlike the other oxygen experiments, the surface was observed during oxygen exposure: the solid vertical line represents when exposure began and the dashed line when it ended.

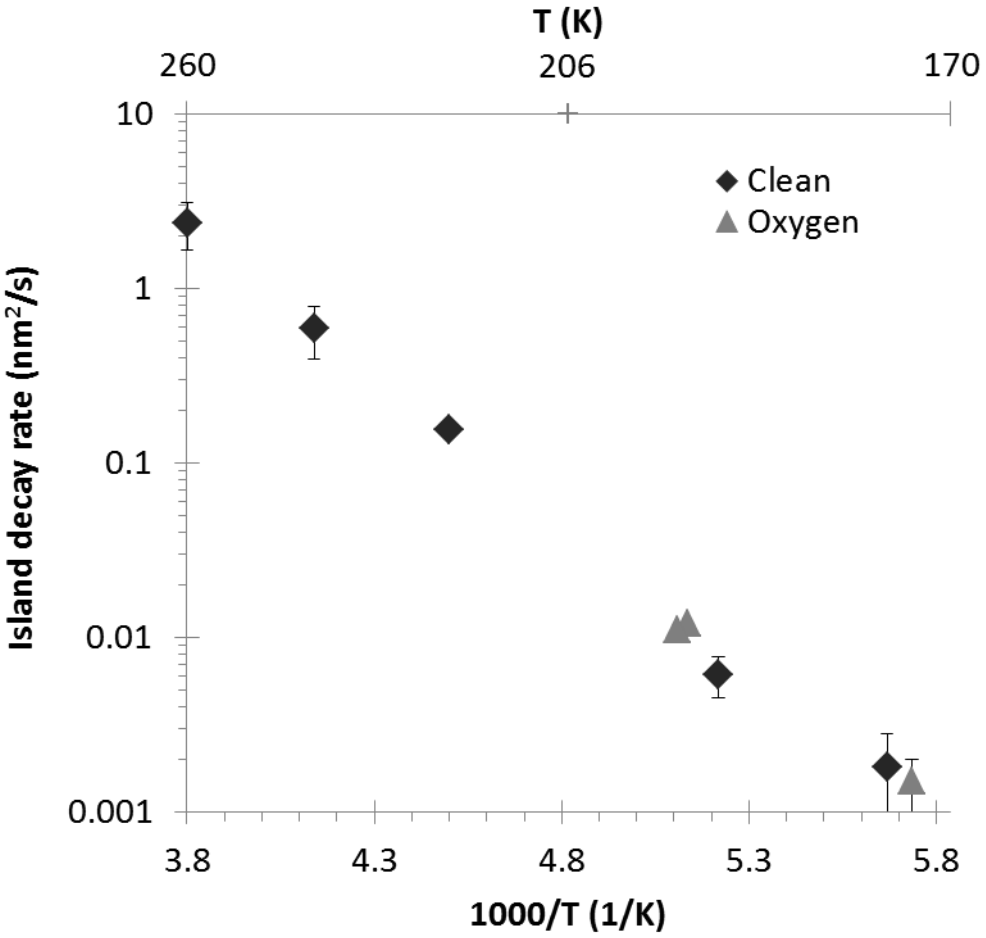

Figure 9. Individual island decay rate as a function of temperature for the clean system (ARL: 190 – 260 K,[53] SMR *et al.*: 175 K) and after oxygen exposure (SMR *et al.*). Islands were all initially less than 500 nm^2, except islands at 260 K were 946 to 3779 nm^2.

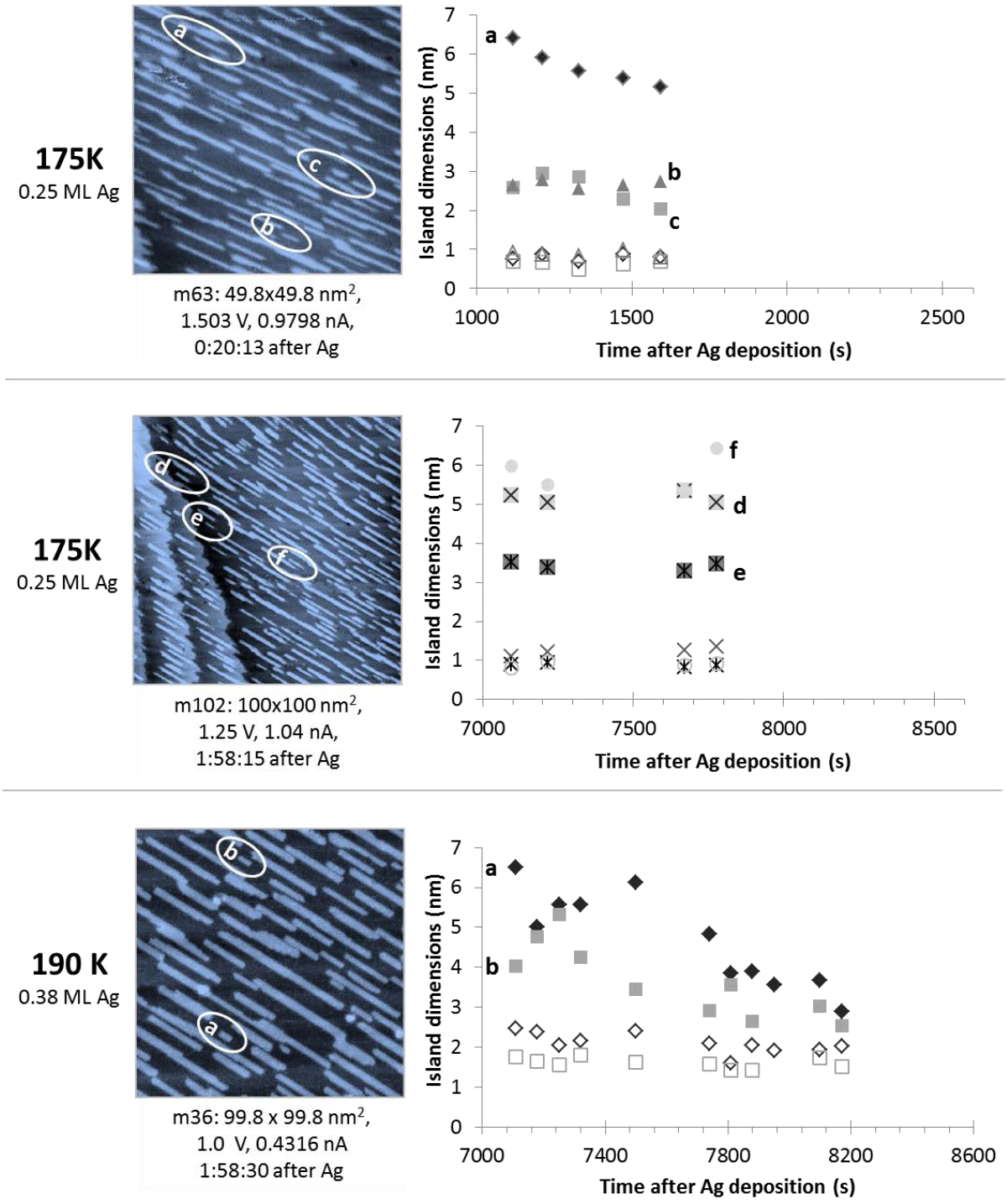

This figure continues on the following page.

Figure 10. Clean-surface, individual island decay along the long <110> (filled points) and short <001> (open points) directions at different temperatures, 175 – 260 K. All with flux = 45 mML/s, except at 175 K where the flux was 21 mML/s.

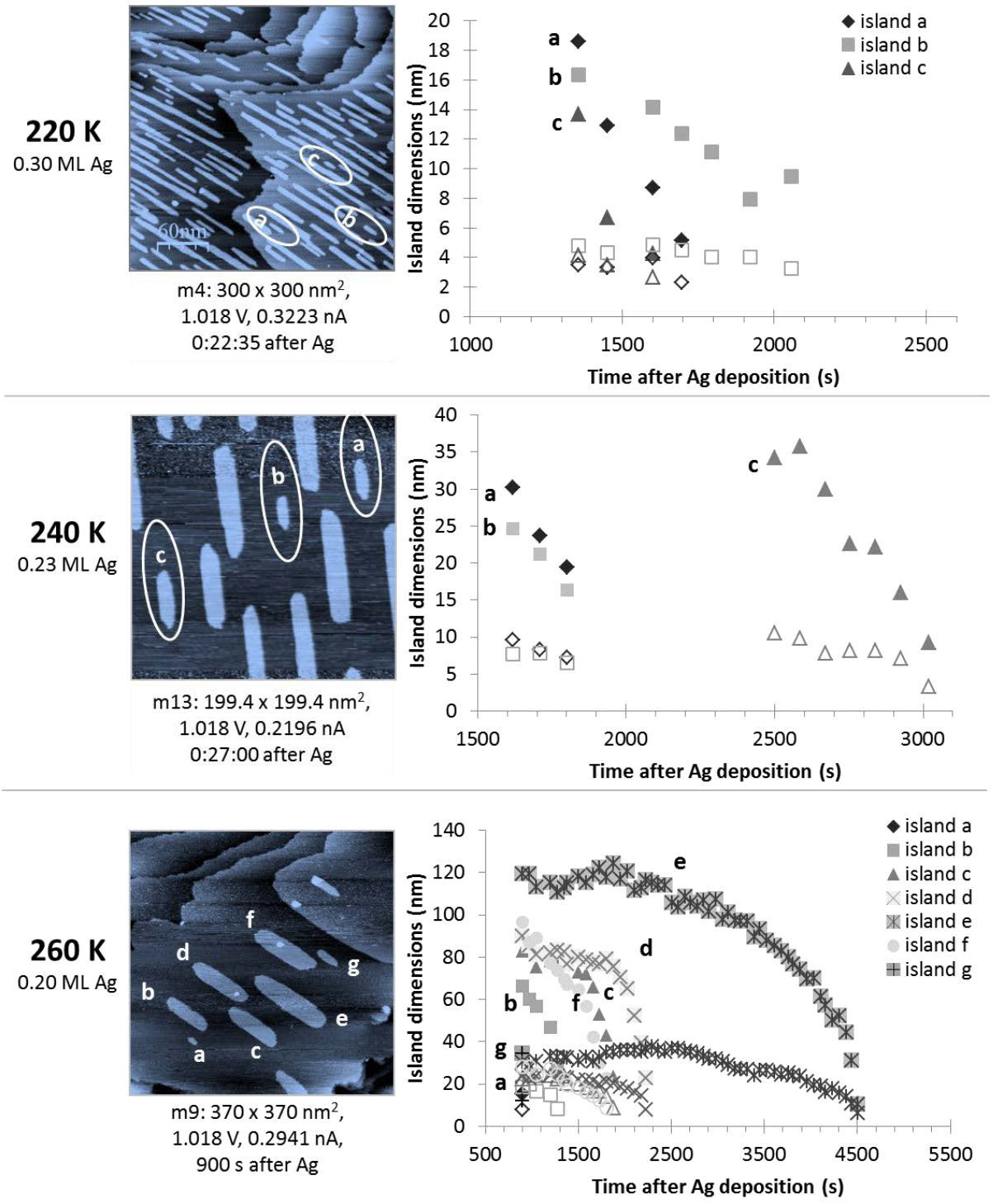

Figure 10. continued.

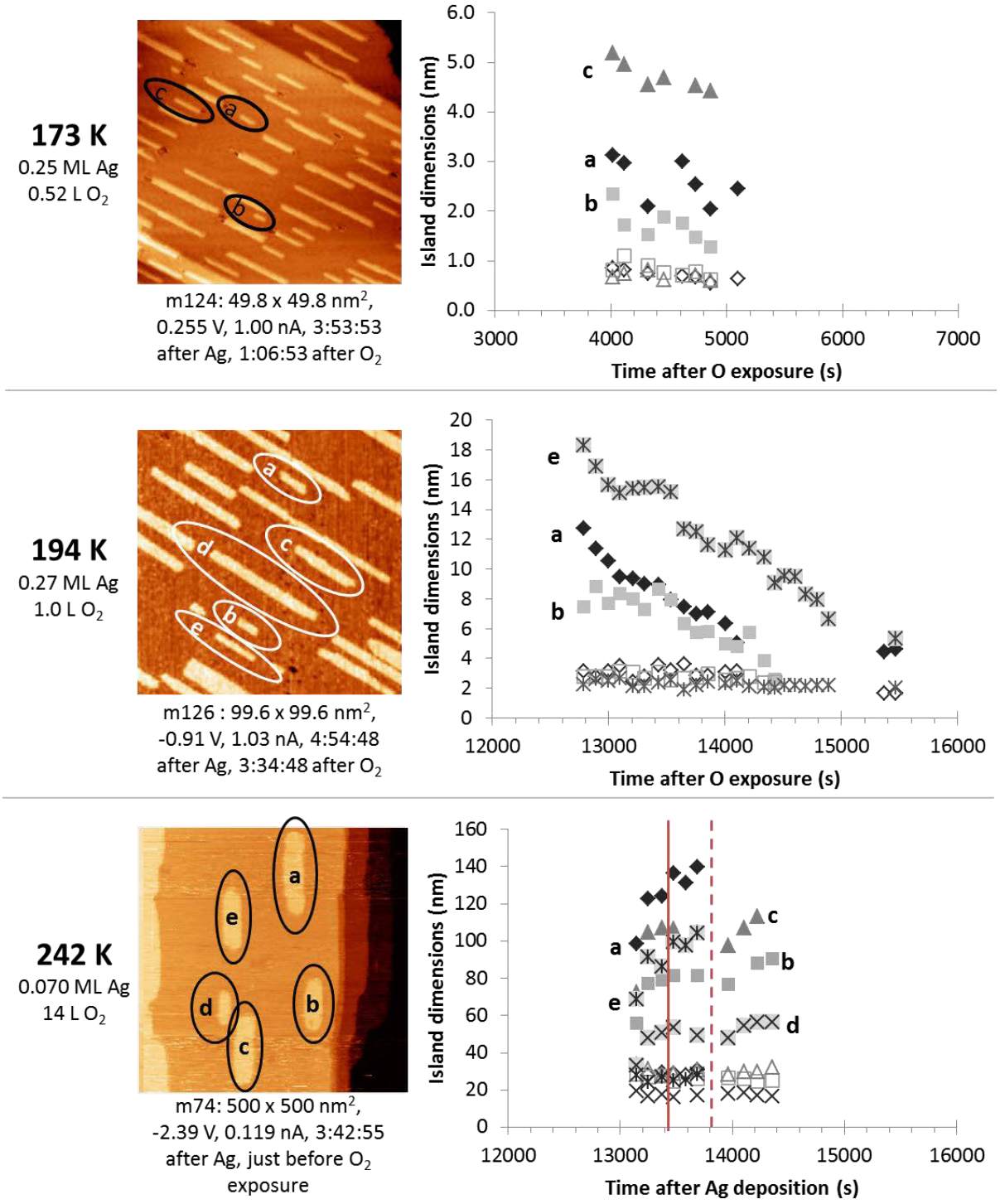

Figure 11. Individual island decay with oxygen, along the long <110> (filled points) and short <001> (open points) axes. At 242 K, the solid vertical line represents when O_2 exposure began, the dashed line when it ended.

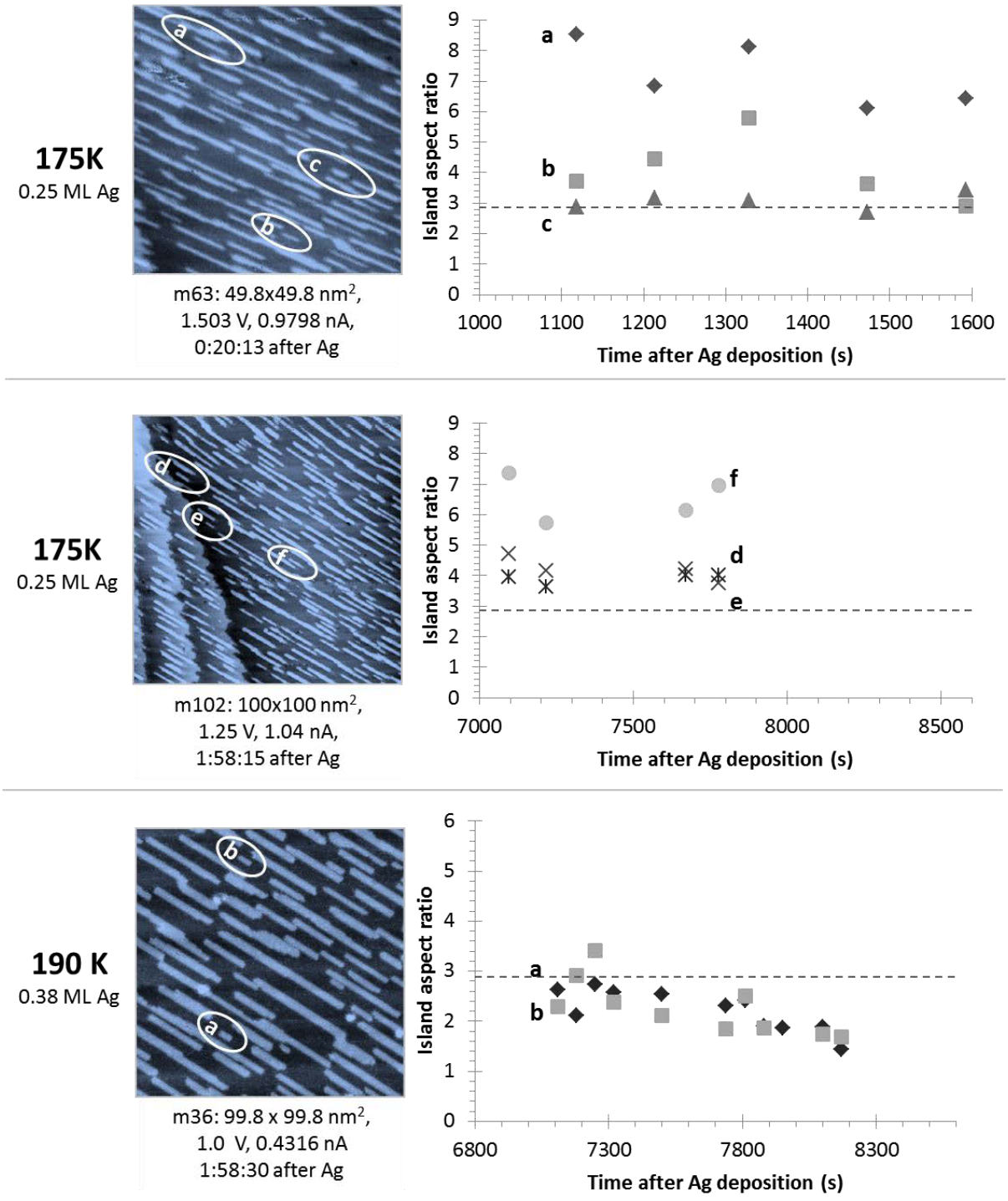

This figure continues on the following page.

Figure 12. Individual island aspect ratio evolution at different temperatures, 175 – 260 K. The horizontal dashed line marks reported $R_{eq} = 2.9 \pm 0.4$.[39]

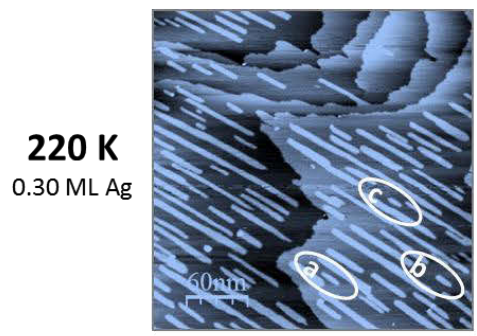

220 K
0.30 ML Ag

m4: 300 x 300 nm^2,
1.018 V, 0.3223 nA
0:22:35 after Ag

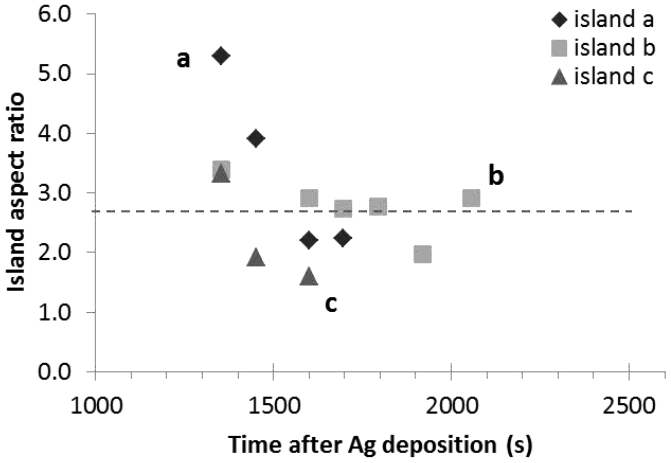

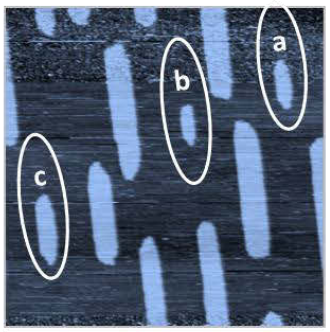

240 K
0.23 ML Ag

m13: 199.4 x 199.4 nm^2,
1.018 V, 0.2196 nA
0:27:00 after Ag

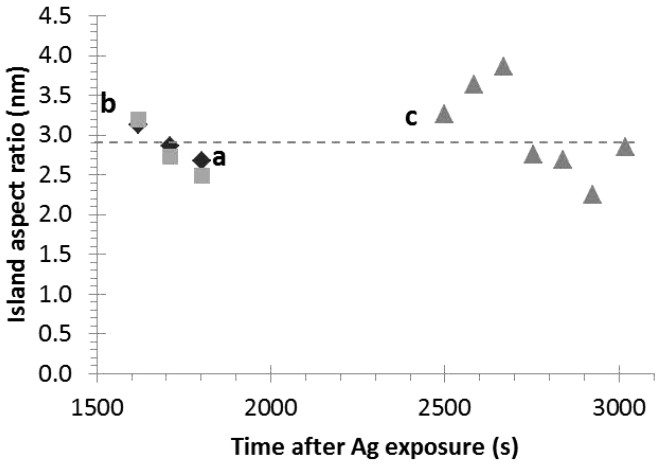

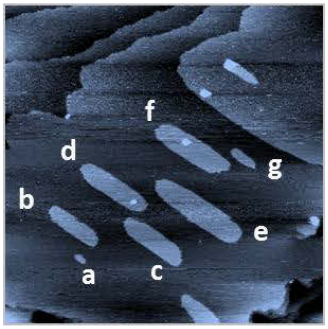

260 K
0.20 ML Ag

m9: 370 x 370 nm^2,
1.018 V, 0.2941 nA,
900 s after Ag

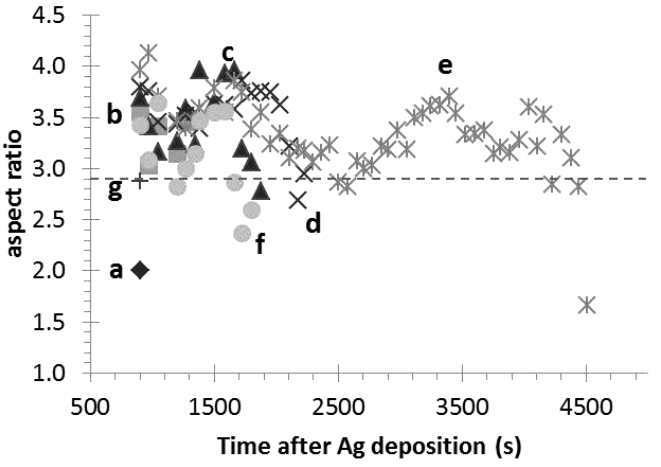

Figure 12. continued.

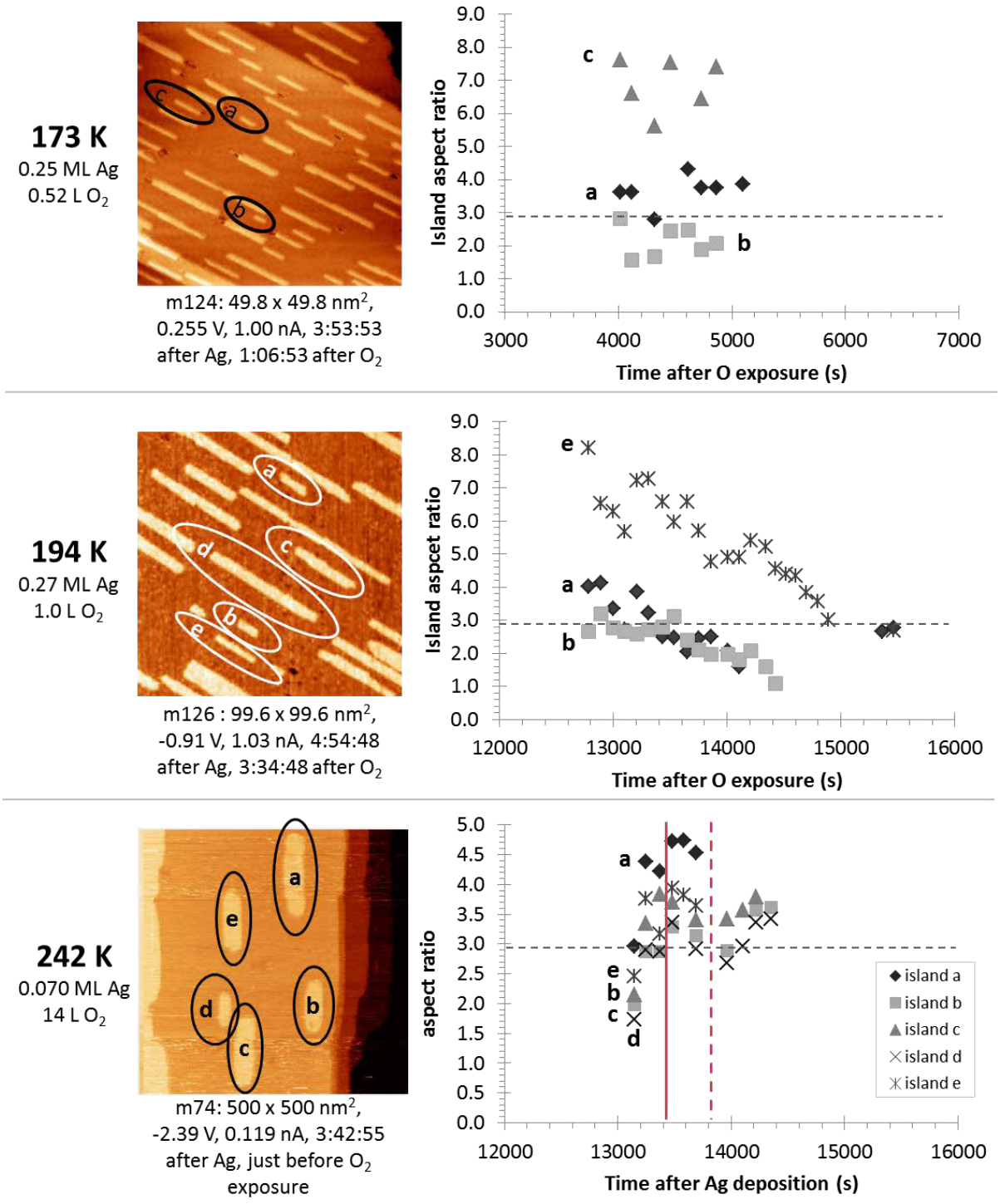

Figure 13. Individual island aspect ratio evolution at different temperatures and oxygen exposures. The horizontal dashed line marks the equilibrium ratio of 2.9 ± 0.4.[39]

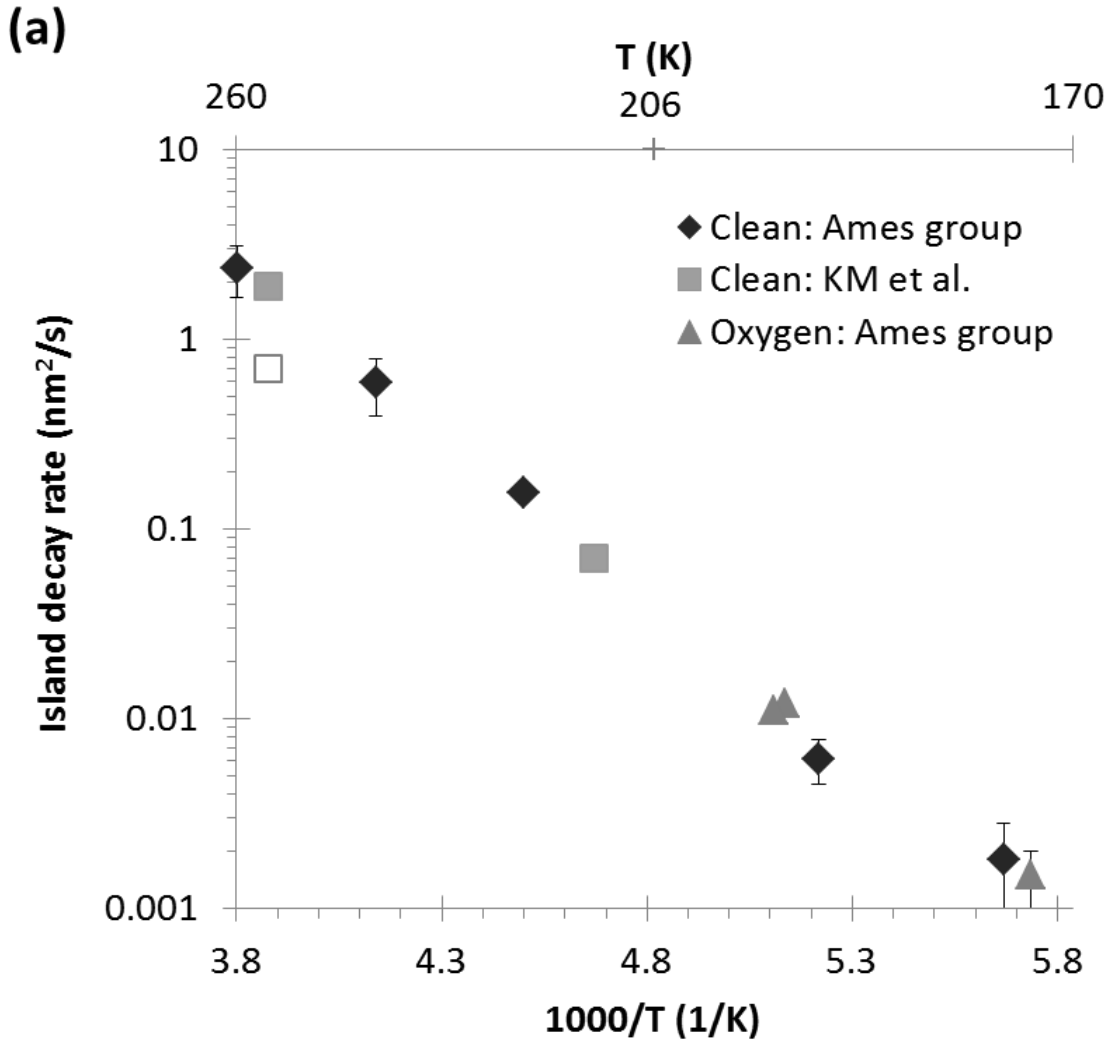

This figure continues on the following page.

Figure 14. Individual island decay rate as a function of temperature for the clean system, comparing our data (ARL: 190 – 260 K,[53] SMR *et al.*: 175 K) with K. Morgenstern *et al.*'s data.[39] The data at 255 K are for the same island with the open square representing the overall rate from initial island size 2900 to 0 nm^2, and the filled square representing the rate after the island size reached 100 nm^2. Islands in the Ames group data were all initially less than 500 nm^2, except islands at 260 K were initially 946 to 3779 nm^2. (b) Data presented in (a) with different axes. The slope of the best-fit line through all filled points is -3909.8 K with a R^2 value of 0.9957, which gives an effective activation barrier, E_{eff} of 0.34 eV.

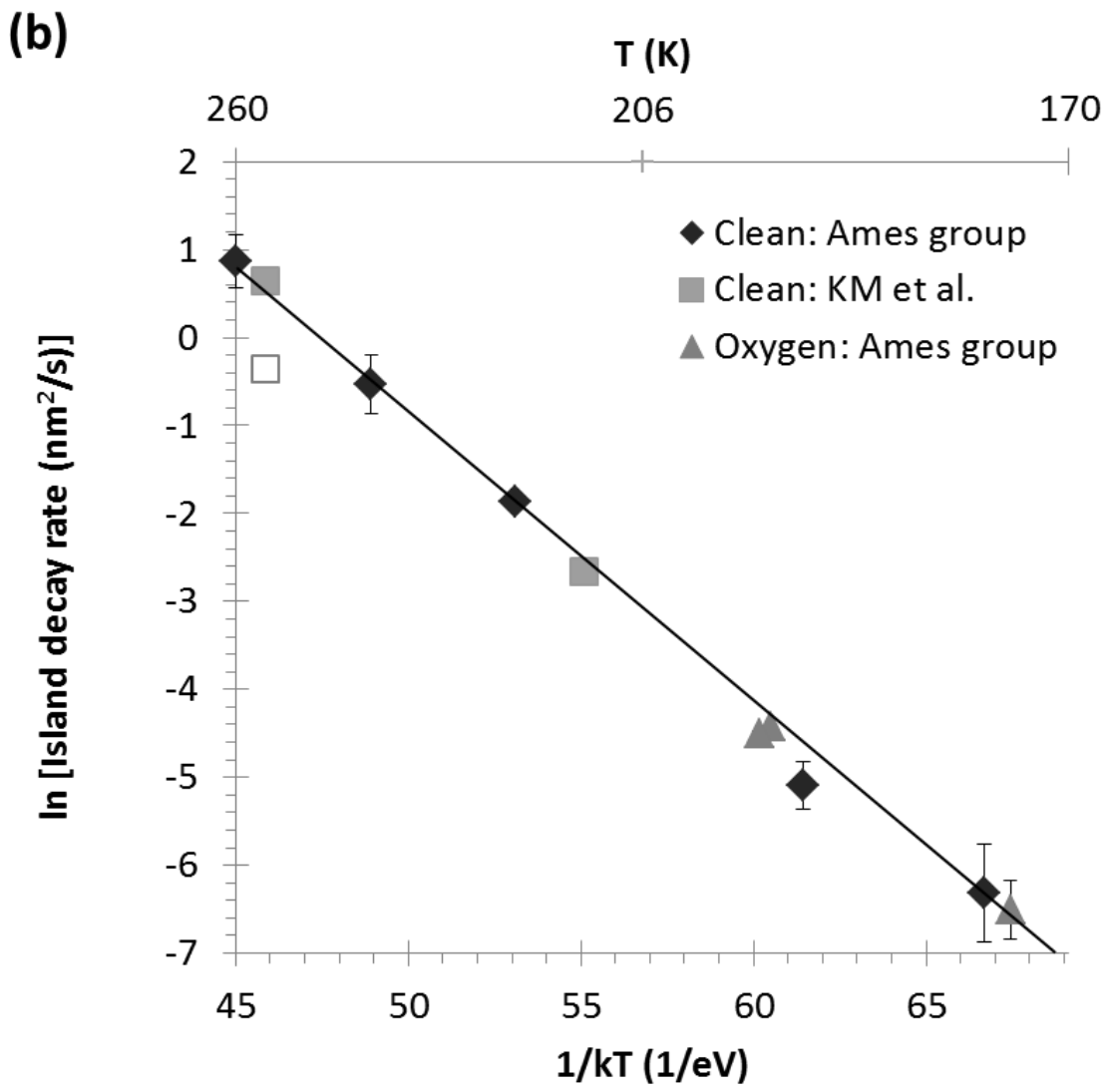

Figure 14. continued.

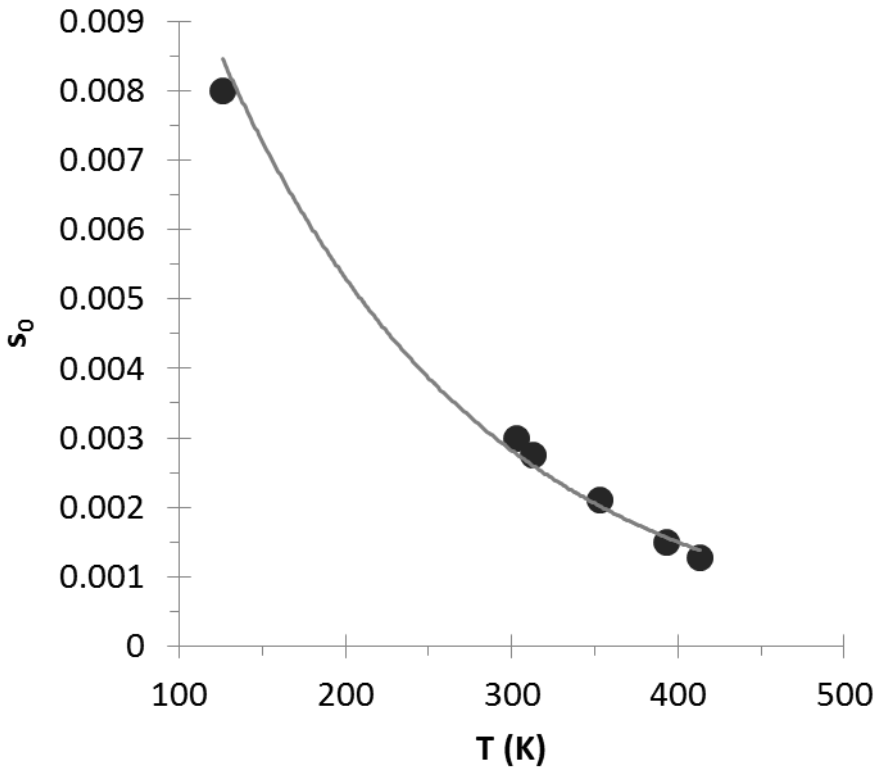

Figure 15. Initial sticking coefficient s_0 of O_2 on Ag(110) as a function of temperature. Experimental data at 303 K and higher are from Engelhardt and Menzel[70] and datum at 126 K is from Barteau and Madix[71] (who also reproduce the room temperature point). The best fit gives line equation $s_0 = 0.0187$ K ($e^{-0.006\ T}$). This data is used to estimate s_0 under our experimental conditions to provide an estimate of the oxygen coverage in monolayers (ML). Results in Table III.

.

Tables

Table I. Ag/Ag(110) island decay rates without oxygen exposure, derived from data presented in Fig. 7, Fig. 10, and Fig. 12. Rates are taken from linear fits across all points; negative slopes indicate shrinkage. The error associated with such a fit can be quite high as the plots are not necessarily linear. Hence, these data are presented as a guide to the trends observed. Comparison between islands and between experiments should be made with caution.

	Island	Initial area (nm^2) [at beginning of t range]	Area decay rate (nm^2/s)	Dimension decay rate		Aspect ratio		Time t range (s)
				Long (nm/s)	Short (nm/s)	Decay rate (1/s)	Mean ratio	
175 K 5/24/2010 0.31 ML Ag	a	4.89	-0.0027	-0.0025	0.00010	-0.0041	7.21	all
	b	1.61	-0.0010	-0.0015	0.000007	-0.0023	4.10	all
	c	3.31	-0.0033	0.000030	-0.00010	0.00050	3.05	all
	d	5.80	-0.0011	0.000020	0.00030	-0.00090	4.20	all
	e	2.85	-0.0014	0.00030	-0.00010	0.00030	3.90	all
	f	4.64	-0.0011	-0.00010	0.000060	-0.00020	6.54	all
	mean	**3.85**	**-0.002**	**-0.0006**	**0.00004**	**-0.001**	5	—
	std.dev.	1.54	0.001	0.0011	0.00015	0.002	2	—
190 K 12/19/2000 0.38 ML Ag	a	13	-0.0073	-0.0028	-0.00040	-0.0009	2.22	all
	b	8	-0.0050	-0.0020	-0.00020	-0.001	2.28	all
	mean	**10**	**-0.006**	**-0.0024**	**-0.0003**	**-0.00095**	2.25	—
	std.dev.	4	0.002	0.0006	0.0001	0.00007	0.04	—
220 K 1/3/2000 0.30 ML Ag	a	71	-0.16	-0.038	-0.0022	-0.0094	3.41	all
	b	83	-0.085	-0.012	-0.0019	-0.0012	2.79	all
	c	58	-0.176	-0.037	-0.0022	-0.0066	2.27	all
	mean	**71**	**-0.139**	**-0.029**	**-0.0021**	**-0.0057**	**2.82**	
	std.dev.	12	0.048	0.015	0.0002	0.0042	0.57	
240 K 1/4/2000 0.23 ML Ag	a	258	-0.80	-0.059	-0.0130	-0.0025	2.89	all
	b	189	-0.43	-0.046	-0.0064	-0.0039	2.80	all
	c	427	-0.53	-0.018	-0.0043	-0.00050	3.16	all
	mean	**292**	**-0.6**	**-0.04**	**-0.008**	**-0.002**	**3.0**	—
	std.dev.	123	0.2	0.02	0.005	0.002	0.2	—

This table continues on the following page.

Table I. continued.

	Island	Initial area (nm^2) [at beginning of t range]		Area decay rate (nm^2/s)	Dimension decay rate		Aspect ratio		Time t range (s)
					Long (nm/s)	Short (nm/s)	Decay rate (1/s)	Mean ratio	
260 K 1/6/2000 0.20 ML Ag	a	98	—	—	—	—	—	—	—
	b	1209	[946]	-2.1	-0.10	-0.026	3.32	3.41	975-1275
	c	1727	[1484]	-2.3	-0.093	-0.013	3.46	3.41	1350-1880
	d	1857	[1164]	-3.5	-0.17	-0.0081	3.52	3.60	1955-2225
	e	3046	[3779]	-1.6	-0.036	-0.0054	3.32	3.33	2296-4508
	f	2369	[2100]	-2.4	-0.077	-0.0021	3.13	3.11	975-1800
	g	364	—	—	—	—	—	—	—
	mean	**1524**		**-2.4**	**-2.4**	**-0.10**	**-0.011**	**3.3**	—
	std.dev.	1054		0.7	0.7	0.05	0.009	0.2	—

Table II. O/Ag/Ag(110) rates extrapolated from data presented in Figs. 8, 11, and 13. Determined in the same way as the data in Table I. The asterisked (*) values at 194 K include only the asterisked islands.

	Island	Initial area (nm^2)	Area decay rate (nm^2/s)	Dimension decay rate		Aspect ratio		Time t range (s)
				Long (nm/s)	Short (nm/s)	Decay rate (1/s)	Mean ratio	
173 K 5/20/2010 0.25 ML Ag 0.52 L O_2	a	3.70	-0.0019	-0.00060	-0.00020	0.00040	3.68	all
	b	1.94	-0.0010	-0.00080	-0.00040	-0.00020	2.14	all
	c	4.11	-0.0015	-0.00080	-0.00010	-0.00007	6.88	all
	mean	**3.25**	**-0.0015**	**-0.0007**	**-0.0002**	**0.00004**	**4**	—
	std.dev.	1.15	0.0005	0.0001	0.0002	0.00032	2	—
193 K 7/7/2010 0.10 ML Ag 13 L O_2	a	8.09	-0.0012	-0.00050	-0.000030	-0.0030	2.15	all
194 K 5/26/2010 0.27 ML Ag 1.0 L O_2	a*	39.4	-0.011	-0.0028	-0.00050	-0.00050	2.83	all
	b*	18.2	-0.011	-0.0031	-0.00030	-0.00090	2.34	all
	c	87.5	-0.0084	-0.0016	-0.00020	-0.0018	6.67	all
	d	197	-0.015	-0.0019	-0.000040	-0.00050	10.6	all
	e*	45.0	-0.011	-0.0047	-0.00010	-0.0018	5.35	all
	mean	**77.5**	**-0.011**	**-0.003**	**-0.0002**	**-0.0011**	**6**	—
	std.dev.	71.6	0.002	0.001	0.0002	0.0007	3	—
	mean*	**34.2**	**-0.0110**	**-0.004**	**-0.0003**	**-0.0011**	**4**	—
	std.dev.*	14.2	0.0004	0.001	0.0002	0.0007	2	—
242 K 2/16/2012 0.07 ML Ag 14 L O_2	a	2857	0.70	0.064	-0.0035	0.025	4.26	all
	b	1476	0.24	0.017	-0.0019	0.00090	3.03	all
	c	2163	-0.0076	0.017	-0.00040	0.00070	3.40	all
	d	629	0.014	0.011	-0.0005	0.00070	2.91	all
	e	2094	0.23	0.054	-0.0013	0.0018	3.46	all
	mean	**1844**	**0.2**	**0.03**	**-0.002**	**0.006**	**3.4**	—
	std.dev.	837	0.3	0.02	0.001	0.011	0.5	—

Table III. Estimated initial sticking coefficient and oxygen coverage based on data in Fig. 15.

T (K)	L O_2	s_0	ML O_2
173	0.52	0.0066	0.003
174	1.1	0.0066	0.007
193	13	0.0059	0.08
194	1.0	0.0058	0.006
242	14	0.0044	0.06

Table IV. Experiment summary.

Sample T (K)	Ag coverage (ML)	Flux (mML/s)	O_2 exposure (L)	Estimated O coverage (ML)	Date
140	0.20	45			1/7/2000
160	0.19	48			1/23/2000
173	0.25	16	0.52	0.003	5/20/2010
175	0.26	45			12/12/1999
175	0.31	21	1.1	0.007	5/24/2010
190	0.38	45			12/19/1999
193	0.10	6.6	13	0.08	7/7/2010
194	0.27	18	1.0	0.006	5/26/2010
205	0.35	45			12/21/1999
220	0.30	45			1/2/2000
240	0.23	45			1/4/2000
242	0.07	70	14 *during imaging*	0.06	2/16/2012
245	0.11	57	20 *during imaging*	0.09	2/25/2012
260	0.20	45			1/6/2000

Table V. Tunneling conditions during O/Ag/Ag(110) experiments.

Expt. →		173 K 5/20/2010		175 K 5/24/2010		194 K 5/26/2010		193 K 7/7/2010		242 K 2/16/2012		245 K 2/25/2012	
STM tip material →		Etched W		Etched W		Etched W		Etched W		Cut PtIr		Cut PtIr	
↓ Condition		**bias (V)**	**current (nA)**	**bias (V)**	**current (nA)**	**bias (V)**	**current (nA)**	**bias (V)**	**current (nA)**	**bias (V)**	**current (nA)**	**bias (V)**	**current (nA)**
after Ag	**mean**	**-1.34**	**1.05**	**1.17**	**0.93**	**-1.28**	**0.98**	**-1.68**	**0.99**	**-2.27**	**0.160**	**-1.61**	**0.120**
	std.dev.	0.25	0.77	0.93	0.25	0.21	0.28	0.28	0.13	0.24	0.097	0.12	0.057
	median	-1.50	0.95	1.50	0.97	-1.26	1.00	-1.54	1.00	-2.26	0.141	-1.59	0.100
	max.	-1.01	5.02	2.75	1.47	-1.00	1.57	-1.42	1.24	-1.56	0.434	-1.10	0.205
	min.	-1.73	0.11	-1.51	0.04	-1.47	0.06	-2.38	0.17	-2.73	0.025	-1.70	0.046
during O_2 exp.	**mean**									**-2.41**	**0.081**	**-1.70**	**0.072**
	std.dev.									0.07	0.040	0.00	0.008
	median									-2.37	0.084	-1.70	0.069
	max.									-2.37	0.120	-1.70	0.084
	min.									-2.49	0.040	-1.70	0.065
after O_2 exp.	**mean**	**-0.90**	**1.29**	**-1.16**	**1.23**	**-0.82**	**0.96**	**-1.42**	**1.00**	**-2.03**	**0.060**	**-1.70**	**0.066**
	std.dev.	1.19	1.77	0.95	1.17	0.64	0.31	0.00	0.25	0.24	0.034	0.00	0.014
	median	-1.00	0.99	-1.06	0.97	-0.91	0.99	-1.42	1.02	-2.03	0.061	-1.70	0.062
	max.	2.37	9.90	2.54	6.80	1.60	1.93	-1.42	1.47	-1.76	0.092	-1.70	0.087
	min.	-3.61	0.01	-3.33	0.03	-2.23	0.06	-1.42	0.05	-2.30	0.027	-1.70	0.048
overall	**mean**	**-1.16**	**1.14**	**0.12**	**1.07**	**-0.93**	**0.96**	**-1.55**	**1.00**	**-2.26**	**0.143**	**-1.64**	**0.105**
	std.dev.	0.80	1.27	1.49	0.82	0.59	0.30	0.24	0.19	0.24	0.095	0.11	0.054
	median	-1.38	0.96	1.25	0.97	-0.91	0.99	-1.42	1.01	-2.26	0.136	-1.70	0.087
	max.	2.37	9.90	2.75	6.80	1.60	1.93	-1.42	1.47	-1.56	0.434	-1.10	0.205
	min.	-3.61	0.01	-3.33	0.03	-2.23	0.06	-2.38	0.05	-2.73	0.025	-1.70	0.046

Appendix 1. Island density decay

Looking at the initial island density N decay as a function of temperature may approximately give the effective activation barrier to OR

$$N_{isl}(t) = N_{isl}(0)\left(1+\frac{t}{\tau}\right)^{-n}$$

with characteristic time τ and effective coarsening barrier E_{eff}

$$\tau = \tau_0 \exp\left(-E_{eff}/kT\right)$$

then

$$\frac{dN_{isl}}{dt} = \left[\frac{n}{\tau_0}\left(N_{isl}(0)\right)^{-1/n}\left(N_{isl}(t)\right)^{(n+1)/n}\right]e^{\left(-E_{eff}/kT\right)}$$

and at t = 0

$$\frac{dN_{isl}}{dt(t=0)} = \left[\frac{n}{\tau_0}\left(N_{isl}(0)\right)\right]e^{\left(-E_{eff}/kT\right)}$$

$$\ln\frac{\frac{dN_{isl}(t)}{dt(t=0)}}{N_{isl}(0)} \propto \frac{-E_{eff}}{kT}$$

Figure A.1.1 shows that the low temperature data is in better agreement with E_{eff} determined from individual island decay in Section 4.1. above. The results are summarized in Table A.I.

Table A1.I. Effective coarsening barrier from initial island density decay

Data set	E_{eff}	R^2
ARL	0.0793	0.9344
SMR	0.4324	0.7942
all	0.1059	0.4303
below 200 K	0.3475	0.6559
above 200 K	0.0661	0.7707

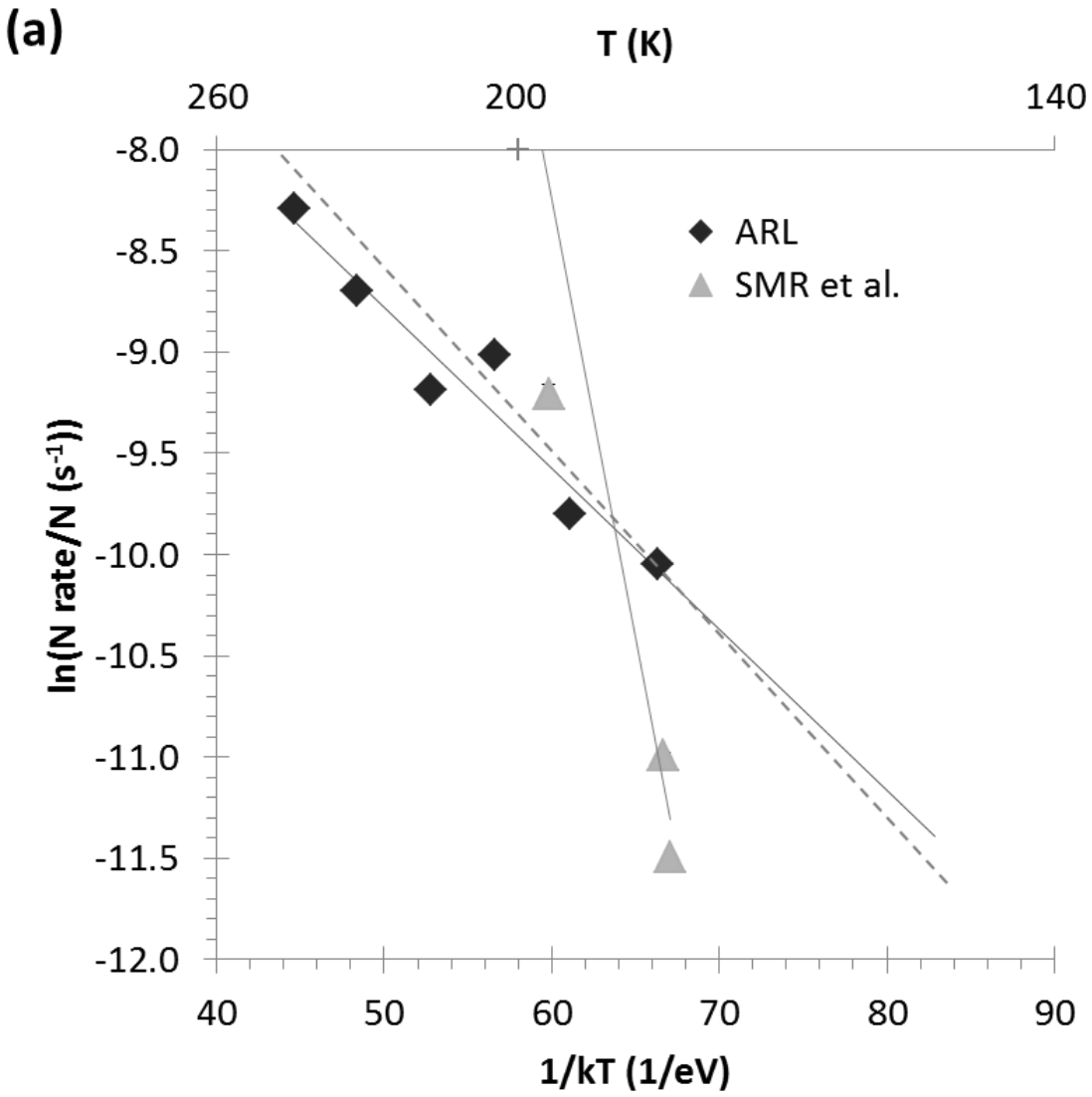

This figure continues on the following page.

Figure A1.1. Island density decay rate as a function of temperature for the clean system. (a) The slope gives another estimate effective activation barrier to OR: ARL = 0.079 eV, SMR *et al.* = 0.43 eV, both data sets = 0.11 eV. (b) There appears to be a break at ~200 K, considering just the points below 200 K, E_{eff} ~ 0.35 eV. Continues on the following page.

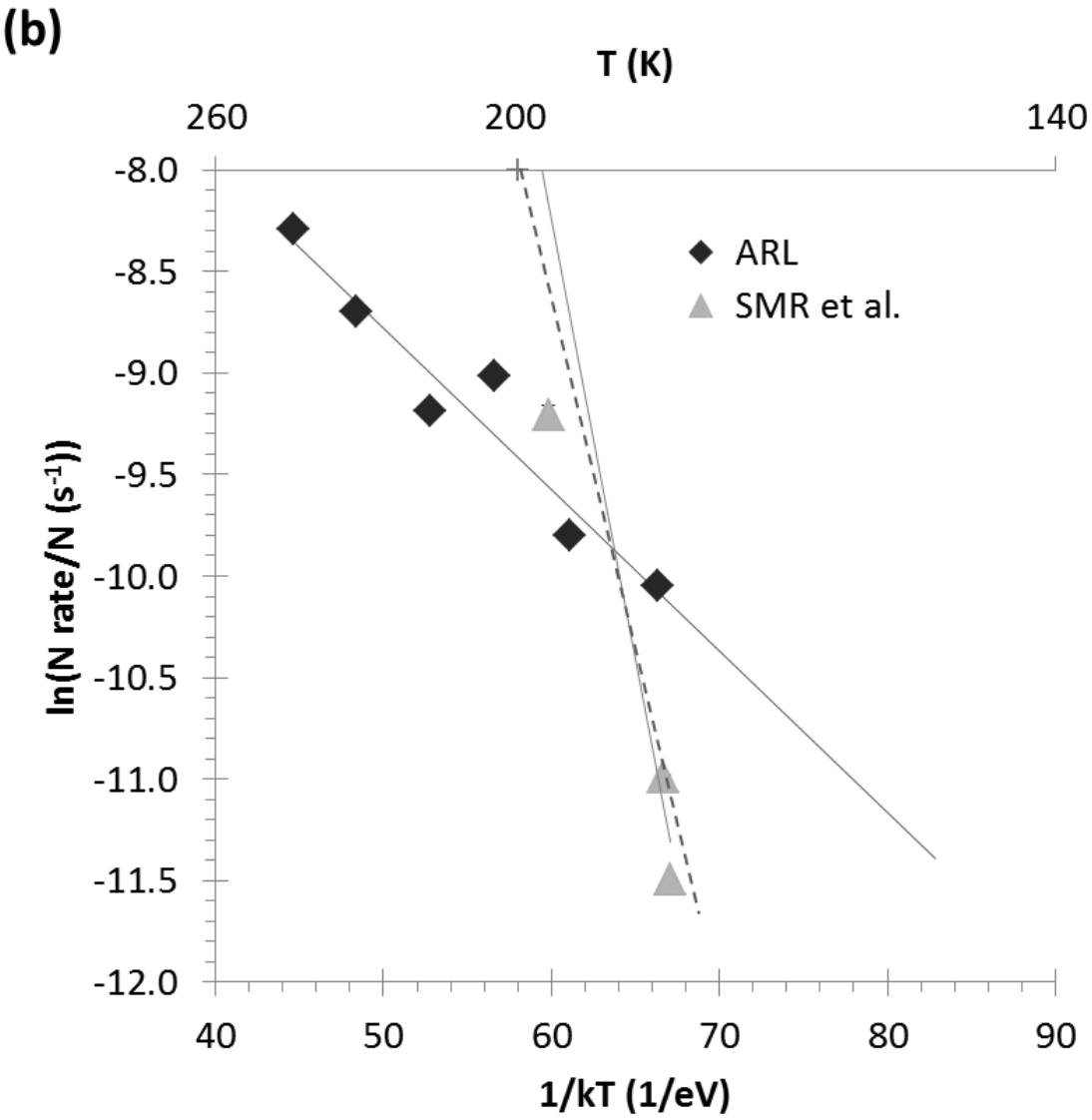

Figure A1.1. continued.

Appendix 2. Labeled Arrhenius plot

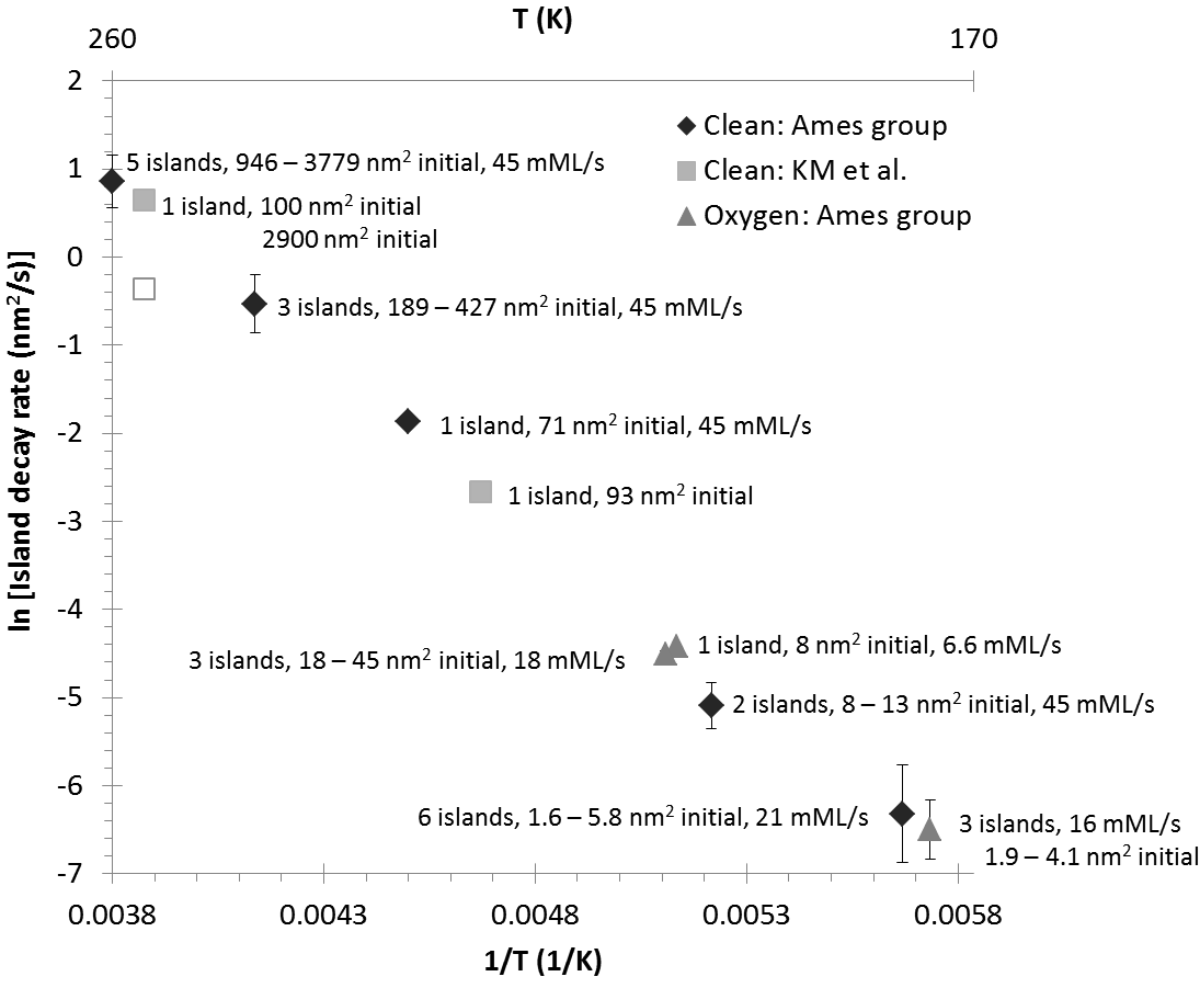

Figure A1.2. Individual island decay rate as a function of temperature for the clean system, comparing our data (ARL: 190 – 260 K,[53] SMR *et al.*: 175 K) with K. Morgenstern *et al.*'s data[39]. The data at 255 K are for the same island with the open square representing the overall rate from initial island size 2900 to 0 nm^2, and the filled square representing the rate after the island size reached 100 nm^2. Islands in the Ames group data were all initially less than 500 nm^2, except islands at 260 K were initially 946 to 3779 nm^2.

References

(1) Harris, P. J. F. *International Materials Reviews* **1995**, *40*, 97.

(2) Bowker, M. *Physical Chemistry Chemical Physics* **2007**, *9*, 3514.

(3) Burda, C.; Chen, X.; Narayanan, R.; El-Sayed, M. A. *Chemical Reviews* **2005**, *105*, 1025.

(4) Campbell, C. T.; Parker, S. C.; Starr, D. E. *Science* **2002**, *298*, 811.

(5) Yang, H. G.; Zeng, H. C. *Journal of Physical Chemistry B* **2004**, *108*, 3492.

(6) Brandstetter, T.; Wagner, T.; Fritz, D. R.; Zeppenfeld, P. *Journal of Physical Chemistry Letters* **2010**, *1*, 1026.

(7) Antczak, G.; Ehrlich, G. *Surface Science Reports* **2007**, *62*, 39.

(8) Ostwald, W. *Lehrbuch der Allgemeinen Chemie*; W. Engelmann: Leipzig, Germany, 1902; Vol. 2.

(9) von Smoluchowski, M. *Physikalische Zeitschrift* **1916**, *17*, 557.

(10) Bardotti, L.; Stoldt, C. R.; Jenks, C. J.; Bartelt, M. C.; Evans, J. W.; Thiel, P. A. *Physical Review B* **1998**, *57*, 12544.

(11) Stoldt, C. R.; Cadilhe, A. M.; Bartelt, M. C.; Jenks, C. J.; Thiel, P. A.; Evans, J. W. *Progress in Surface Science* **1998**, *59*, 67.

(12) Bardotti, L.; Bartelt, M. C.; Jenks, C. J.; Stoldt, C. R.; Wen, J. M.; Zhang, C. M.; Thiel, P. A.; Evans, J. W. *Langmuir* **1998**, *14*, 1487.

(13) Cadilhe, A. M.; Stoldt, C. R.; Jenks, C. J.; Thiel, P. A.; Evans, J. W. *Physical Review B* **2000**, *61*, 4910.

(14) Pai, W. W.; Wendelken, J. F.; Stoldt, C. R.; Thiel, P. A.; Evans, J. W.; Liu, D.-J. *Physical Review Letters* **2001**, *86*, 3088.

(15) Thiel, P. A.; Evans, J. W. *Journal of Physical Chemistry B* **2004**, *108*, 14428.

(16) Caspersen, K. J.; Stoldt, C. R.; Layson, A. R.; Bartelt, M. C.; Thiel, P. A.; Evans, J. W. *Physical Review B* **2001**, *63*, 085401.

(17) Thiel, P. A.; Evans, J. W. *Journal of Physical Chemistry B* **2000**, *104*, 1663.

(18) Stoldt, C. R.; Jenks, C. J.; Thiel, P. A.; Cadilhe, A. M.; Evans, J. W. *Journal of Chemical Physics* **1999**, *111*, 5157.

(19) Thiel, P. A.; Evans, J. W. In *Morphological Organization in Epitaxial Growth and Removal*; Zhang, Z., Lagally, M. G., Eds.; World Scientific Publishing Co. Pte. Ltd.: Singapore, 1998; Vol. 14, p 384.

(20) Stoldt, C. R.; Cadilhe, A. M.; Jenks, C. J.; Wen, J. M.; Evans, J. W.; Thiel, P. A. *Physical Review Letters* **1998**, *81*, 2950.

(21) Zhang, C. M.; Bartelt, M. C.; Wen, J. M.; Jenks, C. J.; Evans, J. W.; Thiel, P. A. *Journal of Crystal Growth* **1997**, *174*, 851.

(22) Pai, W. W.; Swan, A. K.; Zhang, Z.; Wendelken, J. F. *Physical Review Letters* **1997**, *79*, 3210.

(23) Wen, J.-M.; Evans, J. W.; Bartelt, M. C.; Burnett, J. W.; Thiel, P. A. *Physical Review Letters* **1996**, *76*, 652.

(24) Wen, J. M.; Chang, S. L.; Burnett, J. W.; Evans, J. W.; Thiel, P. A. *Physical Review Letters* **1994**, *73*, 2591.

(25) Morgenstern, K.; Rosenfeld, G.; Poelsema, B.; Comsa, G. *Surface Science* **1996**, *352-354*, 956.

(26) Morgenstern, K.; Rosenfeld, G.; Comsa, G. *Physical Review Letters* **1996**, *76*, 2113.

(27) Eßer, M.; Morgenstern, K.; Rosenfeld, G.; Comsa, G. *Surface Science* **1998**, *402-404*, 341.

(28) Rosenfeld, G.; Morgenstern, K.; Beckmann, I.; Wulfhekel, W.; Laegsgaard, E.; Besenbacher, F. *Surface Science* **1998**, *402-404*, 401.

(29) Morgenstern, K.; Rosenfeld, G.; Lægsgaard, E.; Besenbacher, F.; Comsa, G. *Physical Review Letters* **1998**, *80*, 556.

(30) Morgenstern, K.; Rosenfeld, G.; Comsa, G. *Surface Science* **1999**, *441*, 289.

(31) Rosenfeld, G.; Morgenstern, K.; Esser, M.; Comsa, G. *Applied Physics A* **1999**, *69*, 489.

(32) Schlößer, D. C.; Morgenstern, K.; Verheij, L. K.; Rosenfeld, G.; Bensenbacher, F.; Cosma, G. *Surface Science* **2000**, *465*, 19.

(33) Morgenstern, K.; Rosenfeld, G.; Comsa, G.; Sørensen, M. R.; Hammer, B.; Lægsgaard, E.; Besenbacher, F. *Physical Review B* **2001**, *63*, 45412.

(34) Carlon, E.; van Beijeren, H. *Physical Review Letters* **1996**, *76*, 4191.

(35) Lorensen, H. T.; oslash; rskov, J. K.; Jacobsen, K. W. *Physical Review B* **1999**, *60*, R5149.

(36) Mottet, C.; Ferrando, R.; Hontinfinde, F.; Levi, A. C. *Surface Science* **1998**, *417*, 220.

(37) Ferrando, R.; Hontinfinde, F.; Levi, A. C. *Physical Review B* **1997**, *56*, R4406.

(38) Perkins, L. S.; DePristo, A. E. *Surface Science* **1994**, *317*, L1152.

(39) Morgenstern, K.; Laegsgaard, E.; Stensgaard, I.; Besenbacher, F.; Böhringer, M.; Schneider, W. D.; Berndt, R.; Mauri, F.; Devita, A.; Car, R. *Applied Physics A* **1999**, *69*, 559.

(40) Morgenstern, K.; Lægsgaard, E.; Besenbacher, F. *Physical Review B* **2002**, *66*, 115408.

(41) Buatier de Mongeot, F.; Costantini, G.; Boragno, C.; Valbusa, U. *Physical Review Letters* **2000**, *84*, 2445.

(42) Morgenstern, K.; Lægsgaard, E.; Stensgaard, I.; Besenbacher, F. *Physical Review Letters* **1999**, *83*, 1613.

(43) De Giorgi, C.; Aihemaiti, P.; de Mongeot, F. B.; Boragno, C.; Ferrando, R.; Valbusa, U. *Surface Science* **2001**, *487*, 49.

(44) Ferrando, R. *Physical Review Letters* **1996**, *76*, 4195.

(45) Hontinfinde, F.; Ferrando, R. *Physical Review B* **2001**, *63*, 121403.

(46) Hontinfinde, F.; Ferrando, R.; Levi, A. C. *Surface Science* **1996**, *366*, 306.

(47) Montalenti, F.; Ferrando, R. *Physical Review B* **1999**, *59*, 5881.

(48) Mottet, C.; Ferrando, R.; Hontinfinde, F.; Levi, A. C. *European Physical Journal D* **1999**, *9*, 561.

(49) Rusponi, S.; Boragno, C.; Ferrando, R.; Hontinfinde, F.; Valbusa, U. *Surface Science* **1999**, *440*, 451.

(50) Morgenstern, K.; Lægsgaard, E.; Besenbacher, F. *Physical Review Letters* **2001**, *86*, 5739.

(51) Stahrenberg, K.; Herrmann, T.; Esser, N.; Sahm, J.; Richter, W.; Hoffmann, S.; Hofmann, P. *Physical Review B* **1998**, *58*, R10207.

(52) Layson, A. R.; Thiel, P. A. *Surface Science* **2001**, *472*, L151.

(53) Layson, A. R. *The effect of oxygen on the growth and relaxation of silver thin films and associated nanostructures deposited on silver(100).* Ph.D. thesis, Iowa State University, (2001).

(54) Shen, M.; Russell, S. M.; Liu, D.-J.; Thiel, P. A. *Journal of Chemical Physics* **2011**, *135*, 154701.

(55) Shen, M. *Sulfur adsorption, structure, and effects on coarsening on Ag(111) and Ag(100).* Ph.D. thesis, Iowa State University, (2009).

(56) Shen, M.; Liu, D.-J.; Jenks, C. J.; Evans, J. W.; Thiel, P. A. *Surface Science* **2009**, *603*, 1486.

(57) Shen, M.; Liu, D.-J.; Jenks, C. J.; Thiel, P. A.; Evans, J. W. *Journal of Chemical Physics* **2009**, *130*, 094701.

(58) Verykios, X. E.; Stein, F. P.; Coughlin, R. W. *Journal of Catalysis* **1980**, *66*, 147.

(59) Verykios, X. E.; Stein, F. P.; Coughlin, R. W. *Catalysis Reviews* **1980**, *22*, 197.

(60) Serafin, J. G.; Liu, A. C.; Seyedmonir, S. R. *Journal of Molecular Catalysis A* **1998**, *131*, 157.

(61) Li, W.-X.; Stampfl, C.; Scheffler, M. *Physical Review B* **2003**, *68*, 165412.

(62) Li, W.-X.; Stampfl, C.; Scheffler, M. *Physical Review Letters* **2003**, *90*, 256102.

(63) Wodiunig, S.; Keel, J. M.; Wilson, T. S. E.; Zemichael, F. W.; Lambert, R. M. *Catalysis Letters* **2003**, *87*, 1.

(64) Reichelt, R.; Günther, S.; Rössler, M.; Wintterlin, J.; Kubias, B.; Jakobi, B.; Schlögl, R. *Physical Chemistry Chemical Physics* **2007**, *9*, 3590.

(65) Nguyen, N. L.; Piccinin, S.; de Gironcoli, S. *Journal of Physical Chemistry C* **2011**, *115*, 10073.

(66) Zhou, L.; Madix, R. J. *Langmuir* **2010**, *26*, 16282.

(67) Rovida, G.; Pratesi, F.; Maglietta, M.; Ferroni, E. *Journal of Vacuum Science & Technology* **1972**, *9*, 796.

(68) Heiland, W.; Iberl, F.; Taglauer, E.; Menzel, D. *Surface Science* **1975**, *53*, 383.

(69) Rovida, G.; Pratesi, F. *Surface Science* **1975**, *52*, 542.

(70) Engelhardt, H. A.; Menzel, D. *Surface Science* **1976**, *57*, 591.

(71) Barteau, M. A.; Madix, R. J. *Surface Science* **1980**, *97*, 101.

(72) Bowker, M.; Barteau, M. A.; Madix, R. J. *Surface Science* **1980**, *92*, 528.

(73) Campbell, C. T.; Paffett, M. T. *Surface Science* **1984**, *143*, 517.

(74) Outka, D. A.; Madix, R. J. *Surface Science* **1984**, *137*, 242.

(75) Bange, K.; Madey, T. E.; Sass, J. K. *Chemical Physics Letters* **1985**, *113*, 56.

(76) Prince, K. C.; Paolucci, G.; Bradshaw, A. M. *Surface Science* **1986**, *175*, 101.

(77) Sault, A. G.; Madix, R. J. *Journal of Physical Chemistry* **1988**, *92*, 6025.

(78) Capote, A. J.; Roberts, J. T.; Madix, R. J. *Surface Science* **1989**, *209*, L151.

(79) Chua, F. M.; Kuk, Y.; Silverman, P. J. *Physical Review Letters* **1989**, *63*, 386.

(80) Kuk, Y.; Chua, F. M.; Silverman, P. J.; Meyer, J. A. *Physical Review B* **1990**, *41*, 12393.

(81) Rajumon, M. K.; Prabhakaran, K.; Rao, C. N. R. *Surface Science* **1990**, *233*, L237.

(82) Hashizume, T.; Taniguchi, M.; Motai, K.; Lu, H.; Tanaka, K.; Sakurai, T. *Ultramicroscopy* **1992**, *42-44*, 553.

(83) Besenbacher, F.; Nørskov, J. K. *Progress in Surface Science* **1993**, *44*, 5.

(84) Rocca, M.; Vattuone, L.; Boragno, C.; Valbusa, U. *Journal of Electron Spectroscopy and Related Phenomena* **1993**, *64-65*, 577.

(85) Schimizu, T.; Tsukada, M. *Solid State Communications* **1993**, *87*, 193.

(86) Ozcomert, J. S.; Pai, W. W.; Bartelt, N. C.; Reutt-Robey, J. E. *Physical Review Letters* **1994**, *72*, 258.

(87) Ricart, J. M.; Torras, J.; Clotet, A.; Sueiras, J. E. *Surface Science* **1994**, *301*, 89.

(88) Vattuone, L.; Boragno, C.; Pupo, M.; Restelli, P.; Rocca, M.; Valbusa, U. *Physical Review Letters* **1994**, *72*, 510.

(89) Vattuone, L.; Rocca, M.; Boragno, C.; Valbusa, U. *Journal of Chemical Physics* **1994**, *101*, 713.

(90) Vattuone, L.; Rocca, M.; Boragno, C.; Valbusa, U. *Journal of Chemical Physics* **1994**, *101*, 726.

(91) Vattuone, L.; Rocca, M.; Restelli, P.; Pupo, M.; Boragno, C.; Valbusa, U. *Physical Review B* **1994**, *49*, 5113.

(92) Bare, S. R.; Griffiths, K.; Lennard, W. N.; Tang, H. T. *Surface Science* **1995**, *342*, 185.

(93) Canepa, M. *Surface Science* **1995**, *331-333*, 183.

(94) Pawela-Crew, J. *Surface Science* **1995**, *339*, 23.

(95) Butler, D. A.; Raukema, A.; Kleyn, A. W. *J. Chem. Soc.-Faraday Trans.* **1996**, *92*, 2319.

(96) de Mongeot, F. B.; Rocca, M.; Valbusa, U. *Surface Science* **1996**, *363*, 68.

(97) Kleyn, A. W.; Butler, D. A.; Raukema, A. *Surface Science* **1996**, *363*, 29.

(98) Barth, J. V.; Zambelli, T.; Wintterlin, J.; Schuster, R.; Ertl, G. *Physical Review B* **1997**, *55*, 12902.

(99) Bird, D. *Surface Science* **1997**, *377-379*, 555.

(100) Butler, D. A.; Sanders, J. B.; Raukema, A.; Kleyn, A. W.; Frenken, J. W. M. *Surface Science* **1997**, *375*, 141.

(101) de Mongeot, F. B.; Cupolillo, A.; Valbusa, U.; Rocca, M. *Journal of Chemical Physics* **1997**, *106*, 9297.

(102) de Mongeot, F. B.; Cupolillo, A.; Valbusa, U.; Rocca, M. *Chemical Physics Letters* **1997**, *270*, 345.

(103) de Mongeot, F. B.; Rocca, M.; Valbusa, U. *Surface Science* **1997**, *377-379*, 691.

(104) Fernandez, V.; Pahlke, D.; Esser, N.; Stahrenber, K.; Hunderi, O.; Bradshaw, A. M.; Richter, W. *Surface Science* **1997**, *377-379*, 388.

(105) Pazzi, V. *Journal of Molecular Catalysis A* **1997**, *119*, 289.

(106) Pazzi, V. I.; Tantardini, G. F. *Surface Science* **1997**, *377-379*, 572.

(107) Hansen, J. K.; Bremer, J.; Hunderi, O. *Physica Status Solidi (a)* **1998**, *170*, 271.

(108) Valbusa, U.; Mongeot, F. B. D.; Rocca, M.; Vattuone, L. *Vacuum* **1998**, *50*, 445.

(109) Savio, L.; Vattuone, L.; Rocca, M. *Journal of Physics: Condensed Matter* **2002**, *14*, 6065.

(110) Zambelli, T.; Barth, J. V.; Wintterlin, J. *Journal of Physics: Condensed Matter* **2002**, *14*.

(111) Bonini, N.; Kokalj, A.; Dal Corso, A.; de Gironcoli, S.; Baroni, S. *Physical Review B* **2004**, *69*, 195401.

(112) Hahn, J. R.; Ho, W. *Journal of Chemical Physics* **2005**, *123*, 214702.

(113) Rzeźnicka, I. I.; Lee, J.; Yates, J. T. *Journal of Physical Chemistry C* **2007**, *111*, 3705.

(114) Valdes, J.; Vargas, P.; Guillemot, L.; Esaulov, V. A. *Nuclear Instruments and Methods in Physics Research Section B* **2007**, *256*, 81.

(115) Kuk, Y.; Chua, F.; Silverman, P.; Meyer, J. *Physical Review B* **1990**, *41*, 12393.

(116) Jensen, F.; Besenbacher, F.; Laegsgaard, E.; Stensgaard, I. *Physical Review B* **1990**, *41*, 10233.

(117) Coulman, D. J.; Wintterlin, J.; Behm, R. J.; Ertl, G. *Physical Review Letters* **1990**, *64*, 1761.

(118) Kern, K.; Niehus, H.; Schatz, A.; Zeppenfeld, P.; Goerge, J.; Comsa, G. *Physical Review Letters* **1991**, *67*, 855.

(119) Eierdal, L.; Besenbacher, F.; Lægsgaard, E.; Stensgaard, I. *Ultramicroscopy* **1992**, *42–44*, 505.

(120) Roux, C. D.; Bu, H.; Rabalais, J. W. *Chemical Physics Letters* **1992**, *200*, 60.

(121) Taniguchi, M.; Tanaka, K.-i.; Hashizume, T.; Sakurai, T. *Chemical Physics Letters* **1992**, *192*, 117.

(122) Schimizu, T.; Tsukada, M. *Surface Science* **1993**, *295*, L1017.

(123) Sasaki, K.; Suzuki, H.; Tanaka, K.-i.; Okawa, Y. *Surface Science* **1995**, *327*, 33.

(124) Leibsle, F. M. *Surface Science* **1995**, *337*, 51.

(125) Pai, W. W.; Bartelt, N. C.; Peng, M. R.; Reutt-Robey, J. E. *Surface Science* **1995**, *330*, L679.

(126) Pai, W. W.; Reutt-Robey, J. E. *Physical Review B* **1996**, *53*, 15997.

(127) Butler, D. A.; Raukema, A.; Kleyn, A. W. *Surface Science* **1996**, *357-358*, 619.

(128) Reiff, S.; Block, J. H. *Surface Science* **1996**, *345*, 281.

(129) Courths, R.; Hüfner, S.; Kemkes, P.; Wiesen, G. *Surface Science* **1997**, *376*, 43.

(130) Katagiri, H. *Surface Science* **1999**, *424*, 322.

(131) Pascal, M.; Lamont, C. L. A.; Baumgärtel, P.; Terborg, R.; Hoeft, J. T.; Schaff, O.; Polcik, M.; Bradshaw, A. M.; Toomes, R. L.; Woodruff, D. P. *Surface Science* **2000**, *464*, 83.

(132) Nakagoe, O.; Ohta, M.; Watanabe, K.; Takagi, N.; Matsumoto, Y. *Surface Science* **2003**, *528*, 144.

(133) Duan, X.; Warschkow, O.; Soon, A.; Delley, B.; Stampfl, C. *Physical Review B* **2010**, *81*, 075430.

(134) Poulain, C.; Wiame, F.; Maurice, V.; Marcus, P. *Surface Science* **2012**, *606*, L26.

(135) Thijssen, W. H. A.; Marjenburgh, D.; Bremmer, R. H.; vannbspRuitenbeek, J. M. *Physical Review Letters* **2006**, *96*, 026806.

(136) Guillemot, L.; Bandurin, Y.; Bobrov, K.; Esaulov, V. A. *Journal of Physics: Condensed Matter* **2008**, *20*, 355008.

(137) Kürpick, U.; Meister, G.; Goldmann, A. *Applied Surface Science* **1996**, *99*, 221.

(138) Meister, G.; Goldmann, A. *Journal of Electron Spectroscopy and Related Phenomena* **1997**, *84*, 1.

(139) Brandstetter, T.; Wagner, T.; Fritz, D. R.; Zeppenfeld, P. *Surface Science* **2010**, *604*, 2016.

(140) Single crystals were synthesized at the Materials Preparation Center. Ames Laboratory USDOE, Ames, IA.-Ames Laboratory USDOE, Ames, IA. www.ameslab.gov/mpc

(141) Single crystals were purchased from Surface Preparation Laboratory, The Netherlands. www.spl.eu. Aligned within 0.5 degree or better, polished, with roughness 0.03 micron or better, and dimensions 9.0 x 3.0 x 1.5 mm. Purchased February 2010 by Thomas Duguet from René Koper. SPL#210027.

(142) Single crystals were purchased from Surface Preparation Laboratory, The Netherlands. www.spl.eu. Aligned within 0.5 degree or better, polished, with roughness 0.03 micron or better, and dimensions 9.0 x 3.0 x 1.0 mm. Purchased 2011 by Selena Russell from René Koper. SPL#211060

(143) Canepa, M.; Terreni, S.; Narducci, E.; Mattera, L. *Journal of Chemical Physics* **1999**, *110*, 2257.

(144) Thiel, P. A.; Shen, M.; Liu, D.-J.; Evans, J. W. *Journal of Vacuum Science & Technology A* **2010**, *28*, 1285.

(145) Rocca, M.; Savio, L.; Vattuone, L.; Burghaus, U.; Palomba, V.; Novelli, N.; Buatier de Mongeot, F.; Valbusa, U.; Gunnella, R.; Comelli, G.; Baraldi, A.; Lizzit, S.; Paolucci, G. *Physical Review B* **2000**, *61*, 213.

CHAPTER VI

Diffusion and Restructuring of Silver Islands on Ag(100) with Oxygen and Sulfur

Selena M. Russell,[a] Mingmin Shen,[b] Anthony R. Layson,[c] J. W. Evans,[d] and P. A. Thiel[a,e]

1. Introduction

Both oxygen and sulfur interact strongly with Ag(100) and induce reconstructions on the Ag(100) surface in which terrace Ag atoms are replaced by chalcogens.[1-3] Oxygen preferentially adsorbs to kink sites and vacancies,[2] while sulfur prefers 4-fold hollow sites.[4] In addition, these chalcogens accelerate coarsening in coinage metal homoepitaxial systems.[5]

Coarsening occurs through two mechanisms: coalescence, also called Smoluchowski ripening (SR) or evaporation-condensation, also called Ostwald ripening (OR). In the former case (SR), islands diffuse and merge into a larger island, which restructures over time to regain an equilibrium shape. In the latter (OR), coarsening occurs without collision of islands; rather, there is a net transport of material from small islands to large islands by carriers. For Ag on Ag(100), the island shape mimics the square substrate and the islands are square with the edges aligned along the close-packed <110> directions. SR is favored over OR by 0.15 eV [0.77(0.85) - 0.62 = 0.15(0.23) eV][6] and SR is the observed coarsening mechanism (under the conditions of our experiments, specifically island size, separation, and temperature).[6-10] SR occurs by islands diffusing and colliding, so SR depends on the diffusion coefficient of Ag islands. Pai *et al.* found that Ag islands 5.0 to 72.7 nm^2 in area diffuse at 0.0185 ± 0.0045 nm^2/s on Ag(100), with the exact rate depending on island size.[11] As temperature decreases, one expects diffusion rates to decrease. We previously reported

[a] Department of Chemistry, Iowa State University, Ames, Iowa 50011
[b] Current address: Materials and Chemical Sciences Division, Fundamental and Computational Sciences Directorate, Pacific Northwest National Laboratory, Richland, WA 99352
[c] Current address: Jannen School of Arts and Sciences, Trine University, One University Avenue, Angola, Indiana 46703
[d] Departments of Physics & Astronomy and Mathematics, Iowa State University, Ames, Iowa 50011
[e] Department of Material Science & Engineering, Iowa State University, Ames, Iowa 50011

that at 250 K, Ag islands diffused negligibly, so that the island density remained essentially constant over a few hours.[12,13]

In general, clusters on surfaces may move via single atom jumps or by collective displacement.[14] Silver islands on Ag(100) move by Ag atoms diffusing around the perimeter of the island, randomly relocating the island's center of mass. This process is known as periphery diffusion (PD). The rate of PD depends on the type of perimeter or edge a Ag atom traverses; hence, the effective barrier to SR depends on the diffusion barrier along close-packed edges, open edges, and around kinks and corners.[6,10] When islands collide corner-to-corner, a concave connection forms between the islands, giving the conjoined island a dumbbell-shape.[10] Diffusing Ag atoms along the island edge fill in the connection and the conjoined larger island regains a square shape. Earlier studies in our group found that larger islands require more time to relax, with the characteristic relaxation time τ approximately equal to the island side length L, raised to a power n, $\tau \sim L^n$, with $n \approx 3.1$.[15] [In this paper, dimensions such as L will be given in units of either nm or surface lattice constants, a, where a = 0.289 nm for Ag(100).]

Oxygen and sulfur enhance coarsening by changing the dominant mechanism from SR to OR.[4,16] In both cases, OR is terrace diffusion limited, meaning that island decay depends on the carrier diffusion rate and density. The identity of the carrier in the O/Ag/Ag(100) system is unclear. The experimental and theoretical results support the AgS_2 cluster as the carrier in the S/Ag/Ag(100) system.[4] While OR dominates the coarsening pathway, SR continues, but the effect of chalcogens on SR is unknown. In this paper, we address the question: Does oxygen and/or sulfur have any effect on SR, specifically on Ag island diffusion and restructuring?

2. Experimental details

All experiments were performed in a stainless-steel ultrahigh vacuum (UHV) chamber with base pressure of 1×10^{-10} Torr (1.33×10^{-8} Pa), equipped with a variable temperature scanning tunneling microscope (VT-STM) (Omicron GmbH, Germany). The Ag(100) samples were grown by the Ames Laboratory Materials Preparation Center[17] and were cleaned in vacuum by repeated cycles of Ar^+ sputtering (0.5 to 1 keV, ~2 μA, 8 – 20

min) and annealing (625 – 700 K, 10 – 60 min). All STM images were collected using electrochemically etched W tips in constant-current mode. Tunneling conditions were typically 1.0 to 5.0 nA current and -1.5 or 1.0 V tip bias; exact conditions are given in the figure captions. The oxygen experiments took place at 245 to 250 K with the sample actively cooled in the STM stage during all depositions and exposures. The sulfur experiments took place with the sample at room temperature, 300 K. The true temperature of the sample was within ± 5 K of the reported value and was held constant during each experiment. Uncertainties in experimental values were always calculated as $\pm$ 1 standard deviation, unless noted otherwise.

Silver was deposited via an Omicron EFM3 UHV evaporator containing Ag (99.99% pure). The average Ag coverage was 0.28 ± 0.07 monolayer (ML) and ranged from 0.10 to 0.35 ML. The average Ag flux was 14 ± 6 mML/s and ranged from 2.5 to 21 mML/s. Silver coverage and flux were determined by the method outlined in the Introduction to this thesis.

Prior to O_2 exposure or S deposition, the surface was allowed to stabilize for at least 1 hr. One of the authors, ARL, conducted the oxygen experiments in calendar year 2000. The chamber was backfilled with O_2 gas through a leak valve to ~10^{-8} Torr (10^{-6} Pa) in a continuous flow while the chamber was continuously pumped with an ion pump. Oxygen exposure is reported in Langmuir (1 L = 10^{-6} Torr s) and ranged from 2.0 to 36 L. Oxygen coverage ranged approximately from 0.0005 to 0.009 ML, estimated from the initial adsorption probability (sticking coefficient, s_0) of 1.30×10^{-4} at 250 K determined by Rocca *et al.*[18] The actual coverage might differ significantly, as adsorption and dissociation depend on the availability of kink sites along step edges, i.e. specific surface morphology.

Two of the authors, SMR and MS, conducted the sulfur experiments in calendar years 2008 and 2009. S_2 gas was generated within UHV in a solid-state electrochemical Ag|AgI|Ag_2S|Pt cell, following the design of Wagner.[19] Sulfur flux was in the range of (7 to 20)×10^{-5} ML/s. Sulfur coverage, θ_S, given as the ratio of sulfur atoms to Ag atoms, is expressed as ML and ranged from 0.034 to 0.21 ML. After each STM experiment the S(LMM)/Ag(MNN) AES intensity ratio was measured and converted to coverage, following a calibration established by Schwaha, *et al.*[20] and corroborated by Rovida and Pratesi.[21] This procedure has been supported by an STM study.[22]

Throughout this paper, visual clues are used to differentiate quickly between experiment types: blue indicates an image without O or S and orange indicates an image after O exposure or S deposition. STM data file names are provided in the figure captions: the date refers to the experiment date and folder name and m# refers to the image file. Data analysis files are named for the experiment date.

3. Results

Figures 1 and 2 illustrate oxygen and sulfur's effect on pre-adsorbed Ag islands on Ag(100). Initially, Ag islands are square, with edges oriented along the close-packed <011> directions. Upon oxygen or sulfur adsorption, these islands become rounder, showing some edges along the more open <001> directions.[4,23] The extent of edge deviation from the <011> directions increases with increasing chalcogen coverage, moving left to right across a row in Fig. 1 and 2. The systems evolve over time moving down a column. These data are consistent with previous analyses which showed that oxygen and sulfur accelerate Ag island coarsening and that both SR and OR occur with oxygen and sulfur.[4,23]

3.1. Diffusion

The mean square displacement $\langle \Delta r^2 \rangle$ or position of an island is measured as a function of time during STM observation, to obtain the diffusion coefficient, D

$$D = \frac{\langle \Delta r^2 \rangle}{zt} \tag{1}$$

where z is the number of neighboring adsorption sites and t is time. Considering the energetic barrier to diffusion, the coefficient can be written as

$$D = \frac{\upsilon_0 l^2}{z} e^{-E_d/kT} \tag{2}$$

where υ_0 is the attempt or hop frequency, l is the adsorption site distance, E_d is the diffusion barrier, k is the Boltzmann constant, and T is the temperature. On the square Ag(100) surface, z equals 4. This ratio is often abbreviated as D_0. Island position is measured relative to another, similarly sized island (type I analysis), or relative to a fixed position, such as a

defect or pinning site (type II analysis). Type II analysis is preferred as it directly gives the trajectory of one particular island, but is not always possible due to a lack of permanent features in some experiments. Type I analysis gives the combined trajectory of an island pair. The diffusion coefficient of a single island is approximated by dividing the diffusion coefficient *D* in half; therefore, the island sizes must be very similar in the pair.

3.1.1. Oxygen

The results for the island diffusion measurements (type II) for the experiment with 0.1 ML Ag and 2.0 L O_2 at 245 K are shown in Fig. 3b. The region pictured in Fig. 3a was observed continuously for 167 min. The mean square displacement was measured over this full time range for the lifetime of each island contained within a circle, and the results are represented by diamonds in Fig. 3b. However, the island areas are not stable with time as shown in Fig. 3c; the islands with initial area greater than 30 nm^2 fluctuate by 38 ± 13 % (islands a, b, e, and f) and the initially smaller islands (~20 nm^2, islands c and d) decay and disappear. Therefore, the mean square displacement was also determined for islands, which were relatively stable over a more limited time range (areas varied by 10 ± 6 %), and this result is shown as squares in Fig. 3b. Taking the data for all of the islands over the whole time range, the diffusion rate was $D = (1.1 \pm 0.7)\times10^{-4}$ nm^2/s. For islands with relatively stable areas over a more limited time range (islands a, b, d, and f), the diffusion rate was $D = (0.6 \pm 0.4)\times10^{-4}$ nm^2/s. Within the scatter in the experimental data, there is no trend in D as a function of island size (see Fig. 3b).

3.1.2. Sulfur

Type II analysis of Ag islands with 0.034 and 0.083 ML sulfur at 300 K is shown in Fig. 4. (Note that this is a different temperature than for the oxygen experiments in Section 3.1.1, so the data are not directly comparable. Temperature correction will be applied in Section 4, and the data will be compared there.) The island pair areas were 7.0% different or less, and remained relatively stable over the analysis period (varied by 8 ± 5 %). The islands approximately 53 nm^2 diffused at a rate of $D = (4 \pm 1)\times10^{-5}$ nm^2/s, while the smaller islands 22 nm^2 diffused at a rate of $D = (4.2 \pm 0.2)\times10^{-5}$ nm^2/s.

3.2. Restructuring

Fig. 5 shows an example of corner-to-corner pair coalescence. In part (a) the island environment is shown before and after coalescence, and in part (b), sequential STM images of the islands merging are shown. In this paper, we will focus on corner-to-corner coalescence events, since the time-evolution of island shape is more distinctive and it is easier to follow quantitatively. Fig. 5b shows sequential STM images of two square islands with area 33.7 and 13.0 nm^2 colliding corner-to-corner and reshaping into one larger, square island. Initially, a concave connection forms along the <001> direction, giving the conjoined islands a dumbbell shape. Restructuring occurs rapidly at first, but slows as the connection becomes less concave and the island approaches its equilibrium shape. (We will call the concave connection between two islands a 'neck.') During relaxation, we measure the island's neck width, height, and area. The neck width is defined as the narrowest distance across the concave connection. The height is the longest distance across the island; in this case, it is the distance from left corner to right corner. Fig. 5c shows the evolution of these parameters with time. During restructuring, the neck width increases non-linearly while the height decreases non-linearly, and the total, combined island area remains constant. These changes occur because the two islands connect and move closer together.

To describe the kinetics of such an event quantitatively, we define two new parameters. (please number your equations.) The first parameter is L_{eff}, which is the edge length of a square that would contain the combined area of the two merging islands:

$$L_{eff} = \sqrt{A_{avg}} = \frac{A_1 + A_2}{2} \tag{3}$$

The second is the time, τ, required for the neck width to increase from $L_{eff}/2$ to L_{eff}. (Note that $L_{eff}/2$ in the data is often close to the initial neck width, but this is coincidental. Similarly, L_{eff} is sometimes close to the asymptotic neck width, but this too is coincidental.) We will define the relaxation rate to be the slope of the line, in units of a/min, that connects the data points between $L_{eff}/2$ and L_{eff}.[15]

3.2.1. Oxygen

Ag islands coalesce after oxygen exposure, in the same way as on the clean surface. Fig. 6 shows islands with area 17.3 and 24.2 nm^2 after 2.0 L O_2 at 250 K. They merge corner-to-corner and reshape. Again, the neck width and height trend toward the same value non-linearly and the area remains relatively constant. Fig. 7 provides more examples under the same conditions as Fig. 6. Fig. 7f illustrates the size dependence of the relaxation rate with 2.0 L O_2.[15] The exponent of the best-fit line is 3.72 min/a, where a equals 0.289 nm. (If all of the different O_2 exposure experiments are considered together, $n = 2.9$.) Fig. 8 and 9 give several examples of island coalescence with 12 and 36 L O_2. The relaxation rates for all O_2 exposures and relaxation times for all sizes are plotted in Fig. 10a-b. The relaxation time increases as the combined island size increases, as shown in Panel (a). In addition, islands that are exposed to more oxygen tend to restructure faster than those exposed to less oxygen, as shown in Panel (b).

3.2.2. Sulfur

Ag island reshaping depends on the sulfur coverage. Compare Fig. 11 and 12. Islands well below the average island size tend to disappear, coarsening via OR. Islands with area close to or greater than the average island size tend to grow larger via OR. Therefore, SR is not generally observed for small islands as they tend to disappear before diffusing far enough to collide with another island. In most experiments, the average island size shortly after S deposition was 30 ± 8 nm^2 and ranged from 18 to 43 nm^2.

With S, the Ag islands do not always connect corner-to-corner along the open <001> directions. Because the islands become round, and their shapes rotate to varying degrees with increasing coverage. the islands may connect corner-to-corner and side-to-side in addition to round-edge-to-round-edge with no apparent relationship to open or closed directions. Fewer than half of the analyzed islands connect along or slightly off the open <001> directions: Fig. 13c shows a corner-to-corner collision; Fig. 14a,c corner-to-corner; Fig. 15a corner-to-corner; Fig. 16b round-edge-to-round-edge; and Fig. 17a side-to-side. Even small amounts of S cause deviation from the clean coalescence picture. With 0.034 ML S, two of the islands in Fig. 13a-b merge corner-to-corner, but along the <110> directions rather than the <001>

directions. Examples of connection along or slightly off the close packed <110> directions occur in every experiment: Fig. 14b shows a corner-to-corner collision; Fig. 15b-c side-to-side and round-edge-to-round-edge; Fig. 16a round-edge-to-round-edge; Fig. 17b-c corner-to-corner and side-to-side; and Fig. 18a-b corner-to-corner. Regardless, for all of the analyzed islands, a concave neck forms between each island pair, and relaxes at similar rates for a given island size, Fig. 19b.

At low sulfur coverages, island coalescence at room temperature mimics reshaping on the clean surface and with the oxygen exposures discussed above. Between 0.034 and 0.10 ML S, the neck width and height progress at comparable rates with a ratio of 1.0 ± 0.4 ranging 0.2 to 1.4. In these experiments, the average island pair analyzed was 50 ± 23 nm^2 (25 ± 15 nm^2 individually) and the area changed by (6 ± 5)%. The average islands on the terraces were 27 ± 7 nm^2. Two considerably larger islands were analyzed in two different experiments (their results are not included in the numbers reported in the previous sentences). With 0.034 ML, a conjoined island of area 122 nm^2 has a similar neck width to height ratio of 1.4, but decreases in area by 21%; see Fig. 13a. The other large island, with 0.083 ML S and 108 nm^2 conjoined island area, has a considerably larger neck width to height ratio of 6.0, due to the height decreasing slowly while the neck width increases rapidly. This island's area increases by 29%. The evolution of these parameters is show in Fig. 15b.

With 0.15 ML S, islands slightly larger than the average size coalesce with a neck width to height ratio of 2.1 ± 0.4. See Fig. 17. The average island pair analyzed was 74 ± 4 nm^2 (37 ± 7 nm^2 individually) and the average island on the terraces was 30 nm^2. The analyzed islands' areas change by -4.5 to +24%.

In the highest S coverage experiment, 0.21 ML S, the islands are 43 nm^2 on average shortly after S deposition. The island pairs range in size from 67.0 to 197 nm^2 and reshape in a different manner than in the low S coverage experiments. Compare Fig. 11to Fig. 12 and Fig. 18. With 0.21 ML, the island height *increases* slightly while the neck width increases during restructuring, resulting in a neck width to height ratio of 7.9 ± 0.9. During reshaping, the island area increases by 41 to 117%. Hence, all parameters of these large islands increase with high sulfur coverage.

The relaxation time τ, measured as the increase in the neck width between $L_{eff}/2$ and L_{eff}, is shown as a function of island size in Fig. 19b. Some of the experiments exhibit a size dependence, in which $\tau \sim L^n$, where $n = 2.5$ for 0.034 ML S, 3.4 for 0.083 ML S, and 3.1 for 0.21 ML S. However, the data for other experiments is too closely grouped to determine the dependence. (If all of the different S coverage experiments are considered together, $n = 2.6$.)

Island coalescence with ascending step edges also can be observed in the oxygen and sulfur experiments, but this type of event was not extensively analyzed.

4. Discussion

4.1. Oxygen

Oxygen activates silver island coarsening (via OR)[16] and enhances silver island diffusion and restructuring. Silver islands diffuse and reshape 1 to 2 orders of magnitude faster with oxygen than without. In Fig. 20 we compare our data with that of Pai *et al.*[11] The clean diffusion data was recorded at room temperature, but our experiment was conducted at 245 K. We compensate for the temperature difference by adjusting the rate, which is proportional to exp[-*E*/*kT*]. In this case *E* equals the effective barrier to SR, 0.62 eV.[6]

$$\frac{rate_{300}}{rate_{250}} = exp\left[\left(\frac{0.62\text{e}}{k}\right)\left(\frac{1}{245} - \frac{1}{300}\right)\right] = 218 \qquad (4)$$

Fig. 3, compares the island diffusion coefficient of islands after oxygen exposure to clean islands in the literature. The islands diffuse much faster with oxygen, regardless of changes in the island area. Fig. 21 shows that oxygen also increases the restructuring rate. (The temperature compensation between oxygen, 250 K, and clean, 300 K, experiments was calculated using Equation 4.) Given that island area does change with time, evaporation-condensation may also play a role in island diffusion, in addition to PD. On the other hand, island reshaping with oxygen mimics reshaping without oxygen; the neck width, height, and area evolve in the same ways (increasing, decreasing, and ~ constant). Therefore, it is likely that island diffusion and restructuring occur predominantly by the same mechanism as on the clean surface, via Ag adatom diffusion along island edges (PD).

Oxygen may enhance island diffusion and reshaping by providing more easily traversed island edges and facilitating Ag atom kink escape. On Ag(100), oxygen gas adsorbs and dissociates preferentially at step edges, preferring kink or vacancy sites, which facilitate dissociation due to (110) microfacets.[2,24] After dissociation, high coverages of atomic O can induce a missing-row reconstruction on Ag(100), in which Ag atoms along the <001> direction are replaced by two oxygen atoms.[2] Kink sites along the energetically favorable <011> edges provide additional, high-coordination adsorption sites. So oxygen atoms prefer to adsorb along open <001> edges or kinks along close-packed <011> edges. This preference explains why islands tend to round or rotate with oxygen coverage[16]. Earlier experiments on the clean system, in our group, found that PD depends on step orientation and is more efficient along open <001> steps than along close-packed <011> steps.[10] Potentially, Ag atoms diffuse quickly along oxygen stabilized <001> edges. In addition, oxygen adsorption at kink sites may reduce the kink escape barrier for Ag atoms, thus supplying more Ag atoms for PD.

4.2. Sulfur

Like oxygen, sulfur changes the predominant coarsening mechanism on the Ag(100) surface from SR to OR.[4] However, sulfur exerts a minimal effect on silver island diffusion and coalescence. The silver island diffusion rate actually decreases slightly with sulfur adsorption, based on comparison with data from Pai *et al.* in Fig. 22.[11] The neck-reshaping rate remains within an order of magnitude for all S coverages, which is illustrated in Fig. 23. Based on the behavior of the island areas and heights, the necks do not fill in solely by Ag atoms diffusing around the island edges. Instead, the islands regain an equilibrium shape via evaporation and condensation. Transport of material between islands is the only way to explain islands increasing in size, for example observed in Fig. 18, without coalescing with another island. The mobile AgS_2 complex that mediates OR also appears to mediate the observed SR after sulfur deposition.

Sulfur adsorbed at step edges and kink sites may actually diminish PD, From earlier DFT results, we know that S stabilizes kink sites by adsorbing to the upper step edge in the 4-fhs adjacent to the kink.[3] In the S/Ag/Ag(100) system, coarsening strongly accelerates as

the sulfur coverage approaches 0.25 ML, due to forced S population of step edges (which is required for AgS_2 formation). In Fig. 23a the rate appears to be slightly higher 0.041 and 0.083 ML S relative to the clean surface, or relative to higher S coverage, e.g. 0.15 ML S. However, there is significant scatter and these variations may be due to noise in the data, or due to a real S coverage effect. Sulfur causes islands to round by stabilizing open <001> step edges and kink sites, which inhibits Ag atom kink escape.[3] This could reduce the density of Ag atoms available at the step edges for PD.

4.3. Relationship to OR

In PD, adatoms diffuse around island edges and in OR adatoms or vacancies diffuse across terraces between islands.[6] On Ag(100), oxygen preferentially adsorbs to kink sites and vacancies.[2] Two O atoms may occupy opposite corners of the same Ag vacancy, whereas 4 sulfur atoms will replace 5 silver atom vacancies in a reconstruction. It is therefore reasonable to assume that oxygen and sulfur (at sufficient coverage) can stabilize vacancies, so OR via vacancies seems unlikely. Alternatively, the adsorbate may increase the density of Ag adatoms or their diffusion coefficient, or change the carrier, e.g. from a Ag adatom to a Ag-X cluster. In the S/Ag/Ag(100) system, adsorbed sulfur does not facilitate Ag adatom formation or diffusion. Instead, a mobile AgS_2 complex forms at edges and diffuses rapidly across the terrace, accelerating silver island coarsening.[3] However, for the O/Ag/Ag(100) system, OR occurs at an appreciable rate even with small amounts of adsorbed oxygen,[16] but our collaborators (Dr. Da-Jiang Liu and Prof. Jim Evans) have been unable to find a stable Ag-O cluster with DFT.

4.4. Surface geometry and additive

Oxygen on Ag(100) and S on Ag(111) first adsorb at step edges and enhance coarsening at low coverages (0.0005 to 0.009 ML O at 250 K and 0.010 to 0.035 ML S at 300 K), presumably through different mechanisms (OR mediated by adatoms or clusters). On the other hand, O on Ag(110) and S on Ag(100) first adsorb at terrace sites and either have no effect on coarsening at low coverage (0.003 to 0.08 ML O at 173 to 260 K) or a moderate affect at intermediate coverages (0.034 to 0.21 ML S at 300 K). Sulfur accelerates

coarsening via Ag-S clusters on the Ag(111) and Ag(100) surfaces, whereas the details of the oxygen mechanisms on Ag(100) and Ag(110) are unclear.

5. Conclusions

Oxygen accelerates the diffusion and coalescence of Ag islands strongly, by factors of 10 to 100×. During coalescence, with oxygen, the total area of Ag islands remains constant. In contrast, sulfur does not accelerate the diffusion of Ag islands nor the rate of coalescence. However, it has a very strong effect on the mechanism of coalescence. This is apparent from the fact that area is not constant during Ag island coalescence in the presence of sulfur. The effects of oxygen and sulfur on kink sites and vacancies at island edges may explain these differences.

Acknowledgements

SMR thanks Steven L. Yeninas for assistance writing a procedure in Igor Pro to calculate mean square displacement from raw measurements. This work was supported by the National Science Foundation (NSF) Grant No. CHE- 1111500. The work was performed at Ames Laboratory, which is operated for the USDOE by Iowa State University under Contract No. DE-AC02-07CH11358.

Figures

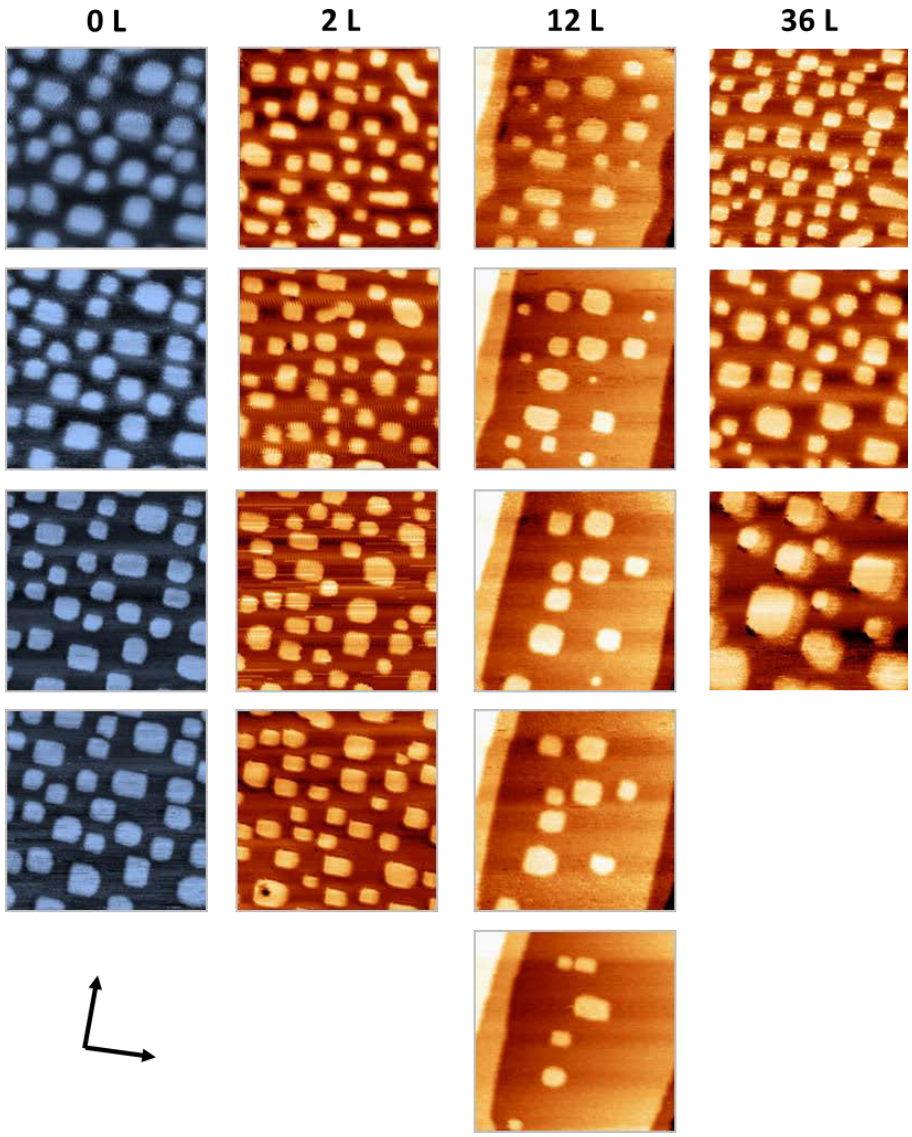

Figure 1. STM images showing Ag island coarsening with different O_2 exposures at 250 K, images in ~1 hr intervals. Oxygen was exposed 60 to 90 min after silver deposition. For a given experiment, the same region is shown, except for the last image with 36 L oxygen. The black arrows delineate the close-packed <110> directions. Clean, no oxygen on 0.29 ML Ag, 61, 120, 185, 233 min after silver deposition 49.5×49.5 nm^2, I = 0.3405 nA, V_{tip} = 1.178 V (2/23/2000 m12, 30, 50, 65). 2.0 L oxygen on 0.32 ML Ag, 7, 59, 120, 180 min after oxygen exposure 49.5×49.5 nm^2, I = 0.3531 nA, V_{tip} = 1.178 V (2/20/2000 m6, 35, 75, 100). 12 L oxygen on 0.25 ML Ag, 28, 59, 121, 179, 235 min after oxygen exposure, 50×50 nm^2, I = 0.3051 nA, V_{tip} = 0.8961 V (2/29/2000 m5, 21, 53, 88, 121). 36 L oxygen on 0.30 ML Ag, 12, 57, 109 min after oxygen exposure, 49.8×48.8 nm^2, I = 0.2236 nA, V_{tip} = 0.9814 V (2/27/2000 m3, 29, 39).

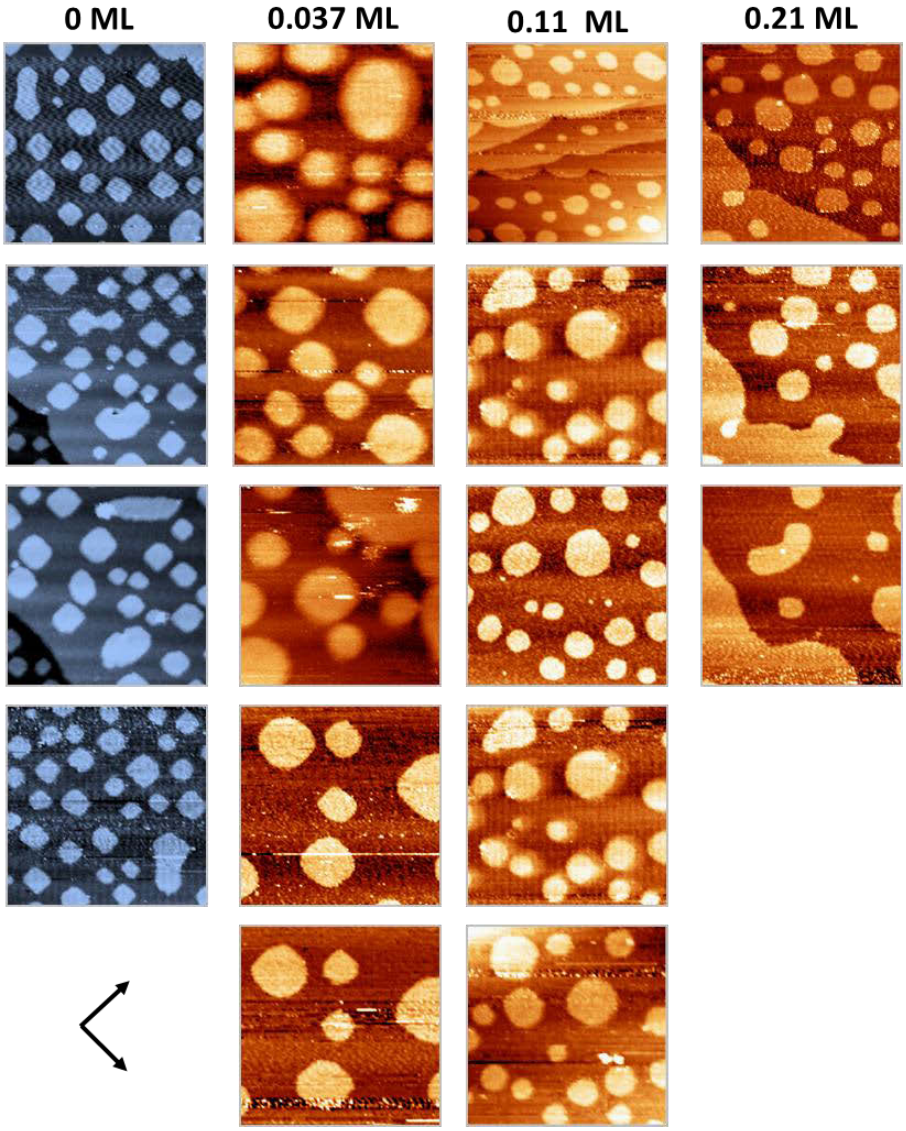

Figure 2. STM images showing Ag island coarsening at different S coverages at 300 K, images in ~1 hr intervals. For a given experiment, the same region is shown, except the first and last images without S, the first 3 images with 0.037 ML S, and the first image with 0.11 ML S. The black arrows delineate the close-packed <110> directions. Clean, no oxygen, 55, 121, 181, 254 min after silver deposition 49.6×49.6 nm^2, I = 0.3405 nA, V_{tip} = 1.178 V (12/5/2008 m 50, 85, 120, 148; m85 and 120 are the same region). 0.037 ML sulfur, 319, 371, 432, 491, 552 min after silver deposition (7, 59, 120, 179, 240 min after sulfur deposition) 49.6×49.6 nm^2, (12/5/2008 m161, 184, 203, 231, 265; m231 – 265 are the same region). 0.11 ML sulfur, 55, 78, 119, 180, 240, 300, 360 min after silver deposition (18, 60, 120, 181, 240, 300 min after sulfur deposition) 49.6 x49.6 nm^2, I = 1.8 nA, V_{tip} = -1.50 V (1/21/2009 m64, 86, 121, 156, 184, 215; m86 – 215 are the same region). 0.21 ML sulfur, 107, 132, 191 min after silver deposition (36, 61, 120 min after sulfur deposition) 49.6×49.6 nm2, (1/6/2009 m47, 61, 94; all are the same region). See Appendix I, Fig. 1 for more examples.

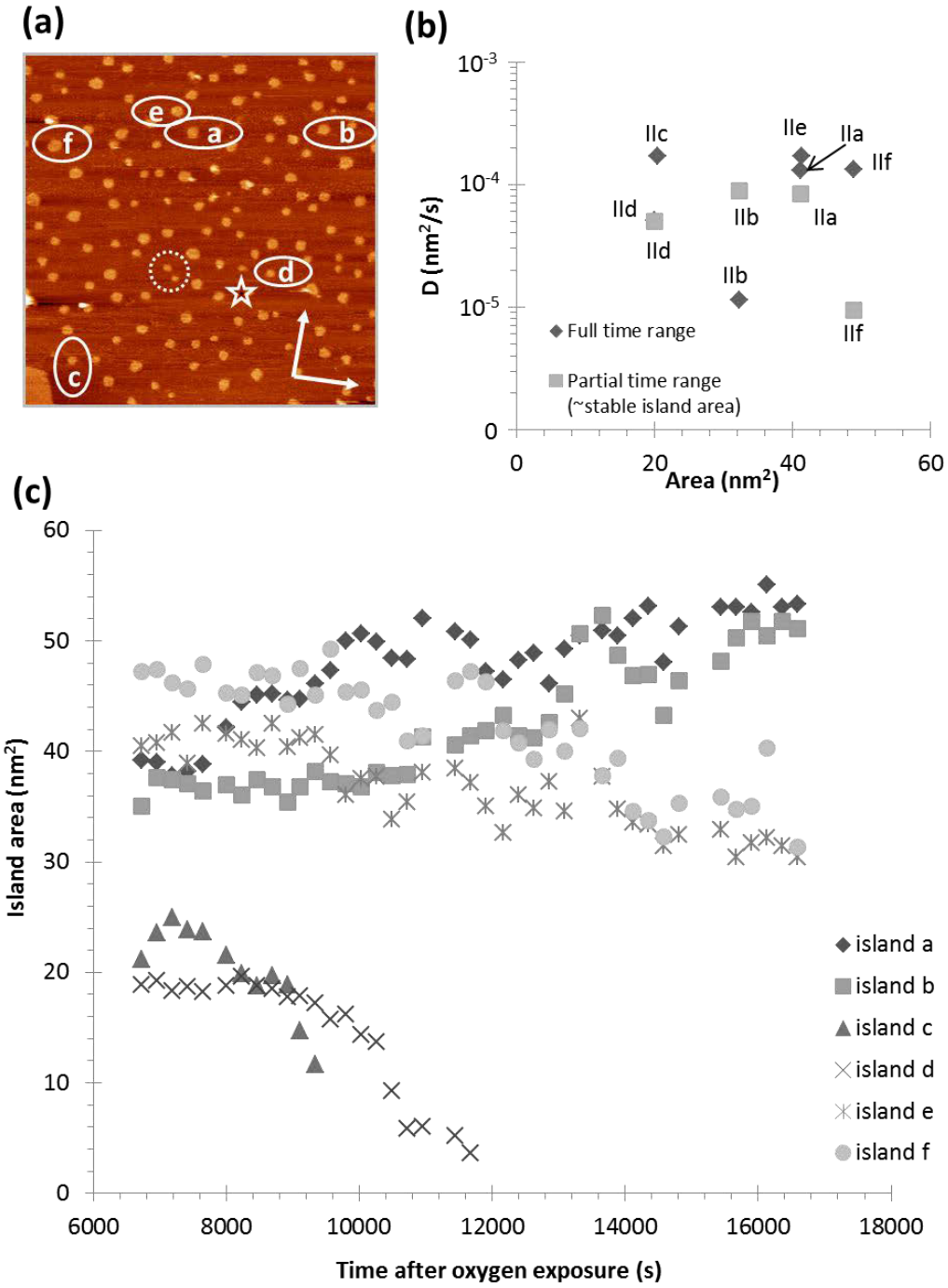

Figure 3. Ag island diffusion after exposure of 12 L O_2 on 0.1 ML Ag at 245 K. Island displacement was measured from the starred defect in (a). The same region was observed for 167 min. (a) 88 min after O exposure, 212×212 nm^2, I = 1.552 nA, V_{tip} = 1.364 V (5/9/2000 m23). (b) Island diffusion over the whole observation time (diamonds) and while island area was stable (squares). (c) Island area (average of every three points shown, error bars not shown) vs. time after oxygen exposure. The MSD of the island pair (type I) in the dotted circle is given in the Appendix.

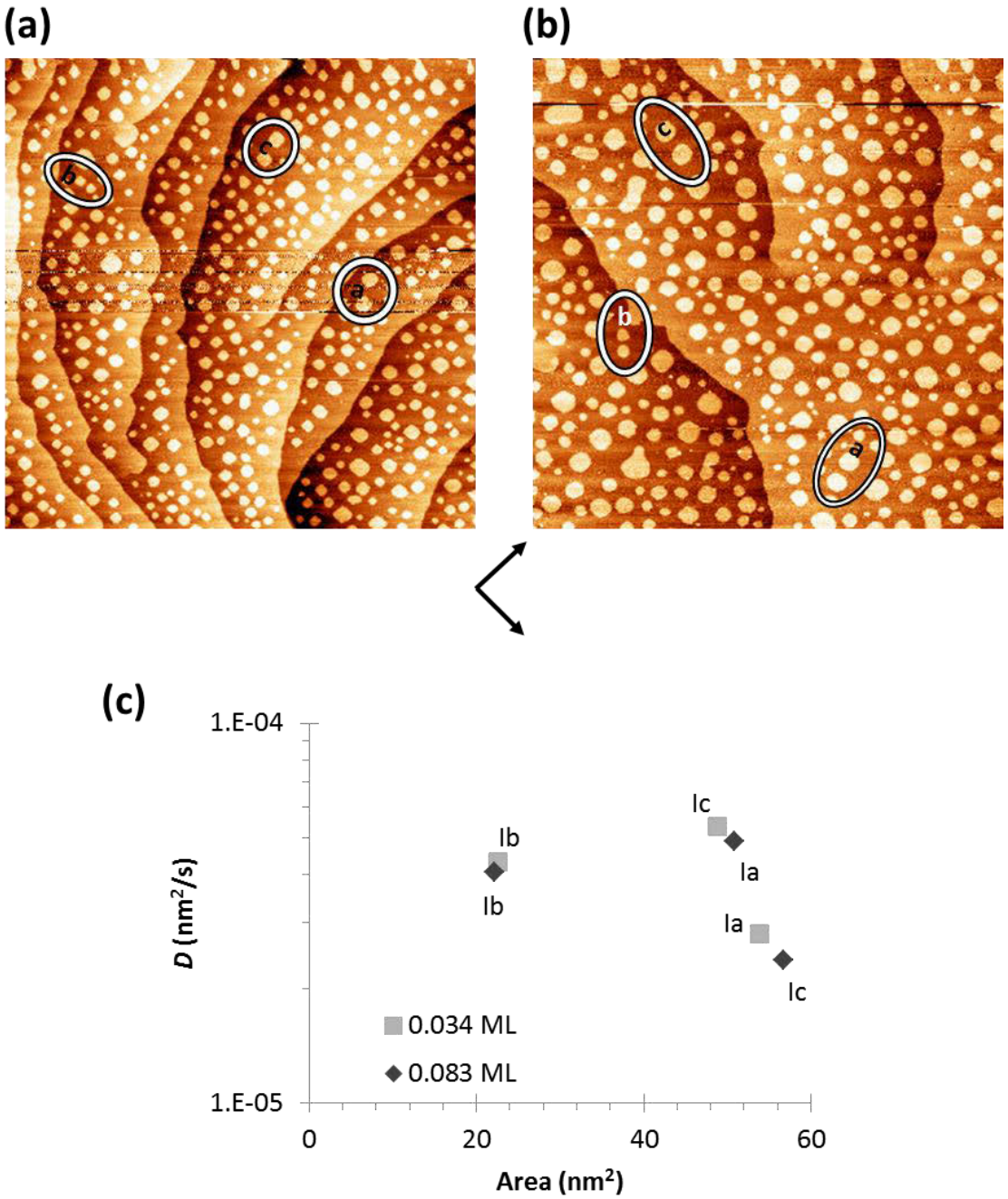

This figure continues on the following page.

Figure 4. Ag island diffusion with sulfur on 0.3 ML Ag at 300 K (a) 0.034 ML S, 127 min after Ag deposition and 84 min after S deposition, 250×250 nm^2, I = 1.26 nA, V_{tip} = -1.503 V (12/22/2008 m73). (b) 0.083 ML S, 117 min after Ag deposition and 44 min after S deposition, 200×200 nm^2, I = 1.73 nA, V_{tip} = -1.502 V (1/26/2009 m83). (c) Island diffusion with different sulfur coverages over the whole observation time. (d-e) Island area (average of every three points shown) vs. time after sulfur deposition of (d) 0.34 ML (12/22/2008) (e) 0.083 ML (1/26/2009).

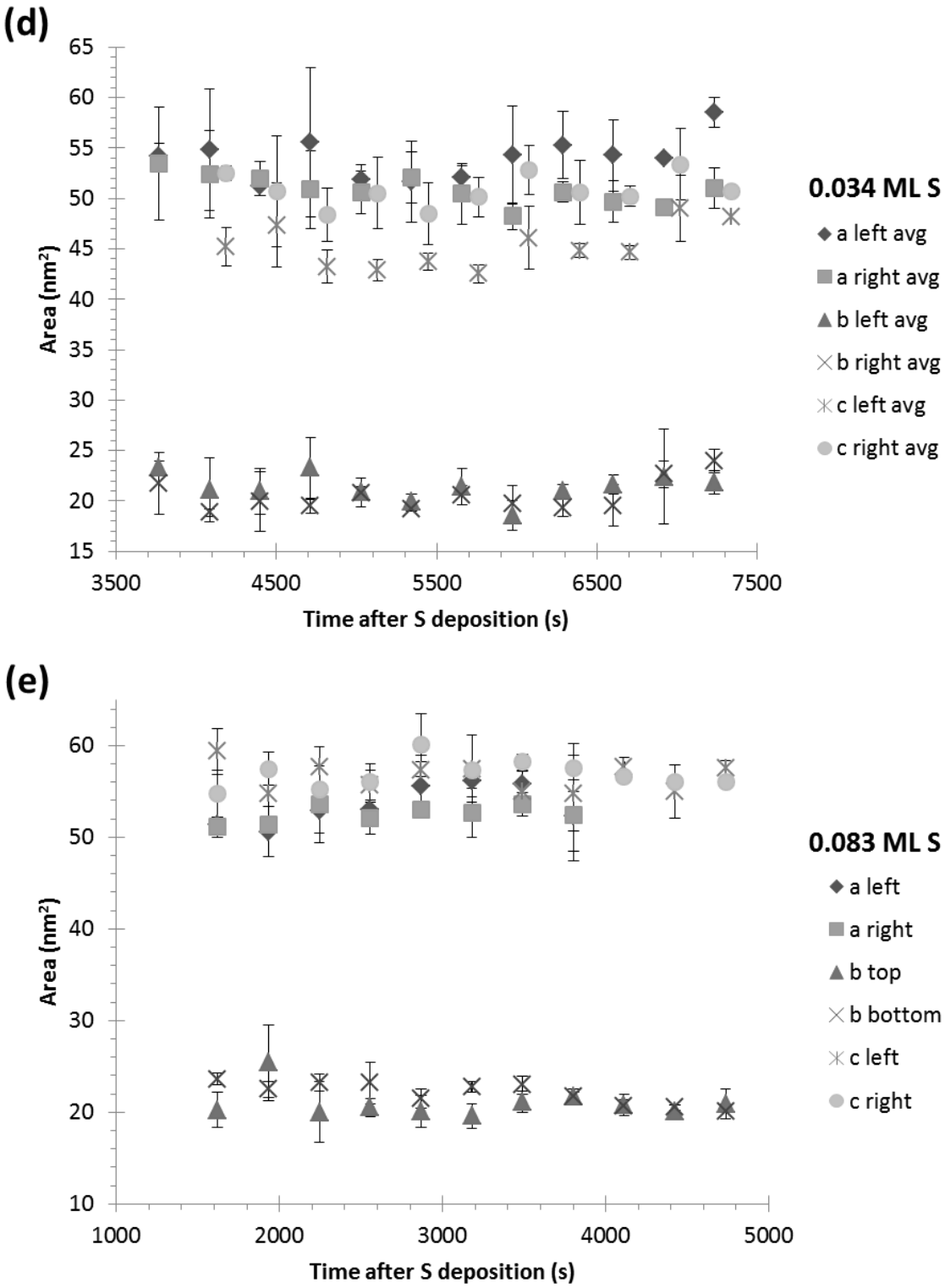

Figure 4. continued.

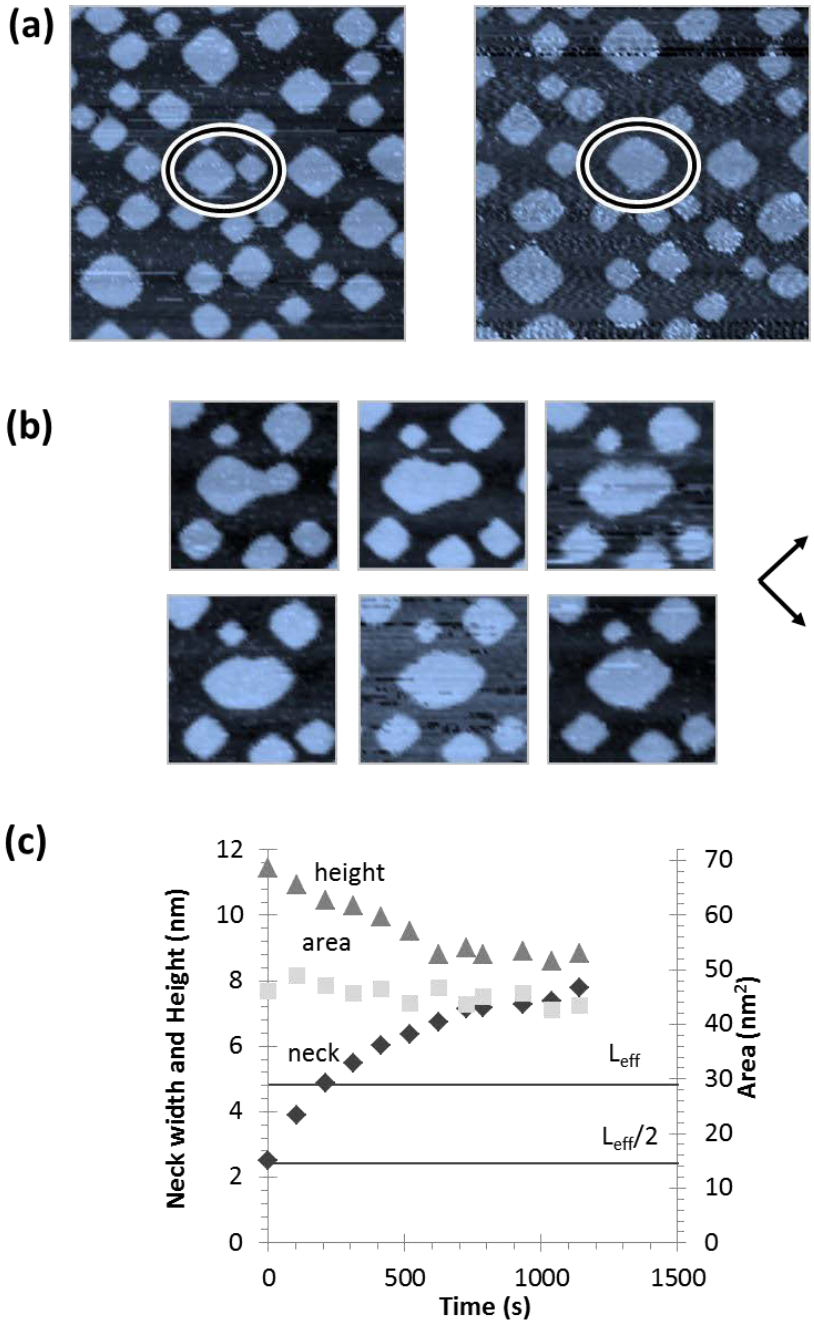

Figure 5. Corner-to-corner coalescence of to two Ag islands on the clean Ag(100) surface at 300 K. (a) Before and after collision and reshaping. Left: Just before the islands touch, and 110 min after Ag deposition. Right: 5411 s or 90 min after first contact, 202 min after Ag deposition, and 80 min after the last image in (b). 49.6 x49.6 nm^2 (12/5/2008 m70, 132). (b) Sequential images of the island in (a) at 1.7 min intervals, 19.1×19.1nm^2 (12/5/2008 m80 – 85). (c) Evolution of the island's neck width, height, and area with time, t = 0 at first imaged contact. The islands relax at 1.113×10^{-2} nm/s or 2.346 a/min over 208 s. The horizontal lines indicate L_{eff} and $L_{eff}/2$, based on the combined area of the islands, $L_{eff} = \sqrt{A_{avg}}$.

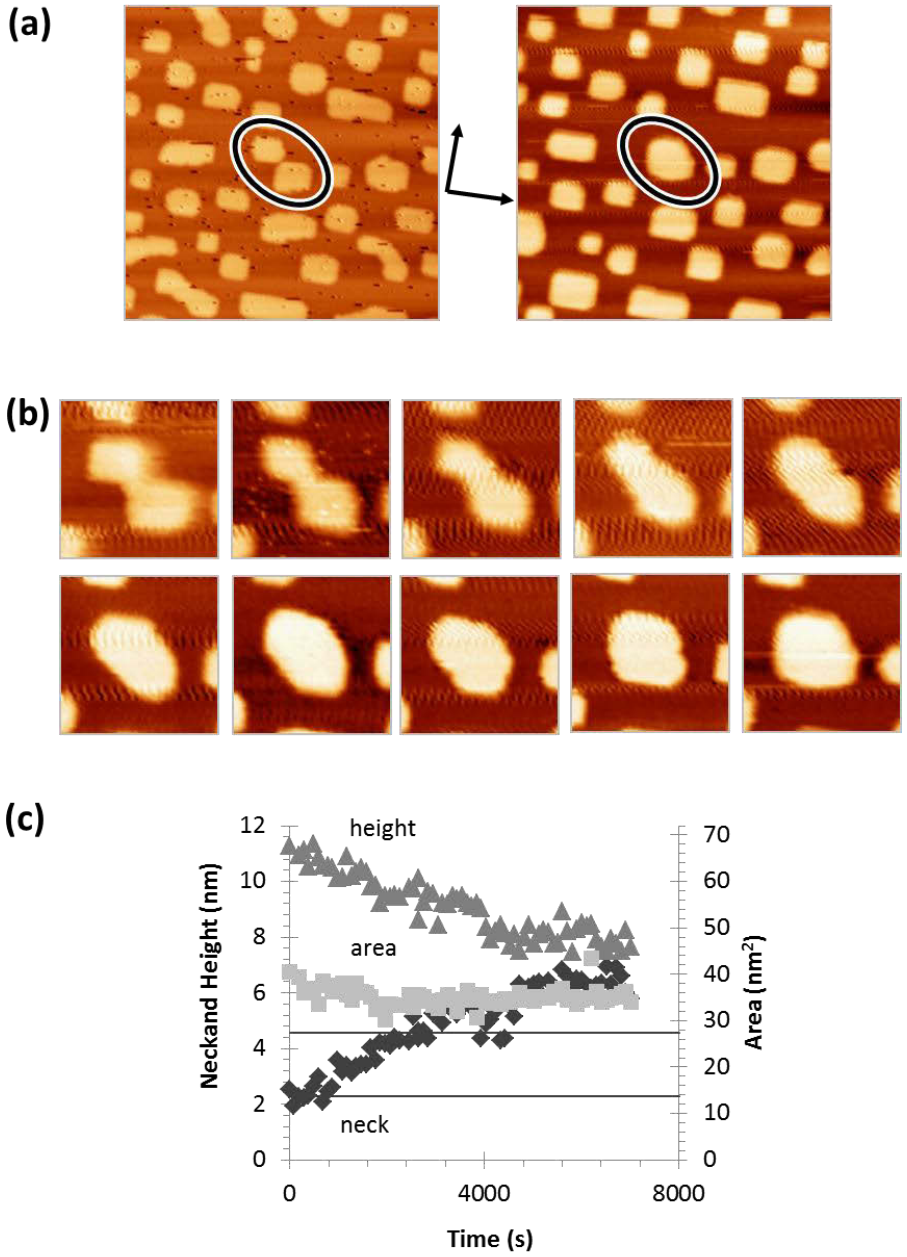

Figure 6. Corner-to-corner coalescence of to two Ag islands after exposing 2.0 L O_2 on 0.3 ML Ag at 249 K. The islands are initially 17.3 and 24.2 nm^2 in area and connect along the <100> . I = 0.4818 nA, V_{tip} = 1.178 V. (a) Just before the islands touch (left), 103 min after Ag deposition, 13 min after O exposure and 6610 s or 110 min after first contact (right), 205 min after Ag deposition, 115 min after O exposure. 49.5×49.5 nm^2 (2/20/2000 m10, 72; merge 4). (b) Island evolution from first contact at 10 min intervals, 14.4×14.4 nm^2 (2/20/2000 m11, m17, m23, m29, m36, m42, m47, m54, m60, m66). (c) Evolution of the island's neck width, height, and area with time, t = 0 at first imaged contact. The combined island relaxes at a rate of 9.982×10^{-4} nm/s or 0.2072 a/min over 2280 s, determined from the slope of the neck curve between L_{eff} and $L_{eff}/2$.

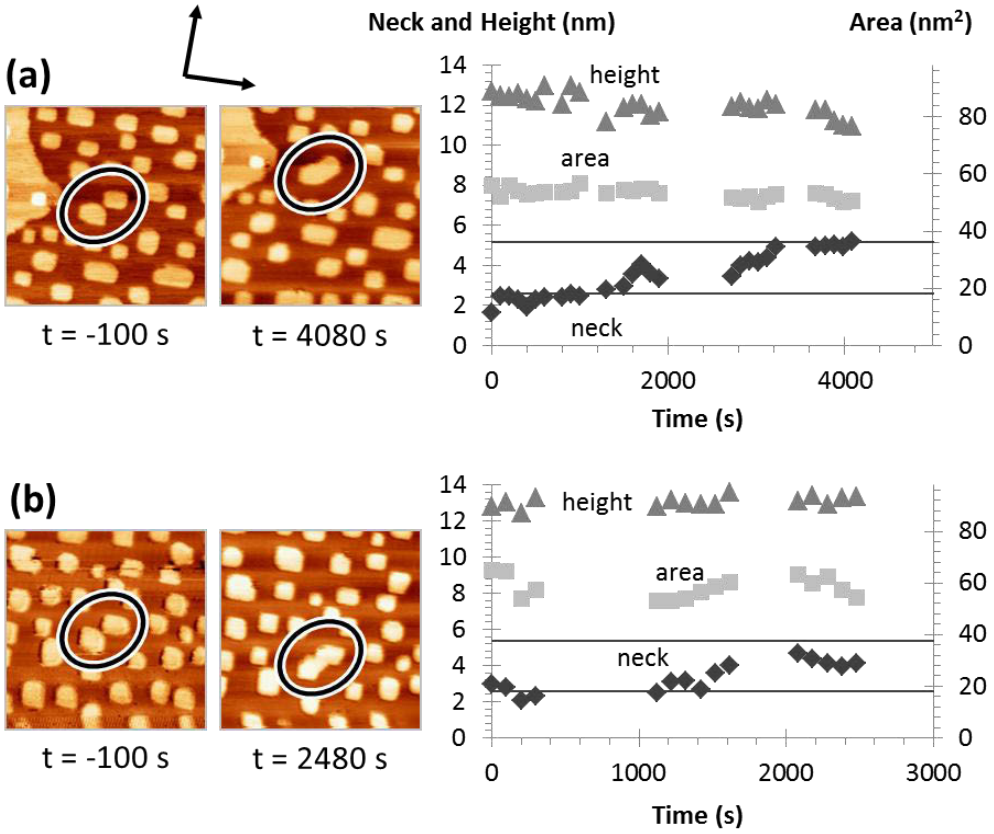

This figure continues on the following page.

Figure 7. Coalescence of Ag islands with 2 L O_2 and 0.3 ML Ag (25 nm^2 average island area) at 249 K, 50×50 nm^2, I = 0.4818 nA, V_{tip} = 1.178 V. The plots show how the restructuring islands relax with time, t = 0 at first imaged contact. The horizontal lines indicate L_{eff} and $L_{eff}/2$. (a) Islands with initial areas 29.4 and 23.8 nm^2 connect corner-to-corner along <100> and relax at 8.182×10^{-4} nm/s or 0.1699 a/min over 3150 s. Initial image recorded 207 min after Ag deposition and 117 min after O exposure (2/20/2000 m73, 104; merge1). (b) Islands with initial areas 28.4 and 29.5 nm^2 connect corner-to-corner along <100> and relax at 1.994×10^{-3} nm/s or 0.4139 a/min over 1350 s. Initial image recorded 232 min after Ag deposition and 142 min after O exposure (2/20/2000 m88, 104; merge 2). (c) Islands with initial areas 31.2 and 13.5 nm^2 connect corner-to-corner along <100> and relax at 9.885×10^{-4} nm/s or 0.2052 a/min over 2390 s. Initial image recorded 217 min after Ag deposition and 127 min after O exposure (2/20/2000 m79, 103; merge 3). (d) Islands with initial areas 7.27 and 6.99 nm^2 connect corner-to-corner along <100> and relax at 6.845×10^{-3} nm/s or 1.421 a/min over 195 s. Initial image recorded 222 min after Ag deposition and 232 min after O exposure (2/20/2000 m82, 86; merge 5). (e) Islands with initial areas 13.9 and 10.1 nm^2 connect corner-to-corner along <100> and relax at 3.645×10^{-3} nm/s or 0.7567 a/min over 475 s. Initial image recorded 185 min after Ag deposition and 95 min after O exposure (2/20/2000 m60, 69; merge 6). (f) Relaxation time τ versus effective length L_{eff} for islands in (a-e) of this figure and Fig. 6. L_{eff} is given in units of surface lattice constant, a = 0.289 nm. The slope of the best-fit line in is 3.7169 min/a.

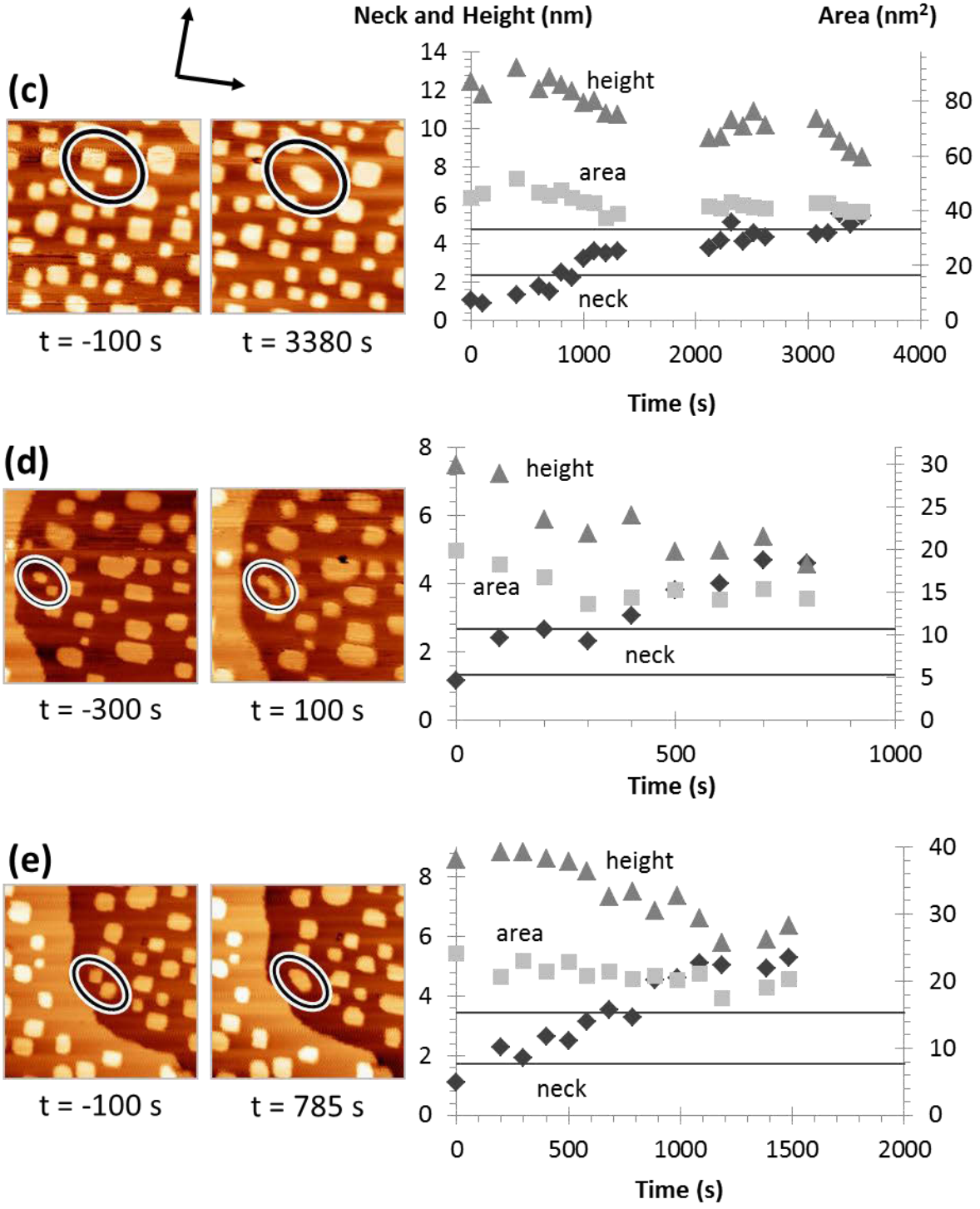

This figure continues on the following page.

Figure 7. continued.

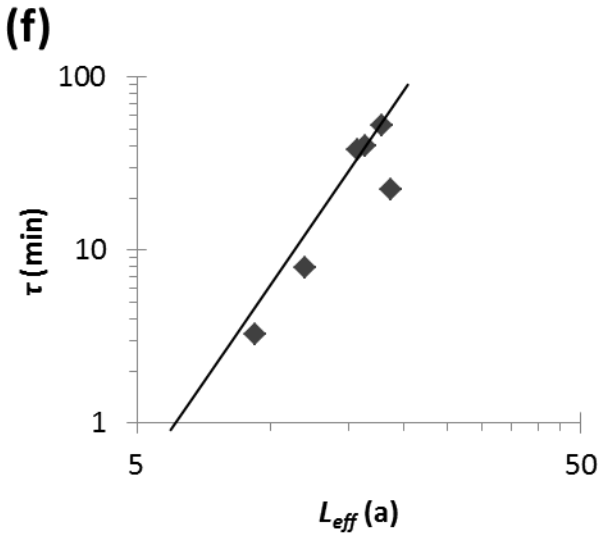

Figure 7. continued.

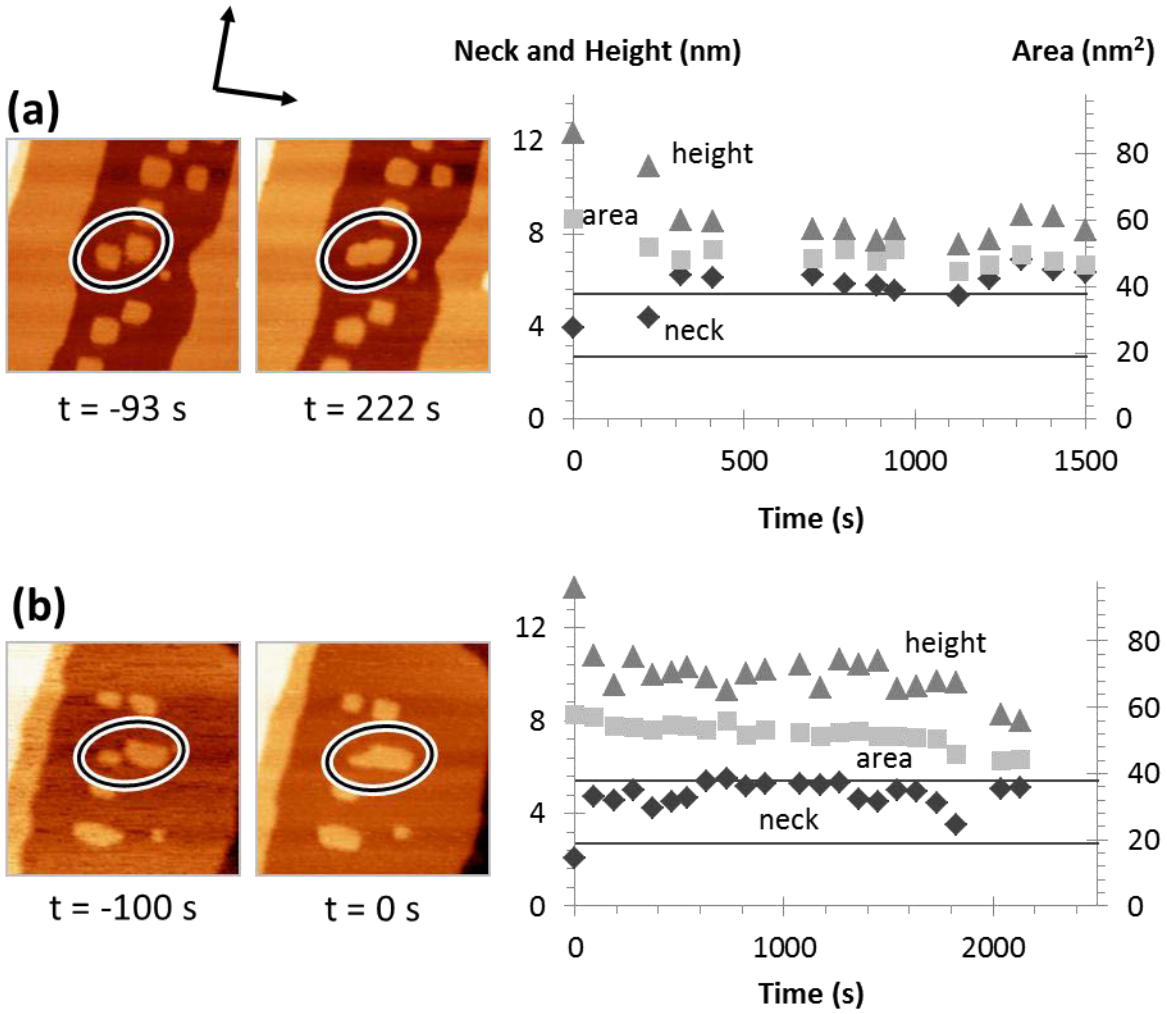

Figure 8. Coalescence of Ag islands with 12 L O_2 and 0.3 ML Ag (22 nm^2 average island area) at 250 K, 50×50 nm^2, I = 0.3051 nA, V_{tip} = 0.8961 V. The plots show how the restructuring islands relax with time, t = 0 at first imaged contact. The horizontal lines indicate L_{eff} and $L_{eff}/2$. (a) Islands with initial areas 26.2 and 32.3 nm^2 connect corner-to-corner along <100> and relax at 8.182×10^{-4} nm/s or 0.1699 a/min over 3150 s. Initial image recorded 93 min after O exposure (2/29/2000 m38, 40; merge1). (b) Islands with initial areas 12.8 and 37.8 nm^2 connect corner-to-corner off <100>, and relax at 3.590×10^{-4} nm/s or 0.7453 a/min over 701 s. Initial image recorded 93 min after O exposure (2/29/2000 m99, 100; merge2). Portion of images in (b) have been published.[16] Copyright (2002) by the American Physical Society.

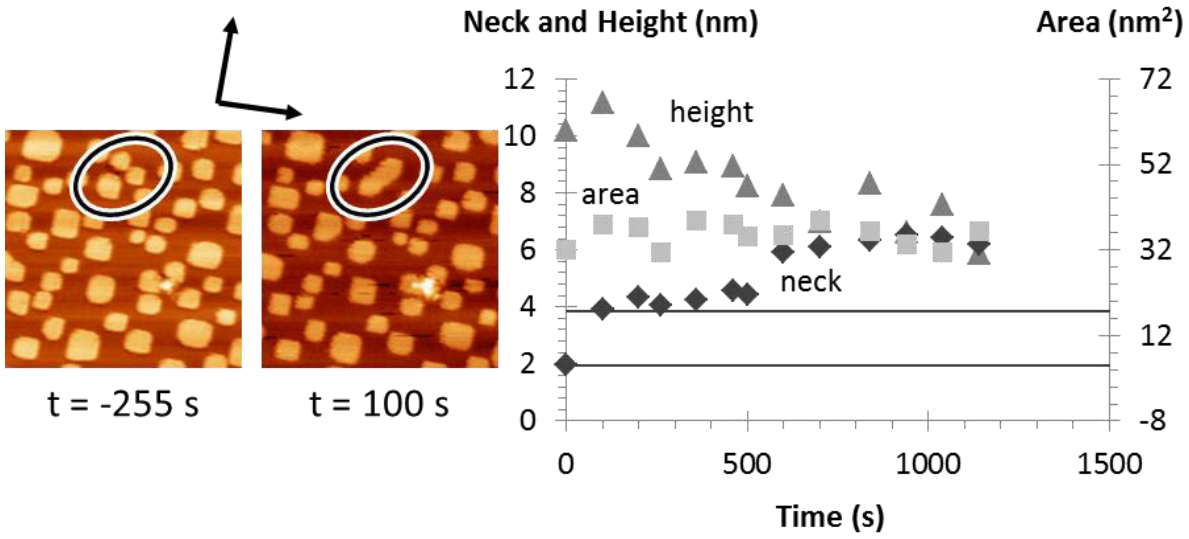

Figure 9. Coalescence of Ag islands with 12 L O_2 and 0.3 ML Ag (17 nm^2 average island area) at 250 K, 50×50 nm^2,. The plots show how the restructuring islands relax with time, t = 0 at first imaged contact. The horizontal lines indicate L_{eff} and $L_{eff}/2$. Islands with initial areas 14.4 and 15.21 nm^2 connect corner-to-round edge along <100> and relax at 0.107 nm/s or 2.23 a/min over 179 s. Initial image recorded 34 min after O exposure (2/27/2000 m12, 16; merge1).

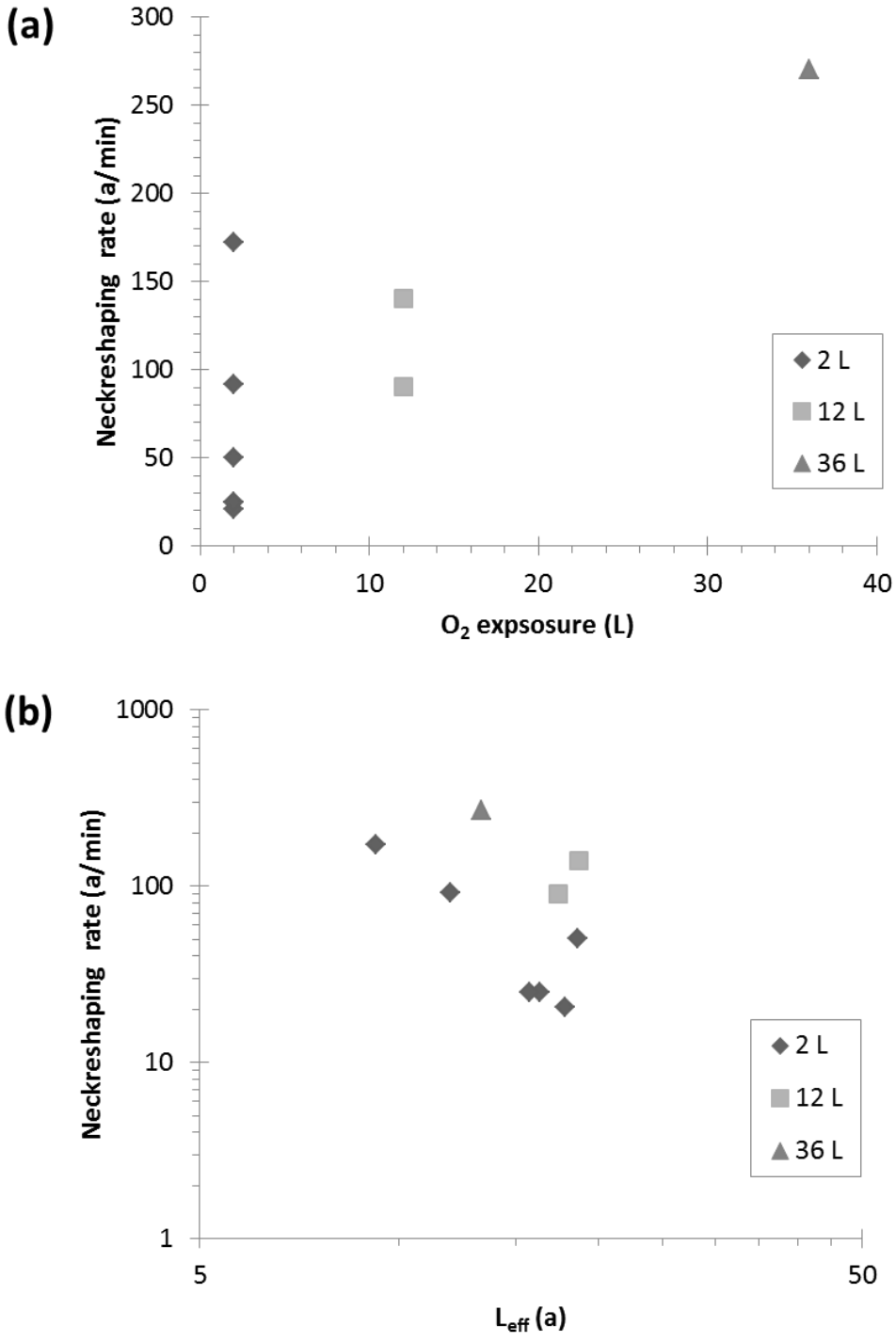

This figure continues on the following page.

Figure 10. Silver island relaxation with different oxygen exposures on 0.3 ML Ag at 250 K. Rates at which islands of all sizes relax depending on O_2 exposure (a) and effective length L_{eff} (b) (with temperature compensation). (c) Island relaxation time τ versus L_{eff} (without temperature compensation).

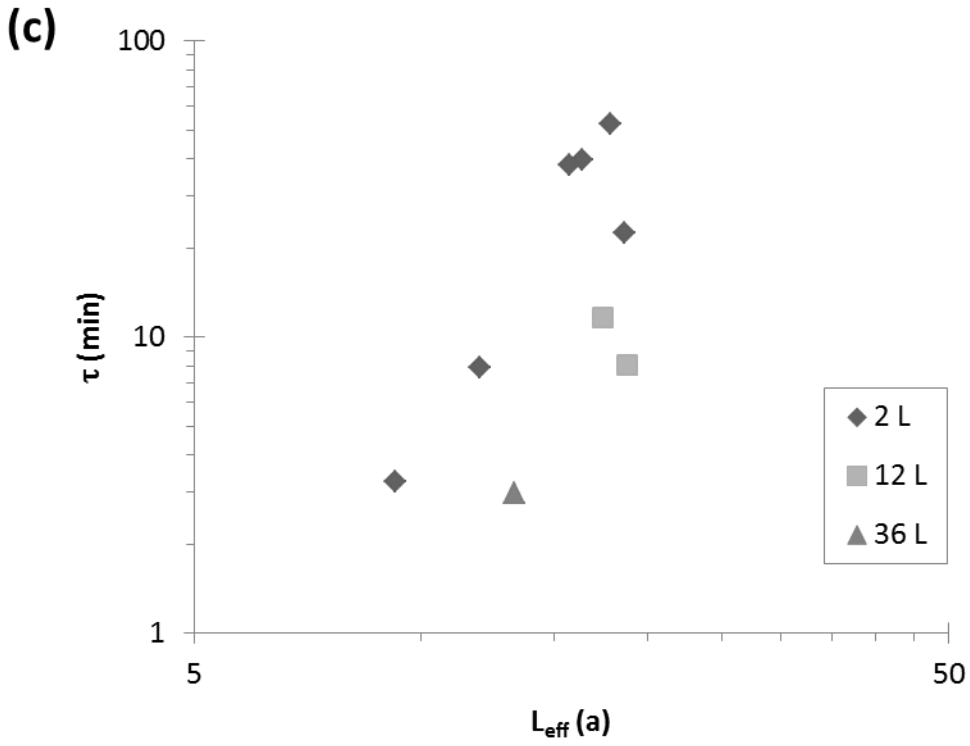

Figure 10. continued.

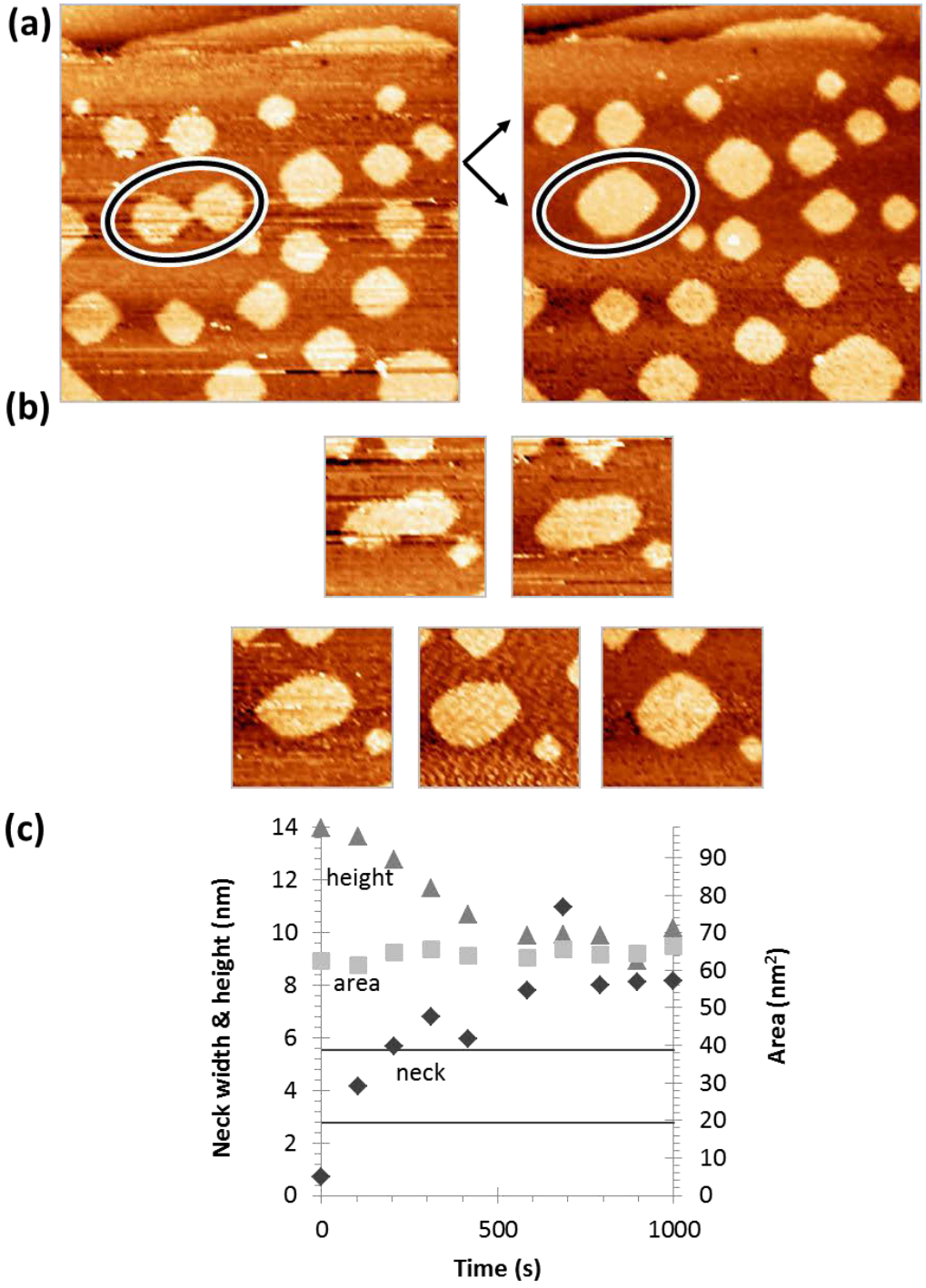

Figure 11. Coalescence of islands with area 31.9 and 29.4 nm^2 connect corner-to-corner along <100> with 0.041 ML sulfur and 0.3 ML Ag at 300 K,. (a) Just when the islands touch (left), 126 min after Ag deposition (72 min after S deposition) and (right) 687 s or 12 min after first contact, 138 min after Ag deposition (83 min after sulfur deposition), 50×50 nm^2 (12/15/2008 m88, 94; merge3). (b) Sequential STM images showing island evolution at 1.7 min intervals from first contact, 19.1×19.1 nm^2 (12/15/2008 m89-93).

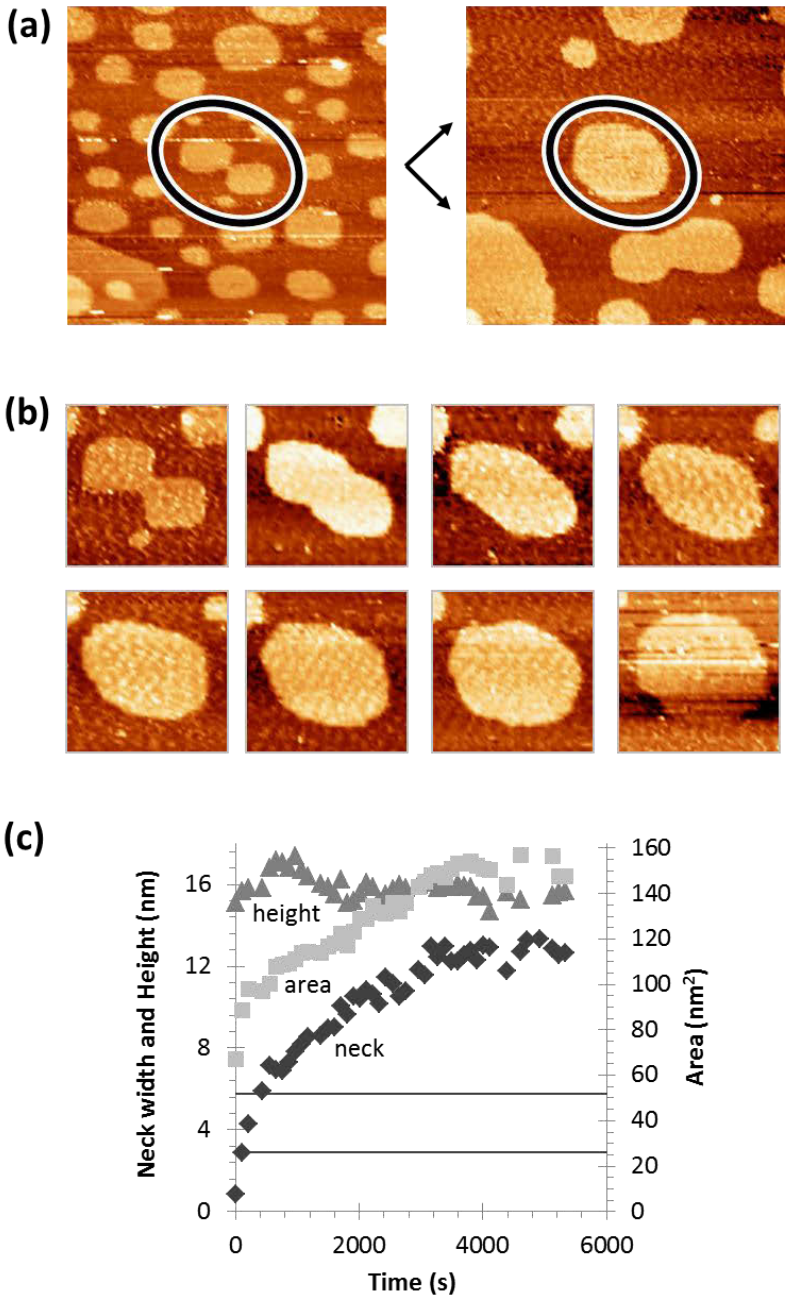

Figure12. Coalescence of two islands with area 36.5 and 30.5 nm^2 connecting corner-to-corner along <110> with 0.21 ML sulfur and 0.3 ML Ag at 300 K,. (a) Just when the islands touch (left), 105 min after Ag deposition (8 min after sulfur deposition) and 106 s or 89 min after first contact (right), 194 min after Ag deposition (123 min after sulfur deposition), 50×50 nm^2 (1/6/2009 m46, 96; merge 2). (b) Island evolution at 10 min intervals from first contact, 19.1×19.1 nm^2 (1/6/2009 m47, 52, 57, 63, 69, 74, 80, 91). (c) Evolution of the island's neck width, height, and area with time, t = 0 at first imaged contact. The combined island relaxes at a rate of 1.052×10^{-2} nm/s or 2.185 a/min, determined from the slope of the neck curve between L_{eff} and $L_{eff}/2$, represented by the horizontal lines.

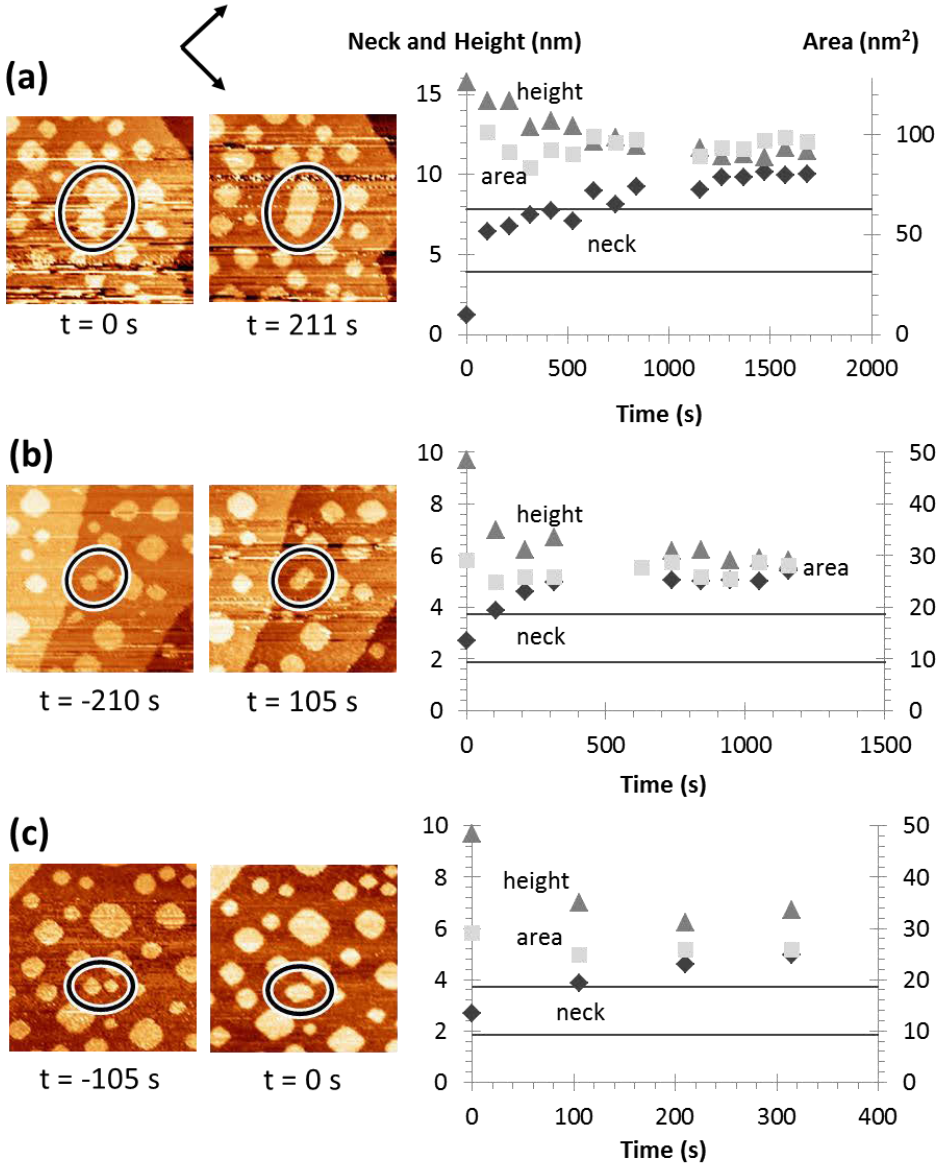

Figure 13. Coalescence of Ag islands with 0.034 ML S and 0.3 ML Ag (28 nm^2 average island area) at 300 K, 50×50 nm^2. The plots show how the restructuring islands relax with time, t = 0 at first imaged contact. The horizontal lines indicate L_{eff} and $L_{eff}/2$. (a) Islands with initial areas 62.9 and 59.1 nm^2 connect corner-to-corner off <110> and relax at 7.44×10^{-3} nm/s or 1.54 a/min over 525 s. The island area decreases by -21%. Initial image recorded 104 min after Ag deposition and 61 min after S deposition (12/22/2008 m60, 62; merge1). (b) Islands with initial areas 15.3 and 12.6 nm^2 connect corner-to-corner along <110> and relax at 1.20×10^{-2} nm/s or 2.50 a/min over 155 s. The island area increases by 0.9%. Initial image recorded 109 min after Ag deposition and 66 min after S deposition (12/22/2008 m63, 66; merge2). (c) Islands with initial areas 16.0 and 9.1 nm^2 connect corner-to-corner along <100> and relax in less than 105 s. The island area decreases by 4.8%. Initial image recorded 125 min after Ag deposition and 82 min after S deposition (12/22/2008 m72, 73; merge3).

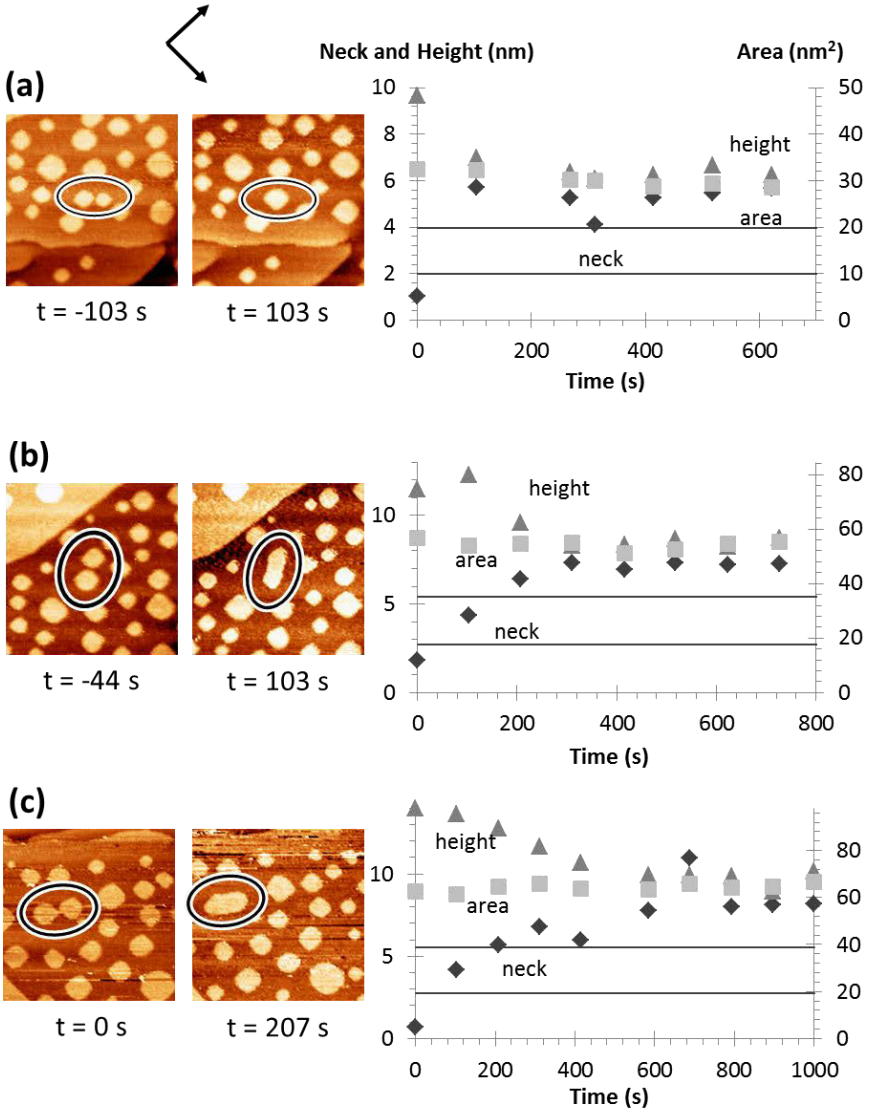

Figure 14. Coalescence of Ag islands with 0.041 ML S and 0.3 ML Ag (18 nm^2 average island area) at 300 K, 50×50 nm^2. The plots show how the restructuring islands relax with time, t = 0 at first imaged contact. The horizontal lines indicate L_{eff} and $L_{eff}/2$. Note that (a) and (b) occur in close proximity to several screw dislocations. (a) Islands with initial areas 18.2 and 13.1 nm^2 connect corner-to-corner along <100> and relax at 1.09×10^{-2} nm/s or 2.26 a/min over 182 s. The island area increases by 2.4%. Initial image recorded 63 min after Ag deposition and 9 min after S deposition (12/15/2008 m54, 56; merge1). (b) Islands with initial areas 31.3 and 26.9 nm^2 connect corner-to-corner off <110> and relax at 2.07×10^{-2} nm/s or 4.31 a/min over 130 s. The island area decreases by 6.0%. Initial image recorded 66 min after Ag deposition and 12 min after S deposition (12/15/2008 m57, 59; merge2). (c) Islands with initial areas 31.9 and 29.4 nm^2 connect corner-to-corner along <100> and relax at 2.22×10^{-2} nm/s or 4.60 a/min over 125 s. The island area increases by 8.5%. Initial image recorded 126 min after Ag deposition and 72 min after S deposition (12/15/2008 m88, 90; merge3).

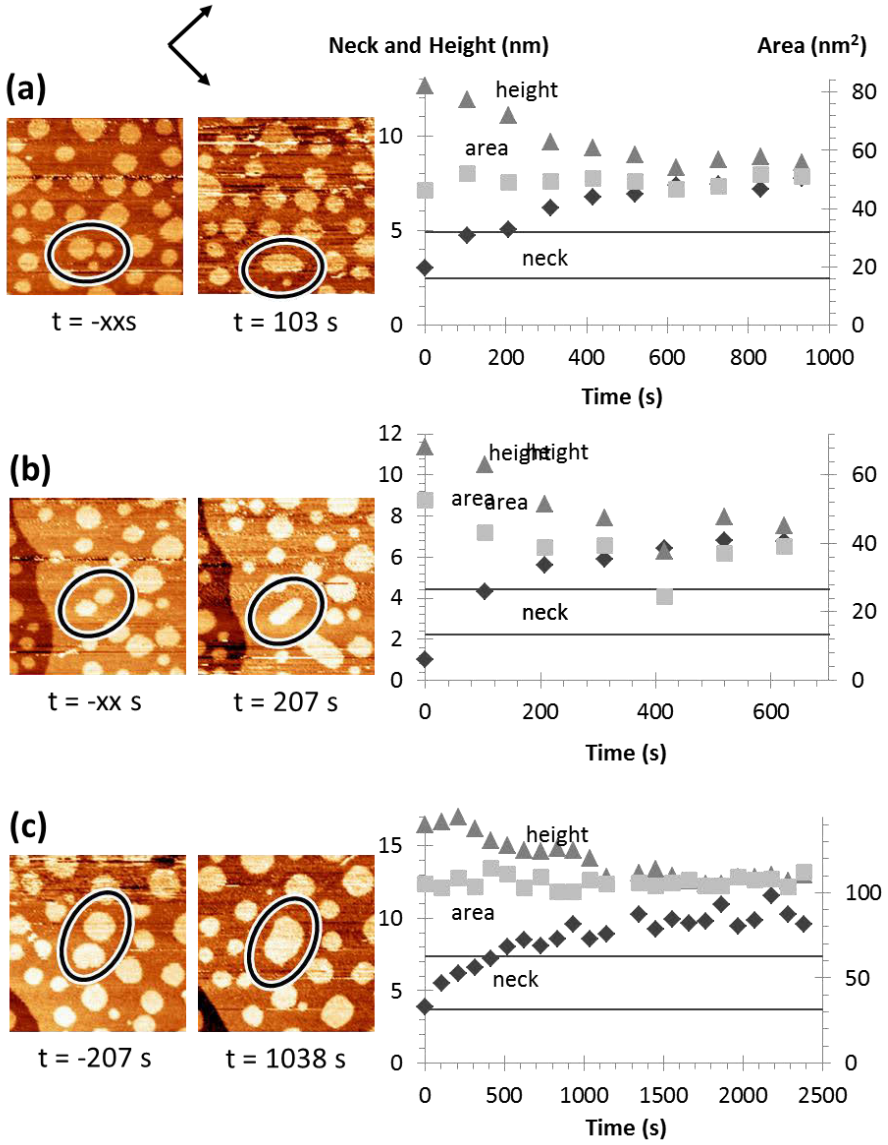

Figure 15. Coalescence of Ag islands with 0.083 ML S and 0.3 ML Ag (30 nm^2 average island area) at 300 K, 50×50 nm^2. The plots show how the restructuring islands relax with time, t = 0 at first imaged contact. The horizontal lines indicate L_{eff} and $L_{eff}/2$. (a) Islands with initial areas 33.0 and 15.6 nm^2 connect corner-to-corner along <100> and relax at 1.89×10^{-2} nm/s or 3.93 a/min over 130 s. The island area increases by 10%. Initial image recorded 100 min after Ag deposition and 27 min after S deposition (1/26/2009 m73, 77; merge1). (b) Islands with initial areas 22.6 and 17.1 nm^2 connect side-to-side along <110> and relax at 2.93×10^{-2} nm/s or 6.08 a/min over 76 s. The island area decreases by 26%. Initial image recorded 100 min after Ag deposition and 27 min after S deposition (1/26/2009 m73, 76; merge2). (c) Islands with initial areas 57.1 and 51.0 nm^2 connect round edge-to-round edge off <110> and relax at 8.45×10^{-3} nm/s or 1.75 a/min over 435 s. The island area increases by 7%. Initial image recorded 112 min after Ag deposition and 39 min after S deposition (1/26/2009 m80, 92; merge3).

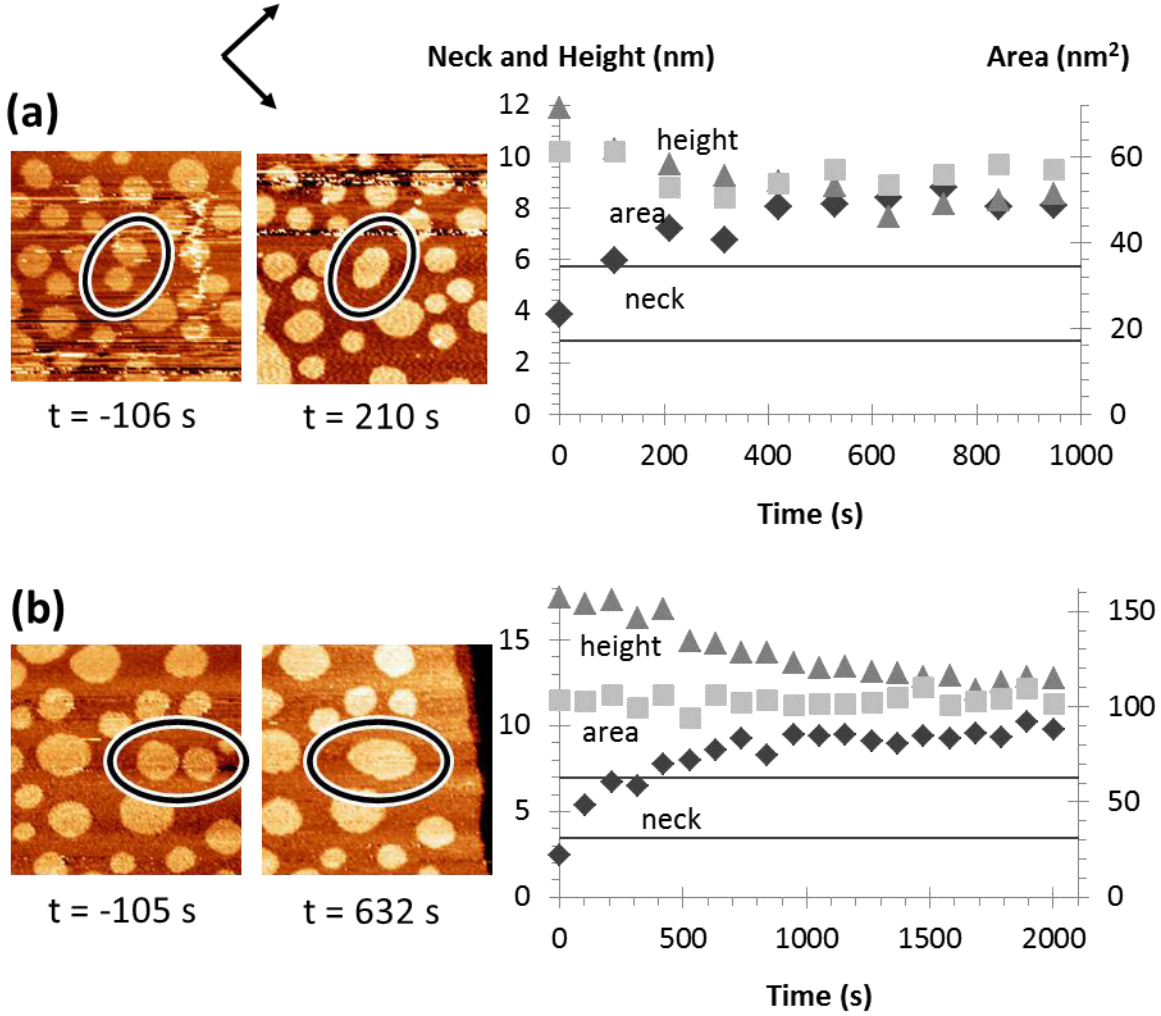

Figure16. Coalescence of Ag islands with 0.10 ML S and 0.35 ML Ag (33 nm^2 average island area) at 300 K, 50×50 nm^2. The plots show how the restructuring islands relax with time, t = 0 at first imaged contact. The horizontal lines indicate L_{eff} and $L_{eff}/2$. (a) Islands with initial areas 59.2 and 37.4 nm^2 connect round edge-to-round edge off <110> and relax at 1.44×10^{-2} nm/s or 2.98 a/min over 200 s. The island area decreases by 13%. Initial image recorded 107 min after Ag deposition and 36 min after S deposition (2/16/2009 m46, 48; merge1). (b) Islands with initial areas 59.2 and 37.4 nm^2 connect round edge-to-round edge along <100> and relax at 1.28×10^{-2} nm/s or 2.66 a/min over 175 s. The island area increases by 13%. Initial image recorded 137 min after Ag deposition and 108 min after S deposition (2/16/2009 m63, 70; merge2).

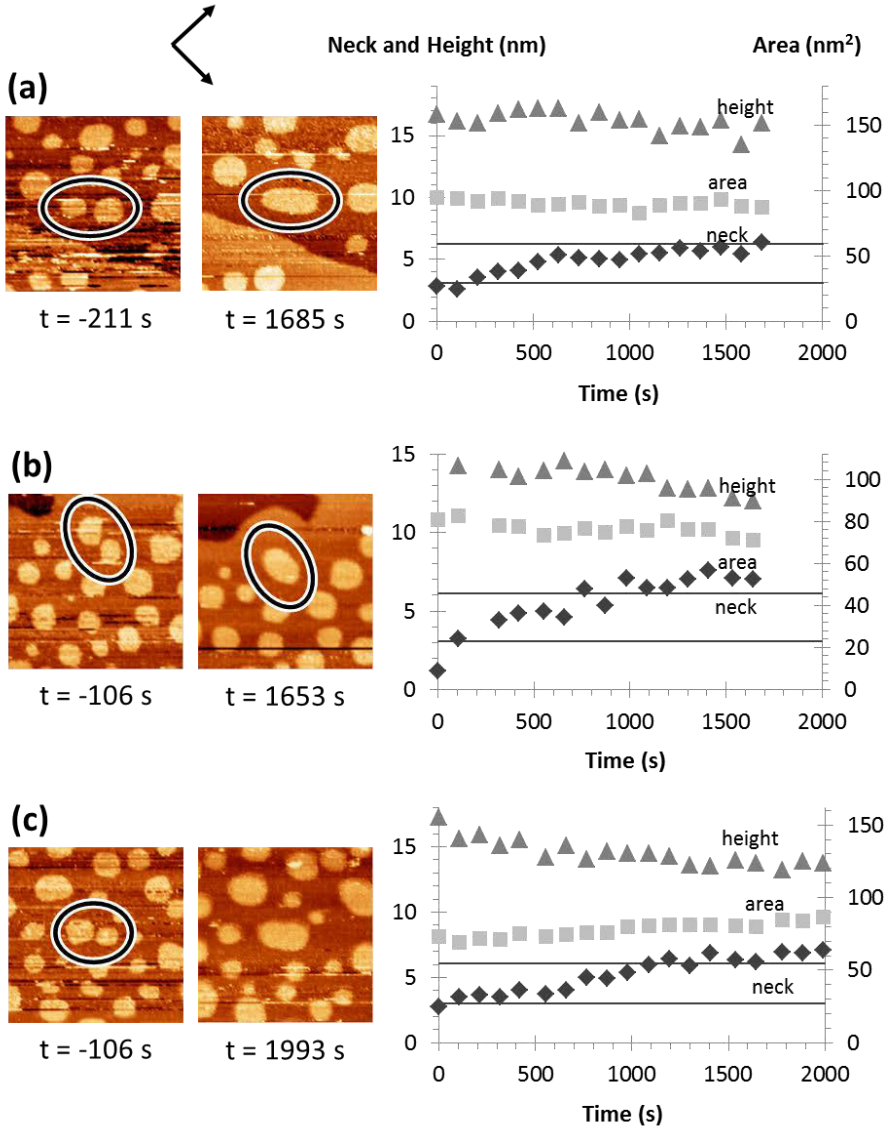

Figure 17. Coalescence of Ag islands with 0.15 ML S and 0.32 ML Ag (30 nm^2 average island area) at 300 K, 50×50 nm^2. The plots show how the restructuring islands relax with time, t = 0 at first imaged contact. The horizontal lines indicate L_{eff} and $L_{eff}/2$. (a) Islands with initial areas 32.7 and 44.8 nm^2 connect side-to-side along <100> and relax at 2.11×10^{-3} nm/s or 0.438 a/min over 1475 s. The island area increases by 13%. Initial image recorded 207 min after Ag deposition and 121 min after S deposition (3/2/2009 m99, 117; merge1). (b) Islands with initial areas 42.2 and 32.2 nm^2 connect corner-to-corner along <110> and relax at 3.50×10^{-3} nm/s or 0.728 a/min over 870 s. The island area decreases by 4%. Initial image recorded 129 min after Ag deposition and 44 min after S deposition (3/2/2009 m60, 76; merge2). (c) Islands with initial areas 42.4 and 27.4 nm^2 connect side-to-side along <110> and relax at 2.86×10^{-3} nm/s or 0.593 a/min over 1035 s. The island area increases by 24%. Initial image recorded 129 min after Ag deposition and 44 min after S deposition (3/2/2009 m60, 79; merge3).

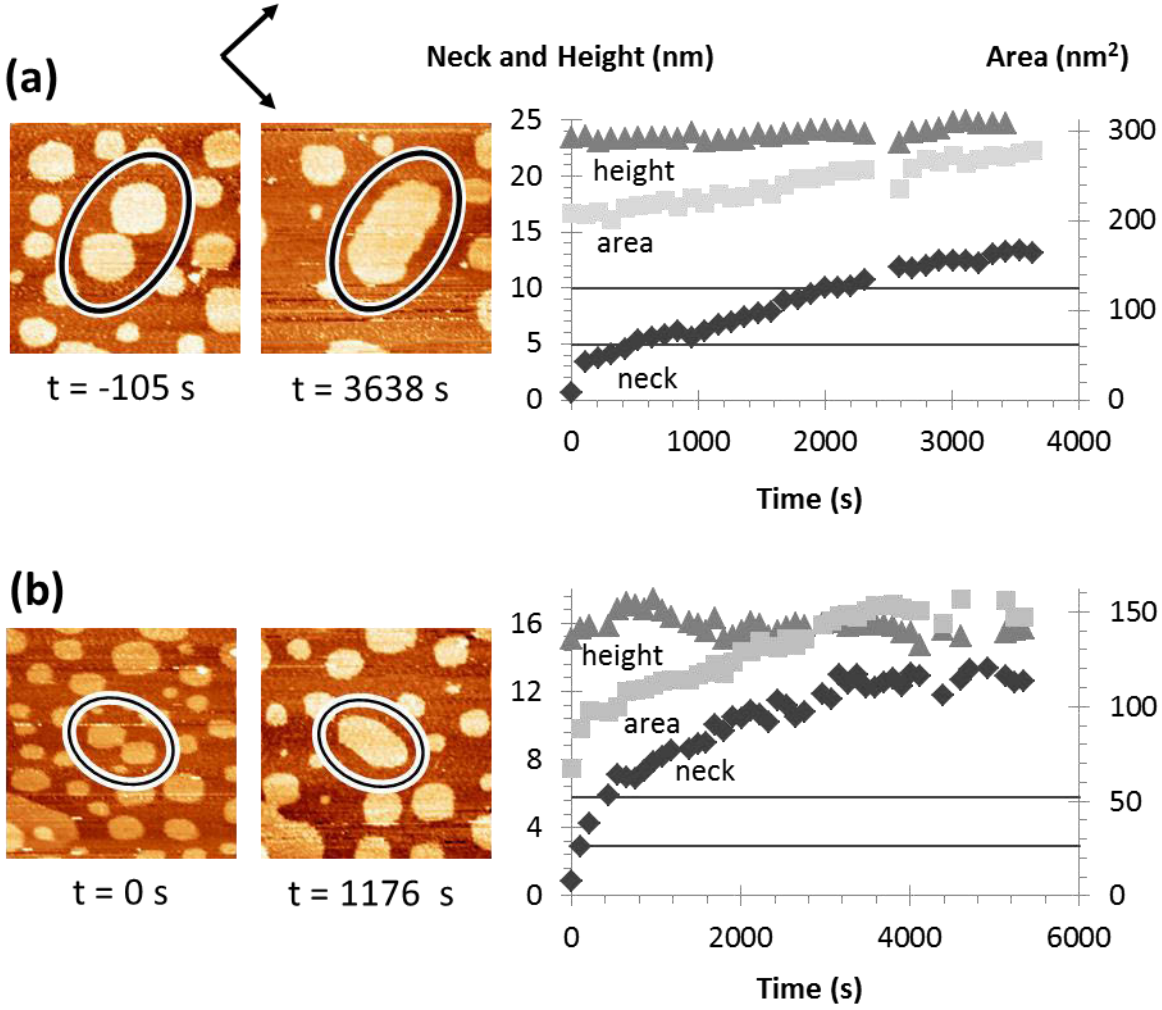

Figure 18. Coalescence of Ag islands with 0.21 ML S and 0.3 ML Ag (43 nm^2 average island area) at 300 K, 50×50 nm^2. The plots show how the restructuring islands relax with time, t = 0 at first imaged contact. The horizontal lines indicate L_{eff} and $L_{eff}/2$. (a) Islands with initial areas 105 and 92.2 nm^2 connect corner-to-corner along <110> and relax at 3.319×10^{-3} nm/s or 0.6891 a/min over 1495 s. The island area increases by 41%. Initial image recorded 134 min after Ag deposition and 37 min after S deposition (1/6/2009 m62, 97; merge1). (b) Islands with initial areas 36.5 and 30.5 nm^2 connect corner-to-corner along <110> and relax at 1.05×10^{-3} nm/s or 1.19 a/min over 275 s. The island area increases by 120%. Initial image recorded 105 min after Ag deposition and 8 min after S deposition (1/6/2009 m46, 57; merge2).

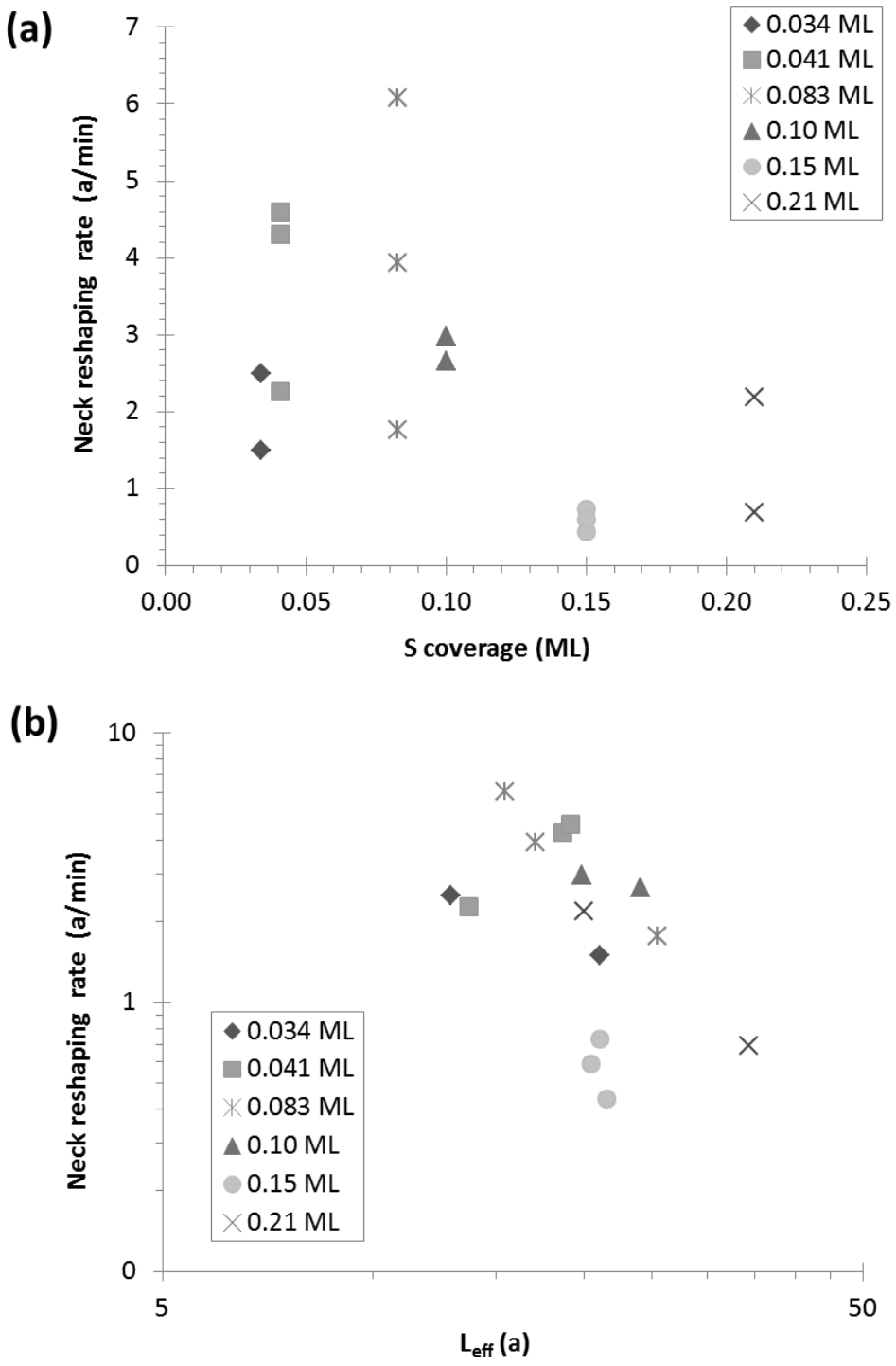

This figure continues on the following page.

Figure 19. Silver island relaxation with different sulfur depositions on 0.3 ML Ag at 300 K. Rates at which islands of all sizes relax depending on S coverage (a) and effective length L_{eff} (b). (c) Island relaxation time τ versus L_{eff} .

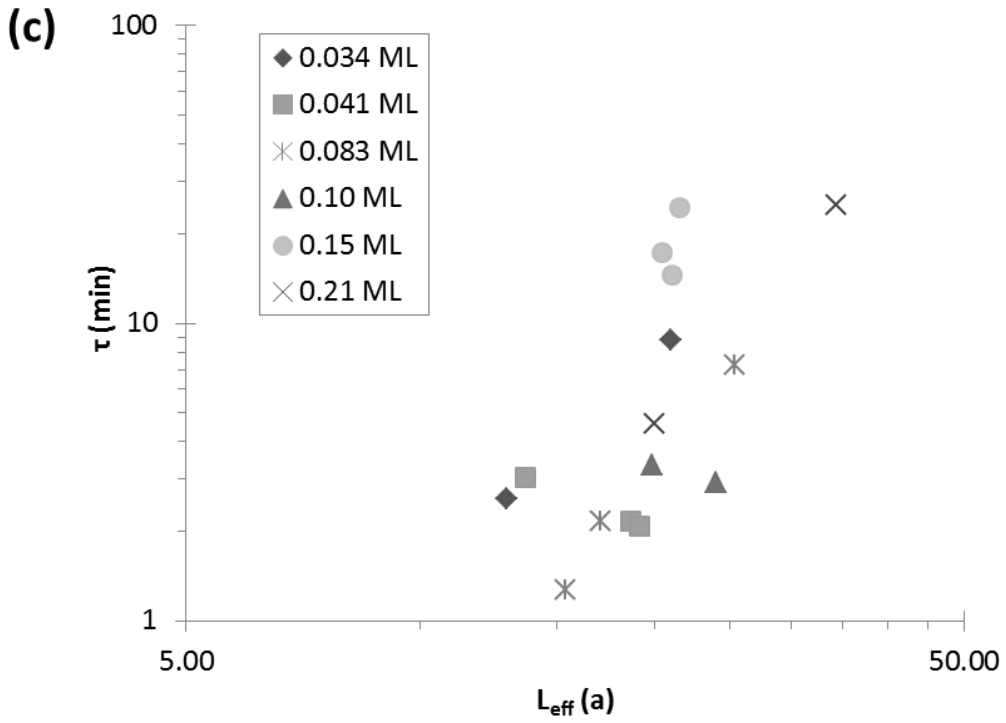

Figure 19. continued.

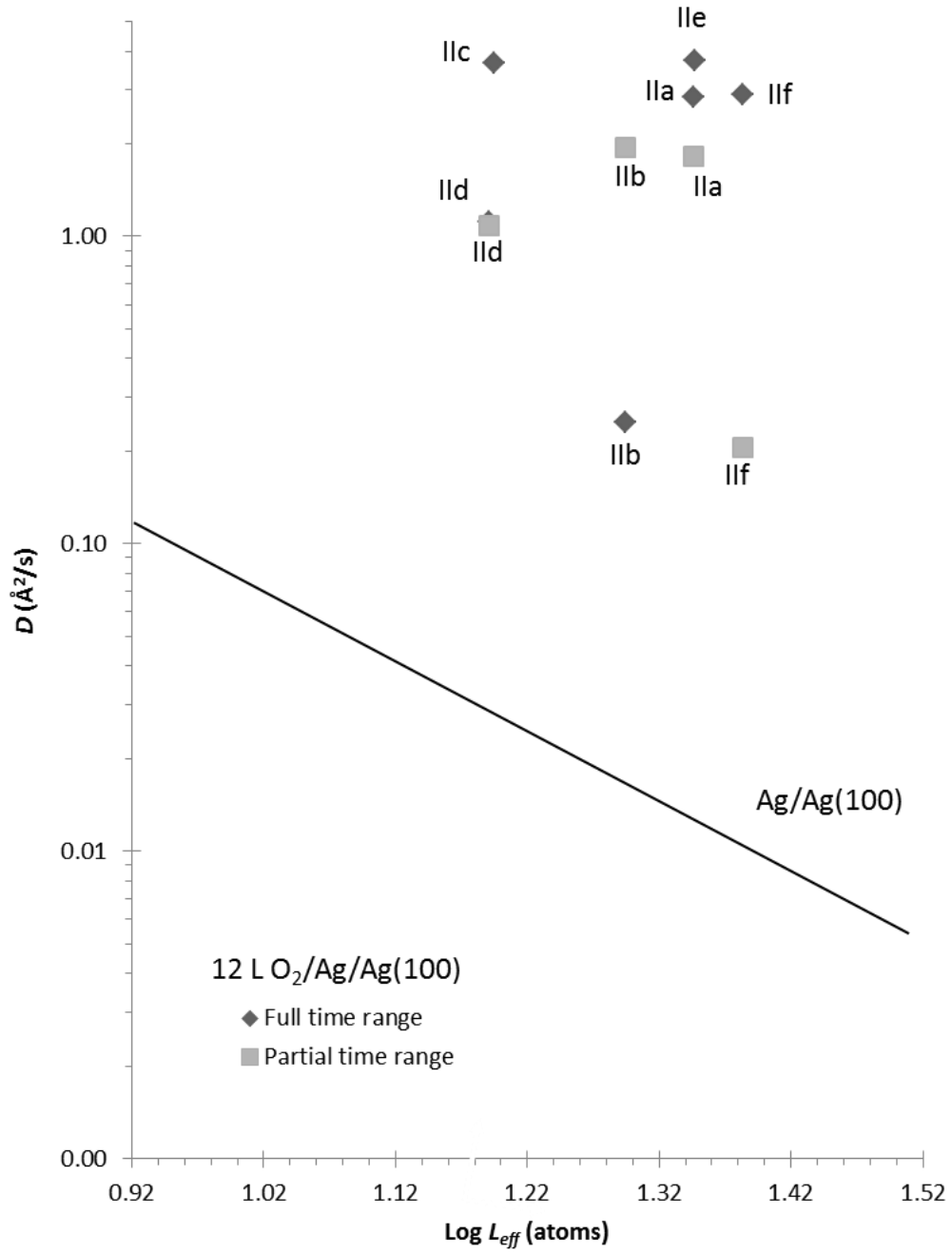

Figure 20. Ag island diffusion after exposure of 12 L O_2 on 0.1 ML Ag at 245 K; the rates have been adjusted to 300 K from the values reported in Fig. 3 (5/9/2000). Island diffusion over the whole observation time (diamonds) and while island area was stable (squares). The black solid line represents clean data reported by Pai *et al.* at 300 K.[11]

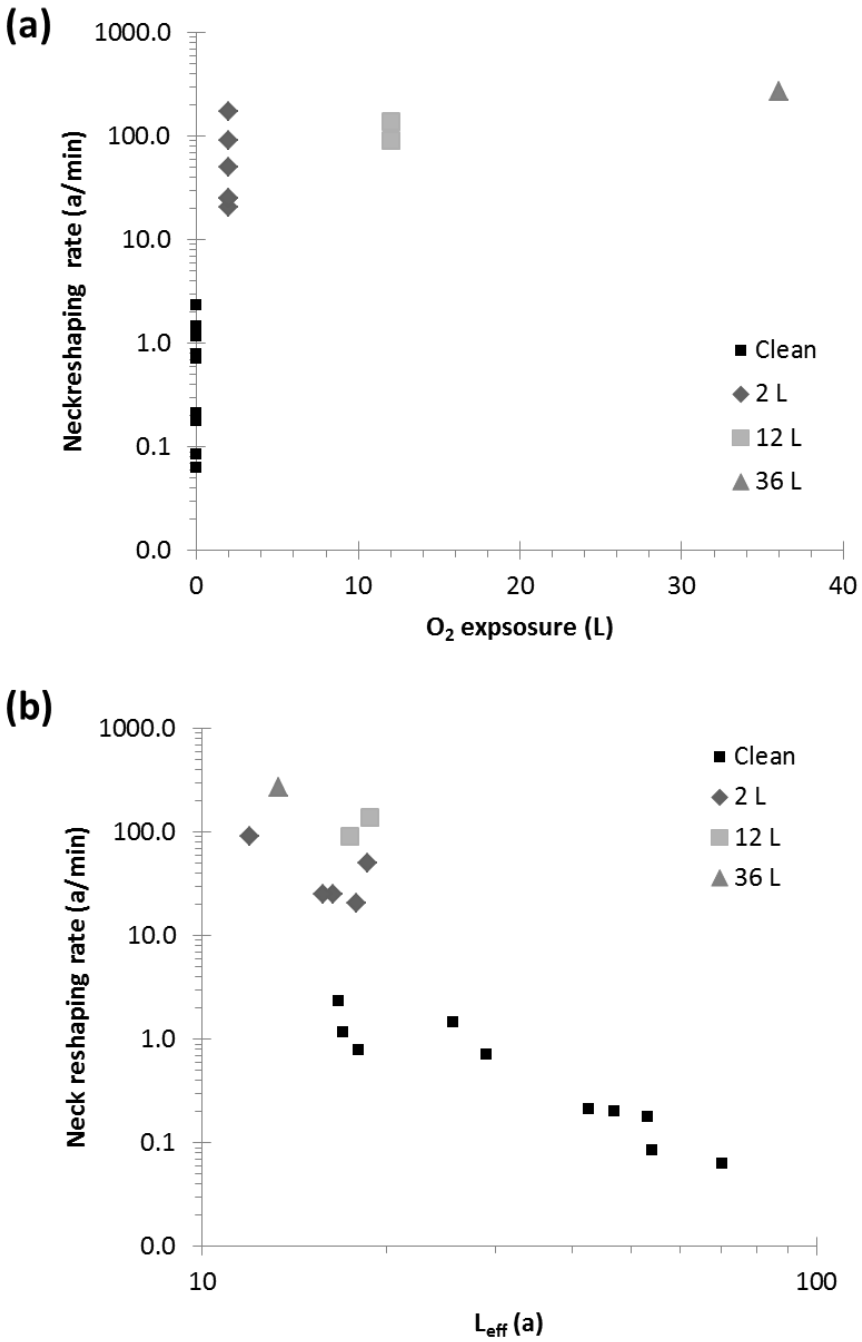

This figure continues on the following page.

Figure 21. Silver island relaxation with different oxygen exposures on 0.3 ML Ag at 250 K. (a) Rates at which islands of different sizes relax, including temperature compensation to 300 K, (b) the dependence of the reshaping rate on island size and (c) the relaxation time τ versus effective length L_{eff} , without temperature compensation. (a-c) compared to corner-to-corner reshaping on the clean surface, black squares and line, at 300 K where $\tau \sim L^n$, with $n \approx 3.1$.[15] Same oxygen data that is presented in Fig. 10. Surface lattice constant a = 0.289 nm.

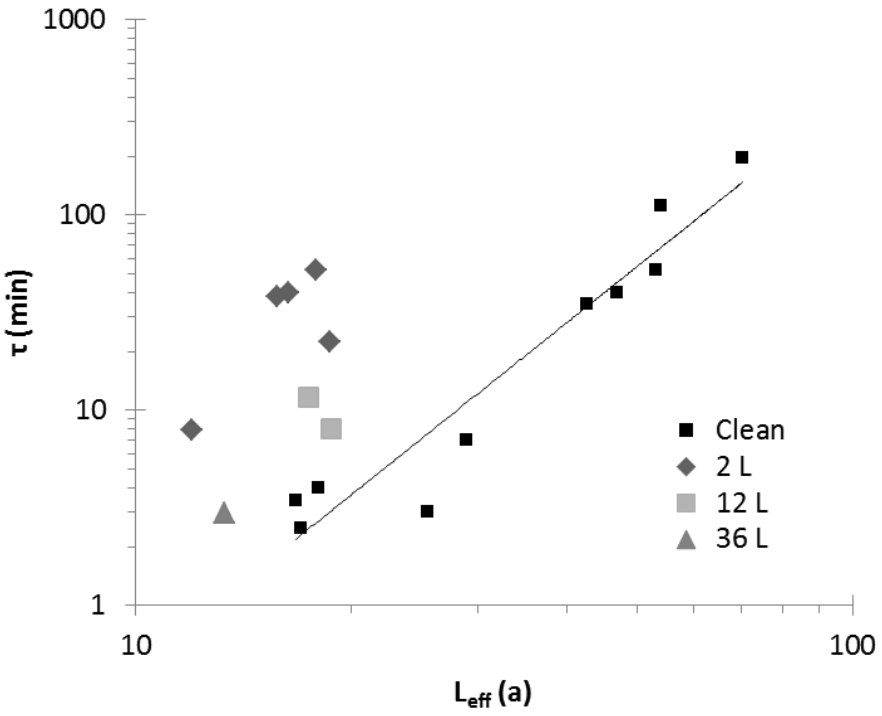

Figure 21. continued.

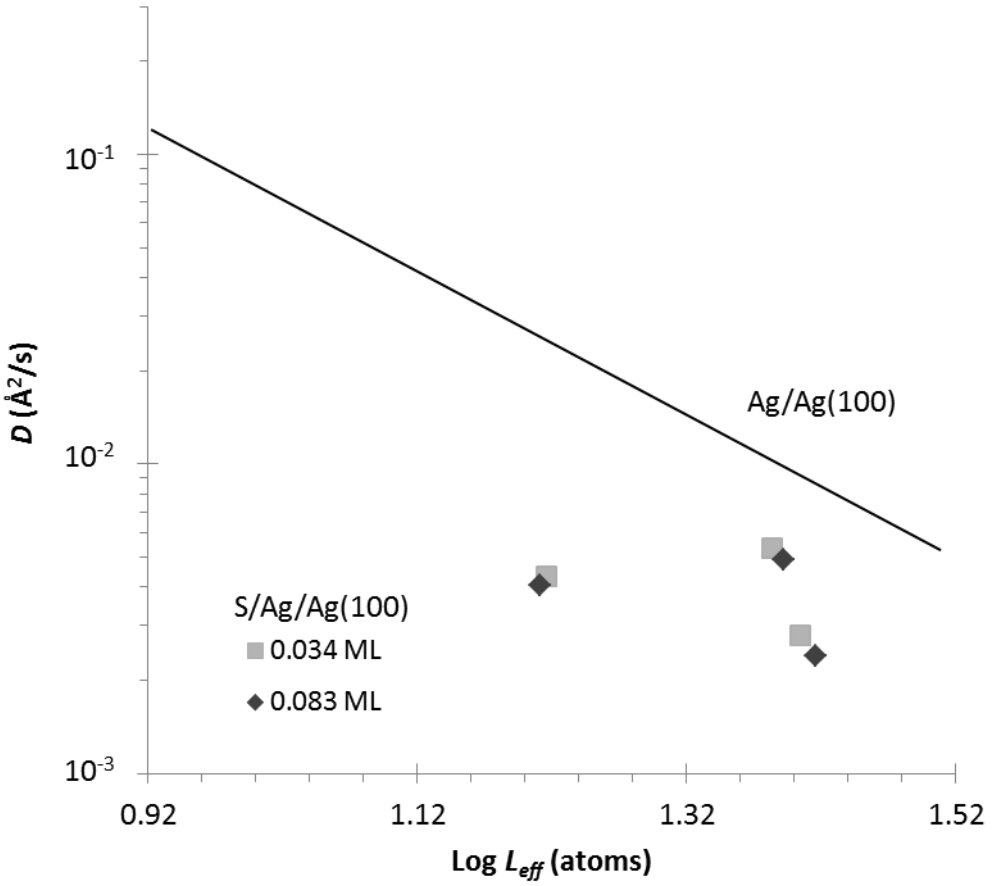

Figure 22. Ag island diffusion after different sulfur depositions on 0.3 ML Ag at 300 K (12/22/2008 and 1/26/2009). Island diffusion over the whole observation time. The black solid line represents clean data reported by Pai *et al.* at 300 K.[11]

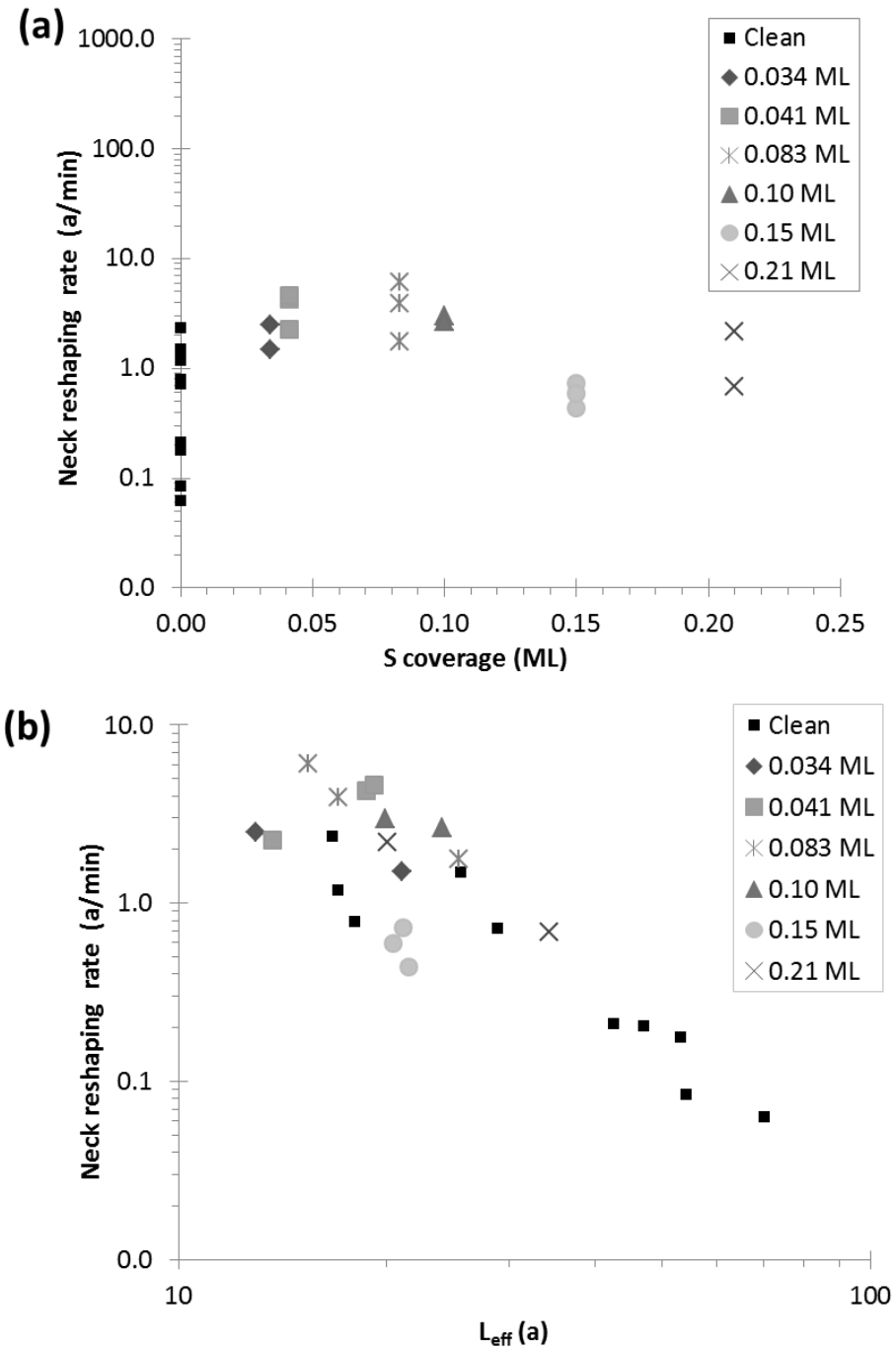

This figure continues on the following page.

Figure 23. Silver island relaxation with different sulfur coverages on 0.3 ML Ag at 300 K. (a) Rates at which islands of different sizes relax, (b) the dependence of the reshaping rate on island size, and (c) the relaxation time τ versus effective length L_{eff} , without temperature compensation. (a-c) compared to corner-to-corner reshaping on the clean surface, black squares and line, at 300 K where $\tau \sim Ln$, with $n \approx 3.1$.[15] Same oxygen data that is presented in Fig. 19. Surface lattice constant a = 0.289 nm.

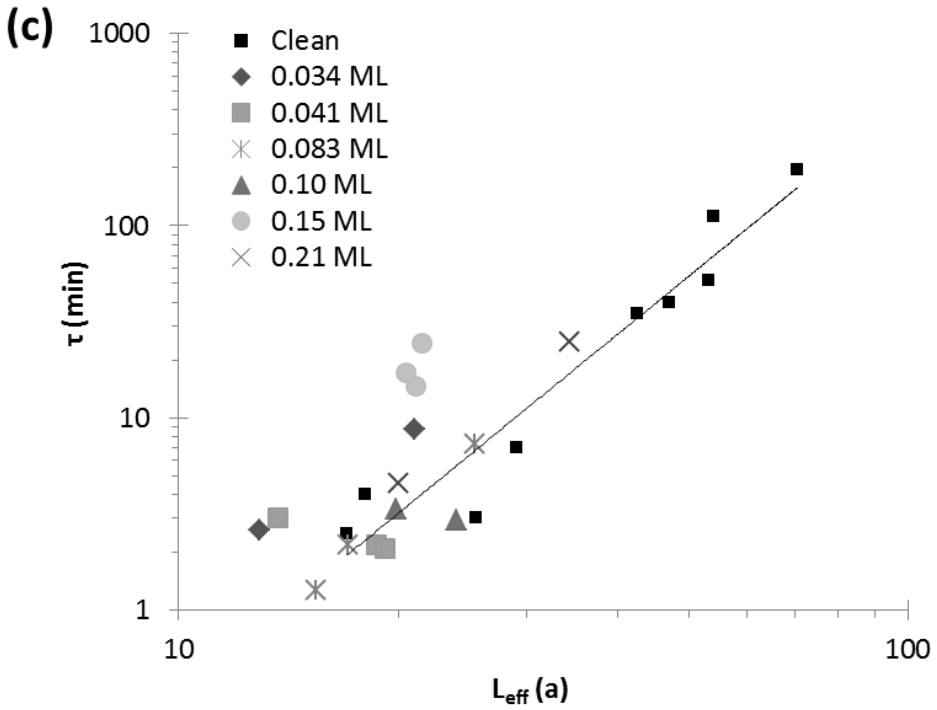

Figure 23. continued.

Tables

Table I. O/Ag/Ag(100) island diffusion 0.1 ML Ag with 12 L O_2 at 245 K and rate adjusted to 300 K (T comp.). The MSD plots are given in the Appendix.

Expt. Date	Type island	initial area, nm^2		Full time range		Partial time range (~stable island area)		
		1st	2nd	D, $\times10^{-4}$ nm^2/s	T comp. D, $\times10^{-2}$ nm^2/s	time range, s	D, $\times10^{-5}$ nm^2/s	T comp. D, $\times10^{-2}$ nm^2/s
5/9/00	Ia	18.5	19.4	5.38	11.7	up to 7049	51.7	11.3
	IIa	41.2		1.30	2.84	after 9815	8.38	1.82
	IIb	32.4		0.114	0.248	up to 10508	8.90	1.94
	IIc	20.5		1.69	3.67			
	IId	20.1		0.513	1.12	up to 9122	4.97	1.08
	IIe	41.4		1.70	3.71			
	IIf	48.9		1.32	2.89	up to 12184	0.942	0.205

Table II. O/Ag/Ag(100) island restructuring: Neck width reshaping rate.

Expt.	O_2 exposure, L	Merge	L_{eff}		$L_{eff}/2$		Neck rate, a/min	T comp. Neck rate, a/min	τ, s	τ, min	τ vs. L_{eff} power fit, n
			nm	a	nm	a					
2/20/2000	2.0	1	5.2	17.84	2.58	8.92	0.17	32.73	3150	53	3.72
		2	5.4	18.63	2.69	9.32	0.41	79.73	1350	23	
		3	4.7	16.35	2.36	8.18	0.21	39.53	2390	40	
		4	4.6	15.75	2.28	7.88	0.21	39.91	2280	38	
		5	2.7	9.24	1.34	4.62	1.42	273.73	195	3	
		6	3.5	11.98	1.73	5.99	0.76	145.75	475	8	
2/29/2000	12	1	5.4	18.72	2.71	9.36	1.16	223.15	485	8	
		2	5.0	17.40	2.51	8.70	0.75	143.56	701	12	
2/27/2000	36	1	3.8	13.31	1.92	6.66	2.23	429.54	179	3	

Table III. S/Ag/Ag(100) island diffusion with 0.3 ML Ag at 300 K. The MSD plots are given in the Appendix.

Expt. Date	ML S	Type island	initial area, nm^2		Full time range
			1st	2nd	D, $\times10^{-5}$ nm^2/s
12/22/08	0.034	Ia	54.2	53.5	2.78
		Ib	23.4	21.8	4.32
		Ic	45.2	52.5	5.35
1/26/09	0.083	Ia	51.4	50.4	4.89
		Ib	20.3	24.0	4.05
		Ic	57.8	55.7	2.39

Table IV. S/Ag/Ag(100) island restructuring

Expt. date	S coverage, ML	Average island area, nm^2	Merge	Individual initial area, nm^2		Pair initial area, nm^2	% difference between individual and average area		% difference between conjoined and average area	Rate over whole time range			Neck / height	Neck / area
										Neck width, $x10^{-3}$ nm/s	Height, $x10^{-3}$ nm/s	Area, $x10^{-3}$ nm^2/s		
12/22/08	0.034	28	1	62.9	59.1	122	77	72	126	3.3	-2.3	2.1	1.4	1.6
			2	15.3	12.6	28	-58	-75	0.39	1.5	-2.2	-2.1	0.7	0.7
			3	16.0	9.1	25	-54	-101	-10	1.1	-5.3	-7.4	0.2	0.1
12/15/08	0.041	18	1	18.2	13.1	31	3	-30	56	4.9	-5.8	-6.8	0.8	0.7
			2	31.3	26.9	58	56	41	107	6.2	-5.4	-1.8	1.1	3.4
			3	31.9	29.4	61	57	50	111	6.5	-4.7	2.8	1.4	2.3
1/26/09	0.083	30	1	33.0	15.6	49	10	-63	47	4.4E	-4.5	1.5	1.0	2.9
			2	22.6	17.1	40	-28	-55	28	7.9	-5.9	-23	1.3	0.3
			3	57.1	51.0	108	62	52	113	0.60	-0.10	4.2	6.0	0.1
2/16/09	0.1	33	1	59.2	37.4	97	55	11	97	3.8	-3.3	-1.7	1.2	2.2
			2	59.2	37.4	97	55	11	97	2.2	-2.5	1.7	0.9	1.3
3/2/09	0.15	30	1	32.7	44.8	78	9	40	89	1.9	-0.80	-3.2	2.4	0.59
			2	42.2	32.2	74	34	7	85	3.1	-1.4	-4.0	2.2	0.78
			3	42.4	27.4	70	35	-9	80	2.2	-1.3	7.6	1.7	0.29
1/6/09	0.21	43	1	105.0	92.2	197	84	73	129	2.9	0.40	21	7.3	0.14
			2	36.5	30.5	67	-16	-33	44	1.7	0.20	13	8.5	0.13

Table V. S/Ag/Ag(100) island restructuring: Neck width reshaping rate.

Expt.	ML S	Avg. L_{eff}, nm	Merge	L_{eff}		$L_{eff}/2$		Connect type	Connect direction	Neck FWHM linear fit			τ vs. L_{eff}
				(nm)	(a)	(nm)	(a)			Rate (nm/s)	Rate (a/min)	τ (s)	power fit, n
12/22/08	0.034	5.3	*1**	*7.813*	*27.03*	*3.906*	*13.52*	*c-to-c*	*<110>*	*0.00744*	*1.54*	*525*	2.50
			2	3.735	12.92	1.867	6.46	c-to-c	<110>	0.0120	2.50	155	
			3	3.538	12.24	1.769	6.12	c-to-c	<001>				
			Avg.	**5.028**	**17.40**	**2.51**	**8.70**			**0.0097**	**2.02**	**340**	
			Std. dev.	2.413	8.35	1.21	4.17			0.0033	0.68	262	
12/15/08	0.041	4	1	3.955	13.68	1.977	6.84	c-to-c	<001>	0.0109	2.26	182	-1.10
			2	5.391	18.66	2.696	9.33	c-to-c	<110>	0.0207	4.31	130	
			3	5.538	19.16	2.769	9.58	c-to-c	<001>	0.0222	4.60	125	
			Avg.	**4.96**	**17.17**	**2.48**	**8.58**			**0.0179**	**3.72**	**146**	
			Std. dev.	0.87	3.03	0.44	1.51			0.0061	1.28	32	
1/26/09	0.083	5	1	4.926	17.04	2.46	8.52	c-to-c	<001>	0.0189	3.93	130	3.35
			2	4.454	15.41	2.23	7.71	s-to-s	<110>	0.0293	6.08	76	
			*3**	*7.350*	*25.43*	*3.67*	*12.7*	*r-to-r*	*<110>*	*0.00845*	*1.75*	*435*	
			Avg.	**5.58**	**19.30**	**2.79**	**9.65**			**0.0189**	**3.92**	**214**	
			Std. dev.	1.55	5.38	0.78	2.69			0.0104	2.16	194	
2/16/09	0.10	6	1	5.74	19.87	2.87	9.93	r-to-r	<110>	0.01435	2.98	200	-0.70
			2	6.95	24.05	3.47	12.02	r-to-r	<001>	0.01280	2.66	175	
			Avg.	**6.35**	**21.96**	**3.17**	**10.98**			**0.01358**	**2.82**	**188**	
			Std. dev.	0.85	2.96	0.43	1.48			0.00110	0.23	18	
3/2/09	0.15	5	1	6.224	21.54	3.112	10.77	s-to-s	<001>	0.00211	0.438	1475	5.7903
			2	6.099	21.10	3.049	10.55	c-to-c	<110>	0.00350	0.728	870	
			3	5.910	20.45	2.955	10.22	s-to-s	<110>	0.00286	0.593	1035	
			Avg.	**6.08**	**21.03**	**3.04**	**10.52**			**0.00282**	**0.59**	**1127**	
			Std. dev.	0.16	0.55	0.08	0.27			0.00070	0.14	313	
1/6/09	0.21	7	1	9.92	34.3	4.96	17.2	c-to-c	<110>	0.003319	0.6891	1495	3.14
			2	5.79	20.0	2.89	10.0	c-to-c	<110>	0.01052	2.185	275	
			Avg.	**7.86**	**27.2**	**3.93**	**13.6**			**0.00692**	**1.4368**	**885**	
			Std. dev.	2.93	10.1	1.46	5.1			0.00509	1.0575	863	

Table VI. Clean Ag/Ag(100) island reshaping at 300 K. Data analyzed by Conrad Stoldt.[15]

Expt.	Merge	L_{eff} (a)	Neck rate (a/min)	τ (min)
12/5/2008		17	2.35	3.47
8/31/1993	1	70	0.06	195
	2	54	0.08	111
5/28/1994		47	0.20	40
	4	53	0.18	52
12/8/1997	2	29	0.72	7
	3	26	1.48	3
12/16/1997	2	17	1.18	2.5
12/11/1997	1	18	0.78	4
	2	43	0.21	35

Appendix. Mean squared displacement plots

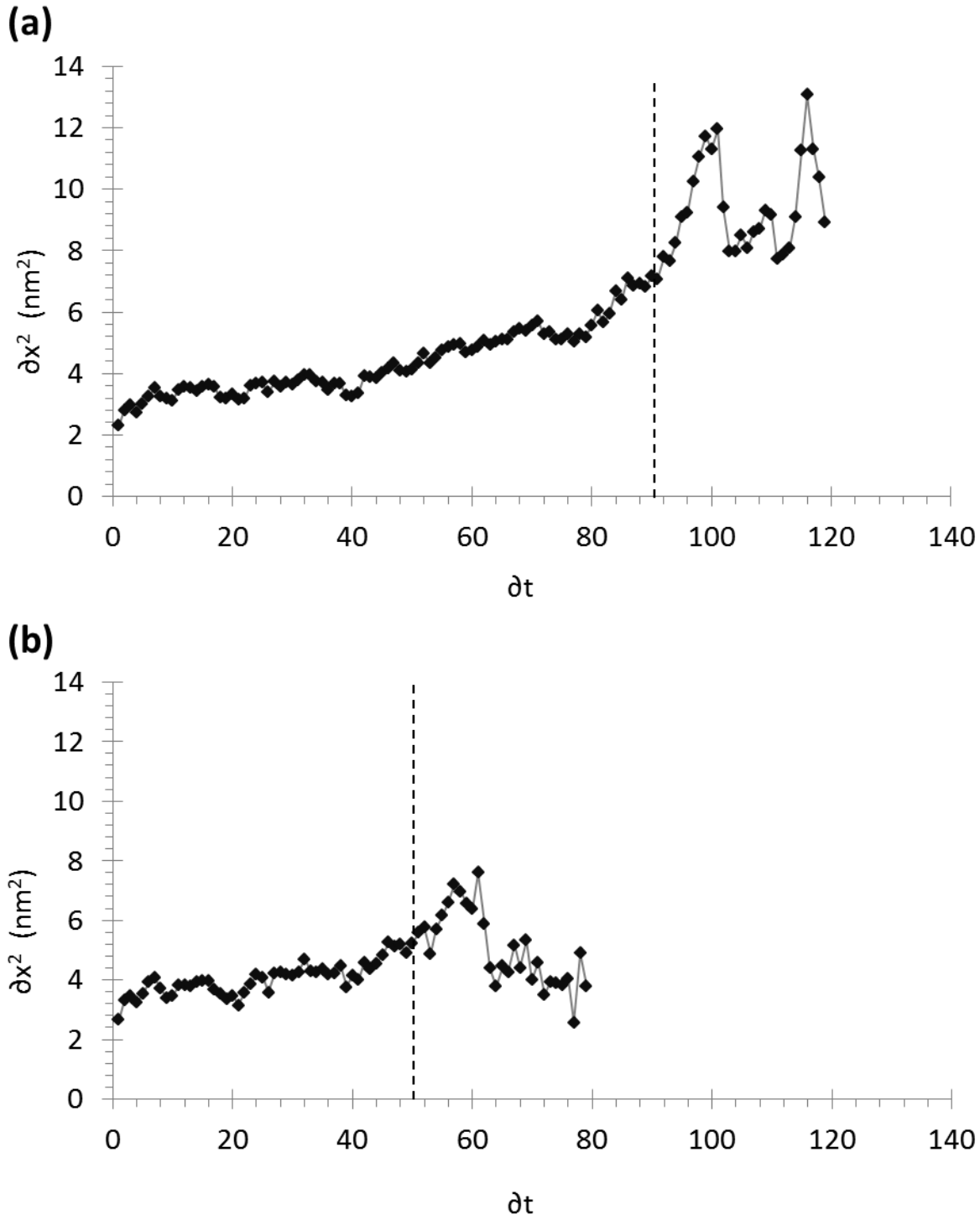

Figure A.1. Diffusion of island a after exposure of 12 L O_2 on 0.1 ML Ag at 245 K. Island designations are given in Fig. 3a. The dashed vertical line marks the cutoff for determining the slope of the line. (a) MSD over the whole observation period. (b) MSD while the island area was stable, after 9815 s.

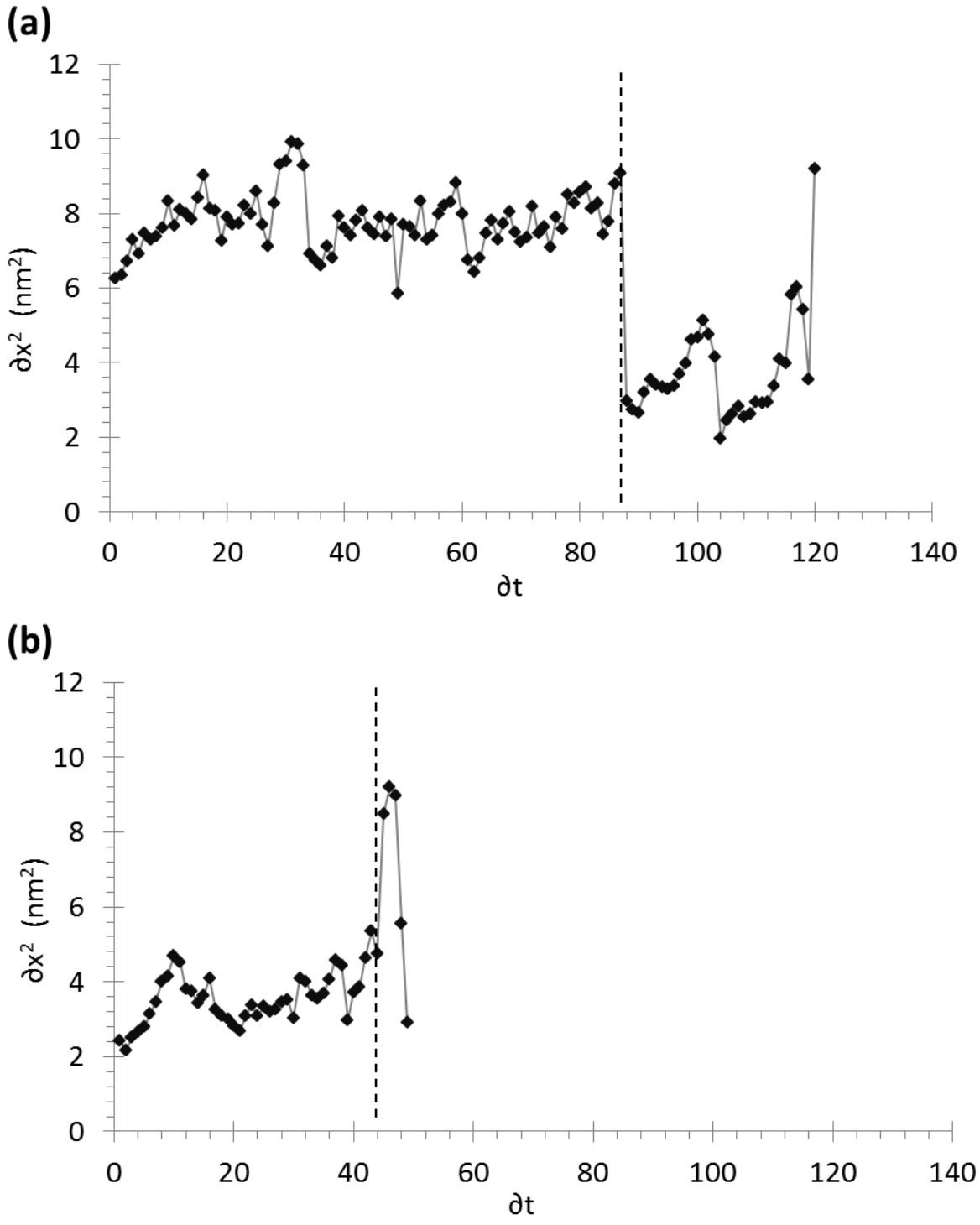

Figure A.2. Diffusion of island b after exposure of 12 L O_2 on 0.1 ML Ag at 245 K. Island designations are given in Fig. 3a. The dashed vertical line marks the cutoff for determining the slope of the line. (a) MSD over the whole observation period. (b) MSD while the island area was stable, up to 10508 s.

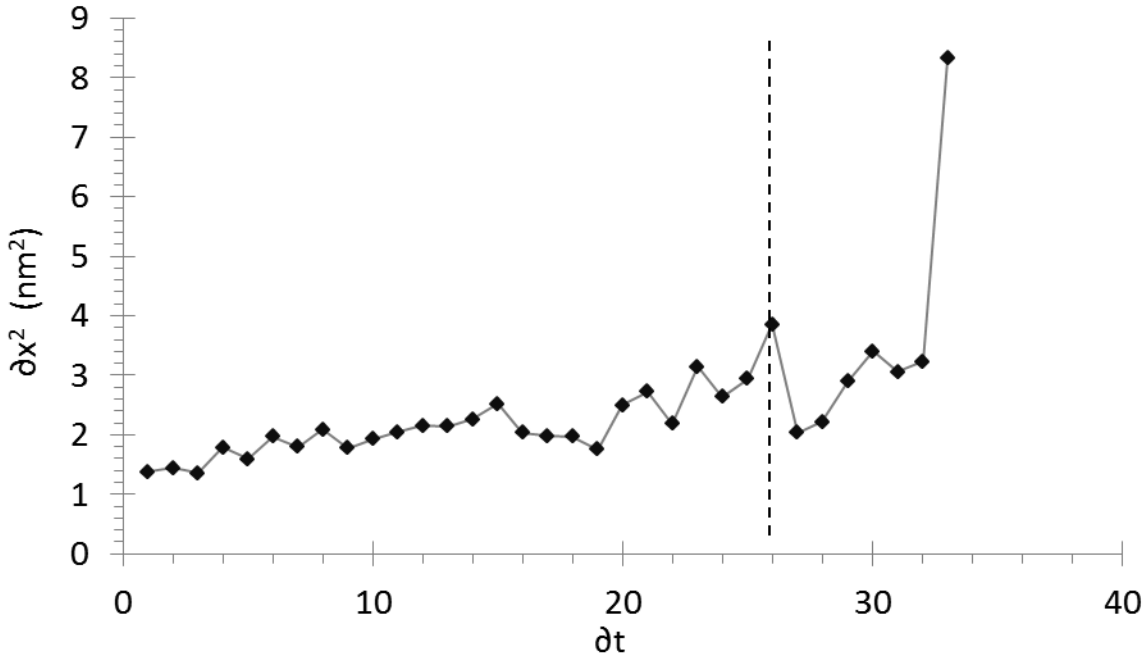

Figure A.3. Diffusion of island c after exposure of 12 L O_2 on 0.1 ML Ag at 245 K. Island designations are given in Fig. 3a. The dashed vertical line marks the cutoff for determining the slope of the line. MSD over the whole observation period.

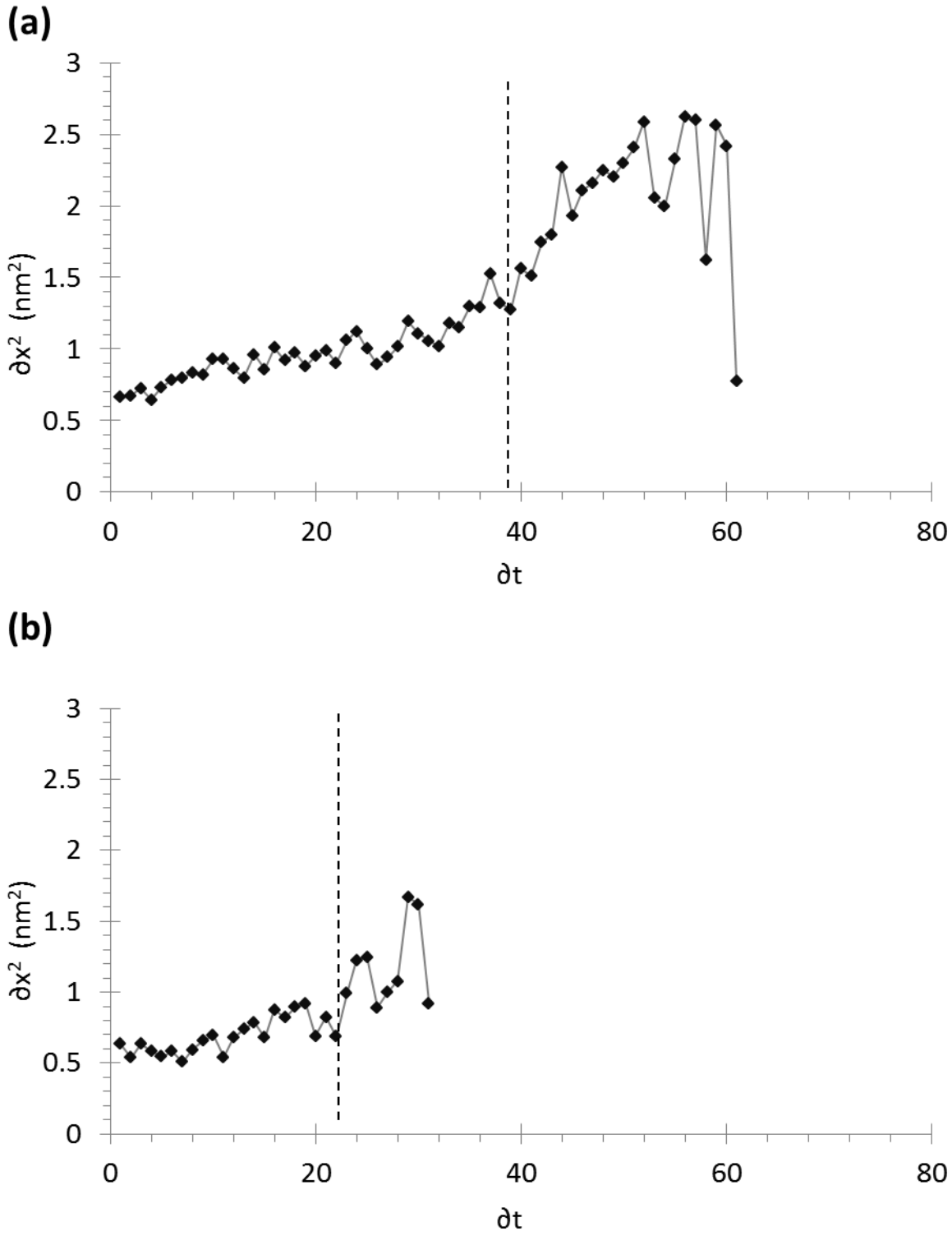

Figure A.4. Diffusion of island d after exposure of 12 L O_2 on 0.1 ML Ag at 245 K. Island designations are given in Fig. 3a. The dashed vertical line marks the cutoff for determining the slope of the line. (a) MSD over the whole observation period. (b) MSD while the island area was stable, up to 9122 s.

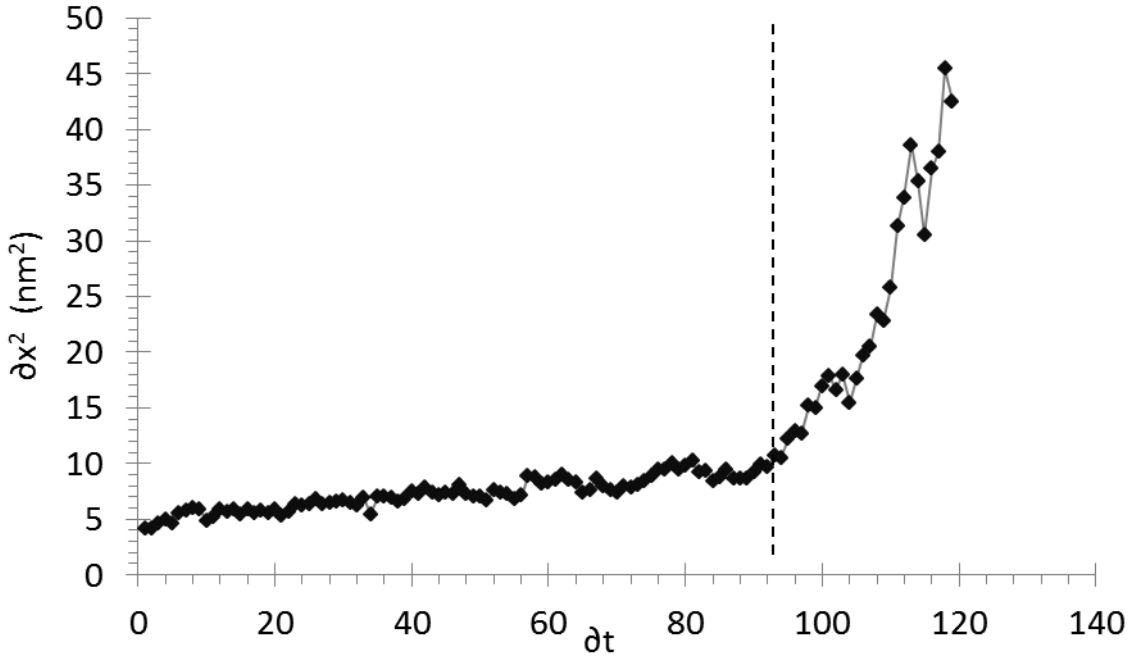

Figure A.5. Diffusion of island e after exposure of 12 L O_2 on 0.1 ML Ag at 245 K. Island designations are given in Fig. 3a. The dashed vertical line marks the cutoff for determining the slope of the line. MSD over the whole observation period.

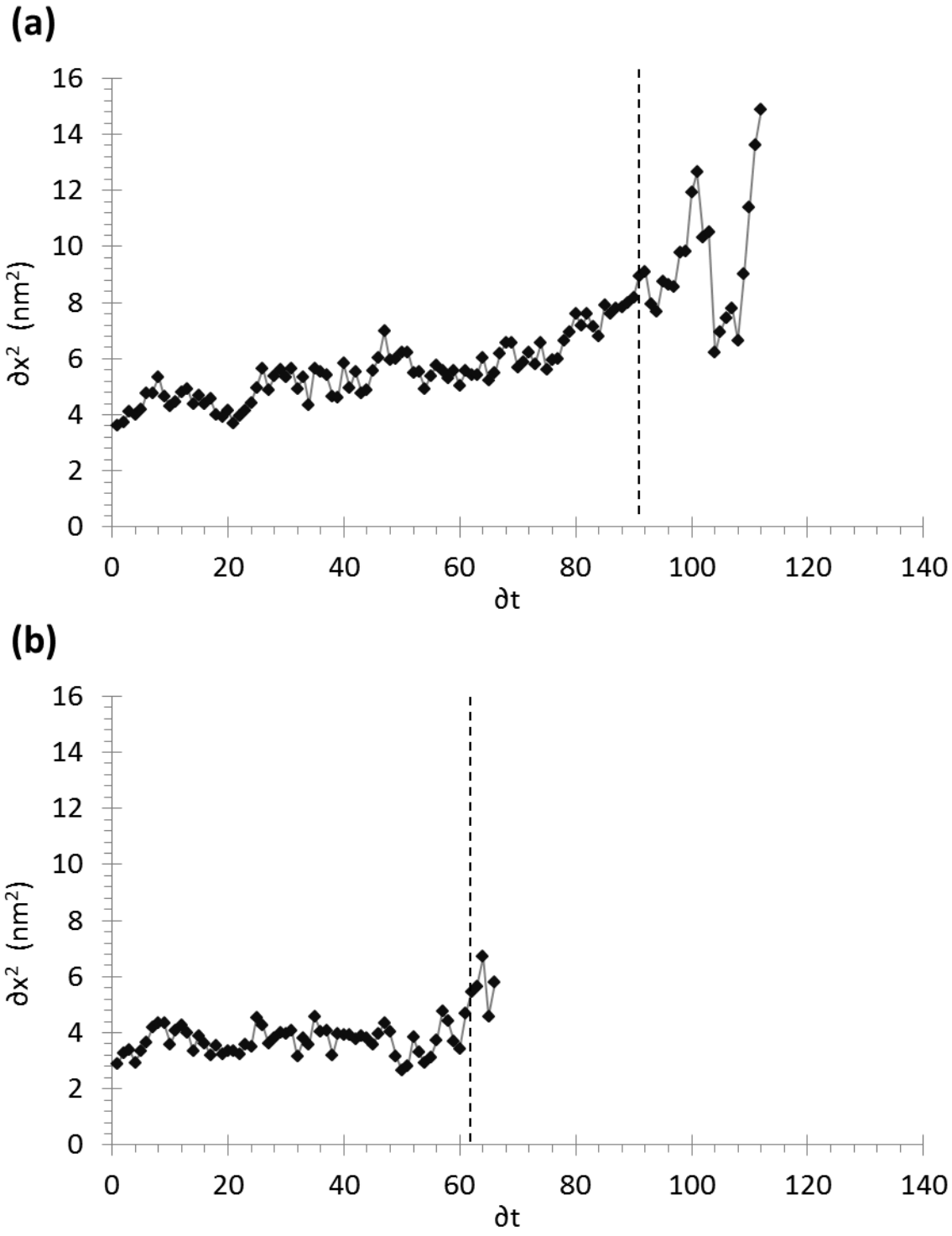

Figure A.6. Diffusion of island f after exposure of 12 L O_2 on 0.1 ML Ag at 245 K. Island designations are given in Fig. 3a. The dashed vertical line marks the cutoff for determining the slope of the line. (a) MSD over the whole observation period. (b) MSD while the island area was stable, up to 12184 s.

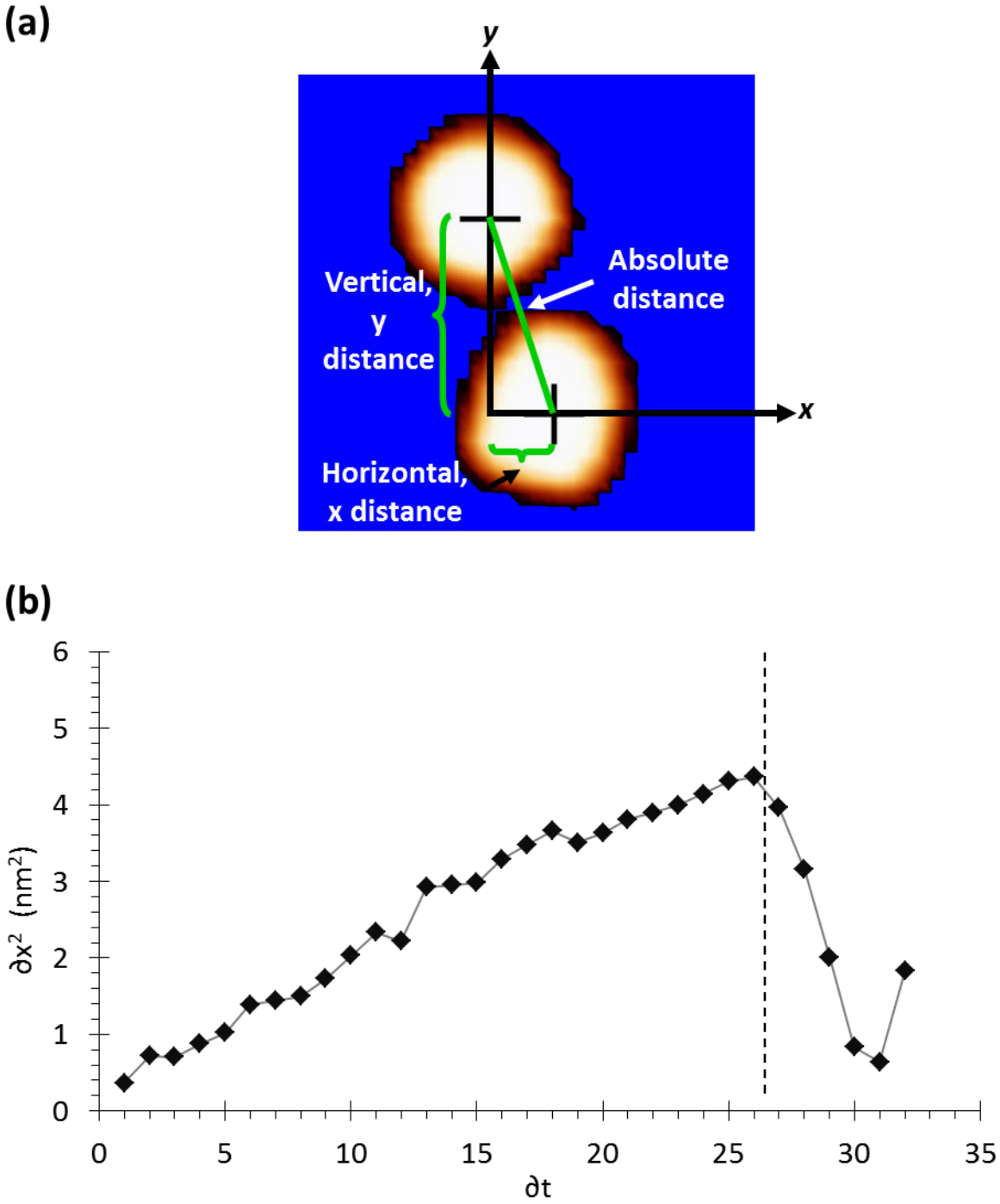

This figure continues on the following page.

Figure A.7. Diffusion of a Ag island pair after exposure of 12 L O_2 on 0.1 ML Ag at 245 K. Island designation is given in Fig. 3a. (a) Smoothed and flooded STM image showing the island centers, 15.3×15.3 nm^2 (5/9/2000 m5). Smoothing does not affect the center position. (b) MSD over the whole observation period. (c) MSD while the island area was stable, up to 7049 s. (b-c) The dashed vertical line marks the cutoff for determining the slope of the line.

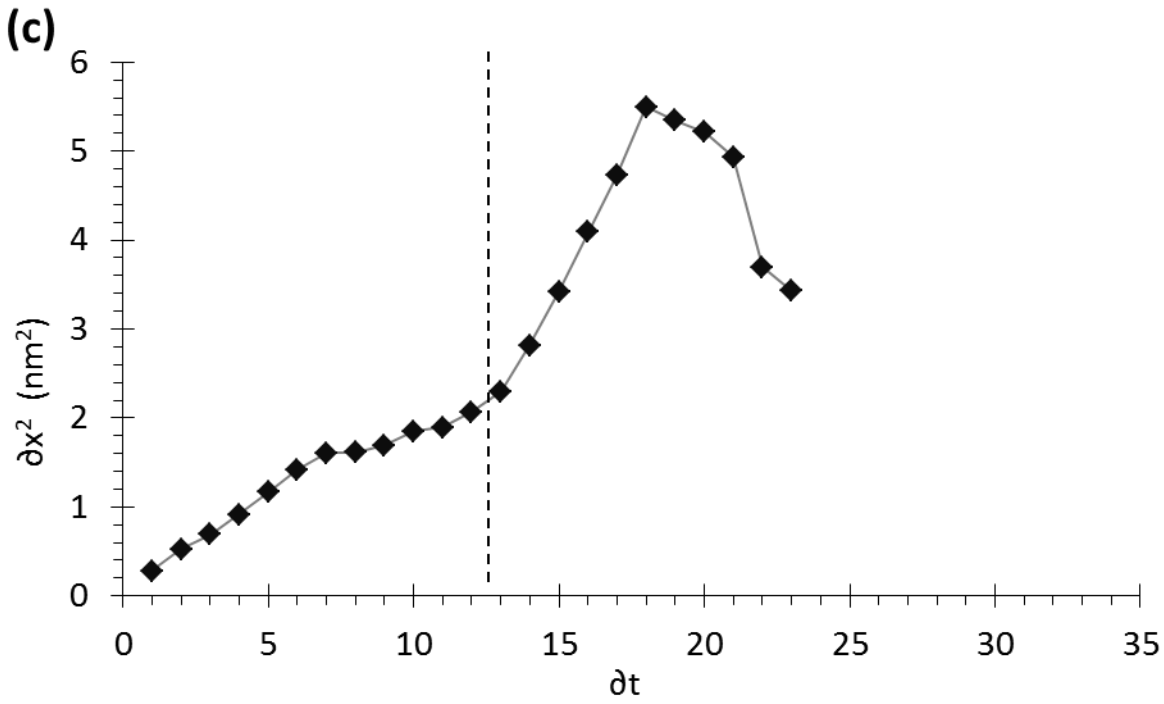

Figure A.7. continued.

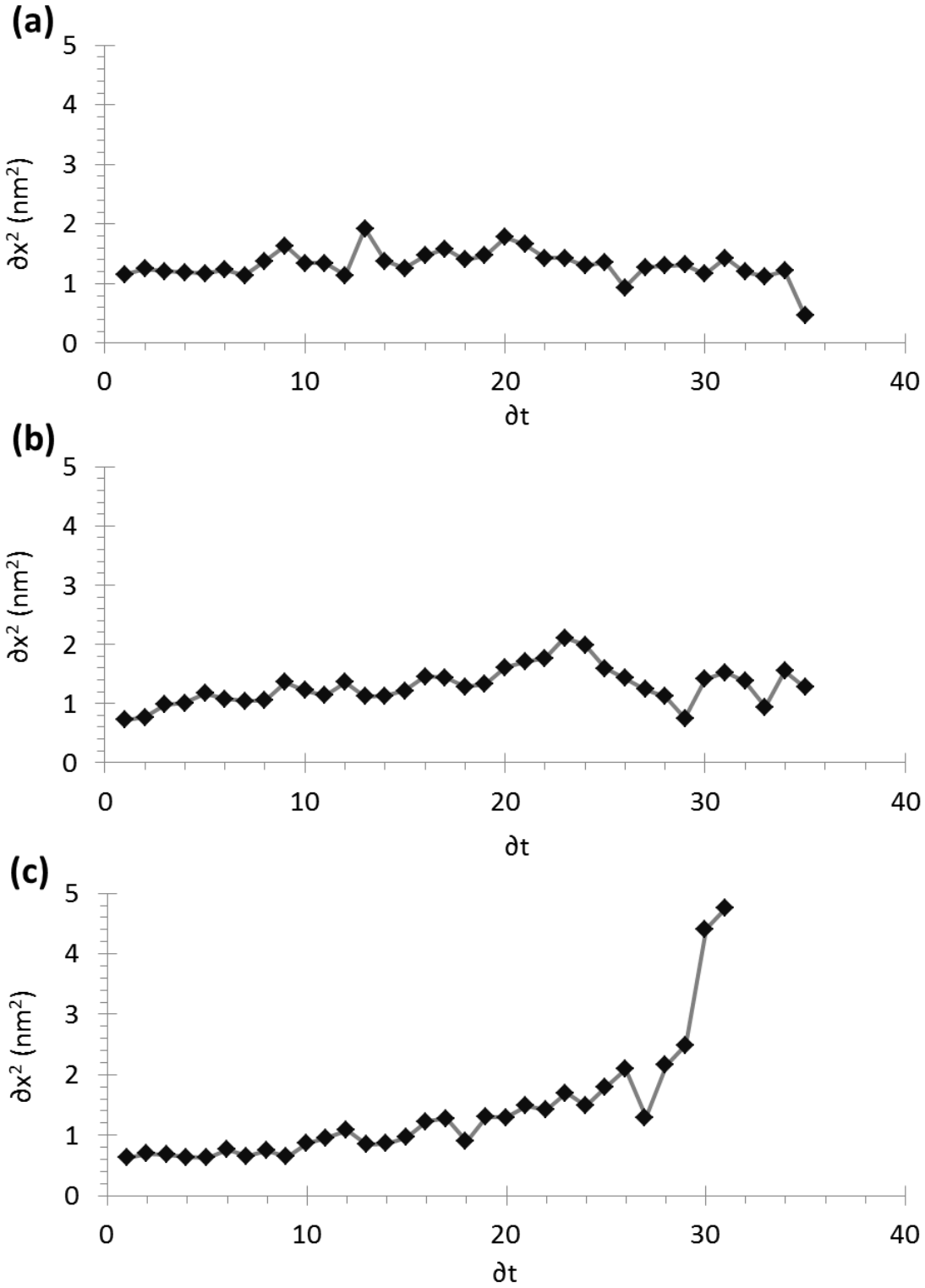

Figure A.8. Diffusion of island pairs after deposition of 0.034 ML S on 0.3 ML Ag at 300 K. Island designations are given in Fig. 4a: (a) pair a, (b) pair b, and (c) pair c. MSD over the whole observation period.

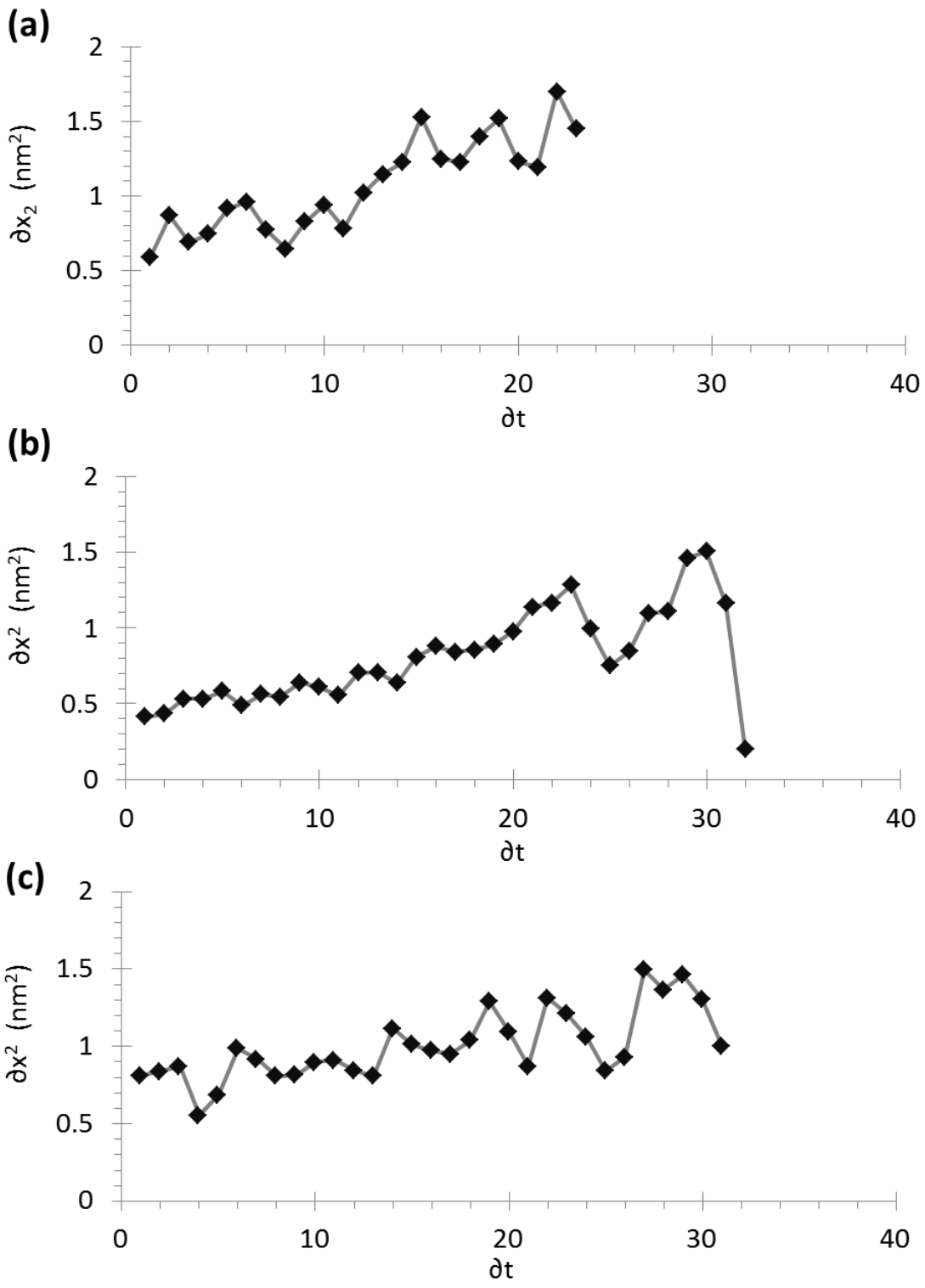

Figure A.9. Diffusion of island pairs after deposition of 0.083 ML S on 0.3 ML Ag at 300 K. Island designations are given in Fig. 4a: (a) pair a, (b) pair b, and (c) pair c. MSD over the whole observation period.

References

(1) Rocca, M.; Savio, L.; Vattuone, L.; Burghaus, U.; Palomba, V.; Novelli, N.; Buatier de Mongeot, F.; Valbusa, U.; Gunnella, R.; Comelli, G.; Baraldi, A.; Lizzit, S.; Paolucci, G. *Physical Review B* **2000**, *61*, 213.

(2) Vattuone, L.; Burghaus, U.; Savio, L.; Rocca, M.; Costantini, G.; de Mongeot, F. B.; Boragno, C.; Rusponi, S.; Valbusa, U. *Journal of Chemical Physics* **2001**, *115*, 3346.

(3) Russell, S. M.; Shen, M.; Liu, D.-J.; Thiel, P. A. *Surface Science* **2011**, *605*, 520.

(4) Shen, M.; Russell, S. M.; Liu, D.-J.; Thiel, P. A. *Journal of Chemical Physics* **2011**, *135*, 154701.

(5) Shen, M.; Liu, D.-J.; Jenks, C. J.; Evans, J. W.; Thiel, P. A. *Surface Science* **2009**, *603*, 1486.

(6) Thiel, P. A.; Shen, M.; Liu, D.-J.; Evans, J. W. *Journal of Physical Chemistry C* **2009**, *113*, 5047.

(7) Wen, J.-M.; Evans, J. W.; Bartelt, M. C.; Burnett, J. W.; Thiel, P. A. *Physical Review Letters* **1996**, *76*, 652.

(8) Stoldt, C. R.; Jenks, C. J.; Thiel, P. A.; Cadilhe, A. M.; Evans, J. W. *Journal of Chemical Physics* **1999**, *111*, 5157.

(9) Stoldt, C. R.; Cadilhe, A. M.; Bartelt, M. C.; Jenks, C. J.; Thiel, P. A.; Evans, J. W. *Progress in Surface Science* **1998**, *59*, 67.

(10) Stoldt, C. R.; Cadilhe, A. M.; Jenks, C. J.; Wen, J. M.; Evans, J. W.; Thiel, P. A. *Physical Review Letters* **1998**, *81*, 2950.

(11) Pai, W. W.; Swan, A. K.; Zhang, Z.; Wendelken, J. F. *Physical Review Letters* **1997**, *79*, 3210.

(12) Caspersen, K. J.; Layson, A. R.; Stoldt, C. R.; Fournée, V.; Thiel, P. A.; Evans, J. W. *Physical Review B* **2002**, *65*, 193407.

(13) Layson, A. R.; Thiel, P. A. *Surface Science* **2001**, *472*, L151.

(14) Antczak, G.; Ehrlich, G. *Surface diffusion : metals, metal atoms, and clusters*; Cambridge University Press: New York, 2010.

(15) Liu, D.-J.; Stoldt, C. R.; Thiel, P. A.; Evans, J. W. *Materials Research Society Symposium Proceedings* **2002**, *749*, W2.8.

(16) Layson, A. R.; Evans, J. W.; Thiel, P. A. *Physical Review B* **2002**, *65*, 193409.

(17) Note *Samples were synthesized at the Materials Preparation Center, Ames Laboratory USDOE, Ames, IA, USA. See: www.mpc.ameslab.gov.*

(18) Rocca, M.; Savio, L.; Vattuone, L.; Burghaus, U.; Palomba, V.; Novelli, N.; Buatier de Mongeot, F.; Valbusa, U.; Gunnella, R.; Comelli, G.; Baraldi, A.; Lizzit, S.; Paolucci, G. *Physical Review B* **2000**, *61*, 213.

(19) Wagner, C. *J. Chem. Phys.* **1953**, *21*, 1819.

(20) Schwaha, K.; Spencer, N. D.; Lambert, R. M. *Surf. Sci* **1979**, *81*, 273.

(21) Rovida, G.; Pratesi, F. *Surf. Sci* **1981**, *104*, 609.

(22) Russell, S. M.; Shen, M.; Liu, D.-J.; Thiel, P. A. *Surf. Sci.* **2011**, *605*, 520.

(23) Layson, A. R.; Thiel, P. A. *Surface Science* **2001**, *472*, L151.

(24) de Mongeot, F. B.; Cupolillo, A.; Valbusa, U.; Rocca, M. *Chemical Physics Letters* **1997**, *270*, 345.

CHAPTER VII
General Conclusions

We have used scanning tunneling microscopy and spectroscopy and density functional theory to investigate the interaction between oxygen and silver or sulfur and silver on the low-index silver surfaces in ultra-high vacuum.

Sulfur and sulfur containing species form a rich variety of structures, which generally involve surface reconstruction when atomic S is adsorbed. On Ag(111), Ag-S clusters form whose exact structure and composition depend on the sample temperature. On Ag(100) between 230 and 300 K, a mixture of the p(2×2) simple adsorption phase and the $(\sqrt{17}\times\sqrt{17})R14^{o}$ reconstruction phase appear irreversibly. In addition, chain-like structures are observed in STM, both at room temperature (where they are dynamic) and below (where they are not). Preliminary results for S on Ag(110) shown in Appendix II indicate that this surface also reconstructs to a row phase. Sulfur adsorbs to its preferred sites with adsorption energies of 3.74 and 4.16 eV on the Ag(111) and Ag(100) surfaces respectively. However, H_2S interacts more weakly with Ag(111), with adsorption energy of 0.15 eV. The potential energy surface is very flat for molecular H_2S on Ag(111) at low temperature. The intermolecular interactions more strongly influence the observed surface structures than do the adsorbate-substrate interactions.

The phases sulfur forms on silver surfaces are similar to those formed on copper surfaces of the same geometry. However, these S phases are dissimilar to those formed by oxygen on the same silver or copper surfaces. Oxygen also forms the same phase on silver or copper surface of the same geometry. Therefore, the nature of the chalcogen (O vs. S) seems to have a larger influence on surface structures than does the nature of the metal (Cu vs. Ag).

Chalcogens generally accelerate coinage metal mass transport, which we measure quantitatively through coarsening experiments. However, the detail mechanisms by which oxygen or sulfur enhance coarsening are not necessarily the same. Both oxygen and sulfur introduce Ostwald ripening as the dominant pathway for island coarsening on Ag(100). Oxygen accelerates the diffusion and coalescence of Ag islands strongly, by factors of 10 to 100×. In contrast, sulfur does not accelerate the diffusion of Ag islands nor the rate of

coalescence, but it has a very strong effect on the mechanism of coalescence. The effects of oxygen and sulfur on kink sites and vacancies at island edges may explain these differences. The low oxygen coverage on Ag(110) had a negligible effect on island coarsening. However, with comparable coverage, oxygen strongly accelerated coarsening on Ag(100). Sulfur exerts a much weaker effect on the rate of coarsening on Ag(100) than it does on Ag(111). This is consistent with DFT, which shows that the difference between $E^{Ag\ carrier}_{OR}$ with and without sulfur, is also much smaller on Ag(100) than on Ag(111). The results presented here in conjunction with earlier results from our group, support the hierarchy of OR coarsening rates on the silver surfaces: (110) > (111) > (100).

APPENDIX I

Destabilization of Ag Nanoislands on Ag(100) by Adsorbed Sulfur

A paper published in *The Journal of Chemical Physics.*[a]

Mingmin Shen,[b,c] Selena M. Russell,[b] Da-Jiang Liu,[d] and Patricia A. Thiel [b,d,e]

Abstract

Sulfur accelerates coarsening of Ag nanoislands on Ag(100) at 300 K, and this effect is enhanced with increasing sulfur coverage over a range spanning a few hundredths of a monolayer, to nearly 0.25 monolayers. We propose that acceleration of coarsening in this system is tied to the formation of AgS_2 clusters primarily at step edges. These clusters can transport Ag more efficiently than can Ag adatoms (due to a lower diffusion barrier and comparable formation energy). The mobility of isolated sulfur on Ag(100) is very low so that formation of the complex is kinetically-limited at low sulfur coverages, and thus enhancement is minimal. However, higher sulfur coverages force the population of sites adjacent to step edges, so that formation of the cluster is no longer limited by diffusion of sulfur across terraces. Sulfur exerts a much weaker effect on the rate of coarsening on Ag(100) than it does on Ag(111). This is consistent with theory, which shows that the difference between the total energy barrier for coarsening with and without sulfur, is also much smaller on Ag(100) than on Ag(111).

1. Introduction

Coarsening (ripening) is a pervasive phenomenon in ensembles of small clusters, because it serves to reduce total interfacial area or length, and thus the energy cost associated with these interfaces. This is achieved by a decrease in the number density of clusters, with a

---

[a] Shen, M.; Russell, S. M.; Liu, D.-J.; Thiel, P. A. *The Journal of Chemical Physics* **2011**, *135*, 154701.
[b] Department of Chemistry, Iowa State University, Ames, IA 50011
[c] Current address: Materials and Chemical Sciences Division, Fundamental and Computational Sciences Directorate, Pacific Northwest National Laboratory, Richland, WA 99352
[d] Ames Laboratory – USDOE, Iowa State University, Ames, IA 50011
[e] Department of Materials Science & Engineering, Iowa State University, Ames, IA 50011

corresponding increase in average size. The most commonly anticipated mechanism of coarsening is Ostwald ripening (OR), in which mass is carried between clusters by smaller particles. In general, the nature of the carriers is unknown. Identifying them may open opportunities to manipulate and control ripening, which in some cases is desirable (e.g. ripening can allow control of size distributions[1,2]) and in some cases not (e.g. sintering of heterogeneous catalysts reduces activity[3]).

Surfaces are good model systems for understanding coarsening. Surfaces of the coinage metals are particularly appealing for model studies, since coarsening and surface mass transport can proceed at reasonably low temperature. For *clean* surfaces of Ag and Cu, it is established that single metal atoms are usually the mass carriers. However, the electronegative adsorbate sulfur can accelerate coarsening of homoepitaxial islands on (111) surfaces of these metals by several orders of magnitude.[4-8] It has been proposed that the acceleration of coarsening is due to a change in the nature of the carrier, from single metal atoms to small clusters that contain both metal (M) and sulfur atoms. Two different clusters have been identified as potential carriers on the (111) surfaces: MS_2 and M_3S_3.[8] The former cluster is linear, while the latter is shaped like a flat triangle of M, decorated by a sulfur atom on each edge. For the M_3S_3 clusters, tt has been proposed that these clusters are more abundant than single metal atoms, to a degree which offsets their slower diffusion and makes them more efficient transporters overall.[5, 7]

Both types of clusters have analogs in other systems. Alkanethiols on Au(111) form clusters with Au atoms that can be described as $M(SR)_2$, where R is an alkyl group.[9-12] These are analogous to MS_2. On Ni(111), a triangular Ni_3S_3 cluster has been identified, although its role in coarsening was not studied.[13] On Cu(111), a triangular Cu_3S_3 cluster has been proposed on the basis of density functional theory (DFT)[5] and kinetic measurements.[4] Finally, for coarsening of Co islands on Ag(111) and Au(111) in the presence of adsorbed sulfur, a carrier similar to M_3S_3 has been identified: M_3S_4, which is a M_3S_3 triangle capped by a central sulfur atom.[14,15]

These studies open the question of whether and how sulfur affects coarsening on substrates other than (111), particularly since the M_3S_3 clusters would not match the symmetry of other substrates. One would not expect to find them on a (100) surface, for

instance, although analogs such as square M_4S_4 might be anticipated. This question motivates the present study of a Ag(100) surface. Its answer may contribute to a general understanding of adsorbate-enhanced coarsening of metals.

The system under investigation can be described as S/Ag/Ag(100), since Ag islands are prepared by deposition of Ag on Ag(100), followed by adsorption of sulfur. Background information about both of the simpler systems, S/Ag(100) and Ag/Ag(100), is available. In the first, sulfur on Ag(100) forms two ordered structures at room temperature: a chemisorbed p(2×2) phase with ideal coverage 1/4 = 0.25 monolayers (ML), and a (√17×√17)R14° phase (abbreviated √17) with ideal coverage 8/17 ≈ 0.47 ML.[16-18] Between 0.25 and 0.47 ML, these phases co-exist. The √17 is a reconstruction in which Ag atoms are ejected from the surface plane to form new islands on top of the terraces.[18] A number of possible alternative structures have been investigated with DFT, including the square M_4S_4 cluster mentioned above.[18] With one exception, none of the alternatives are competitive with the two observed structures, at coverages up to 0.47 ML. The exception is a p(2×2) structure with c(2×2)-like domain boundaries, which is only slightly more favorable than the mixed p(2×2) + √17 phase above 0.25 ML. There is some indication that it may exist below room temperature.[18]

In the second system, Ag/Ag(100), Ag forms homoepitaxial islands via nucleation and growth on sufficiently-large Ag(100) terraces. The islands tend to be square-shaped, with close-packed step edges. At 300 K, these islands coarsen through island diffusion and coalescence,[19-21] rather than OR. The diffusion-coalescence mechanism is termed Smoluchowski ripening (SR).[22]

This paper is organized as follows. Details, both of experiments and computations, are combined in Section 2. Results and interpretations from experiment and computations are given in Sections 3 and 4, respectively, followed by a combined discussion in Section 5.

2. Experimental and computational details

The Ag(100) sample was grown by the Ames Laboratory Materials Preparation Center.[23] The details of sample preparation and experimental procedures were very similar to those reported in a previous study of sulfur on Ag(111).[24] Notably, S_2 gas was generated within UHV in a solid-state electrochemical Ag|AgI|Ag_2S|Pt cell, following the design of

Wagner.[25] Sulfur flux was in the range (7 to 20) $\times 10^{-5}$ ML/s. The Ag flux was ~0.018 ML/s, and Ag coverage was around 0.3 ML in all experiments. Tunneling conditions for the STM images (all constant-current) were typically 1.0 nA current and -1.5 V tip bias. All experiments took place at 300 K. Data file names are provided in the figure captions: the date refers to the experiment date and folder name and "m#" refers to the image file.

Uncertainties in experimental values were always calculated as $\pm$ 1 standard deviation, unless noted otherwise (as in Fig. 2).

Sulfur coverage, θ_S, is given as the ratio of sulfur atoms to Ag atoms, also expressed as ML. After each STM experiment the S(LMM)/Ag(MNN) AES intensity ratio was measured and converted to coverage, following a calibration established by Schwaha, et al.[26] and corroborated by Rovida and Pratesi.[16] This procedure has been supported by an STM study.[18]

DFT calculations were performed using the VASP[27-29] total energy code, with Perdew-Burke-Ernzerhof (PBE)[30] generalized gradient approximation (GGA). The projected augmented-wave (PAW)[31] method was used, utilizing a new PAW potential with improved treatment of the f channels[32] for Ag instead of the potential in the standard VASP package. Energetic values were obtained from Ag slabs, as described below, with the bottom layer of atoms fixed at their bulk positions. Adsorbates were attached to one side of the slab, with the induced artificial dipole interactions compensated by an external electrostatic field.[33] The lattice constant was set to 0.415 nm, the bulk PBE value at zero temperature using the new PAW potential (versus the experimental value of 0.409 nm). Methfessel-Paxton[34] smearing of the occupancy function (with $N = 1$ and $\sigma = 0.2$ eV) was used for efficiency. The energy cutoff was 280 eV for all calculations. The vacuum spacing between slabs was 1.2 nm.

Due to the need to compare energetics from calculations using various supercells, it is necessary to carefully consider convergence of DFT numbers to their bulk limit from calculations on finite slab thickness and with finite k-point grids. We find that surface energetics on Ag(100) and Cu(100) generally display variations with the slab thickness with a period of 5 ML.[35] An effective method to achieve highly accurate energies on these surfaces is to average over results for a range of slab thickness.[35] In this work, that range is 5 to 9 ML. The numerical errors, which are mainly due to finite slab thickness and finite k-

point grids, can be estimated from the standard deviation of the results divided by the number of samples (5 in this paper). Note that this is different from the calculation of errors that are due to statistical noise in the samples.

DFT calculations of an AgS molecule using different approximations of the exchange-correlation functionals[18] show that local density approximation and PBE produce stronger binding between Ag and S, while a revision of PBE known as RPBE,[36] and the hybrid HSE06,[37] produce weaker binding. Below, we present results for the S/Ag/Ag(100) system using the PBE approximation exclusively. However, we note that the adsorption energy calculated using RPBE is weaker for S/Ag(100). For instance, for isolated sulfur atoms, it is 0.40 eV (about 10%) lower. From this we conclude that there is a significant level of uncertainty in the absolute value of the adsorption energy from DFT.

3. Experimental results and interpretation

Figure 1 shows a series of STM images at different θ_S and times, with 0.3 ML Ag pre-adsorbed. The θ_S values range from 0.00 to 0.21 ML. Column (a) is the sulfur-free surface. STM confirms that the evolution of Ag islands on this Ag(100) surface proceeds through SR, as expected. There is no observable OR, even for very small islands (about 8 atoms on a side). Column (b) shows a different experiment after sulfur adsorption to θ_S = 0.034. Most Ag islands stay square but their corners are slightly more rounded. Column (c) shows ripening at θ_S = 0.083. The islands are irregularly shaped, with many rounded regions, and some straight regions that are not quite aligned with the original step orientation on the clean surface. Column (d) shows the progression of STM images at θ_S = 0.12, and column (e) reveals fast island decay at θ_S = 0.21. Here the Ag islands display linear edges with various orientations, many of which seem to be rotated by about 45º with respect to the original Ag island orientation on the clean Ag(100) surface. Round edges are also common. Through the entire coverage range θ_S = 0.034 to 0.21, there is evidence for OR in addition to SR. For instance, the dumbbell-shaped island in the first image of Column (d) is evidence of a collision and merger between two islands.[38] The contribution from OR increases with θ_S, however. This means that sulfur introduces OR as a competitive ripening pathway. Oxygen

exerts a similar effect on the mechanism of Ag island ripening on Ag(100), i.e. conversion from SR to OR.[39]

Experiments at $\theta_S \geq 0.25$ are complicated by the fact that a $\sqrt{17}$ phase develops, in which Ag atoms are displaced from the terrace plane.[18] These Ag atoms form new islands of $\sqrt{17}$ phase on the surface. It is impossible to tell whether a Ag island is a result of this reconstruction, or is a vestige of Ag deposition before sulfur adsorption. Therefore, $\theta_S = 0.21$ is the highest coverage studied for coarsening.

One measure of the coarsening rate for either OR or SR is the growth rate of the average island size. For OR, this can be calculated using the Lifschitz-Slyosov-Wagner theory.[40] However, specifically for OR, a valuable alternative experimental approach which does not require analyzing large ensembles of islands on broad terraces is to assess the decay rate of smaller individual islands. Figure 2 shows this type of data, for OR at different θ_S. In all cases, the initial island size is 10.0 ± 0.3 nm^2 and the island edge is close to a terrace step (4.9 ± 1.6 nm away), so the terrace step acts as a strong sink for Ag atoms. The results are not significantly different if islands are chosen that are surrounded by much-larger islands in the middle of terraces. As shown in the plot, the island decay rate changes little from 0.03 to 0.12 ML, then begins to increase significantly at 0.15 ML. The highest rate is reached at the highest measured coverage, 0.21 ML.

In Fig. 2, the OR decay rate changes from about 0.0022 nm^2/s at 0.034 ML to 0.013 nm^2/s at 0.21 ML. This implies an enhancement of 6x in the coarsening rate. However, this is not an enhancement relative to the clean surface. A comparison with experimental OR data for the clean surface is impossible, since there OR is not observed. However, the corresponding rate of OR for the clean surface can be calculated as 0.0006 nm^2/s. This value is shown by the open square in Fig. 2. Relative to this value, the average rate at 0.21 ML is 22x higher. For simplicity, we will refer to the enhancement as being about an order of magnitude.

For sulfur-induced OR, one can ask, what is the rate-limiting step? In traditional discussions, two possibilities are usually suggested: either attachment and detachment of particles from island edges (AD), or diffusion of particles across terraces (TD). In the former case, an island's rate of decay or growth is independent of its environment, which provides a

way to test the kinetics experimentally. For S/Ag/Ag(100), evidence for terrace diffusion (TD) limited OR at $\theta_S = 0.12$ is shown in Fig. 3. The area of a shrinking island (indicated by an arrow) is shown. This island first decays slowly while a neighboring smaller island (circled) is present. When the smaller island disappears, the rate increases abruptly. Hence, the decay rate of the island depends strongly on the surrounding islands, which is a signature of TD-limited kinetics. We caution, however, that even for additive-free systems, one can find systems with features of AD and TD behavior.[41] For more complex systems such as S/Ag/Ag(100) where OR can be mediated by complexes involving chemical additives, one must also consider other regimes associated with reaction-limited behavior.[4,7]

In summary, the main experimental observations are these:

(1) Sulfur can accelerate the rate of Ag island coarsening on Ag(100) by a factor of 6-22 at 300 K. The effect increases with θ_S over the measured range of 0.03 to 0.21 ML.

(2) With increasing θ_S, the Ag islands become rounder and more irregular. Some edges are rotated by about 45° from their sulfur-free orientation.

(3) Sulfur changes the mechanism of ripening of Ag islands, from SR to TD-limited OR.

We now turn to a model that can explain these observations, based upon DFT.

4. Theoretical results and interpretation

4.1. Sulfur adlayer structure and equilibration (sulfur diffusion)

The highest experimental coverage, 0.21 ML, is just below the ideal coverage of the p(2×2). From previous DFT work,[18] we know that sulfur atoms in the p(2×2) occupy the 4-fold hollow (4fh) site. We also know that the p(2×2) forms because of repulsive interactions at nearest-neighbor (NN), second-NN, and fourth-NN sites (in order of decreasing strength). The existence of fourth-NN repulsions means that the phase diagram is qualitatively similar to that of Se/Ni(100)[42] and O/Rh(100)[43]. It can be reasonably assumed that, if it were in equilibrium, the sulfur layer would be disordered at low θ_S, and would progress to p(2×2)

order close to 0.25 ML. In experiment, a p(2×2) is observed near 0.25 ML, but its development at lower coverages has not been studied systematically.

From DFT, we find that—for isolated sulfur—the diffusion barrier is very high, 0.84 eV. This corresponds to a hop rate of only ~1/min. at 300 K. Therefore, it is unlikely that the adlayer is in equilibrium, at least at low coverage. As coverage approaches 0.25 ML, repulsive interactions between sulfur atoms probably enhance the mobility of sulfur and facilitate equilibration. This would explain observation of the well-ordered p(2×2).[18]

In the picture developed in the following sections, formation of Ag-S clusters at steps is responsible for enhanced coarsening, but slow sulfur diffusion at low coverage is responsible for kinetic limitations to enhancement in this regime. This feature will be key to understanding coarsening behavior in this system.

4.2. DFT: Adsorption of sulfur atoms on terraces and near steps

The structure of the clean Ag(100) surface is shown in Fig. 4. There are two types of steps. One is close-packed, i.e. parallel to the <0 1 -1> direction. In this type of step, there can be defects–kink sites–like the one circled. The second type of step is open and parallels the <001> direction. It can be considered a continuous chain of kink sites. Corners, where close-packed steps meet, often display properties that are similar to kink sites.[44] In our calculations, small Ag clusters—like those in Fig. 5—serve as models for step edges.

Consider first the adsorption energies, E_{ad}, of *single* sulfur atoms. Figure 5 shows local minima in the energy landscape, and the corresponding values of E_{ad}. A sulfur atom binds more strongly at a 4fh site in the middle of a terrace [Fig. 5(a)] than at any other site. Sites at or adjacent to step edges are all less favorable, as shown by the examples in Fig. 5(b-e).

Figure 6 shows (meta)stable configurations of *pairs* of sulfur atoms near a square cluster of Ag atoms. The value of E_{ad} for each panel is half the total E_{ad} for the pair. The configuration in Fig. 6(a) resembles a combination of the single-atom configurations in Fig. 5(b) and 5(c), but there are important differences. First, the Ag and sulfur atoms have shifted slightly, becoming more linear than a superposition of the two single-atom configurations. The shift includes a displacement of the Ag atom slightly away from the other Ag atoms.

Second, the value of E_{ad} is lower than the average of Fig. 5(b) and 5(c). We can attribute this to an attractive interaction that spans the two sulfur atoms and the Ag atom between them. Together, these factors lead us to interpret the configuration in Fig. 6(a) as an incipient linear AgS_2 cluster.

There are a number of other local energy minima for pairs of sulfur atoms around a step edge, but we have found none as favorable as that in Fig. 6(a). Figures 6(b)-(c) show two examples. In both cases, the S-Ag-S unit is nearly linear, and the Ag atom is displaced slightly away from the other Ag atoms. The existence of these configurations supports a propensity for nascent linear AgS_2 clusters at step edges.

Figure 7 shows adsorption energies of pairs of sulfur atoms near extended clusters that mimic steps with different orientations. These results show that the adsorption energy of a pair of sulfur atoms at a kink site exceeds that at a close packed step edge. This should make the step energy for the open step closer to that of the close-packed step. This means that sulfur should make the Ag islands rounder than islands on clean surfaces, in agreement with the experimental results in Fig. 1.

4.3. DFT: Energetics of coarsening

Acceleration in coarsening generally requires a reduction in the effective activation barrier for Ostwald ripening, E_{OR}. This is the total energy barrier for a carrier to leave a kink site and move far out into the terrace. For a specific mechanism involving a metal carrier X, this can be broken down into three components:

$$E^X_{OR} = E^X_d + E^X_{form} + E^X_{att} \quad (1)$$

where E^X_d is the terrace diffusion barrier of the carrier, E^X_{form} is the formation energy of the carrier, and E^X_{att} is any *extra* barrier to attachment or detachment at step edges. (These quantities are illustrated in Fig. 8, 9 and 11.) The term E^X_{form} controls the density of carriers of type X on terraces. The term E^X_{att} is zero or negligible for TD-limited kinetics.

The natural benchmark for assessing acceleration of coarsening, and E_{OR}, is the sulfur-free surface. Based upon experiment, the hierarchy of coarsening rates on Ag(100) must be

OR(clean) < SR(clean) < OR(with sulfur). In other words, any OR mechanism involving sulfur must be faster than OR *would be* if it occurred on the clean surface.

OR on the clean surface would be controlled by detachment of Ag atoms from (or attachment to) kink/corner sites as illustrated in Fig. 8(a), plus Ag diffusion across the terrace, i.e. X = Ag. The pathway that would be followed is illustrated in Fig. 8(b). The local maxima in the curve represent saddle points in the energy landscape as the Ag atom moves from the kink/corner site (at 0.0 eV) toward an isolated 4fh site on the terrace. The total barrier in Fig. 8(b) is $E^{Ag}_{OR} = 0.84$ eV. An alternative way to assess E^{Ag}_{OR} is to evaluate the individual components of E^{Ag}_{OR} expressed in Eq. (1). Accurate values for two of those components, $E^{Ag}_{form} = 0.42$ eV and $E^{Ag}_{d} = 0.44$ eV, have been obtained previously from DFT.[35] Their sum, 0.86 eV [Fig. 8(c)], is close to the total barrier of 0.84 eV calculated from the energy landscape [Fig. 8(b)]. This indicates that $E^{Ag}_{att} \approx 0$ and so from this approach $E^{Ag}_{OR} = 0.86$ eV. The small discrepancy between the two methods (0.84 eV vs. 0.86 eV) is likely due to the small (4x4) supercell used in the energy landscape calculations, where interactions between Ag atoms and clusters probably have some residual effect.[35]

We have investigated whether the presence of a sulfur atom at the step edge sites marked S1 and S2 in Fig. 8(a) could affect the OR energetics of the Ag atom carrier. At S1, sulfur has a negligible effect on E^{Ag}_{OR}. At S2, sulfur actually stabilizes the kink site and E^{Ag}_{OR} increases to about 1 eV. Hence, adsorption of a single sulfur atom at a step site fails to enhance coarsening via Ag atom carriers.

Another possibility is that sulfur on the terraces enhances coarsening by lowering the diffusion barrier of Ag, E^{Ag}_{d}. At the highest observed enhancement (at 0.21 ML), much of the terrace is covered by p(2×2). However, for a single Ag adatom in a sulfur p(2×2) matrix, we calculate that $E^{Ag}_{d} = 0.46$ eV. Since this is slightly *higher* than the value for the sulfur-free surface, 0.44 eV, it seems that sulfur does not accelerate diffusion of Ag atoms.

Coarsening *can* be accelerated significantly if the nature of the carrier changes to AgS_2. The total barrier for the AgS_2 cluster to detach from the kink/corner site of a model Ag cluster is 0.70 eV, as illustrated on the left side of Fig. 9. This means $E^{AgS_2}_{OR} \approx 0.70$ eV, which is considerably lower than the value of $E^{Ag}_{OR} = 0.86$ eV. This difference could lead to a strong enhancement in the coarsening rate.

It is useful to examine the formation energy and diffusion barrier of AgS_2 (shown on the right side of Fig. 9). First, the sum of these two quantities is 0.67 eV, only slightly lower than $E^{AgS_2}{}_{OR} \approx 0.70$ eV from above, meaning that there is no significant *extra* barrier to attachment/detachment ($E^{AgS_2}{}_{att} \approx 0$). In turn, this is consistent with TD-limited OR. Second, comparison with Ag shows that $E^{AgS_2}{}_{form} = 0.45$ eV, only slightly higher than $E^{Ag}{}_{form} = 0.42$ eV. However, the diffusion barriers are much different: $E^{AgS_2}{}_{d} = 0.22$ eV, whereas $E^{Ag}{}_{d} = 0.44$ eV. Therefore, the reason for the lower $E^{AgS_2}{}_{OR}$ lies in the lower diffusion barrier of AgS_2.

The diffusion of AgS_2 is key to enhanced coarsening. Diffusion of this species along the chain direction is very easy, but the cluster cannot easily hop across, or rotate out of the channel that it lies in. These features will result in unusual diffusion trajectories.

If AgS_2 formation at step edges is responsible for enhanced coarsening, why does the coarsening rate increase with θ_S? One might think that at low θ_S, an energy penalty for bringing an isolated sulfur atom to the step edge (from the terrace) must be added to the quoted values for $E^{AgS_2}{}_{form}$ and $E^{AgS_2}{}_{OR}$ making this OR pathway less favorable. Then these energies would be reduced at higher θ_S where population of step sites is forced. However, this is not the case. Relative to terrace sites, there *is* a small energy penalty for having two sulfur atoms individually at step sites that are closest to those occupied in the nascent AgS_2 cluster. Compare Fig. 5(a) where $E_{ad} = -4.16$ eV, with Fig. 5(b) and (c) where on average $E_{ad} = -4.08$ eV. However, there *is no* significant energy penalty for simultaneously having two sulfur atoms at the step edge in the form of an actual nascent AgS_2 complex. Compare Fig. 5(a) where $E_{ad} = -4.16$ eV, with Fig. 6(a) where $E_{ad} = -4.14$ eV. Thus, $E^{AgS_2}{}_{form}$ and $E^{AgS_2}{}_{OR}$ should not depend significantly on θ_S.

Instead, we propose that the increase in coarsening rate is essentially a non-equilibrium effect due to slow sulfur diffusion at low θ_S. (See Sec. 4.1 and 5.1).

Finally, we have considered the possibility that Ag vacancies are involved in sulfur-enhanced coarsening. On the clean Ag surface, coarsening by vacancies is only slightly less favorable than coarsening by Ag atoms, and sulfur might tip the balance in favor of vacancy coarsening. However, DFT shows that this mechanism, plus several other vacancy-mediated mechanisms are unlikely. Details are in the Appendix.

5. Discussion

5.1. Comments about the mechanism proposed for accelerated coarsening in S/Ag/Ag(100)

The experimental data clearly show that sulfur accelerates coarsening of Ag islands on Ag(100). Based upon DFT, the following explanations can be ruled out:

i) Reduction of the total energy barrier to OR via single Ag atom carriers, E^{Ag}_{OR}. Specifically, sulfur near a kink site does not reduce the total detachment barrier, and p(2×2) sulfur on the terrace does not reduce the diffusion barrier of a Ag atom, relative to the sulfur-free surface.

ii) Reduction of the extra barrier to attachment/detachment via Ag vacancies, E^{V}_{att}. On the clean surface, this extra energy barrier is the main factor that makes vacancies less efficient than Ag atoms as carriers. Sulfur does not change this balance. We also checked that sulfur does not change the formation energy or the diffusion barrier of Ag vacancies.

The following explanation *is* supported by DFT. Acceleration of coarsening in this system is tied to the formation of AgS_2 clusters primarily at step edges. These AgS_2 clusters can detach from step edges according to the path illustrated in Fig. 9. There is no appreciable extra barrier to attachment/detachment, meaning that the kinetics should be TD-limited as observed. The main difference between the potential energy surface for detachment of a AgS_2 cluster and a Ag atom—and the reason why a AgS_2 cluster can enhance coarsening—lies in the diffusion barrier. At $E^{AgS_2}_{d} \approx 0.22$ eV and $E^{Ag}_{d} = 0.44$ eV, the cluster has a clear advantage over the Ag atom. However, to contribute to coarsening, formation of AgS_2 clusters and their equilibration with edges of Ag islands must be facile. We claim that due to the very limited mobility of isolated sulfur atoms on terraces, these conditions are only achieved for high θ_S, and correspondingly the coarsening rate increases as θ_S increases.

In TD-limited OR, the traditional picture is that there is complete local equilibration of surface species, in which case the details of adsorption at step edges should not strongly impact OR kinetics. (They may have a weak effect by changing step energies.) However, for systems with a propensity for formation of clusters such as AgS_2 or Ag_3S_3, TD-like OR does not imply complete local equilibration of all adspecies. This richer and more complicated

type of behavior was noted first for S/Cu/Cu(111)[4] and later for S/Ag/Ag(111).[7] In both systems, there are distinct regimes of OR with different degrees of local equilibration, depending on θ_S. For S/Ag/Ag(100), there may well be complete local equilibration for higher S coverages where TD-like behavior was observed. However, our picture is that a lack of complete equilibration at lower S coverages behavior can be sensitive to details of the kinetics of cluster formation/dissociation.

In our model, it is implicitly assumed that clusters do not form on terraces. No doubt there are kinetic limitations to cluster formation on terraces at low θ_S related to slow sulfur diffusion. The situation is less clear at higher θ_S. However, even if clusters do form on terraces, we anticipate that this does not necessarily enhance coarsening as effectively as clusters formed at step edges. This is because enhancement would require strong coupling between the cluster and Ag atom concentrations on terraces, which seems unlikely.[4, 7]

The mechanism proposed here for coarsening acceleration is plausible because it is qualitatively consistent with experimental data. A more quantitative test using detailed modeling, like that implemented for S/Ag/Ag(111),[7] is planned.

5.2. Comparison with accelerated coarsening in S/Ag/Ag(111)

In two ways, the mechanism proposed here for S/Ag/Ag(100) is the *opposite* of the mechanism proposed for S/Ag/Ag(111). First, on Ag(111), sulfur saturates the step edges *before* the terrace sites, because the step edges present pseudo-4fh sites whereas the terraces present less-favorable 3fh sites. Second, on Ag(111), sulfur at the steps plays no direct role in coarsening, whereas on Ag(100) sulfur at steps is crucial to accelerated coarsening.

On Ag(111), both Ag_3S_3 and AgS_2 have been proposed to play a role in accelerated coarsening. On Ag(100), we propose here that AgS_2 is important. Elsewhere, we have shown that this type of cluster is energetically feasible as a carrier on Cu(111) and Au(111) surfaces also.[8] It may be generally important on coinage metal surfaces. Experiments planned for the Ag(110) surface will test this possibility.

Interestingly, local linear S-Ag-S arrangements can be found in the √17 reconstruction of S/Ag(100). Two examples of local S-Ag-S units are enclosed by ovals in Fig. 10, and the unit cell is shown by the square. This √17 structure was deduced from DFT

calculations of energies, and supported by comparison of measured and predicted STM images.[18]

In this paper, we have not discussed any cluster analogs of Ag_3S_3 as possible Ag carriers on Ag(100). The natural geometric analogs would be square Ag_4 clusters decorated by sulfur, but their formation energy is prohibitively high–at least 1.2 eV. (See Fig. S2 of Ref. [18].) The driving force for formation of Ag_3S_3 on Ag(111) is the creation of pseudo-4fh sites for sulfur at the edges of the Ag_3 triangles. This driving force does not exist on Ag(100), since the terraces already have 4fh sites. On Ag(100), AgS_2 has lower formation energy than any other cluster.[18]

The magnitude of the enhancement in coarsening rate is considerably larger for S/Ag/Ag(111) than for S/Ag/Ag(100). For S/Ag/Ag(111), at 300 K, the rate of OR increases by at least 3 orders of magnitude, in going from zero to 0.035 ML.[7,8] This is comparable to the enhancement observed for S/Cu/Cu(111) (at higher temperature), which is about 2.5 orders of magnitude in going from zero to 0.014 ML. For S/Ag/Ag(100), we estimate that the enhancement is only about 1 order of magnitude, occurring over a much wider θ_S range, spanning 0.2 ML. (See Section 3.)

This trend correlates with the findings from DFT, which shows that $E^{AgS_2}{}_{OR}$ is somewhat lower than $E^{Ag}{}_{OR}$ on Ag(100), the difference being 0.84 - 0.67 = 0.17 eV. However, $E^{AgS_2}{}_{OR}$ is *much* lower than $E^{Ag}{}_{OR}$ on Ag(111)–where the difference is between 0.45 and 0.55 eV.[7,8] This line of reasoning is valid also if Ag_3S_3 is the carrier on Ag(111), because then the difference is 0.35 eV.

In summary, from experiment, sulfur enhancement of OR is much smaller on Ag(100) than on Ag(111). From DFT, the difference between $E^{Ag\ carrier}{}_{OR}$ with and without sulfur is also much smaller on Ag(100) than on Ag(111). These two findings are self-consistent.

5.3. Comparison with accelerated coarsening in O/Ag/Ag(100)

We have previously investigated coarsening in the O/Ag/Ag(100) system.[39,45] From experiment, oxygen bears three main similarities to sulfur: (1) it accelerates coarsening relative to the clean Ag(100) surface; (2) it introduces OR as an observable ripening

mechanism; and (3) it causes re-orientation of Ag island edges. However, the low adsorption probability of O_2(gas), and problems with measuring oxygen coverage with AES, prevented us from quantitatively correlating these observations with oxygen coverage.

DFT also reveals some similarities between oxygen and sulfur in this system. First, the energy landscapes are similar for single oxygen atoms and single sulfur atoms near Ag island edges. Our preliminary DFT results for isolated adsorbed oxygen atoms are consistent with those reported by Savio et al., for oxygen adsorption on a surface vicinal to Ag(100).[46] Furthermore, our DFT suggests that incipient, AgO_2-like clusters or chains may form at Ag step edges, analogous to the incipient AgS_2 clusters/chains of Fig. 6 or Fig. 7. However, DFT shows that the exact mechanism by which coarsening is enhanced in O/Ag/Ag(100) is not the same as for S/Ag/Ag(100). Details will be reported elsewhere.

6. Conclusions

Using STM, we find that sulfur can accelerate the rate of Ag island coarsening on Ag(100) by about an order of magnitude at 300 K. The effect increases with θ_S over the measured range of 0.03 to 0.21 ML. With increasing θ_S, the Ag islands become rounder and more irregular. Sulfur also changes the mechanism of ripening of Ag islands, from SR to TD-limited OR. These observations can all be explained by a model in which a linear AgS_2 cluster forms and detaches from step edges. The barrier to diffusion for this cluster is only half that of a single Ag atom, while the formation energy is about the same, so the AgS_2 cluster plausibly enhances the rate of coarsening. It also stabilizes kink sites, which accounts for the rounder shape of the Ag islands. The total barrier for detachment of AgS_2 is close to the sum of its formation energy and its diffusion barrier, meaning that OR should be TD-limited in the presence of sulfur, as observed. AgS_2 formation is kinetically-limited at low θ_S, because of the low mobility of sulfur atoms, and thus enhancement increases with θ_S. Other possible mechanisms for accelerated coarsening, involving Ag vacancies or Ag atoms as carriers, have been examined but are not viable based on DFT.

Sulfur exerts a much weaker effect on the rate of coarsening on Ag(100) than it does on Ag(111). This is consistent with DFT, which shows that the difference between $E^{Ag\ carrier}_{OR}$ with and without sulfur, is also much smaller on Ag(100) than on Ag(111).

Acknowledgements

The experimental component of this work was supported by NSF Grant CHE-1111500. The theoretical component (DJL's contribution) was supported by the Division of Chemical Sciences, Basic Energy Sciences, US Department of Energy (USDOE). The work was performed at Ames Laboratory, which is operated for the USDOE by Iowa State University under Contract No. DE-AC02-07CH11358. We thank J.W. Evans for a useful critique of this work.

Figures

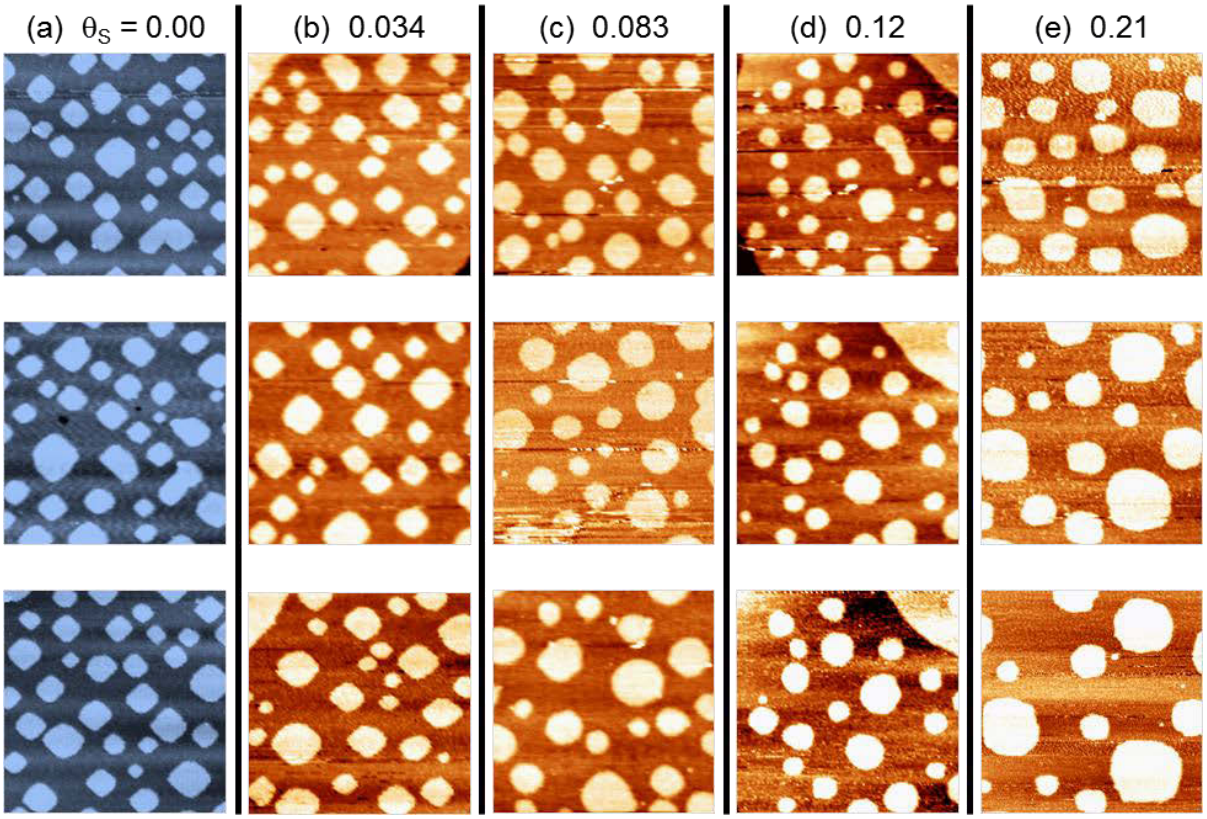

Figure 1: STM images showing Ag island coarsening at different θ_S, at 300 K. Ag coverages are all 0.3 ML, and STM images are 50×50 nm^2. Column (a): clean Ag/Ag(100), 86, 145, 210 min after Ag deposition. Column (b): 0.034 ML sulfur on Ag/Ag(100), 78, 120, 154 min after Ag deposition (14, 58, 90 min after sulfur deposition). Column (c): 0.083 ML sulfur on Ag/Ag(100), 90, 155, 215 min after Ag deposition (20, 85, 145 min after sulfur deposition). Column (d): 0.12 ML sulfur on Ag/Ag(100), 78, 124, 168 min after Ag deposition (9, 55, 99 min after sulfur deposition). Column (e): 0.21 ML sulfur on Ag/Ag(100), 99, 150, 204 min after Ag deposition (2, 53, 107 min after sulfur deposition). Files: (a) 12/5/2008 m65, 99, 136. (b) 12/22/2008 m50, 73, 91. (c) 1/26/2009 m72, 110, 145. (d) 12/30/2008 m48, 75, 100. (e) 1/6/2009 m47, 76, 105.

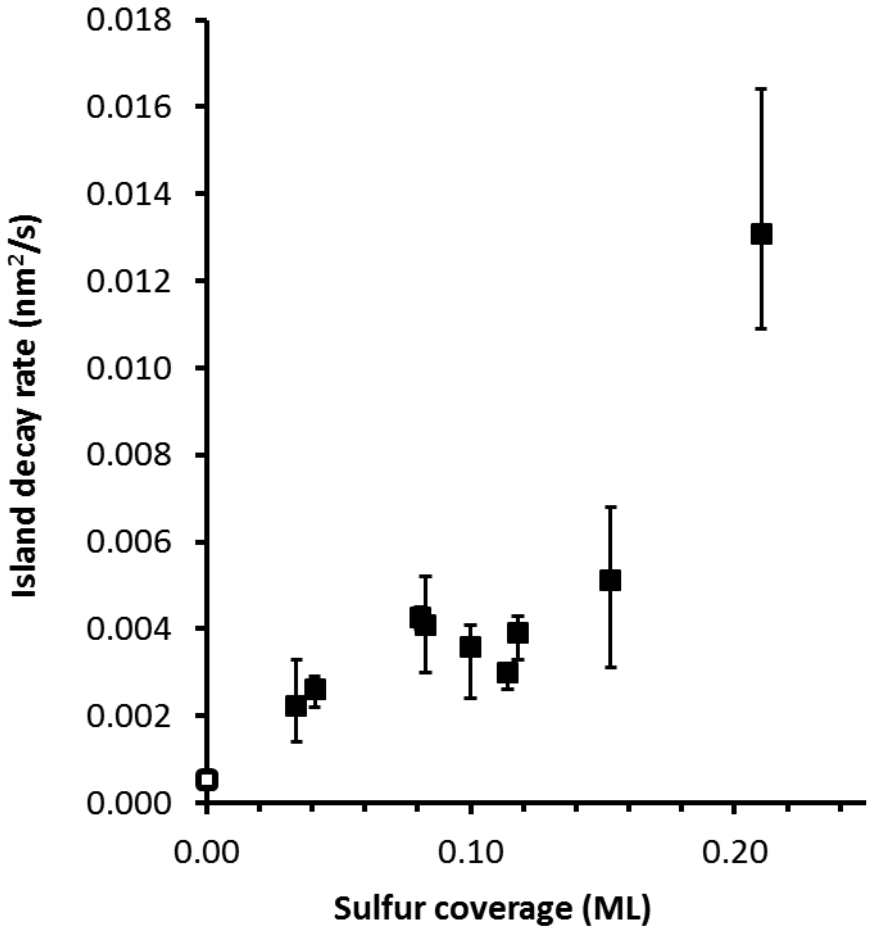

Figure 2: Individual Ag island decay rate at different S coverages on Ag/Ag(100). Each filled square is an average value, and the error bars show the entire range of rates measured for a given θ_S. The open square at zero coverage is an estimate of the rate of OR for a Ag island in the absence of sulfur: 0.0006 nm^2/s.

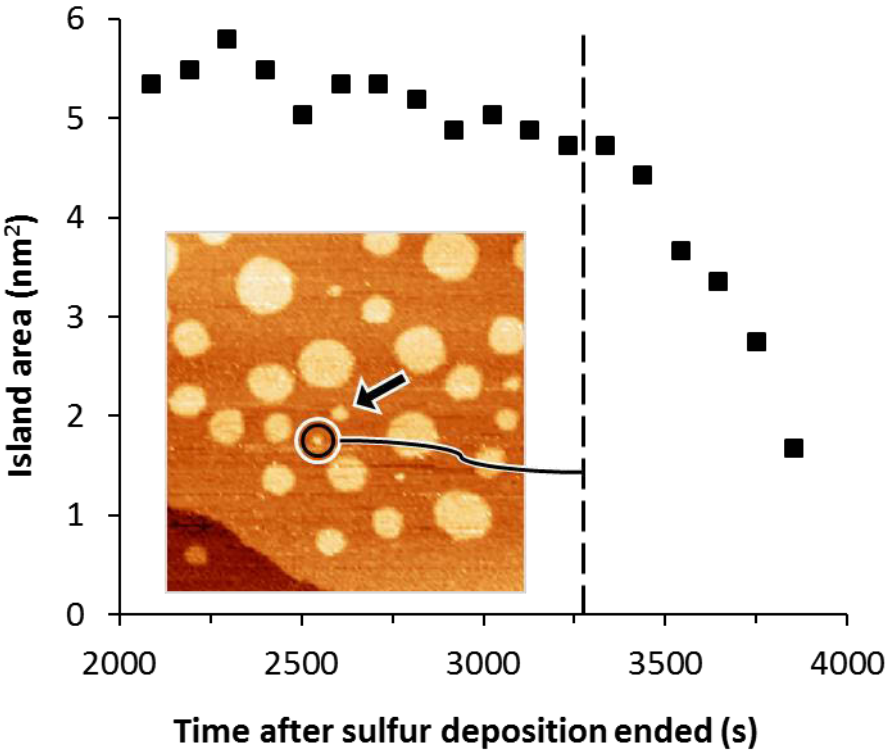

Figure 3: Island area vs. time at $\theta_S = 0.12$ on Ag/Ag(100). The arrow in the STM inset shows the island monitored. The circle shows a small island that disappears at about 3300 s, as indicated by the vertical dashed line. The STM image was recorded 3126 s after sulfur deposition ended and its size is 49.6×49.6 nm^2 (12/30/2008 m72).

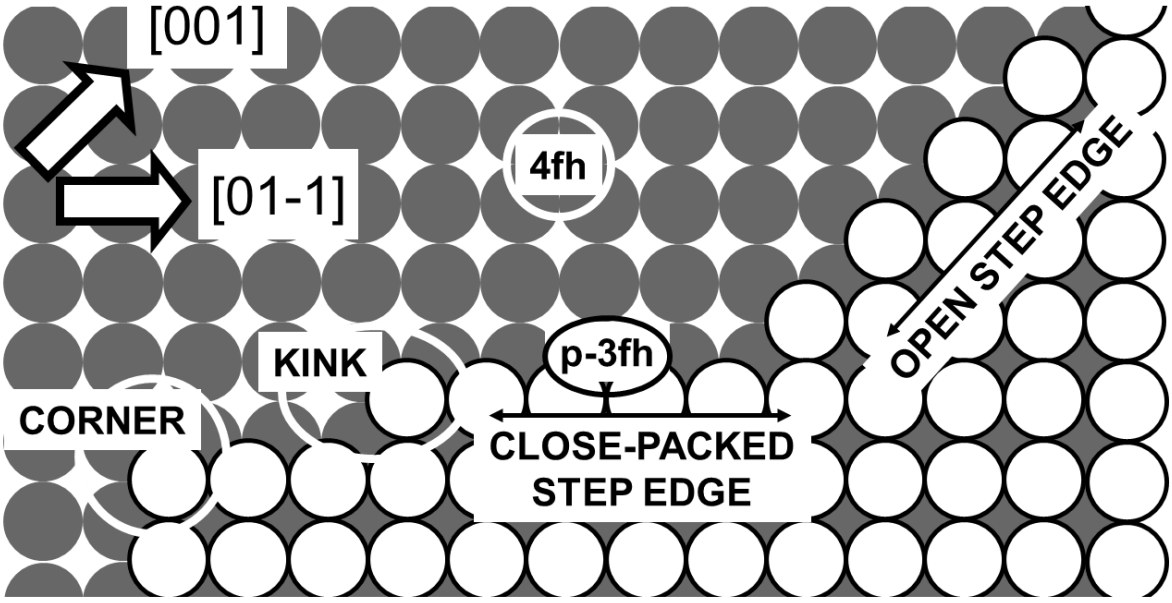

Figure 4: Schematic of the different types of sites, and step edges, on Ag(100).

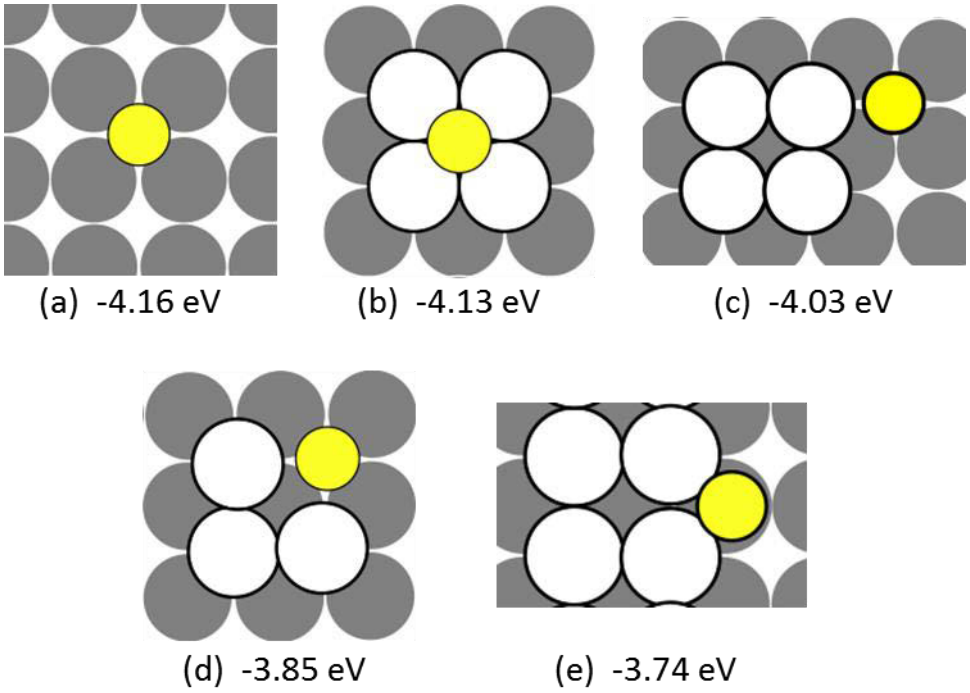

Figure 5: Schematic of possible adsorption sites for single sulfur atoms. For each configuration, the adsorption energy per sulfur atom is given. In (a – d), the surface unit cell used in DFT is p(3×3). (a): Sulfur at a 4fh site on a terrace. There is no difference in E_{ad} for a p(2×2) unit cell, within numerical uncertainties. (b): Top sulfur at a 4fh site adjacent to a corner/kink site. (c): In-plane sulfur at a 4fh site adjacent to a corner/kink site. (d): In-plane sulfur at a 4fh site adjacent to two Ag atoms. (e) In-plane sulfur at a pseudo-3fh site along a close-packed step. The surface unit cell in DFT is p(3×2).

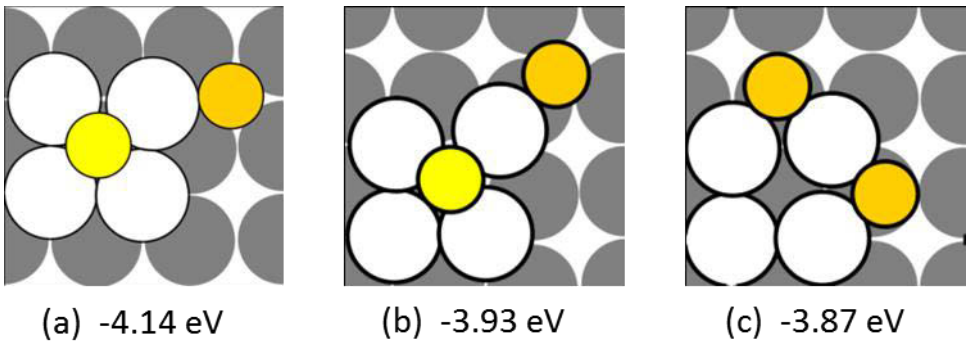

Figure 6: Clusters of 4 Ag atoms with 2 S atoms. For each system, the adsorption energy per sulfur atom is given. In-plane sulfur atoms are slightly darker (orange on-line) than on-top sulfur atoms (yellow on-line). In (a), the surface unit cell in DFT is p(4×4); results are similar for a p(3×3). In (b) and (c), the surface unit cell in DFT is p(3×3).

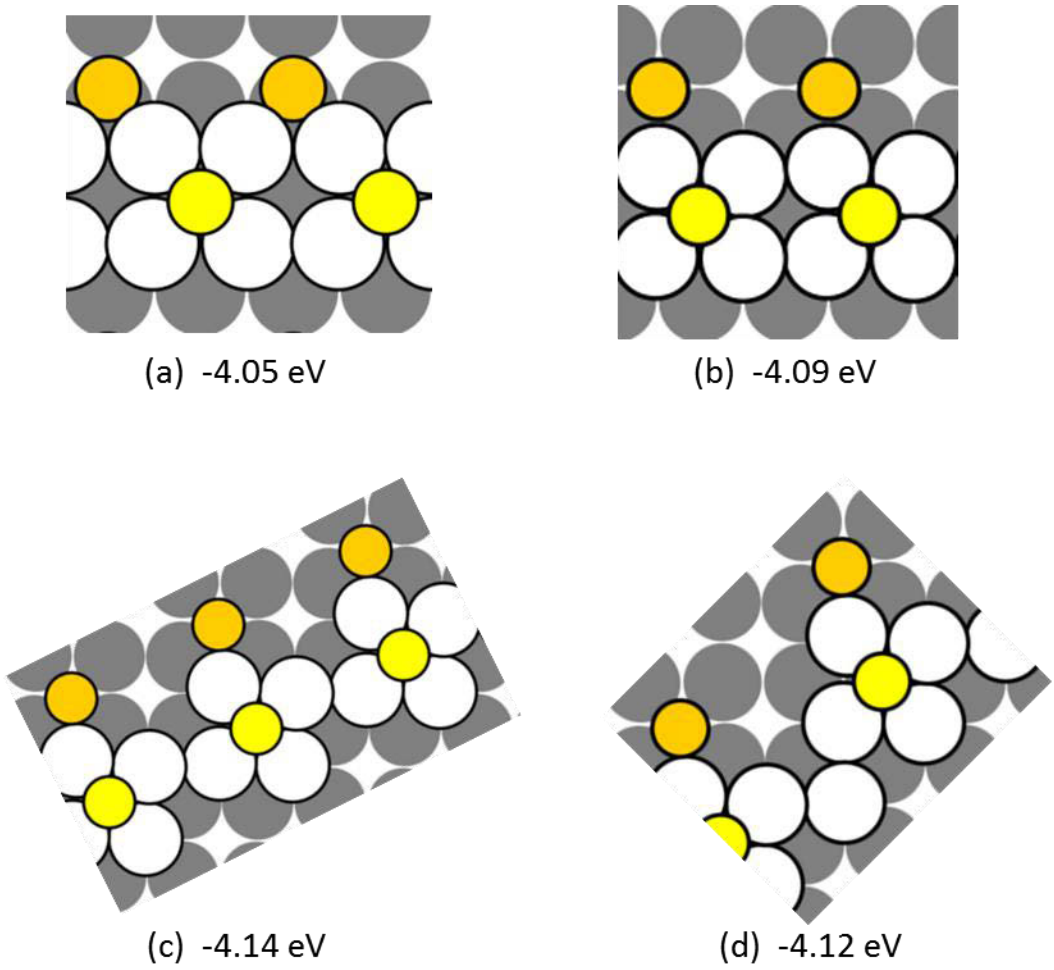

Figure 7: Models of possible Ag step configurations decorated by sulfur. For each configuration, the adsorption energy per sulfur atom is given. In-plane sulfur atoms are slightly darker (orange on-line) than on-top sulfur atoms (yellow on-line). (a, b): Models of close-packed steps. (c, d): Models of steps with kink sites.

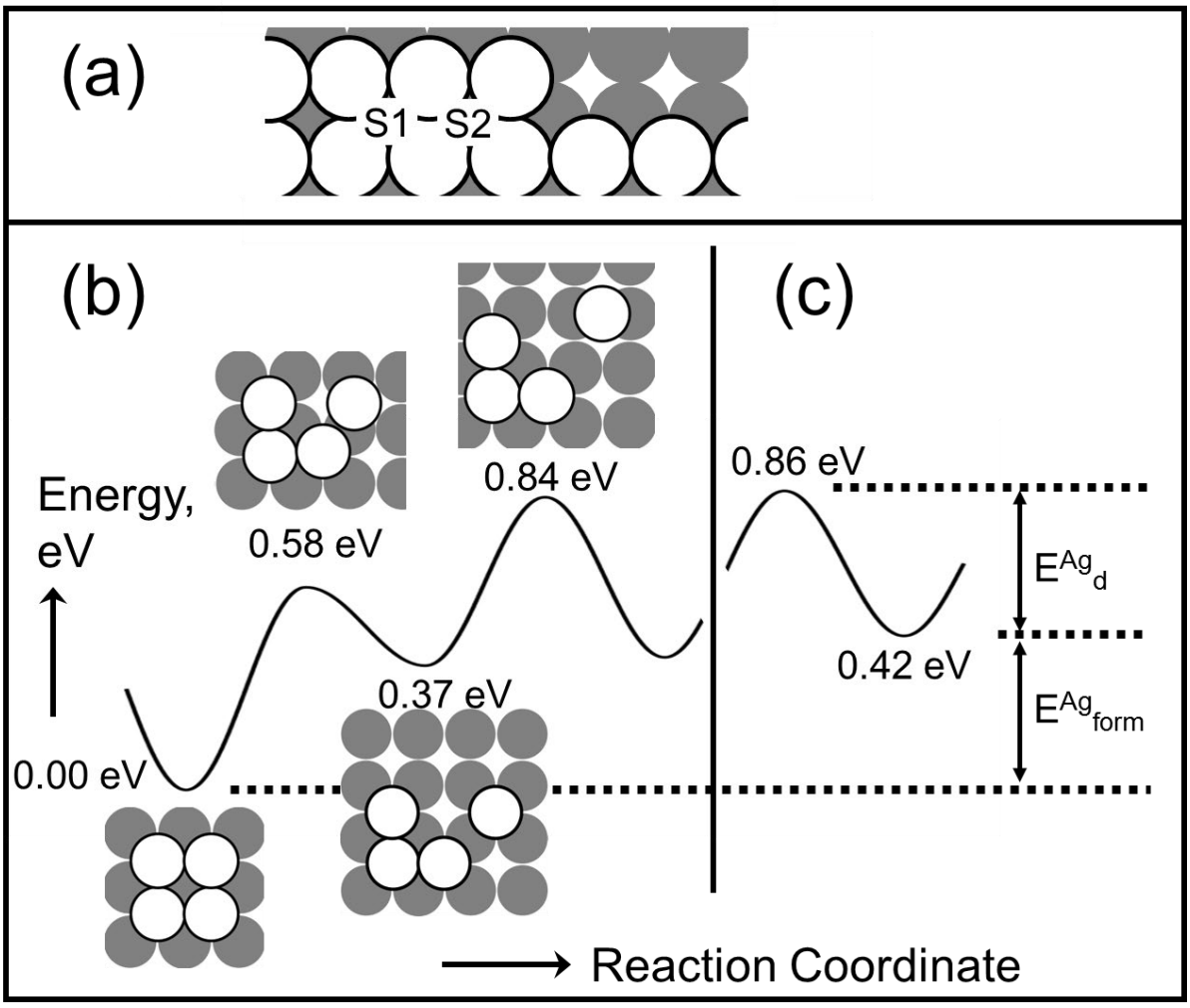

Figure 8: (a) Schematic of an extended, close-packed step edge, with a kink site. S1 and S2 show potential sulfur adsorption sites. (b) Potential energy surface for a Ag atom detaching from a four-atom Ag cluster as illustrated in the schematics. The surface unit cell in DFT is p(4×4). (c) Extrapolation of the potential energy surface to a Ag atom far away from the Ag cluster, using DFT calculations of isolated Ag atoms.[35]

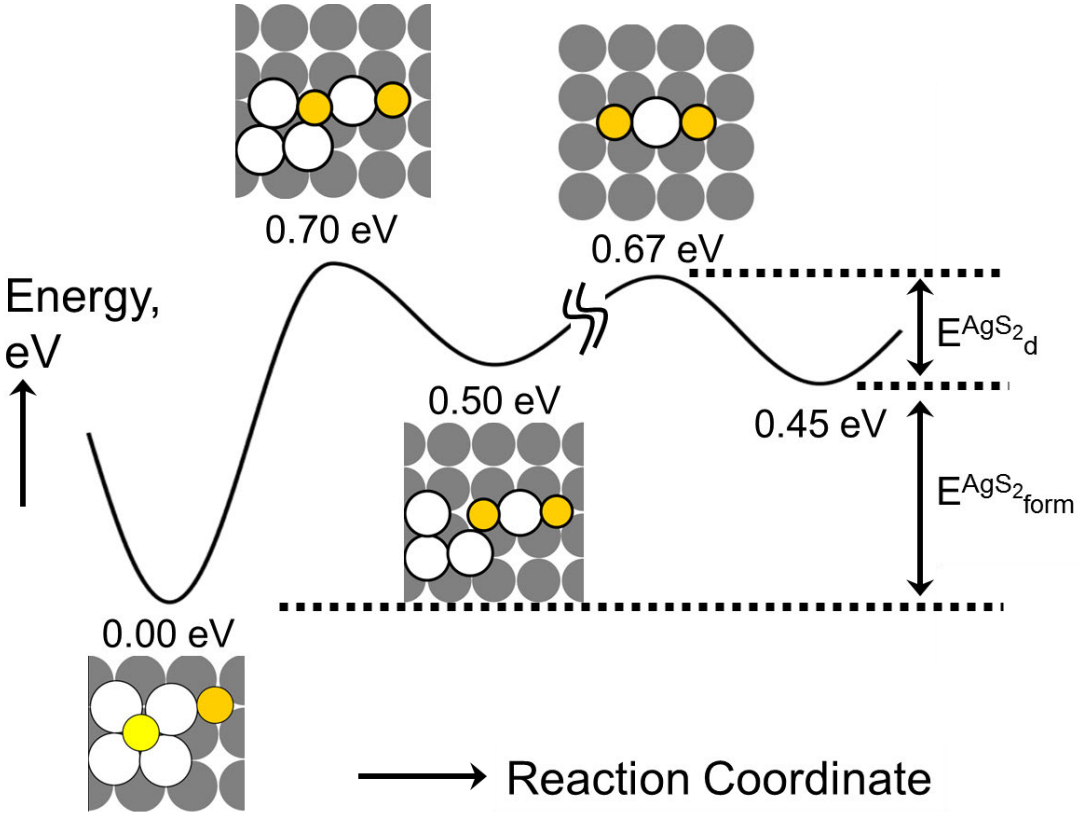

Figure 9: Left side: Potential energy surface for a AgS_2 cluster detaching from a four-atom Ag cluster, as illustrated in the schematics. The surface unit cell in DFT is p(4×4). In-plane sulfur atoms are slightly darker (orange on-line) than on-top sulfur atoms (yellow on-line). Right side: Extrapolation of the potential energy surface far from the Ag cluster, using DFT calculations of isolated AgS_2 clusters, as illustrated in the schematics. The formation energy of AgS_2 is calculated relative to sulfur in the p(2×2) overlayer.

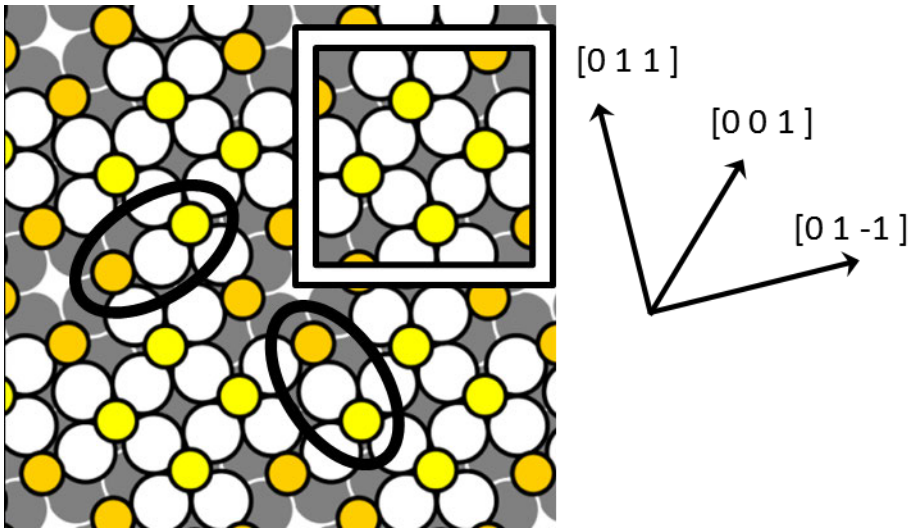

Figure 10: Schematic of the (√17×√17)R14° structure for sulfur on Ag(100), discussed in detail elsewhere.[18] Ovals encase S-Ag-S motifs like those favored at extended step edges, with one top sulfur and one in-plane sulfur. The square shows the √17 surface unit cell. In-plane sulfur atoms are slightly darker (orange on-line) than on-top sulfur atoms (yellow on-line).

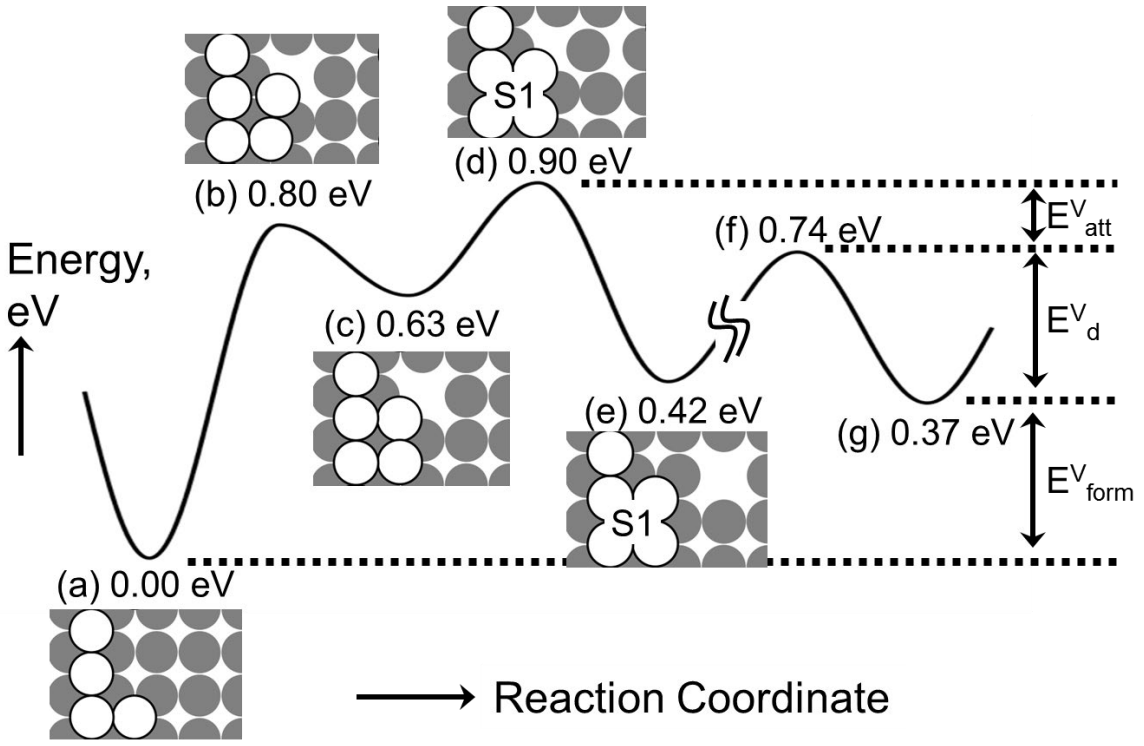

Figure 11: Left side: Potential energy surface for a Ag vacancy detaching from a model kink site, as shown in the schematics. The site marked S1 is a sulfur adsorption site used to test sulfur's effect on the energy barrier going from (e) to (d), for reasons described in the text. The surface unit cell used in DFT is p(4×3). Right side: Extrapolation of the potential energy surface far from the Ag cluster, using DFT calculations of isolated Ag vacancies.[35]

Appendix 1. Energetics of coarsening with carriers containing Ag vacancies

First, consider a type of coarsening mechanism in which adsorbed sulfur facilitates Ag vacancies as the agents of Ag transport, rather than Ag atoms or clusters containing Ag atoms. We have previously determined the formation energy (0.37 eV) and diffusion barrier (0.37 eV) for vacancies on clean Ag(100).[35] There is an additional energetic component, due to the difficulty of attaching/detaching vacancies to/from a kink/corner site, which involves interlayer movement of Ag atoms. One pathway is illustrated in Fig. 11. From left to right, the kink position moves upward because a vacancy is created. We have explored other pathways, including a more cooperative process like that proposed for Cu/Cu(100).[47] But the process illustrated in Fig. 11 is the most competitive we have found for Ag/Ag(100).

Two parts of the process are energetically costly. The first is creation of the vacancy in the vicinity of the kink (a to c in Fig. 11), and the second is diffusion of the vacancy away from the kink (c to e). We find that the second process is associated with the higher saddlepoint (cf. Fig. 11). The total barrier, E^{V}_{OR} = 0.90 eV, is larger than the sum of the formation energy and diffusion barrier of vacancies (0.74 eV),[35] which means there is an *extra* attachment/detachment barrier E^{V}_{att}=0.16 eV for vacancies.

(Note that E^{V}_{OR} =0.90 eV is slightly larger than E^{Ag}_{OR} =0.86 eV, consistent with the assertion in Section 4.3 that OR on the clean surface would occur via Ag atom carriers, not via vacancy carriers.)

It is thus reasonable to ask whether adsorbed sulfur might simply reduce E^{V}_{att}. This energy manifests at the highest saddlepoint along the reaction coordinate, i.e. at Fig. 11(d). To determine the effect of sulfur on this saddlepoint, we calculate the energy barrier for a Ag vacancy to move from (e) to (c) with a sulfur atom on the site labeled S1 in Fig. 11(d) and (e). With sulfur, the energy barrier is about 0.54 eV, slightly *higher* than 0.48 eV for the sulfur-free surface. The conclusion is that sulfur does not reduce E^{V}_{att}.

Finally, we have investigated the formation energy and the diffusion barrier of vacancies in the presence of sulfur. The main conclusion is that for low θ_S, neither is affected significantly. This, plus the fact that E^{V}_{att} cannot be reduced by sulfur, means that vacancies are not likely to be responsible for acceleration of coarsening.

It is noteworthy that at higher θ_S (above 0.25 ML), the vacancy formation energy *can* be lowered. This requires rather complex structures, which have been investigated but are not shown here. Along these lines, the √17 structure observed experimentally (Fig. 10) has an ideal coverage of 0.47 ML, and can be regarded as a complex network of sulfur-stabilized Ag vacancies.

Appendix 2. Details of decay analysis

Table A2.I. Ag island decay rates

Monolayers of S	Average decay rate, nm^2/s	Standard deviation	Slowest decay rate, nm^2/s	Fastest decay rate, nm^2/s	Number of islands evaluated
0.034	0.0022	0.0010	0.0014	0.0033	3
0.041	0.0026	0.0004	0.0022	0.0029	3
0.081	0.0043	0.0004	0.0040	0.0045	2
0.083	0.0041	0.0016	0.0030	0.0052	2
0.100	0.0036	0.0008	0.0024	0.0041	4
0.114	0.0030	0.0003	0.0026	0.0032	3
0.118	0.0039	0.0005	0.0033	0.0043	3
0.153	0.0051	0.0018	0.0031	0.0068	4
0.210	0.0131	0.0026	0.011	0.016	4

Table A2. II. Initial conditions of individual Ag islands evaluated to determine decay rate as shown in Fig. 2.

	Average	Standard deviation	Maximum	Minimum	Count
Initial island area, nm^2	9.97	0.25	10.83	9.31	29
Distance to descending step, nm	5.87	2.35	10.33	1.99	24
Distance to ascending step, nm	6.70	3.49	17.43	2.69	21
Distance to nearest step, nm	4.92	1.58	8.38	1.99	28
Number of surrounding islands	3	2	7	0	29
Distance to surrounding islands, nm	9.09	4.69	28.61	3.30	76
Area of surrounding islands, nm^2	29.68	18.98	101.17	0.92	81

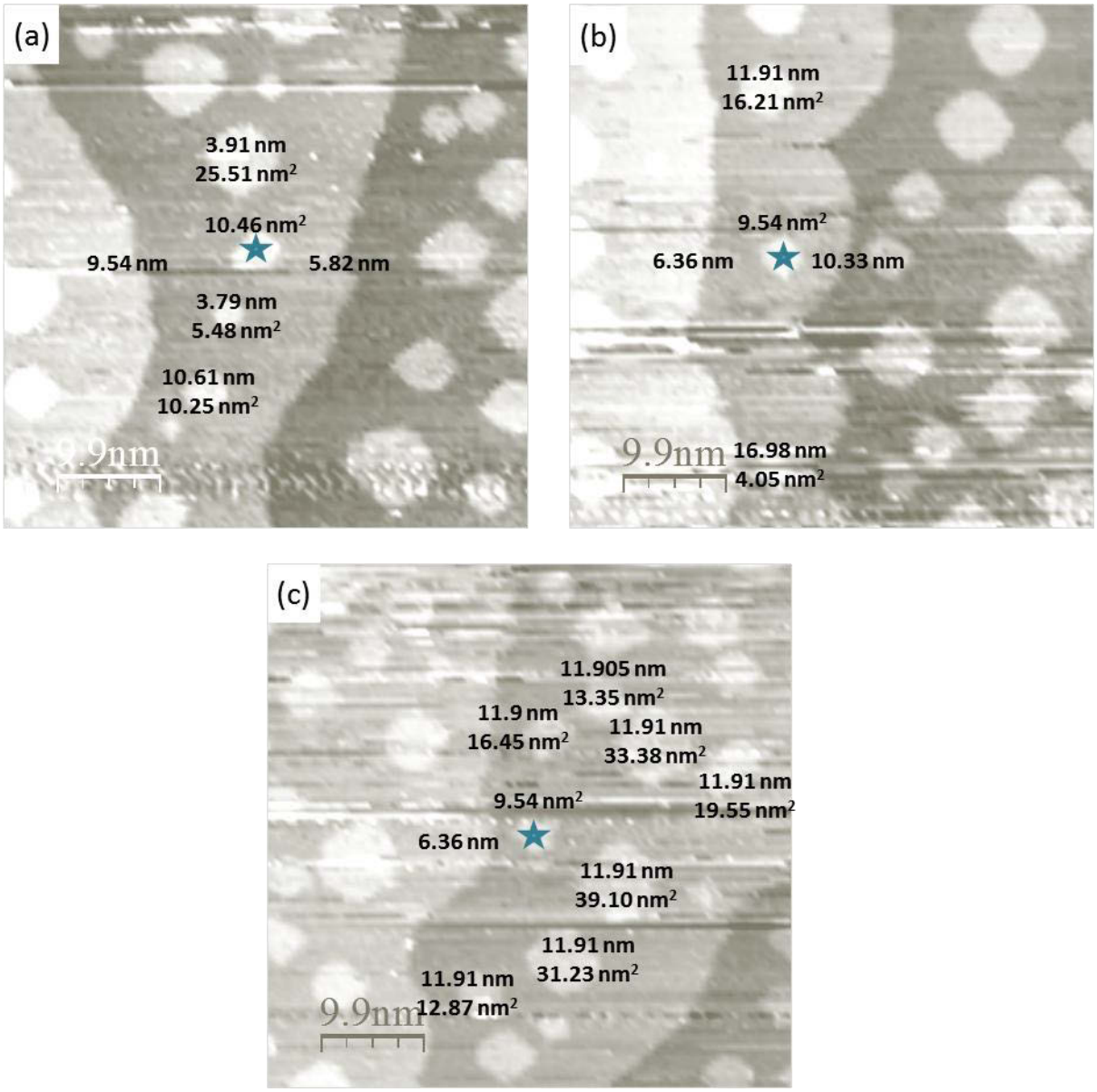

Figure A2.1. Initial conditions of individual Ag islands evaluated marked with a blue star. 0.034 ML sulfur on Ag/Ag(100); 6254, 7095, and 4841 s after Ag deposition; 3661, 4502, and 2248 s after sulfur deposition. STM images 49.3×49.3 nm^2 of islands (a) 2, (b) 3, and (c) 4 (12/22/2008 m68, 60, 49).

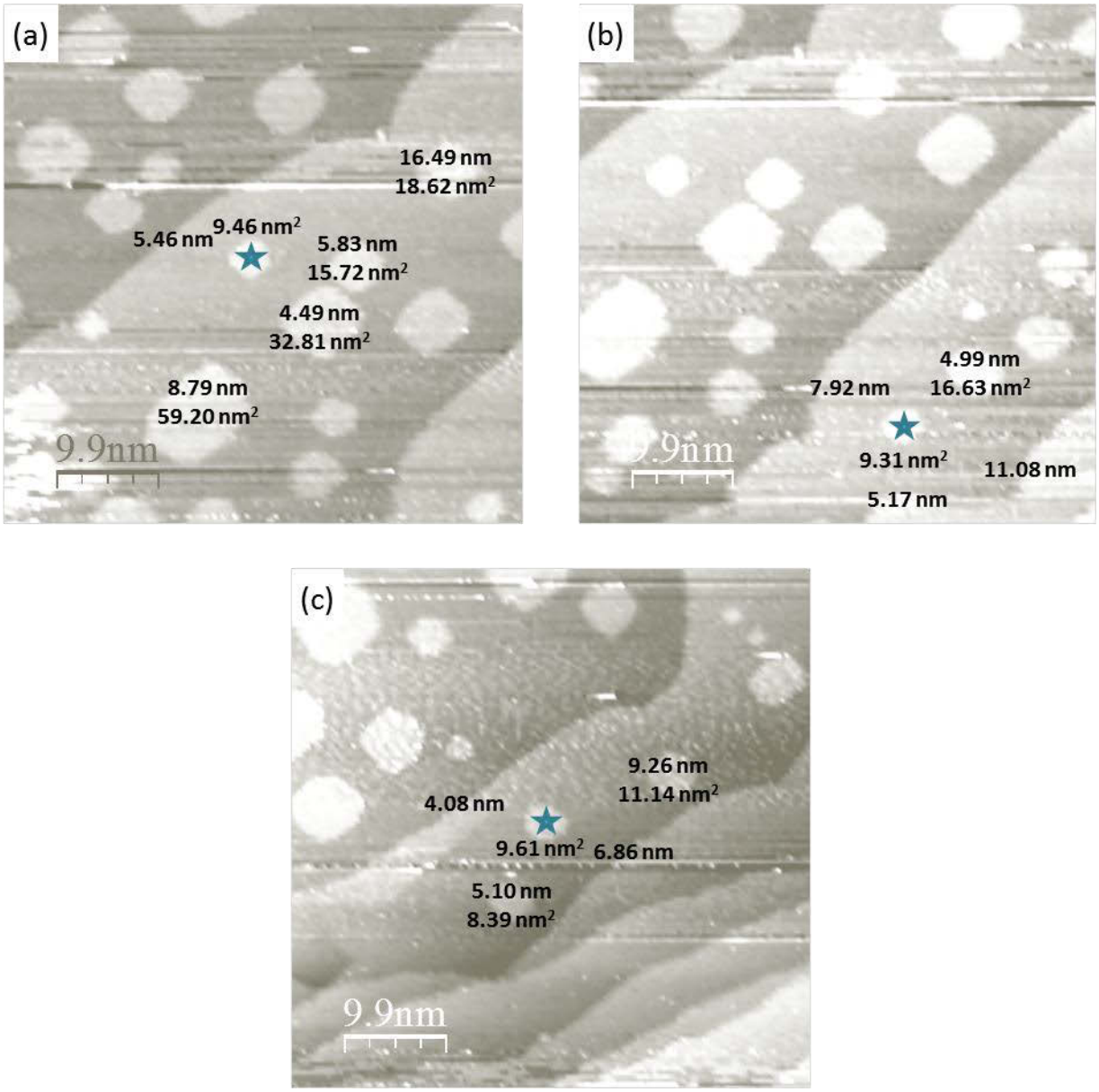

Figure A2.2. Initial conditions of individual Ag islands evaluated marked with a blue star. 0.041 ML sulfur on Ag/Ag(100); 6492, 6492, and 6699 s after Ag deposition; 3222, 3222, 3429 s after sulfur deposition. STM images 49.6×49.6 nm^2 of islands (a) 1, (b) 4, and (c) 5 (12/15/2008 m78, 78, 80).

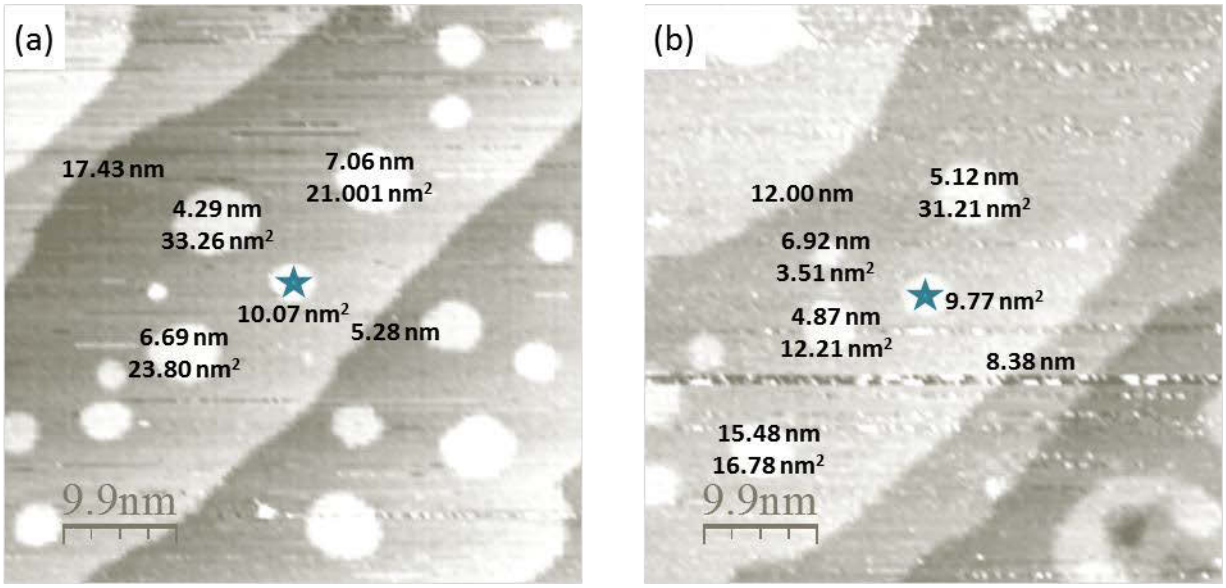

Figure A2.3. Initial conditions of individual Ag islands evaluated marked with a blue star. 0.081 ML sulfur on Ag/Ag(100); 10801 and 13225 s after Ag deposition; 3061 and 5485 s after sulfur deposition. STM images 49.6×49.6 nm^2 of islands (a) 2 and (b) 3 (2/5/2009 m64, 84).

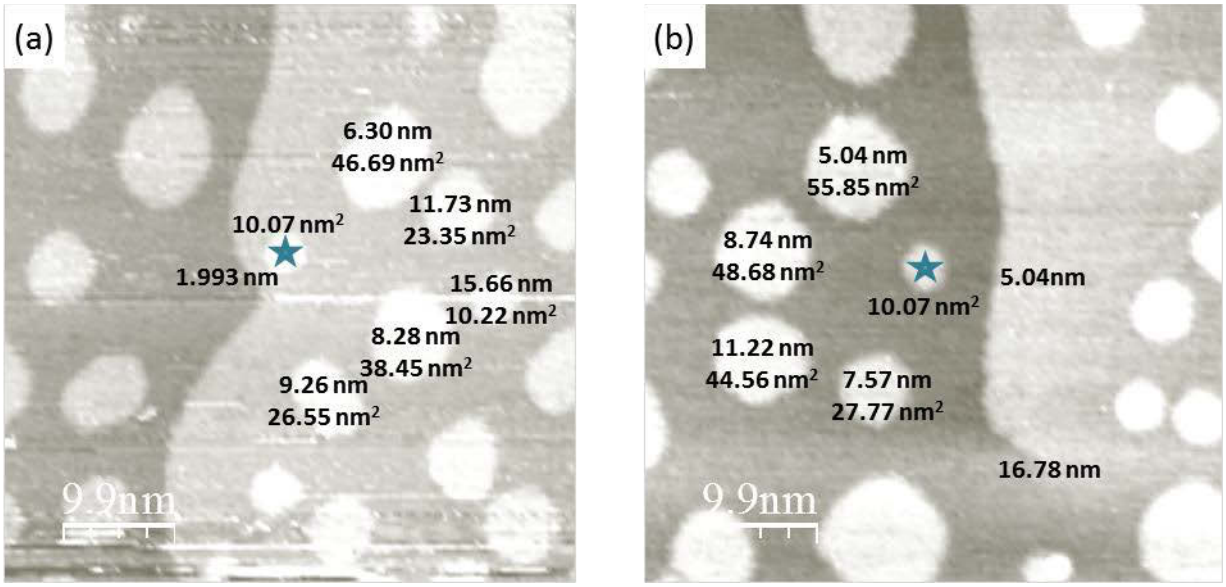

Figure A2.4. Initial conditions of individual Ag islands evaluated marked with a blue star. 0.083 ML sulfur on Ag/Ag(100); 5610 and 12936 s after Ag deposition; 1246 and 8572 s after sulfur deposition. STM images 49.6×49.6 nm^2 of islands (a) 3 and (b) 4 (1/26/2009 m70, 141).

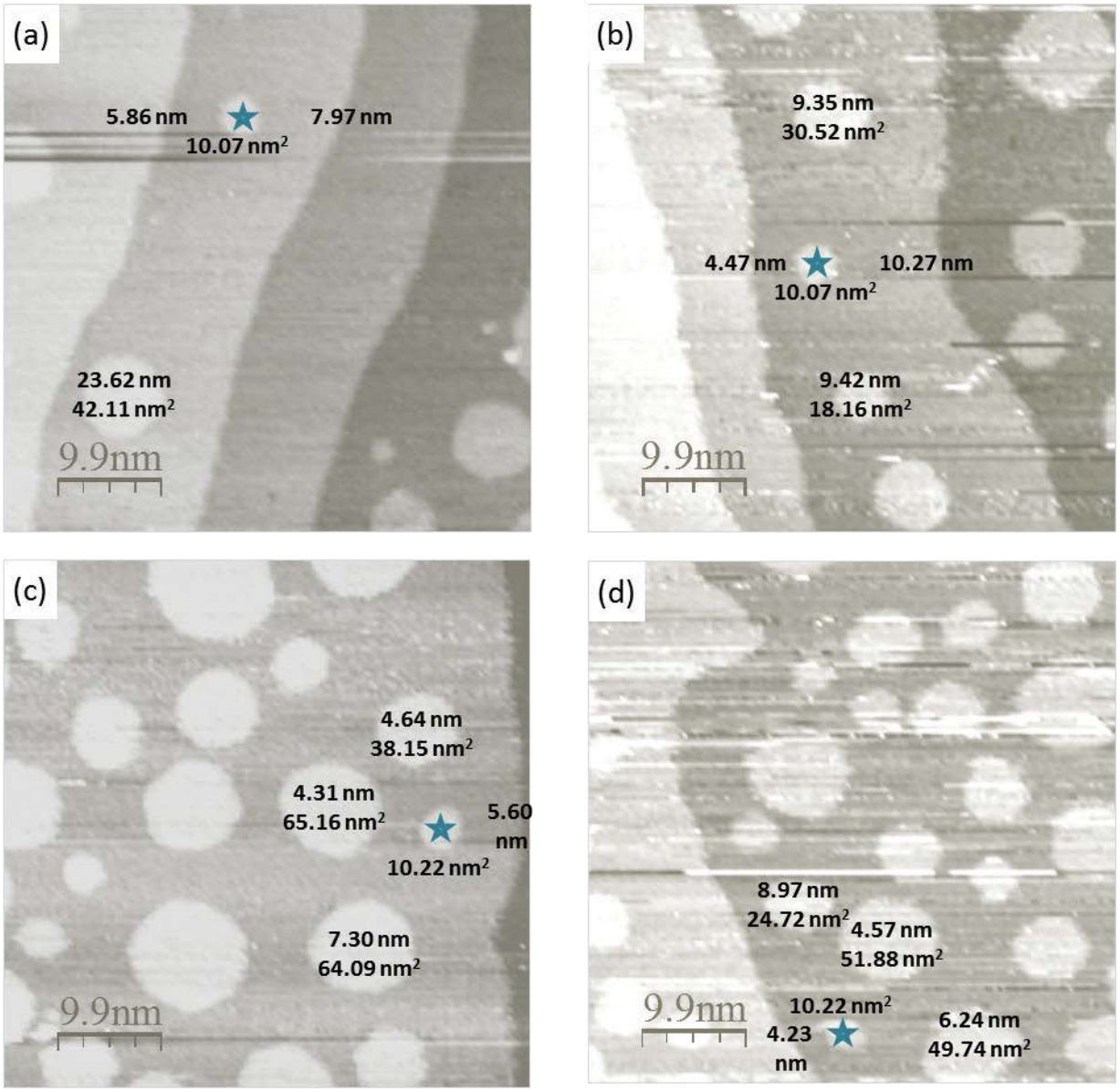

Figure A2.5. Initial conditions of individual Ag islands evaluated marked with a blue star. 0.10 ML sulfur on Ag/Ag(100); 10417, 11576, 8522, and 6520 s after Ag deposition; 6277, 7436, 4382, and 2380, s after sulfur deposition. STM images 49.6×49.6 nm^2 of islands (a) 2, (b) 3, (c) 4, and (d) 5 (2/16/2009 m84, 95, 66, 47).

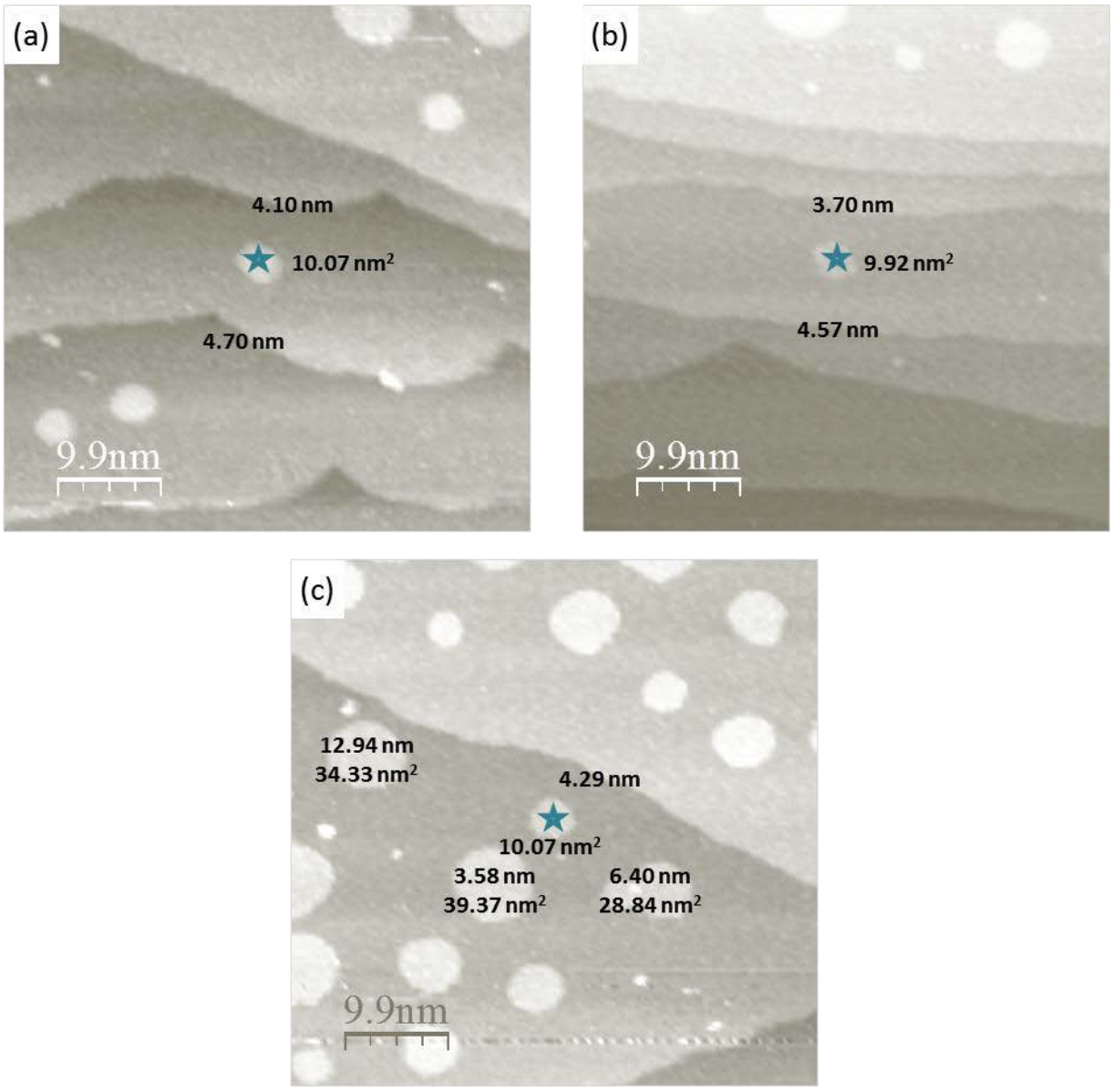

Figure A2.6. Initial conditions of individual Ag islands evaluated marked with a blue star. 0.11 ML sulfur on Ag/Ag(100); 10274, 9340, and 10274 s after Ag deposition; 6090, 5156, and 6090 s after sulfur deposition. STM images 49.6×49.6 nm^2 of islands (a) 3, (b) 4, and (c) 5 (1/21/2009 m116, 116, 107).

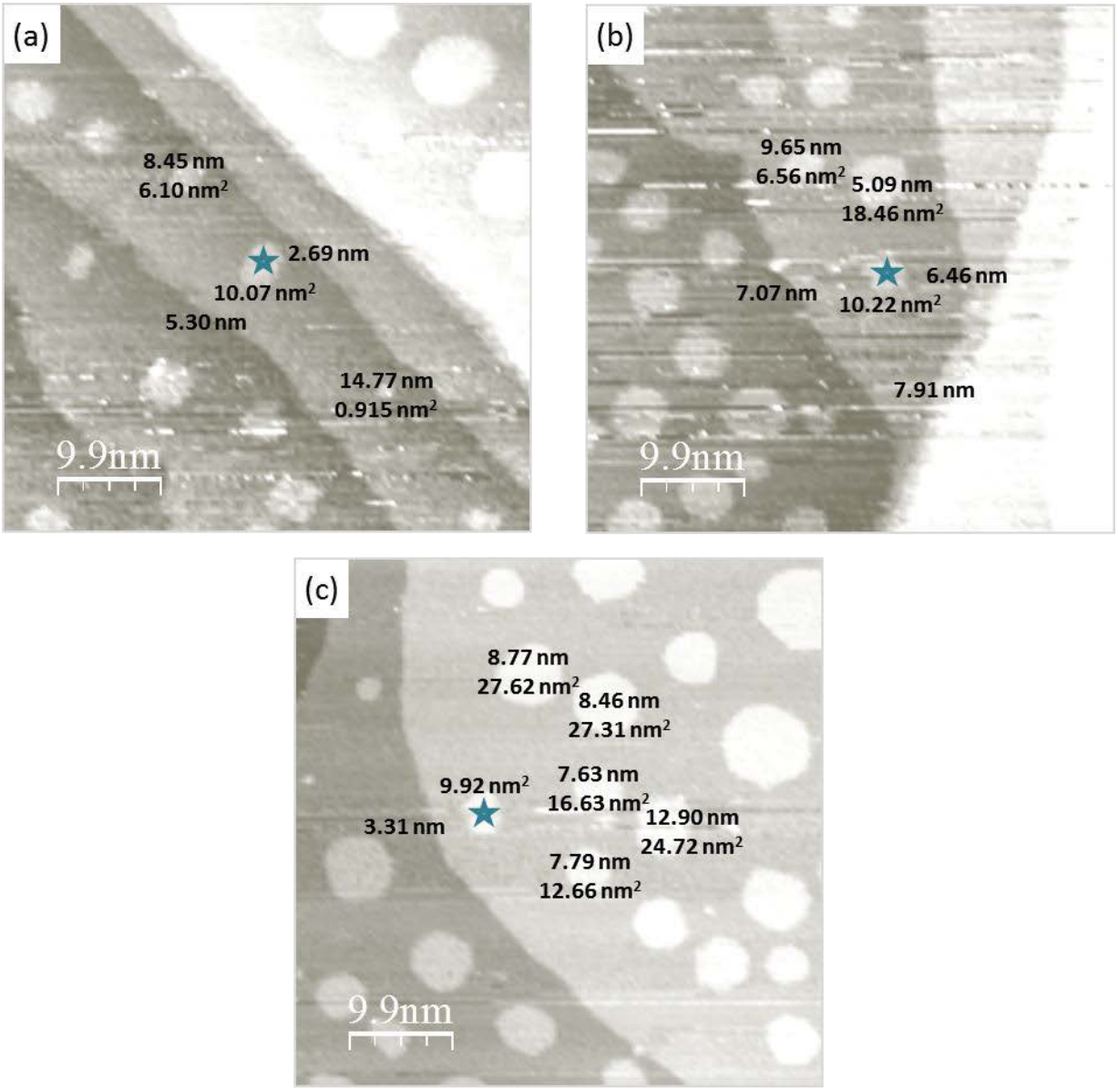

Figure A2.7. Initial conditions of individual Ag islands evaluated marked with a blue star. 0.12 ML sulfur on Ag/Ag(100); 5535, 5431, and 7095 s after Ag deposition; 735, 631, and 2295 s after sulfur deposition. STM images 49.6×49.6 nm^2 of islands (a) 4, (b) 5, and (c) 6 (12/30/2008 m49, 48, 64).

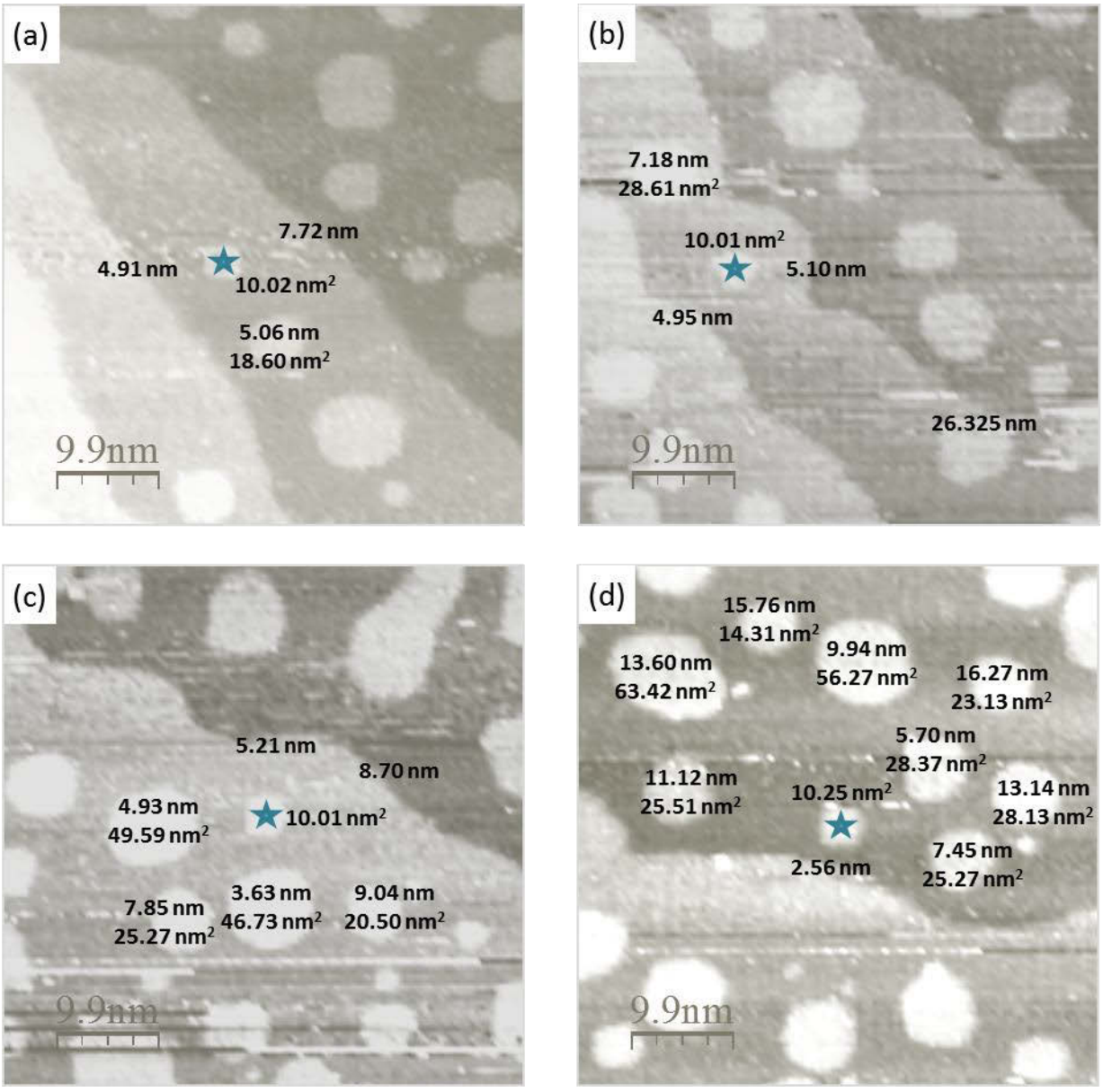

Figure A2.8. Initial conditions of individual Ag islands evaluated marked with a blue star. 0.15 ML sulfur on Ag/Ag(100); 7112, 6261, 7955, and 8830 s after Ag deposition; 2012, 1161, 2855, and 3730 s after sulfur deposition. STM images 49.6×49.6 nm^2 of islands (a) 1, (b) 3, (c) 4, and (d) 5 (3/2/2009 m62, 46, 54, 70).

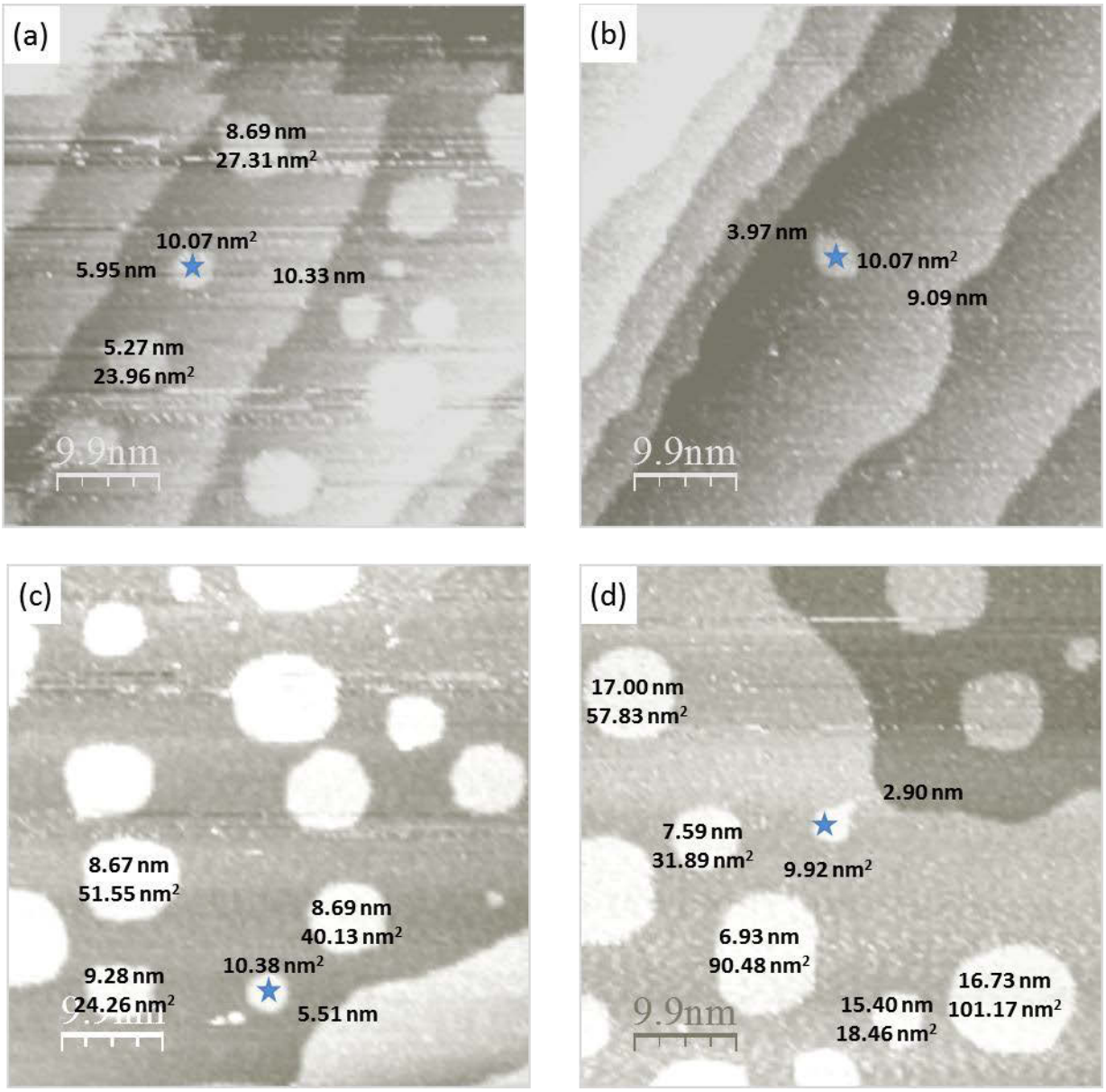

Figure A2.9. Initial conditions of individual Ag islands evaluated marked with a blue star. 0.21 ML sulfur on Ag/Ag(100); 6863, 7913, 9174, and 8228 s after Ag deposition; 1043, 2093, 3354, and 2408 s after sulfur deposition. STM images 49.6×49.6 nm^2 of islands (a) 2, (b) 3, (c) 4, and (d) 5 (1/6/2009 m51, 61, 73, 64).

References

(1) Zheng, H.; Smith, R. K.; Jun, Y.-W.; Kisielowski, C.; Dahmen, U.; Alivisatos, A. P. *Science* 2009, *324*, 1309.

(2) Brune, H.; Kern, K. *Phys. Low-Dim. Struct.* 1994, *1*, 67.

(3) Harris, P. J. F. *Int. Mat. Rev.* 1995, *40*, 97.

(4) Ling, W. L.; Bartelt, N. C.; Pohl, K.; de la Figuera, J.; Hwang, R. Q.; McCarty, K. F. *Phys. Rev. Lett.* 2004, *93*, 166101.

(5) Feibelman, P. J. *Phys. Rev. Lett.* 2000, *85*, 606.

(6) Shen, M.; Liu, D.-J.; Jenks, C. J.; Thiel, P. A. *Surf. Sci.* 2009, *603*, 1486.

(7) Shen, M.; Liu, D.-J.; Jenks, C.; Thiel, P.; Evans, J. *J. Chem. Phys.* 2009, *130*, 094701.

(8) Thiel, P. A.; Shen, M.; Liu, D.-J.; Evans, J. W. *J. Vac. Sci. Technol. A* 2010, *28*, 1285.

(9) Maksymovych, P.; Voznyy, O.; Doughterty, D. B.; Sorescu, D. C.; Yates Jr., J. T. *Prog. Surf. Sci.* 2010, *85*, 206.

(10) Voznyy, O.; Dubowski, J. J.; Yates Jr., J. T.; Maksymovych, P. *J. Am. Chem. Soc.* 2009, *131*, 12980.

(11) Maksymovych, P.; Yates Jr., J. T. *J. Am. Chem. Soc.* 2008, *130*, 7518.

(12) Maksymovych, P.; Sorescu, D. C.; Yates Jr., J. T. *Phys. Rev. Lett.* 2006, *97*, 146103.

(13) Yamada, M.; Hirashima, H.; Kitada, A.; Izumi, K.; Nakamura, J. *Surf. Sci.* 2008, *602*, 1659.

(14) Morgenstern, K.; Laegsgaard, E.; Besenbacher, F. *Surf. Sci.* 2008, *602*, 661.

(15) Kibsgaard, J.; Morgenstern, K.; Laegsgaard, E.; Lauritsen, J. V.; Besenbacher, F. *Phys. Rev. Lett.* 2008, *100*, 116104.

(16) Rovida, G.; Pratesi, F. *Surf. Sci* 1981, *104*, 609.

(17) Sotto, M. P.; Boulliard, J. C. *Surf. Sci.* 1985, *162*, 285.

(18) Russell, S. M.; Shen, M.; Liu, D.-J.; Thiel, P. A. *Surf. Sci.* 2011, *605*, 520.

(19) Wen, J.-M.; Chang, S.-L.; Burnett, J. W.; Evans, J. W.; Thiel, P. A. *Phys. Rev. Lett.* 1994, *73*, 2591.

(20) Wen, J.-M.; Evans, J. W.; Bartelt, M. C.; Burnett, J. W.; Thiel, P. A. *Phys. Rev. Lett.* 1996, *76*, 652.

(21) Pai, W. W.; Swan, A. K.; Zhang, Z.; Wendelken, J. F. *Phys. Rev. Lett.* 1997, *79*, 3210.

(22) Smoluchowski, M. V. *Phys. Z.* 1916, *17*, 585.

(23) Note *Samples were synthesized at the Materials Preparation Center, Ames Laboratory USDOE, Ames, IA, USA. See: www.mpc.ameslab.gov.*

(24) Shen, M.; Liu, D.-J.; Jenks, C.; Thiel, P. A. *J. Phys. Chem. C* 2008, *112*, 4281.

(25) Wagner, C. *J. Chem. Phys.* 1953, *21*, 1819.

(26) Schwaha, K.; Spencer, N. D.; Lambert, R. M. *Surf. Sci* 1979, *81*, 273.

(27) Kresse, G.; Furthmüller, J. *Phys. Rev. B* 1996, *54*, 11169.

(28) Kresse, G.; Hafner, J. *Phys. Rev. B* 1994, *49*, 14251.

(29) Kresse, G.; Hafner, J. *Phys. Rev. B* 1993, *47*, 558.

(30) Perdew, J. P.; Burke, K.; Ernzerhof, M. *Phys. Rev. Lett.* 1996, *77*, 3865.

(31) Kresse, G.; Joubert, D. *Phys. Rev. B* 1999, *59*, 1758.

(32) Kiejna, A.; Kresse, G.; Rogal, J.; De Sarkar, A.; Reuter, K.; Scheffler, M. *Phys. Rev. B* 2006, *73*, 035404.

(33) Neugebauer, J.; Scheffler, M. *Phys. Rev. B* 1992, *46*, 16067.

(34) Methfessel, M.; Paxton, A. T. *Phys. Rev. B* 1989, *40*, 3616.

(35) Liu, D.-J. *Phys. Rev. B* 2010, *81*, 035415.

(36) Hammer, B.; Hansen, L. B.; Norskov, J. K. *Phys. Rev. B* 1999, *59*, 7413.

(37) Krukau, A. V.; Vydrov, O. A.; Izmaylov, A. F.; Scuseria, G. E. *J. Chem. Phys.* 2006, *125*, 224106.

(38) Stoldt, C. R.; Cadilhe, A. M.; Jenks, C. J.; Wen, J.-M.; Evans, J. W.; Thiel, P. A. *Phys. Rev. Lett.* 1998, *81*, 2950.

(39) Layson, A. R.; Evans, J. W.; P.A.Thiel *Phys. Rev. B* 2002, *65*, 193409.

(40) Ratke, L.; Voorhees, P. W. *Growth and coarsening: Ostwald ripening in material processing*; Springer-Verlag: Berlin, 2002.

(41) Theis, W.; Bartelt, N. C.; Tromp, R. M. *Phys. Rev. Lett.* 1995, *75*, 3328.

(42) Bak, P. *Phys. Rev. Lett* 1985, *54*, 1539.

(43) Liu, D.-J. *J. Phys. Chem. C* 2007, *111*, 14698.

(44) Evans, J. W.; Thiel, P. A.; Bartelt, M. C. *Surf. Sci. Reports* 2006, *61*, 1.

(45) Layson, A. R.; Thiel, P. A. *Surf. Sci.* 2001, *472*, L151.

(46) Savio, L.; Giallombardo, C.; Vattuone, L.; Kokalj, A.; Rocca, M. *J. Phys. Cond. Matt.* 2008, *20*, 224006.

(47) Hannon, J. B.; Klünker, C.; Giesen, M.; Ibach, H.; Bartelt, N. C.; Hamilton, J. C. *Phys. Rev. Lett.* 1997, *79*, 2506.

APPENDIX II

Sulfur Adsorption on Ag(110)

Selena M. Russell[a] and Patricia A. Thiel[a,b]

1. Experimental Results

At 117 to 162 K, 0.17 ML S appears as amorphous islands on the surface. Between 162 and 196 K, where the surface looks like it has "squiggles" like Ag(100). Example images from this experiment are shown in Fig. 1.

After depositing 0.42 ML S and heating the sample to 204 K, an ordered structure appears. See Fig. 2. Rows appear along the open, [001] direction and are separated by approximately 0.886 nm. This agrees very well with $3a'/\sqrt{2} = 0.866623$ nm. Protrusions within these new rows are visible. Also note the highly facetted nature of the step edges.

Fig. 3 outlines the temperature dependence of the surface phases with 0.73 ML S adsorbed on the surface. The high coverage of sulfur causes the surface to appear very rough. Between 234 and 260 K, islands appear on terraces and jutting out from step edges, and pits appear within terraces. These changes indicate that the surface undergoes reconstruction involving the removal of terrace Ag atoms. At room temperature, the islands appear rectangular, elongated along the [1-10] direction. The pits are less prevalent. The step edges are also highly faceted, and often appear brighter, taller, than the ascending terrace.

Depositing 0.88 ML of sulfur caused significant changes to the surface, as shown in Fig. 4. However, imaging became very difficult due to the high coverage, so there are only a few clear images using very weak tunneling conditions. At 164 K, terraces appear very rough with much material that shows no order. At 202 K, the surface is still very rough and I had difficulty identifying large terraces. Some small areas do appear smooth. At 236 K, all I could image were long strips. At 299 K, I observed rectangular islands, highly faceted step

[a] Department of Chemistry, Iowa State University, Ames, IA 50011
[b] Department of Materials Science & Engineering, and Ames Laboratory – USDOE, Iowa State University, Ames, IA 50011

edge, and rectangular pits. The flat areas are striped. Based on earlier coarsening studies, the stripes are in the [1 -1 0] close-packed direction.

2. Experimental Details

All experiments were performed in a stainless-steel ultrahigh vacuum (UHV) chamber with base pressure of 1×10^{-10} Torr (1.33×10^{-8} Pa), equipped with a variable temperature scanning tunneling microscope (VT-STM) (Omicron GmbH, Germany). The Ag(110) samples were cleaned by repeated cycles of Ar^+ sputtering (1 keV, ~ 2 μA, 8 – 16 min) and annealing (625 – 670 K, 10 min). The experiments conducted were on two samples from the Surface Preparation Laboratory in the Netheralnds.[1,2]

All STM images were collected using electrochemically etched W tips and cut PtIr tips in an Omicron VT-STM. The true temperature of the sample is within ± 5 K of the reported value and was held constant during each experiment, unless otherwise noted. Tunneling conditions are given in the figure captions.

Sulfur was generated within UHV in a solid-state electrochemical Ag|AgI|Ag_2S|Pt cell, following the design of Wagner.[3] Sulfur coverage, θ_S, is given as the ratio of sulfur atoms to Ag atoms, also expressed as ML. After each STM experiment the S(LMM)/Ag(MNN) AES intensity ratio was measured and converted to coverage, following a calibration established by Schwaha, et al.[4] and corroborated by Rovida and Pratesi.[5] This procedure has been supported by an STM study.[6]

In the figures, yellow arrows indicate S deposition, and red arrows indicate heating the sample in the STM stage.

Acknowledgements

This work was supported by NSF Grant CHE-1111500. The work was performed at Ames Laboratory, which is operated for the USDOE by Iowa State University under Contract No. DE-AC02-07CH11358.

Figures

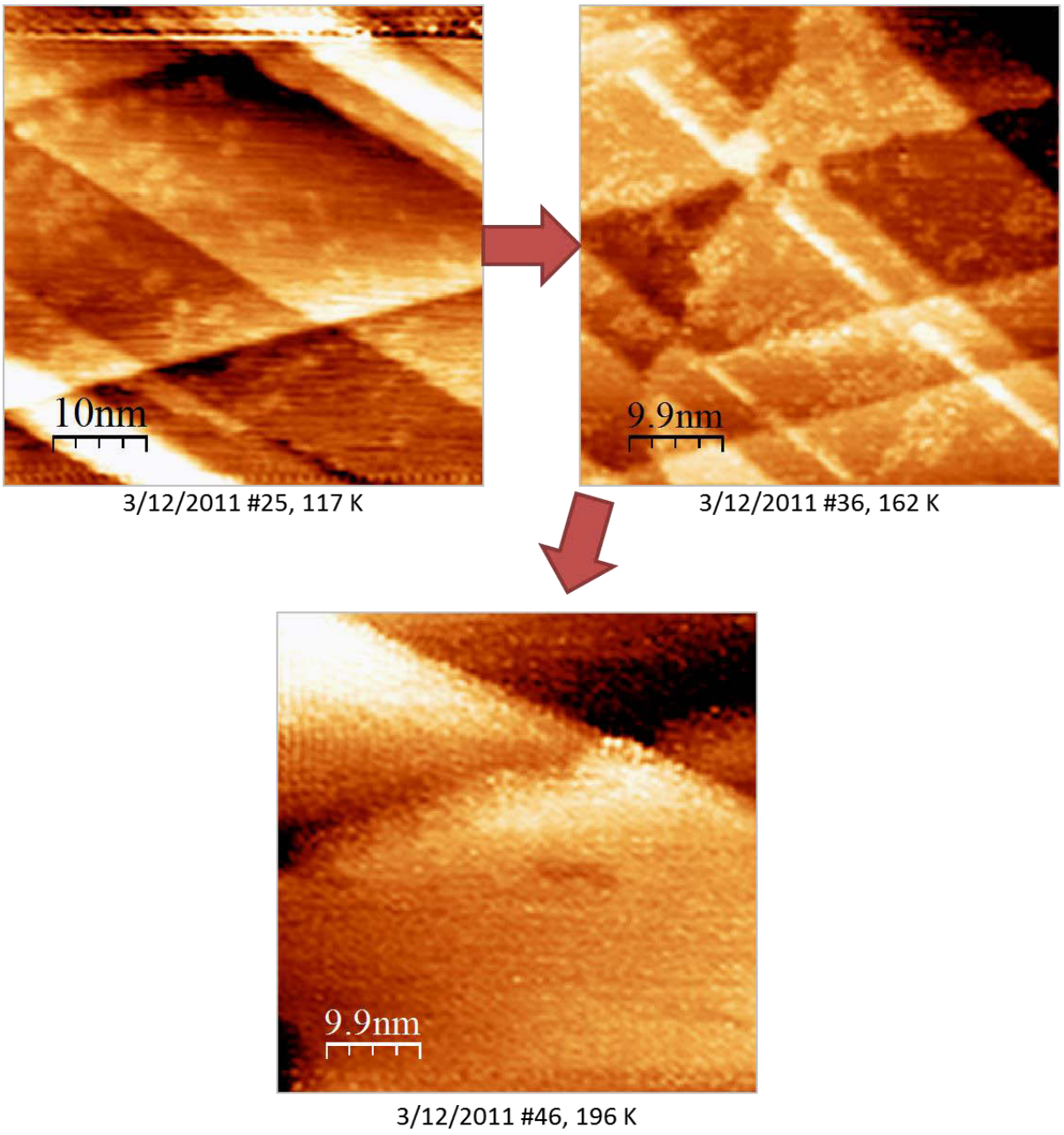

Figure 1. 0.17 ML S deposited on Ag(110) at 117 K and heated in steps to 196 K.

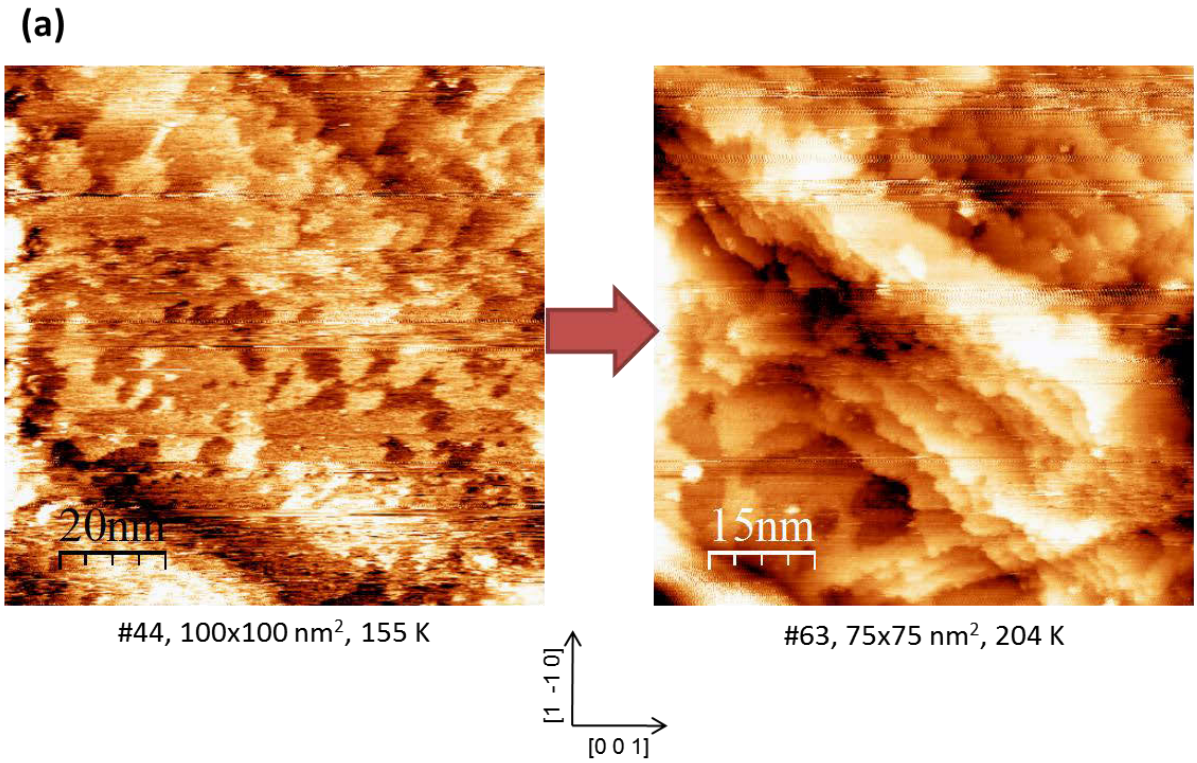

This figure continues on the next page.

Figure 2. 0.42 ML S deposited on Ag(110) at 155 K and heated to 204 K (a). Details of the surface at 204 K (b).

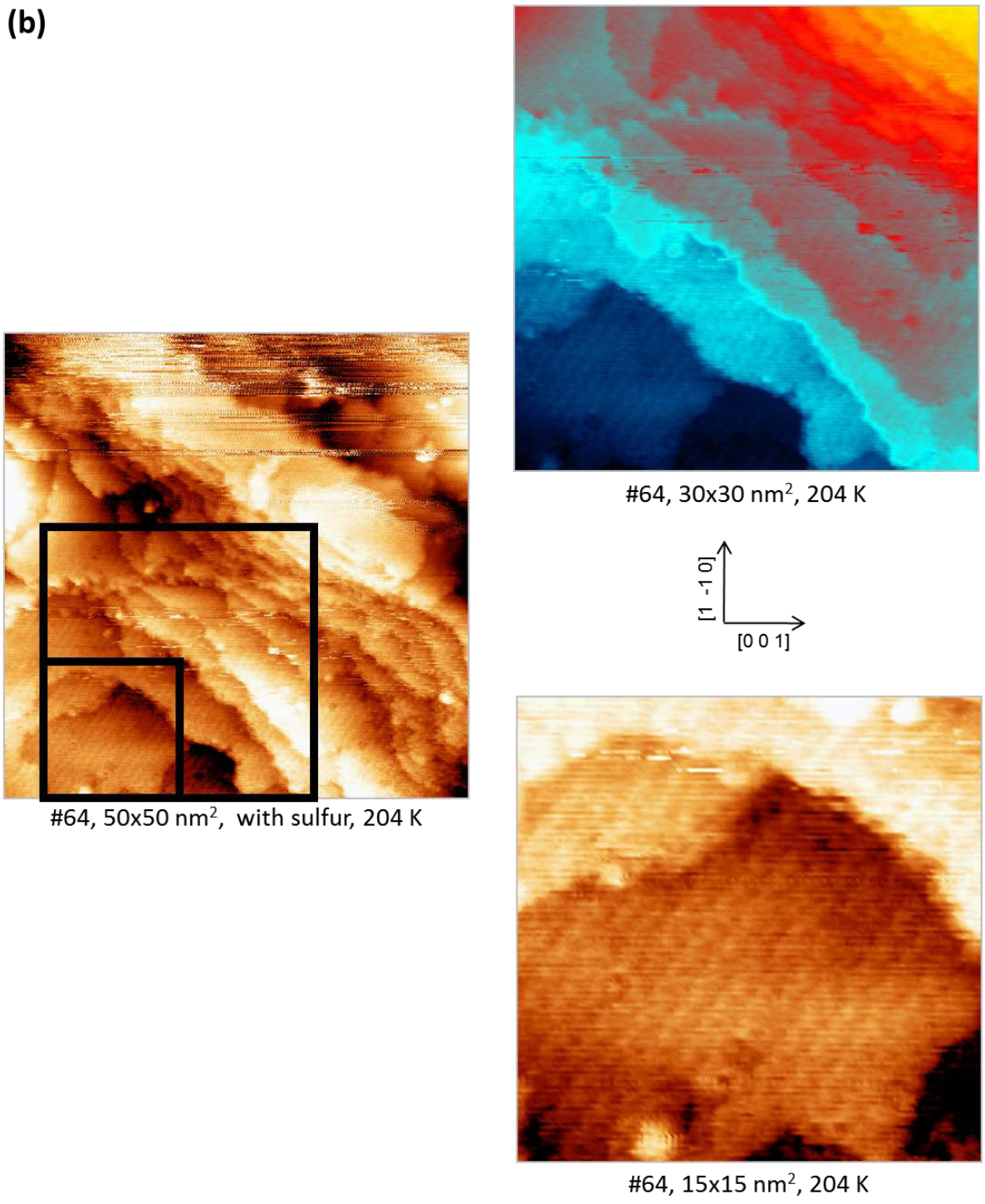

Figure 2. continued.

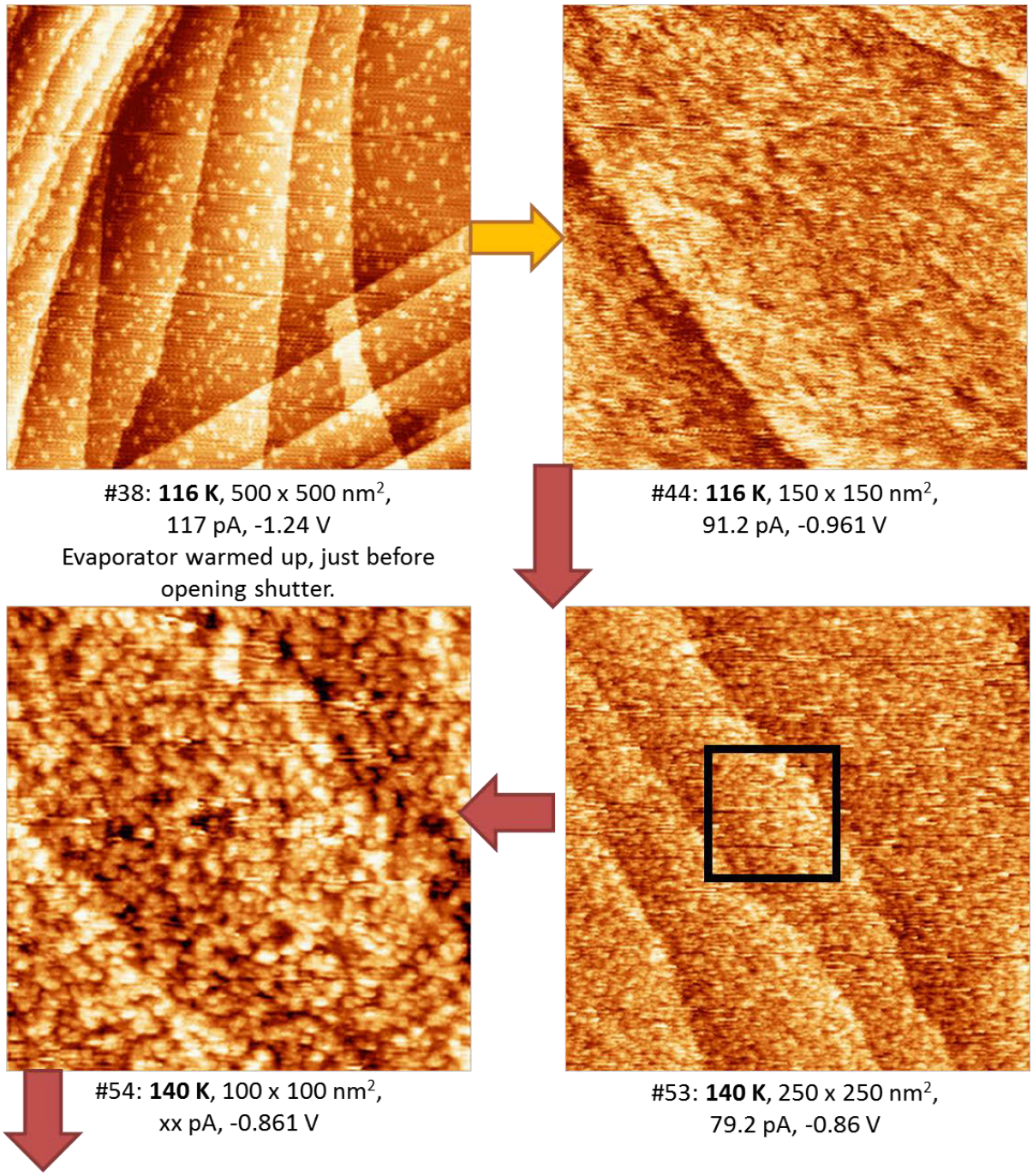

This figure continues on the next page.

Figure 3. 0.73 ML S deposited on Ag(110) at 117 K and heated in steps to 300 K.

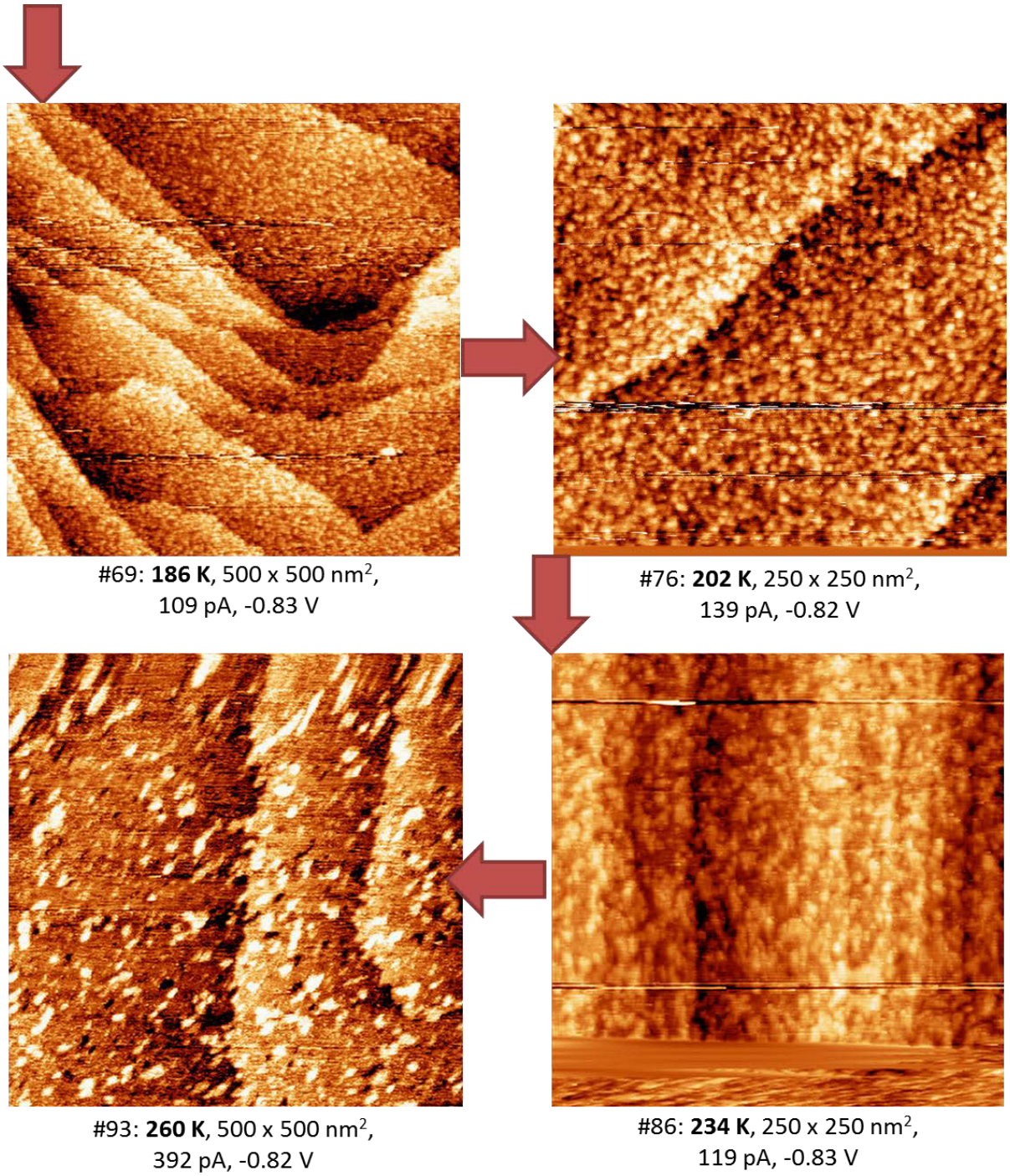

This figure continues on the next page.

Figure 3. continued

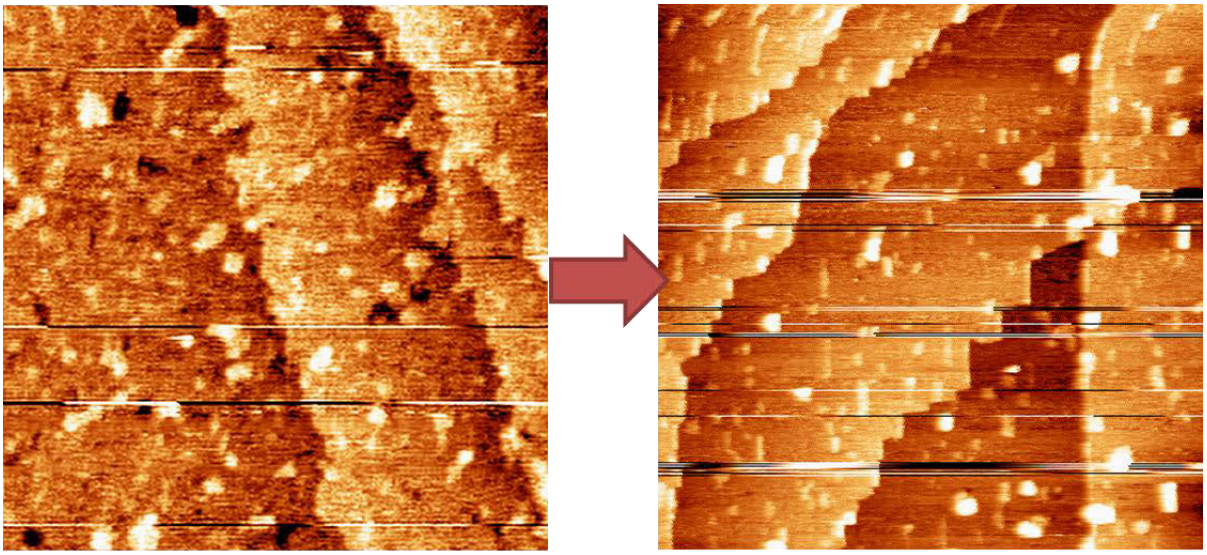

#97: **260 K**, 250 x 250 nm^2,
15.0 pA, -0.82 V

#123: **RT**, 500 x 500 nm^2,
108 pA, -0.73 V

Figure 3. continued

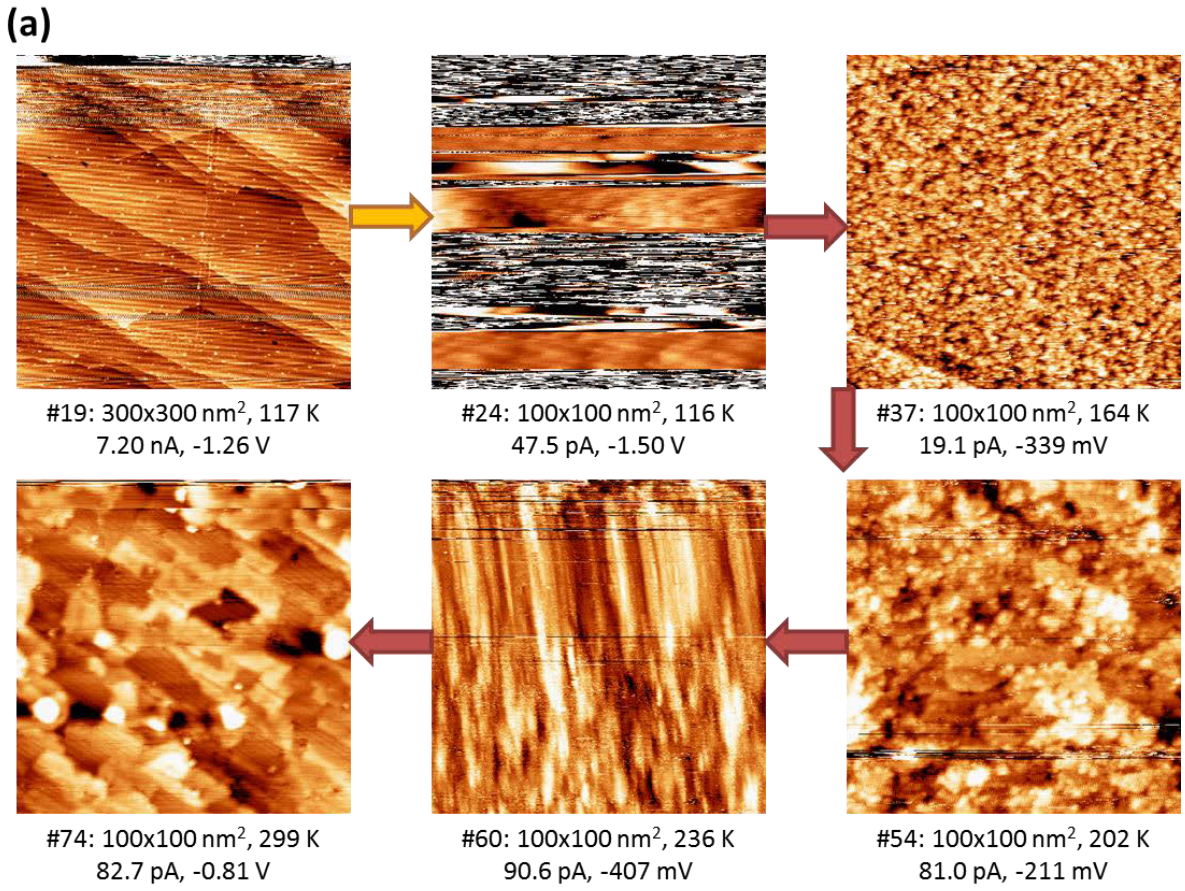

This figure continues on the next page.

Figure 4. 0.88 ML S deposited on Ag(110) at 117 K and heated in steps to 299 K (a). Details of the surface at room temperature (b).

(b)

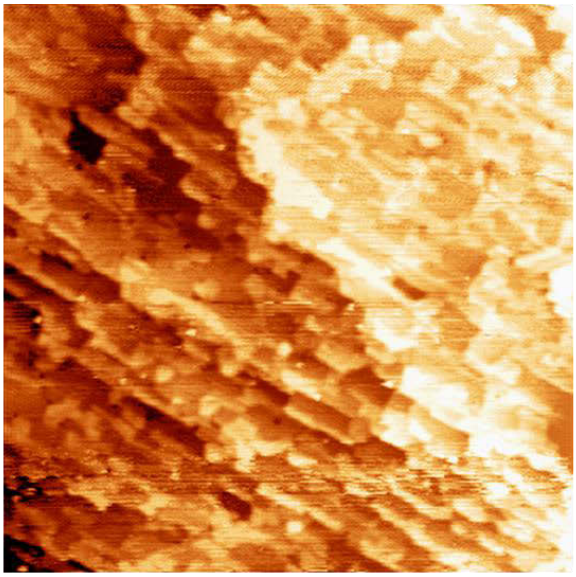

#69: 200x200 nm^2, 299 K, 109 pA, -229 mV

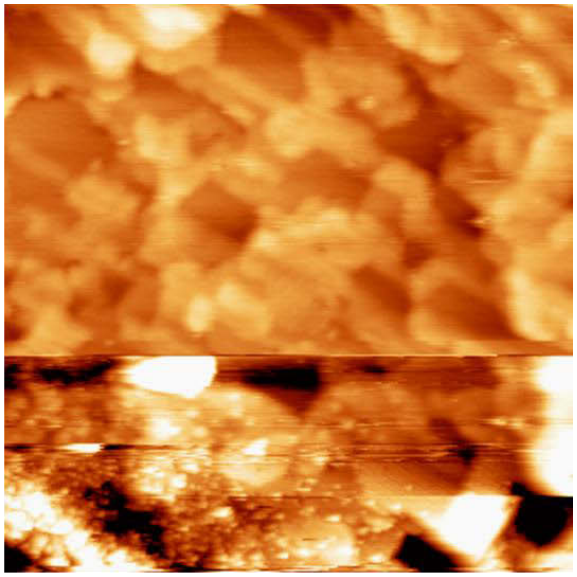

#81: 100x100 nm^2, 299 K, 48.9 pA, -1.00 V

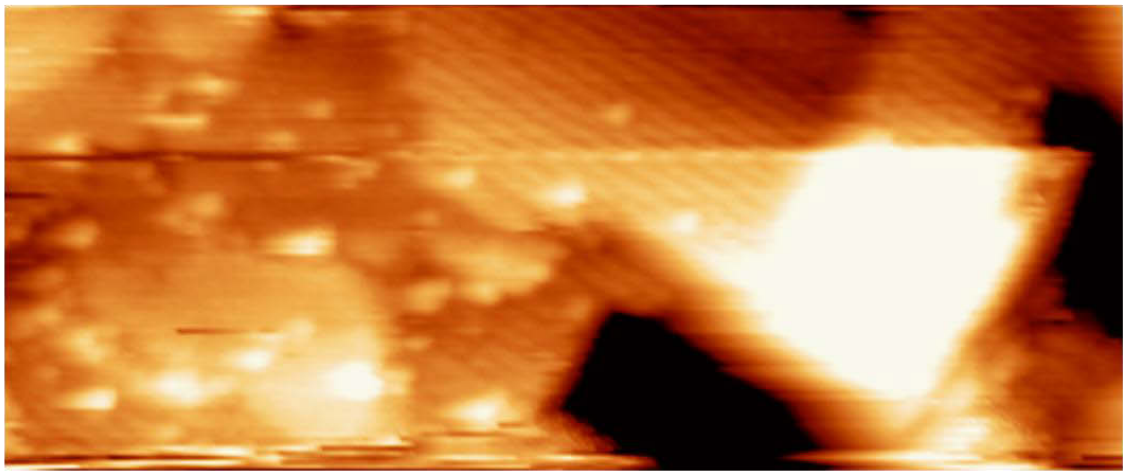

#81: 47.3x19.7 nm^2, 299 K, 48.9 pA, -1.00 V

Figure 4. continued.

References

(1) Single crystals were purchased from Surface Preparation Laboratory, The Netherlands. www.spl.eu. Aligned within 0.5 degree or better, polished, with roughness 0.03 micron or better, and dimensions 9.0 x 3.0 x 1.5 mm. Purchased February 2010 by Thomas Duguet from René Koper. SPL#210027.

(2) Single crystals were purchased from Surface Preparation Laboratory, The Netherlands. www.spl.eu. Aligned within 0.5 degree or better, polished, with roughness 0.03 micron or better, and dimensions 9.0 x 3.0 x 1.0 mm. Purchased 2011 by Selena Russell from René Koper. SPL#211060

(3) Wagner, C. *J. Chem. Phys.* **1953**, *21*, 1819.

(4) Schwaha, K.; Spencer, N. D.; Lambert, R. M. *Surf. Sci* **1979**, *81*, 273.

(5) Rovida, G.; Pratesi, F. *Surf. Sci* **1981**, *104*, 609.

(6) Russell, S. M.; Shen, M.; Liu, D.-J.; Thiel, P. A. *Surf. Sci.* **2011**, *605*, 520.

APPENDIX III
Sulfur evaporator

1. Introduction

Chalcogens are deposited on surfaces through various methods in ultra-high vacuum (UHV) including vapor exposure, thermal evaporation, sputtering and ablation, and electrochemical vapor generation.

Deposition from the gas phase involves backfilling the chamber with the appropriate gas (O_2, NO_2, H_2S, SO_2, or H_2Se) with the sample at a temperature sufficient for the molecule to adsorb and dissociate. Early surface science experiments often employed H_2S as the sulfur source. On copper surfaces H_2S readily dissociates at room temperature and the reaction is exothermic.[1-3] However, silver surfaces are relatively unreactive toH_2S gas.[4] The dissociation reaction is slightly exothermic and the barrier is higher than for H_2S dissociation on copper or gold.[3,5] In order to adsorb S atoms on the low-index silver surfaces, Rovida and Pratesi found that high H_2S pressures (greater than 10^{-3} Torr) were required.[6] Backfilling a UHV chamber with such large amounts of hazardous and corrosive gas is less than desirable.

Chalcogens heavier than oxygen may also be deposited via thermal or electrochemical techniques. Thermal methods include evaporation of pellets and dissociation of metallic rods. The electrochemical method described here provides a cleaner and more direct chalcogen deposition than gas exposure or thermal techniques.[7]

The solid-state electrochemical cell Ag|AgI|Ag_2S|Pt produces molecular sulfur vapor.[8-17] At 473 K, AgI becomes an excellent ionic conductor and Ag_2S decomposes giving mobile S molecules. Applying a voltage of ~200 mV releases S vapor, mostly comprised of S_2 molecules. However, sulfur molecules of various size comprise the vapor, including S_6, S_7, S_5, and S_8.[12] The exact vapor composition depends on the cell voltage and temperature. At 200 mV, the partial pressure of S_2 is ten times greater than that of any other sulfur molecule.[12] Based on experimentally observed surface phases, the sulfur molecules dissociate on the Ag surface between 120 and 200 K.

Most solid-state electrochemical chalcogen or halogen sources prepare the cell by pouring the molten silver compounds into glass tubes with the Pt, Ag and thermocouple

wires. The method ensures excellent contact between the materials, which is very important for cell function. However, with use the source becomes depleted of the chalcogen or halogen and the raw materials must be replenished.

Mingmin Shen designed and built a solid-state electrochemical sulfur source at Iowa State University during calendar years 2005 and 2006 with the assistance the Ames Laboratory Machine Shop and the Iowa State University Chemistry Glass Shop. Her design was based on that of Heegemann *et al.*[13] and Jones[16] and is discussed in Appendix III of her thesis.[18] Shen mounted the S evaporator May 2006 on the VT-STM chamber in 331 Spedding Hall. We have used that source in all of the S deposition experiments conducted at Iowa State University. To simplify the refilling process, we employ solid, pressed pellets of the silver compounds. To ensure good contact between the cell components, we physically press the materials in the cell with a stainless steel or ceramic rod acting as a plunger. The evaporator has been refilled and rebuilt on numerous occasions with only slight modifications. Recently, a Maria or glass collar has been added to the glass cell housing. The Maria on the Pyrex glass tube allows the cell to be held at the correct height relative to the stainless steel plunger, ensuring good contact between the cell materials.[19]

2. Design and construction

I built an evaporator analogous to the one discussed above during June and July 2010 at The RIKEN Institute with the help of their Rapid Engineering Team and the Kawai and Kim research groups. A photograph and schematic of the sulfur source is shown in Fig. 1. I brought most of the raw materials from Iowa State U. However, the wires, metal mesh, some ceramics, stainless steel rod, connectors, and all mounts were provided by the Kawai and Kim groups. The first assembly did not yield significant amounts of S. During my February and March 2012 visit, I rebuilt the evaporator and successfully deposited appreciable amounts of S. The results of both experiment sets are described in Chapter III.

The evaporator was mounted on a linear motion arm that could be isolated from the LT-STM chamber and evacuated through the exchange chamber. The Kawai and Kim groups had previously employed this configuration for thermal evaporation. Therefore, I used the existing linear motion arm, housing, feedthroughs, and gate valve. The evaporator chamber is

pictured in Fig. 2. Fig. 3 illustrates the configuration of the evaporator in relationship to the wobble stick, and therefore the sample during the July 2010 experiments. During the March 2012 experiments, the evaporator chamber configuration was the same as in Fig. 3, except that it was mounted on the preparation chamber. To deposit sulfur on the sample surface, the sample was brought within a couple centimeters of the source by appropriately positioning the cell via the linear motion arm and the sample via the wobble stick or manipulator.

2.1. Electrochemical cell housing

We modified the stainless steel-quartz tube to accommodate this configuration and the requirements of the cell. The configuration in UHV requires that the evaporator emits S to the side, perpendicular to the long axis of the cell, rather than from the end, along the long axis of the cell as in the Iowa State evaporator. The glass end of the tube was modified following the drawing in Fig. 4b. The end was sealed and port 1 opened, from which sulfur vapor flows. The ground and thermocouple wires pass through port 2, as shown in Fig. 5a-b. The lips or rods adjacent to both ports help hold the W filament and Pt anode wires in place. The glass stops within the tube, to the left (down tube) from port 1 are very important. The cell components must be held together tightly for the cell to function properly, and the stops hold the anode side of the cell in the tube, as pictured in Fig. 5d-e. The exact length of the metal-glass tube is not important, but the glass portion should be long enough to ensure that the filament is well separated from the joint area to avoid thermal expansion near weakening the joint weakening it.

Two pieces were fabricated to mount the evaporator to the linear motion arm and hold the chemicals in place. A solid machinable ceramic (Macor) rod acts as the plunger in this cell design, pushing the cell components firmly against each other. The dimensions are given in Fig. 4c. The rod diameter is critical, as the rod must be thin enough to slide pass the narrow metal-glass joint, but wide enough to push against the wire spring (between the rod and the Ag plate; see Fig. 1) without the end of the spring being caught between the glass tube and the rod. The ceramic rod length is more flexible, with the key requirements being that it begins before the metal-joint area and ends before reaching port 2 of the glass tube (so that the ground and thermocouples may pass through the port when the evaporator is fully

assembled.). Fig. 4e shows how these components are assembled. The ceramic rod butts up against a stainless steel rod in the metal region of the tube. Therefore, one end of the stainless steel rod is flat. The other end screws into the linear motion arm (with a nut, pictured at the far left in Fig. 5a). Again, the diameter is very important, as the rod must fit within the metal tube, and the exact length is less important. The evaporator is mounted on the linear motion arm by bolting the stainless steel rod to the arm, and spot welding the metal-glass tube to the rod (metal shims may also be used to help hold the tube in place). The spot weld is easily broken (to repair the cell), so multiple welds should be made to securely hold the tube during mounting and use.

2.2. Electrochemical cell materials

The electrochemical cell show in Fig. 1 consists a W coiled wire spring (ground) and filament, Ag plate (cathode), pressed AgI (ionic conductor) and Ag_2S pellets, Pt mesh and wire (anode), and the wire bundle which connects the cell to the feedthrough. A type K thermocouple attached to the cell end of the spring was used to measure the cell temperature. The W wire is 0.25 mm in diameter and was coiled around a 10-24 bolt. The length of wire is sufficient to provide the correct placement of the ceramic rod, short of port 2. The spring electrically connects the cathode to ground. In addition, the spring bulges out of port 2, so I have reinforced the spring in this area by combining multiple springs. The same W wire was coiled around a bolt so that the inner diameter of the coil equals the outer diameter of the glass tube. The length is sufficient to coil around the tube and connect the wire bundle to the evaporator. The silver plate or disk is 99.9999% Ag with a diameter of ~4.4 mm and ~1.3 mm thick. Both silver compounds were hand pressed into pellets using an IR pellet quick press and dye borrowed from a group at Iowa State and cut down to a diameter that fit in the tube with a razor blade. The silver iodide is 99.999% AgI and was used as received from Acros Organics (New Jersey, USA). The pressed AgI pellet was 3-4 mm thick. The silver sulfide is 99.9% Ag_2S and was used as received from Sigma-Aldrich (St. Louis, MO, USA). The pressed Ag_2S pellet was 2 mm thick. Both silver compounds are light sensitive (and may decompose in air). The anode consists of a Pt wire (1 mm diameter, 99.999% pure) and fine Pt mesh. One end of the wire was wound a few turns and spot welded to a disk of fine Pt

mesh (cell side). The free end of the wire passes through port 1 and bends back to connect to the wire bundle.

The wire bundle connects the cell to the feedthrough. The wires in the bundle are insulated twists of Cu wires. The evaporator is moved in and out of the UHV chamber for deposition, so the wire bundle wraps around the transfer arm. The wires are long enough to allow the evaporator to extend to the appropriate distance into the UHV chamber, but short enough so as not to be bulky. The connections between the cell and bundle employ barrel connectors or the wires are looped and spot welded. The connections must be wrapped or insulated so they do not short to the chamber wall. Moving the evaporator (in line or rotating) strains these connections and this is a weak point with the current evaporator. More robust connections should be employed.

2.3. Rebuilding and mounting

As assembled June and July 2010, the evaporator did not yield appreciable amounts of S on the Ag(111) surface, so I reassembled the evaporator with fresh electrochemical cell materials and improved the connections during my February to March 2012 visit. The rebuilt evaporator, before use, is shown in Fig. 6.

While reassembling the evaporator, many of the materials frequently became lodged in the tube, requiring me to try to free them by poking with long, thin stiff rods (such as an Allen key) and forceps, and tapping the tube. While putting cell materials in the tube, I broke the glass at port 2. Fortunately, the Rapid Engineering Team was able to repair the tube quickly. (I would bring a spare, modified metal-glass tube in case the existing one is irreparably damaged in the future.)

I insulated the wires and connections with ceramic tubing and refrasil brought from Iowa State. The connection insulation is an improvement, but not executed perfectly. The refrasil should have been slipped onto the wires *before* connecting the wires. To reduce strain on the connections, I spot welded foil ribbons around the wire bundle and linear motion arm, which is pictured at the left of Fig. 6a. However, some of the connections were still weak resulting in unreliable contact, which affected S deposition. The evaporator continuity after assembly and pumping down is given in Table I.

The March 2012 experiments allowed S to be deposited at room temperature, so the evaporator was mounted on the preparation, rather than the STM, chamber. A schematic and photo of the chamber is shown in Fig. 5 in Chapter I. The evaporator was mounted on the same linear motion arm as in the calendar year 2010 experiments, and this assembly was mounted behind a gate valve on the preparation chamber. During deposition, the sample was brought very close to port 1. The photograph in Fig. 7 was taken during deposition and shows the sample - evaporator configuration.

The S evaporator was mounted just below the mass spectrometer (MS) on the preparation chamber. The spectra recorded for different positions of the evaporator relative the MS is shown in Fig. 8. With port 1 of the evaporator pointing up toward the MS, the S_2 peak increases, in addition to the background gas peaks. The evaporator was more than 20 cm away from the MS. During deposition the evaporator was within 1 cm of the sample.

2.4. Future designs

The diameter of all the cell components should be as large as possible, but small enough to pass through the tube, especially in the narrower metal-glass joint area. However, I often loaded components through port 2 as measuring the inner diameter of the joint is not straight forward, and materials become lodged in the joint area. This should be considered in determining the size of port 2. A large port 2 enables facile loading and wire pass through, but also allows the spring to buckle out of the port. Therefore, the size of port 2 should balance these two factors (the latter may be alleviated by different shape and material of the spring wire). The spring is round W wire because it was readily available, but may not be the best material. It would be better if the spring wire was not round but elliptical and of a material with a larger spring constant. The round wire coil bulges and shifts, so the chemicals are not always held tightly. The inner diameter of the tube dictates the diameter of cell materials, so if materials sized for one tube may not be readily placed in a tube of different size.

Port 1 should be large enough to manipulate the Pt wire with tweezers. Adding a lip/rod both sides of the port (rather than just the one) would hold both the filament and anode wires in place. Ideally, the stops would be located a few millimeters to a centimeter

from the edge of port 1 so the filament may evenly heat the cell components by ending past the chemicals.

Also, the current ceramic rod could be a bit longer and port 2 moved closer to the sealed glass end.

In the future, a considerably larger tube could be used, for example a tube with the inner diameter equal to the diameter of the dye used to press the silver compound pellets would be very convenient, provide more raw material for the cell, and larger surface area for the components to interact. In addition, the glass need not be quartz glass, but can be any UHV compatible glass that can be easily worked according to the modifications described above with a thermal expansion coefficient compatible with 304 stainless steel up to ~525 K, and mechanically strong. The linear temperature expansion coefficient of 304 stainless steel is 17.3×10^{-6} m/mK between 273 and 588 K. The coefficient of quartz over the same temperature range is $(0.55 \text{ to } 1.4)\times10^{-6}$ m/mK. The evaporator at Iowa State University employs a Pyrex tube (no welded metal component). The coefficient of Pyrex over the same temperature range is 4.0×10^{-6} m/mK.

3. Operation

3.1. Evacuation

The evaporator chamber, housing the S source on the linear motion arm was generally isolated from the STM or preparation chambers, so it was pumped independently from those chambers. During the July 2010 and the first March 2012 experiments, the exchange chamber evacuated the evaporator. However, as the exchange chamber is directly mounted on the vacuum system (attached to the preparation chamber), pumping on this chamber induced vibrations visible in STM. In addition, the base pressure of the exchange chamber was 10^{-8} Torr (10^{-6} Pa), though it was frequently in the 10^{-6} Torr (10^{-4} Pa) range. After the first S deposition attempt March 2012 we switched the evacuation from the exchange chamber to a portable miniature (mini) chamber. The mini chamber's base pressure was frequently 10^{-8} Torr (10^{-6} Pa). Thus, the mini chamber more effectively evacuated the evaporator chamber and minimized vibration.

The evaporator was always outgassed and warmed up isolated from the STM or preparation chambers to minimize contamination. The gate valve isolating the evaporator was open long enough for the evaporator to be positioned, then the sample to be positioned, and finally for the evaporator to be retracted. The deposition times given in Tables II and III refer to the time the sample was directly in front of the evaporator. Therefore, the total time the gate valve was open between the chambers was several seconds to a minute longer than the deposition time. Once the evaporator was retracted, the gate valve was closed and the evaporator turned down.

3.2. Control

The S source requires two power supplies to function, one to control the filament current, and the other to control the cell voltage. The power supply used to provide filament current during sample anneal was also used to supply filament current to the evaporator and is pictured in Fig. 9b. The power supply pictured in Fig. 9c controlled the cell voltage. Both power supplies must support the demands of the evaporator, particularly control over low voltage. These power supplies were controlled manually.

3.3. Low-temperature deposition

To replicate experiments conducted by Shen at Iowa State, we wanted to deposit S below room temperature in the LT-STM at RIKEN. Unlike the VT-STM, the sample cannot be easily held at specific temperatures (above the imaging temperature) in the LT-STM. However, the sample will warm up to room temperature in a predictable way upon removal from the STM stage at 4.7 K. Therefore, the sulfur source was mounted on the LT-STM chamber. The chamber is shown in Fig. 5 in Chapter I.

The experiments conducted July 2010 aimed to deposit S below a sample temperature of 100 K, so the evaporator was mounted on the STM chamber. The results are described in Appendix 3 of Chapter III. These experiments did not result in appreciable S deposition. (The AES on STM-1 does not work, so surface composition cannot be verified and STM provides the only surface specie information.) Mass spectra recorded at the time indicated that evaporator generated a 62 m/z peak, but I do not have copies of these spectra. Qualitatively,

the spectra appeared similar to that in Fig. 8. The relative position of the evaporator to the MS is different in the STM chamber than in the preparation chamber, described above; they are further apart in the STM chamber by 10s of centimeters and the evaporator could not directly point at the MS.

Sulfur deposition was attempted six times during July 2010, but the sample was not cleaned between each deposition. Fig. 10 summarizes when the experiments took place and the sample conditions. Deposition lasted for 35 s or less so the sample temperature remained below 100 K. To deposit S, one person manipulated the cryostats and sample (usually Dr. Kim), while another person positioned the evaporator (SMR). Filament power of 3 ± 1 W resulted in evaporator temperature of 477 ± 10 K. (Due to the location of the thermocouple, the internal cell temperature may differ from the reported value.) The voltage applied to the electrochemical cell was 290 ± 90 mV on average, resulting in a current of 23 ± 5 mA. The parameters for each deposition are given in Table II.

Pressure in the exchange chamber evacuating the evaporator reached the mid 10^{-8} Torr (10^{-6} Pa) range. The STM base pressure ranged from the mid 10^{-11} Torr (10^{-9} Pa) to low 10^{-10} Torr (10^{-8} Pa) range, but because the depositions were quick and required two people, I did not record the STM pressure during deposition.

The photographs in Fig. 5 were taken February 2012, after the evaporator had been used last in July 2010. Fig. 5d shows that with use, Ag dendrites formed between the Ag plate and AgI pellet. In addition, something appeared to form at the interface between the AgI and Ag_2S pellets. Compare Fig. 5d and Fig. 6c, which was taken before the cell was used, July 2012. All of the interfaces between the cell components appear smooth. In our experience with the S evaporator at Iowa State University, the Ag dendrites and irregular (not smooth) interfaces lead to poor cell function. However, the cause is not clear.

3.4. Room temperature deposition

In June and July 2012, I rebuilt the S source as described in Section 2.3 and mounted it on the preparation chamber. The evaporator worked very well during these experiments. The results are described in Chapter III.

Sulfur was deposited in five individual experiments at 300 K resulting in either a low coverage (estimated to be ~0.01 ML in Chapter III, Section 4.2) or a high coverage, in which the bare Ag(111) substrate was not visible. Fig. 11 summarizes when the experiments took place and the sample conditions. The deposition time ranged 47 to 60 s in the low coverage experiments and 54 to 281 s. Filament power of 3.7 ± 0.5 W resulted in evaporator temperature of 473 ± 19 K. (Due to the location of the thermocouple, the internal cell temperature may differ from the reported value.) In the low coverage experiments, the cell voltage ranged from 238 to 268 mV. The parameters for each deposition are given in Table III. During deposition the sample was held in the XYZ manipulator, so deposition could be performed by one person, who positioned the evaporator. Fig. 7 shows the placement of the evaporator relative to the sample.

Pressure in the exchange or mini chamber evacuating the evaporator reached the mid 10^{-7} Torr (10^{-5} Pa) range. The pressure in the preparation chamber during deposition increased slightly, but remained the base pressure range. The preparation base pressure was usually 10^{-9} Torr (10^{-7} Pa). Comparing the July 2010 and March 2012 experiments, the pressure in the evaporator - exchange/mini chamber just before or during S deposition was about 1 order of magnitude higher in the successful March 2012 experiments.

The S evaporator chamber was left mounted to the preparation chamber of STM-1 upon my departure March 21, 2012. The evaporator has likely been dismounted from the preparation chamber and the linear motion arm. Supplies that I left behind are stored in a labeled drawer on the spot welding cart. The electrochemical cell assembly, included the stainless steel bolt plunger, may also be located in this drawer or in cabinet next to the work bench. The welding cart and work bench are located in the STM-1 and STM-2 room, on the first floor of the Nanoscience Joint Laboratory building in the South Area of the Wako campus.

Acknowledgements

This work was supported by NSF Grant CHE-1111500; a Grant-in-Aid for Scientific Research on Priority Areas “Electron Transport Through a Linked Molecule in Nano-scale”; and a Grant-in-Aid for Scientific Research(S) “Single Molecule Spectroscopy using Probe

Microscope" from the Ministry of Education, Culture, Sports, Science, and Technology (MEXT) of Japan.

Figures

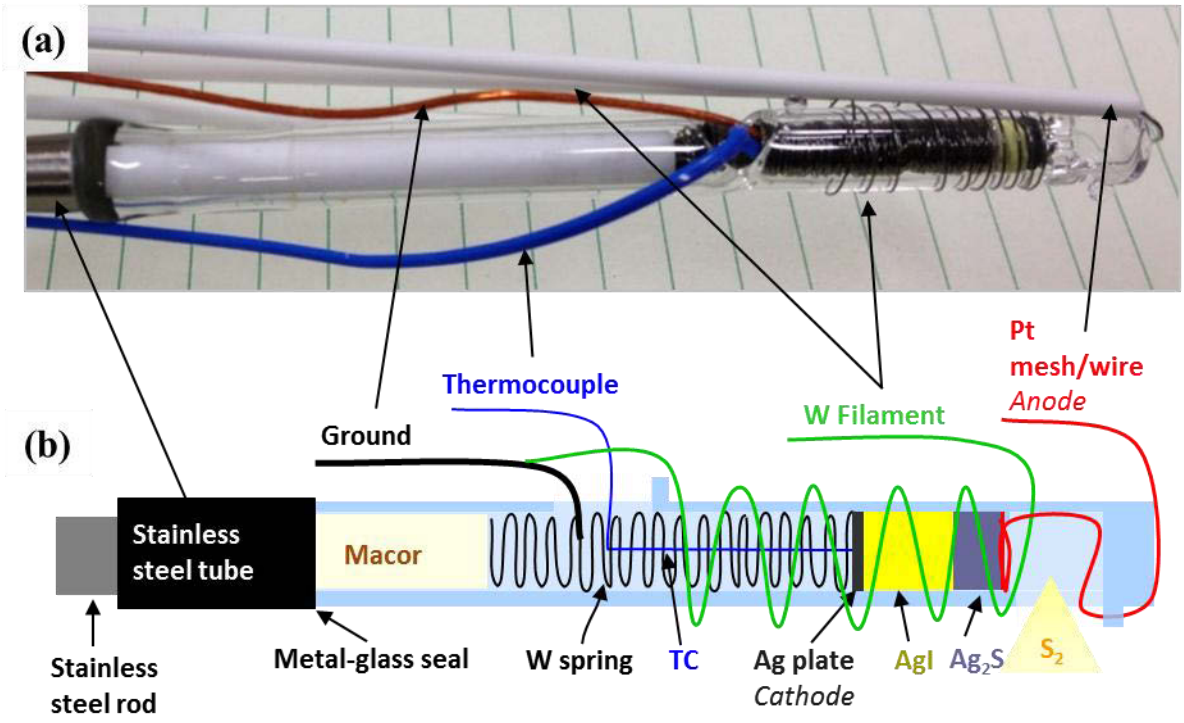

Figure 1. Electrochemical cell (a) and schematic, not to scale (b).

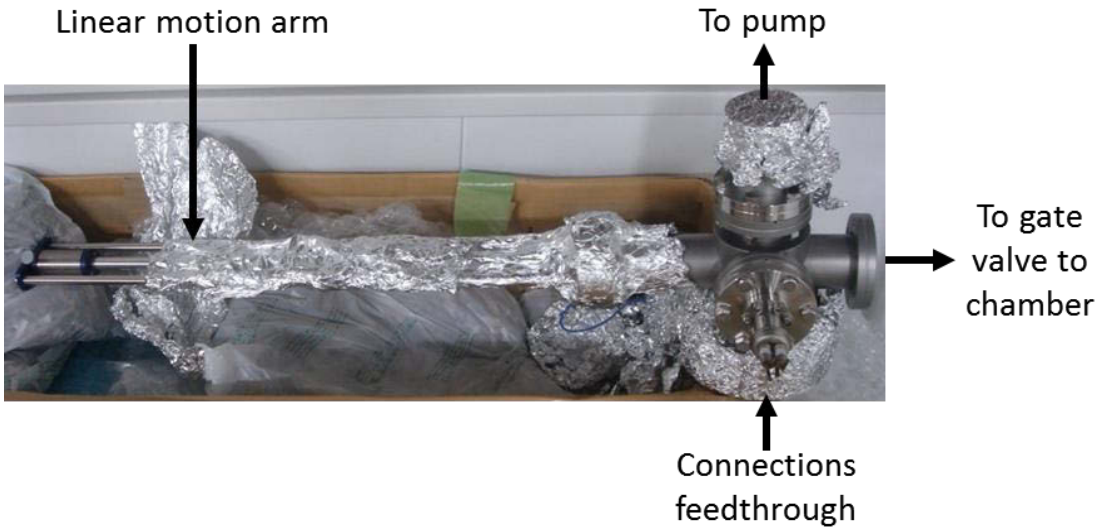

Figure 2. Existing evaporator chamber.

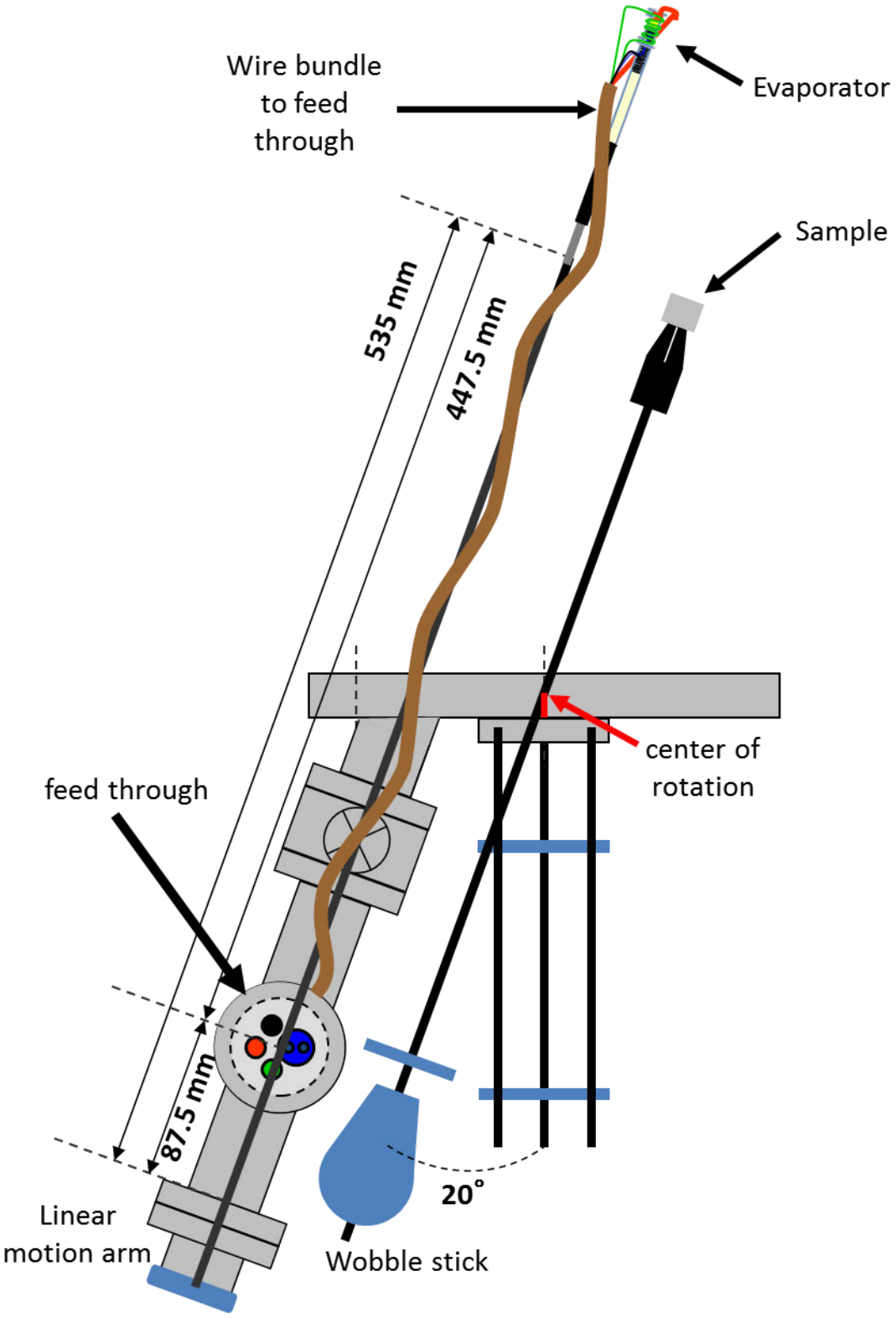

Figure 3. Mounting of the evaporator, to scale. This schematic depicts the set up for low temperature deposition experiments conducted calendar year 2010.

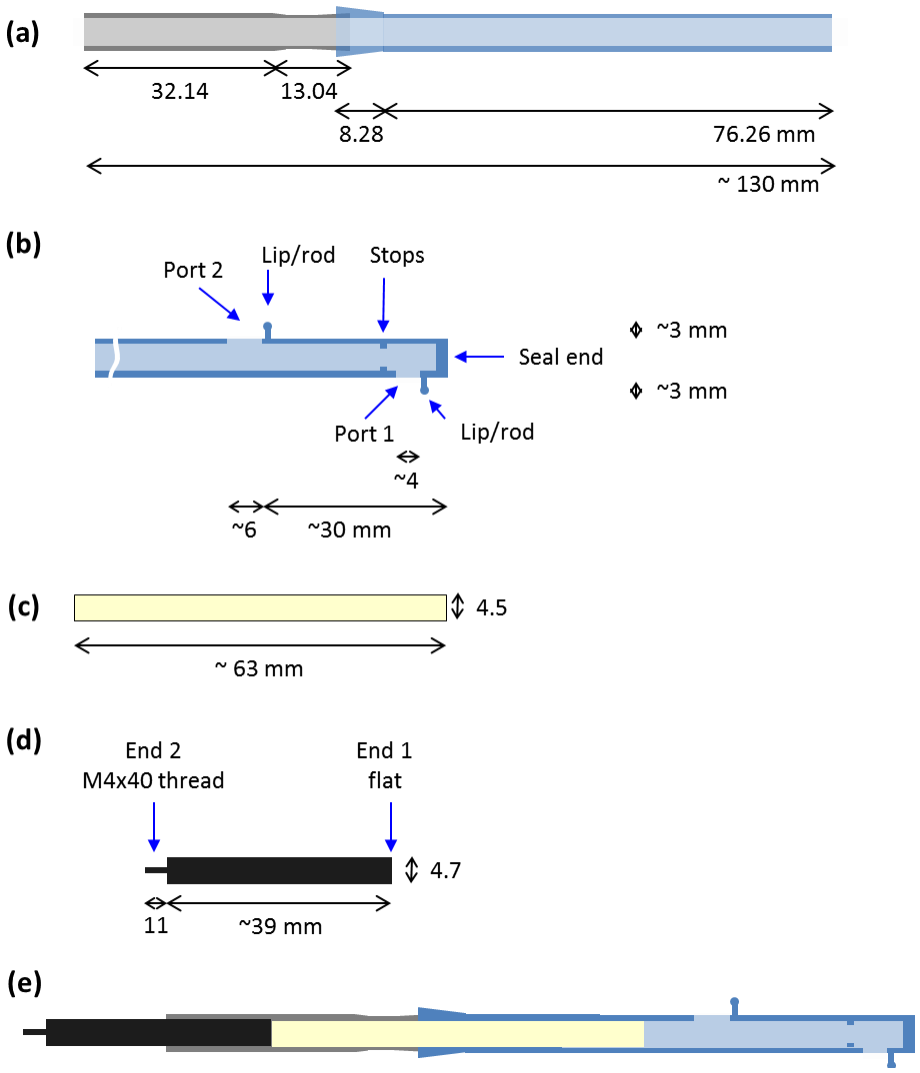

Figure 4. Evaporator housing, to scale. (a) Stainless steel-quartz glass tube as purchased from Kurt J. Lesker. Dimensions: metal O.D. 6.35 mm, 6.55 mm at joint, I.D. 5.36 mm; glass O.D. 7.02 mm, 8.85 mm at joint, I.D. 4.91 mm. Tube is slightly narrower in area joining the metal and glass. (b) Modified glass end of the metal-glass tube. Sealed the open end. Opened two ports into the tube approximately 4 and 6 mm in diameter (better to err on the small side). The second, larger port is approximately 30 mm from the sealed end. Two glass lips or rods approximately 3 mm tall were added near one edge of both ports (the edge closest to the sealed end, to hold the filament wire in position). Glass stops were added within the tube (to hold the chemical discs in position, away from port 1). Diameters of alumina (c) and stainless steel (d) rods must fit within this tube. (c) Alumina/ceramic rod must slide past the metal-glass joint and end before port 2 in (b). Material must be non-conducting, not brittle or soft, and UHV compatible. Dimensions: 63 mm long, 4.5 mm diameter. Both ends smooth and flat. (d) Stainless steel rod. Material must be low carbon steel, such as 304. Dimensions: 63 mm long, 4.5 mm diameter. End 1: smooth and flat. End 2: screw, M4x40, 11 mm long, but threads only 10 mm long. (e) Assembled: (c) and (d) slide into (a).

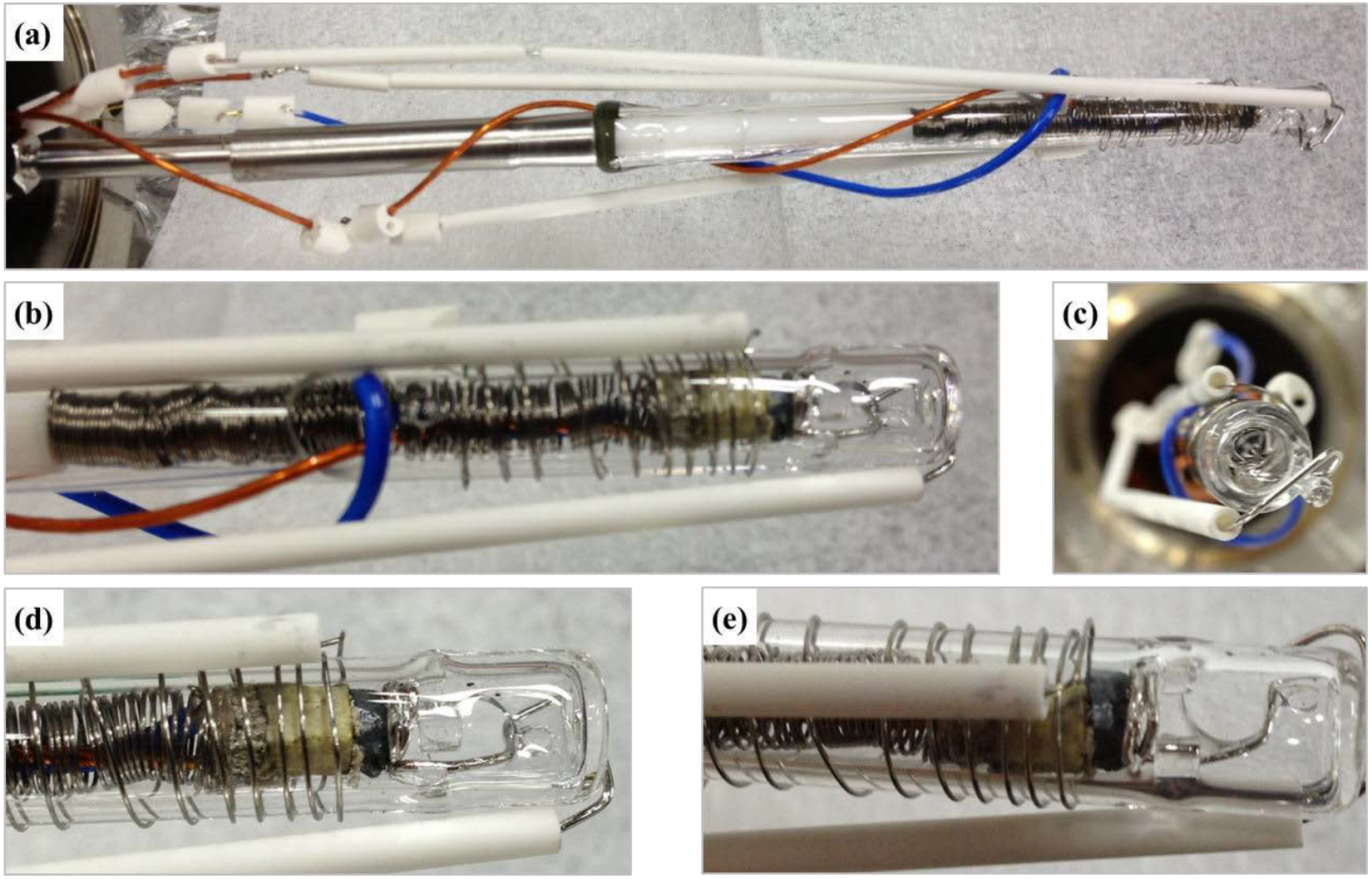

Figure 5. Photos of the mounted S evaporator taken March 2012, *after* use during July 2010.

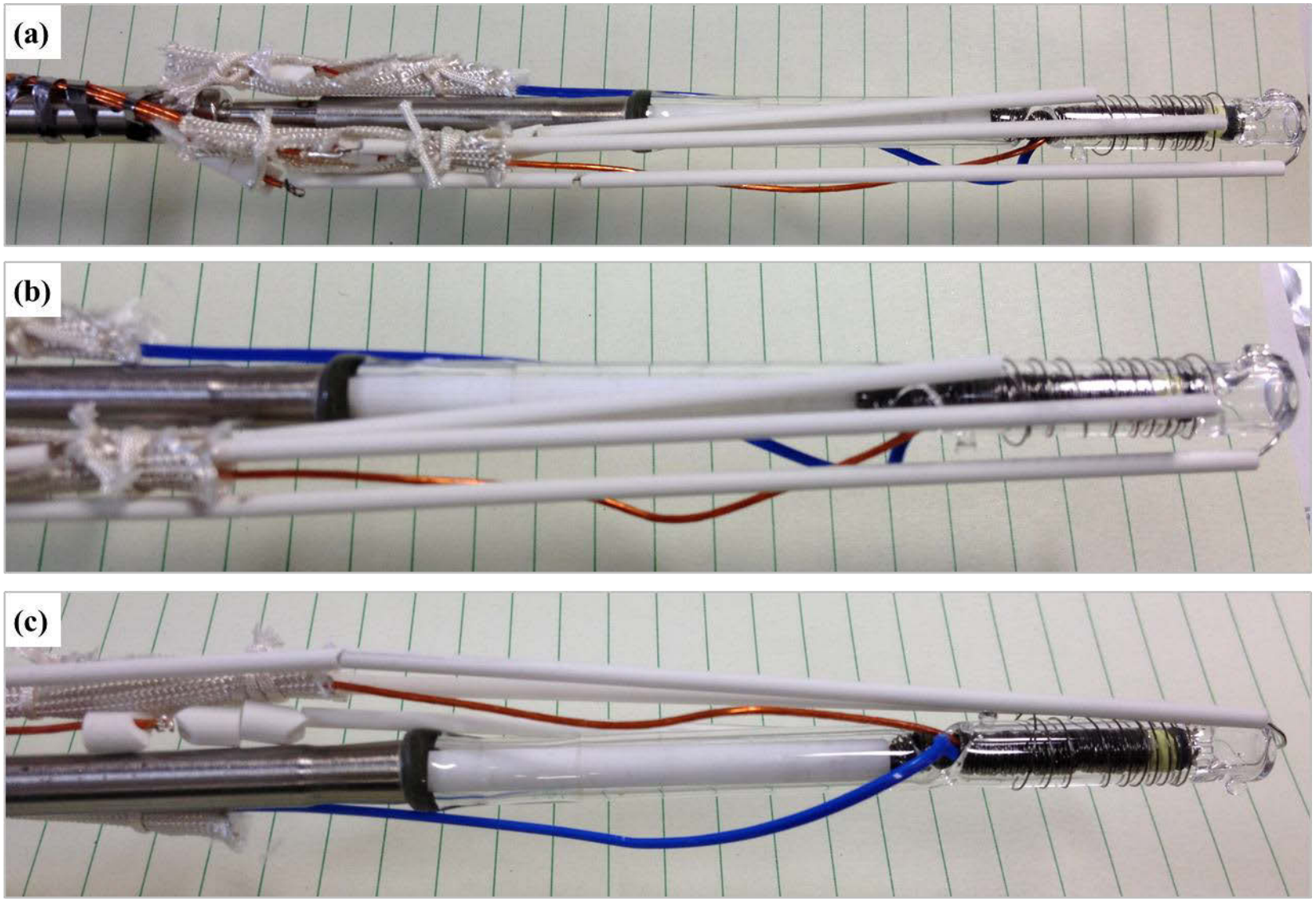

Figure 6. Photos of the mounted S evaporator taken July 2010, before mounting on the chamber and before use.

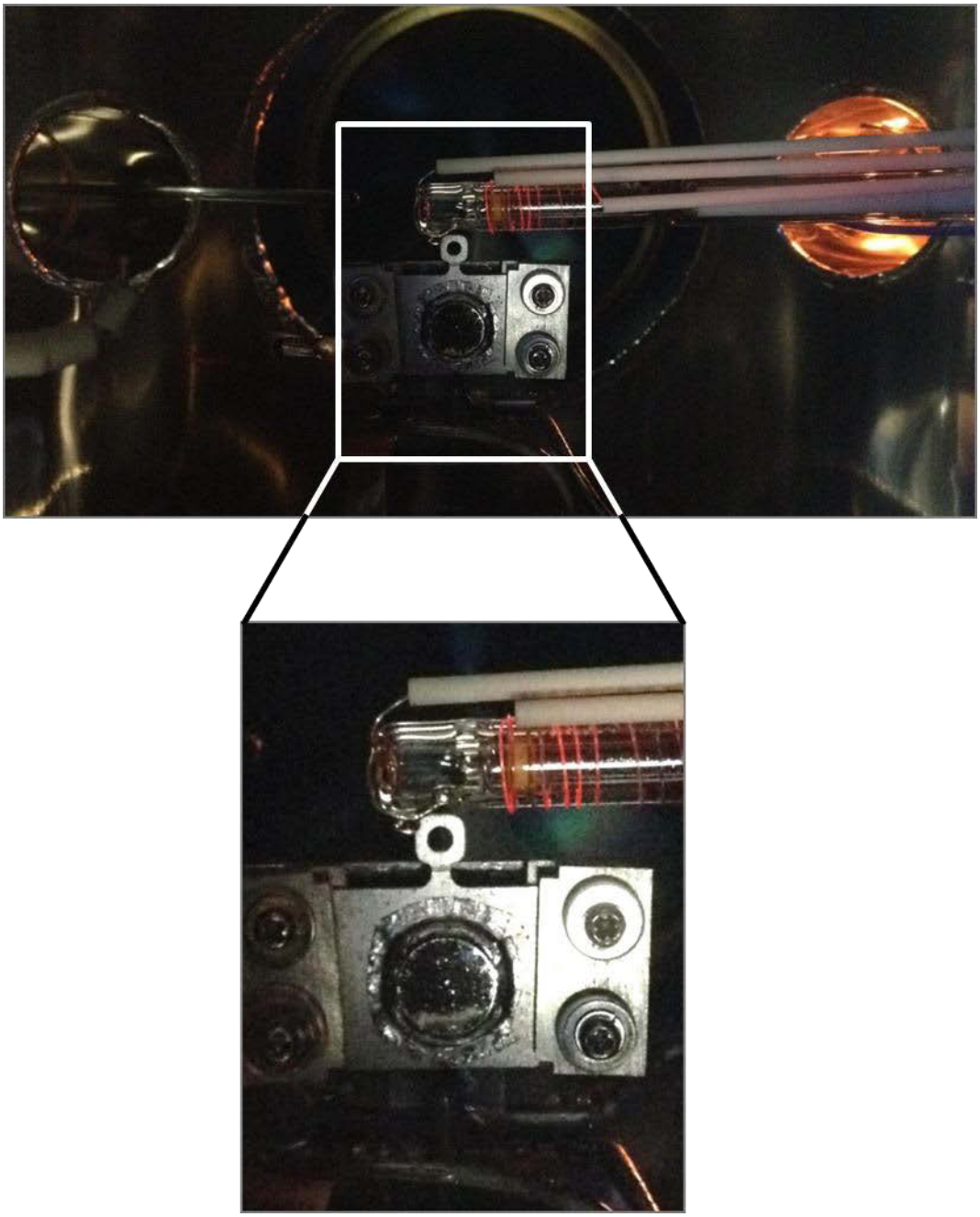

Figure 7. Room temperature deposition occurred in the preparation chamber attached to the STM chamber. The same evaporator mounting on the linear motion arm,**Figure** as in Fig. 3, was attached on the preparation chamber for these experiments conducted calendar year 2012. During S deposition, the source was brought very close to the sample via the linear motion arm.

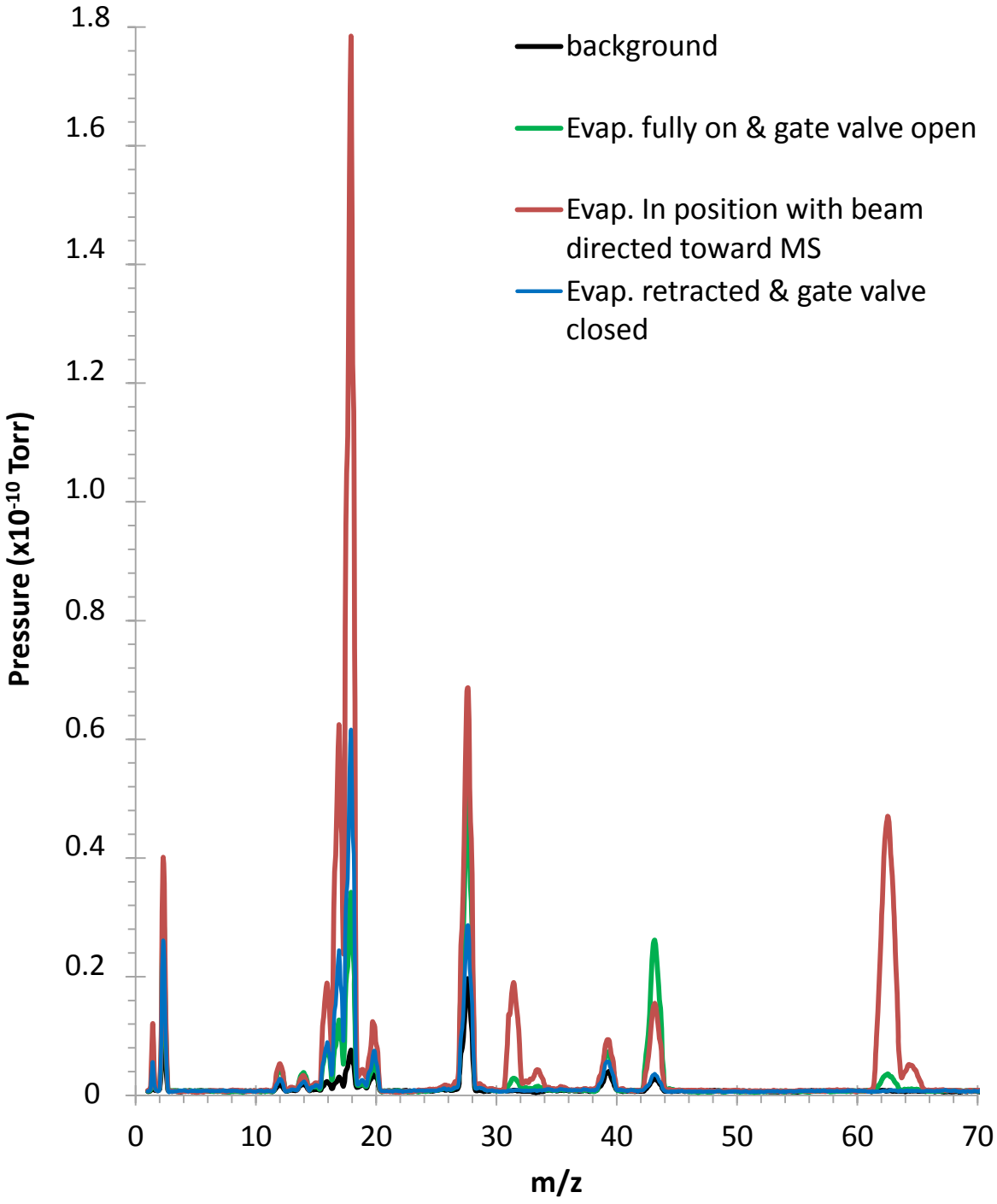

Figure 8. Mass spectra recorded in the preparation chamber. Mass 62 increases, indicating that S_2 is emitted from the evaporator. Background gasses also increase, due to the poorer vacuum in the exchange or mini chambers evacuating the evaporator assembly and atmospheric gases and water trapped in the evaporator. Spectra were recorded on 3/2/2012, cycles 4, 6, 13, and 32 or 32 shown.

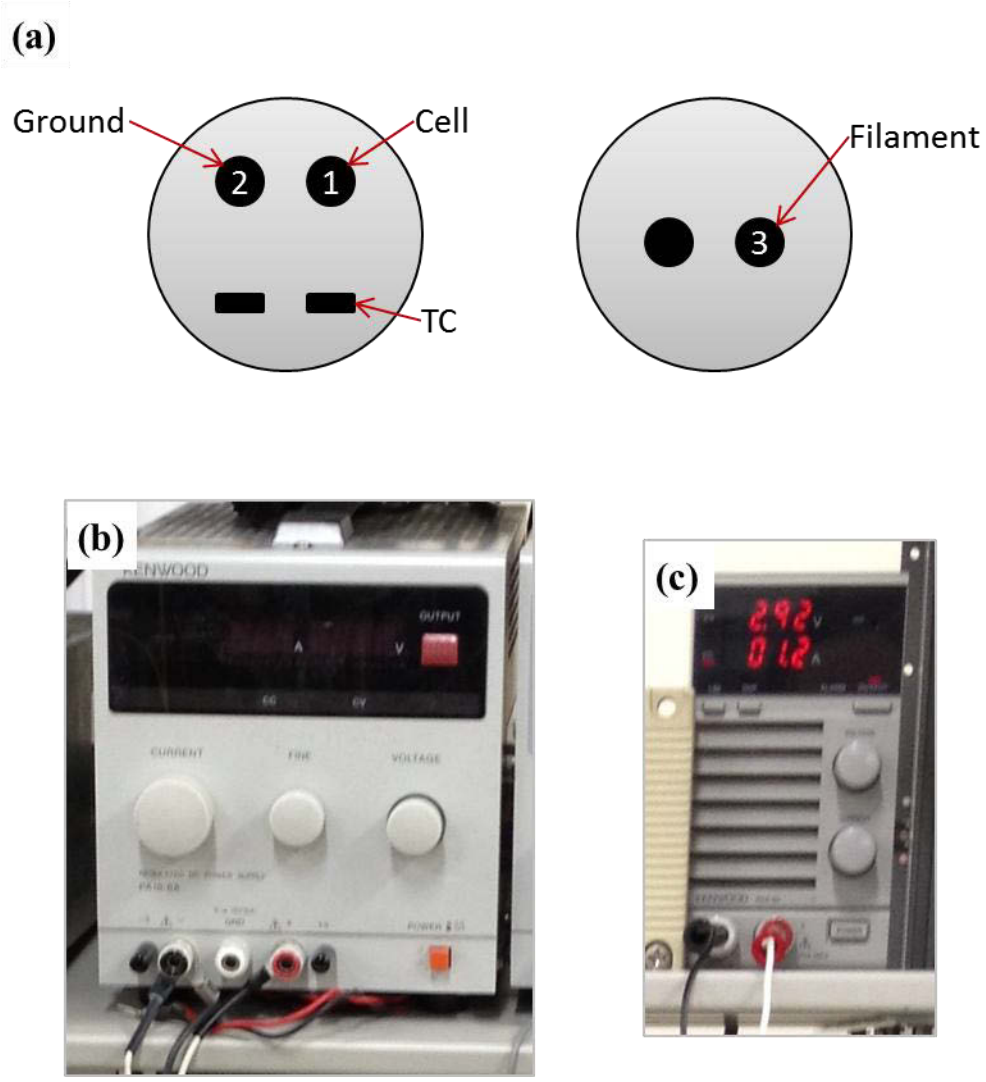

Figure 9. Evaporator connections and power: feedthrough configuration (a) and power supplies to control the filament current (b) and cell voltage (c) during the July 2012 experiments.

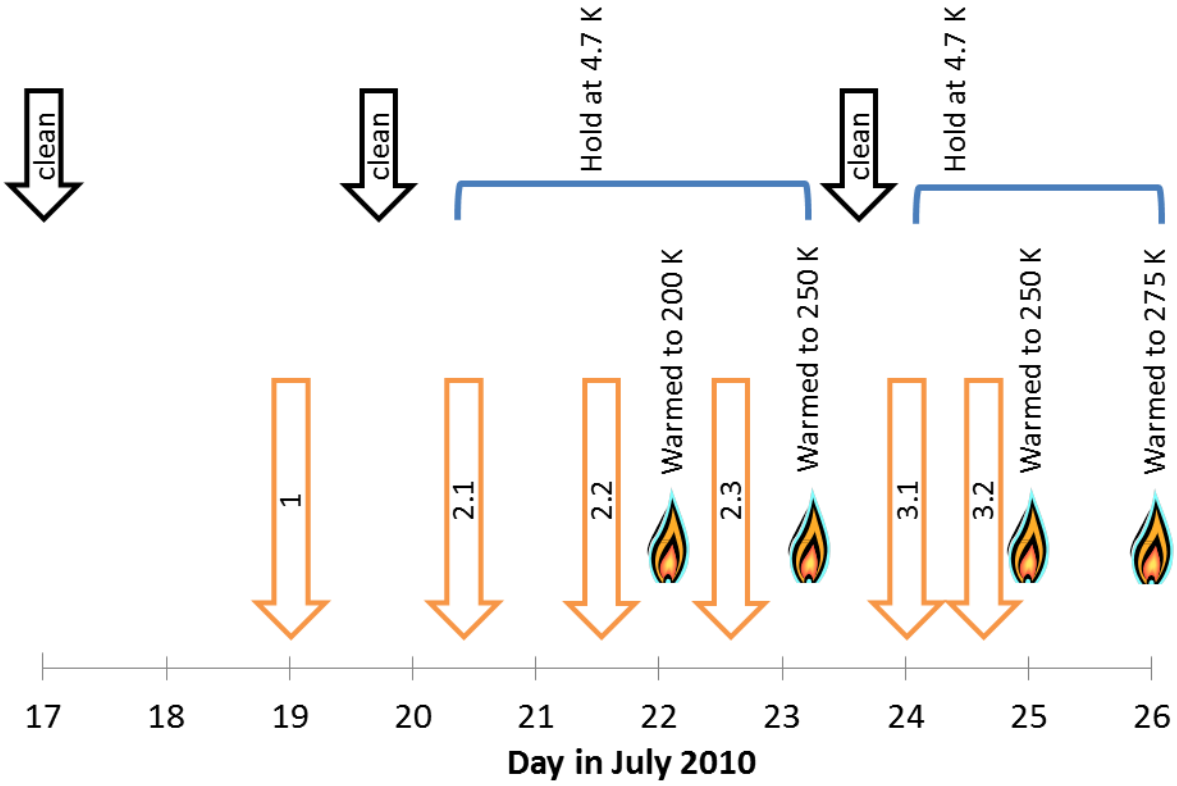

Figure 10. Experiment summary of the calendar year 2010 experiments. Sulfur deposition is marked by the orange, down arrows in the lower level.

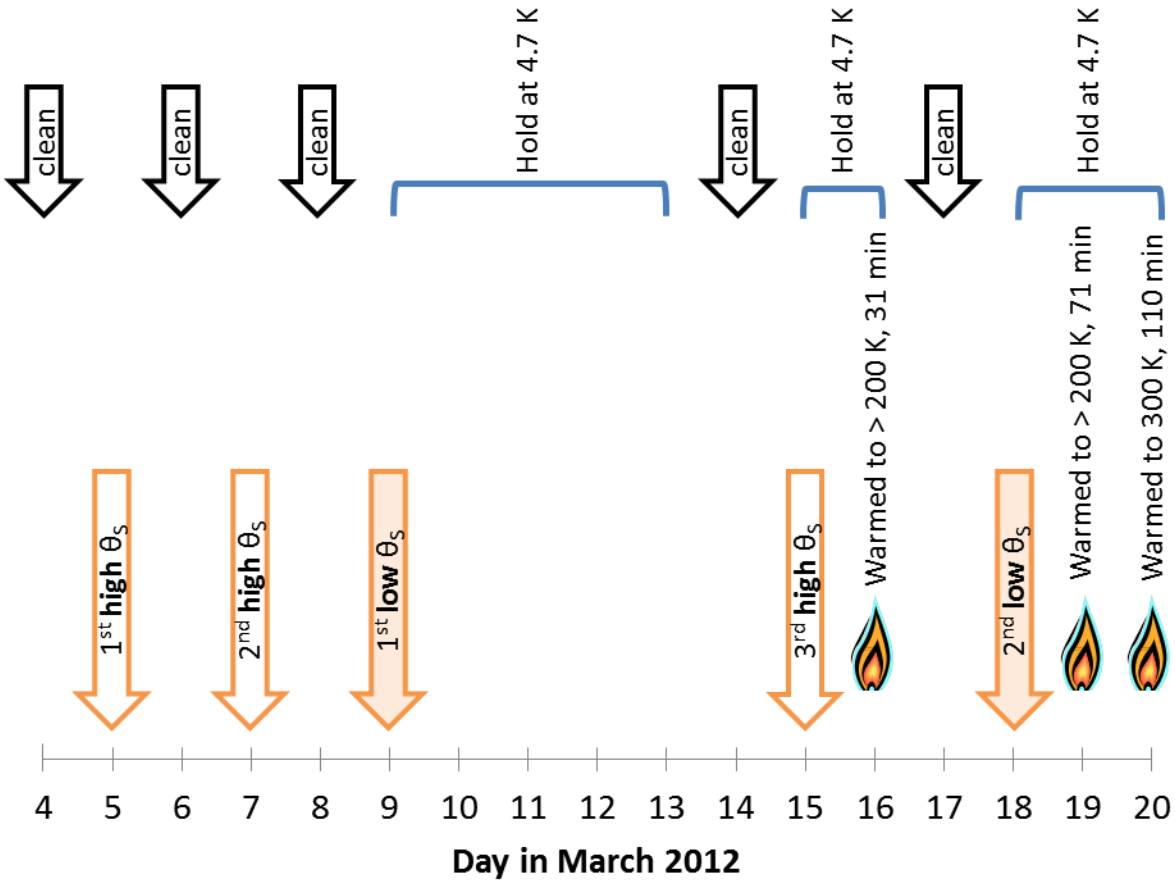

Figure 11. Experiment summary of the calendar year 2012 experiments. Sulfur deposition is marked by the orange, down arrows in the lower level.

Tables

Table I. Sulfur evaporator connections February 29, 2012. See notebook 5, page 48 for details.

		Resistance
Vacuum side	Anode - ground	0.680↑ MΩ
	Filament - ground	0.8 Ω
Vacuum to Air side	Anode - pin 1	0.2 Ω
	Filament - pin 3	0.5 Ω
	Ground - pin 2	0.8 Ω
Air side after mounting and pumping down to low 10^{-6} Torr	Anode - ground	~1↑ MΩ
	Filament - ground	0.8 Ω
	TC - TC	16.3 Ω
	All - Chamber	∞

Table II. S deposition attempts below 100 K, calendar year 2010.

Date	Expt.	Filament		Cell		Deposition time	Temperature (K)		Exchange chamber pressure (Pa)	STM notes
		(A)	(V)	(mV)	(mA)	(s)	Evap.	Sample		
7/19/10	1	1.3	1.4	230	20	30	492	82	5.87×10^{-6}	poor resolution
7/20/10	2.1	1.4	1.7	230	20	28	475	42	8.00×10^{-6}	amorphous adsorbate groupings
7/21/10	2.2	1.3	1.4	230	20	34	461	49	5.33×10^{-6}	amorphous adsorbate groupings, step decoration
7/22/10	2.4	1.2	3	250	30	10	479	63	3.07×10^{-6}	high coverage, amorphous adsorbate groupings, step decoration; Ordered rectangular islands upon warming
7/24/10	3.1	1.4	1.8	330	20	30	475	67	2.27×10^{-6}	very little material on surface
7/25/10	3.2	1.4	3.2	450	30	30	481	45	3.73×10^{-6}	amorphous adsorbate groupings, step decoration; Step modification with vaguely dot like protrusions upon warming

Table III. Sulfur deposition attempts at 300 K, calendar year 2012.

Date	Expt.	Filament		Cell		Deposition time	Temperature (K)		Exchange or mini chamber pressure (Pa)	Preparation chamber pressure (Pa)	STM notes
		(A)	(V)	(mV)	(mA)	(s)	Evap.	Sample			
3/5/12	1^{st} high θ_S	1.3	3	210-58	10	281	477	300	2.15×10^{-5}	8.73×10^{-7}	Failed (cell potential dropped, poor connection in vacuum)
3/7/12	2^{nd} high θ_S	1.1	2.9	250	~80	240	451	300	3.99×10^{-6}	1.17×10^{-6}	High coverage with linear features
3/9/12	1^{st} low θ_S	1.4	3.3	268-239		60	467	300	3.11×10^{-5}	5.51×10^{-7}	Step decoration & chain clusters
3/15/12	3^{rd} high θ_S	1.4	2.4	270		54	503	300	7.95×10^{-5}	2.91×10^{-6}	High coverage, poor resolution. No improvement upon warming.
3/18/12	2^{nd} low θ_S	1.3	2.9	238		47	469	300	1.40×10^{-4}	–	Step decoration & chain clusters. Stable upon warming to ~200 and 300 K.

References

(1) Campbell, C. T.; Koel, B. E. *Surface Science* **1987**, *183*, 100.

(2) Leung, K. T.; Zhang, X. S.; Shirley, D. A. *Journal of Physical Chemistry* **1989**, *93*, 6164.

(3) Alfonso, D. R. *Surface Science* **2008**, *602*, 2758.

(4) Yu, Y.; Dixon-Warren, S. J.; Astle, N. *Chemical Physics Letters* **1999**, *312*, 455.

(5) Qin, C.; Whitten, J. L. *Surface Science* **2005**, *588*, 83.

(6) Rovida, G.; Pratesi, F. *Surface Science* **1981**, *104*, 609.

(7) Electrochemical cells have been used to generate S, Se, Te, Cl, and Br. See the following references for some examples.

(8) Keller, H.; Rickert, H.; Detry, D.; Drowart, J.; Goldfinger, P. *Zeitschrift für Physikalische Chemie* **1971**, *75*, 273.

(9) Reinhold, H. *Zeitschrift für Elektrochemie und Angewandte Physikalische Chemie* **1934**, *40*, 361.

(10) Wagner, C. *Journal of Chemical Physics* **1953**, *21*, 1819.

(11) Detry, D.; Drowart, J.; Goldfing.P; Keller, H.; Rickert, H. *Berichte der Bunsengesellschaft für Physikalische Chemie* **1968**, *72*, 1054.

(12) Detry, D.; Drowart, J.; Goldfinger, P.; Keller, H.; Rickert, H. *Zeitschrift für Physikalische Chemie* **1967**, *55*, 314.

(13) Heegemann, W.; Meister, K. H.; Bechtold, E.; Hayek, K. *Surface Science* **1975**, *49*, 161.

(14) Schwaha, K.; Spencer, N. D.; Lambert, R. M. *Surface Science* **1979**, *81*, 273.

(15) Spencer, N. D.; Goddard, P. J.; Davies, P. W.; Kitson, M.; Lambert, R. M. *Journal of Vacuum Science & Technology A: Vacuum, Surfaces, and Films* **1983**, *1*, 1554.

(16) Jones, J., University of New Hampshire, 2003.

(17) Ratchford, R. J.; Rickert, H. *Zeitschrift für Elektrochemie, Berichte der Bunsengesellschaft für physikalische Chemie* **1962**, *66*, 497.

(18) Shen, M., Iowa State University, 2009.

(19) See notebook 4, pages 80 and106 for design notes and photographs regarding the Maria.

APPENDIX IV.

Experimental Database

Abbreviations

Expt.	Experiment	v.	very
Nb-Pg	Notebook number - Page number	STS	Scanning Tunneling Spectroscopy
RT	Room Temperature	IETS	Inelastic Electron Tunneling Spectroscopy
Isl.	Island		
Evap.	Evaporator (usually the S source)	AS	Action Spectroscopy
		√17	(√17×√17)R14° reconstruction

Table I. Silver samples

Surface	Sample	Description	Form / Geometry	Current condition	Dates
Ag(111)	1	MaTecK GmbH (new)	tiered disk (top hat)	unknown	Sept. 2009
	2	MaTecK GmbH (new)		unknown	July 2010
	3	MaTecK GmbH (not new)		low-medium	Feb. to Mar. 2012
Ag(100)	1	Ames Lab Materials Preparation Center	rectangle	re-polished	May 2008 to Oct. 2008
	1*	re-polished in group		very poor	Nov. 2008 to Apr. 2009
	2	Ames Lab Materials Preparation Center		very poor	Apr. 2009 to Oct. 2010
	3	Surface Preparation Laboratory #210027, 9x3x1.5 mm^3 (1st commercial)		good	May 2012 to present
Ag(110)	1	Surface Preparation Laboratory #210027, 9x3x1.5 mm^3 (1st commercial)	rectangle	re-polished	Apr. 2010 to Mar. 2011
	1*	re-polished in group		very poor	Mar. 2011 to May 2011
	2	Surface Preparation Laboratory #211060, 9x3x1 mm^3 (2nd commercial)		excellent	June 2011 to present

Table II. Ag(111) experiments with H_2S conducted at The RIKEN Institute.

Expt.	Date	Description, T sample (K)	Nb-Pg	File name	Notes
	9/20/09	clean surface, 4.7 K	5-7	2090920 Ag111	
	9/21/09	clean surface, 4.7 K	5-8	2090921 Ag111	atomic resolution #8-20
1	9/22/09	clean surface, 4.7 K	5-9	2090922 Ag111, m1-10	
		after H_2S exposure, 20 K	5-9	2090922 Ag111, m11-22	step edge decoration #11, contamination #15?
		after warming to RT	5-9	2090922 Ag111, m23-27	noise
2	9/22/09	clean surface, 4.7 K	5-10		
		after H_2S exposure, 30 K	5-10	2090922 H2S Ag111_2	Island and protrusions
	9/23/09	after resting over night , 4.7 K	5-10	2090923 H2S Ag111, m1-39	Islands remain, step decoration
		after warming to 197 K	5-11	2090923 H2S Ag111, m40-57	Dirty, but no islands or signs of H_2S
3	9/23/09	after H_2S exposure, > RT	5-11	2090923 H2S Ag111, m58-	
4	9/28/09	after H_2S exposure, RT	5-13	2090928 H2S Ag111, m1-16	step edge decoration
		after H_2S exposure, RT	5-14	2090928 H2S Ag111, m17-24	high coverage
		after warming to 140 K	5-14	2090928 H2S Ag111, m25-33	disordered adsorbates
		after warming to 197 K	5-14	2090928 H2S Ag111, m34-36	disordered adsorbates
5	9/28/09	after H_2S exposure, RT	5-14	2090928 H2S Ag111_2, m1-17	Step regions with adsorbate; "bar" structure #10-15
		after warming to 250 K	5-15	2090928 H2S Ag111_2, m18-	Several structures, #27
6	9/29/09	clean surface, 4.7 K	5-15	2090929 H2S Ag111, m1-3	
		after H_2S exposure, RT & slowly cooled	5-15	2090929 H2S Ag111, m4-40	large domains of ordered structures
		after H_2S exposure, RT	5-15	2090929 H2S Ag111, m41-	hexagonal ordered structure
		after resting over night , 4.7 K	5-16	2090930 H2S Ag111 contd	Structure not visible in all regions
	9/30/09	clean surface, 4.7 K	5-16	2090930 Ag111	
	10/1/09	clean surface, 4.7 K	5-17	2091001 Ag111	atomic resolution #14-25
7	10/1/09	after H_2S exposure, 20 K	5-18	2091001 H2S Ag111	Same molecular clusters, unstable with tip bias
	10/2/09	after resting over night , 4.7 K	5-18	2091002 H2S Ag111	No change overnight. Break up clusters to get individual H_2S
	10/3/09	after resting over night , 4.7 K	5-18	2091003 H2S Ag111	No change over night.STS: IETS difficult, AS at 150 V (#88-109), 200 mV (#48-68), 250 mV (#68-88)

Table III. Ag(111) experiments with S conducted at The RIKEN Institute.

Expt.	Date	Description, T sample (K)	Nb-Pg	File name	Notes
	7/7/10	clean surface, 4.7 K	5-34	1100707 Ag111	rough and dirty
	7/10/10	clean surface, 4.7 K	5-35	1100710 Ag111	
	7/18/10	clean surface, 4.7 K	5-39	1100718 Ag111	
1	7/19/10	after S deposition, 82 K	5-39	1100719 S Ag111	poor resolution
2	7/20/10	clean surface, 4.7 K	5-41	1100720 Ag111	
		after S deposition, 42 K	5-41	1100720 S Ag111	amorphous adsorbate groupings
	7/21/10	after resting over night, 4.7 K & depositing more S, 49 K	5-42	1100721 S Ag111	amorphous adsorbate groupings, step decoration
		after warming to 200 K	5-42	1100721 S Ag111 warmed	islands stable to scanning
	7/22/10	after resting over night, 4.7 K & depositing more S, 63 K	5-43	1100722 S Ag111	high coverage, amorphous adsorbate groupings, step decoration
		after warming to 250 K	5-43	1100722 S Ag111 warmed	ordered rectangular islands
	7/23/10	after resting over night , 4.7 K		1100723 S Ag111 contd	ordered rectangular islands
3	7/24/10	after S deposition, 67 K	5-45		very little material on surface
		after S deposition, 45 K		1100724 S Ag111, m1-m51	amorphous adsorbate groupings, step decoration;
	7/25/10	after resting over night , 4.7 K		1100724 S Ag111, m52-	No apparent changes
		after warming to 250 K		1100725 S Ag111 warmed	No islands; Step modification: protrusions in ~hexagonal arrangement
	7/26/10	after warming to 275 K & after resting over night, 4.7 K	5-45	1100726 S Ag111 rewarmed	Step faceting and large protrusions near step edges
	2/29/12	clean surface, 4.7 K	5-51	1120229 Ag11	rough and dirty
	3/3/12	clean surface, 4.7 K	5-55	1120303 Ag111	tip unstable, check with other sample: tip ok, surface dirty
	3/4/12	clean surface, 4.7 K	5-55	1120304 Ag111	Atomic resolution #5; small terraces
1^{st} high θ_S	3/5/12	after S deposition, RT	5-57	1120305 S Ag111	No S deposited; cell failure

This table continues on the following page.

Table III. S/Ag(111) experiments continued.

Expt.	Date	Description, T sample (K)	Nb-Pg	File name	Notes
2^{nd} high θ_S	3/7/12	after S deposition, RT	5-59	1120307 S Ag111	High coverage with linear features in rotational domains
1^{st} low θ_S	3/9/12	after S deposition, RT	5-61	1120309 S Ag111	Step decoration & very stable chain clusters (topography inverts -5 to -6 V)
	3/10/12	after resting over night , 4.7 K	5-62	1120310 S Ag111 continued	No change overnight; Try STS; atomic resolution #21
	3/11/12	after resting over night , 4.7 K	5-62	1120311 S Ag111 continued	No change overnight; atomic resolution #13
	3/12/12	after resting over night , 4.7 K	5-62	1120312 S Ag111 continued	No change overnight; STS
	3/13/12	after resting over night , 4.7 K	5-64	1120313 S Ag111 continued	No change overnight; STS, at - V central chain protrusion minimized and outer region enhanced
3^{rd} high θ_S	3/15/12	after S deposition, RT	5-67	1120315 S Ag111	High coverage, poor resolution
	3/16/12	after resting over night , 4.7 K	5-67	1120316 S Ag111 continued	No change overnight
	3/16/12	after warming to ~199 K	5-67	1120316 S Ag111 warmed	No change overnight or with warming
2^{nd} low θ_S	3/18/12	after S deposition, RT	5-70	1120318 S Ag111	Step decoration & chain clusters. Stable upon warming to ~200 and 300 K.
	3/19/12	after resting over night, 4.7 K & after warming to ~202 K	5-70	1120319 S Ag111 continued warmed	No change with resting or warming
	3/20/12	after resting over night, 4.7 K & after warming to 300 K	5-70	1120319 S Ag111 continued warmed	No change with resting or warming

Table IV. Ag(100) experiments with S conducted at Iowa State.

Date	Sample	Image	Description, T cooling block (K)	S coverage (ML)	Nb-Pg	Notes
6/23/08	1	1-6	clean surface, RT		1-51	
		7-10	clean surface, 120 K			
		11-16	after S deposition, 120 K	trace		S on terraces near edge & in meandering domains
		17-19	after heating, 160 K			
		22-23	after heating, 240 K			
		24-27	after heating, RT			
7/22/08	1	1-10	clean surface, RT		1-68	large terraces; pinning sites
		11-18	clean surface, 120 K			
		19-31	after S deposition, 120 K	0.37		S bumps
		32-41	after heating, 170 K			random small islands
		42-63	after heating, 230 K			
		64-104	after heating, RT			chewed edges; large islands; p(2x2) + √17
		105-121	after cooling, 230 K			√17 islands more square; less of p(2x2) phase
		122-145	after heating, RT			more of p(2x2) phase
7/30/08	1	1-3	clean surface, RT		1-72	large terraces
		4-10	clean surface, 120 K			
		11-27	after S deposition, 120 K	0.25		random islands
		28-35	after heating, 170 K			chewed edges; random islands; maybe order
		36-50	after heating, 240 K			less chewed edges; maybe island coalescence; rotational domains
		51-91	after heating, RT			less √17, more p(2x2)
		92-107	after cooling, 230 K			
2/12/09	1*	1-61	clean surface, RT		2-4	poor image quality, tip bad
		62-101	after S deposition, RT	0.09		no obvious step-edge fluctuation
2/23/09	1*	1-9	clean surface, RT		2-9	noisy
		10-33	clean surface, 223.4 K			
		34-97	after S deposition, 223.4 K	0.08		dislocations / step-edge move (67-90)

This table continues on the following page.

Table IV. S/Ag(100) experiments continued.

Date	Sample	Image	Description, T cooling block (K)	S coverage (ML)	Nb-Pg	Notes
3/9/09	1*	1-14	clean surface, RT			
		15-42	after cooling, 104.3			
		43-55	after S deposition, 107.9 K	0.23		altered step edges
		56-72	after heating, 160.4 K			
		73-95	after heating, 222.4 K			rough, scalloped, lightly chewed edges
		96-117	after heating, 301.3			something like "roads/chains" or p(2x2) (See LEED images)
3/10/09	1*	1-	after resting overnight at RT & annealing: 0.55 A, 1 hr, ~500 K			no √17, smooth step edges(See LEED images)
11/15/09	2	1-14	clean surface, RT		2-124	
		15-35	clean surface, 116 K			
		36-41	after S deposition, 115 K	0.47		tons of material, tip unstable, lots of reconstruction?
		44-42	after heating, 166.9 K			can't see anything!
		45-47	after heating, 296.2 K			new tip. Large irregular shaped islands, √17. cannot clearly see p(2x2)
		48-	after annealing: 1.20A, 30min, ~667K			root17 in-terrace everywhere! No islands. Step edge faceted.
11/19/09	2	1-34	clean surface, RT		2-127	
		35-67	clean surface, 117.0 K			
		68-71	after S deposition, 116.5 K	0.56		lots of material, affects tip.
		72-80	after heating, 161.0 K			blobs of S, poor resolution, #77 best
		81-92	after heating, 222.3 K			blobs, #84 best
		93-95	after heating, 247.3			
		96-103	after heating, RT			hints of surface structure, horrible resolution
		104-	after annealing: 0.70 A, 15min, ~533 K			cannot see anything
9/29/10	2	1-11	clean surface, RT		3-60	No improvement
		12-21	clean surface, 107.84 K			
		22-	after S deposition, 106.0 K	xx		

Table V. Ag(100) experiments with submonolayer coverage of Ag or Au conducted at Iowa State.

Date	Sample	Image	Description, T cooling block (K)	Nb-Pg	Note
8/5/08	1	1-7	clean surface, RT	1-75	pinning sites
		8-21	after Ag deposition: 660 nA, 25 s, RT		tiny square islands; square pits
8/18/08	1	1-5	clean surface, RT	1-80	
		6-60	after Ag deposition:660 nA, 60 s, RT		multi layers of Ag
9/16/08	1	1-16	clean surface, RT	1-90	
		17-55	after Ag deposition: 670 nA, 30 S, RT		distortion: not 90° corners
9/18/08	1	1-20	clean surface, RT	1-91	
		21-105	after Ag deposition: 490 nA, 33 s, RT		distortion
10/15/08	1	1-23	clean surface, RT	1-103	
		24-33	after Ag deposition: 400 nA, 100 s, RT		no distortion: resolved issue at STM stage base
11/20/08	1*	1-4	clean surface, RT	1-120	
		5-8	after Ag deposition: 2.0 μA, 8 min, RT		hexagonal islands
		9-13	after annealing: 1.20 A, 30 min		
2/26/09	1*	1-12	clean surface, RT	2-11	
		13-20	clean surface, 219 K		
		21-44	after Ag deposition: 485 nA, 16 s, 218.5 K		wormy islands, high coverage
		45-56	after heating, RT		square island, mostly large
2/27/09	1*	1-18	clean surface, RT	2-12	
		19-29	after Ag deposition: 300 nA, 60 s, RT		coverage too high?
6/12/12	3	1-10	clean surface, RT	4-130	larger terraces, still bunchy
		11-12	clean surface, 195 K		
		13-46	after Au deposition: 96-999 nA, 5s, 195 K		Small islands, poor resolution, appear roundish / elongated
		47-64	after heating, 221 K		Islands ~ same shape and size. Maybe slight density decrease. Poor resolution
		65-75	after heating, 245 K		Islands more elongated (tip effect? see 70-71)

Table VI. Ag(100) experiments with submonolayer coverage of Ag and **S** conducted at Iowa State.

Date	Sample	Image	Description, T cooling block (K)	S coverage (ML)	Ag deposition		Nb-Pg	Note
					Flux (mML/s)	Coverage (ML)		
9/30/08	1	1-14	clean surface, RT				1-96	
		15-26	after Ag deposition: 460 nA, 35 s, RT					distortion
		27-44	after S deposition, RT	0.23				Ag island density decreased, irregular shape
12/1/08	1*	1-38	clean surface, RT				1-124	
		39-73	after Ag deposition: 460 nA, 40 s, RT		13	~0.53		
		74-123	after S deposition, RT	0.009				
12/5/08	1*	1-36	clean surface, RT				1-128	
		37-155	after Ag deposition: 490 nA, 20 s, RT		18	0.35		SR, observed 3+ hr
		156-	after S deposition, RT	0.036				OR, observed 5 hr
12/10/08	1*	1-20	clean surface, RT				1-132	
		21-45	after S deposition, RT	0.046				streaky images
		46-108	after Ag deposition: 495 nA, 20 s, RT		16	0.31		lower island density, approximately halved after 2 hr, OR
12/15/08	1*	1-22	clean surface, RT				1-135	
		23-44.5	after Ag deposition: 485 nA, 20 s, RT		15	0.30		
		44.5-49	during S deposition, RT					
		50-111	after S deposition, RT	0.040				
12/22/08	1*	1-22	clean surface, RT				1-138	
		23-37	after Ag deposition: 505 nA, 18 s, RT		17	0.30		
		40-95	after S deposition, RT	0.034				
12/30/08	1*	1-22	clean surface, RT				1-140	
		23-44	after Ag deposition: 490 nA, 18 s, RT		7	0.12		
		45-100	after S deposition, RT	0.12				part of islands changed orientation R45°. All images 200x200nm^2

This table continues on the following page.

Table VII. S/Ag/Ag(100) experiments continued.

Date	Sample	Image	Description, T cooling block (K)	S coverage (ML)	Ag deposition		Nb-Pg	Note
					Flux (mML/s)	Coverage (ML)		
1/6/09	1*	1-16	clean surface, RT				1-143	
		17-45	after Ag deposition: 495 nA, 18 s, RT		17	0.30		
		46-105	after S deposition, RT	0.21				islands maybe rotated 45°
1/13/09	1*	1-20	clean surface, RT				1-145	
		21-31	after Ag deposition: 500 nA, 18 s, RT		17	0.30		
		32-116	after S deposition, RT	0.27				√17 (prefers step & isl edges) & p(2x2) phases, islands irregularly shaped, tip damage when zoom in
1/21/09	1*	1-38	clean surface, RT				1-149	
		39-63	after Ag deposition: 490 nA, 16 s, RT		19	0.30		
		64-229	after S deposition, RT	0.11				round islands, v. few rotated 45°, some still not rotated
1/26/09	1*	1-37	clean surface, RT				1-152	
		38-61	after Ag deposition: 490 nA, 16 s , RT		20	0.32		slightly larger islands
		62-167	after S deposition, RT	0.083				v. slow, more coalescence events than at higher coverage, islands square, round & hexagonal
1/29/09	1*	1-15	clean surface, RT				1-154	
		16-38	after Ag deposition: 475 nA, 15 s, RT		21	0.32		
		39-152	after S deposition, RT	0.094				Checked coverage 2/3/09 (AES computer crash)
2/5/09	1*	1-16	clean surface, RT				2-1	
		17-42	after Ag deposition: 490 nA, 15 s, RT		20	0.30		
		43-160	after S deposition, RT	0.081				
3/2/09	1*	1-17	clean surface, RT				2-13	
		18-37	after Ag deposition: 470 nA, 16 s, RT		20	0.32		
		38-117	after S deposition, RT	0.15				islands rotate, square

Table VII. Ag(110) experiments with submonolayer coverage of Ag conducted at Iowa State.

Date	Sample	Image #	Condition	T sample (K)	Ag deposition		Nb-Pg	Notes
					Flux (mML/s)	Coverage (ML)		
4/30/10	1	1-19	clean surface	300			2-151	after 15 cycles: 200nm+ terraces, able to image over 1um (new tip)
		20-33	after Ag deposition	300		--		no islands, diffuse to step edges?
		34-44	after Ag deposition	300		--		rough, bumpy step edges
		45-55	after cooling	250				
		56-81	after Ag deposition	250	13	0.40		large long islands, OR; need larger terraces, use lower flux & time
5/9/10	1	1-19	clean surface	300			2-155	larger terraces
		20-44	clean surface	120				noisy
		45-56	after Ag deposition	120		--		no islands?
		57-	after Ag deposition	120				v. v. noisy, must use high bias
5/13/10	1	1-18	clean surface	300			2-156	clean, tip better
		19-35	clean surface	175				
		36-54	after Ag deposition	175	16	0.28	3-1	tiny elongated islands, jagged step edges, depletion zone along descending [001] steps
		55-83	after heating	196				SR? coarsening during warm up, smoother step edges, larger depletion zone
		84-97	after heating	215				OR, dramatic coarsening during warm up, v. smooth step edges
2/7/12	2	1-11	clean surface	300			4-88	
		12-36	clean surface	248				
		37-41	after Ag deposition	246	27	0.82		long, wide step flow. High coverage
		42-45	after heating	300				fingers remain, but terraces smoother
		46-61	after cooling	235				
		62-	after Ag deposition	234	23	0.34		Islands! Wide and long.

This table continues on the following page.

Table VII. Ag/Ag(110) experiments continued.

Date	Sample	Image #	Condition	T sample (K)	Ag deposition		Nb-Pg	Notes
					Flux (mML/s)	Coverage (ML)		
2/12/12	2	1-3	clean surface	300			4-91	difficult to image. Still dirty
		4-26	clean surface	245				Much cleaner right of scratch.
		27-	after Ag deposition	244	49	0.74		Step flow. Fat finger islands
2/13/12	2	57-71	clean surface	300			4-91	200-300 nm wide terraces. Tip dirty.
		72-94	clean surface	244				
		95-	after Ag deposition	244	85	0.17		Islands! Tip horrible. Low coverage, but ok density. Repeat.
2/29/12	2	83-102	clean surface	300			4-96	Cut PtIr tip.
		103-127	after Ag deposition	243	0.078	39		thermally unstable. Slope compensation issues
3/7/12	2	1-13	clean surface	300			4-96	Cut PtIr tip.
		14-50	clean surface	242				thermally unstable
		51-86	after Ag deposition	241	0.071	36		islands. Thermally unstable.
4/5/12	2	1-3	clean surface	300			4-98	Cut PtIr tip.
		4-9	clean surface	244				
		10-	after Ag deposition	244	0.067	33		V. few islands in tip shadow, move to the left. Tip drift into surf., difficult to find isl., no O exposure.
4/9/12	2	1-4	clean surface	300			4-100	Cut PtIr tip. Very noisy.
		5	clean surface	243				extremely noisy, cannot image step-edges.
		6-12	clean surface	300				Previous cut PtIr tip. Less noise. Tip easily cleaned.
		13-28	clean surface	243				
		29-	after Ag deposition	243	0.10	50		Islands elongate and OR with time. Difficult to find islands (low density b/c smaller terraces?)

Table VIII. Ag(110) experiments with submonolayer coverage of Ag and O_2 exposures up to 20 L conducted at Iowa State.

Date	Sample	Image #	Condition	T sample (K)	O_2 exposure (L)	Ag deposition		Nb-Pg	Notes
						Flux (mML/s)	Flux (mML/s)		
5/20/10	1	1-13	clean surface	300				3-3	
		14-50	clean surface	173					
		51-99	after Ag deposition	173		16	0.25		
		100-	after O exposure	173	0.52				
5/24/10	1	1-34	clean surface	300				3-4	
		35-58	clean surface	175					
		59-122	after Ag deposition	175		21	0.31		
		123	after O exposure	174	1.1				
5/26/10	1	1-16	clean surface	300				3-5	
		17-31	clean surface	196					
		32-64	after Ag deposition	195		18	0.27		Depletion zone near step edges. Small islands OR, large islands also SR
		65-	after O exposure	194	1.0				Island shapes change with each image.
7/7/10	1	69-81	clean surface	300				3-22	
		82-113	clean surface	197					
		114-181	after Ag deposition	193		6.6	0.099		Initially difficult to image.
		182-	after O exposure	193	13				Isl. density decrease. Aspect ratio change: wider

This table continues on the following page.

Table VIII. O/Ag/Ag(110) experiments continued.

Date	Sample	Image #	Condition	T sample (K)	O_2 exposure (L)	Ag deposition		Nb-Pg	Notes
						Flux (mML/s)	Flux (mML/s)		
2/16/12	2	1-12	clean surface	300				4-93	Approach difficult. Tunnel 305 pA, -2.60 V
		13-43	clean surface	244					Noisy. **Lower time constant** (2.60 --> 0.615 at image 20)
		44-45	after Ag deposition	243			--		No islands or obvious step flow.
		46-74	after Ag deposition	242		70	0.070		Num of islands increases as coarse move right. Watch an area with 5 islands for a bit. OR
		75-77	during O exposure	242	14				
		78-81	after O exposure	242					No drastic change. Lots of material on surface. Ok island resolution for a few images, then tip drift.
2/25/12	2	1-9	clean surface	300				4-95	
		10-47	clean surface	246					thermally unstable
		49-73	after Ag deposition	245		57	0.11		big islands
		74-82	after O exposure	236	20				thermally unstable. Islands stable

Table IX. Ag(110) experiments with submonolayer coverage of Ag and S coverages up to 0.88 ML conducted at Iowa State.

Date	Sample	Image #	Description, T cooling block (K)	S coverage (ML)	Nb-Pg	Notes
7/12/10	1	1-30	clean surface, RT		3-25	
		31-	after S deposition, RT	0		evaporator working?
7/14/10	1	1-16	clean surface, RT		3-26	
		17-37	clean surface, 192 K			
		38-	after S deposition, 191 K	0		evaporator working?
7/16/10	1	1-19	clean surface, RT		3-28	
		20-31	clean surface, 189 K			
		32-	after S deposition, 189 K	0		evaporator working?
1/27/11	1	1-8	clean surface, RT		3-88	dirty! Pressure increased during experiment to 7.3x10^-10 Torr
		9-23	clean surface, 103 K			
		24	after S deposition 102 K	0.88		can't see anything, spiky
		25-38	after heating, 153 K			rough surface; 218 pA and -340 mV
		39-55	after heating, 194 K			some smooth terraces, but "chewed" #48
		56-66	after heating, 231 K			vertical stripes, blurry
		67-83	after heating, 298 K			rectangular islands and pits, highly faceted edges; stripes/chains! *81 bottom
2/4/11	1	1-19	clean surface, RT		3-91	difficult to find lg terraces; tip was dirty, surf looks ok
		20-27	clean surface, 103 K			dirty cannot find terraces
		28-35	after S deposition, 103 K	trace?		maybe sulfur? Electrochemical cell potential too low?
		36-43	after heating, 172 K			step edge faceting?
2/17/11	1	1-5	clean surface, RT		3-95	marginally better than yesterday after 2 cycles
		6-12	clean surface, 117 K			can only find terraces on RHS, visually next to screw
		13-29	clean surface, 105 K			Stacks / columns like Ag(100) sample
		30-38	after S deposition, 104 K	0.42		
		39-55	after heating, 143 K			step and pit edges rough in all directions, rounded
		56-59	after heating, 174 K			
		60-79	after heating, 196 K			Pattern! Edges faceted
		80-83	after heating, 225 K			blurry, noisy
		84-	after heating, 297 K			

This table continues on the following page.

Table IX. S/Ag(110) experiments continued.

Date	Sample	Image #	Description, T cooling block (K)	S coverage (ML)	Nb-Pg	Notes
2/24/11	1	1-9	clean surface, RT		3-98	~80 nm wide terraces near each other! Clean, except highly stepped areas. Turbo on.
		10-37	clean surface, 121 K			eventually found terraces
		38-	after S deposition, 121 K	0.16		cannot find anything!
3/12/11	1	1-3	clean surface, RT		3-104	terraces
		4-19	clean surface, 105 K			
		20-27	after S deposition, 103 K	0.15		faint blobs
		28-43	after heating, 151 K			something on surface, no order, maybe faceting
		44-50	after heating, 188 K			
		51-	after heating, 233 K			
9/7/11	2	1-12	clean surface, RT		4-16	200 nm wide terraces
		13-35	clean surface, 99 K			ghost features
		36-39	after S deposition, 99 K	0		noisy
		40-43	after heating, 131 K			noisy
		44-51	after heating, 220 K			poor resolution. Small terraces and large vacancy islands.
		--	after heating, RT			Tip crashed into surface upon manual approach and cannot retract. Move a little in +-y to free.
9/11/11	2	1-4	clean surface, RT		4-19	large terraces, clean.
		5-35	clean surface, 103 K			Poor resolution due to tip interaction with surface
		36-40	after S deposition, 102 K	trace?		Poor resolution due to tip interaction with surface
		41-58	after heating, 123 K			Black spots and faint blobs. Must use very weak tunneling conditions.
		59-69	after heating, 152 K			Edges more stable. Tiny linear features on a few terraces.
		70-71	after heating, 177 K			
		72-77	after heating, 220 K			black dots.
		78-83	after heating, 260 K			easier to image at low I.
		84-	after heating, RT			No pattern, domains, etc.

This table continues on the following page.

Table IX. S/Ag(110) experiments continued.

Date	Sample	Image#	Description, T cooling block (K)	S coverage (ML)	Nb-Pg	Notes
9/19/11	2	1-11	clean surface, RT		4-23	good terraces. Noisy, must use very low current
		12-38	clean surface, 101 K			Noisy. Blobs appear on surf while evap. warming up (shutter closed)
		39-47	after S deposition, 101 K	0.73		Light and dark blobs. Noisy
		48-61	after heating, 126 K			Surface bumpy / rough. Step edges poorly defined.
		62-68	after heating, 149 K			Rough.
		69-73	after heating, 176 K			Looks the same.
		74-84	after heating, 194 K			rough, edges unaffected.
		85-90	after heating, 228 K			elongated blobs. Rough. Poor resolution.
		91-110	after heating, 256 K			Smoother, islands of blobs. Edges more angular. Small Pits. Rectangular features. Poor resolution.
		111-132	after heating, RT			Rectangular features. Edges faceted and brighter often. Rectangular islands. Poor resolution.
9/29/11	2	1-11	clean surface, RT		4-29	Use low current.
		12-35	clean surface, 100 K			Ghost features. Tip noisy
		36-39	after S deposition, 100 K	0.008		difficult to image, maybe S.
		40-66	after heating, 146 K			Blobs. Edges maybe faceted.
		67-86	after heating, 173 K			Ghost features. Blobs and faceted edges.
		87-105	after heating, 195 K			Rectangular and shapeless pits, cannot resolve in pits. Bright blobs. Facetted edges.
		106-119	after heating, 228 K			Poor resolution
		120-125	after heating, 255 K			No blobs. Edges fringe with tip.
		126-140	after heating, RT			Edges fringe. #103 and 135 very clear in part.
		141-144	after cooling, 257 K			Edges fringe. Very smooth surface.
		145-149	after cooling, 226 K			Edges fringe a little. Nothing observable on terraces.
		150-	after cooling, 193 K			Edges faceted. No blobs or pits.

This table continues on the following page.

Table IX. S/Ag(110) experiments continued.

Date	Sample	Image#	Description, T cooling block (K)	S coverage (ML)	Nb-Pg	Notes
10/3/11	2	1-10	clean surface, RT		4-31	
		11-26	clean surface, 104 K			Ghost features. Clean but lobs appear on surf while evap. warming up (shutter closed)
		27-36	after S deposition, 102 K	0		Ghost features. Blobs on terraces & step edges. Compare #33-36.
		37-45	after heating, 150 K			Ghost features. Dark blobs with bright ring, or all bright (bias independent). Some edges facetted.
		46-61	after heating, 173 K			Black spots and faint blobs. S or evap./tip junk?
		62-69	after heating, 195 K			Dark features, most small, some very large. Edges faceted, don't fringe.
		70-85	after heating, 227 K			Dark pits, ~rectangular (#80)
		86-97	after heating, 256 K			No details. Bowties.
		98-	after heating, RT			Edges fringe. Bowties, defects.
10/10/11	2	1-10	clean surface, RT		4-35	Turbos on. Dirty?
		11-23	clean surface, 100 K			Dirty. Stuff on surf while S evap. warm up.
		24-26	after S deposition, 100 K	0		Blobs.
		27-33	after heating, 171 K			Turbos off. S or tip debris on surface.
		34-38	after heating, 192 K			Black spots, mostly small, a few large. Double tip.
		39-	after heating, RT			Nothing.
10/15/11	2	1-5	clean surface, RT		4-37	Turbo on. Large terraces, mostly clean.
		6-26	clean surface, 100 K			Nothing new on surf during S evap. warm up.
		27-34	after S deposition, 100 K	0		Amorphous blobs, everywhere, but concentrated at upper edges. Bias independent
		35-47	after heating, 193 K			Turbos off. Dark pit like features & bright blobs. Terrace edge faceting.
		48-61	after heating, 228 K			Pits / blobs, bias independent. Some edges fringe, others don't.
		62-82	after heating, 252 K			Dark depressions/pits, not bowtie shaped. ~0.2 nm deep. Pits shapes become more angular as scan.
		83-93	after heating, RT			

This table continues on the following page.

Table IX. S/Ag(110) experiments continued.

Date	Sample	Image#	Description, T cooling block (K)	S coverage (ML)	Nb-Pg	Notes
11/14/11	2	1-3	clean surface, RT		4-49	
		4-13	clean surface, 120 K			
		14-16	after S deposition, 120 K	0.0090		
		17-	after heating, RT			
12/3/11	2	27-33	clean surface, RT		4-57	
		34-39	clean surface, 105K			
		40-41	after S deposition, 100 K			*could not record AES, S coverage unknown
		42-53	after heating, 194 K			
		54-	after heating, 295 K			
12/20/11	2	1-5	clean surface, RT		4-66	
		6-24	clean surface, 104 K			
		25	after S deposition, 103 K	0.046		Poor resolution. Blobs before open shutter.
		26-33	after heating, 195 K			
		34-	after heating, 295 K			
12/30/11	2	1-2	clean surface, RT		4-68	
		3-19	clean surface, 108 K			
		20-22	after S deposition, 105 K	0.0030		pre-deposition material on surface.
		23-28	after heating, 197 k			#27 step facet?
		29-	after heating, RT			#35 not all edges fringy
1/16/12	2	1-48	clean surface, RT		4-78	turbo on. New tip not performing well.
		49-70	clean surface, 103 K			pre dep. stuff
		71-78	after S deposition, 102 K	0		irregular blobs
		79-92	after heating, 193 K			edges faceted
		93-	after heating, RT			

This table continues on the following page.

Table IX. **S**/Ag(110) experiments continued.

Date	Sample	Image#	Description, T cooling block (K)	S coverage (ML)	Nb-Pg	Notes
1/23/12	2	1-12	clean surface, RT		4-82	
		13-29	clean surface, 103 K			
		30-34	after S deposition, 108 K	0		
		35-56	after heating, 199 K			
		57-	after heating, RT			
1/27/12	2	1-10	clean surface, RT		4-84	
		11-31	clean surface, 104 K			pre-deposition junk
		32-37	after S deposition, 102 K	0		
		38-65	after heating, 195 K			
		66-	after heating, RT			
2/1/12	2	1-2	clean surface, RT		4-86	
		2-24	clean surface, 105 K			
		25-26	after S deposition, 104 K	0.0079		
		27-34	after heating, 195 K			maybe edge faceting
		35-	after heating, RT			nothing

APPENDIX V.

Instrument and Apparatus Maintenance

Table I. Vacuum break and chamber bake list.

Date	Notebook: page
05/21/2008	1: 28
06/9/2008	1: 42
10/9/2009	1: 98
10/9/2009	1: 108
03/11/2009	2: 20
03/17/2009	2: 26
03/26/2009	2: 32
07/22/2009	2: 87
07/31/2009	2: 93
08/5/2009	2: 98
09/25/2009	2: 107-111
12/11/2009	2: 130-132
02/25/2010	2: 133-136
04/23/2010	2: 147
05/27/2010	3: 7-9
06/3/2010	3: 11
06/21/2010	3: 16
07/23/2010	3: 32
08/4/2010	3: 36-39
08/17/2010	3: 44-48

Date	Notebook: page
11/15/2010	3: 65
11/23/2010	3: 69
12/4/2010	3: 73
12/7/2010	3: 75
12/15/2010	3: 79
03/30/2011	3: 107
06/13/2011	3: 128-131
06/23/2011	3: 135-141
07/4/2011	3: 143
07/11/2011	3: 146-151
08/10/2011	4: 3
08/23/2011	4: 8-10
10/18/2011	4: 40
10/26/2011	4: 45-46
11/18/2011	4: 51-54
12/5/2011	4: 57-62
01/2/2012	4: 69
04/23/2012	4: 105-120
06/5/2012	4: 126
06/14/2012	4: 132-136

Table II. Repair list for the 331 VT-STM chamber at ISU.

Equipment	Comments	Date	Notebook: page
Ionization gauges	Replaced fuses 2 and 3. Changed connection from filament 2 to filament 1.	June 2011	3: 133
	Replaced filament with tungsten twin filament with ceramic food. Connect filament 1. Degased. Calibrated. Checked emission current.	June 2011	3: 138, 142
Ion pump	Apply Torr Seal around leaky flange (heater side, closest to window)	Nov. 2010	3: 69, 73, 75
	Green crud on HV connector & feedthrough causing popping noise. Replace resistor in controller and HV connector. Clean feedthrough.	May 2011	3: 120
	Inside: fine, granular Ti dust everywhere, tried to remove some. Replaced HV feedthrough.	June 2011	3: 135
	Remove Ti dust with electronics vacuum. Dust in all areas of the chamber.	June 2011	3: 137
	HV connector & feedthrough: Clean/remove crud, coat ceramic and pin in grease, and cover backing spring in refrasil.	Sept. 2011	4: 15
	REMOVE Varian pump, replace with NEW Agilent pump	Apr. 2012	4 :105
Titanium sublimation pump	Replaced filaments A and B	Mar. 2009	2: 20
	Replaced all filaments	June 2011	3: 136
	Filament A deformed with black coating. Filaments A and C loose at bottom. Ti build up on ceramics. Replace all filaments, though A will not fully fit in to mount.	Dec. 2011	4:57
Turbo-molecular pumps	Replaced power supply in large turbo pump controller.	Oct. 2008	1: 109
Ion sputter gun	Cleaned original ceramics and put back into gun.	July 2009	2: 87
	Replaced with gun from SPA-LEED chamber. *Performed by Thomas D.*	Jan. 2010	
Manipulator	Fixed rotation. Rotating arm too close to holder mount causing grinding; cannot remove screw.	July 2009	2: 88-89
	Sample holder: Remove thermocouple coated in Teflon. Replaced Mo spring. Cleaned ceramics.	July 2009	2: 88-89
	Installed K type thermocouple leads insulated with fiberglass, no Teflon. Chromel in double fiberglass. Allen bolt holding head on the stripped.	June 2011	3: 135
	Insulation on AL lead shifted, short to ground. Install additional insulation.	June 2011	3: 146
	Direct heating (Ta plate 2,3) wire broke at sample head. Replaced.	June 2011	3: 146
	Cleared out old lubricant from screw track. Added Fromblin.	Sept. 2011	

Table III. Repair list continued.

Equipment	Comments	Date	Notebook: page
Omicron metal evaporator	Cap fell off (perhaps heated too quickly). Fixed	Oct. 2008	1: 98
	Mount home built Cu evaporator on STM flange 6 (back). Later removed due to leaks.	Dec. 2009	2: 130
	Change metal, Ag to Cu. Move in 7.5 mm. *Performed by Thomas D.*	Dec. 2009	2: 132
	Change metal, Cu to Ag. Move out 20 mm. *Performed by Thomas D.*	Apr. 2010	2: 147
Mantis metal evaporator	NEW! Check all connections before mounting (empty).	Apr. 2012	4 :107
	Test / outgas in vacuum. Power very unstable	Apr. 2012	4: 110
	Add metals to pockets 1-4 (Ni, Al, Au, Cu)	Apr. 2012	4: 111
	Test / outgas in vacuum.	Apr. 2012	4: 112
	Checked source condition: 1-Ni) extensive melting, 2-Al) coating everything in its path, 3-Au) filled 2/3, 4-Cu) not melted	June 2012	4: 126
	3-Au) Flux monitor shorted to ground. Au film on all areas surrounding pocket and STM stage. Ag sample does not appear gold. Cleaned flux monitor.	June 2012	4: 132
Sulfur evaporator	Replace chemicals and broken thermocouple wire.	Oct. 2008	1: 108
	Replace chemicals. Polish Ag plate. Check flag arm tightness.	Mar. 2009	2: 20
	Replace insulation with ceramic.	Mar. 2009	2: 26
	Replace chemicals, only use hand press to form pellets!	Mar. 2009	2: 32
	Replace chemicals, W filament, and Ta flag.	June 2010	3: 10
	Replace chemicals. Load in correct order. *Performed by Chad Y.*	July 2010	3: 32
	Re-assemble with all new materials, including refrasil and chemicals, to repair electronic issues.	Aug. 2010	3: 36
	Replace AgI	Aug. 2011	4: 2
	E. chem. cell disconnected from feedthrough (cap popped off). Put cap back on and gently bent Pt wire to push down and to keep clear of filament. NEXT TIME: file a groove in feedthrough and use Ta wire to secure cap.	Oct. 2011	4: 40
	Short in cell due to a Ag dendrite between Ag plate and Ag_2S, across AgI pellet; replace compounds with commercial reagents and buff Ag plate	Dec. 2011	4: 57
	Very high resistance across cell (16 MΩ), pyrex tube not held tightly, can move up, weakening connection. Tighten. Increased flag size. Add "maria" to tube, see pg 80.	Jan. 2012	4: 70
	Replace filament, glass tube (now with maria), Pt cap, W springs, and refrasil. Modified s.s. clamp to accommodate new tube design. Reattached TCs to feedthrough. MOVE to STM flange 6, back (new Manits evaporator will be mounted where S evap. had been).	Apr. 2012	4 :106-107
	Gas line: Replace leaky Nupro valve between line and load-lock, with new Nupro valve.	June 2012	4: 134

Table IV. Repair list continued.

Equipment	Comments	Date	Notebook: page
LEED / AES	Recoat LEED screen, by Alex B.	July 2009	2: 91
	Clean LaB6 ceramic mount. Search for root of electronic problem.	Aug. 2009	2: 94-105
	Replaced LaB_6 filament with W filament and Wehnelt cap	Sept. 2009	2: 106
	Short between W filament and Wehnelt. Shipped back to OCI. *Performed by Mingmin S.*	Sept. 2009	2: 106
	Remount e-gun with W filament. No electron beam. Cable problem.	Sept. 2009	2: 107
	Send optics, electronics, LaB6 and W filaments to OCI for cleaning, recoating, and repair.	Feb. 2010	2: 133
	Reinstalled after OCI recoated screen; gassy and factor setting too weak.	May 2010	3: 7
	Linear motion gears loose; tighten set screws.	Dec. 2011	4: 57
	Tighten motion set screw.	Jan. 2012	4: 70
	Recoat LEED screen, by Mark W. and David A.	Apr. 2012	4 :108
	Screen will not light in LEED mode.	Apr. 2012	4 :117 - 120
	Rebuilt gun.	June 2012	4: 126
	Still not working, so checked all connection in optics. Found nothing, but rebuilt gun and optics.	June 2012	4: 132
	Tested in vacuum: not working. Found infinite resistance across screen, ITO absent. Send screen to OCI for recoating.	June 2012	4: 133-134
	Mounted recoated screen (photos in notebook) and all connections good.	July 2012	4: 134-136
STM	NEW controller from RHK	Aug. 2008	1: 82
	PIC feedthrough: Grounding short caused image distortion. Wire insulation worn. Enlarge surrounding screen opening.	Oct. 2008	1: 95-99
	RHK tip cable: Several pins loose.	May 2009	2: 57
	Push pull drive: Replace block on air-side and adjust screw.	May 2010	3: 7
	Tip motor: Cannot move tip in +y direction. Move motor stage manually to free. Vacuum out and wipe up Ti dust.	Aug. 2011	4: 1

Table V. Repair list continued.

Equipment	Comments	Date	Notebook: page
Other	Wobble stick: Jaws not fully opening. Hold head and tighten outer screw body.	Oct. 2008	1: 99
	Wobble stick: Head popped off. Replaced missing screw and added washers.	May 2010	3: 7
	Table legs: Adjust so evenly float.	May 2010	3: 119
	Main gate valve: replace HVA valve (leak at viton gasket) with MDC valve from SPA-LEED chamber.	June 2011	3: 135
	Approachable TC: Removed from below sputter window. Will ask machine shop to put a W ball at the end to touch to samples.	June 2011	3: 136
	Windows: Clean 3 most used windows with hydrogen peroxide.	June 2011	3: 137
	Pump traps: All 3 roughing pump traps baked	Aug. 2011	3: 156
	Load-lock: Valve leak between chambers. Replace with new VAC valve. (The case of the mysterious He leak.)	Aug. 2011	4: 7
	Load-lock: Transfer arm movement rough (dropped tips) due to Ti dust. Dismanteled and cleaned.	Nov. 2011	4: 51
	Tip flash device: Tip stuck in flasher, Ag on W tip melted	Nov. 2011	4: 51
	Load-lock: Replace valve between chamber (VAT to rebuilt MDC)	Apr. 2012	4 :105
	Load-lock: Major leak at valve between chambers, replace (rebuilt MDC to VAT)	Apr. 2012	4 :113
	Gas line: Replace leaky Nupro valve between line and load-lock, with new Nupro valve.	June 2012	4: 134

ACKNOWLEDGEMENTS

I would like to express my deep gratitude to my advisor Professor Patricia A. Thiel. Working with Prof. Thiel has been a wonderful experience. I have especially enjoyed preparing publications with her, as I have learned so much about thinking about science and how to communicate science. She has provided tremendous research , professional, and learning opportunities. I would like to offer my special thanks to Professor James W. Evans for our illuminating discussions and data analysis guidance. I am grateful to Prof. Evans and Dr. Da-Jiang Liu for their insights into my experimental data and their assistance, with Prof. Thiel, in developing a deeper understanding of this research. I would like to thank Professor Maki Kawai for inviting me to research in her group at The RIKEN Institute and the opportunity to work with Dr. Yousoo Kim. I would like to express my very great appreciation to Prof. Kawai and Dr. Kim for welcoming into their groups. I am grateful to Dr. Kim, who regularly provides professional support and encouragement. I would also like to thank Professors James W. Evans, Gordon Miller, Theresa Windus, Sriram Sundararajan who have served on my Program of Study Committee. I have been lucky enough to take at least one class by each of these professors. I might not have studied at Iowa State if not for the advice and encouragement of Professor John J. Kozak at DePaul University. I would like to express my very great appreciation to all of the Chemistry Professors at DePaul University. You made the switch to Chemistry a very happy choice. I would like to acknowledge my fifth grade teacher, Mrs. Dee LeFevour, who encouraged me to participate in my first science fair.

I would like to thank the Thiel group members, past and present, for their discussions, assistance, and camaraderie. In particular, I thank Mingmin Shen for getting me started in the group and training me. I appreciate the guidance and friendship the Kawai and Kim groups bestowed on me during my three visits to The RIKEN Institute.

I would like to express my appreciation for my family and friends who encouraged me to follow this path and their support in achieving my goal. I am particularly grateful for my parents' belief in me and their unconditional love. Many friends at home, in Ames, and in Japan have helped me through my graduate studies. I would like to especially thank Steven Yeninas and Teresa Rasmussen.